Bundesanstalt für Wasserbau
Federal Waterways Engineering and Research Institute

4th MASHCON

International Conference on Ship Manoeuvring in Shallow and Confined Water with Special Focus on Ship Bottom Interaction

Bundesanstalt für Wasserbau: Klemens Uliczka, Carl-Uwe Böttner, Marko Kastens
Flanders Hydraulics Research: Katrien Eloot, Guillaume Delefortrie
Ghent University: Marc Vantorre, Maxim Candries, Evert Lataire
Editors

Proceedings of the 4th International Conference on Ship Manoeuvring in Shallow and Confined Water with Special Focus on Ship Bottom Interaction
Hamburg, Germany
23 to 25 May 2016

4th MASHCON

Editors

Klemens Uliczka, Carl-Uwe Böttner, Marko Kastens
Bundesanstalt für Wasserbau (BAW)

Katrien Eloot, Guillaume Delefortrie
Flanders Hydraulics Research

Marc Vantorre, Maxim Candries, Evert Lataire
Ghent University

Published by:Bundesanstalt für Wasserbau
Federal Waterways Engineering and Research Institute
e-mail:info@baw.de
www.baw.de

BAWProceedings
ISBN 978-3-939230-38-0 (online)
ISSN 2700-8444 (online)

Table of Contents

Squat

Ship-Bank and Ship-Ship Interaction Effects

Preface

An event being organized for the fourth time at regular intervals evokes a certain level of continuity. After three successful editions, it seemed worth spending some time to choose an acronym, which would make referring to the Fourth *International Conference on Ship **MA**noeuvring in **SH**allow and **CON**fined Water* much easier. This allows us to welcome you at ***MASHCON 2016*** **!**

As for the first three editions, MASHCON 2016 is open for all contributions related to hydrodynamic aspects of ship manoeuvring in navigation areas with restricted dimensions in horizontal and/or vertical direction. For both scientific researchers and nautical experts, ship behaviour in shallow and confined water remains a niche domain. As a matter of fact, seagoing ships are only being confronted with such conditions in harbours and their approach channels, unlike inland vessels, for which shallow and confined waters can be considered as a natural habitat. Nevertheless, each conference so far has put a spotlight on one specific topic within this scope. After ship-bank, ship-ship and ship-lock interaction, this edition will be particularly dedicated to ***ship-bottom interaction***.

While the effects due to the close vicinity of the bottom are the core of shallow water ship hydrodynamics, the selection of this main topic has been inspired by the increasing interest in the phenomena occurring in the gap between the keel of a ship and the bottom of a waterway. Different motivations can be identified for this interest. As a result of increasing accuracy of methods for determining a ship's position, also in vertical sense, bottom surveys, maintenance dredging techniques and water level prediction tools, the margins with respect to the required under keel clearance can possibly be reduced, which of course has a beneficial impact on maintenance dredging cost. On the other hand, smaller margins are only appropriate when the overall risk remains within acceptable limits. It should be borne in mind that a minimum UKC is not only required to avoid bottom contact due to squat, response to waves, passing ships. A minimum UKC is also required to guarantee a minimum level of manoeuvrability and controllability. Another issue arising in many navigation areas concerns the problematic definition of the boundary between bottom and water. On the one hand, ship induced flows may cause erosion and sedimentation of the bottom, but on the other hand, a ship's behaviour may be fundamentally changed due to interaction with fluid mud layers covering the solid bottom. Eventually, a considerable share of the contributions to MASHCON 2016 appear to be related to the main topic, which confirms the interest from different viewpoints.

The main purpose of organising a conference is, of course, to provide a meeting opportunity to discuss progress in scientific research and to stimulate mutual contacts between experts in practical and theoretical aspects. The Knowledge Centre *Manoeuvring in Shallow and Confined Water* intends to offer an added value to participants of the conference by making benchmark model test data available for the validation of mathematical and numerical models and tools. On the occasion of the call for papers for MASHCON 2016, a selection was made among model test data which were obtained at Flanders Hydraulics Research with the DTC container carrier at low under keel clearance in the framework of the European SHOPERA project. The data present time series of sinkage and trim, surge and sway forces, and yaw and roll motions, during captive harmonic sway and yaw tests. It is appreciated that the full benchmark data which were released last year have been requested by eleven researchers. This finally led to the submission of three papers, while the other applicants informed us they have not been able to finalise their research yet due to time constraints and/or limited resources. It is also encouraging to notice that some of the benchmark data distributed on the occasion of the former conferences are being used for validation purposes in the contributions to this Conference. Numerical methods are in full development and are quite promising. They are potentially able to provide more insight into the detailed flow in the limited area between keel and bottom, but validation data are required to assess their reliability and applicability. By publishing open model test data, the Knowledge Centre wishes to make a modest contribution to this evolution.

In order to offer some continuity to the target audience we aim to address, a return period of two to three years seems to be optimal. On the other hand, the full organisation of a conference places an important workload to the research groups within the Knowledge Centre partners. For this reason, we try to alternate conference venues in our home cities with locations abroad, relying on partner institutions with common interest. In 2011, MARINTEK and NTNU relieved us of hosting the second conference, and at present, we highly appreciate the efforts of our local host, the Federal Waterways Engineering and Research Institute or Bundesanstalt für Wasserbau (BAW), who was found willing and enthusiastic to

take the organisation of MASHCON 2016 on their shoulders. As a result, Hamburg is the fourth city to host our Conference, after Antwerp (2009), Trondheim (2011) and Ghent (2013).

Contacts between the Knowledge Centre partners, Flanders Hydraulics Research (FHR) and Ghent University, and the Hamburg office of the Bundesanstalt für Wasserbau already go back many years. This is not surprising: FHR and BAW are both governmental institutions, with a core task to provide consultancy to the administrations with respect to issues relating to waterways engineering. Both institutions have been confronted with the need for broadening their activities from purely hydraulic issues to topics related to the behaviour of a ship in confined waterways. It is not a coincidence that both institutions are interested in common topics such as ship's squat, effect of muddy bottoms on navigation, ship-bank interaction, and often rely on model test techniques for acquiring more insight into the physical background of the governing effects. The problems with which the maritime ports and inland waterways have to cope in both countries, are actually very comparable. Antwerp and Hamburg not only meet each other as competitors for silver and bronze on the European container ports winner's podium, but also experience common opportunities and challenges as ports connected to sea by a long channel dredged in a natural river with an important tidal regime. To mention another example, the problems related to sedimentation and fluid mud in German and Flemish ports can be considered as variations on the same theme, although solutions may in practice be quite different.

One change with respect to the former conferences needs to be mentioned: contrary to the three first editions, MASHCON 2016 is no longer co-organised by the Royal Institution of Naval Architects. Nevertheless, the efforts of the Institution in spreading the call for papers and the announcements for the conference is quite substantial. We are grateful to the R.I.N.A. for their support in the starting up of this Conference series, and look forward to further co-operation in the future.

34 contributions by authors from all over the world, an interesting excursion program, a committed local organising staff, a city full of activity exuding a maritime atmosphere.
Welcome to MASHCON 2016, welcome to Hamburg!

Katrien Eloot

Flanders Hydraulics Research
&
Ghent University

Marc Vantorre

Ghent University

Maxim Candries

Ghent University

On behalf of the Knowledge Centre
Manoeuvring in shallow and confined water

Organisation

Members of the International Scientific Committee

Dr. Tor Einar Berg	Marintek - Sintef, Norway
Dr. Carl-Uwe Böttner	Federal Waterways Engineering and Research Institute (BAW), Germany
Prof. Andrés Cura Hochbaum	ILS, Technical University Berlin, Germany
Dr. Larry Daggett	Waterway Simulation Technology, USA
Dr. Guillaume Delefortrie	Flanders Hydraulics Research, Belgium
Dr. Jonathan Duffy	Australian Maritime College, Australia
Prof. Bettar Ould el Moctar	ISMT, University of Duisburg Essen, Germany
Prof. Katrien Eloot	Flanders Hydraulics Research, Belgium
Prof. Yoshitaka Furukawa	Department of Marine Systems Engineering, Kyushu University, Japan
Dr. Tim Gourlay	Centre for Marine Science and Technology, Curtin University, Australia
Dr. Andreas Gronarz	Development Centre for Ship Technology and Transport Systems, Germany
Prof. André Hage	ANAST, University of Liège, Belgium
Prof. Alexander Härting	Department of Maritime Studies, Jade University Elsfleth, Germany
Prof. Katsuro Kijima	Professor emeritus of Kyushu University, Japan
Prof. Nikolai Kornev	Faculty of Mechanical Engineering and Marine Technology, University of Rostock, Germany
Dr. Evert Lataire	Division of Maritime Technology, Ghent University, Belgium
Prof. Bjørnar Pettersen	Norwegian University of Science and Technology, Norway
Frans Quadvlieg	MARIN, The Netherlands
Marc Steinwand	Schiffbau-Versuchsanstalt Potsdam GmbH, Germany
Prof. Fred Stern	IIHR - Hydroscience & Engineering, The University of Iowa, USA
Dr. Klemens Uliczka	Federal Waterways Engineering and Research Institute (BAW), Germany
Prof. Marc Vantorre	Division of Maritime Technology, Ghent University, Belgium
Dr. Michael Woodward	National Centre for Maritime Engineering and Hydrodynamics, Australian Maritime College, University of Tasmania

Review Co-Ordination

Dr. Maxim Candries	Ghent University, Belgium

Members of the Local Organising Committee

Dr. Carl-Uwe Böttner	Federal Waterways Engineering and Research Institute (BAW), Germany
Susane Holz	Federal Waterways Engineering and Research Institute (BAW), Germany
Sabine Johnson	Federal Waterways Engineering and Research Institute (BAW), Germany
Marko Kastens	Federal Waterways Engineering and Research Institute (BAW), Germany
Simone Knobloch	Federal Waterways Engineering and Research Institute (BAW), Germany
Dr. Klemens Uliczka	Federal Waterways Engineering and Research Institute (BAW), Germany
Ellen Vyncke,	Ghent University, Belgium
Christine Wallisch	Federal Waterways Engineering and Research Institute (BAW), Germany

Supporting Institutions

MASHCON 2016 was supported by the following institutions:

Bundesanstalt für Wasserbau
Federal Waterways Engineering and Research Institute

Federal Waterways Engineering and Research Institute (BAW)

Kussmaulstrasse 17, 76187 Karlsruhe, Germany

Flanders Hydraulics Research

Flanders
State of the Art

The Knowledge Centre Manoeuvring in Shallow and Confined Water

co-operation between

Flanders Hydraulics Research, FHR
Berchemlei 115, 2140 Antwerp, Belgium

and

EA15 - Maritime Technology Division,
Ghent University
Tech Lane Ghent Science Park – Campus A 904,
9052 Gent, Belgium

Federal Ministry
of Transport and
Digital Infrastructure

Federal Ministry of Transport and Digital Infrastructure, Germany

Invalidenstr. 44, 20115 Berlin, Germany

The Royal Institution of Naval Architects

8 - 9 Northumberland Street, London,
WC2N 5DA, UK

Exhibition and Sponsorship

Exhibitors

Federal Waterways Engineering and Research Institute (BAW)

Kussmaulstrasse 17, 76187 Karlsruhe, Germany

Sponsors Category I

Port of Zeebrugge

P. Vandammesluis, Isabellalaan 1, 8380 Zeebrugge, Belgium

Mediterranean Shipping Company

MSC Belgium NV
Noorderlaan 127A, 2030 Antwerpen, Belgium

Esterline - Simulation Visual Systems

Esterline Belgium BVBA
President Kennedypark 35A, 8500 Kortrijk, Belgium

CVBA BRABO

Noorderlaan 21 - Haven 28, 2030 Antwerpen, Belgium

Sponsors Category II

Exmar

Exmar Marine NV
De Gerlachekaai 20, 2000 Antwerpen, Belgium

MDK

Agentschap Maritieme Dienstverlening en Kust
Koning Albert II laan 20 bus 5, 1000 Brussel, Belgium

ArcelorMittal Belgium NV

Keizerinlaan 66, 1000 Brussel, Belgium

HB-plus

Hermeslaan 1A, 1831 Diegem, Belgium

4th MASHCON

International Conference on Ship Manoeuvring in Shallow and Confined Water with Special Focus on Ship Bottom Interaction

23 - 25 May 2016

Elbcampus, Hamburg, Germany

CONFERENCE PROGRAMME

22 MAY 2016 (SUNDAY)

18:00 – 21:00	**Registration + Icebreaker Party**

23 MAY 2016 (MONDAY)

8:00 - 9:00	**Registration**
9:00 - 9:15	**Opening address**
9:15 - 10.00	**Invited Keynote Speech** by Capt. Wolfgang Hintzsche, German Shipowners' Association (VDR)
	SESSION A1 Ship Bottom Interaction / C1: Ship Behaviour in Locks (Chair: Prof. N. Kornev)
10:00 - 10.25	*Ship-induced sediment transport in coastal waterways (SeST)* K. Uliczka and B. Kondziella Federal Waterways Engineering and Research Institute, Germany
10:25 - 10:50	*Calculation of hydrodynamic interaction forces on a ship entering a lock using CFD* S.L. Toxopeus and K. Bhawsinka MARIN, The Netherlands
10:50 - 11:05	**Refreshment break**
	SESSION B1: Squat (Chair: Dr. T. Gourlay)
11:05 - 11:30	*Development of a squat formula based on numerical calculations* A. Gronarz Development Centre for Ship Technology and Transport Systems, Germany
11:30 - 11:55	*Squat in berthed ship - passing ship interaction for restricted water cases* S.P. Denehy, J.T. Duffy, D. Ranmuthugala and M.R. Renilson AMC Search Ltd, Australia ; Australian Maritime College, Australia
11:55 - 12:20	*Impact of banks on ship squat* E. Lataire, M. Vantorre and G. Delefortrie Ghent University, Belgium ; Flanders Hydraulics Research, Belgium

12:20 - 13:30	**Lunch**
	SESSION C2: Ship Bottom Interaction (Chair: Prof. Y. Furukawa)
13:30 - 13:55	*Effect of lateral and depth restriction on ship behavior using computational fluid dynamics* D.B. Poojari and A.R. Kar Indian Register of Shipping, India
13:55 - 14:20	*Interaction between ship-induced stress and associated characteristics of turbidity records* S. Niehueser, M. Ulm, A. Arns, J. Jensen, V. Kelln, K. Uliczka and B. Kondziella Research Institute for Water and Environment, University of Siegen, Germany ; Federal Waterways Engineering and Research Institute, Germany
14:20 - 14:45	*Ship Manoeuvring Behaviour in Muddy Navigation Areas: State of the Art* G. Delefortrie and M. Vantorre Flanders Hydraulics Research, Belgium ; Ghent University, Belgium
14:45 – 15:10	*Numerical analysis of the flow in the gap between the ship hull and the fairway bottom in extremely shallow water* I. Shevchuk, C.-U. Böttner and N. Kornev University of Rostock, Germany ; Federal Waterways Engineering and Research Institute, Germany
15:10 - 15:25	**Refreshment break**
	SESSION C3: Ship Bottom Interaction (Chair: Dr. K. Uliczka)
15:25 - 15:50	*A simplified maneuvering performance of a large container ship passing through the Suez Canal* Y. You and W. Kim Daewoo Shipbuilding & Marine Engineering Co., Ltd., Rep. of Korea
15:50 - 16:15	*A new slender body theory for shallow water and comparison of the results with experimental and two other numerical methods* M. Alidadi, O. Gören, D.B. Danişman and S. Calisal University of British Columbia, Vancouver, Canada ; Istanbul Technical University, Istanbul, Turkey ; Piri Reis University, Istanbul, Turkey
16:15 - 16:40	*The definition of the nautical bottom in muddy navigational areas* M. Druyts and P. Brabers MDCE bvba, Belgium; Demco nv, Belgium

24 MAY 2016 (TUESDAY)

8:00 – 09:15	**Registration**
	SESSION D1: Manoeuvring in Shallow Water (Chair: Dr. C.-U. Böttner)
09:15 – 09:40	*Captive model tests based 6 DOF shallow water manoeuvring model* G. Delefortrie, K. Eloot, E. Lataire, W. Van Hoydonck, M. Vantorre Flanders Hydraulics Research, Belgium ; Ghent University, Belgium
09:40 - 10:05	*Experimental study on the manoeuvrability of KVLCC 2 in shallow water* D.J. Yeo, K. Yun and Y. Kim Korea Research Institute of Ships and Ocean Engineering, Rep. of Korea
10:05 - 10.30	*Shallow water effects on longitudinal components of hydrodynamic derivatives* Y. Furukawa, H. Ibaragi, Y. Nakiri and K. Kijima Kyushu University, Japan
10:30 – 10:45	**Refreshment break**
	SESSION E1: Ship-Bank and Ship-Ship Interaction Effects (Chair: Dr. G. Delefortrie)
10:45 - 11:10	*Progress on real-time prediction of ship-ship-shore interactions based on potential flow* J.A. Pinkster PMH bv, The Netherlands
11:10 - 11:35	*Passing ships interaction in the oil terminal of São Sebastião (Brazil): an applied study to define the operational limits* F. Ruggeri, R.A. Watai and E.A. Tannuri Argonáutica Engineering & Research, Brazil ; Numerical Offshore Tank of the University of São Paulo (TPN-USP), Brazil
11:35 - 12:00	*Parametric study of a modified panel method in application to the ship-to-ship hydrodynamic interaction* S. Sutulo and C. Guedes Soares Centre for Marine Technology and Ocean Engineering, Instituto Superior Técnico, University of Lisbon, Portugal
12:00 – 12:25	*Shallow water and interaction effects in ECDIS real-time motion prediction system* A. Ozersky and E. Rogozhina Transas Technologies, Russia
12:25 - 13:30	**Lunch**
	SESSION F1: Experimental Measurements (Chair: Dr. J. Duffy)
13:30 – 13:55	*The Towing Tank for Manœuvres in Shallow Water* G. Delefortrie, S. Geerts and M. Vantorre Flanders Hydraulics Research, Belgium ; Ghent University, Belgium

13:55 - 14:20	*Measured ship motions in Port of Geraldton approach channel* J.H. Ha, T.P. Gourlay and N. Nadarajah Centre for Marine Science and Technology, Curtin University, Australia ; Global Navigation Satellite Systems Research Centre, Curtin University, Australia
14:20 - 14:45	*Manoeuvring with negative underkeel clearance: 2nd full scale field test in the Port of Delfzijl* R. Barth, C.J.A.W. van der Made, L. Bourgonjen, J. van Dijken, M. Vantorre and J. Verwilligen Wiertsema & Partners, The Netherlands ; Groningen Seaports, The Netherlands; Ghent University, Belgium ; Flanders Hydraulics Research, Belgium
14:45 - 15:10	*Running sinkage and trim of the DTC container carrier in harmonic sway and yaw motion: open model test data for validation purposes* K. Eloot, M. Vantorre, G. Delefortrie and E. Lataire Flanders Hydraulics Research, Belgium ; Ghent University, Belgium
15:10 – 15:25	**Refreshment break**
	SESSION C4: Ship Bottom Interaction (Chair: Prof. O. el Moctar)
15:25 - 15:50	*Numerical simulation of the ship bottom interaction of DTC container carrier for different keel clearance in pure sway motion* R. He, Z.Z. Zhang, X.Z. Wang and D.K. Feng School of Naval Architecture and Ocean Engineering, Huazhong University of Science and Technology, P. R. Of China
15:50 – 16:15	*RANS-based Numerical Simulation of Captive Model Tests in Shallow Water for the DTC Container Carrier* Y. Liu, Z.-J. Zou and L. Zou School of Naval Architecture, Ocean and Civil Engineering, Shanghai Jiao Tong University, China ; State Key Laboratory of Ocean Engineering, Shanghai Jiao Tong University, China ; Collaborative Innovation Center for Advanced Ship and Deep-Sea Exploration, Shanghai, China
16:15 – 16:40	*Investigation of ship-bank, ship-bottom and ship-ship interactions by using potential flow method* Z.-M. Yuan, A. Incecik Department of Naval Architecture, Ocean and Marine Engineering, University of Strathclyde, UK
16:40 – 17:05	*CFD simulation of PMM motion in shallow water for the DTC container ship* G.B. Deng, A. Leroyer, E. Guilmineau, P. Queutey, M. Visonneau and J. Wackers METHRIC, LHEEA/UMR 6598 CNRS, Ecole Centrale de Nantes, France
18:00 – 19:30	***International Maritime Museum***
19:30 – 23:00	**Conference Dinner at the *International Maritime Museum***

25 MAY 2016 (WEDNESDAY)

08:00 - 09:00	**Registration**
	SESSION B2: Squat (Chair: Dr. A. Gronarz)
9:00 – 9:25	*Validation studies on numerical prediction of ship squat and resistance in shallow water* P. Mucha, G. Deng, T. Gourlay and O. el Moctar University of Duisburg-Essen, Germany ; Federal Waterways Engineering and Research Institute (BAW), Germany ; Ecole Centrale de Nantes, France ; Curtin University, Australia
09:25 – 09:50	*Water level forecasts and squat calculation for the Traverse du Nord* S. Mercier, B. Cayer, D. Lefaivre, G. Sauvé and A. D'Astous Corporation des pilotes du Bas Saint-Laurent, Canada; Fisheries and Oceans Canada / Maurice Lamontagne Institute, Canada; Innovation maritime, Canada
09:50 – 10:15	*Applicability of artificial neural networks to squat prediction of Very Large and Ultra Large Container Vessels based on measurements on the Elbe estuary* B. Reiter, T. Albers, F. Treuel and H. Jansch von Lieberman GmbH, Germany ; Hamburg University of Technology, Germany ; Federal Waterways Engineering and Research Institute, Germany
10:15 – 10:40	*Application of potential flow methods to ship squat in different canal widths* T. Gourlay, E. Lataire and G. Delefortrie Curtin University, Australia ; Ghent University, Belgium ; Flanders Hydraulics Research, Belgium
10:40 – 10:55	**Refreshment break**
	SESSION E2: Ship-bank and ship-ship interaction effects (Chair: Prof. A. Härting)
10:55 – 11:20	*Simultaneous ship-to-ship interaction and bank effect on a vessel in restricted water* A.Y. Sian, A. Maimun, Y. Ahmed and Rahimuddin Marine Technology Centre, Universiti Teknologi Malaysia, Malaysia ; Universitas Hasanuddin, Indonesia
11:20 – 11:45	*Numerical modelling of propeller-induced flow velocities on embankments* S. Leschka, B. Xu, L. Yde, O. Stoschek and J. Best DHI Deutschland GmbH, Germany; DHI Water & Environment (S) Pte. Ltd., Singapore and Hamburg Port Authority AöR, Germany
11:45 – 12:10	*Bank effects modelling in Real-Time Manoeuvring Simulations* R. Redondo, R. Atienza, I. Trejo, I. Verdugo and J.R. Iribarren Siport21, Spain
12:10 – 12:30	**Closing Words**
12:30 – 13:30	**Lunch**
14:00 - 17:00	**Technical excursion to the Port of Hamburg**

26 MAY 2016 (THURSDAY)

09:00	**Meet at Elbcampus**
09:15	**Departure/Bustransfer to BAW**
10:00	**Visit at BAW**
12:00	**Small Lunch**
13:00	**Departure to CentralStation / Airport**

Invited Keynote Speech

by **Wolfgang Hintzsche** (Capt., BSc, Marine Director)
German Shipowners' Association (VDR)

The key note is given by Wolfgang Hintzsche, who will provide the ship-owners' perspective on harbour and waterway management and approach channel restrictions.

Capt., Bsc., Wolfgang Hintzsche is Marine Director at VDR, the German Ship-Owners Association, and is the representative of the German Ship-Owners at the IMO.

The German Shipowners' Association (VDR):

The German Shipowners' Association (Verband Deutscher Reeder, VDR) is responsible for representing the common business and social policy interests of German shipping companies at federal and state government level. The VDR was founded in 1907 and merged with the Association of German Coastal Shipowners (Verband der Deutschen Küstenschiffseigner) in 1994. With approximately 220 members, the German Shipowners' Association represents the lion's share of the German merchant navy. Further particulars are available at www.reederverband.de.

Ship Bottom Interaction

4th MASHCON, Hamburg - Uliczka et al. (eds) - © 2016 Bundesanstalt für Wasserbau ISBN 978-3-939230-38-0 (Online)
DOI: 10.18451/978-3-939230-38-0_1

SHIP-INDUCED SEDIMENT TRANSPORT IN COASTAL WATERWAYS (SeST)

K Uliczka and **B Kondziella,** Federal Waterways Engineering and Research Institute, Germany

SUMMARY

The question of the extent to which the residual sediment transport in estuaries is influenced by the passage of ever larger vessels has repeatedly been discussed during the last decade. In the context of the natural (tidal) transport of sediment and suspended matter in coastal waterways and the increased sedimentation in port basins and marinas along the estuaries following a series of extension measures. Measurements carried out in "still" water illustrated not only the available options but also the limitations of the various measurement techniques for recording the increased sediment concentration which is induced in the water column by sailing vessels. The use of redundant measurement techniques permits a scientifically confirmed evaluation and provides initial insights into the magnitude of the increased ship-induced sediment concentration in coastal waterways depending on the passing vessels.

1 INTRODUCTION

In the context of the natural (tidal) transport of sediment and suspended matter in coastal waterways and the increased sedimentation in port basins and marinas along the estuaries following a series of extension measures. The question of the extent to which this residual sediment transport is influenced by the passage of ever larger vessels has repeatedly been discussed during the last decade.
Research in the literature showed that on the one hand, studies of ship-induced sediment transport have been carried out to investigate the resuspension or erosion of shore zones due to ship-induced wave systems in inland waterways and coastal waters (e.g. [12], [5], [11]) and enable the ship-induced increase in suspended matter in the cross section of the water body to be estimated by integration in relation to naturally induced values (e.g. [4]). However, the majority of such works have been concerned with the passage of pusher craft, coasters, smaller ships and recreational craft in inland waterways and rivers (e.g. [10], [1]). Furthermore, simple analytical approaches have been developed, mathematical models used and compared (e.g. [6]) and existing approaches called into question on the basis of new numerical models and field measurements, for example with respect to the impacts of propeller wash (e.g. [15]).
As container ships continue to increase in size and new plans are devised to adapt the fairways of coastal waterways for container shipping, the recognition that ship-induced sediment transport contributes to the sediment regime of tidal estuaries takes on growing importance.
Whether or not this increased vessel size could also have a tangible influence on the sediment transport regime of tidal estuaries is explained and debated in the following with reference to preliminary basic measurements carried out in the KIEL CANAL in the framework of the BAW's R&D project on ship-induced sediment transport (SeST).

The interaction between the sailing ship and the coastal waterway, and in particular with ship-induced suspended sediments, is not considered further in this work because the sediment concentration in the water column is relatively low compared to fluid mud and therefore no significant interactions are anticipated. Additional comprehensive studies of the ship dynamics of ultra large vessels in coastal waterways of limited width and depth are being undertaken by the BAW on behalf of the German Federal Waterways and Shipping Administration (WSV) (currently e.g. [13]).

2 THE SeST RESEARCH PROJECT

The main overarching objectives of the BAW's ongoing research project on coastal waterways, which was launched in 2011, are to record basic information on ship-induced sediment transport (SeST), to differentiate this information spatially and according to processes, to develop empirical-analytical approaches for estimating SeST in coastal waterways in the near field, the far field and the shore zone and to determine SeST as a proportion of the total volume transported in a tidal estuary.

Figure 1 illustrates this spatial and process-oriented differentiation by dividing sediment transport between the near field (approximately two ship widths), the far field (transition from the fairway to shallow water) and the bank zone.

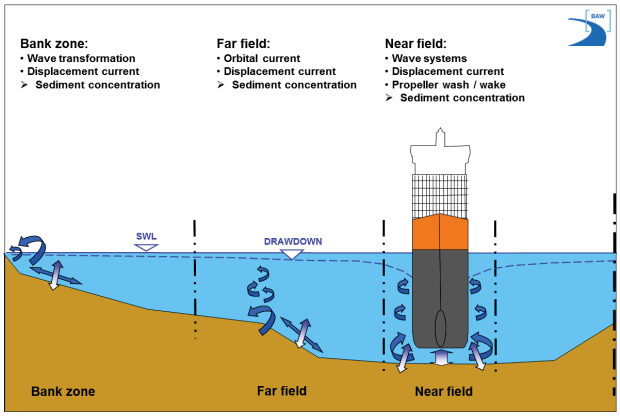

Figure 1. Diagrammatic view of ship-induced sediment loading differentiated spatially and according to processes.

The conceptual model of transient, ship-induced flow and turbulence development, including the influence of the propeller, is presented as a side view in Figure 2.

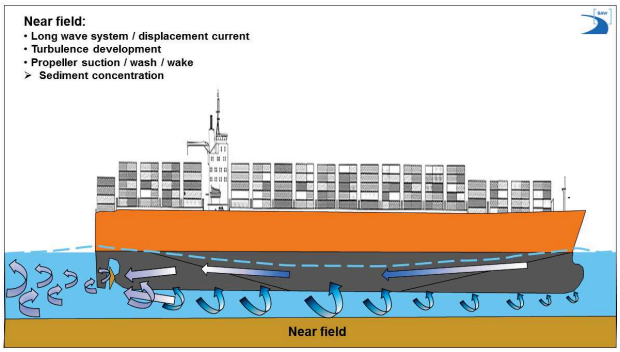

Figure 2. Schematic model showing the development of transient, ship-induced turbulence and flow in a ship's near field (vertical exaggeration)

Owing to the interdependence of the tidal and ship-induced physical processes which influence ship-induced sediment transport (SeST) in a coastal waterway, measurements carried out in the field are essential in order to gain an insight into the relevant interactions. SeST measurements in the near and far fields as well as in the bank zone are required for a holistic view.
The methodological structure of the BAW research project is shown in the diagram below (Figure 3), which groups the various sub-projects on the top level (planning, recording, evaluation and implementation) together with their respective work packages. Some of the work packages under the recording and analysis sub-projects are processed concurrently.

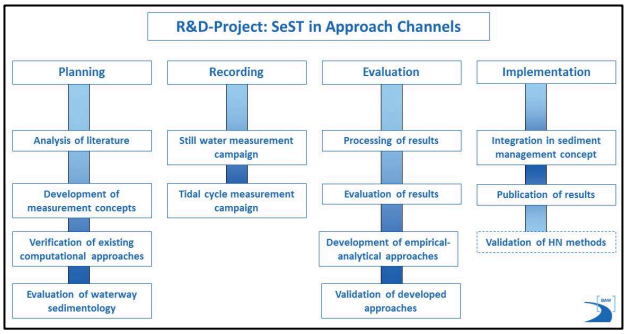

Figure 3. Diagram of the realisation concept for the BAW SeST R&D project

The first measurements were required to be carried out under controlled conditions in "still water", for instance in the KIEL CANAL, with a minimum of "background noise"; after verifying the measurement techniques in this way, the next step was to embark on more measurement campaigns under tidal conditions.
The near-field analyses of passing vessels were intended to provide detailed insights into the physical processes both of the water flowing around these vessels and of ship-induced sediment transport, to enable the influence of the displacement flow, propeller wash and the wake, for example, to be determined. To permit a complete description of ship-induced sediment transport in a cross profile, it was necessary to simultaneously record SeST in the far field as well as in the bank zone.
Various measurement techniques such as ADCP/PDT from Aqua Vision, a cooperation partner in the Netherlands, backed up by sample collection and a few other systems including an Innomar SES2000 supported by the NIAH at HafenCity University Hamburg (HCU), a project partner, as well as single probes (turbidity, flow, water level) needed to be tested and their suitability established for the task at hand.
The results of the hydrodynamics measurements and the measurements of ship-induced sediment transport in each zone then had to be analysed according to processes, formulated as empirical-analytical approaches and assessed with regard to their accuracy and limits of applicability.

3 MEASUREMENTS IN THE KIEL CANAL

The measurements in "still water" without any "background noise" due to flow-related turbidity were carried out in the KIEL CANAL, which links the North Sea to the Baltic, at approximately km 18 not far from the Hochdonn viaduct [7]. The sediment at the bottom of this canal section is comprised of about 75% fine to medium sand ($62 < \mu m < 500$), which could be suspended as a result of passing vessels.
The measurement configuration in cooperation with the Waterways and Shipping Office (WSA) Brunsbüttel and Aqua Vision is summarised in Figure 4 and consists of the following individual components:

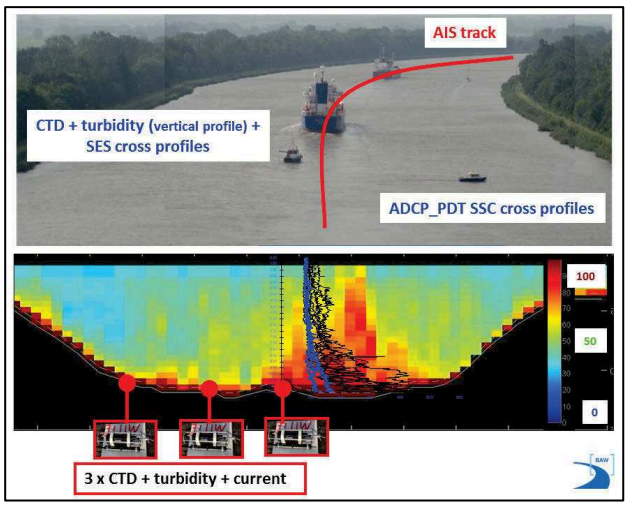

Figure 4. Measurement configuration for recording ship-induced sediment transport in the "still water" of the KIEL CANAL

- Three autonomous CTD, OBS turbidity and VECTOR flow probes installed near the bottom of the cross profile as a stationary, continuous measurement system.
- Ship-based ADCP/PDT cross profile measurements before and after the passage of vessels ([2]).

- Ship-based profiles in the wake with lowered CTD and OBS turbidity probes.
- Ship-based SES cross profiles for analysing the acoustic signal in the wake.
- AIS for detecting passing vessels and determining their ship parameters.

Stationary measurements were performed during the period from 17 to 25 September 2012 at the three points near the bottom for 506 passing vessels (both convoys and single vessels).

In addition, 79 passing vessels were recorded by means of ship-based measurements during the period from 18 to 20 September 2012; 161 profiles with lowered probes (CTD + SSC) and 175 SES cross profiles (acoustic signature) were measured on these three days while measurements for a further 523 ADCP/PDT cross profiles (SSC + v) were conducted and documented.

4 EVALUATION OF THE RESULTS

The various systems used for the measurements are presented in the following for selected events, which are representative of the large number of passing vessels recorded. After discussing the results and analysing their fitness, the suitability of each system for future recordings of ship-induced sediment transport is assessed.

4.1 SHIP-BASED MEASUREMENTS

4.1 (a) Profile measurements in the wake with lowered probes

Profiles were calculated in the wake of passing vessels using a ship-based system of lowered CTD and OBS turbidity probes, in order to measure the vertical distribution of ship-induced turbidity.
Figure 5 shows five time-dependent profile measurements in the wake of a feeder ship. Turbidity concentrations between 150 and 300 g/m^3 were measured at a water depth h of approximately 10 m as a function of time.

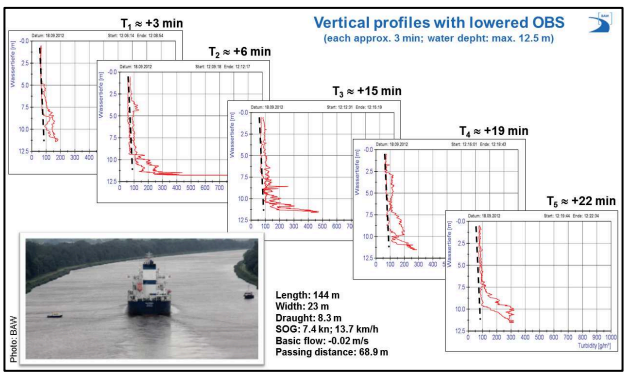

Figure 5. Vertical turbidity profiles in the wake of a passing vessel in the KIEL CANAL as a function of time

However, these values can only be taken as a guide to the time-dependent vertical turbidity distribution because even experienced shipmasters were unable to keep the measurement vessels stationary in a particular position owing to the strong flows and turbulences in the wake. The original idea of an unequivocal spatial assignment of the vertical profile to cross profile and stationary point measurements could therefore no longer be realised, which is why a more detailed evaluation and "blending" with the results of the stationary measurements near the bottom were dispensed with.

This ship-based measurement technique was considered to be unsuitable for scientifically confirmed data analyses – and hence also for further measurement campaigns, especially in the tidal estuary – owing to the insufficient positioning stability in the wake of a ship.

4.1 (b) SES cross profile measurements

As an alternative to profiles with lowered CTD/OBS probes for recording the vertical turbidity distribution, cross profile measurements were carried out using an Innomar SES2000 system (sediment echo sounder or sub-bottom profiler), to enable the ship-induced acoustic signature in the wake to be recorded and subjected to a qualitative analysis. Initial experience with this system was gained on the Lower Elbe as well as in the KIEL CANAL with assistance from the Hydrographic Laboratory and the NIAH at HCU Hamburg [3].

Figure 6 shows the acoustic signature in the wake immediately after the passing of a vessel and at various intervals as an example of SES measurements in the wake. It is interesting to note the "rising" hydroacoustic signals as a function of time, which is an indication of air bubbles and eddies in the wake but says nothing about sinking, ship-induced suspended sediment.

It is presently impossible to separate these acoustic signatures according to individual influences (air ingress, eddies and suspended sediment); complex research projects by specialists in acoustics will consequently be necessary in future.

Selected SES cross profiles were post-processed in order to assess the quality of the ADCP/PDT results.

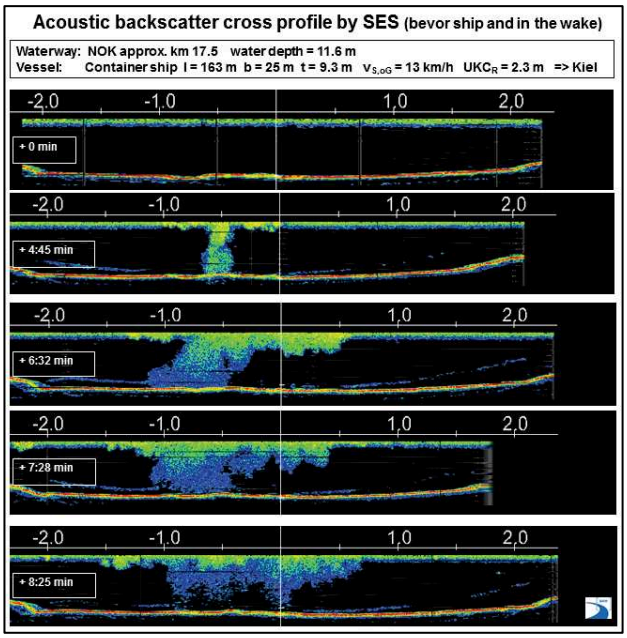

Figure 6. SES cross profile measurements for detecting the acoustic signature in the wake of a feeder ship in the KIEL CANAL as a function of time

4.1 (c) ADCP/PDT cross profile measurements

Wide-area recording of the vertical suspended sediment concentration in the water column using a ship-based Aqua Vision ADCP/PDT (Acoustic Doppler Current Profiler / Plume Detection Tool) is a tried and tested acoustic technique in tidal waters (e.g. [8], [14]). The ship carrying out the measurements crosses the waterway from one bank to the other at a speed as constant as possible. The acoustic backscatter signals recorded by the ADCP/PDT allow conclusions to be drawn regarding the sediment concentration in the individual depth cells. Calibration with the suspended matter samples taken from the water column during the measurement campaign is necessary for this purpose. A second ADCP, inclined 20°, was used to record the sediment concentration close to the bottom. The measurements were conducted with the ADCP/PDT parametrised for depth cells with a vertical extent of 0.5 m. Hence, sediment concentration information was obtained for 22 depth cells in the KIEL CANAL, which has a water depth of about 11 m.

The fact that the waterway was traversed several times shows how the concentration of ship-induced suspended sediment changes over time in the cross section of the water body. The measurements and evaluations for the investigations of the KIEL CANAL described here were undertaken by the Dutch firm Aqua Vision BV on behalf of the BAW in [2].

Cross profile measurements were carried out in the narrowest possible time frame immediately after each vessel had passed, in order to estimate the ship-induced sediment concentration in the water column as a function of time. The graphs in Figure 7 summarise the ship-induced acoustic backscatter signals, converted to give the sediment concentration, obtained with the ADCP/PDT cross profile measurements in the wake of the vessel from the first journey (T_1 = 0 min) up to the time T_5 = +7.0 min.

Based on the experience with SES measurements in connection with the acoustic signature comprised of air bubbles, eddies and sediment concentration in the wake, the cross profile measurements at the times T_1 = 0 min, T_2 = +1.1 min and T_3 = +4.0 min were not evaluated because it is impossible to separate the backscatter owing to sediment concentration. The concentration values can only be estimated as of T_4 = +5.5 min and T_5 = 7.0 min, since a vertical concentration distribution which increases towards the bottom is only clearly discernible when these intervals are reached (Figure 7). It is obvious for this reason that acoustic measurement techniques are not adequate on their own for recording ship-induced sediment transport in the near field of a vessel, because it is not currently possible to record the maximum ship-induced sediment concentration in the cross profile of a waterway after a vessel has passed.

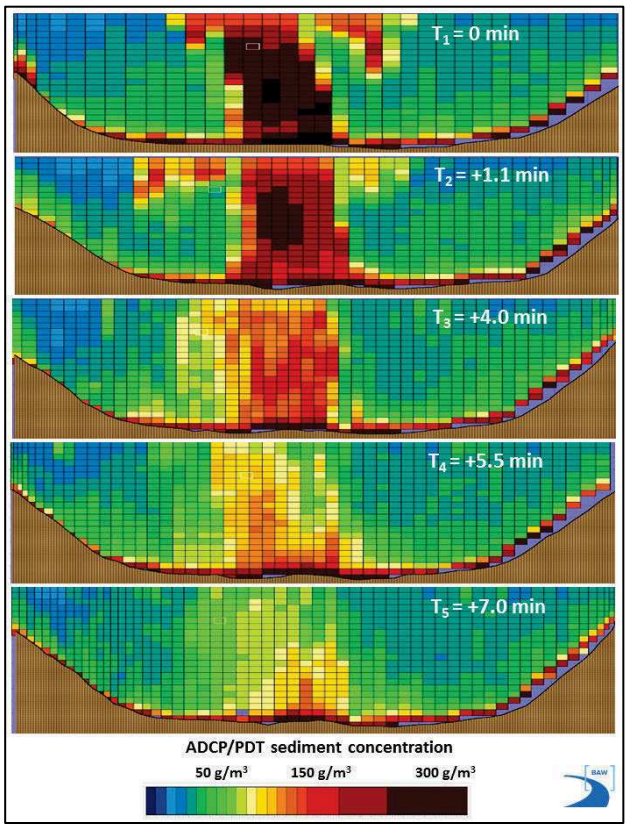

Figure 7. Ship-induced acoustic backscatter signals obtained with the ADCP/PDT cross profile measurements in the wake of a feeder ship as a result of air ingress, eddies and sediment concentration (converted to SSC according [2])

Two individual SES and ADCP/PDT profiles are compared in the following in order to evaluate the results of the acoustic methods; they serve to illustrate why it is problematic to employ these measurement techniques for

investigations in a ship's near field (Figure 8). The information on passing vessels is included as a guide (top part of the diagram with the positions of the stationary measuring instruments; red, green and blue lines).

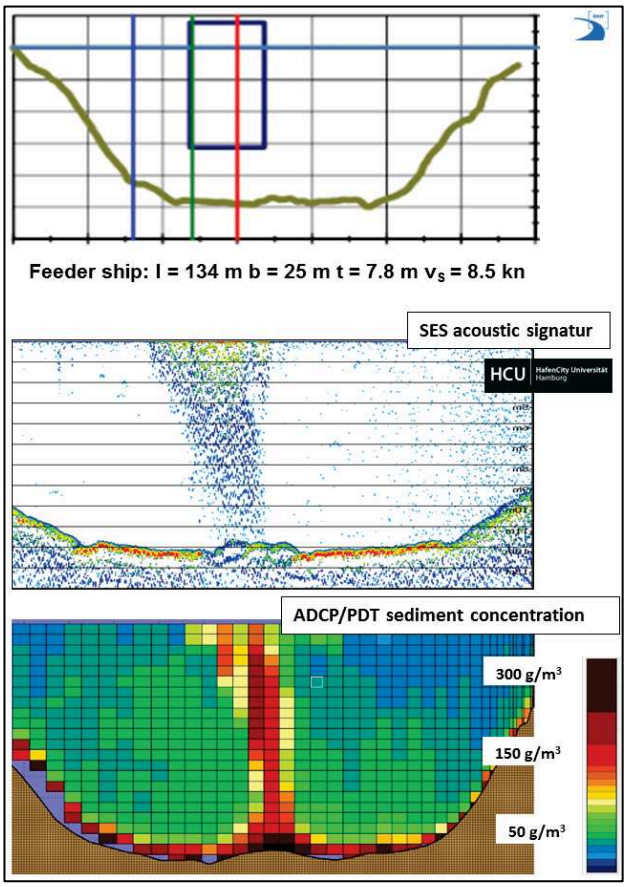

Figure 8. Comparison and evaluation of ship-induced acoustic backscatter signals for a passing feeder ship – interpretation of air ingress, turbulence and sediment concentration (example)

To enable the magnitude of the ship-induced sediment concentration and the corresponding dry matter in the measurement cross section to be estimated in spite of the many scientific reservations, the time intervals T_4 = +5.5 min and T_5 = +7.0 min were evaluated in relation to the "basic turbidity" previously recorded at the time T_0 = -12 min (Figure 9).

Based on the ADCP/PDT measurements at km 18 in the KIEL CANAL (bottom material: fine to medium sand 62 < µm < 500), the total dry matter in the measured cross profile is SeSS = +28 kg/m approximately 5 minutes after the passing of a large feeder ship or SeSS = +20 kg/m after 7 minutes.

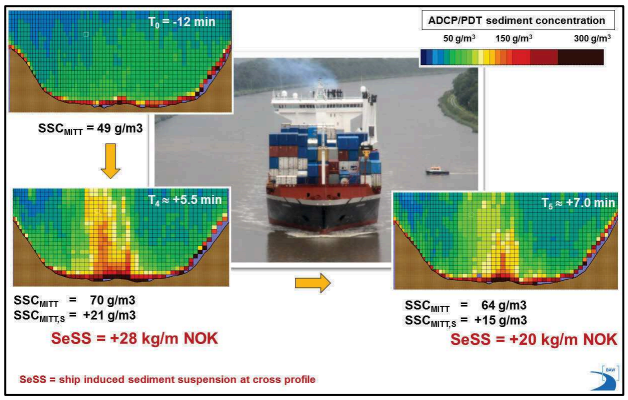

Figure 9. Estimated ship-induced suspended sediment (SeSS) as a function of time in the measurement cross section based on ADCP/PDT measurements of a passing feeder ship in the KIEL CANAL (according [2])

4.2 STATIONARY MEASUREMENTS

The time series for the water level, the standard deviation σ of the individual flow components, the turbulent energy derived from this where TKE = ½ ($\sigma_X^2 + \sigma_Y^2 + \sigma_Z^2$) and the turbidity measured near the bottom are shown below as representative of the stationary measurements conducted at three points in the cross section of the KIEL CANAL (Figure 10). The values were recorded during the passage of a feeder ship with a length l_{oa} = 155 m, a width b = 25 m and a draught t = 7.8 m, which navigated through the water at a speed v_S = 8.5 kn and a passing distance from the bank L = 59 m (ship sailing in the middle, north measuring point = red line).

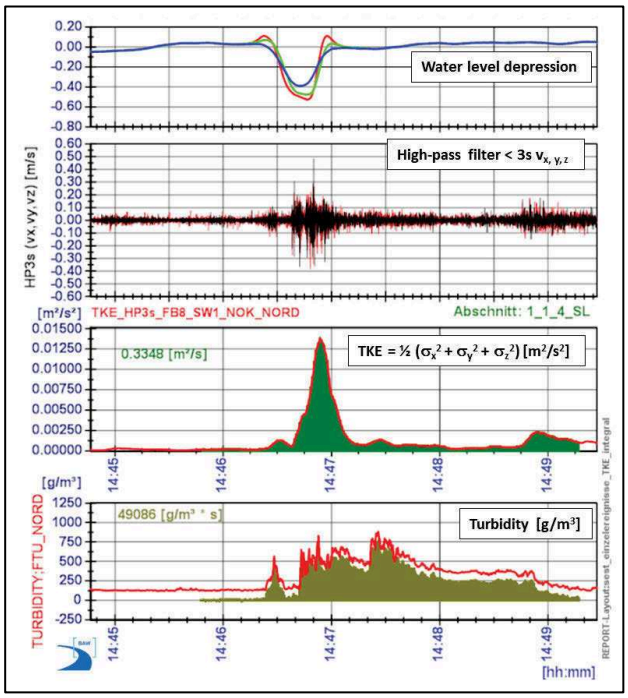

Figure 10. Change in the water level, flow components, derived TKE and turbidity near the bottom for a feeder ship passing approximately in the middle

These time series enable the change in the water level at the three stationary points to be unequivocally assigned along with the ship-induced standard deviation of the flow and hence also the TKE.

It was not possible to assign characteristic turbidity profiles unequivocally either to selected parameters of the passing vessels (length, width, draught, speed, course) or the TKE during the initial evaluations because the influencing parameters – even in a canal – proved to be far more complex than was originally assumed.

The integral of the offset-corrected turbidity time series over a period of about 3.5 minutes yielded approximately 49 kg/m^3·s of suspended dry matter near the bottom (converted from nephelometric turbidity units (NTU) with a factor of 1.6).

A preliminary detailed analysis of the ship-induced turbidity near to the bottom was undertaken in order to determine the dependence on the draught. The time series for the turbidity measurements of 59 passing vessels sailing roughly in the middle were selected for this purpose; the median was subsequently determined, separated according to the draught t < 6.1 m ≤ t and plotted in Figure 11.

The separation of the median into two typical draught classes for the KIEL CANAL (t < 6.1 m ≤ t) clearly illustrates the influence of the draught both on the change in ship-induced turbidity over time and on the maximum turbidity value. It is conceivable that the ship-induced suspended particle diameter of the bottom material also has an effect on this draught-dependent turbidity characteristic, and this will be the object of a further investigation to be carried out with the Research Institute for Water and Environment (fwu), a project partner at the University of Siegen [9].

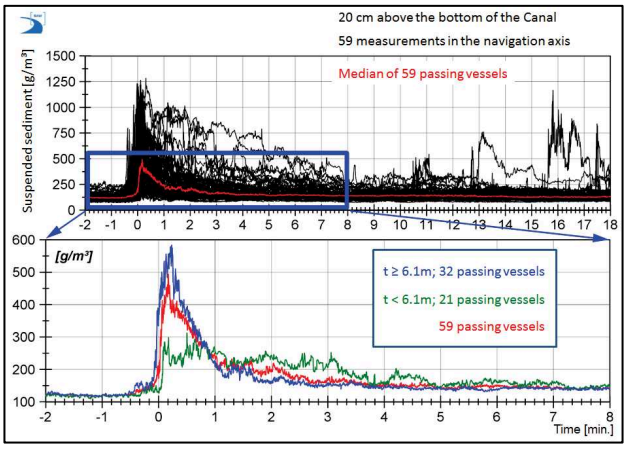

Figure 11. Classification of turbidity measurements near the bottom according to the draught in the KIEL CANAL (59 passing vessels sailing in the middle)

The representative measurements described here and the first evaluations raised a whole series of broader questions concerning the way the processes are understood as well as the interactions between passing ships and ship-induced turbidity characteristics; these issues will be dealt with subsequently in the framework of the SeST research project with fwu, the BAW's university research partner.

5 CONCLUSIONS AND NEXT STEPS

The first measurements carried out in "still" water – in this case in the KIEL CANAL – within the BAW's SeST R&D project illustrated not only the available options but also the limitations of the various measurement techniques for recording the increased sediment concentration which is induced in the water column by sailing vessels. When analysing the acoustic backscatter signals in the wake of these vessels, it is necessary to separate the portions attributable firstly to propeller-induced turbulences and air bubbles, for example, and secondly to the increased sediment concentration and to then consider their possible mutual interactions. The use of redundant measurement techniques permits a scientifically confirmed evaluation and provides initial insights into the magnitude of the increased ship-induced sediment concentration in coastal waterways depending on the passing vessels.

In accordance with the realisation concept for the SeST R&D project, further measurements were conducted in the tidal Elbe estuary in autumn 2015. In addition to the six stationary measuring points near the bottom shown in Figure 12, ADCP/PDT cross profiles were undertaken at the main measurement cross section – in spite of the known scientific drawbacks described above – in order to estimate the magnitude of the ship-induced sediment concentration in relation to natural (tidal) sediment transport.

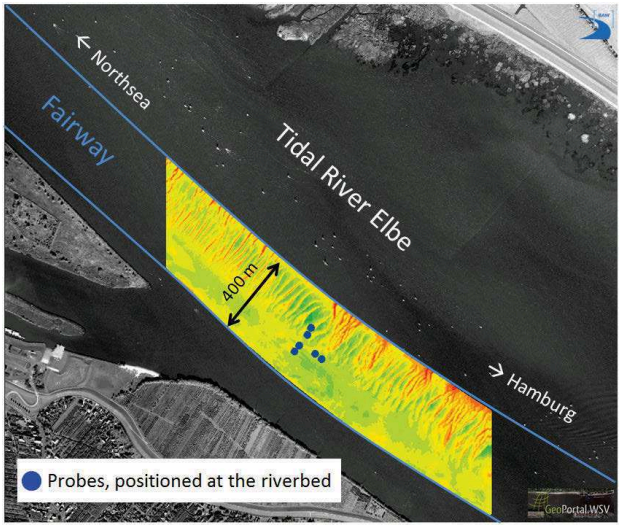

Figure 12. Positions of the stationary measurement probes installed near the bottom of the tidal Elbe at Lühesand (seawards from Hamburg) for recording ship-induced sediment transport and relating it to the natural sediment regime

In accordance with the realisation concept, the various approaches for estimating ship-induced sediment transport developed together with fwu, the BAW's research partner, will be validated based on the results of the stationary measurements conducted in the tidal Elbe as a starting point for further research work on this complex topic.

6 REFERENCES

1. Althage, J. (2010). Ship-Induced Waves and Sediment Transport in Göta River, *Master Thesis, University of Lund, Sweden*

2. Aqua Vision BV (2012). Suspended sediment measurements in the Kiel Canal. *Report AC_DOC_120149 Concept, Utrecht, Netherlands (unpublished)*

3. Böder, V.; Prokoph, A.; Sauer, A. (2012). Erfassung des Gewässerbetts und von Sedimenten im Nordostseekanal (NOK) mit hydroakustischen Methoden. *Northern Institute of Advanced Hydrographics, HafenCity University (HCU) Hamburg, Germany (unpublished)*

4. Davis, S.E.; Allison, J.B.; Driffill, M.J.; Zhang, S. (2009). Influence of vessel passages on tidal creek hydrodynamics at Aransas National Wildlife Refuge (Texas, AUS): Implication on materials exchange. *Journal of Coastal Research, Vol. 25 (2), West Palm Beach, Florida, USA*

5. Erm, A.; Soomere, T. (2006). The impact of fast ferry traffic on underwater optics and sediment resuspension. *Oceanologia, 48 (S), Institute of Oceanology PAS, Sopot, Poland*

6. Hamdi, S. (2007). Mathematical modelling of ship induced sediment resuspension – Derivation of analytical solutions and numerical solutions with practical applications in seabed mechanics. *Seminaires Laboratoire de Mecanique des Solides, University of Toronto, Canada*

7. Kondziella, B.; Böder, V.; Prokoph, A.; Sauer, A. (2012). Forschung und Entwicklung zum schiffserzeugten Sedimenttransport (SeST) im NOK und in der Elbe. *Bundesanstalt für Gewässerkunde, Veranstaltungen Koblenz 5/2013, Germany*

8. Maushake, Ch. (2007). Untersuchungen zur Schwebstoffdynamik im Elbeästuar auf Basis von ADCP-Messungen. *"Die Küste", Issue 72, Germany*

9. Niehüser, S.; Ulm, M.; Arns, A.; Jensen, J.; Kelln, V.; Kondziella, B.; Uliczka, K. (2016). Interaction between ship-induced stress and associated characteristics of turbidity records. *Proceedings of 4th MASHCON, Hamburg, Germany (submitted)*

10. Parchure, T.M.; McAnally Jr., W.H.; Teeter, A.M. (2001). Desktop method for estimating vessel-induced sediment suspension. *Journal of Hydraulic Engineering, Vol. 127, No. 7, ASCE, USA*

11. Rapaglia, J.; Zaggia, L.; Ricklefs, K.; Gelinas, M.; Bokuniewicz, H. (2011). Characteristics of ships' depression waves and associated sediment resuspension in Venice Lagoon, Italy. *Journal of Marine Systems (85)*

12. Ravens, Th. M.; Thomas, R.C. (2008). Ship wave-induced sedimentation of a tidal creek in Galveston Bay. *Journal of Waterway, Port, Coastal and Ocean Engineering Vol. 134, Issue 1.*

13. Reiter, B.; Albers, Th.; Jansch, H. (2016). Applicability of artificial neural net-works to squat prediction of ultra large container vessels based on measurements on the Elbe estuary. *Proceedings of 4th MASHCON, Hamburg, Germany (submitted)*

14. Van Santen, P.; Mol, J.-W. (2011). Sediment and hydrodynamic measurements in the German estuaries 2006-2011. *AquaVision AV_DOC_110023, Utrecht, Netherlands (unpublished)*

15. Williams, R.; Wang, T.; Whelan, M.; Shepsis, V.; Poon, Y. (2006). Methodology for estimating effects from propeller wash: Case Studies. *Poster Session No. 50, 30th ICCE, San Diego, California, USA*

7 AUTHORS' BIOGRAPHIES

Klemens O. K. Uliczka, Dr.-Ing., currently holds the position of Senior Research Engineer at the Federal Waterways Engineering and Research Institute (BAW), Hamburg Office, Germany. He is responsible for the task of ship/waterway interaction in the coastal department. His previous experiences includes coastal engineering, tidal dynamic in estuaries, ship dynamic in fairways and design of river structures at approach channels.

Bernhard Kondziella, Dipl.-Ing. (FH), currently holds the position of Research Engineer at the Federal Waterways Engineering and Research Institute (BAW), Hamburg Office, Germany. He conducts investigations into ship/waterway interaction for the coastal department; he is responsible for field measurements in the SeST research project. His previous experiences includes model and field measurements with respect on estuaries and approach channels.

4th MASHCON, Hamburg - Uliczka et al. (eds) - © 2016 Bundesanstalt für Wasserbau ISBN 978-3-939230-38-0 (Online)
DOI: 10.18451/978-3-939230-38-0_2

EFFECT OF LATERAL AND DEPTH RESTRICTION ON SHIP BEHAVIOR USING COMPUTATIONAL FLUID DYNAMICS

D B Poojari and **A R Kar**, Indian Register of Shipping, India

SUMMARY

Ship to bank interaction is extremely important for navigational purposes. Restriction in waters is basically a solid boundary on the sides of the hull as in canals or at the bottom of the hull or both. This lateral and vertical restriction brings with it complications in the flow around the hull. These flow complications have a direct effect on the hydrodynamic forces and moments acting on the hull form and thus influence the ship motion. Information of the vessel's navigational characteristics under such conditions is essential and will prove useful. The conventional experimental methods (model testing) is time consuming and expensive and also it does not capture the actual picture of the flow around the hull. Computational fluid dynamics (CFD) on the other hand being a visualization tool provides a clear image of the flow in the domain making it more vivid although we still see some limitations and accuracy problems with it. The current work aims at predicting the behavior of a tanker ship when it moves through a location with both lateral and vertical restrictions. Two bank shapes namely rectangular and surface piercing bank with a slope and a fixed under keel clearance of h/T=1.5 were used to predict vessel behavior under such severe conditions. Squat prediction for these types of restrictions are also carried out which is another important aspect under such blockage. The simulations are carried out for two different starboard offset from the bank. RANS based CFD solver is used for force and moment predictions, the modeling and meshing carried out with a combination of ICEM and SHIPFLOW®.

NOMENCLATURE

L_{pp}	Length between perpendicular
Y'	Non-dimensionalised Sway Force
N'	Non-dimensionalised Yaw Moment
K'	Non-dimensionalised Roll Moment
h	depth
T	Draft
U	Forward speed
y_b	Clearance from the bank
R'	Non-dimensional Resistance
C_B	Block coefficient
C_T	Total Resistance coefficient
B	Breadth
$Y+$	Y plus value
w	Wake fraction
v_a	Inflow velocity at the propeller plane

1 INTRODUCTION

The green house gas emission control to mitigate the global warming is on the priority list of IMO. Although shipping contributes to the larger part of transport, the emissions from them are relatively much lower compared to that of other transport system. Most efficient, cost effective and environment friendly mode of transport is the maritime transport system. During the last few decades the shipping community has seen a phenomenal scale enlargement and speed increase but utilization of this shipping for transportation has not witnessed much growth. India is one of the biggest peninsulas in the world with a coastline spanning 7500km but the freight movement by coastal ships is only about 7%. There is an enormous potential to utilize, explore and enhance coastal and inland shipping which eventually will aid reduction in carbon emissions which is higher in other modes of transportation.

Increase in size and speed of ships showcases an impressive progress made in the field. This also imposes severe concerns on various aspects of its behavior, one such concern is when it operates in a restricted environment. The probability of collision, grounding etc increases which raises concerns about oil leakage, traffic curtailment, repair costs, loss due to out of service condition to name a few. Perceiving the ship behavior in confinements can save millions and bring a sense of safety. Transfer of ship into a shallow depth condition switches it to a sluggish or less reactive behavior compared to open sea. This can be credited to the restrictions that modify flow around the hull. In addition to this if a transverse restriction is bought in the complications will exaggerate.

Several RANS based force and moment prediction methods for numerical captive model tests are established. Some of them are [4], [6], [7], [8] and [9]. Investigations/Studies have been carried out in the past for analyzing the ship behavior in confinements. The study carried out by [5] and [10] brings out the effect of shallow waters and the bank effect with variable bank configuration on the ship also the ship to ship interaction is presented here. A numerical method to predict ship squat is presented and detailed in [2]. Simulations and experiments conducted by [3] details about the pressure, velocity and force moment changes observed in restricted conditions for an LNG carrier.
The use of numerical tool to analyze the flow behavior although not wholly reliable is a good source of information on various aspects of flow around a ship. Computational hydrodynamics is an evolving tool and is more or less helping designers resolve various issues in comparatively feasible time. The prime focus of the paper is to bring out the use of CFD in predicting the changes observed when a ship is put in a restricted region. The

changes in forces, moments and the flow visuals are presented. The likely changes in the flow and the effects on propeller for a given depth are also presented. The effect of the changes in bank clearance on squat is also explored. Viscous solver from SHIPFLOW® tool is used for the RANS computations.

2 NUMERICAL COMPUTATION

The simulations are carried out using a naval architect specific computational tool SHIPFLOW®. The tool is a hybrid steady state solver with both potential and viscous computation sources. The present study works on the global approach using the viscous solver XCHAP

2.1 DOMAINS

The numerical simulations were carried out for different cases. First the study was done for a vessel in shallow depth with freedom in the lateral direction. While another case for lateral depth restriction with two canal configuration was simulated. The domains chosen for the investigations are shown in Fig 1(a) and Fig 1(b).

2.1 (a) Canal 1

The canal is rectangular in shape with both the canal walls vertical. The second canal configuration is a surface piercing sloped wall with slope 1:4.

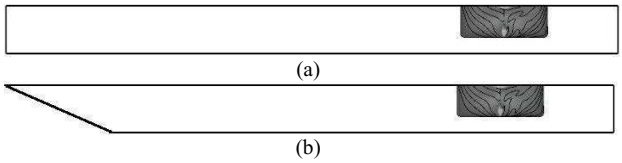

Figure 1. a) Vertical wall canal b) Sloped wall canal

2.1 (b) Mesh

The domain is discretized with overlapping grid. H_O type structured grid automatically generated using XGRID module around the hull is immersed in H_H type structured grid imported from ICEM meshing. This combination helps to achieve better Y+ values and thus resolve the viscous sub layer effectively and also the number of elements to resolve the physics is also reduced. The mesh in XGRID extends 0.1Lpp ahead of the ship and 0.1Lpp aft with a radial distance of 0.15Lpp and the canal grid extends 0.75Lpp ahead and 2Lpp aft of the ship. The total number of interpolation cells used is 0.3 million to get the simulation time in control and also to capture better results.

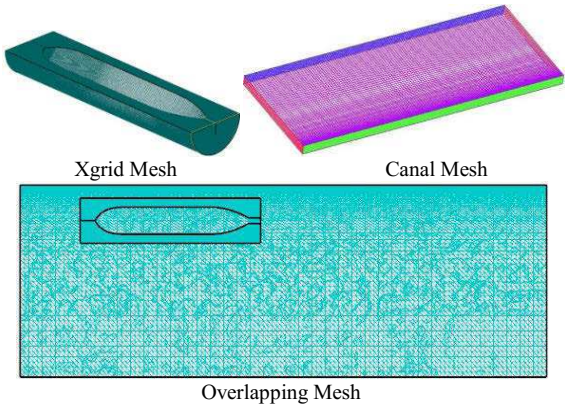

Figure 2. Overlapping structured mesh and component mesh

2.1 (c) Boundary conditions

The boundary conditions play a very crucial role in numerical computations, with the type of computations the boundary conditions are to be assigned to achieve the best possible reality aspects in the computations. In this case the conventional boundary conditions suffice to capture the details. The assigned boundary conditions are shown in the Fig 3.

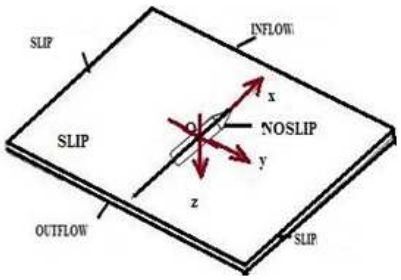

Figure 3. Boundary conditions

2.1 (d) Turbulence modeling:

The solver provides EASM, kω SST and kω BSL turbulence models for resolving the closure problem. The choice of an appropriate model confirms the accuracy of the computation. Although EASM works well with XCHAP, the kω SST was chosen which works better in capturing the desired physics in the type of flows that is dealt with here.

3 CASE STUDY

3.1 SHIP PARTICULARS

The investigation was carried out for famous benchmark ship KVLCC2 tanker model scale. The paper studies the lateral and vertical restriction problem for bare hull. The principal particulars of the full scale and model scale ship is given in the table.

Table 1. Full scale and model scale particulars

PARTICULARS	FULL SCALE	MODEL SCALE
Length (L_{pp})	320 m	4.97 m
Breadth (B)	58 m	0.90625 m
Draft (T)	20.8 m	0.325 m
Block Coefficient (C_B)	0.8098	0.8098
Vessel Speed (U)	7.6 m/s	0.984 m/s

3.2 SHALLOW WATER EFFECT

The study was carried out for shallow water condition predicts the forces and moments acting on the ship when moving through a harbor, port or canals. The simulations were carried out for a variable depth to draft ratio. The simulations reveals that the change in depth brings an evident transformation in the ship behavior as presented in [7]. The Fig 4 shows the resistance plot which clearly depicts the inverse relation of depth and resistance.

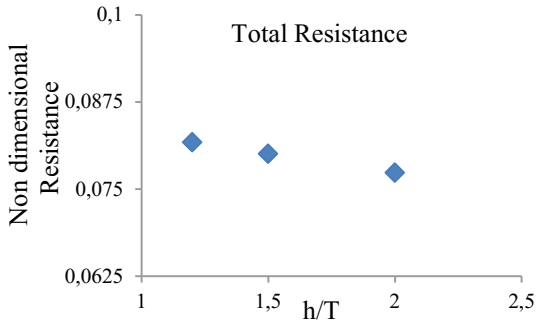

Figure 4. Resistance variation with h/T

3.3 BANK EFFECT

The ship bank interaction investigations were carried out for two variants of canals. The computations did not consider wave as the ship moved at a very low speed of 0.384m/s (6knots for full scale). The canal wall close to the ship remained vertical and the canal wall away from the ship was modified to a sloped wall. The effect of change in shape of the canal wall away from the ship was taken up to investigate possibilities of its influence on ship behavior. The depth of the canal was fixed at h/T-1.5. The two shapes of the canal used for investigation are shown in Fig 1.

3.4 RESULTS

The simulations were carried out for a Froude number of 0.055 and a Reynolds number of $1.926*10^6$.The results for a fixed water depth and two ship bank clearances are given in this section. The sway force (Y'), yaw moment (N'), rolls moment (K') and resistance measured in the numerical test are presented.

3.4 (a) Canal 1

The simulations investigate two ship bank clearances with y_b/L_{pp} of case (1) 0.237 and case (2) 0.264. An attempt to measure the forces and moments acting on the ship was made in the paper. The results show a drop in sway force, resistance and roll moment with increase in the clearance whereas the yaw moment increase with the increased clearance. This can be credited to the pressure distribution which changes with the distance from the canal wall. The pressure distribution on the hull shows in Fig 6 the unsymmetrical distribution on the ship bottom for case1 whereas the distribution seems more or less symmetrical for case 2.

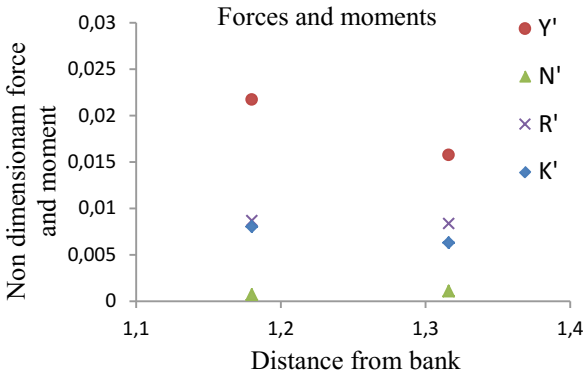

Figure 5. Force and moment variation with change in ship bank clearance

Figure 6 are depicts the pressure distributions on the hull when placed in canal 1with two different bank clearances The pressure distribution around the hull projects the suction effect caused due to the high velocity and low pressure in the region closer to the canal wall. The side of the hull closer to the bank wall shows drop in pressure as compared to the side away from the bank wall. It can also be visualized that as the bank clearance increases the severity of low pressure subsides. The effect of lateral blockage is seen not only on the sides but also notable on the hull bottom.

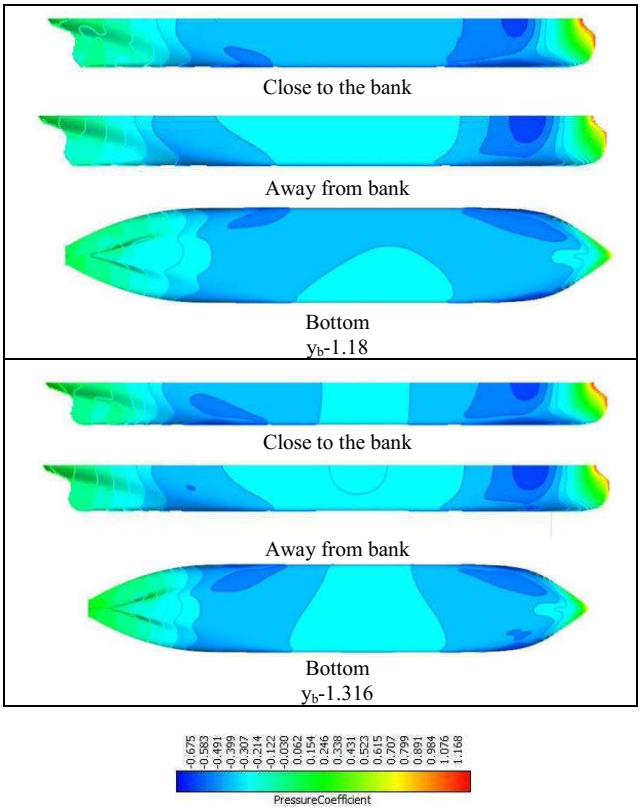

Figure 6. Pressure distribution on the hull

Another factor worth noting is the effect of the flow pattern change at the propeller location. The propeller performance is reflected by the pattern of the flow coming from the hull. The amount of wake in which the propeller works characterizes its performance. The flow reversals at the propeller plane can render the propeller producing zero thrust for half of its rotation. In order to avoid such objectionable situation assessment of the flow at the propeller plane is necessary. This will aid the understanding of the flow behavior and help make appropriate design changes so as to avoid vibrations, noise etc. caused by flow separations. The predicted flow pattern at the propeller plane is presented in Fig 7.

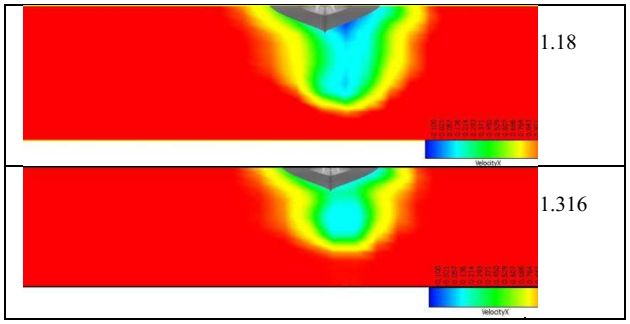

Figure 7. Axial velocity at the propeller plane

The wake distribution is unsymmetrical about the centerline. The flow separation is higher towards the region closer to the bank. The suction effect observed along the length of the hull also prominently affects the flow to the propeller. This will hinder the propeller performance and also affect the rudder effectiveness and make the ship stubborn to turn. Moving away from the canal wall relieves the severity of flow separation. It can be inferred that the closer the ship to the canal wall more probability of collision due to pressure drop and lowered propeller and rudder performance credited to the zero or negative axial flow at the propeller. So an optimal distance from the wall must be maintained to avoid any undesired outcome.

3.4 (b) Canal 2

Similar tests were carried out for a ship placed in a canal with surface piercing wall with slope 1:4. Will this change of slope on the wall away from the ship bring about any change in the ship behavior? To get a clarification on this, a starboard clearance of 0.237 L_{pp} was investigated for h/T=1.5. The forces and moments calculated numerically for both canals are compared and presented in the table 2.

Table 2. Force and Moment comparison

Yb=1.18	Non Dimensional values			
	Y	N	K	CT
Canal 1	2.17E-02	-7.04E-04	8.02E-03	8.67E-03
Canal 2	2.09E-02	-7.86E-04	7.94E-03	8.56E-03
Percentage difference	-3.47%	11.65%	-1.06%	-1.30%

It is evident from the results presented that the forces acting on the hull are more of a function of its distance from the wall closer to it. The table shows the yaw moment variation is about 11.6% and roll moment of about 1%, sway force variation is 3.5 % and the resistance variation of 1.3%. So a shape change of the wall away from the ship alters the sway force and yaw moment predominantly which plays an important role in maneuverability aspect of the ship. The pressure distribution shown in Fig 8 on the hull asserts the change observed. The unsymmetrical distribution seen about the midship section in canal 1 becomes more symmetrical when placed in canal 2 modifying the moments acting on the vessel.

The flow pattern is affected by the sloped wall. The sloped canal wall affects the hull bottom pressure and the axial velocity distribution at the propeller plane. The axial flow onto the propeller is better with the sloped canal than vertical canal wall. The intense drop in axial flow onto the propeller is eased by the sloped wall. The sloped canal wall although away from ship has not much effect on the magnitude of forces and some moments acting on the hull; it influences the overall flow characteristics around the ship.

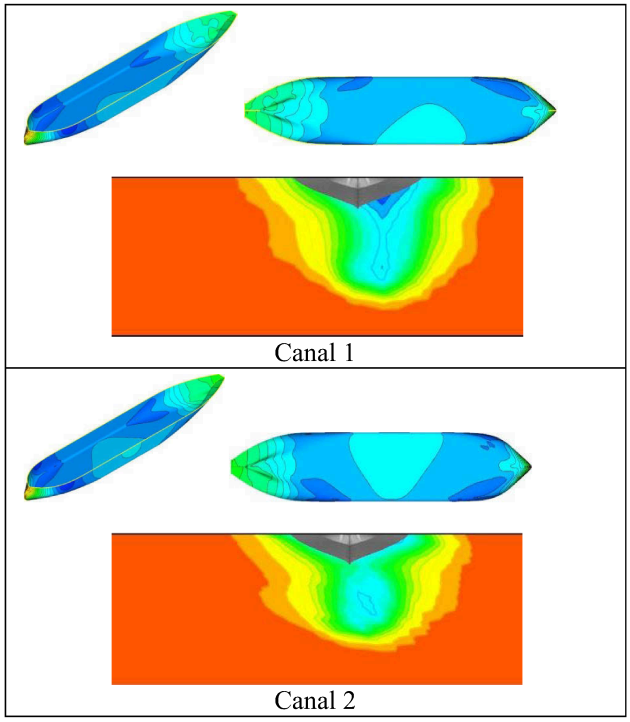

Figure 8. Pressure distribution on the hull and Axial velocity at the propeller plane comparison for canal 1 and canal 2 for y_b-1.18

4 SQUAT

Ship passing a confined water pushes the water ahead of her, this water flows through the sides or the bottom of the ship. This flow pushes itself through the limited space available squeezing the streamlines together increasing the flow velocity. The water level around the hull reduces and this drops the vessel vertically down. This sinking is squat. Squat has existed forever but for the past forty years the increase in vessel size and speed has led to the reduction of under keel clearance to around 1.0 to 1.5 m alarming increased possibility of grounding in shallow and confined conditions.

The under keel pressure distribution at the ship centerline is compared for lateral restriction and open waters respectively.

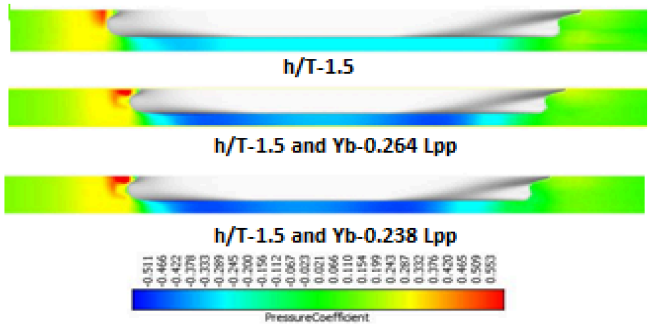

Figure 9. Pressure distribution below the ship

There is a remarkable drop in the pressure with the lateral restriction. The severity increases with the ship moving closer to the canal wall. The low pressure region confined to bow area with shallow depth spreads to 75% of the vessel length with both vertical and lateral restrictions.

Sinkage predictions were carried out for the canal 1 using the potential method for a fixed h/T=1.5 and ship bank clearance of 0.264 L_{pp} and 0.238 L_{pp} at different speeds. It is observed that the reduction of the bank clearance by 9.8 % has zero impact on sinkage. The speed is a deciding factor on the amount of sinkage the vessel undergoes. The higher the speed the higher is the squat shown in Fig 10.

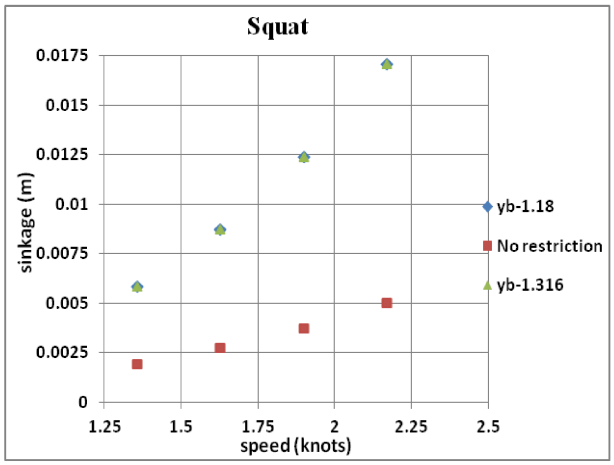

Figure 10. Squat predicted using potential method

5 SCALE EFFECT ON WAKE

The flow phenomenon is most sensible to the scale effect at the propeller. The computations were carried out for a scale of 1:64 which confines the output to the model scale; the scale effect will lead to wrong predictions at the full scale. The measurement of flow velocity observed at the propeller plane is a clear indication of the wake field observed at that plane for that scale. The wake fraction is measured as

$$w = 1 - \left(\frac{v_a}{U}\right)$$

The axial velocity plot at the propeller plane is an indication of the axial velocity into the propeller v_a and the probable wake. In order to investigate the scale effect the simulations were carried out for three different scales 1:110, 1:64 and full scale. Observation of the axial flow pattern indicates the variation in wake fraction with scale. The observed flow pattern at the propeller plane is shown in the Fig 11.

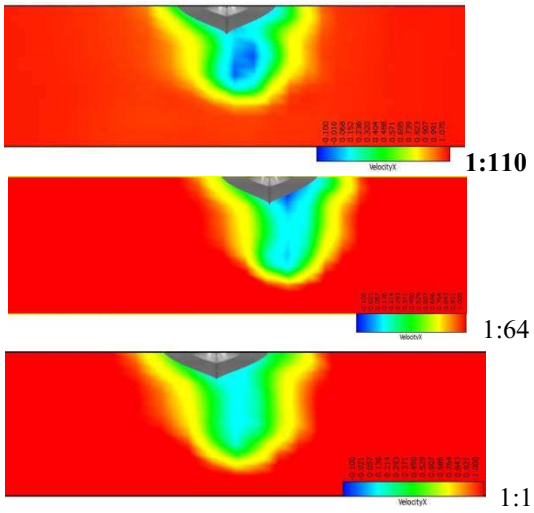

Figure 11. Axial velocity comparison for different scale

The figure 11 shows the changes in the axial flow pattern with scale change, this confirms reduction in the intensity of negative flow with increasing scale ratio. It can therefore be interpreted from the simulation results that the wake on full scale is less intense than the model and hence lower is the risk of vibrations or noise induced. The scale effect influences the scaled up results and must be accounted when scaling the results to full scale.

6 CONCLUSION

The investigation for lateral and vertical restrictions in the flow leads to the following conclusions.

1) The forces and moments shoot up with the addition of lateral restriction to the prevailing vertical blockage. This complicates the flow around the hull and renders the ship sluggish and stubborn making it difficult to maneuver.
2) The slope change of the bank wall away from the ship has a nominal effect on the forces acting on the hull but affects the yaw moment also the flow characteristics are modified.
3) The closer the ship to the canal wall higher the suction and chances of collision.
4) The axial flow to the propeller is also affected by the movement of the ship closer to the wall. The closer the ship to the wall the higher is the reversed flow observed, unsymmetrical wake at the propeller plane deteriorates its performance and reduces the thrust producing capacity at a given rpm.
5) Squat comparison for open water and lateral restriction shows indisputable increase with reduction in the ship bank clearance. Closer the ship to the canal wall higher is the squat.
6) Speed plays a vital role in measuring the sinkage of the ship. The change of ship bank clearance by 11% does not bring any effect on the sinkage and hence the squat.
7) Flow visuals provide a very close look into the actual pattern of the flow and guide the designers to accommodate all the design changes with utmost care and clarity.
8) The scale effect investigation leads to a conclusion that the wake is sensitive to scale effect and must be accounted for applying on full scale.

7 ACKNOWLEDGEMENTS

The authors deeply acknowledge and thank Björn Regnström (FLOWTECH) for his constant support and suggestions in resolving the issues faced. Also authors thank Michal Orych (FLOWTECH) for his valuable inputs. Authors also express gratitude to Sharad Dhavalikar (Indian register of shipping) for his frequent inputs and suggestions.

8 REFERENCES

1. Bertram, V. (2000) *Practical Ship Hydrodynamics*, Butterworth Publications.

2. Debaillon, B.; Lataire, E.; Vantorre, M. (2009). Comparison of bank effects on ship squat between experimental measurements and a numerical modeling system, *International Conference on Ship Manoeuvring in Shallow and Confined Water: Bank Effects*, Antwerp, Belgium: pp. 31-38.

3. Nakisa, M.; Maimun, A.; Sian, A.Y.; Ahmed, Y.M.; Priyanto, A.; Jaswar; Behrouzi, F. (2013). Three-dimensional numerical analysis of restricted water effects on the flow pattern around hull and propeller plane of LNG ship, *International journal of mechanics*, Vol. 7(3): pp. 234-241.

4. Poojari, D.; Janardhanan, S.; Kar, A.R. (2014). Maneuverability Assessment of a container ship using Steady RANS method **,** *Proceedings of the Twenty-fourth (2014) International Ocean and Polar Engineering Conference*, Busan, Korea**.**

5. Zou, L.; Larsson, L.; Delefortrie G.; Lataire E. (2011). CFD Prediction and Validation of Ship-Bank Interaction in a Canal. In: *Proceedings of the 2nd International Conference on Ship Manoeuvring in Shallow and Confined Water, Trondheim, Norway*.

6. Poojari, D.; Saj, A.V.; Janardhanan, S., Kar, A.R. (2014). Effect of Environmental Loads on the Maneuverability of a Tanker. *International Conference on Computational and Experimental Marine Hydrodynamics, MARHY* 2014, Chennai, India.

7. Janardhanan, S.; Krishnankutty, P. (2010). Estimation of sway-velocity based hydrodynamic derivatives in surface ship maneuvering. *International Journal of Ocean and Climate Systems,* Vol 1, No 3 and 4, pp 167-178.

8. Janardhanan, S.;Krishnankutty P. (2009) Prediction of Ship Maneuvering Hydrodynamic Coefficients Using Numerical Towing Tank Model Tests, *12th Numerical Towing Tank Symposium*, Cortona, Italy..

9. Poojari, D.; Saj, A.V.; Janardhanan, S.; Kar, A.R. (2015). Numerical Captive Model Tests and Trajectory Prediction for Ship Maneuverability in Shallow Water, *ICSOT INDIA: Coastal and Inland Shipping.*

10. Zou, L.; Larsson, L. (2013). Confined water effects on the viscous flow around a tanker with propeller and rudder. *International Shipbuilding Progress* 60(1): 309-343.

11. Broberg, L.; Regnstrom B.; Ostberg M. (2013). *SHIPFLOW Theoretical Manual*, FLOWTECH International AB., Gothenburg, Sweden,

12. Briggs, M.J.; Kopp, P.J.; Ankudinov, V.; Silver A.L. (2011). Ship Squat Comparison and Validation Using PIANC, Ankudinov and BNT Predictions. In: *Proceedings of the 2nd International Conference on Ship Manoeuvring in Shallow and Confined Water, Trondheim, Norway*.

13. Barass, B.; Derrett, D.R. (2006). *Ship Stability for Masters and Mates, Sixth Edition*

14. ITTC Recommended Procedures (2002), Manoeuvrability- Captive model test procedure," *Proceedings of 23rd ITTC.*

15. Pinkster, J.A.; Bhawsinka K. (2013). A real-time simulation technique for ship-ship and ship-port interactions. *The 28th International Workshop on Water Waves and Floating Bodies (IWWWFB 2013)*.

9 AUTHORS' BIOGRAPHIES

Deepti B Poojari (Deepti.Poojari@irclass.org) currently holds the position of Surveyor (Hydrodynamics Group-Research & Innovation cell) at Indian Register of Shipping. She leads the manoeuvring research team and is involved in other consultancy work carried out in the division.

A R Kar (kar@irclass.org) holds the position of Senior Principal Surveyor at Indian Register of Shipping. He is the Head of the Dept for Hydrodynamics and Risk & Reliability Group-RIC division.

4th MASHCON, Hamburg - Uliczka et al. (eds) - © 2016 Bundesanstalt für Wasserbau ISBN 978-3-939230-38-0 (Online)
DOI: 10.18451/978-3-939230-38-0_3

INTERACTION BETWEEN SHIP-INDUCED STRESS AND ASSOCIATED CHARACTERISTICS OF TURBIDITY RECORDS

S Niehueser, M Ulm, A Arns, J Jensen and **V Kelln**, Research Institute for Water and Environment, University of Siegen, Germany
K Uliczka and **B Kondziella**, Federal Waterways Engineering and Research Institute, Germany

SUMMARY

In a joint research project between the German Federal Waterways Engineering and Research Institute and the Research Institute for Water and Environment of the University of Siegen the ship-induced sediment transport as a proportion of the totally transported volume is investigated. Therefore, a field campaign in the Kiel Canal was conducted in 2012 and ship-induced loads were recorded. This paper highlights the preliminary results from analyzing the observed variables. First independent samples of observed passages were created and used to calculate correlations between the individual parameters. In a next step, high frequency turbidity records were separated into a common signal and linked to a critical sediment grain diameter. This procedure led to a classification depending on the ship-induced flow velocities because common characteristics of the turbidity measurements could be found. For further analyses the groups could be associated with AIS-transmitted parameters.

1 INTRODUCTION

Foreign trade is a vitally important factor in most economies. In Germany, inland navigation accounted for approximately 230 million tons of transported goods in 2014 (www.destatis.de, German Federal Statistical Office) indicating the demand for a robust and reliable transport infrastructure. However, both natural effects and anthropogenic interventions can cause sediment deposits in shipping channels and harbors which need to be dredged to maintain the infrastructures main function. Over the last decades, sediment dynamics have extensively been studied and a comprehensive review particularly dealing with transport issues in the San Francisco Bay Coastal System is provided in [1].
Sediment transport is generally described having extraordinary complex physical characteristics. The reason for that is the variety of parameters which directly influence the process [2]. Examples are the high turbulent hydrodynamical conditions as well as the sediment itself with different densities, shapes, grain diameters, grain size distributions, and storage conditions. Taking all these factors into account highlights that sediment transport is governed by quickly changing conditions in every time step. Another key challenge in this context is to quantify the amount of sediment deposit which is directly induced by the ship's passage and how the consequent sediment transport can be described as a function of the ship-induced load. The ship-induced load can be described e.g. by waves caused by the ship's passage, hereafter referred to as ship waves.
Investigations on ship waves are usually based on one of the following three methods: A first method is to perform expensive field measurements including all relevant processes as e.g. turbulences and other predominant conditions as e.g. tidal influences (e.g. [3], [4], [5], [6], [7], [29]). A second method for calculating the ship-induced waves is setting up a computational fluid dynamics (CFD) model (e.g. [8]) or using Boussinesq-type equations (e.g. [9], [10]). Such models are generally restricted by the underlying boundary conditions (e.g. ship's hull, inlet/outlet conditions). A third method is to rely on laboratory data of ship waves recorded in physical model experiments but these are limited to certain vessel types and waterway conditions [11]. Outcomes based on all three methods are often empirical formulas for describing wave parameters as e.g. the significant wave height but these formulas are usually only valid within a pre-defined range (e.g. [12], [13]). Furthermore, such empirical formulas are widely used for the calibration and validation of field measurements or numerical models (e.g. [11], [14], [29]).
In general, when moving along a waterway, a vessel usually generates a typical wave pattern which is divided into primary and secondary components (e.g. [15], [16], [11], [17]). The long-period primary wave is reflected alongside the ship and causes a fluctuation of the water level. These fluctuations are caused by the pressure and velocity distribution along the ship's hull showing pressure increases at the bow and stern and decreased pressure alongside of the ship. Consequently, rising water levels are found at the bow and stern (bow and stern wave) and a decreasing water level along the ships' side (drawdown). The drawdown corresponds to a reverse flow from the bow to the stern of the ship.
Replacement processes caused by the different pressure conditions induce the short-period secondary wave system. This system is mainly characterized by divergent and transverse waves (Kelvin waves) travelling away from both sides of the ship's hull with the ridges at an angle of 19.47° to the vessel's moving direction. The predominant contribution to the entire water level fluctuation can either originate from the primary or from the secondary wave system but depending on the waterway conditions. The primary waves prevail in restricted waterways while the secondary wave systems are more influential in unrestricted waterways [15].
In a joint research project the German Federal Waterways Engineering and Research Institute (BAW) and the Research Institute for Water and Environment (fwu) of

the University of Siegen aim at determining the ship-induced sediment transport as a proportion of the total volume transported in a tidal estuary [18]. Here, preliminary results are introduced, linking turbidity records with ship characteristics (e.g. geometry) and ship-induced stress (e.g. ship wave) using observational data from a field campaign that covers a large number of ship passages. The measurements were conducted at one specific cross-section of the Kiel Canal located in northern Germany and include but are not limited to turbidity records as well as geometries and velocities of and nearby the ships. Due to the limitation to stationary measurements this paper focusses on the aspect of sediment entrainment. Conclusions about the suspended sediment concentration in the entire water column or the sediment transport itself cannot be drawn directly.
However, the intention of this paper is to describe the interaction between ship and waterway with regard to the entire system and not for individual vessels.

2 STUDY AREA

The Kiel Canal is the most frequented artificial waterway in the world and has a total length of about 100 km connecting Brunsbüttel at the tidal Elbe River with Kiel at the Baltic Sea (see Figure 1) (e.g. [19], [20]). This artificial waterway reduces the route between the German North Sea and the Baltic Sea by nearly 450 km and the ships can avoid travelling all around northern Denmark.

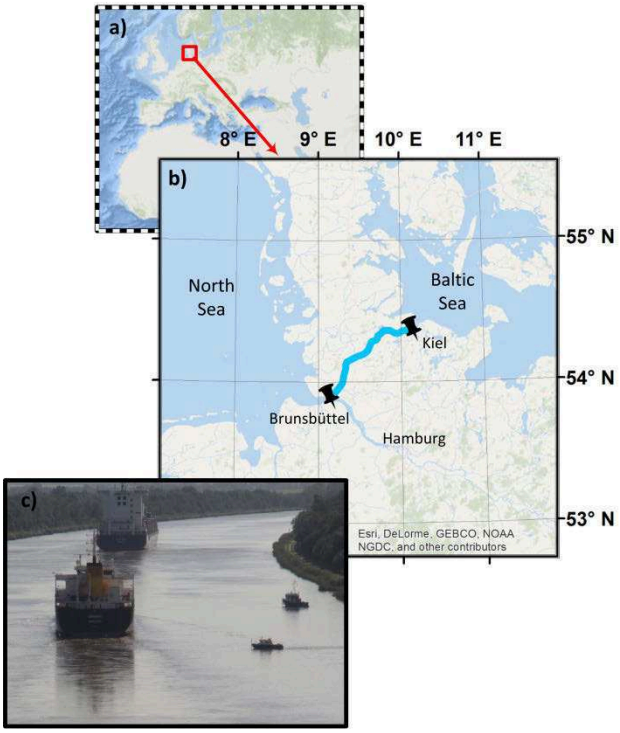

Figure 1. The Kiel Canal and a picture of the selected cross section during the field campaign (Photo: BAW).

In September 2012, the BAW carried out a field campaign in the Kiel Canal covering a period of approximately one week. The selected cross section is located at km 17.925 (near Brunsbüttel). In 2012 ~35,000 vessels passed through the Kiel Canal, i.e. more traffic than e.g. in the Suez Canal (http://www.wsa-kiel.wsv.de/Nord-Ostsee-Kanal/).
The Kiel Canal provides very constant and assessable conditions and is neither affected by tides nor strong currents (mostly from drainage processes). This very specific study site can thus be considered as field laboratory, one of the main reasons for selecting it for the field campaign.

3 DATA

The above mentioned measuring campaign provides both measurements at the bottom of the Kiel Canal as well as in the total water column by means of ship-based methods. Here, the focus is on stationary measurements at the bottom of the cross section. Figure 2 (top) shows the positions of the probes in the cross section having distances from the south bank as follows: 43.31 m (probe 1), 66.61 m (probe 2), and 82.85 m (probe 3).

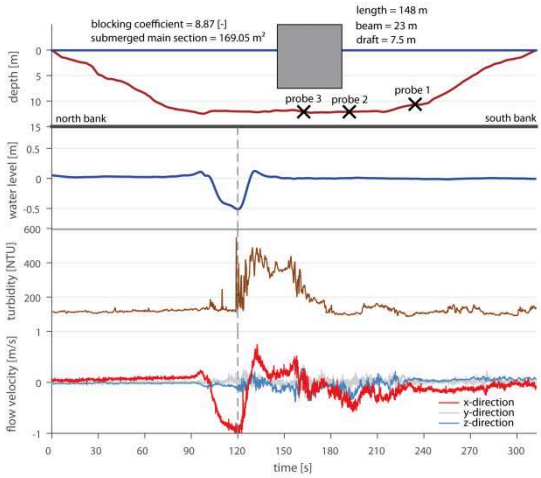

Figure 2. Overview of the recorded and investigated parameter (from top to bottom: idealized ship geometry and location of the probes, water level fluctuation, turbidity, flow velocity).

For the investigations different parameters were processed including water level, ship-induced flow velocities at the bottom (three-dimensional, recorded as x, y, z components) and turbidity information. Temporal resolutions are different for individual parameters with 8 Hz for the CTD probe (Conductivity, Temperature, Depth) and the turbidity probe (type: SeaPoint, STM), and 32 Hz for the flow probe. All datasets were recorded between September 17th 10:00 and September 25th 12:30. In this period a total number of 509 vessels passed the cross section. Observed parameters are exemplarily shown in Figure 2 considering the passage of one individual vessel. The grey dashed line is located at time step 120 s, a relative time with respect to the starting point of the passage. This point was chosen as a common reference point for

all observed passages as follows: In the data preprocessing, times of individual ship passages were reduced in order to match the maximum trough to the reference point.
Additionally, the ship provided AIS-signal (Automatic Identification System) was also recorded containing all relevant information of the passing ship. More specifically, AIS data sets provide length, beam, draft, speed and course over ground together with the ship's name and identifier. Furthermore, soil samples were taken in the cross section to obtain reliable information on the mass fraction of the particle size distribution. In Table 1 the main grain diameters are listed which represent the majority of the soil in the observed cross section. Therefore our investigations focus on these grain diameters. For further details of the field campaign in the Kiel Canal refer to [18].

Table 1. Grain size distribution [21].

Class name	grain diameter [µm]	mass fraction [%]
Very fine sand	62-125	19.0
Fine sand	125-250	38.4
Medium sand	250-500	17.6
		$\sum = 75.0$

According to the characteristics of the Kiel Canal, a separation of the measurements in natural and ship-induced effects is not needed. Therefore, the investigations can directly be performed. This distinguishes the presented work from other analyses like e.g. in [6]. Furthermore, effects of the propeller on the sediment entrainment have been ruled out in this study, since it is not possible to separate the amount of the propeller in the given measurements. A principal model of the propeller related impact in the near field of a vessel is given in [18] while the effect of propeller wash is investigated in [27].

4 METHODS

Aiming at robust and reliable results, different samples were created by either applying two different criteria (sample 1) ensuring all passages being independent and unaffected or also a third criterion (sample 2) intended to reduce the spatial influence of the observed parameters. Specifically, the criteria were as follows:

- the interval between consecutive ship passages (2 minutes before and 10 minutes after the reference point),
- the availability of the AIS-signal for the individual recorded ship passages,
- the distance of the individual recorded ship passages from the nearest probe (±2 m).

Since sample 1 is used for a correlation analysis, sample 2 is used for smoothing the turbidity record as well as for investigations concerning the critical grain diameter. The reason for using two different samples is that the absolute values of the measured parameters decrease with increasing distance to the probes as shown in Figure 3. The example shows how the fluctuation in the water level develops from the middle of the cross section to the southern canal bank. In this case, the vessel directly passed over the probe in the middle of the cross section (distance between ship's axis and probe 3 <5 cm) thus it can be assumed that the surface elevation is fully formed.

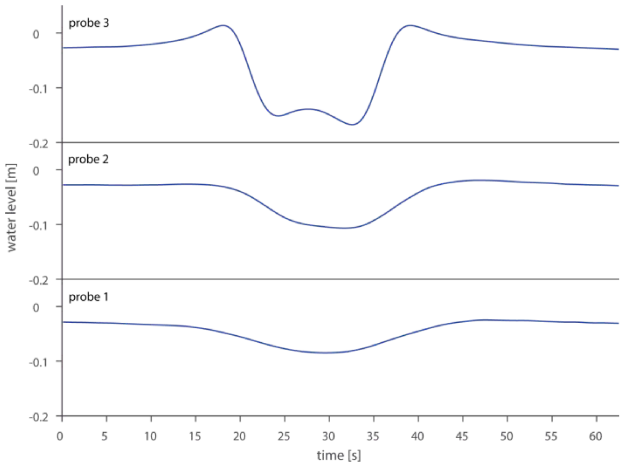

Figure 3. Development of the fluctuation in the water level from the middle of the cross section to the southern bank.

For the correlation analysis the absolute values of the parameters are less important because these analyses aim at describing the linear relationship between two recorded parameters as the tendency to move in the same/different direction. This is different when looking at the critical grain diameter which is estimated based on the smoothed turbidity records. Here, the absolute values of the time series are more important to examine the ship-induced amount of sediment in the water column. A drawback, however, is a reduced size of sample 2 compared to sample 1.
Before investigating the turbidity records in detail, some previous analyses need to be performed. In a first step, correlation coefficients between relevant parameters are computed. Detecting the relevant parameters is mainly based on the observational records. Therefore, available vessel parameters like speed over ground, length, beam, draft, submerged main section of the ship, and the blocking coefficient are taken into account. The blocking coefficient combines ship and waterway parameters to account for the interaction between the vessel and the characteristics of the observed cross section. The coefficient is defined as the submerged main section of the ship divided by the cross sectional area of the waterway at the observed site.
Further parameters are related to the primary wave system. The focus is on the three main values bow wave, drawdown, and stern wave. Also the maximum resulting flow velocity components (x, y, z direction) and the recorded turbidity maximum are considered.
The correlation coefficient R between two recorded parameters is defined as

$$R = \frac{C(x,y)}{\sqrt{C(x,x)\cdot C(y,y)}} \quad (1)$$

where C is the covariance which is defined for two random variables x and y as

$$\mathrm{Cov}(x,y) = \frac{1}{n-1}\sum_{i=1}^{n}(x_i - \mu_x)\cdot(y_i - \mu_y) \quad (2)$$

where n is the length of x and y and μ is the mean of x and y. Thus, the correlation coefficient ranges from -1 to 1, whereas correlation coefficients below zero show negative correlation, correlation coefficients equal to zero point out no correlation, and correlation coefficients larger than zero reveal a positive correlation.
The significance test is based on an approximate test for the hypothesis of no correlation. The estimation uses

$$p = |R|\sqrt{\frac{n-2}{1-R^2}} \quad (3)$$

and compares p with critical values from the t-distribution with n-2 degrees of freedom [22]. The critical values are chosen on a significance level of 5% which means, if $p \leq 0.05$, the correlation is significant.
In the next step two smoothing methods, namely moving average and principal component analysis (PCA), were tested and applied to the turbidity records of sample 2. The smoothing is required as the high frequency turbidity records also include spikes and outliers which need to be eliminated for further analyses. Additionally, some of the smoothing techniques enable to extract a common signal from likewise ship passages needed to describe the general system behavior. The results are later on used to derive a generalized and robust description of the high-resolution turbidity data and to avoid misinterpretations in the temporal location and/or in magnitude of the detected maximum.
The moving average (also called running mean) is an example for a low-pass filter technique removing higher frequencies from time series and thus smoothing the data. This method as well as other linear smoothing methods is reviewed in [23]. During the procedure, every n^{th}-value of the original time series Y is substituted by the mean of the n^{th}-value, the q previous and the q subsequent values of Y:

$$X_n = \frac{1}{2q+1}\cdot\sum_{j=-q}^{+q} Y_{n-j} \quad (4)$$

The successive calculation of the mean for all values of Y with a moving window of 2q+1 values that is continuously pushed forward is responsible for the method's name. The smoothing intensity can be controlled by changing the window size. A larger q leads to a larger window and therefore to a stronger decrease in the variance of Y. A disadvantage in this context is the missing availability of smoothing several data sets simultaneously. Each time series has to be smoothed individually.
In contrast, the PCA is a multivariate statistical method to detect the common signals in multidimensional data sets like a set of turbidity time series. The main advantage in this context is the possibility of identifying patterns in the data set. This allows showing up the similarities as well as the differences. Furthermore, the dimensions of the original dataset can be reduced by discarding certain information [24]. However, vessels with identical characteristics can be classified and then subsequently analyzed in groups.
[25] give a short description on how to use the PCA approach. The first step is the calculation of the eigenvalues and the eigenvectors of the covariance matrix. This builds a decomposition of the data set into orthogonal components based on the criterion of maximum variability. The eigenvectors are composed by one component for each dimension of the data set respectively (in this case turbidity time series for each vessel). Furthermore, the eigenvectors represent the principal components while the corresponding eigenvalues constitute the proportion of the total variance explained by the individual principal components. The original set of time series can be reconstructed by taking all the principal components into account. If the aim is to reduce the vessel's turbidity time series to the main common signal, not all principal components should reasonably be used for the analyses but these which explain most of the variance in the turbidity records.
The smoothed time series of the turbidity records will be used for investigating the relationship between ship-induced stress and the turbidity. In particular, the turbulent flow velocity at the bottom of the cross section is regarded to determine the entrainment of the sediments and the resuspension process. To get a first idea, a grain-diameter-based Froude number is used for the analyses [26]:

$$360 = \frac{v_m^2}{d_{crit}\cdot g} \quad (5)$$

where v_m is the mean velocity of the flow at the bottom of the cross section, d_{crit} is the critical grain diameter, and g is the gravitational acceleration. As mean flow velocity at the bottom of the cross section, the resulting ship-induced flow velocity at the bottom of the cross section is used. Hence, the results may be considered as approximation to describe the interaction between a passing ship and the waterway even if there are more detailed approaches for calculating the entrainment of the sediments.
Afterwards a threshold classification based on the critical grain diameter was conducted yielding in a general description of the turbidity curve for each group. In the last step, the groups are assigned to directly measurable parameters e.g. to AIS data like the length or the draft of a ship.

5 RESULTS

5.1 DATA ASSIMILATION

The data assimilation was performed using the described criteria for selecting unaffected ship passages. After that 257 passages remain for sample 1 (correlation analysis)

and 54 for sample 2 (turbidity record smoothing, investigations concerning the critical grain diameter). In case of sample 1, 195 of the 257 ships have been maneuvered above probe 3 in the center of the canal, 61 over probe 2 and 1 over probe 1 located close to the southern bank.

5.2 CORRELATION ANALYSIS

The results of the correlation analysis based on 257 recorded vessels are shown in Figure 4. The outcome is provided as matrix giving a quick overview of the selected parameters each of which is briefly characterized below. Correlations between individual parameters are shown as circles with the correlation coefficient inside. If the calculated correlation is not significant, the circle is drawn in white color. Otherwise, the circle is colored ranging from -1 (light green) to 1 (red) depending on the value of the correlation coefficient.
The correlation analysis indicates low or no significant correlations for the speed over ground with all other parameters since most ships passed with a speed of approximately 15 km/h, the official maximum speed in the Kiel Canal for all vessels. In contrary to that, strong dependencies are found between the ship's geometry and parameters of the primary wave system. This can be seen, in particular, in the draft and the drawdown ($R = 0.80$). The same is valid for the correlation between the maximum resulting flow velocity and the drawdown/draft ($R = 0.88/R = 0.82$). It is thus concluded that the maximum resulting flow velocity can be used for the characterization of a specific vessel. The maximum recorded turbidity shows significant correlations with almost all parameters but coefficients are rather small ($R < 0.35$) in contrast to the correlation between other parameters. Similar results for the correlations were found by [29] and further on used to predict ship-induced wave heights with empirical formulas. Regression analyses were performed as well to predict the maximum turbidity based on the bed shear stress.

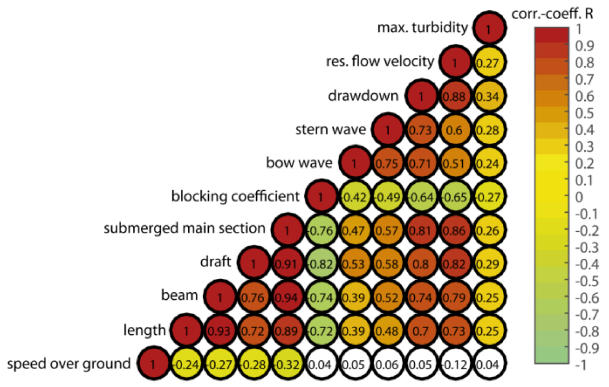

Figure 4. Correlation analysis.

A preliminary conclusion here is that the maximum turbidity also cannot be directly described by the chosen parameters. Furthermore, the maximum turbidity is probably not the ideal parameter for characterizing the turbidity records because of the complex physical ship/waterway-interaction and the fluctuations in the measurements due to the high frequency recording. Therefore, another method is introduced in the next chapters.

5.3 SMOOTHING TECHNIQUES

The correlation analysis above highlighted that the maximum recorded turbidity cannot be used to properly describe the entire ship-induced turbidity. A possible reason is the high sampling rate of 8 Hz. Infrequent outliers lead to a misinterpretation in temporal location and/or absolute value of the detected maximum. Figure 5 shows four arbitrary examples for those cases.

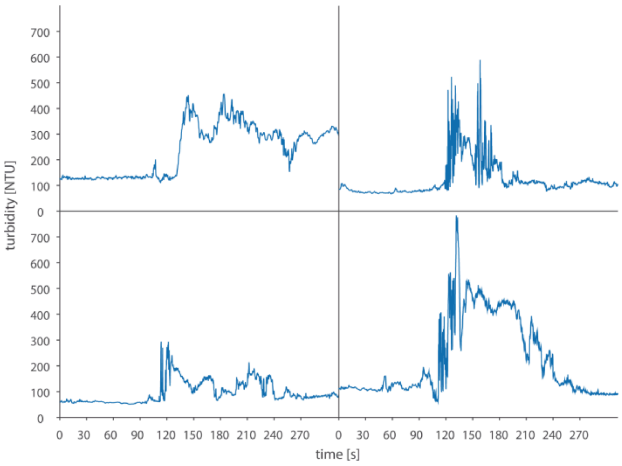

Figure 5. High frequency turbidity records.

Therefore, only the first and the second principal component were used to compress the information in the vessel's turbidity time series for the analyses. This enables to explain approximately 75 % of the variability of the turbidity records regardless of the sample. Each remaining principal component does not exceed 10 %.
Figure 6 finally summarizes the results of the smoothing techniques applied to two different turbidity records. The grey line in the background shows the observed high frequency turbidity time series. The red line is the moving average with a window size of 10 s (assumed to be appropriate for this issue without losing too much information but gaining a good result in smoothing at the same time) and the black line represents the reconstruction of the turbidity records based on the first and second principal component of sample 2 with 54 measurements of unaffected ship passages. The explained variance sums up to 76.4 % showing that only signals in the measurements have been removed that show strong individual characteristics of each vessel and of the prevailing environmental conditions during the vessel passage.
Figure 6 essentially shows the advantages and disadvantages of the applied methods. While the moving average fits very well to the original data, the PCA-approach shows a more general description. This fact is owed to the mathematical background of the methods. The moving average shows better results with increasing window sizes. Downside is the loss of information about the actu-

ally recorded peak. Contrary, this loss is much smaller when using the PCA. However, the detailed description is less good.
Since the following investigations focus on the general characteristic and on describing the peak values, the PCA-approach is used in the next chapter.

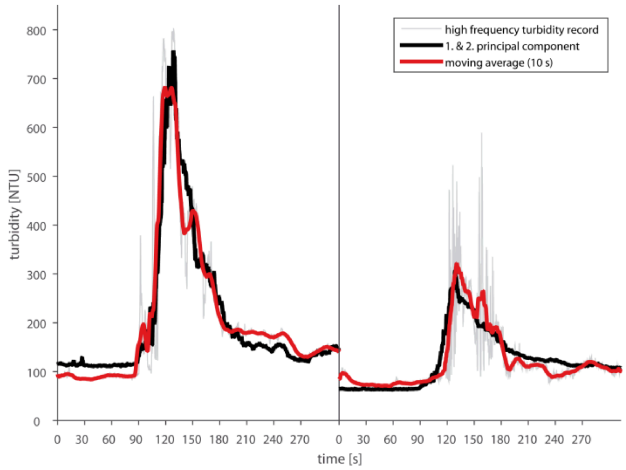

Figure 6. Summarized smoothing techniques.

5.4 CRITICAL GRAIN DIAMETER

The results of the grain diameter analyses are shown in Figure 7 for two exemplarily chosen vessels representing two different cases. The graphs are divided in two subplots. The upper plot shows the (calculated) critical grain diameter for each time step using equation (5) based on the flow velocity at the bottom of the cross section. The color shaded areas are classified by the grain diameters considering very fine sand, fine sand, and medium sand. The lower subplot shows the recorded high frequency turbidity in black as well as the first and second principal component reconstruction in red taking 54 measurements of unaffected ship passages (sample 2) into account.

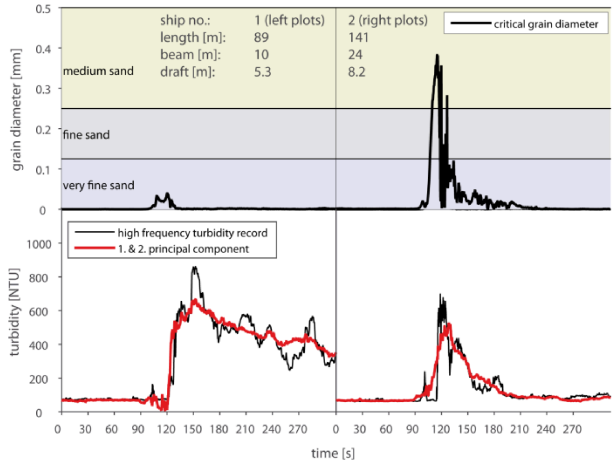

Figure 7. Recorded turbidity and calculated grain diameter.

However, the two different turbidity records in Figure 7 still have characteristics in common. Both time series in the lower part of the figure show a basic turbidity around 100 NTU. Due to the passing ship the turbidity quickly increases and reaches a maximum just after the occurrence of the trough (reference point at 120 s). Afterwards, the turbidity decreases until reaching the basic concentration again. The main difference in the shown examples is the time the turbidity remains in the water column. The critical grain diameters, shown in the upper subplots, allow for linking the different residence times to the flow velocity. As figured out on the left, the turbidity decreases slowly (consequently the residence time is long) in case that the recorded flow velocity at the bottom does not exceed the first threshold. The critical grain diameter shows that the recorded velocity only has the ability to resuspend very fine sand. In contrast to this, the turbidity decrease is much faster (therefore the residence time is short) in case that the flow velocity is large enough to resuspend medium sand, as shown by the large critical grain diameter. The physical background of the described behavior can only be assumed since the available measurements only provide information about the sediments on the canal bed and not about the sediment distribution in the water column. First, the different densities of the sediment fractions may impact the residence time. Medium sand with a higher density sinks faster than very fine material with a lower density. Another additional explanation for the shorter residence time in case that medium sand was resuspended might be that fast sinking grains affect slowly sinking particles and increase their sinking speed. As mentioned before, a verification of these explanations requires further but actually not available information.
Nevertheless, the critical grain diameter was mainly used as auxiliary parameter to classify the observed 54 vessels for further investigations. Since the shown behavior was found for all turbidity time series, this approach constitutes an appropriate classification methodology, regardless of the detailed allocation of the physical processes. Therefore, three classes were set up using the grain diameters as class limits as shown in Table 2. The individual time series were classified according to the maximum critical grain diameter.

Table 2. Classification based on the grain diameter.

Class name	range [mm]	number
Grain group 1	≤0.125	24
Grain group 2	>0.125 ≤0.250	16
Grain group 3	>0.250	14

In Figure 8 three subplots of the specific grain groups are shown. The gray marked lines in the background show the first and second principal component of the individual turbidity time series in the individual grain groups. The black line represents the mean time series of all ships in that group and the red shaded area highlights the standard deviation of each time step. Noticeable is the characteristic behavior which was already shown in Figure 7. Here the mean time series show the same behavior: ship passages that induced a rather small flow velocity at the canal bed were assigned to group 1 which shows a

low sink rate resulting in a long residence time. In contrast all ships that induced a rather high flow velocity were assigned to group 3 which shows a characteristic fast decrease of turbidity resulting in a shorter residence time. Another point is that, regarding the mean time series the maximum turbidity increases with the group number. This is shown better recognizable in Figure 9 where the three mean time series are plotted one upon the other.

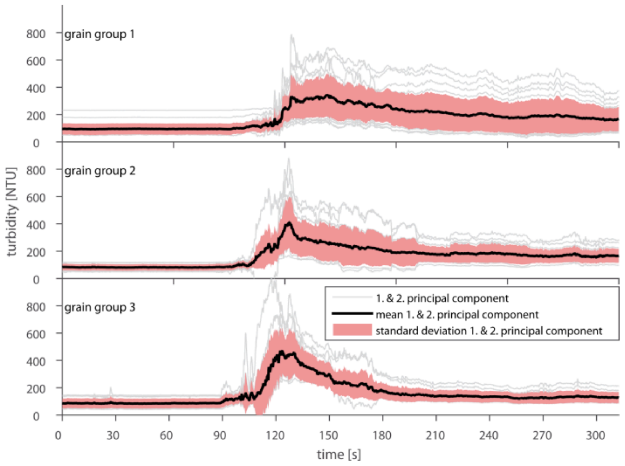

Figure 8. Mean turbidity of the grain groups including the standard deviations.

Furthermore, individual time series of a group have been tested for a systematic behavior, e.g. checking all time series that tend to be higher than the group mean for exceeding a certain draft. These tests did not show up any dependencies and clarify that the ship-induced sediment resuspension is a complex physical process which cannot be linked to single parameters. Sediment behavior like flocculation as well as environmental effects in the particular waterway cross section affects the results.

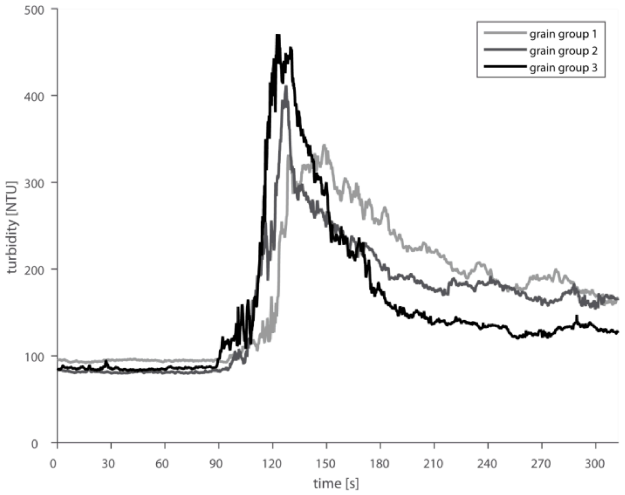

Figure 9. Mean turbidity of the grain groups.

However, for the given section of the Kiel Canal the described classification approach allows splitting the given data set of observed ship passages based on the critical grain diameter resulting in three groups, each with a characteristic behavior and a significant difference in turbidity residence time. The three groups are shown in Figure 9, the black time series marks the development of grain group 3, the dark grey line of grain group 2 and the light grey line of grain group 1.

With the flow velocity at the canal bed, the chosen classification needs a parameter which is usually not available. Therefore the next step considers permanent available ship parameters like the AIS-data. Furthermore, it is necessary to quantify the uncertainties in terms of the spread around the mean values in this case with the standard deviation. Figure 10 shows four parameters and their distribution over the three grain groups exemplarily. The mean is displayed as a red line, the blue box around the mean represents the spread in terms of the standard deviation and the horizontal black lines below and above the box are the minimum and maximum of each parameter. The plot clearly shows a strong dependency between the parameters and the grain groups. The larger the resuspended grain diameter, the larger are the mean parameters. Except for the flow velocity the spread decreases with an increasing grain group. The strong dependency between the resulting flow velocity at the bottom and the grain groups results from calculating the critical grain diameter on base of the flow velocity. Here, the range of the flow velocities assigned to each grain group representing an idealized characteristic of the turbidity should be shown. However, same results are valid for other parameters not shown in Figure 10.

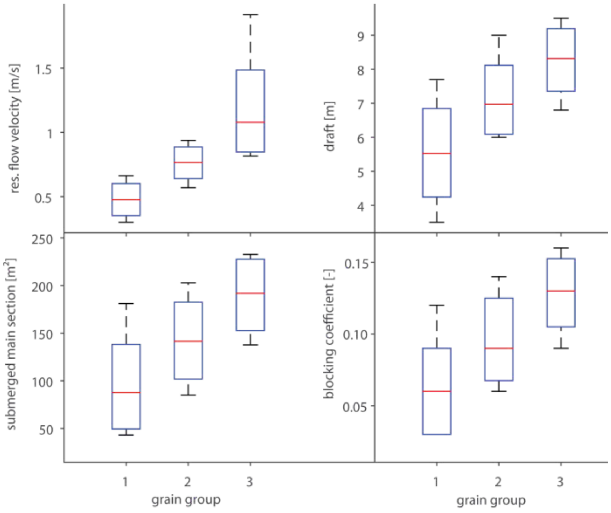

Figure 10. Grain groups vs. ship parameters.

6 CONCLUSIONS

In this paper, a field campaign in the Kiel Canal was evaluated. The analyses have been performed during a joint research project between the German Federal Waterways Engineering and Research Institute and the Research Institute for Water and Environment of the University of Siegen. Strong dependencies between the ship's geometry and the primary wave system parameters or the maximum resulting flow velocity at the bottom of the cross section were identified. However, the correlation analysis also revealed that the turbidity is a highly sensitive parameter requiring higher effort to be de-

scribed compared to e.g. afore mentioned parameters. Therefore, the principal component analysis was used to find out common patterns in the turbidity measurements. The common signal in the turbidity records in terms of the first and second principal component were used to link a critical grain diameter and the corresponding flow velocity at the bottom of the cross section. This approach was used to classify the turbidity records and not to describe the underlying physical processes in detail. The classification shows appropriate results and can additionally be directly assigned with AIS-transmittable parameters (e.g. length or draft of a ship). A validation of the chosen grain diameter approach is still needed and should include comparisons with other studies. Thresholds of sediment movement are e.g. described by [28].

In a next step, further effort is on deriving a generalized description of the classified turbidity time series since the high resolution records still contain individual characteristics. On this basis, the maximum but also the total shape of the generalized turbidity curves can be taken into account depending on the specific issue. An estimation of the ship-induced sediment transport will then be possible with the residence time from the generalized turbidity time series (assuming a higher amount of suspended sediment concentration during the residence time). The proportion of ship-induced sediment transport including uncertainties can then be approximated for waterways based on AIS-transmitted parameters.

Furthermore, combined with AIS-parameters a future sediment transport can also be estimated based on the expected ship traffic.

However, the current results are still limited to the Kiel Canal. To achieve a general description of the sediment transport the developed methods have to be applied to other (tidal) waterways, e.g. the Elbe river.

7 ACKNOWLEDGEMENTS

The shown analyses are derived from the research project "Schiffserzeugter Sedimenttransport an Seeschifffahrtsstraßen (SeST)" funded by the German Federal Waterways Engineering and Research Institute (BAW). The authors of the Research Institute for Water and Environment at the University of Siegen are grateful to the corresponding personnel at the BAW who are also co-authors of this paper and who run the field measurements, prepared and provided the large variety of data as well as helpful comments within the research project.

8 REFERENCES

1. Barnard, P.L.; Schoellhamer, D.H.; Jaffe, B.E.; McKee, L.J. (2013). Sediment transport in the San Francisco Bay Coastal System: An overview, *Marine Geology* 345: pp. 3-17. doi:10.1016/j.margeo.2013.04.005.

2. Simons, D.B.; Sentürk, F. (1992). Sediment Transport Technology: Water and Sediment Dynamics, *Water Resources Publication*, Colorado, USA.

3. Johnson, J.W. (1957). Ship waves in navigation channels, *Proceeding of the 6th coastal Engineering Conference*, Gainesville, Florida. ASCE: pp. 666–690.

4. Schoellhammer, D.H. (1996). Anthropogenic sediment resuspension mechansim in a shallow microtidal estuary, *Estuar. Coast. Shelf Sci.* 43: pp. 533-548. doi:10.1006/ecss.1996.0086.

5. Houser, C. (2011). Sediment Resuspension by Vessel-Generated Waves along the Savannah River, Georgia, *Journal of Waterway, Port, Coastal, and Ocean Engineering* 137: pp. 246-257. doi:10.1061/(ASCE)WW.1943-5460.0000088.

6. Rapaglia, J.; Zaggia, L.; Ricklefs, K.; Gelinas, M.; Bokuniewicz, H. (2011). Characteris-Tics Of Ship's Depression Waves And Associated Sediment Resuspension In Venice Lagoon, Italy, *Journal of Marine Systems* 85: pp. 45-56. doi:10.1016/j.jmarsys.2010.11.005.

7. Rapaglia, J.; Zaggia, L.; Parnell, K.; Lorenzetti, G.; Vafeidis, A.T. (2015). Ship-wake induced sediment remobilization: Effects and proposed management strategies for the Venice Lagoon, *Ocean & Coastal Management* 110: pp. 1-11. doi:10.1016/j.ocecoaman.2015.03.002.

8. Ji, S.; Ouahsine, A.; Smaoui, H.; Sergent, P. (2014). 3D Modeling of sediment movement by ships-generated wakes in confined shipping channel, *International Journal of Sediment Research* 29: pp. 49-58. doi:10.1016/S1001-6279(14)60021-4.

9. Madsen, P.A.; Sørensen, O. (1992). A new form of Boussinesq equations with improved linear dispersion characteristics. Part 2. A slowly-varying bathymetry, *Journal of Coastal Engineering* 18: pp. 183-204. doi:10.1016/0378-3839(92)90019-Q.

10. Dam, K.T.; Tanimoto, K.; Nguyen, B.T.; Akagawa, Y. (2006). Numerical study of propagation of ship waves on a sloping coast, *Journal of Ocean Engineering* 33: pp. 350-364. doi:10.1016/j.oceaneng.2005.05.003.

11. Sorensen, R.M. (1997). Prediction of vessel-generated waves with reference to vessels common to the upper Mississippi river system, *Technical report*, Department of Civil and Environmental Engineering, Lehigh University, Bethlehem, PA, USA.

12. Krey, K. (1913). Fahrt der Schiffe auf beschränktem Wasser, *Schiffbau* 14.

13. Dand, J.W.; White, W.R. (1978). Design Of Navigation Canals, *Symposium on aspects of navigability of constraint waterways including harbour entrances*, Delft, Netherlands.

14. Jensen, J.; Kelln, V.; Niehüser, S.; Uliczka, K.; Kondziella, B. (2015). Entwicklung empirisch-analytischer Ansätze als Proxy für schiffserzeugten Sedimenttransport an Seeschifffahrtsstraßen, *HTG Kongress 2015*, Bremen, Deutschland, HTG: pp. 231-240.

15. Jensen, J. (1998). Ermittlung von schiffserzeugten Belastungen an Wasserstraßen, *Tagungsband Numerische Verfahren in der Wasserbaupraxis*, Verein zur Förderung der wissenschaftlichen Weiterbildung an der Universität-Gesamthochschule Siegen e.V. (fww): pp. 125-136.

16. Bertram, V. (2000). Practical ship hydrodynamics, *Butterworth-Heinemann*, Oxford, UK.

17. BAW (2006). Anpassung der Fahrrinne von Unter- und Außenelbe an die Containerschifffahrt, *Gutachten zu den ausbaubedingten Änderungen der schiffserzeugten Belastung*, (BAW-Nr. A3955 03 10062).

18. Uliczka, K.; Kondziella, B. (2016). Ship-induced sediment transport in coastal waterways (SeST), *Proceedings of 4th MASHCON*, Hamburg, Germany. (submitted).

19. Brockmann, J.; Heeling, A.; Pohl, P.; Uliczka, K. (2008). The Kiel Canal (Nord-Ostsee-Kanal), *Die Küste* 74: pp. 317-332.

20. Thormählen, C. (2010). Modernisation of the Brunsbüttel locks, *PIANC Yearbook* 2010: pp. 131-134.

21. Aqua Vision BV (2012). Suspended sediment measurements in the Kiel Canal. *Report AC_DOC_120149 Concept*, Utrecht, Netherlands. (unpublished).

22. Von Storch, H.V.; Zwiers, F.W. (1999). Statistical analysis in climate research, *1st edn. Cambridge University Press*, Cambridge, UK.

23. Buja, A.; Hastie, T.; Tibshirani, R. (1989). Linear smoothers and additive models (with discussion), *The Annals of Statistics* 17: pp. 453–555. URL:http://www.jstor.org/stable/2241560.

24. Smith, L.I. (2002). A tutorial on Principal Components Analysis, *Cornell University*, USA.

25. Marcos, M.; Gomis, D.; Monserrat, S.; Alvarez-Fanjul, E.; Perez, B.; Garcia-Lafuente, J. (2005). Consistency of long sea-level time series in the northern coast of Spain, *Journal of Geophysical Research* 110: C03008. doi:10.1029/2004JC002522.

26. Kresser, W. (1964). Gedanken zur Geschiebe- und Schwebstofffführung der Gewässer, *Österreichische Wasserwirtschaft* 16: pp. 6-11.

27. Williams, R.; Wang, T.; Whelan, M.; Shepsis, V.; Poon, Y. (2006). Methodology for estimating effects from propeller wash: Case Studies, *Poster Session No. 50, 30th ICCE*, San Diego, California, USA.

28. Komar, P.D.; Miller, M.C. (1973). The threshold of sediment movement under oscillatory water waves, *Journal of Sedimentary Petrology* 43: pp. 1101−1110.

29. Göransson, G.; Larson, M.; Althage, J. (2014). Ship-Generated Waves and Induced Turbidity in the Göta Älv River in Sweden, *Journal of Waterway, Port, Coastal, Ocean Engineering*: doi:10.1061/(ASCE)WW.1943-5460.0000224.

9 AUTHORS' BIOGRAPHIES

Sebastian Niehüser, M.Sc., is the lead author of this paper and research associate of the Research Institute for Water and Environment at the University of Siegen. He is responsible for engineering as well as research projects in the field of extreme value analysis, probabilistic methods and flooding risks at coastal and inland sites. Since 2014 he is working on issues in relation to the interactions between the ship-induced stress and the corresponding sediment transport within the research project SeST.

Marius Ulm, M.Sc., is a research associate at the Research Institute for Water and Environment of the University of Siegen. He is responsible for research and engineering projects in the field of coastal and inland hydraulic engineering. In particular, he is mainly involved in the SeST research project from which the presented outcomes result from. His previous experience includes data and time series analysis as well as numerical modeling.

Arne Arns, Dr.-Ing., is employed at the Research Institute for Water and Environment (fwu) of the University of Siegen. He is currently Research Fellow and team leader of the coastal extremes group. He has experience in publishing scientific results, teaching, engineering and applying for, working on, and coordinating research projects.

Jürgen Jensen, Prof. Dr.-Ing., has a full professorship in Hydraulics, Hydraulic Structures and Coastal Engineering at the University of Siegen and is head of the Research Institute Water and Environment (fwu). His experience ranges from coastal engineering, probabilistic and statistical methods, physical and numerical models for the optimization of hydraulic and coastal structures to ship waves and interactions with the waterways.

Vitalij Kelln, Dipl.-Ing., holds the current position of a research associate at the Research Institute for Water and Environment (fwu) at the University of Siegen. He is responsible for the research project SeST, hydraulic engineering projects, and teaching of hydrodynamic numerical modeling. His previous experience includes

time series analysis, extreme value statistics, and hydrodynamic numerical modeling.

Klemens Uliczka, Dr.-Ing., holds the current position of Senior Research Engineer at the Federal Waterways Engineering and Research Institute (BAW), Hamburg Office, Germany. He is responsible for the task of interaction ship/waterway at the coastal department. His previous experiences include coastal engineering, tidal dynamic in estuaries and design of banks and revetments at approach channels.

Bernhard Kondziella, Dipl.-Ing (FH), holds the current position of Research Engineer at the Federal Waterways Engineering and Research Institute (BAW), Hamburg Office, Germany. He runs investigations about the interaction ship/waterway at the coastal department and since 2011 he is responsible for the field measurements in the research project SeST. His previous experiences include model and field measurements in estuaries and approach channels.

4th MASHCON, Hamburg - Uliczka et al. (eds) - © 2016 Bundesanstalt für Wasserbau ISBN 978-3-939230-38-0 (Online)
DOI: 10.18451/978-3-939230-38-0_4

SHIP MANOEUVRING BEHAVIOUR IN MUDDY NAVIGATION AREAS: STATE OF THE ART

G Delefortrie, Flanders Hydraulics Research, Belgium
M Vantorre, Ghent University, Belgium

SUMMARY

The manoeuvring behaviour of vessels is highly affected by their small under keel clearance in access channels and harbours. If sedimentation and the formation of mud layers occur in these areas the manoeuvring behaviour becomes even more challenged, especially because the exact location of the bottom is not unequivocally determined. In such areas the nautical bottom definition, as stated by PIANC, is useful: *The nautical bottom is the level where physical characteristics of the bottom reach a critical limit beyond which contact with a ship's keel causes either damage or unacceptable effects on controllability and manoeuvrability.* Over the past decades research has been focussing on both the determination of the physical characteristics of the mud and the manoeuvring behaviour in such areas. The paper tends to give an overview of this research and of practical applications in harbours worldwide, and to provide an outlook for future research.

NOMENCLATURE

A	ship's cross section area (m²)
g	gravity constant (m/s²)
h	depth (m)
h^*	hydrodynamically equivalent depth (m)
L_{PP}, L_{OA}	ship length (m)
m	blockage (-)
U	ship speed (m/s)
W	channel width (m)
z_A	sinkage aft perpendicular (m)
z_F	sinkage fore perpendicular (m)
η	dynamic viscosity (Pa.s)
ρ	density (kg/m³)
τ_y	yield stress (Pa)
Φ	fluidization parameter (-)

Subscripts

1	denotes water layer
2	denotes mud layer

1 INTRODUCTION

When studying the manoeuvring behaviour of vessels in shallow water the bottom of a harbour or access channel is almost always considered to be solid. In reality this is not always the case. Due to the erosive effect of the currents in rivers, particles are transported over a certain distance until they settle again. If those settlements are concentrated in a certain area the formation of a mud layer is possible, depending on the grain size. To avoid excessive formation of mud layers maintenance dredging works are needed so that a minimal under keel clearance can be guaranteed.

The question arises how much of the present mud layer has to be dredged. The mud layer consists of a material, the characteristics of which change with the depth. In general mud characteristics like viscosity or density increase with increasing depth. Therefore the upper part of the mud layer can rather be considered as black water. If the ship's keel touches this upper part it is unlikely that any damage can occur; on the other hand, when a ship navigates above a mud layer an undulation of the water-mud interface can be observed. This undulation can possibly have adverse effects on the manoeuvring behaviour of the vessel.

For these reasons PIANC has introduced the nautical bottom concept [1, 2]: *The nautical bottom is the level where physical characteristics of the bottom reach a critical limit beyond which contact with a ship's keel causes either damage or unacceptable effects on controllability and manoeuvrability.* The nautical bottom concept can be applied to any bottom so that safety and manoeuvrability for the shipping traffic can be guaranteed.

A successful application of the concept implies knowledge on both the physical characteristics of the nautical (in this case muddy) bottom, as well as on the manoeuvring behaviour of the vessels in the vicinity of the nautical bottom. Although in this paper the focus will be more on the latter, some basic information on the behaviour of the mud and how to measure this behaviour will be given in the next paragraph. The remainder of the article will summarize the performed experimental and numerical research on the manoeuvring behaviour in muddy areas and how this information has been used to perform real-time simulations in different harbours all over the world. An outlook on future research and open research topics will be provided as well.

2 BEHAVIOUR OF MUD

2.1 MUD CHARACTERISTICS

Mud layers are formed due to the decrease of kinetic energy that causes sediment particles to deposit on the bottom of a channel. If an increasing amount of particles is settling down the base sediment layer will be subjected to increased pressure due to the weight of the upper layers. As a result water is expelled from the base layers and

the sediments are compacted. This process is called consolidation and depends on the variation of permeability, which is the water flux through a unit gross sectional area, and the effective stress, which is the total stress minus pore water pressure [3]. On the other hand, the disturbances in the upper water layer, caused by e.g. currents, waves, shipping traffic, also affect the mud layer characteristics; the fraction of water in the mud layer can consequently increase. This phenomenon results in the opposite effect of consolidation, and is usually called liquefaction (driven by shear stress) or fluidization (driven by fluctuating pore pressure). The combination of these phenomena with internal transports within the mud layer results in the formation of a mud layer with characteristics changing with the depth. One important aspect of the different conditions of the mud layer is that its behaviour not only is location and time dependent, but also varies according to its recent deformation history. The latter is also known as thixotropy. This is also of importance when the rheology of the mud layer has to be measured. An example is shown in Figure 1, where the yield stress decreases with the number of cycles of increasing and subsequently decreasing shear rate.

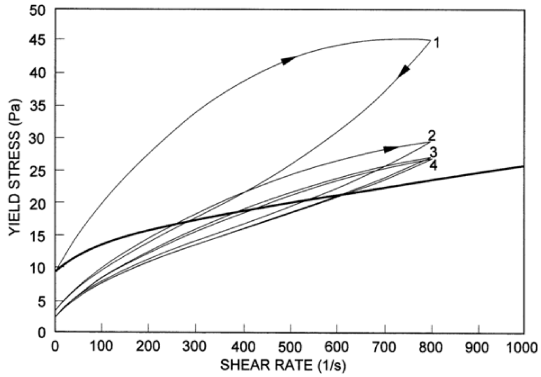

Figure 1. Measuring the rheology of hectorite. Adapted from [4].

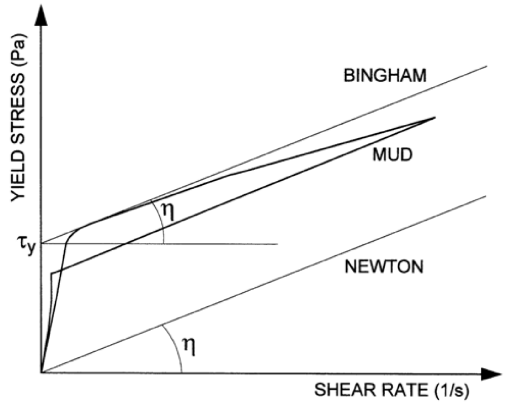

Figure 2. Classification of fluids based on their rheology behaviour.

Another point of interest is the initial yield stress or rigidity. In order for the mud to move an initial resistance has to be overcome. Such a behaviour can be characterized by a Bingham fluid, contrary to a Newton fluid like water, see Figure 2. For numerical purposes the Bingham model, determined by two parameters, is still too simple. More appropriate models could be used, such as Worrall-Tuliani [5] or Toorman [6], involving up to five parameters. A detailed explanation of such models falls outside the scope of this article.

The actual behaviour of the mud highly depends of its composition, e.g. organic matter and sand content play an important role.

2.2 MEASURING TOOLS

2.2 (a) Echo-sounding

In 2012 a questionnaire was organized on the use of in situ measurements to assess mud characteristics [7]. The results cannot be interpreted as real market share, but in 63% of the cases echo sounding was used to determine the nautical bottom. This high percentage can be ascribed to the simple setup. An electromagnetic wave is emitted that reflects at the bottom. The time between emission and reception and the intensity of the received wave is then a measure for the local depth. The frequency of the wave is closely related to its sensitivity for reflection. In case of a soft mud layer on the bottom, a high frequency echo of 210 kHz will reflect on top of the water-mud interface. A lower frequency (e.g. 33 kHz) will reflect at a level somewhat deeper into the mud (Figure 3). However it is unclear whether this corresponds to the position of the nautical bottom.

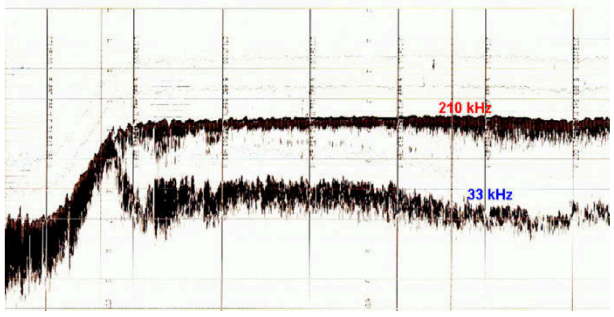

Figure 3. Example of an echo-sound result in the harbour of Zeebrugge [8].

2.2 (b) Monitoring the mud density

The density of the mud layer can be measured with a variety of methods. The acoustic method is based on the relationship between the propagation of sound in a fluid and the density of that fluid. A more accurate method is the nuclear method, which is based on the behaviour of gamma-radiation in mud suspension.

The measurement of the density of the mud can mostly be automated and results are typically presented in combination with echo-sounding, as shown in Figure 4. According to the questionnaire [7], a density based method is used in 31% of the cases.

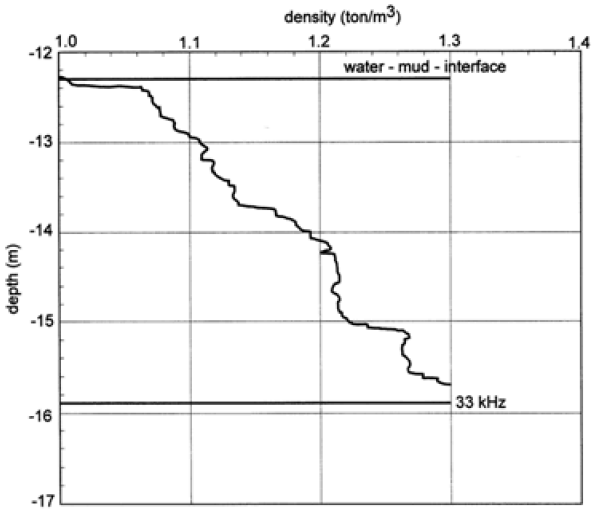

Figure 4. Density profile in function of the water depth.

2.2 (c) Monitoring the mud rheology

Rheology measurements commonly focus on the measurement of the yield stress (viscosity measurement). These measurements are mostly more labour intensive, because single point measurements have to be carried out and post-processing of the measurements is needed to take account of the thixotropic and hysteresis of the mud. For that reason only a small percentage in [7] uses rheology like methods.

2.2 (d) Ongoing research

At present none of the mentioned tools is capable of capturing the actual physical limit in the fluid mud layer. For this reason FHR (Flanders Hydraulics Research) built a Sediment Test Tank [9] to better observe the behaviour of natural mud and to test the actual instruments on the market in a controlled environment. To determine the mud properties in an unequivocal way a measurement protocol has been established together with KU Leuven, dotOcean and Antea Group [10].

2.3 NAUTICAL BOTTOM CRITERION

Due to the complex structure and behaviour of the mud it is indeed difficult to find a straightforward physical limit. Moreover variations in time of the mud layer's characteristics require a rather continuous monitoring of this physical limit.

In most cases the mud density is used as a critical limit. This does not mean that mud density is the critical parameter, but that at a certain value of this density a rheological transition in the mud behaviour occurs, which is more easily monitored afterwards when linked to a density value, see Figure 5 for an example in the port of Zeebrugge. In Zeebrugge, the critical density was initially decided to be 1.15 ton/m³, but was later increased to 1.20 ton/m³. Other examples of this approach are Rotterdam (1.20 ton/m³), Nantes (1.20 ton/m³), Paramaribo (1.23 ton/m³), Bangkok (1.20 ton/m³), Cayenne (1.27 ton/m³), and Chinese harbours (1.20 to 1.30 ton/m³) [11, 12].

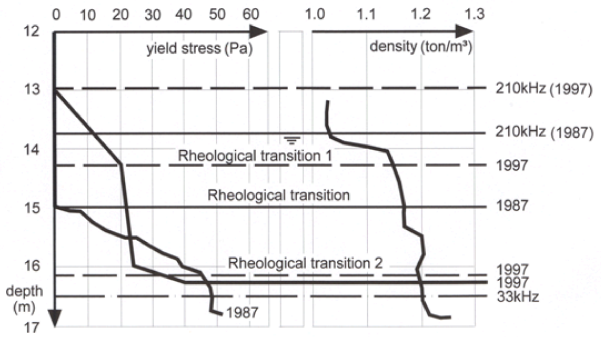

Figure 5. Rheology profile of the mud layer in the harbour of Zeebrugge. Comparison between the 1987 and the 1997 measurement campaign. The single curve for the density is illustrative.

In some harbours alternative methods are used; for instance, in Emden the focus is put on the organic content of the mud layer, which must remain large enough to limit the yield stress to 100 Pa. In this way the harbour remains navigable [13].

In all cases the measurement of mud layer characteristics implies simplifying the mud layer. On top of that most invasive measurement techniques change the characteristics of the mud layers [3].

3 EXPERIMENTAL RESEARCH

3.1 OVERVIEW

Experimental research on navigation in muddy areas is rather scarce. In this section a distinction will be made between model scale and full scale research.

3.2 MODEL SCALE

3.2 (a) Scaling

Since William Froude's experiments with small-scale tests on ship hulls in the 1860s, model tests have been playing an major role in understanding a ship's hydrodynamic behaviour. However, ship model tests have an important drawback: when the speed scale is selected in such a way that Froude's scale law is fulfilled, dynamic similarity will occur between the inertia forces and the gravity and pressure induced forces. A correct scaling of viscous forces, on the other hand, require Reynolds' scale law to be met, which is practically impossible when a free surface is present. In order to overcome this difficulty, empirical correction methods have been developed to deal with scale effects on e.g. resistance tests.

Accounting for the difficulties caused by the viscous effects due to the properties of a fluid with a rather sim-

ple rheology such as water, which as a Newtonian fluid can be characterised by its dynamic or kinematic viscosity as the only parameter, a correct scaling of the effects caused by the presence of a fluid mud layer, for which five parameters are required to describe the rheological characteristics in a proper way [6], is not realistic. Moreover, the mud characteristics should even be varied with the depth to model a realistic mud layer. Another difficulty concerns the thixotropy of the mud: the use of a thixotropic material during model tests would make it by definition impossible to perform systematic tests under constant bottom conditions. Most model tests for investigating the effect of the presence of fluid mud layers on a ship's hydrodynamics were therefore conducted with a homogeneous mud-simulating fluid with the correct density ratio with respect to the water in the test facility. For practical reasons, often a material with a Newtonian rheology is selected which is immiscible with water, which guarantees constant test conditions. Sometimes real mud or artificially composed mud has been used as well.

Summarized, model testing for investigating mud-ship interaction always implies an important simplification of the physical reality. Test results should therefore be interpreted cautiously.

In the remainder of this section, a brief summary will be given of the test programs conducted over the past 40 years with respect to the effect of mud layers on ship behaviour.

3.2 (b) MARIN (Wageningen, NL)

Both captive and free running model tests were carried out with a 1/82.5 scale model of a tanker sailing above or in contact with an artificial mud layer of rather small viscosity which was immiscible with water [14]. Two densities and up to three mud layer thicknesses were varied.

One important observation was the undulation pattern that occurred in the water-mud interface when a ship is passing. The amplitude of these undulations increases with the thickness of the mud layer and with decreasing mud density and affect the propeller efficiency as was observed during the free running trials.

3.2 (c) SOGREAH (Grenoble, F)

Model scale tests were conducted in a looped wave flume [15] with a scale model of a tanker (at different scale factors) focussing at resistance and squat variations above an artificially composed mud layer, with properties very close to natural mud. It is the only case where the tested mud layer included a density gradient over the depth; moreover, layers with different yield stresses were applied. Also in this case undulations of the water-mud interface had been observed which show the same behaviour.

3.2 (d) Flanders Hydraulics Research (Antwerp, B)

At FHR experimental research was carried out in three phases. In a first phase self-propelled tests were carried out with scale models of an LNG-tanker and a hopper dredger along a guiding rail above a mud-substituting layer with a negligible viscosity which was immiscible with water [16]. Mud density, mud layer thickness and water depth variations were included in the program. The undulations of the water mud interface could be linked to three different speed ranges (see 5.2). The reaction of the ship models due to these undulations was analogous to the observations by MARIN. Additionally, a limited number of similar model tests were conducted above an artificially composed mud layer, as well as a series of tests with a ship-like body towed above natural mud layers. Although the bottom layers were both miscible with water, similar tendencies were observed. Moreover, the water-mud interface appeared to be relatively stable under the ship; as mixing only occurred behind the ship, this only had a minor effect on ship behaviour.

A second, and more comprehensive research [17], was performed with an extensive captive test program with three different ship models (two container carriers and one tanker) in a variety of artificial muddy environments, including mud thickness variation, water depth variation, densities ranging between 1.10 ton/m³ and 1.26 ton/m³ and dynamic viscosities varying between 0.03 and 0.33 Pa.s (Table 1). During this program the undulations of the water-mud interface were also registered, and similar observations could be made, although the larger viscosity also plays a significant role.

Table 1. FHR: tested mud conditions on prototype scale [17]

Mud	Density [kg/m³]	Viscosity [Pa.s]
B	1179	0.10
C	1149	0.06
D	1108	0.03
E	1257	0.29
F	1206	0.11
G	1248	0.33
H	1207	0.19

An additional, third research specifically focussed on the effect of the muddy environments C and D on a container carrier equipped with a bow thruster [18]. This research was again carried out self-propelled, along a guiding rail.

3.2 (e) Bundesanstalt für Wasserbau (BAW, Hamburg, D)

BAW conducted model tests with a 1/40 scale model of a container vessel to study the sinkage and trim above highly concentrated natural mud [19].

3.3 FULL SCALE

3.3 (a) Rotterdam

In 1975 full scale tests were carried out with a 318 000 deadweight tanker (SS Lepton). The tests consisted of entering the harbour and monitoring the effect of the under keel clearance during a course change [20]. This was done by analysing the steering capacity, i.e. the maximal percentage of available rudder and propulsion and the speed of the vessel during the manoeuvre. The presence of undulations of the water-mud interface could be confirmed during the full scale tests.

3.3 (b) Zeebrugge

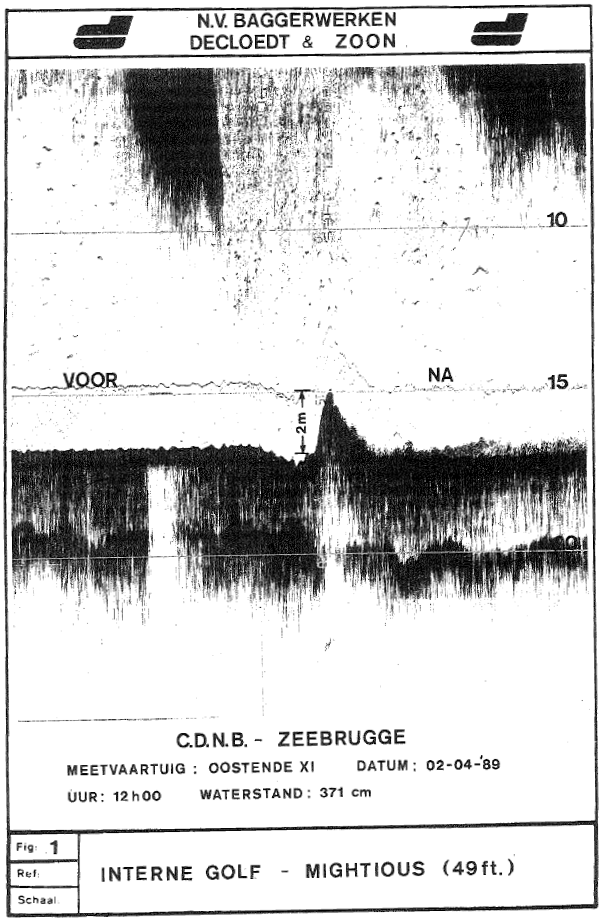

Figure 6. Full scale undulations of the water-mud interface measured in the port of Zeebrugge.

Full scale tests were carried out with the twin screw suction hopper dredger Vlaanderen XVIII (L_{OA} = 124 m) in 1986 and in 1988 [21]. Several test types were performed at under keel clearances varying between -0.35 m and +3 m referred to the water mud interface. It seemed possible to navigate through top mud, with a tested under keel clearance up till -0.35 m, without any major difficulties. On the other hand during one trial the ship became totally uncontrollable. During this trial the ship had intentionally hit the rheological transition level (the nautical bottom). Survey vessels were able to record internal waves in the mud-water interface by their high-frequency echo on several occasions, as illustrated by Figure 6, where a hydraulic jump with a height of about 2 m can be observed due to the passage of a deep-drafted OBO-carrier.

Since 2005 full scale monitoring of deep-drafted container carriers are carried out whenever possible to check the real-time manoeuvring models at FHR.

3.3 (c) Saint-Nazaire

Full scale runs were carried out in the Loire estuary with the tanker Alsace. A good agreement was found with the results of the model scale tests at SOGREAH.

3.3 (d) Delfzijl

In 2013 full scale trials were carried out with the general cargo vessel CSL Rhine in the port of Delfzijl to validate the conclusions from a simulator study [22]. Although tests were conducted at under keel clearances of 14% and larger referred to the top of the mud layer, it could be concluded that both the manoeuvring and propulsion behaviour was influenced by the mud layer at under keel clearances with respect to the water-mud interface smaller than 18%. In 2015 new full scale trials were carried out with the hopper dredger Geopotes 15 at a range of under keel clearances between +14% and -4% referred to the top of the mud layer. In general the ship's behaviour could confirm previous simulation studies [23].

4 NUMERICAL / THEORETICAL RESEARCH

The behaviour of mud has been studied empirically and theoretically by many authors, but mainly for hydraulic and morphologic purposes. Numerical theories have been used to study the ship behaviour in muddy navigation areas [24, 25] indicating that the mud response is especially important at rather slow speeds and that mud viscosity acts as an effective reduction in the total water depth.

The water-mud undulations seem to have a significant influence on the ship's behaviour. In [16] an expression for the critical speed was derived, based on an ideal fluid:

$$U_{crit} = \sqrt{\frac{8}{27} g h_1 \left(1 - \frac{\rho_1}{\rho_2}\right) (1 - m_1)^3} \qquad (1)$$

m_1 is the local blockage factor of the upper fluid layer:

$$m_1 = \frac{A_1}{W h_1} \qquad (2)$$

and A_1 is the ship's cross section area in the upper fluid layer.

Once the ship attains the critical speed, the jump on the water-mud interface occurs behind the ship's stern,

where it obstructs the inflow of propeller and rudder. The theory was confirmed with the model experiments where the viscosity of the mud layer was small (< 0.01 Pa.s).

Recently steps were taken to include the mud behaviour with an appropriate rheological model into CFD. As a first part of this project CFD computations with a cylinder towed through mud were compared with model tests at FHR where the same setup was used with a natural mud layer [26].

5 BEHAVIOUR OF A SHIP IN MUDDY AREAS

5.1 OVERVIEW

Based on experimental and numerical research an overview is given on the behaviour of a ship in muddy areas. In some cases mathematical models were developed for real-time simulation purposes, which will be discussed in paragraph 5.4. However, based on the evolution of the coefficients of these mathematical models, effects of the mud layer on the ship will be explained.

5.2 UNDULATIONS OF WATER – MUD INTERFACE

According to [16] three speed ranges can be detected for the behaviour of the water mud interface:

- At low speed a small sinkage near the fore body is detected, which disappears amidships and turns into an elevation abaft;
- At a certain speed value the sinkage at the entrance changes suddenly into an elevation. The section at which the jump occurs moves abaft with increasing speed;
- If the speed increases more, the rising of the interface occurs behind the stern. The amplitude of the elevation can exceed the mud layer thickness several times.

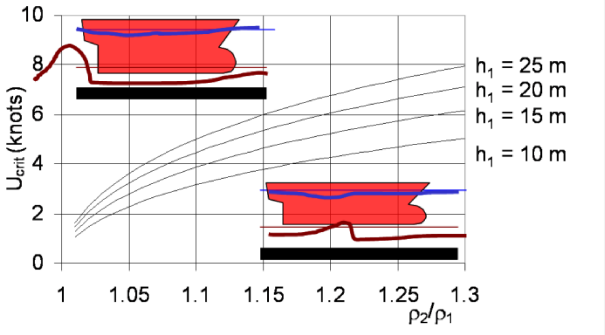

Figure 7. Critical speed in function of water depth and mud density.

The latter occurs at a speed which is given by equation 1 for inviscid fluids. The evolution of this speed is shown in Figure 7. For common manoeuvring speeds in harbour areas, the ship always seems to be in the critical range. However, for larger mud viscosities, equation 1 does not seem applicable [27]. When sailing above the mud layer, the amplitude of the rising is only significant if the viscosity drops below a certain critical value somewhere between 0.12 and 0.18 Pa.s, see Figure 8. Disregarding the viscosity the risings are always significant once the ship's keel touches the mud layer.

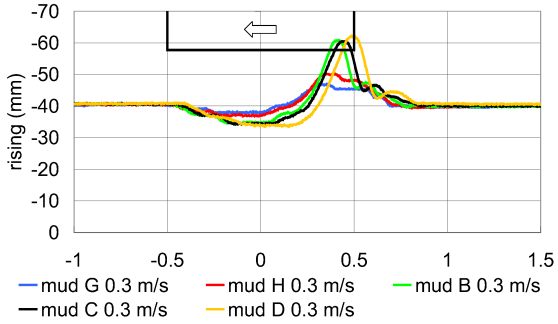

Figure 8. Rising of the water mud interface when a container carrier sails at an under keel clearance of 10% above the top of the mud layer.

The propagation pattern also seems to be influenced by both the viscosity and the speed. At lower speeds, the undulation crests are approximately perpendicular to the ship's heading in case of mud layers with low viscosity (< 0.12 - 0.18 Pa.s), while at higher speeds the undulations seem to behave as a Kelvin pattern (see Figure 9). The perpendicular pattern is observed over a larger speed range in case of mud layers with larger viscosities (> 0.12 - 0.18 Pa.s). The transition between both patterns occurs at a higher speed in case of mud layers of higher viscosity. A more viscous mud layer clearly requires larger speeds to have a critical influence.

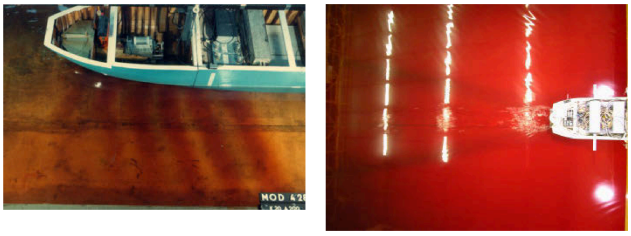

η = 0.002 Pa.s η = 0.030 Pa.s

Figure 9. Propagation pattern of undulations of the water-mud interface.

5.3 SHIP'S SQUAT

The behaviour of the sinkage and trim of a vessel in muddy areas is closely related to the undulations of the water-mud interface [27].

When a ship navigates with a small under keel clearance above the mud, contact can occur between the undulating mud-water interface and the ship's keel. The mud will yield a small increase of buoyancy, which results in a small decrease of the sinkage. Sailing in contact with the mud will always generate an increase of buoyancy, see Figure 10. For an equal total depth, the sinkage is thus larger above a solid bottom than above a muddy bottom. At somewhat higher speed, however, an increase of the

squat may be observed in case of negative under keel clearance with respect to the mud-water interface, as was observed during model tests at SOGREAH (Figure 11).

An interface rising will have the largest influence on the trim when it takes place amidships. The influence will decrease when the rising moves abaft. In all cases a larger rising causes a larger asymmetry and thus a larger trim compared to solid bottom conditions.

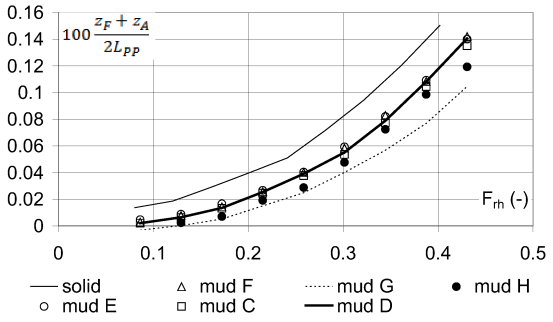

Figure 10. Sinkage in function of the ship speed. Thickness of the mud layer: 1.5 m full scale. No propeller or rudder action. -1.1% under keel clearance referred to the water mud interface [27].

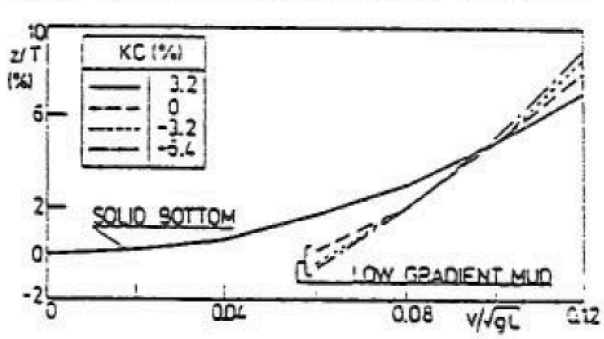

Figure 11. Sinkage in function of the ship speed for different under keel clearances related to low gradient mud. Thickness of the mud layer: 1.5 m full scale. Adapted from [15].

5.4 MATHEMATICAL MANOEUVRING MODELS

5.4 (a) MARIN

Based on the model tests performed at MARIN a mathematical manoeuvring model was developed [14]. The velocity derivatives resulted appreciably higher in muddy conditions (larger damping), while the increase of acceleration derivatives was merely ascribed to the small under keel clearance and not the effect of the mud layer.

Manoeuvres are slower in muddy areas, especially in case of a small positive under keel clearance referred to the water mud interface and when the rising of this interface is high, thus with smaller densities. The mud layer slackens the steady conditions while accelerating the dynamic ones, zigzag tests are for example carried out faster with mud on the bottom, while turning circles are larger in muddy conditions (Figure 12).

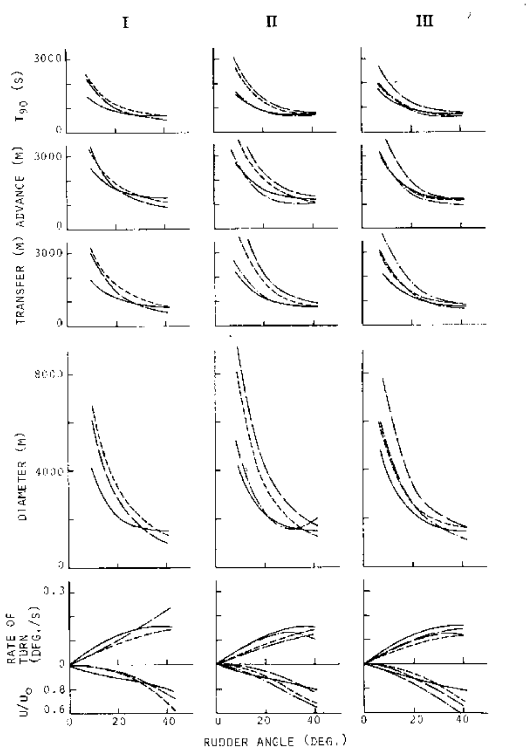

Group	Type of line	Mud: Density (kg/m³)	Mud: Thickness	Keel clearance: To mud	Keel clearance: To bottom
I	———	0	0	—	0·20 T
	- - - - - -	1140	0·07 T	0·15 T	0·22 T
	— — —	1140	0·13 T	0·10 T	0·23 T
II	———	0	0	—	0·20 T
	- - - - - -	1140	0·07 T	0·10 T	0·17 T
	— — —	1140	0·13 T	0·03 T	0·16 T
	— · — · —	1140	0·20 T	−0·03 T	0·17 T
III	— · · ———	0	0	—	0·20 T
	- - - - - -	1140	0·07 T	0·03 T	0·10 T
	— - - —	1140	0·13 T	−0·03 T	0·10 T
	— · — · —	1140	0·20 T	−0·10 T	0·10 T

Figure 12. Turning circles: effect of mud thickness [14].

5.4 (b) FHR

For each of the muddy environments that was tested during the second research phase coefficients of a full four quadrant modular manoeuvring model were determined [28].

The ship's resistance is characterized by a sharp increase once the ship's keel penetrates viscous mud layers. The acceleration derivatives not only increase significantly with decreasing water depth, but also with increasing mud density and viscosity, even if no contact occurs

between ship and mud. In general the presence of a mud layer tends to increase the shallow water effects.

The propeller wake increases above or in contact with low density mud layers, while it decreases in case of high density mud layers, which is in agreement with the behaviour of the undulations of the water-mud interface. A mud layer will always increase the propeller shaft torque, which means that the propeller efficiency decreases, especially when penetrating the mud. The asymmetry effect of a single propeller will also be more significant in muddy areas.

The rudder induced lateral force on the hull is significantly larger in muddy areas. At the same time its application point moves towards midships, so the larger lateral force does not yield a larger turning moment.

At slow speeds (smaller than 3 knots) the effect of a bow thruster seems to diminish once the keel touches a mud layer [29].

The mathematical models were intensely applied for fast-time and real-time simulations (see also 6.1). As an example, the results of turning circle manoeuvres is given in Figure 13, confirming the main conclusions of Figure 12.

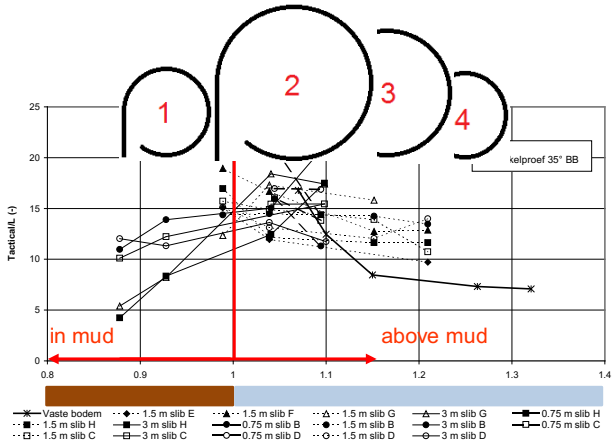

Figure 13. Turning circle tests (full to port) with a 6000 TEU container vessel: tactical diameter as a function of under keel clearance with respect to the mud-water interface for several mud layers [30].

5.5 HYDRODYNAMICALLY EQUIVALENT DEPTH

Based on the fact that the mud layer tends to increase the shallow water effect, a consolidated mathematical model was developed [27, 31, 32] which takes account of mud layer density, viscosity, thickness and water depth based on a hydrodynamically equivalent depth. With h_2 the thickness of the mud layer and h_1 the height of the upper lying water layer, the total depth can be written as:

$$h = h_1 + h_2 \qquad (3)$$

The bottom material can vary from water over soft mud to consolidated mud. If the mud has large viscosity and density values, like sand or clay, the material will hardly move when a ship passes by and its top can be considered as the actual seabed. In this case the hydrodynamically equivalent depth h^* is:

$$h^* = h_1 \qquad (4)$$

On the other hand if the material is very fluid the mud layer cannot be considered as a solid bottom. In the limit condition of two equivalent water layers, the hydrodynamically equivalent depth is:

$$h^* = h_1 + h_2 = h \qquad (5)$$

For intermediate situations a parameter Φ can be defined, so that:

$$h^* = h_1 + \Phi h_2 \leq h \qquad (6)$$

Particular values for the parameter Φ are 0 (hard layer of thickness h_2) and 1 (watery layer of thickness h_2), Φ represents consequently the degree of watery behaviour of the bottom layer and is therefore called the fluidization parameter.

Intuitively the fluidization parameter of the mud covering the seabed depends on the following aspects:

- the rheological properties (e.g. viscosity) of the mud: a decrease of the latter means a more fluid mud layer and will logically result in an increased fluidization parameter;
- the under keel clearance referred to the mud-water interface: the fluidization parameter increases when the ship's keel is located closer to the mud or penetrates the mud. In these conditions the mud layer is stirred and will behave more fluidly.

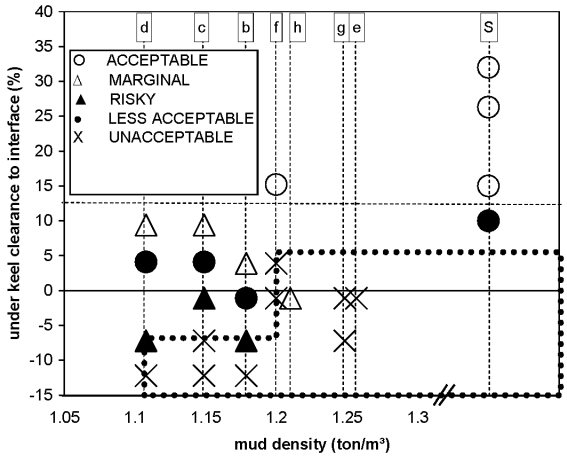

Figure 14. Real time simulations with a 6,000 TEU container carrier, assisted by two tugs of 45 ton bollard pull. Quantitative evaluation for the harbour of Zeebrugge, dotted area = "unacceptable".

6 REAL TIME SIMULATION PROJECTS

6.1 FHR

6.1 (a) Nautical bottom criterion in Zeebrugge

Based on the developed mathematical models [28], real-time simulations were carried out in 2004 [17] to check the position of the nautical bottom in the harbour of Zeebrugge. Based on this real-time simulation program the position of the nautical bottom changed from 1.15 ton/m³ to 1.20 ton/m³. The available tug assistance is critical for the penetration of the ship's keel in the mud, which should be limited to 7% of the ship's draft, see Figure 14.

6.1 (b) Updates to the simulation models

Since 2004 the manoeuvring models were continuously enhanced:

- In 2006 an algorithm was added to cope with the changing characteristics of a mud layer or with a transition from solid bottom towards muddy bottom [33].
- The consolidated model, based on the hydrodynamically equivalent depth, was added to the simulator in 2008.
- In 2010 the nautical bottom criterion was checked against the admittance of container carriers up to 400 m length in the port of Zeebrugge and the effect of mud on bow thrusters was added.

6.2 OTHER INSTITUTES

To the authors' best knowledge no other institutes have developed manoeuvring models in muddy areas to perform real time simulation research. On the other hand, the knowledge developed at FHR on ship behaviour in muddy areas has been used to enable other institutions to perform simulator studies to tackle local navigation problems. Some examples:

- On behalf of Alkyon (nowadays part of Arcadis), FHR suggested modifications to mathematical models for a container vessel, a bulk carrier and a towed barge to simulate manoeuvres in the approach to harbours in Brazil and Surinam.
- A real-time simulation study to investigate the feasibility of introducing the nautical bottom approach in the harbour of Delfzijl (The Netherlands) was performed at the FHR simulators in the frame of a study by Wiertsema & Partners on behalf of Groningen Seaports [23].
- On behalf of USACE, FHR suggested modifications to mathematical models for a tanker to simulate approach manoeuvres to the Calcasieu Ship Channel (USA) at the ERDC simulator facility in the frame of a project executed by RPS Group Plc.

7 CONCLUSIONS AND OUTLOOK

This paper intended to give an overview of the research that has been carried out since 1975 on the manoeuvring behaviour of ships in muddy navigation areas.

Despite the numerous research efforts on the manoeuvring behaviour in muddy navigation areas the question still remains how both parts of the nautical bottom definition by PIANC can be linked. It is still hard to tell what the physical limit is, and how it can be measured adequately in situ. Confirmation is needed whether this physical limit is linked to critical issues with the ship's controllability. It is rather doubtful that this critical limit can be summarized in a single parameter such as the mud density, which is however the most common practice to characterize the mud, besides the echo sounding.

Further research is still needed with regards to the measuring tools. At present each tool claims to measure a level which corresponds to the nautical bottom, but a convergence of the different levels is not reached yet.

The manoeuvring behaviour of the vessels in muddy navigation areas also needs further attention, however the limits of physical scale models are reached, as it is hard to address the influence of density and viscosity gradients and thixotropy on model scale. Therefore a start is made to try to implement the rheological behaviour of the mud into CFD. This is a long term project, as for now only the behaviour of a cylinder submerged in mud without water can be predicted [22].

8 REFERENCES

1. PIANC/IAPH (1997). Approach channels – A guide for design. Final report of the joint Working Group PIANC and IAPH, in cooperation with IMPA and IALA. *Supplement to PIANC Bulletin No. 95*: 108 pp.

2. PIANC (2014). Harbour approach channels design guidelines. Report no. 121, 309 pp.

3. Berlamont, J.; Ockenden, M.; Toorman, E.; Winterwerp, J. (1993). The characterisation of cohesive sediment properties. *Journal of Coastal Engineering* 21: pp. 105-128.

4. Toorman, E. (2005). Mud rheology: implications for navigability. *Workshop Nautical Bottom*, Flanders Hydraulics Research, Antwerp, Belgium, April 29, 2005.

5. Worrall, W.; Tuliani, S. (1964). Viscosity changes during the ageing of clay-water suspensions. *Trans. Brit. Ceramic Soc.* 63: pp. 167-185.

6. Toorman, E.A. (1997). Modelling the thixotropic behaviour of dense cohesive sediment suspensions. *Rheologica Acta* 36(1):56-65.

7. Kruiver, P.; Vermooten, S.; Rutten, G. (2012). Enquête: “De bevaarbare waterdiepte bij slibbodems.” *DELTARES report 1205981-004* (In Dutch).

8. De Brauwer, D. (2005). Maintenance dredging and bottom survey in the harbour of Zeebrugge. *Workshop Nautical Bottom, Flanders Hydraulics Research & Ghent University*, Antwerp, 2005.

9. Claeys, S.; De Schutter, J.; Vantorre, M.; Van Hoestenberghe, T. (2011). Rheology as a survey tool: "We are not there yet". *Hydro International* 15(3): pp. 14-19.

10. Claeys, S.; Staelens, P.; Vanlede, J.; Heredia, M.; Meshkati Shahmirzadi, M. E.; Van Oyen, T.; Van Hoestenberghe, T.; Toorman, E.; Verwaest, T.; Mostaert, F. (2015). Sediment Related Nautical Research: Rheological Measurement Protocol for cohesive sediment. Version 3.0. *WL Reports, 13_117*. Flanders Hydraulics Research & Antea Group, DOTocean and KULeuven: Antwerp, Belgium.

11. McAnally, W.; Teeter, A.; Schoellhamer, D.; Friedrichs, C.; Hamilton, D.; Hayter, E.; Shrestha, P.; Rodriguez, H.; Sheremet, A.; Kirby, R. (2007). Management of Fluid Mud in Estuaries, Bays, and Lakes. II: Measurement, Modeling, and Management. *Journal of Hydraulic Engineering*, Vol. 133, No. 1, pp. 23-38.

12. Lassere, J.L.; Collinet, M. (2003) Base Navale de Dégrad des Cannes (Cayenne) – Etude hydrodynamique et sédimentologique – Phase I, *BRGM/RP-52541-FR*, pp. 42.

13. Wurpts, R.; Torn, P. (2005). 15 Years Experience with Fluid Mud: Definition of the Nautical Bottom with Rheological Parameters. *Terra et Aqua* 99.

14. Sellmeijer, R.; Van Oortmerssen, G. (1983). The effect of mud on tanker manoeuvres. *The Royal Institution of Naval Architect*s, Spring Meetings 1983, paper no. 7.

15. Brossard, C.; Delouis, A.; Galichon, P.; Granboulan, J.; Monadier, P. (1990). Navigability in channels subject to siltation. *22nd International Coastal Engineering Conference*, Delft, The Netherlands: pp. 3088-3101.

16. Vantorre, M.; Coen, I. (1988). On sinkage and trim of vessels navigating above a mud layer. *The Royal Society of Flemish Engineers, Harbour Congress*.

17. Delefortrie, G.; Vantorre, M.; Verzhbitskaya, E.; Seynaeve, K. (2007). Evaluation of Safety of Navigation in Muddy Areas through Real-Time Maneuvering Simulation. *Journal of Waterway, Port, Coastal, and Ocean Engineering*, Vol. 133, No. 2: pp. 125-135.

18. Richter, J.; Vantorre, M.; Delefortrie, G.; Eloot, K.; Mostaert, F. (2009). Port of Zeebrugge - Determination of nautical bottom. Research on nautical implications: Model trial setup and test program. *Version 2_0. WL Reports, 582c*. Flanders Hydraulics Research & Gent University: Antwerp, Belgium.

19. Uliczka, K. (2005). Investigations of the BAW to the nautical bottom. *Workshop Nautical Bottom*, Flanders Hydraulics Research, Antwerp, Belgium, April 29, 2005.

20. Van Bochove, G.; Nederlof, L. (1978). Vaargedrag van diepstekende schepen in slibrijke gebieden. *De Ingenieur*, volume 91, no 30/31: pp. 525-530. (In Dutch).

21. Kerckaert, P.; Vandenbossche, D.; Malherbe, B.; Druyts, M.; van Craenenbroeck, K. (1988). Maintenance dredging at the port of Zeebrugge: procedures to achieve an operational determination of the nautical bottom. *The Royal Society of Flemish Engineers, Harbour Congress*.

22. Verwilligen, J.; Vantorre, M.; Delefortrie, G.; Kamphuis, J.; Meinsma, R.; van der Made, K.J. (2014). Manoeuvrability in proximity of nautical bottom in the harbour of Delfzijl, *33rd PIANC World Congress - Navigating the new millennium*, San Francisco, USA.

23. Barth, R.; van der Made, C.; Bourgonjen, L.; van Dijken, J.; Vantorre, M.; Verwilligen, J. (2016). Manoeuvring with negative underkeel clearance – 2nd full scale field test in the port of Delfzijl. *4th International Conference on Ship Manoeuvring in Shallow and Confined Water (MASHCON)*, Hamburg.

24. Doctors, L.J.; Zilman, G.; Miloh, T. (1996) The influence of a bottom mud layer on the steady-state hydrodynamics of marine vehicles. *21st Symposium on Naval Hydrodynamics*: pp. 727 – 742.

25. Wu, G.X. (1993) The representation of a body advancing in a stratified fluid by singularity distribution, *International Shipbuilding Progress*, Vol. 40, No. 422: pp. 127-135.

26. Toorman, E.A.; Vandebeek, I.; Liste Muñoz, M.; Heredia, M.; Rocabado, I.; Vanlede, J.; Delefortrie, G.; Vantorre, M.; Meersschaut, Y. (2015). Drag on an object towed through a fluid mud layer: CFD versus experiment. *INTERCOH2015: 13th International Conference on Cohesive Sediment Transport Processes*, Leuven, Belgium. VLIZ Special Publication, 74: pp. 114-115.

27. Delefortrie, G.; Vantorre, M.; Eloot, K.; Verwilligen, J.; Lataire, E. (2010). Squat prediction in muddy navigation areas. *Ocean Eng.* 37(16): pp. 1464-1476. dx.doi.org/10.1016/j.oceaneng.2010.08.003.

28. Delefortrie, G.; Vantorre, M.; Eloot, K. (2005). Modelling navigation in muddy areas through captive model

tests. *J. Mar. Sci. Technol.* 10(4): pp. 188-202. dx.doi.org/10.1007/s00773-005-0210-5.

29. Verwerft, B.; Vantorre, M.; Delefortrie, G.; Eloot, K.; Mostaert, F. (2010). Port of Zeebrugge - Determination of nautical bottom. Research on nautical implications: Regression Model from Trials. *Version 2_0. WL Reports, 582c*. Flanders Hydraulics Research & Ghent University: Antwerp, Belgium.

30. Lataire, E. (2014). Effect of fluid mud on navigation of deep-drafted vessels. *Seminário Internacional em Portos e Hidrovias*, Rio de Janeiro, 10 a 12 de setembro 2014. pp. 46 slides

31. Delefortrie, G.; Vantorre, M. (2009). Prediction of the forces acting on container carriers in muddy navigation areas using a fluidization parameter. *Journal of Marine Science and Technology* 14(1): pp. 51-68. dx.doi.org/10.1007/s00773-009-0041-x.

32. Delefortrie, G.; Vantorre, M. (2009) Modelling propeller and rudder induced forces acting on deep drafted vessels in muddy navigation areas. *Journal of Marine Science and Technology* 14(2): pp. 171-184. dx.doi.org/10.1007/s00773-009-0045-6.

33. Vander Donckt, S.; Vantorre, M. (2006). Bepaling van de nautische bodem in de haven van Zeebrugge. Onderzoek nautische implicaties. Fase C: validatie concept nautische bodem. *Third preliminary report. Research project UGent 174F5605, WL Mod. 582C*. Ghent / Antwerp, 2006. (In Dutch).

9 AUTHORS' BIOGRAPHIES

Guillaume Delefortrie, naval architect, is expert nautical research at Flanders Hydraulics Research. Manoeuvring behaviour of container carriers in muddy navigation areas was the subject of his PhD thesis. He is in charge of the research in the Towing Tank for Manoeuvres in Shallow Water and is secretary of the 27th and 28th ITTC Manoeuvring Committee.

Marc Vantorre, naval architect, is full senior professor of marine hydrodynamics and head of the Maritime Technology Division at Ghent University, Belgium. His research focuses on ship behaviour in shallow and confined waters, mainly in close co-operation with Flanders Hydraulics Research in Antwerp. He is member of PIANC Working Groups and former member of the ITTC Manoeuvring Committee. The investigation of manoeuvring behaviour in muddy areas has been a topic throughout his career.

4th MASHCON, Hamburg - Uliczka et al. (eds) - © 2016 Bundesanstalt für Wasserbau ISBN 978-3-939230-38-0 (Online)
DOI: 10.18451/978-3-939230-38-0_5

NUMERICAL ANALYSIS OF THE FLOW IN THE GAP BETWEEN THE SHIP HULL AND THE FAIRWAY BOTTOM IN EXTREMELY SHALLOW WATER

I Shevchuk, University of Rostock, Germany
C-U Böttner, Federal Waterways Engineering and Research Institute, Germany
N Kornev, University of Rostock, Germany

SUMMARY

The paper presents the results of the computational study on the flow around a Post-Panamax container ship cruising in a restricted shallow channel in model scale. The study aimed next to numerical prediction of dynamic sinkage and trim at the analysis of the flow regime in the gap between ship's hull and waterway's bottom.

NOMENCLATURE

L_{wl}	Waterline length (m)
ρ	Density of water (kg/m^3)
B	Ship beam (m)
T	Ship draft (m)
h	Fairway depth (m)
λ	Model scale (-)
U	Ship speed (m/s)
S_B	Squat at the bow (m)
S_H	Squat at the stern (m)
y^+	Dimensionless wall distance (m)

1 INTRODUCTION

Through years of experimental tests in model scale to predict ship induced wave loads on bank protection in channels and waterways at BAW, a comprehensive collection of squat measurements had grown, allowing to draw some principal and systematic conclusions on the squat effect in shallow and restricted waters. One was the observation of a significant increase of the trim angle when water depth to draft ratio is decreased to less than h/T = 1.3. Change in the flow regime was suspected to be responsible for this effect. In order to avoid the complicated experimental investigations it was decided to utilize computational methods to gain an insight into the flow regime and underlying mechanisms of the described effect. In the presented research a series of computations covering a representative range of h/T and different ship speeds were performed using both RANS and a scale-resolving approach - the hybrid RANS/LES model of Kornev et al. [1]

2 CONSIDERED PROBLEM AND COMPUTATIONAL SETUP

2.1 MODEL PARAMETERS

The model PPM55 used for the simulations corresponds to a Post-Panamax container ship to the scale 1:40. The parameters of the model are presented in the Table 1. In this research the bare hull without propeller and rudder was investigated, even though in the experiment the model was self-propelled. Influence of propeller suction force on squat as well as the flow in the bottom is out of the scope of the current study and will be investigated in the further research.

2.2 FAIRWAY PARAMETERS

A symmetric channel with the flat bottom and the bank slope 1:3 was considered, which corresponds to the geometry, used in the BAW model basin for the experimental investigations of squat (see Fig.1). For the RANS calculations the channel depth was varied from h/T=1.15 to h/T=1.75, for hybrid calculations only the lowest value was studied. In order to keep the slope constant for different depths, the breadth of the channel was changed accordingly. The ship was assumed to move in the centre of the channel.

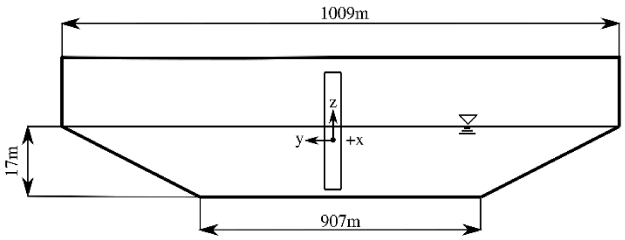

Figure 1. Channel geometry at the full scale, h/T = 1.06

Table 1. PPM55 Parameters

L_{wl}	8.89
B	1.375
T	0.4
C_B	0.689
λ	1:40

2.3 RANS SQUAT COMPUTATION SERIES

The RANS computations were performed for twenty five cases with the parameters listed in the Table 2. The corresponding range of Reynolds numbers is

$$4.3 \cdot 10^6 - 1 \cdot 10^7$$

Numerical solution was obtained using the quasi-steady state VOF-solver LTSInterDyMFoam, which is a development of the chair of modelling and simulation at the University of Rostock, based on a CFD toolkit

OpenFOAM. In the framework of the local time stepping (LTS) method the time step is not constant over the computational domain, rather than it is a scalar field, depending on the local Courant number. This way the solution process can be considerably speeded up, compared to unsteady formulation. The simulation started with the fixed ship attitude and after the convergence of the wave system the model was allowed to sink and trim. For turbulence modelling $k-\omega$ SST model of Menter was used with the automatic wall functions [4]. Unstructured hexa-dominant computational grids were generated by StarCCM® trimmer mesher with the average $y^+ = 40$. The middle line plane was considered a symmetry plane and thus only a half of the ship flow was calculated. For a half a ship meshes about 2M cells were produced. Computational cells near the ship hull had an isotropic cubic form with the edge length of 0.01m at the bow and at the stern and 0.02m in the cylindrical part of the hull. Cells, located at the free surface were refined down to 0.005m in vertical direction. At the inlet and the outlet of the domain the control volumes were stretched in longitudinal direction. Domain length was equal to $5L_{wl}$: $2L_{wl}$ in front of the model and $2L_{wl}$ after (it was chosen according to experience [2])

Table 2. Summary of the considered cases (U in m/s)

h/T \ U	1.15	1.2	1.3	1.5	1.75
0.48	RANS, RANS/LES	RANS	RANS	RANS	RANS
0.64	RANS, RANS/LES	RANS	RANS	RANS	RANS
0.81	RANS, RANS/LES	RANS	RANS	RANS	RANS
0.97	RANS, RANS/LES	RANS	RANS	RANS	RANS
1.13	RANS RANS/LES	RANS	RANS	RANS	RANS

Discretization of convective terms was done using linear upwind interpolation. Diffusive terms were approximated using Green-Gauss scheme with linear interpolation and explicit correction of mesh non-orthogonality. For time-stepping the Euler implicit scheme was employed.

The computational methodology described above had already been successfully applied for the prediction of squat in a restricted fairway [2]. For the description of the OpenFOAM VOF algorithm the reader is referred to [3].

2.4 HYBRID RANS/LES COMPUTATIONS

For the hybrid computations only five cases were selected (see Table 2). There were two reasons for this. First of all hybrid simulations should be conducted on finer meshes compared to RANS ones and therefore they are much more computationally expensive. The second reason is that the aim was to investigate the unsteady effects in the wake and these were assumed to be the most intense at the lowest h/T.

Simulations were carried out using the unsteady VOF solver interDyMFoam. Initial trim and sinkage as well as the initial conditions for velocity, pressure and volume fraction fields were obtained from the local time stepping solver (see section 2.3). As previously, the model was free to sink and trim, but this time rigid body dynamics was also taken into account. For the integration of the equations of rigid body dynamics second order leapfrog method was adopted. Coupling with fluid dynamics was performed in an iterative manner [5].

Since the symmetry condition cannot be applied for scale-resolving simulations, the mesh was constructed for the whole ship and contained about l3M cells. The average y^+ value was approximately 1. The gap between the ship hull and the fairway bottom was resolved using 35 cells, including viscous layers. No wall functions were applied. The viscous layers were also added to the channel bottom.

The RANS/LES turbulence model of Kornev et al. blends the Lilly's version of Germano subgrid stress model with the $k-\omega$ SST model of Menter depending on the ratio between the integral length scale and the local cell size. Details of the model implementation and validation can be found in [6] and will be omitted here. As it was described by some authors [7], application of upwind-biased schemes (even high-order) for the discretization of the convective term can influence the quality of hybrid simulations because of the increase of dissipation and therefore it is recommended to use centred schemes. Unfortunately the latter may become unstable in some regions of the flow and thus the blending between upwind and centred schemes is proposed, in which the blending factor depends on the local flow characteristics (strain rate, vorticity, turbulent viscosity, etc.) [7], so that the scheme turns to upwind in the RANS zone and to a centred one in the LES region. For all the hybrid simulations in the present study the convective term was discretized using the mixture of a second order linear upwind scheme with a centred one. The time stepping was performed by means of the Crank-Nicolson scheme. Diffusive terms were approximated in the same way as in RANS calculations (see Sec. 2.3).

3 RESULTS AND DISCUSSION

3.1 RANS RESULTS

Computational results for the squat effect at the bow and at the stern are presented in the Fig. 2 and 3. From the computed data one can identify the following tendency.

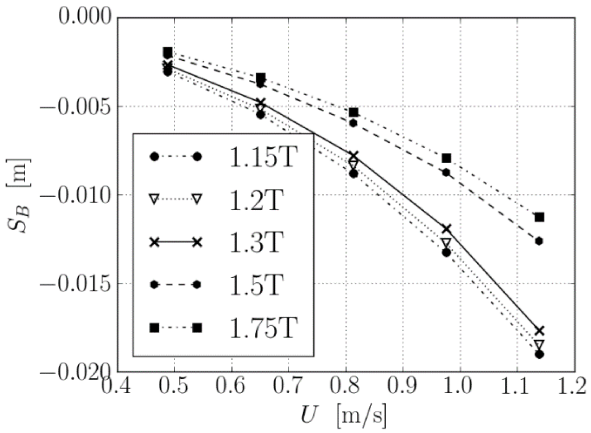

Figure 2. S_B of PPM55 at different speeds and depths

At the small speeds the ship is normally trimmed to the bow ($S_B > S_H$). With the increase of the speed the direction of the trim is changed to the stern. Already at 0.81m/s in all cases the trimming moment was negative. Further speedup of the ship caused the reduction of the under keel clearance (UKC) and the increase of the trim angle. As it is known, squat is in general intensified when the channel depth decreases and the speed increases, which means that the proper tendency was reproduced by the numerical method.

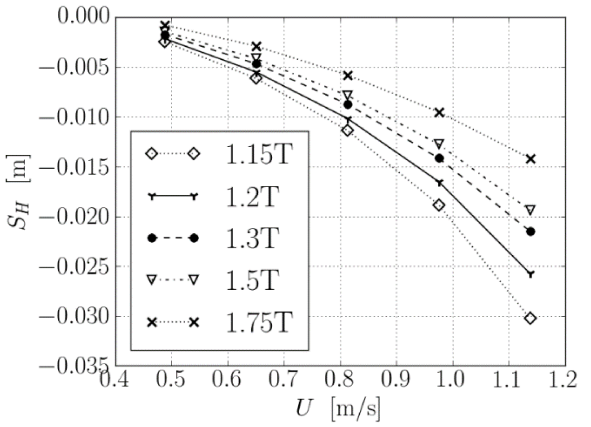

Figure 3. S_H of PPM55 at different speeds and depths

The most interesting results were obtained for the velocity distribution in the gap between the ship and the channel bottom.

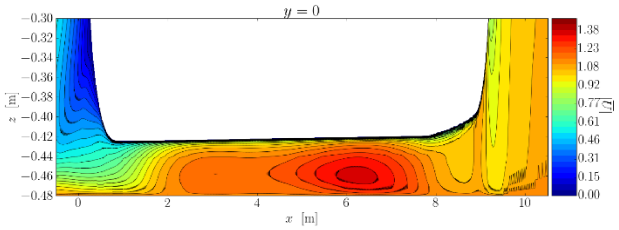

Figure 4. Velocity magnitude distribution at the middle line plane of PPM55 at h/T=1.15, U=1.13m/s. AP at x=0.

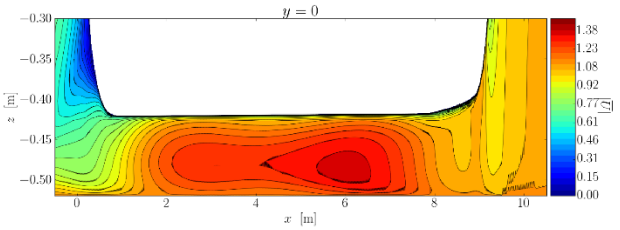

Figure 5. Velocity magnitude distribution at the middle line plane of PPM55 at h/T=1.3, U=1.13m/s. AP at x=0.

In Figures 4, 5 and 6, one can see the distribution of the velocity magnitude at the middle line plane at different depths at the speed of 1.13 m/s. In the presented figures the following phenomenon can be observed. At h/T = 1.75 one can distinguish two separate boundary layers growing in the gap: one on the bottom and one on the ship hull. As h/T decreases, these two get united so that there is no region, for which it could be stated that the viscous effects are negligible there (see Fig. 4). This phenomenon leads to the decrease of the flow velocity starting from the midship. Since the Bernoulli equation in its inviscid form

$$p + \frac{\rho u^2}{2} = const \qquad (1)$$

is no more applicable in this region, the deceleration of the flow does not lead to the increase of pressure and reduction of the trimming moment. Because of the pressure drop Δp due to viscous effects, pressure in the stern p_H decreases even stronger:

$$p_H = p + \frac{\rho(u^2 - u_H^2)}{2} - \Delta p \qquad (2)$$

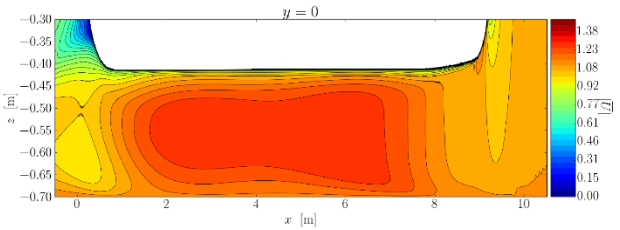

Figure 6. Velocity magnitude at the middle line plane of PPM55 at h/T=1.75. AP at x=0.

Thus, compared to the cases with higher h/T the trimming moment (which is mostly due to the low pressure at the stern) increased, even though the local velocity in the stern area became lower. If one takes the above discussion into account, it becomes clear, why the decrease of h/T results in a substantial trim change. One of the reasons for this is obviously the asymmetric distribution of the pressure loss relative to the midship.

One additional effect which deserves attention is the formation of the flow separation below the stern bulb at lower depths. The separation zone is pronounced in the Fig. 4 and 5 for h/T=1.15, h/T=1.3 respectively, whereas at h/T=1.75 only the moderate separation is observed. The longitudinal evolution of the flow in this separation

region can be seen in the Fig. 7. The boundary layer detaches at approximately x=1.5 and a separation bubble is built up downstream.

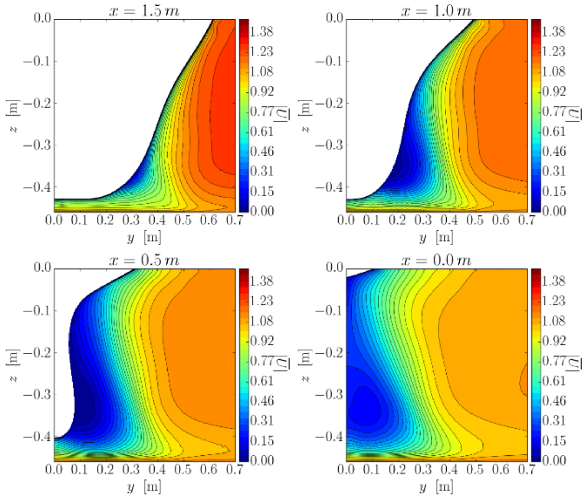

Figure 7. Velocity magnitude distribution at different x-slices in the ship stern. The development of the separation region can be observed. AP at x=0

It is known, that RANS models generally don't perform well in separation regions [8], and therefore in such cases application of hybrid methods or LES is recommended.

3.2 HYBRID RANS/LES RESULTS

In all the RANS/LES simulations periodic oscillations of the trim angle and the squat at the midship were observed.

The period of the oscillations was approximately equal to the eigenfrequency of the model hull and therefore one can say that the observed oscillations are physically adequate.

Since the hybrid simulations started from a RANS solution, it took some time till the instabilities are developed. In the Fig. 8 one can see an example of the time history of squat oscillations at the stern. It can be noticed that the oscillations are periodic ($T_o \approx 1s$) with the amplitude slightly changing in time.

For U=0.48, 0.65, 0.81 m/s the amplitude of S_H and S_B oscillations was approximately equal to 10% of the mean value. The maximum amplitude of fluctuations was observed for U = 0.97 m/s, where the amplitude reached about 50% of the mean value. Further increase of the ship speed led to the reduction of the fluctuation intensity to 3.5%. This stabilization of the ship dynamics can be of a numerical as well as of a physical nature. On the one hand when the gap between the ship and the bottom is getting narrower, the unsteadiness in the stern can become less intense because the amount of water passing under the ship will decrease and this can weaken the vortical structures.

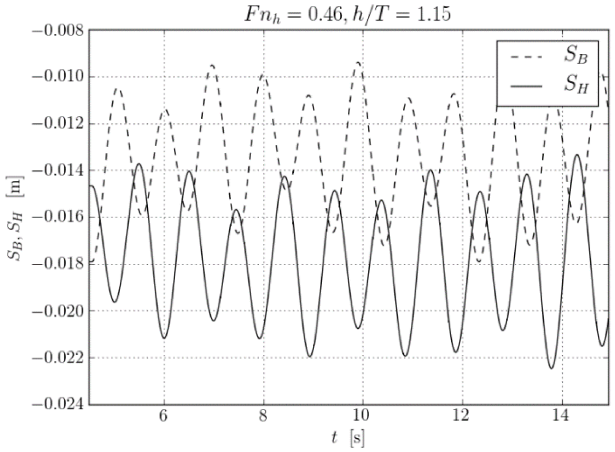

Figure 8. Time history of the stern squat oscillations for h/T=1.15 and U=0.97m/s (figures for other regimes are omitted in the present work)

On the other hand, the decrease of the gap size can force the hybrid model to switch to RANS in a broader region of the flow, causing in this way a stabilization. In order to clarify, which of these scenarios led to the observed effect, additional computations should be conducted. In most cases the application of the hybrid methods did not lead to considerable change of the mean trim and sinkage, even though the oscillations were observed. . The only exception is the case with U = 1.13 m/s, where S_B, S_H increased (signed value) by approximately 5%.

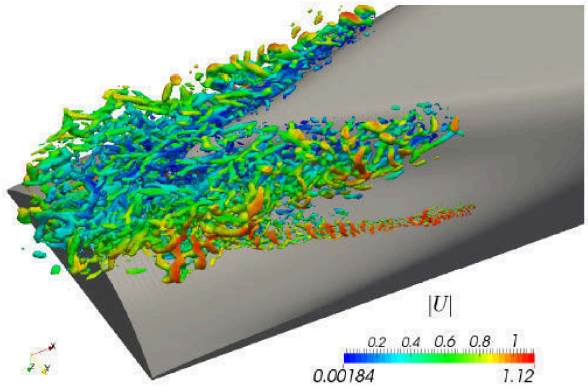

Figure 9. Instantaneous snapshot of the coherent structures at the stern of PPM55 at h/T=1.15, U=0.97m/s

Analysis of the vortical structures in the wake (see Fig 9) has revealed, that the unsteady behaviour of the ship was caused by the hydrodynamic effects. In RANS computations a separation region at the stern bulb was observed, but the dynamics of the bubble could not be resolved in time. On the contrary to RANS the hybrid method switched to LES in the stern region and this way the periodically detaching vortices were captured. These unsteady vortices caused the periodic fluctuations of forces and moments on the hull, which influence can be observed in the Fig. 8. The breadth of the region filled with eddies and the intensity of the latter point out that the hull oscillation amplitude is likely to be realistic.

Once the main part of the hybrid simulations was accomplished it was decided to carry out some additional numerical study in order to determine, whether the observed hull oscillations were caused by the unsteady separations or the flaws of the coupling between the fluid dynamics and rigid body dynamics. For this purpose a few additional RANS/LES simulations with the fixed ship attitude were carried out, during which the velocity fluctuations in the separation bubble were recorded at 3 points along the stern bulb.

The Fourier analysis of the recorded data for the separation bubble (see Fig. 10) with the fixed hull showed, that there is indeed a velocity fluctuation mode close to the eigenfrequency of the hull oscillations (around 1/s). This finding made the authors more confident that the observed unsteady behaviour of the ship had a physical background and was not a result of numerical instabilities.

Unfortunately, since no experimental data for the velocity in the ship wake is available it is hard to conclude, to which extent (quantitatively) the observed effect is close to reality. However, the experience shows, that sometimes during the towing tank as well as self-propelled trials under extreme shallow water conditions ship models can indeed noticeably oscillate.

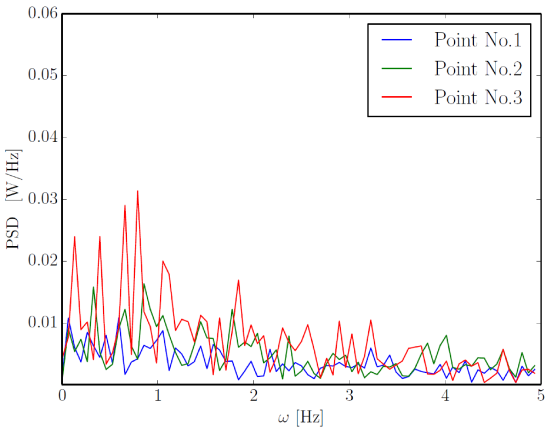

Figure 10. Power spectral density of the velocity fluctuations in the wake of PPM55

4 CONCLUSIONS

The presented paper describes the results of a series of RANS and RANS/LES computations of squat effect under extreme shallow water conditions. The main aim of the numerical study was to determine, which effects lead to the dramatic intensification of squat at $h/T < 1.3$, which is often observed in experiments. After the extensive analysis of the velocity distribution in the flow under the ship and pressure distribution along the hull at different motion regimes it was found out, that at low values of h/T the boundary layers, which grow on the ship hull and at the channel bottom unite, which causes the increase of pressure drop along the hull due to the intensified friction.

Additionally it was shown, that at low depths considerable separations occur in the stern region. Due to the high diffusivity of RANS closure models it is problematic to capture the influence of these separations on the dynamics of the hull. However, if a hybrid model is applied, the unsteady effects in the wake can clearly be seen and they lead to considerable oscillations of the model. Application of the hybrid approach, however, did not lead to any noticeable change in the average values of dynamic trim and sinkage.

5 ACKNOWLEDGEMENTS

The computational resources for the presented study were provided by the North-German Supercomputing Alliance (HLRN) and the German Research Foundation (DFG, grant INST 264/113-1 FUGG).

6 REFERENCES

1. Kornev, N.; Taranov, A.; Shchukin, E.; Kleinsorge, L. (2011). Development of hybrid URANS–LES methods for flow simulation in the ship stern area, *Ocean Engineering* 38: pp. 1831-1838. DOI: 10.1016/j.oceaneng.2011.09.024.

2. Shevchuk, I.; Kornev, N. (2013). Application of OpenFOAM to prediction of ship squat in restricted waterways. *Proc. of 16th Numerical Towing Tank Symposium*, Duisburg, Germany: pp. 147-152.

3. Damian, S.M. (2013). An Extended Mixture Model for the Simultaneous Treatment of Short and Long Scale Interface. *PhD Thesis,* Universidad Nacional del Litoral, Santa Fe, Argentina.

4. Menter, F.; Carregal Ferreira, J.; Esch, T.; Konno, B. (2003). The SST turbulence model with improved wall treatment for heat transfer predictions in gas turbines. In *Proc. of the International Gas Turbine Congress*: pp. 2–7

5. Xing-Kaeding, Y. (2006). Unified approach to ship seakeeping and maneuvering by a RANSE method, *PhD Thesis,* Technical University Hamburg-Harburg, DOI: 10.15480/882.238

6. Abbas, N.; Kornev, N.; Shevchuk, I.; Anschau, P. (2015). CFD prediction of unsteady forces on marine propellers caused by the wake nonuniformity and nonstationarity. *Ocean Engineering* 104: pp. 659–672.

7. Strelets, M. (2001). Detached eddy simulation of massively separated flows, *39th Aerospace Sciences Meeting and Exhibit*, DOI: 10.2514/6.2001-879

8. Spalart, P.R. (2000). Strategies for turbulence modelling and simulations, *International Journal of Heat and Fluid Flow* 21-3, pp. 252-263.
DOI: 10.1016/S0142727X(00)00007-2.

7 AUTHORS' BIOGRAPHIES

Ivan Shevchuk works at the chair of modelling and simulation at the University of Rostock as a PhD student. In the framework of his PhD research he investigates the unsteady hydrodynamic effects in the ship flow under shallow water conditions

Carl-Uwe Böttner, currently works as a Research Engineer with the Federal Waterways Engineering and Research Institute (BAW) in Hamburg on the fields of ship dynamics and ship handling simulation. He is responsible for consulting the authorities in terms of ship handling simulation.

Nikolai Kornev is the head of the chair of modelling and simulation at the University of Rostock.

4th MASHCON, Hamburg - Uliczka et al. (eds) - © 2016 Bundesanstalt für Wasserbau ISBN 978-3-939230-38-0 (Online)
DOI: 10.18451/978-3-939230-38-0_6

A SIMPLIFIED MANEUVERING PERFORMANCE OF A LARGE CONTAINER SHIP PASSING THROUGH THE SUEZ CANAL

Y You and **W Kim,** Daewoo Shipbuilding & Marine Engineering Co., Ltd., Republic of Korea

SUMMARY

In the Suez Canal, it have been consistently reported that ships collided with other ships or inner walls of the Canal, despite the maneuverability of the ships meet the IMO standards. Ship owners are requiring the ship design considering the maneuverability under restricted water, because they thought that those collisions resulted from bad execution in the Canal. In this paper, it is simply tried to evaluate the maneuvering performance to specify the design basis related to the rudder considering the maneuverability of the ship under restricted water such as the Suez Canal. The hydrodynamic coefficients at deep and shallow water are predicted based on the empirical formulae. The bank effects due the walls of the Canal are considered by analyzing the CFD calculation results using the parameters with reference to the empirical formulae. The index as a design basis is developed by evaluating the minimum relative distances between the ship and both walls of the Canal under prescribed environmental conditions.

1 INTRODUCTION

Most of ships in shipyards of South Korea sailing along a planned route in the ocean are large vessels such as container ship, liquefied natural gas carrier (LNGC), very large crude oil carrier (VLCC) et al. It is general that the ships have simplified sailing plan where complex maneuvering behaviors are minimized to secure ship handling safety. Therefore, hull, propeller and rudder design have been conducted by considering typical maneuvering test results such as course keeping ability and turning ability at design speed. For the designed ship, it should be shown whether the maneuverability meet the standards related to the initial turning test, 35° turning test, 10°/10° zigzag test and 20°/20° zigzag test recommended by the International Maritime Organization (IMO) [1]. It have been generally demonstrated using simulation, model test and sea trial. In shipyards, it is frequent that maneuvering performance of a ship is evaluated by simulation, because it is important to confirm whether the ship can meet the IMO standards or not, from the shipbuilding company's point of view. Kijima et al [2] conducted regression analysis based on the model test for various ships and predicted hydrodynamic coefficients of a ship using principal particulars. Based on the research, it is possible to predict maneuverability of a ship using limited information which can be obtained in the initial design stage. Lately, Sung and Park [3] conducted virtual captive model test using the computational fluid dynamics (CFD) and obtained the hydrodynamic coefficients. The maneuvering simulation results using the acquired coefficients are compared with those using coefficients obtained from the model test.

It has been enough to verify the maneuverability of the designed ship using the typical maneuvering test results if the ship has a simple sailing route. However, it is hard to judge the ship handling safety based on the typical test, if complex sailing conditions such as low speed, shallow water and restricted water are additionally included in the sailing plan for financial efficiency and security reasons. It is representative that a large vessel passes through the Suez Canal from Asia to Europe. In the Suez Canal, it have been consistently reported that ships collided with other ships or inner walls of the Canal, despite the maneuverability of the ships meet the IMO standards. Ship owners are requiring the rudder design considering the maneuverability under restricted water, because they thought that those collisions resulted from bad execution in the Canal. However, there is no way like IMO standards to judge the ship handling safety in the canal.

In this paper, it is tried to construct an evaluation method of the maneuvering performance to specify the design basis related to the rudder considering the maneuverability of the ship under restricted water such as the Suez Canal. First of all, a large container ship was chosen to investigate the maneuvering behavior under the restricted water, because there are in great demand for container ships passing through the Suez Canal. And, the hydrodynamic coefficients at deep and shallow water are predicted based on the empirical formulae proposed by Kijima et al [2, 4] and added mass and added mass moment of inertia are predicted based on the empirical formulae suggested by Hooft and Pieffers [5] and Meijing [6]. Rudder lift and drag coefficients are predicted based on the empirical formulae proposed by Fujii and Tsuda [7, 8]. In case of propeller thrust coefficients, they are obtained from the model test results for previous project in the Daewoo Shipbuilding and Marine Engineering Co., Ltd. (DSME). Environmental conditions for the Suez Canal are determined with reference to the sailing directions published by the National Geospatial-Intelligence Agency [9]. Maximum wind speed which is allowed for sailing ship in the Canal is 10.0 knots. The wind load coefficients of the large container ship are predicted using the empirical formulae proposed by Fujiwara [10] and irregular wind speeds are generated using Frøya spectrum proposed by Anderson and Løvseth [11]. The effect of the canal flow on the ship can be considered in the maneuvering equations of motion using the Hwang's method [12]. The bank effects

due the walls of the Canal are considered by analyzing the CFD calculation results using the parameters with reference to the empirical formulae proposed by Norbin [13]. To specify the design basis of maneuverability under the prescribed condition, it is assumed that the ship passes through along the virtual waypoints in the straight canal with same cross section. Rudders have to be controlled for the ship to go straight following the way points, because there are irregular winds, canal flows and bank effects. In the Suez Canal, it is prohibited to operate the autonomous navigation system. Therefore, the ship has to be controlled by a seafarer. To consider the control characteristics of the human seafarer, the fuzzy control proposed by Hasegawa [14] is applied. The maneuvering performance as a design basis is evaluated by calculating the minimum relative distances between the ship and both walls of the Canal under prescribed environmental conditions. The minimum distances for 3 hours obtained according to the wind directions. Four points, which are bow and stern end points in the port and starboard side of the ship, are decided as the reference points for the evaluation. For the reference points, the ship is assumed as a rectangle whose length is same with the length between perpendiculars and width is same with the breadth. Using the evaluated results, it is anticipated that the ship handling safety can be qualitatively compared under the given environmental conditions. In the future, it is possible to be developed as minimum requirement to ensure the performance of a ship which has to pass through any restricted water, after the values for ships in the collision accident are statistically investigated.

2 MODEL SHIP AND MANEUVERING EQUATIONS OF MOTION

As shown in Fig. 1, a large container ship with twin propellers and rudders was chosen in order to calculate the maneuvering behavior of the ship in the Suez Canal. Table 1 shows the principal particulars of the container ship. LCG indicates the distance of the longitudinal center of gravity from midship. In this study, maneuvering equations of motion as shown in equation (1) are solved to evaluate the maneuvering performance of the ship. In equation (1), m indicates the mass of the ship, and I_{zz} means the mass moment of inertia. u , v are the longitudinal and transverse speeds, and r is the rotational angular velocity. $\dot{u}$, $\dot{v}$ indicate the time derivatives of longitudinal and transverse speed. $\dot{r}$ is the time derivatives of angular velocity. X , Y is the longitudinal and transverse forces acting on the ship, and N is the yaw moment.

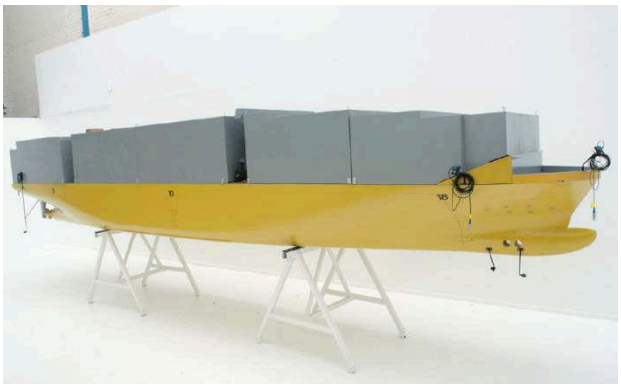

Figure 1. A model of the large container ship with twin propellers and rudders

Table 1. Principal particulars of the container ship

Item	Magnitude
Length overall [m]	About 400.0
Length between perpendiculars [m]	About 375.0
Breadth [m]	59.0
Draft [m]	16.0
Block coefficient [-]	0.700
LCG [m]	7.00
Propeller diameter [m]	9.50
Pitch at 0.7R [m]	6.700
Rudder area [m^2]	60.00
Aspect ratio [-]	1.50

$$\begin{aligned} m(\dot{u} - vr) &= X \\ m(\dot{v} + ur) &= Y \\ I_{zz}\dot{r} &= N \end{aligned} \tag{1}$$

Fig. 2 shows the coordinate system of this research. x_g , y_g indicates the global coordinate axis, δ is the rudder deflection angle. U means the ship speed. Ψ , Ψ_{wind} , $\Psi_{canal\ flow}$ are the heading angle of the ship, incident angle of wind and canal flow, respectively. V_{wind} , $V_{canal\ flow}$ are the speed of wind and canal flow.

The forces and moment acting on the ship can be expressed as equation (2). The subscript “H” indicates the hull of the ship, and “C” means the canal flow. The meaning of “H(C)” is that canal flow load acting on the hull is considered during the calculation of hydrodynamic loads acting on the hull [12]. “P”, “R”, “W” and “B” indicate loads due to the propellers, rudders, wind and bank effect.

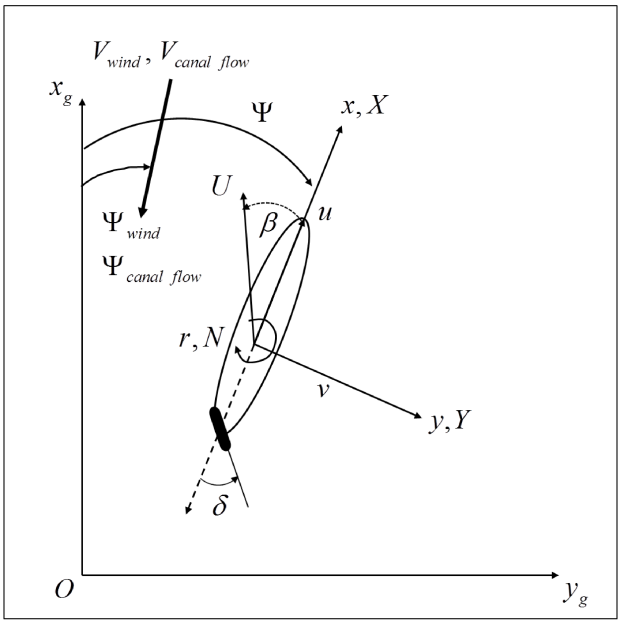

Figure 2. Coordinate system

$$
\begin{aligned}
X &= X_{H(C)} + X_P + X_R + X_W + X_B \\
Y &= Y_{H(C)} + Y_R + Y_W + Y_B \\
N &= N_{H(C)} + N_R + N_W + N_B
\end{aligned} \tag{2}
$$

Because the design of a ship is not confirmed in the initial design stage, it is impossible to acquire the detailed information, accurately. All hydrodynamic coefficients, added mass and added mass moment of inertia, and rudder lift coefficients are predicted using the empirical formulae to consider the limitation on the initial design stages [2, 4, 5, 6, 7, 8]. However, resistance coefficient and information related to propeller thrust are obtained from model test results for previous projects. Hydrodynamic loads are written as shown in equation (3). m_x , m_y indicate the added mass along the longitudinal direction and transverse direction. J_{zz} is the added mass moment of inertia. T means the draft of the ship. x_G indicates the LCG as defined in Table 1.

$$
\begin{aligned}
X_{H(C)} &= -m_x\dot{u} + (m_y + X_{vr})vr + \left(\frac{1}{2}\rho \cdot L_{pp} \cdot T \cdot U^2\right) \cdot X_{uu} \cos^2\beta \\
Y_{H(C)} &= -m_y\dot{v} + m_x ur + Y_H(v', r') \\
N_{H(C)} &= -J_{zz}\dot{r} + N_H(v', r') + x_G \cdot Y_H(v', r')
\end{aligned}
$$

where,

$$
\begin{aligned}
Y_H(v', r') &= \left(\frac{1}{2}\rho \cdot L_{pp} \cdot T \cdot U^2\right) \\
&\cdot \left(Y_v' \cdot v' + Y_r \cdot r' + Y_{vv}' \cdot v' |v'| + Y_{rr}' \cdot r' |r'| + Y_{vvr}' \cdot v'v'r' + Y_{vrr}' \cdot v'r'r'\right) \\
N_H(v', r') &= \left(\frac{1}{2}\rho \cdot L_{pp}{}^2 \cdot T \cdot U^2\right) \\
&\cdot \left(N_v' \cdot v' + N_r \cdot r' + N_{vv}' \cdot v' |v'| + N_{rr}' \cdot r' |r'| + N_{vvr}' \cdot v'v'r' + N_{vrr}' \cdot v'r'r'\right) \\
\beta &= \frac{-v}{\sqrt{u^2 + v^2}},\ v' = v/U,\ r' = r \cdot L_{pp}/U \\
X_{vr} &= \frac{\partial^2 X}{\partial v \partial r},\ X_{uu} = \frac{\partial^2 X}{\partial u \partial u},\ Y_v = \frac{\partial Y}{\partial v}, Y_r = \frac{\partial Y}{\partial r},\ Y_{vv} = \frac{\partial^2 Y}{\partial^2 v},\ Y_{rr} = \frac{\partial^2 Y}{\partial^2 r}, \\
Y_{vvr} &= \frac{\partial^3 Y}{\partial^2 v \partial r}, Y_{vrr} = \frac{\partial^3 Y}{\partial v \partial^2 r}, N_v = \frac{\partial N}{\partial v}, N_r = \frac{\partial N}{\partial r},\ N_{vv} = \frac{\partial^2 N}{\partial^2 v}, \\
N_{rr} &= \frac{\partial^2 N}{\partial^2 r},\ N_{vvr} = \frac{\partial^3 N}{\partial^2 v \partial r}, N_{vrr} = \frac{\partial^3 N}{\partial v \partial^2 r}
\end{aligned} \tag{3}
$$

3 PREDICTION OF ENVIRONMENTAL LOADS SUCH AS WIND, CANAL FLOW AND BANK EFFECT

The cross section of the Suez Canal is defined with reference to the cross sectional area proposed by the National Economic Development as shown in the Fig. 3. Actual cross section is not only same along the canal but also it is not straight. In this research, the geographical characteristics are simplified, even if actual cross section is not always identical. The canal section has two sloped walls whose angles are same at both sides. The width of the bottom is 121 m, and the width of the canal at mean water level is 313 m. And, the depth of the canal is 24m. It is assumed that virtual way points are located at the center of the width at mean water level. Because it is not wide enough to allow two-way passage, two convoys are scheduled to transit the Canal on a typical day, one southbound and northbound. Therefore, a ship always tries to move straight near center in the Suez Canal. Because the draft of the container ship is 16 m, the relative distances between the two reference points at starboard side and bank wall have to be larger than 64.0 m to prevent from colliding with the wall. Likewise, the relative distances between the two reference points at port side and bank wall have to be larger than 64.0 m, as well. Accordingly, the values can be regarded as indices which should be kept to a minimum. The values are defined as C_{STBD} and C_{PORT} .

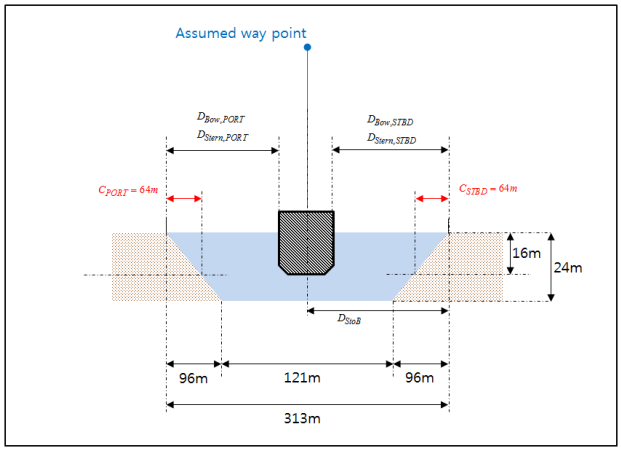

Figure 3. Design section of the Suez Canal

To consider the wind loads acting on the hull, wind load coefficients are obtained from the empirical formulae proposed by Fujiwara [10]. The values to predict the coefficients are shown in Table 2. The maximum allowed wind speed for sailing in the Suez Canal is 10.0 knots. HBR indicates the height to top of superstructure, C is the distance from midship section to center of the superstructure. H_C is the height to center of lateral projected area, AOD is the lateral projected are of superstructure. CBR is the distance from midship section to center of the superstructure. A_T, A_L are the transverse and lateral projected area, respectively.

To generate irregular wind speeds acting on the hull, Frøya spectrum proposed by Anderson and Løvseth is used. The spectral density function is shown in equation (4). U_0 is the 1-hour mean wind speed at 10 m in units of m/s, and z is the height above sea level in units of m. n is 0.468.

The spectral density considering the geographical characteristics of the Suez Canal is shown in Fig. 4. Fig. 5 shows the generated random wind speed based on the acquired spectral density function.

Table 2. Inputs of the large container ship to predict wind load coefficients proposed by Fujiwara (2001)

Item	Magnitude
Design wind speed [*knots*]	10.0
HBR [m]	43.0
C [m]	9.75
H_C [m]	24.7
AOD [m^2]	11445
CBR [m]	14.75
A_T [m^2]	17338.4
A_L [m^2]	3114.4

$$S_U(f) = 320 \cdot \frac{(\frac{U_0}{10})^2 (\frac{z}{10})^{0.45}}{(1+\tilde{f}^n)^{\frac{5}{3n}}} \quad (4)$$

$$(where, \tilde{f} = 172 \cdot (\frac{z}{10})^{\frac{2}{3}} \cdot (\frac{U_0}{10})^{-0.75})$$

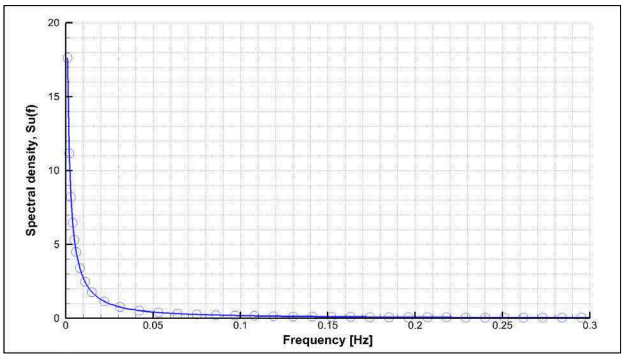

Figure 4. Spectral density of Froya Spectrum

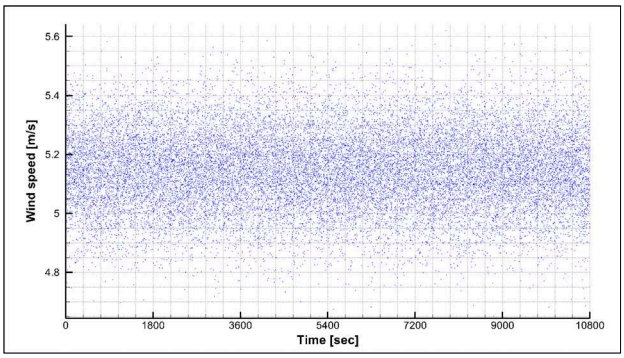

Figure 5. Generated random wind speed

In the canal, there can be canal flow according to the change of the water level in both ends of the Suez Canal. However, it is ignored in this research. Namely, still water condition is only considered.

Bank effect between hull and wall in the canal are obtained from CFD calculation. The loads due to bank effect can be acquired as follows. First of all, X, Y forces and N moment are calculated under the certain conditions with bank wall and they are marked as $X_{w/\ walls}$, $Y_{w/\ walls}$ and $N_{w/\ walls}$, as shown in Table 3. And the forces and moment, which are marked as $X_{w/o\ walls}$, $Y_{w/o\ walls}$ and $N_{w/o\ walls}$, are calculated under same conditions without bank walls. The differences between the values with bank walls and the values without bank walls are regarded as the loads due to the bank walls. And, they are marked as X_B, Y_B and N_B, as shown in equation (5). In this research, the the effect of X_B is ignored to simplify the analysis for the maneuvering performance in the Suez Canal.

Test matrix for CFD calculation written as shown in Table 3. According to the formulae proposed by Norbin, depth, inflow speed and distance from wall to hull are important

parameters. With reference to other research conducted by Ch'ng [15], it is aimed to investigate the effect due to the inflow speed and distance from wall to hull. In Table 3, D_{StoB} indicates the distance from the center line of the ship to the wall in the starboard side. In the empirical formulae proposed by Norbin, it was constructed for the wall in starboard side, only. However, there are two sloped walls in the Suez Canal. Accordingly, the parameter of the CFD calculation is modified with reference to the parameters proposed by Ch'ng [15].

Table 3. CFD calculation matrix to estimate the bank effect on the hull

Depth [m]	Inflow speed [knots]	D_{StoB} [m]
24	5.5, 7.5, 9.5	91.25
		104.3
		130.4
		156.5

In the CFD calculation, it is assumed that there is uniform flow with prescribed speed. In addition, it is assumed that there is no free surface effect acting on the hull. The meaning of no free surface indicates the submerged body is only affected by the canal flow. Namely, there are no waves induced by the hull. Of course, the disturbed free surface and generated waves affect the calculated forces and moment. In reality, the free surface effect is significantly related to the ship speed. Because the magnitude of the values which are induced by the ship moving with low speed may be small, it can be ignored. Fig. 6 shows an example of the pressure distribution on the ship bottom obtained by the CFD calculation. In the figure, there are four solid lines. The solid lines at the top and bottom are the boundaries in the Suez Canal at mean water level. The two lines in the middle show the boundaries at bottom in the Canal. Due to the wall effect acting on the ship bottom, the asymmetric pressure distribution can be observed. Accordingly, as the ship approaches on the wall, the calculated yaw moment have to increase. In the CFD calculation, the scale factor is 39.551, the number of meshes ar about 200 million. The Star CCM+ is used to calculate the bank effect as a CFD tool. A Reynolds-Averaged Navier Stokes (RANS) model with K-epsilon turbulence model is used for simulation.

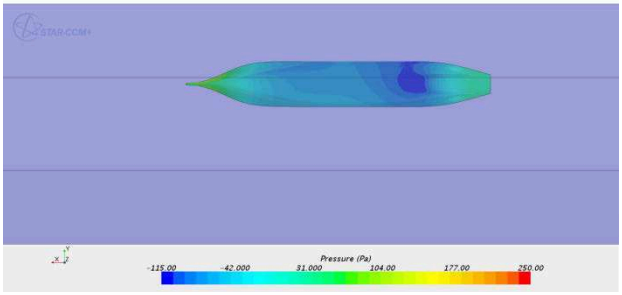

Figure 6. An example of the pressure distribution on the ship bottom obtained by the CFD calculation

To consider the Y forces and N moments due to the banks, the heading angle of the ship is ignored, because the deviation of the heading angle is small. Of course, the effect of heading angle is very significant. In this study, it is only aimed to construct the evaluation method of the maneuvering performance of the ship in the Suez Canal. Fig.7 and 8 show the calculated Y forces and N moments using CFD at 5.5, 7.5 and 9.5 knots. In the figures, the black squares, blue circles and red diamonds indicate the results at 5.5, 7.5 and 9.5 knots. In the calculation, the heading angle of the ship is zero. The acquired Y forces and N moment have increased, as the ship speed increases. Likewise, Y forces and N moment have increased, as the location of ship goes near bank.

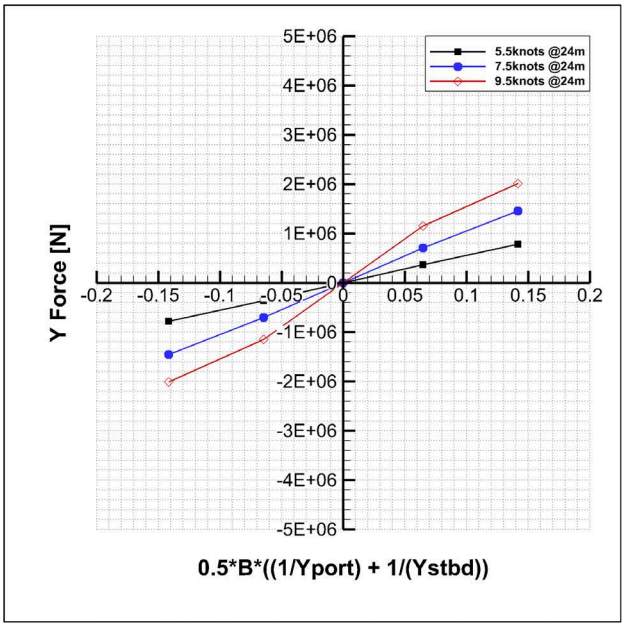

Figure 7. Calculated Y forces according to the ship location in the Suez Canal

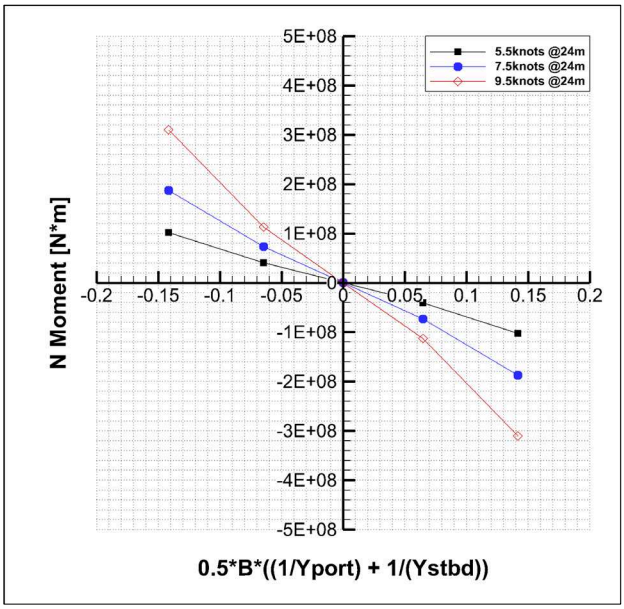

Figure 8. Calculated Y forces according to the ship location in the Suez Canal

4 ESTIMATION OF MANEUVERING PERFORMANCE PASSING THROUGH THE CANAL

As mentioned, the minimum distances between the four reference points and port/starboard banks under the prescribed environmental conditions are acquired as shown in Fig.9. The red solid line indicates minimum value of C_{STBD} and C_{PORT}. And the red dashed line indicates the maximum value of C_{STBD} and C_{PORT}.

If the ship approaches to the bank in starboard side, the calculated relative distances between two reference points in starboard side and bank in starboard side decrease. Otherwise, the calculated relative distances between two reference points in port side and bank in port side increase. If the distances are less than 64.0 m, it indicates the ship collide with the bank. At that time, the relative distances in opposite direction become 249.0 m.

The black line with squares shows the minimum distances for the bow reference point in starboard to the starboard side wall. And the black line with circles shows the minimum distances for the stern reference point in starboard to the starboard side wall. The blue line with empty squares shows the minimum distances for the bow reference point in port to the port side wall. And the blue line with empty circles shows the minimum distances for the stern reference point in port to the port side wall. To mark the acquired values on the same plot, infinitesimal values and overlarge values are marked as 64.0 m and 249.0 m, respectively. As mentioned, if the calculated values are lower than 64.0 m, it means the ship collided with a bank wall. At that time, the calculated values for the opposite direction are larger than 249.0 m.

Because the cross section of the Canal is symmetric, the obtained polar chart is symmetric as well. The relative distance for bow reference points are insignificantly different with that for stern reference points. Based on the acquired polar chart, the ship cannot be safely operated under the wind for 60, 90, 270 and 300 deg. In other conditions, the ship can move without colliding with the bank walls. Based on the results, it is possible to evaluate the maneuvering performance of the ship in the Suez Canal, qualitatively.

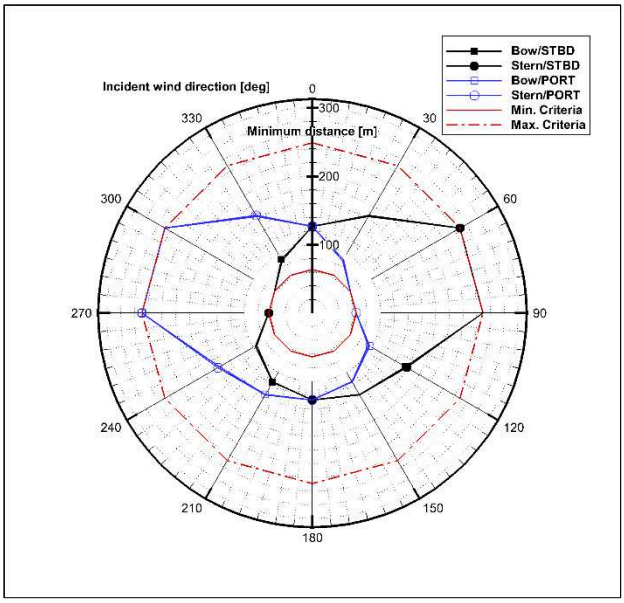

Figure 9. Minimum distances between the ship with 7.5 knots and banks along the Suez Canal under the maximum wind speed

5 CONCLUSIONS

In this paper, it is tried to construct an evaluation method of the maneuvering performance of the ship in the Suez Canal. The hydrodynamic coefficients for the container ship at deep and shallow water are predicted and added mass and added mass moment of inertia are predicted based on the empirical formulae. The maximum environmental conditions for the Suez Canal are determined with reference to the sailing directions. The wind load coefficients of the large container ship are predicted using the empirical formulae and irregular wind speeds are generated using Frøya spectrum. The bank effects due the walls of the Canal are considered by analyzing the CFD calculation results. To specify the design basis of maneuverability under the prescribed condition, the minimum relative distances between the ship and both walls of the Canal are calculated under prescribed environmental conditions.

Based on the results, it can be concluded that the container ship cannot sail in the Suez Canal when the maximum wind comes from 60, 90, 270 and 300 deg.

6 REFERENCES

1. IMO MSC.137(76) (2002). *Standards for ship manoeuvrability*.

2. Kijima, K.; Katsuno, T; Nakiri, Y.; Furukawa, Y. (1990). On the manoeuvring performance of a ship with the parameter of loading condition. *Journal of the Society of Naval Architects of Japan* 168: pp. 141-149.

3. Sung, Y.J.; Park, S.H. (2015). Prediction of Ship Manoeuvring Performance Based on Virtual Captive

Model Tests. *Journal of the Society of Naval Architects of Korea* 52: pp. 407-417.

4. Kijima, K.; Nakiri, Y.; Tsutsui, Y.; Matsunaga, M. (1990). Prediction Method of Ship Manoeuvrability in Deep and Shallow Water. *MARSIM & ICSM*.

5. Hooft, J.P.; Pieffers, J.B.M. (1988). Maneuverability of Frigates in Waves. *Marine Technology* 25.

6. Meijing, L.; Xiuheng, W. (1990). Simulation Calculation and Comprehensive Assessment on Ship Maneuverabilities in Wind, Wave, Current and Shallow Water. *MARSIM & ICSM*.

7. Fujii, J.; Tsuda, T. (1961). Experimental Researches on Rudder Performance (2). *Journal of the Society of Naval Architects of Japan* 110.

8. Fujii, J.; Tsuda, T. (1962). Experimental Researches on Rudder Performance (3). *Journal of the Society of Naval Architects of Japan* 111.

9. National Geospatial-Intelligence Agency (2014). Red Sea and the Persian Gulf. *Pub.172 Sailing Directions (Enroute)*. Twentieth Edition.

10. Fujiwara, T.; Ueno M.; Nimura, T. (2001). An Estimation Method of Wind Forces and Moments acting on Ships. *Mini symposium on prediction of ship manoeuvring performance*.

11. Andersen, O.J.; Løvseth, J. (1992). The Maritime Turbulent Wind Field. Measurements and Models. *Final Report for Task 4 of the Statoil Joint Industry Project*. Norwegian Institute of Science and Technology. Trondheim. Norway.

12. Hwang, W. (1980). *Application of System Identification to Ship Maneuvering*. Ph.D. Thesis. Massachusetts Institute of Technology.

13. Norbin, N. (1974). Bank effects on a ship moving through a short dredged channel. *Symposium of naval hydrodynamics 10th Proceedings*.

14. Hasegawa, K.; Kouzuki, A. (1987). Automatic Collision Avoidance System for Ships Using Fuzzy Control (in Japanese). *Journal of the Kansai Society of Naval Architects* 205: pp.1-10.

15. Ch'ng, P.W.; Doctors, L.J.; Renilson, M.R. (1993). A Method of Calculating the Ship-Bank Interaction Forces and Moments in restricted water. *International Shipbuilding Progress* 40: pp. 7-23.

7 AUTHORS' BIOGRAPHIES

Youngjun You Research engineer at DSME. He is responsible for seakeeping analysis for SEMI-RIGs and maneuvering analysis for merchant ships which are constructed at DSME.

Woojin Kim, Assistant research engineer at DSME. He is responsible for design for merchant ships which are constructed at DSME.

4th MASHCON, Hamburg - Uliczka et al. (eds) - © 2016 Bundesanstalt für Wasserbau ISBN 978-3-939230-38-0 (Online)
DOI: 10.18451/978-3-939230-38-0_7

A NEW SLENDER BODY THEORY FOR SHALLOW WATER AND COMPARISON WITH EXPERIMENTAL AND TWO OTHER NUMERICAL METHODS

M Alidadi, University of British Columbia, Vancouver, Canada,
O Gören and **D B Danişman,** Istanbul Technical University, Istanbul, Turkey,
S Calisal, Piri Reis University, Istanbul, Turkey,

SUMMARY

This study compares the results of a new slender body formulation for shallow water applications with two other well established methods for a Wigley hull. For the slender-body method for shallow water, the velocity potential is decomposed into a double-body potential and a perturbation potential. Using an order of magnitude analysis, the three-dimensional governing equation for the flow field around a slender hull is reduced into a series of two-dimensional problems in cross-flow planes as in the 2D+t methods. An Eulerian-Lagrangian approach is then used to satisfy the free surface condition. An implicit unsteady solver modeling and VOF model are used for the CFD simulations, using Star-CCM+. The numerical results obtained from these two methods for a Wigley hull are then compared with the new results. In addition the wave elevation and wave resistance results are compared against the predictions of Dawson method and experimental data. The effect of shallow water on resistance trim and squat are calculated and a ceiling for speed in shallow water is observed.

NOMENCLATURE

B	Beam of a ship
CFD	Computational Fluid Dynamics
D	Draft of a ship
L	Length of a ship
V	Velocity of the ship (m/s)
Rw	Wave resistance (N)
P	Pressure (N/m^2)
g	Gravitational acceleration (m/s^2)
x, y, z	Coordinates as in figure 1.
n	Normal vector
t	Time (s)
η	Wave elevation (m)
Φ	A potential function
υ	kinematic viscosity (m^2/s)
ρ	Density of water (kg/m^3)

letter subscripts denote differentiation along that direction

1 INTRODUCTION

For decades the experimental testing has been the main tool for research and development in ship hydrodynamics. However this started to change with the improvements of computers since 1970's. Nowadays the computational tools are extensively used in hydrodynamics, as:

- Building and testing of a ship model is expensive.
- Numerical hydrodynamic studies of ship models are becoming cheaper and faster with improved software and hardware.
- Computational methods provide detailed, visual information about the flow field around the hulls.

Most of the early numerical methods such as Michel integral, 2D+t formulation [1] and Dawson methods [14] are based on the potential flow theory. They are fast and provide a relatively good estimation of wave resistance. As the potential flow methods do not take into account the viscosity, the viscous resistance is normally calculated using empirical methods. However in the past decades, CFD methods based on RANS simulations become more popular as the computational power improved. This paper is focused on comparing three numerical methods for ship hydrodynamics for shallow water. A new Slender-body method, an approach based on the Dawson algorithm and a CFD methodology are first explained. Then the wave profiles and wave resistance and shallow water effects are compared against the experimental values for a Wigley hull with principal dimensions Length L=2 m, Beam B=0.2 m and Draft D=.123 m.

2 NEW SLENDER–BODY FORMULATION

The Slender-body methods have been adopted extensively for flow calculation around slender hulls. Numerous researchers at the University of British Columbia did the ground breaking work for what is now called as 2D+t formulation in recent publications for wave pattern and resistance and vortex shedding of slender hulls (see [1, 2], [3], [4, 5]). Maruo and Song [6, 7] used this method to calculate the bow impact and deck wetness on a Wigley hull. Tulin and Wu [8] numerically calculated the divergent waves generated by a Wigley hull using a Slender-body method.

Development of the new Slender-body methods was a result of the desire to apply 2D+t method for shallow water and include some upstream influence in the calculations, assuming that such additions will be improving the results, especially for shallow water applications. This was done by including a double body potential explicitly in the formulation. Using an order of magnitude analysis, the three-dimensional flow problem is then converted into a series of two-dimensional problems which are easier to solve than the original problem.
The free-stream potential is taken as the base potential in the studies mentioned above. However at very low Froude numbers, the flow around a hull can be approximated by the flow around a double-body consisting of the submerged part of the hull and its image about mean free surface [9]. In the new Slender-body formulation presented here, the double-body potential is used as the base potential because it is considered to be a better representation of the actual flow potential than the free-stream potential especially at low Froude numbers and shallow water applications.

2.1 MATHEMATICAL FORMULATIONS OF THE SLENDER-BODY METHOD

The coordinate system for a ship moving at constant speed U through otherwise undisturbed water is shown in Figure 1. It is fixed on the ship with x and y axes on the waterline plane and the origin at amidships and on the center plane. The equation for the Wigley hull geometry in this coordinate system is:

$$y = Y(x,z) = \pm\frac{B}{2}\left(1-\frac{4x^2}{L^2}\right)\left(1-\frac{z^2}{D^2}\right) \qquad (Eq\ 1)$$

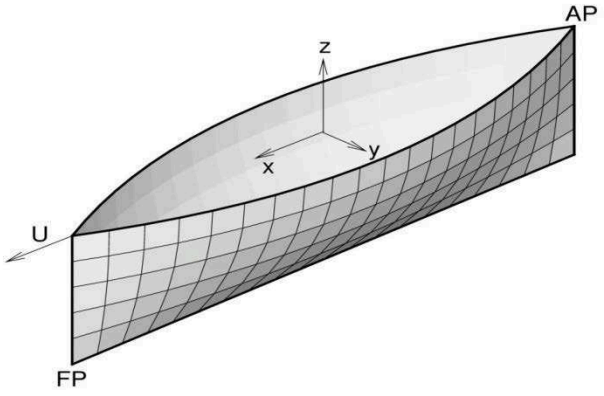

Figure 1. Coordinate system fixed to the hull

The fluid is assumed to be inviscid and incompressible and the fluid motion irrotational. The flow is represented by a velocity potential ψ which satisfies the Laplace's equation

$$\psi_{xx} + \psi_{yy} + \psi_{zz} = 0 \qquad (Eq\ 2)$$

The kinematic and dynamic boundary conditions for the steady free surface represented by $z = \eta(x,y)$ are:

$$\psi_x\eta_x + \psi_y\eta_y - \psi_z = 0 \qquad (Eq\ 3)$$

$$\frac{1}{2}\left(\psi_x^2 + \psi_y^2 + \psi_z^2 - U^2\right) + g\eta = 0 \qquad (Eq\ 4)$$

The impermeable boundary condition on the hull with normal vector $\boldsymbol{n}$ (positive pointing outwards) is

$$\psi_x n_x + \psi_y n_y + \psi_z n_z = 0 \qquad (Eq\ 5)$$

Next we assume that the velocity potential ψ is composed of a perturbation wave potential ϕ and the double-body potential $\bar{\phi}$, i.e.

$$\psi = \phi + \bar{\phi} \qquad (Eq\ 6)$$

where the double-body potential $\bar{\phi}$ satisfies Laplace's Equation 2), then the perturbation potential ϕ must satisfy Laplace's equation

$$\phi_{xx} + \phi_{yy} + \phi_{zz} = 0 \qquad (Eq\ 7)$$

Using an order of magnitude analysis for a slender hull (see Appendix A) and assuming that ϕ_{xx} is much smaller than $\phi_{yy}$and ϕ_{zz}, the governing equation 7 simplifies into :

$$\phi_{yy} + \phi_{zz} = 0 \qquad (Eq\ 8)$$

.

Equation 8 denotes that the flow around a slender hull can be seen as a two-dimensional problem in the cross flow planes along the x axis, which is easier to solve than the original three-dimensional problem (7). A sketch of a cross flow plane is shown in Figure 2.

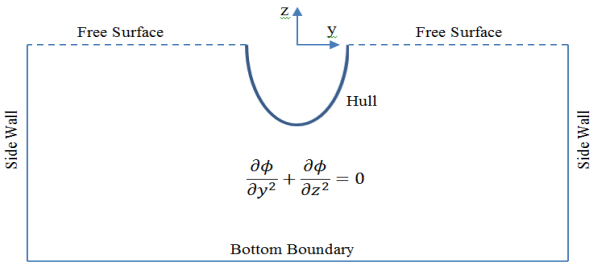

Figure 2. Sketch of a cross flow plane

An order of magnitude analysis of the individual terms in the free surface equations and hull boundary condition results in (see Appendix A) :

$$\left(\bar{\phi}_y + \phi_y\right)\eta_y - \left(\bar{\phi}_z + \phi_z\right) = 0 \qquad (Eq\ 9)$$

$$\frac{1}{2}\left(\bar{\phi}_x^2 + \bar{\phi}_y^2 + \bar{\phi}_z^2 - U^2\right) + \frac{1}{2}\left(\phi_y^2 + \phi_z^2\right) + \left(\bar{\phi}_y\phi_y + \bar{\phi}_z\phi_z\right) + g\eta = 0 \qquad (Eq\ 10)$$

$$\phi_y n_y + \phi_z n_z = -\left(\bar{\phi}_y n_y + \bar{\phi}_z n_z\right) \qquad (Eq\ 11)$$

The kinematic and dynamic boundary conditions are non-linear equations and are applied on the free surface at $z = \eta(x, y)$ which is unknown a priori. These equations were linearized by expanding them about the undisturbed free surface at $z = 0$. Since $\bar{\phi}_z = 0$ on the free surface, the free surface boundary conditions become:

$$\bar{\phi}_y \eta_y - \phi_z = 0 \qquad at\ z = 0 \quad (Eq\ 12)$$

$$\frac{1}{2}\left(\bar{\phi}_x^2 + \bar{\phi}_y^2 + \bar{\phi}_z^2 - U^2\right) + \bar{\phi}_y \phi_y + g\eta = 0 \quad \text{at z=0} \qquad (Eq\ 13)$$

Solving equation 8 in a cross flow plane requires specifying the boundary conditions on the side walls and at the bottom boundaries. Here they are assumed to be impermeable. For the calibration purposes of the new results the side walls are placed 30B away from the body in order to ensure the waves do not reflect into the computational domain. The bottom boundary is specified at various locations and for infinitely deep condition at $30D$ from the body to minimize the bottom effect.

2.2 SOLUTION APPROACH

The time-stepping approach developed by Longuet-Higgins and Cokelet [10] is used for the implementation of the Slender-body method. It involves a two-step procedure divided into an Eulerian boundary element method and a Lagrangian stepping procedure following particles.

2.2 (a) Boundary Element Method

The first step involves solving the two-dimensional Laplace Equation 8 in a cross flow plane using the body boundary condition and the velocity potential ϕ_0 known on the free surface from the previous time step. Applying Green's third identity to the Laplace Equation 8 gives an integral equation for the perturbation potential at a field point q in the cross flow plane (see [11] and [12])

$$\phi(q) = \frac{1}{2\pi}\int_S \left(\frac{\partial \phi}{\partial n}\ln r - \phi\ \frac{\partial}{\partial n}\ln r\right) ds \qquad (Eq\ 14)$$

Where r is the distance from a source point p to a field point q and S is the boundary for the cross flow plane.
In order to calculate the unknown boundary values, the boundary S is divided into a series of panels with constant singularity distributions. Applying boundary conditions to equation 14 gives the system of linear equations:

$$\sum_{j=1}^{N} A_{ij} \left.\frac{\partial \phi}{\partial n}\right|_j + B_{ij}\phi_j = 0 \qquad i = 1, \cdots, N \qquad (Eq\ 15)$$

Where N is the number of panels on the boundaries and coefficients A_{ij} and B_{ij} are defined as:

$$A_{ij} = \frac{1}{2\pi}\int_j \ln r\ ds\ ; B_{ij} = \frac{1}{2\pi}\int_j \frac{\partial}{\partial \mathrm{n}}\ln r\ ds \qquad (Eq15 - b)$$

The coefficient A_{ij} (B_{ij}) represents influence of a panel j with a source (doublet) distribution of unit strength on a panel i [12].

2.2 (b) Lagrangian –Eulerian method

The second step involves a Lagrangian method to calculate the perturbation potential and the free surface location at the next cross-flow plane. This marching from one cross-flow plane to the next one can be viewed as a time-domain problem with a time step:

$$dt = \frac{dx}{\bar{\phi}_x} \qquad (Eq\ 16)$$

where dx is the spatial step along the longitudinal axis. It is set to $dx = 0.001\ m$ in this study.

For obtaining the kinematic and dynamic boundary conditions in the Lagrangian form, the derivative is defined as:

$$\frac{d}{dt} = \bar{\phi}_y \frac{\partial}{\partial y} \qquad (Eq\ 16 - b)$$

Therefore the kinematic and dynamic boundary conditions and in the Lagrangian form can be written as:

$$\frac{d\eta}{dt} = \Phi_x \quad at\ z = 0 \qquad (Eq\ 17)$$

$$\frac{d\phi}{dt} = \frac{1}{2}\left(U^2 - \left(\bar{\phi}_x^2 + \bar{\phi}_y^2\right)\right) - g\eta \quad at\ z = 0 \quad (Eq\ 18)$$

The Lagrangian form of the flow velocity in y direction then becomes:

$$\frac{dy}{dt} = \bar{\phi}_y \qquad (Eq\ 19)$$

Using the two step Adams-Bashforth method, the values for the perturbation potential and free surface location at a new cross flow plane are obtained as :

$$\eta(t + dt) = \eta(t) + \left(\frac{3}{2}\eta_t(t) - \frac{1}{2}\eta_t(t - dt)\right)dt$$
$$\phi(t + dt) = \phi(t) + \left(\frac{3}{2}\phi_t(t) - \frac{1}{2}\phi(t - dt)\right)dt$$
$$y(t + dt) = y(t) + \left(\frac{3}{2}y_t(t) - \frac{1}{2}y_t(t - dt)\right)dt \qquad (Eq\ 20)$$

where η_t, $\phi_t$and $y_t$are determined from equations 19.
The wave resistance R_w is calculated by integrating the pressure field over the still water hull surface:

$$R_w = \int_{-L/2}^{L/2} dx \int_{S_B} p \cdot n_x dA \qquad (Eq\ 21)$$

where S_B represents the girth of the hull section, and p is the pressure obtained from the Bernoulli's equation:

$$p = -\rho\left[U\phi_x + \frac{1}{2}\left(\phi_y^2 + \phi_z^2 + gz\right)\right] \qquad (Eq\ 22)$$

The wave resistance coefficient C_w is determined using the formulation:

$$C_w = \frac{R_w}{0.5\rho U^2 L^2} \qquad (Eq\ 23)$$

For the results presented in this paper, the starting cross section was at $L/4$ upstream of the bow. The perturbation potential and wave elevation values were set to zero on this cross section. We defined 75 panels on the free surface at the starting section. The size of these panels increased toward the impermeable wall in a geometric progression with the initial size $D/10$. We used 10 panels on the hull surface when the cross section intersects the hull.

2.3 CALCULATION OF DOUBLE-BODY POTENTIAL

The double-body potential is calculated using the boundary element method developed by Hess and Smith [13]. The governing equation for this potential is the three-dimensional Laplace equation

$$\nabla^2\overline{\phi} = 0 \qquad (Eq\ 24)$$

subject to the impermeable hull boundary condition

$$\nabla\overline{\phi}\cdot\boldsymbol{n} = 0 \qquad (Eq\ 25)$$

Similar to the methodology described above, the equation (Eq) is converted into a system of linear equations

$$\sum_{j=1}^{M} C_{ij}\sigma_j = \boldsymbol{U}\cdot\boldsymbol{n} \quad for\ i = 1,\cdots,M \qquad (Eq\ 26)$$

where M is the number of quadrilateral panels on the hull surface and its image around the undisturbed free surface, and σ_j is the source strength of a panel j. The coefficient C_{ij} obtained from the relation

$$C_{ij} = \frac{1}{4\pi}\int_j \nabla\left(\frac{1}{r}\right).ndS \qquad (Eq\ 26-b)$$

and represents effect of a source panel j with unit strength on a panel i [12].
The double-body potential is calculated in this study using 50 panels in the x direction and 20 panels in the z direction.

3 DAWSON METHOD

Hess and Smith developed a boundary element method in 1967 for computing the flow around a submerged body in an infinite domain [13]. Dawson modified this method in 1977 for a surface-piercing body. One may refer to the thesis by Raven for a comprehensive explanation on this method [14].

The theoretical essence of Dawson method is based on the low-Froude-number theory. Similar to the method explained in the previous section, the total velocity potential is decomposed into a double-body and a perturbation potential (see equation 6). The double-body potential $\overline{\phi}$ is regarded as a "slowly varying potential" and hence its derivatives are of the order of (U). Newman [15] showed that the perturbation potential ϕ = O(ε^2) and wave elevation $\eta = O(\varepsilon)$ with $\varepsilon \equiv U^2/2g \ll 1$. In another study Calisal et al. showed that η = O(Fr^2) which is parallel to Newman's finding [16]. Based on this analysis the kinematic and dynamic free surface conditions are combined into a single linearized equation with respect to ϕ:

$$\nabla\overline{\phi}\cdot\nabla\left[-(\nabla\overline{\phi})^2 + \nabla\overline{\phi}\cdot\nabla\phi\right] + \frac{1}{2}\nabla\phi\cdot\nabla(\nabla\overline{\phi})^2 + g\phi_z = 0 \quad \text{at } z = 0 \qquad (Eq\ 27)$$

By adopting the definition of derivatives along a streamline, Dawson expressed the above equation as

$$\left(\overline{\phi}_l^2\phi_l\right)_l + g\phi_l = 2\overline{\phi}_l^2\overline{\phi}_{ll} \quad at\ z = 0 \qquad (Eq\ 28)$$

where

$$\overline{\Phi}_l = |\nabla\overline{\Phi}\ \ | = \sqrt{\overline{\Phi}_x^2 + \overline{\Phi}_{ly}^2} \qquad (Eq\ 28-b)$$

The potential flow problem is now reduced into solving the three dimensional Laplace equation $\nabla^2\overline{\phi} = 0$ subject to boundary conditions $\overline{\phi}_n = 0$ on the body and free surface condition 28. The radiation condition is fulfilled in this method by a 4-point backward differentiation scheme. The implementation of this method involves distributing panels on the plane z = 0 and on the hull surface as shown in Figure 3. The solution is then obtained by employing the Hess and Smith's method which uses source panels with constant strength. The wave elevation and pressure in this method are calculated from equations:

$$\eta = \frac{1}{2g}\left[U^2 + \overline{\phi}_l^2 - 2\overline{\phi}_l\phi_l\right] \qquad (Eq\ 29)$$

$$p = -\frac{\rho}{2}\left[U^2 + (\nabla\overline{\phi})^2 - 2\nabla\overline{\phi}\cdot\nabla\phi\right] \qquad (Eq\ 30)$$

The wave resistance is also computed by integrating the pressure over the hull surface (see equation 22).

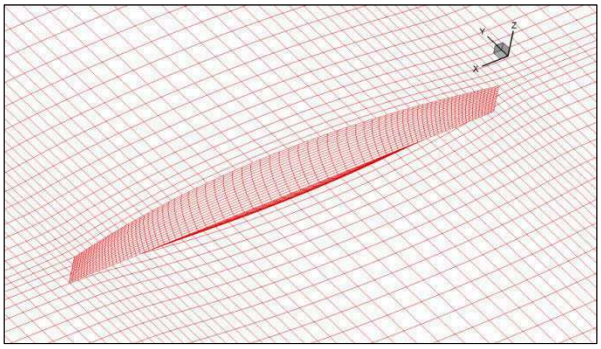

Figure 3. Distribution of panels on the hull and free surface

4 CFD METHOD

The usage of Computational Flow Dynamics (CFD) based on RANS equations is rapidly increasing for marine applications due to the improvements of computers. Here we implemented the CFD method for the Wigley hull by conducting simulations in the Star-CCM+ software. The corresponding coordinate system is at amidships on the undisturbed free surface (see Figure 1). As the hull is symmetric about its center plane of symmetry, only half of it is considered in the simulations. The domain based on hull length L extends from:

- *3.5L* to *-6.5L* in longitudinal direction
- *1L* to *-3L* in vertical direction
- *0* to *3L* in lateral direction

The applied boundary conditions are:

- Symmetry plane at the hull centerplane.
- Symmetry plane at the side of domain
- Hydrostatic pressure corresponding to undisturbed water surface at the outlet boundary
- Inlets with prescribed velocity and volume fraction at the upstream, top and bottom boundaries

The mesh used contains 372212 hexahedral cells. In order to obtain accurate results, we used local refinements and prism layers along the wetted surface of hull. The calculations used a mesh structure on the hull surface and the symmetry plane. In addition we had mesh at the still water level with refinements in the wake region. An implicit unsteady solver with k-omega turbulence modeling and VOF wave's model is used for simulations. The time step is set based on the inlet velocity from the equation:

$$\mathrm{dt} = \frac{\mathrm{L}}{50\mathrm{U}} \qquad (Eq\ 31)$$

5 VALIDATION IN DEEP WATER

One of the main objectives of this study is to estimate the shallow water effects on the sinkage and trim of a ship. A critical and the target case is the sailing of tankers in Vancouver harbor Canada . For these reasons an existing formulation that is 2D+t method is modified and a formulation suitable for shallow water studies is developed. The new code is first tried for deep water studies of the resistance, waterline profile. Once validated the code is then used for finite depth conditions.

Comparisons of different numerical calculations are reported below. The methods described above are implemented for the Wigley hull with dimensions given at section 1.

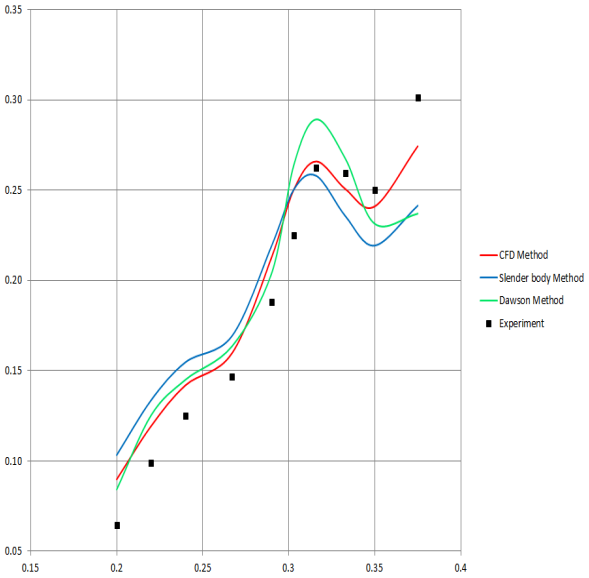

Figure 4. Comparison of numerical wave resistance coefficients with Dawson, new formulation and experimental values

The new code is validated with using the results of other codes for resistance and wave profile first. The general agreement of the resistance prediction with the new formulation with experimental resistance data could be considered as acceptable Figure (4). This is in view of the dispersion of such data coming from different towing tanks. Aanesland [18] gave averaged values from towing tank databases where the Wigley hull was towed fixed and free to trim and squat. Aanesland's numerical results were obtained by a three dimensional linear potential flow formulations similar to Dawson's method. However Kelvin sources were distributed in the outer domain to satisfy wave radiation conditions.

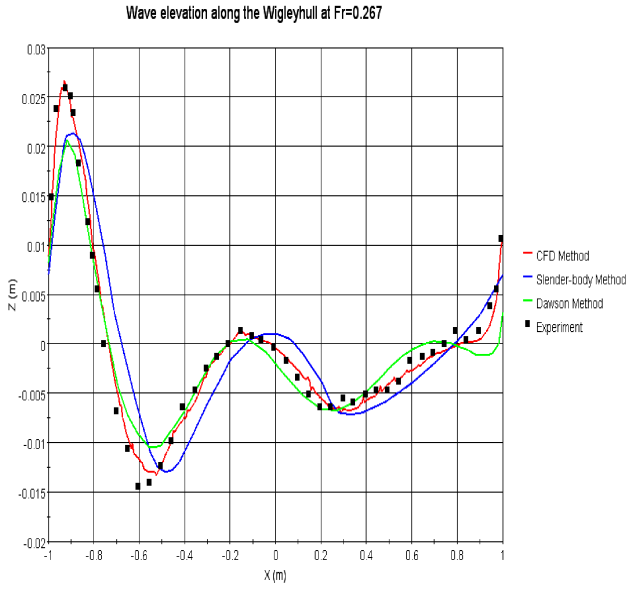

Figure 5. Wave elevation on the Wigley hull side at Fr= 0,267

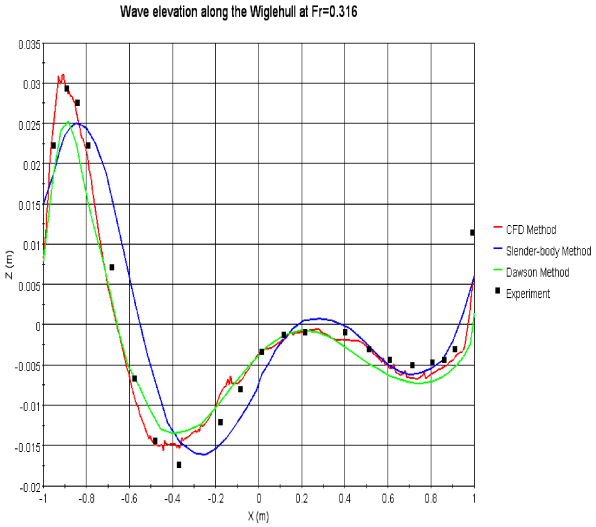

Figure 6. Wave elevation on the Wigley hull side at Fr=0,316

Figure 5 and Figure 6 show the comparison of the wave profiles along the hull at Froude numbers F_R=0.267 and F_R=0.316. The experimental results for F_R=0.267 are from a testing at the department of Naval Architecture and Ocean Engineering at the Yokohama National University [17], while the results for F_R=0.316 are obtained by Maruo and Song from tests on a 6-meter Wigley hull model [6]. The wave profiles of the CFD method are in a good agreement with experiments at both Froude numbers. The CFD predictions for the position and magnitudes of the wave peaks and troughs have a good match with the experimental results. On the other hand, the wave profiles for the Slender-body and Dawson methods have similar trends to the experiments; however there are some discrepancies between them and experimental values, especially around the bow section. The first wave peak is underestimated by both of the potential flow methods which might be due to linearization of the free surface boundary conditions. Also, the Dawson method has a better prediction of the location of wave peaks and troughs than the Slender-body method. This is possibly a result of the order of magnitude analysis used in the development of the Slender-body method. A new way for the start of the calculation is to be implemented soon.

6 FINITE DEPTH EFFECTS

Figure 7 shows that the depth effect for resistance is significant as the depth Froude number increases. Similarly the figure 6 shows that that the trim increases significantly with depth Froude number while the squat coefficient remains almost constant.

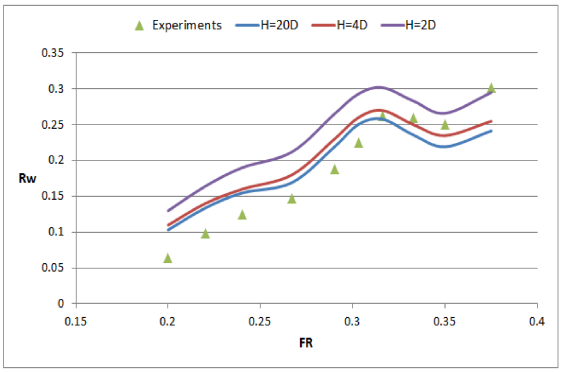

Figure 7. Wave making resistance deep and shallow water comparisons with new formulation compared to averaged experimental values of Aanesland

The results for wave resistance with the new formulation with finite depth or shallow water are reported in figure 7. The shallow water effect becomes significant as the clearance becomes smaller. Deep water sinkage and trim values by the 2D+t method are by Wong and Calisal [5] and shown in Figure 8. Sinkage is nondimensionalized with $U^2/2g$ and trim is given as a percentage of the ship length. the results are then compared with averaged values reported by Aanesland [18]. The nondimensional sinkage calculated by the 2D+t method is in good agreement with the experimental data however it seems to underestimate at higher Froude numbers. In contrast the trim is over estimated in the Froude number range of 0.27 to 0.35. The trim and squat in shallow water at relatively high Froude number with the new formulation are reported in Figure 9 and 10.

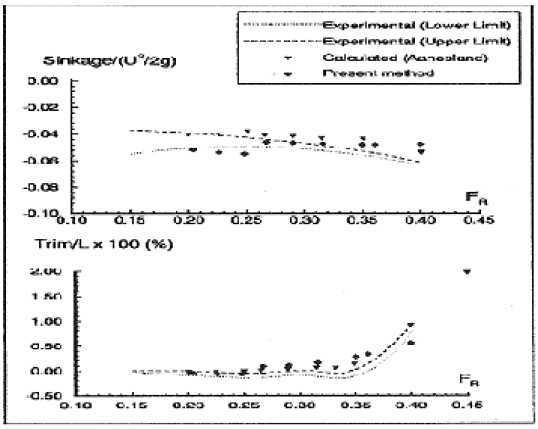

Figure 8. Computed and measured trim and sinkage for Wigley hull deep water with 2D+t formulation

The sinkage and trim angle are calculated assuming the Wigleyhull has a weight eqaul to 10.3 kgf. The pressure distribution is first obtained from the Bernoulli's equation. Then the hull sinkage by is calculated by balancing the hull weight with the hydrodynamic force in the vertical direction. The trim angle is similarly calculated by balancing the hull moment around the y-axis with the y-moment of hydrodynamic forces.

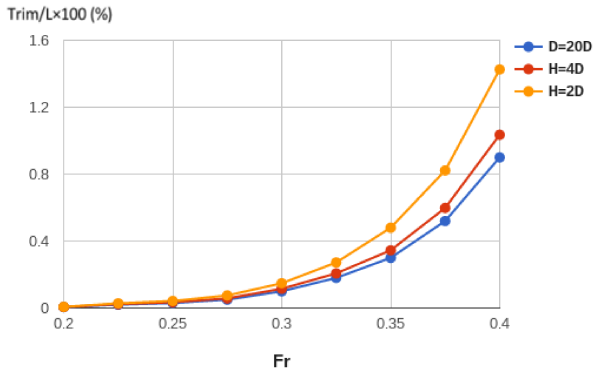

Figure 9. Computed trim variation with new formulation in shallow water with ship Froude number

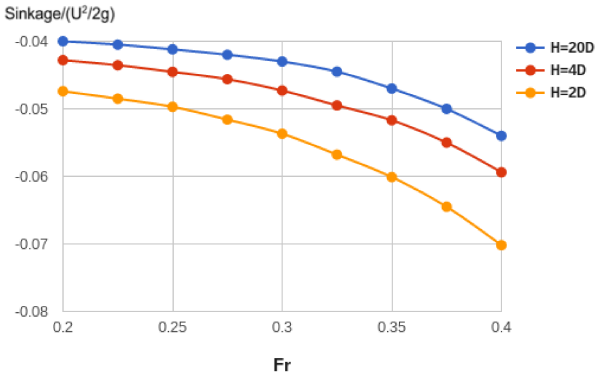

Figure 10. Water depth and Froude number effect on squat for Wigley hull with new formulation.

7 CONCLUSIONS

A new slender body formulation and two existing numerical methods for ship hydrodynamics were compared with the experimental values available for Wigley hull. The New Slender-body and Dawson methods, which are based on the potential flow theory, were easier and faster to implement than the CFD method. However the CFD method, which is based on RANS equations, had the best agreement with the experimental values in the validation in deep water. The CFD method was able to predict the magnitude and location of the wave peaks and troughs more accurately than the potential methods. The CFD results for wave resistance coefficients were also a better match with experimental values than the results obtained from Slender-body and Dawson methods. Some numerical challenge was faced as poor convergence when the depth Froude number is close to 1. A ceiling of ship operational speed is seen as the sinkage and trim increases with increasing speed. Application to shallow water of the new Slender body is expected to improve the earlier results reported above.

8 REFERENCES

1. Calisal, S.M.; Chan, J.L.K. (1989). A numerical calculation for ship bow wave, Ship Research, vol. 33, no. 1, p. 21–28.

2. Calisal, S.M.; Chan, J.L.K. (1993). A numerical procedure for time domain nonlinear surface wave calculations, Ocean Engineering, vol. 20(1), pp. 19-32.

3. Allievi, A.; Calisal, S.M. (1993). A semi-implicit, semi-lagrangian finite element model for nonlinear free surface flow. 6th International Conference on Ship Hydrodynamics.

4. Wong, L.H.; Calisal, S.M. (1994). A numerical solution for potential flows including the effects of vortex shedding, J. Offshore Mech. Arct. Eng. 115(2): pp. 111-115.

5. Wong, L.H.; Calisal, S.M. (1996). Numerical algorithms for slender bodies with vortex shedding and density stratification, Ship Research, vol. 40, no. 1.

6. Maruo, H.; Song, W.-S. (1990). Numerical appraisal of the new slender ship formulation in steady motion, Proceedings of the 18th Symposium on Naval Hydrodynamics, Michigan, pp. 239-256.

7. Song, W.-S.; Maruo, H. (1993). Bow impact and deck wetness: simulation based on nonlinear slender body theory, Proceedings of the 3rd International Offshore and Polar Engineering Conference, Singapore.

8. Tulin, M.; Wu, M. (1996). Divergent bow waves, 21th Symposium on Naval Hydrodynamics, p. 661-679, Trondheim.

9. Faltinsen, O.M.(2005). Hydrodynamics of High-Speed Marine Vehicles, Cambridge University Press.

10. M. S. Longuet-Higgins and E. D. Cokelet, (2005). The Deformation of Steep Surface Waves on Water. I. A Numerical Method of Computation. Proceedings of Royal Society London, vol. 350, pp. 1-26.

11. Brebbia, C.A.; Dominquez, J. (1992). Boundary Elements: An Introductory Course, WIT Press.

12. Katz, J.; Plotkin, A. (2001). Low-Speed Aerodynamics, Cambridge University Press.

13. Hess, J. L.; Smith, A.M.O. (1981). Calculation of potential flow about arbitrary bodies, Progress in Aerospace Sciences, vol. 8, pp. 1-138, 167.

14. Raven, H.C. (1996). A solution method for the nonlinear ship wave resistance problem, PhD Thesis, Technische Universiteit Delft, The Netherlands.

15. Newman, J.N. (1976). Linearized wave resistance theory, Proceedings of the International Seminar on Wave Resistance, p. 31-34, Tokyo.

16. Calisal, S.M.; Goren, O.; Okan, B. (1991). On an iterative solution for nonlinear wave calculations, Journal of Ship Research, vol. 35, no. 1, pp. 9-14.

17. Hayashi, K.; Kunishige, Y. (1988). *Measurement of wave pattern around a yawed ship model*, Graduation Thesis, Yokohama National University, Japan

18. Aanesland V. (1989). A Hybrid Model for Calculating wave Making resistance, *Proceedings of the Fifth International Conference on Numerical Ship Hydrodynamics*, Japan, pp. 657 -666.

9 AUTHORS' BIOGRAPHIES

Mahmoud Alidadi holds a PhD degree in mechanical engineering from University of British Columbia (UBC). As a research fellow at UBC, he worked on development a numerical method for studying hydrodynamics of slender ships.

Ömer Gören received his Ph.D. degree in 1985 from ITU and was then post-doctoral fellow at UBC in 1986-87. Since then he has been a faculty at ITU Dept. of Naval Architecture and Marine Eng. His focus of reserach interests are free surface hydrodynamics and hull shape optimization for resistance.

Devrim Bülent Danışman received his Ph.D. degree in 2004 from ITU. Subsequently, he worked as research fellow at the University of Newcastle during 2000-2001. Currently he is an Assoc.Prof. at ITU. His field of interests are computational and experimental resistance analysis and form optimization.

Sander Calisal did his doctoral work at U Cal Berkeley with late professor J.V. Wehausen and has worked in USNA and UBC Canada and is a professor at Piri Reis University. He researched on ship hydrodynamics and ship design.

10 APPENDIX A: ORDER OF MAGNITUDE ANALYSIS

Replacing the potential ψ from Equation 6 in the kinematic and dynamic boundary conditions Eq. 3 and Eq. 4 gives

$$\left(\overline{\phi}_x + \phi_x\right)\eta_x + \left(\overline{\phi}_y + \phi_y\right)\eta_y - \left(\overline{\phi}_z + \phi_z\right) = 0$$

$$\frac{1}{2}\left(\left(\overline{\phi}_x + \phi_x\right)^2 + \left(\overline{\phi}_y + \phi_y\right)^2 + \left(\overline{\phi}_z + \phi_z\right)^2 - U^2\right) + g\eta = 0 \qquad \text{(A1-A2)}$$

Similarly the hull boundary condition 5 changes to

$$\phi_x n_x + \phi_y n_y + \phi_z n_z = -\left(\overline{\phi}_x n_x + \overline{\phi}_y n_y + \overline{\phi}_z n_z\right) \qquad \text{(A3)}$$

In order to simplify the above equations, non-dimensionalized variables are defined:

$$\tilde{x} = \frac{x}{L} \qquad \tilde{y} = \frac{y}{B} \qquad \tilde{z} = \frac{z}{D}$$

The order of magnitude of the individual terms in the governing equation 8 and boundary conditions A1-A3 are:

$$\phi_{xx} = O\left(\frac{\phi}{L^2\tilde{x}^2}\right) \quad \phi_{yy} = O\left(\frac{\phi}{B^2\tilde{y}^2}\right) \quad \phi_{zz} = O\left(\frac{\phi}{D^2\tilde{z}^2}\right)$$

$$\phi_x = O\left(\frac{\phi}{L\tilde{x}}\right) \quad \phi_y = O\left(\frac{\phi}{B\tilde{y}}\right) \quad \phi_z = O\left(\frac{\phi}{D\tilde{z}}\right)$$

$$n_x = O\left(\frac{n}{L\tilde{x}}\right) \quad n_y = O\left(\frac{n}{B\tilde{y}}\right) \quad n_z = O\left(\frac{n}{D\tilde{z}}\right)$$

$$\eta_x = O\left(\frac{\eta}{L\tilde{x}}\right) \quad \eta_y = O\left(\frac{\eta}{B\tilde{y}}\right)$$

$$\overline{\phi}_x = O\left(\frac{\overline{\phi}}{L\tilde{x}}\right) \quad \overline{\phi}_y = O\left(\frac{\overline{\phi}}{B\tilde{y}}\right)$$

One can conclude that for a slender hull where $O(D) \approx O(B)$ and $B/L \ll 1$

$$\phi_{xx} \ll \phi_{yy}, \phi_{zz} \qquad \phi_x\eta_x \ll \phi_y\eta_y$$

$$\phi_x^2 \ll \phi_y^2, \phi_z^2 \qquad \phi_x n_x \ll \phi_y n_y, \phi_z n_z$$

$$\overline{\phi}_x\eta_x \ll \overline{\phi}_y\eta_y \qquad \overline{\phi}_x\phi_x \ll \overline{\phi}_y\phi_y$$

$$\overline{\phi}_x n_x \ll \overline{\phi}_y n_y, \overline{\phi}_z n_z$$

4th MASHCON, Hamburg - Uliczka et al. (eds) - © 2016 Bundesanstalt für Wasserbau ISBN 978-3-939230-38-0 (Online)
DOI: 10.18451/978-3-939230-38-0_8

THE DEFINITION OF THE NAUTICAL BOTTOM IN MUDDY NAVIGATIONAL AREAS

M Druyts, MDCE bvba, Belgium
P Brabers, Demco nv, Belgium

SUMMARY

When salt water meets fresh water, flocculation occurs and sedimentation starts. During the settling process, estuarine mud particles constantly reduce the mutual distance until, at a specific moment - van der Waals forces and electrostatic forces - the particles form network structures. The nature of the mixture changes from fluid mud to a gel like substance. This phenomenon generates in estuarine mud layers a physical two component structure: one component of low viscosity (fluid mud), and of high viscosity (solid mud). The interface between the two is characterized by a drastic change of the rheological parameters: a rheological transition. During trials with TSHD 'Vlaanderen XVIII' in Zeebrugge, the vessel, navigating with zero under keel clearance relative to this interface, was completely out of control. The rheological transition is, according to the PIANC definition, the Nautical Bottom in muddy navigational areas. Several sounding instruments are capable of measuring the rheological transition level.

1 INTRODUCTION

Since the SHZ 'Vlaanderen XVIII' trials and the publications of Prof. Toorman and Dr. Wurpts, no new trials and/or investigations, relating to the Nautical Bottom concept in muddy navigational areas, were reported. This paper is an attempt to put or to keep the subject on the agenda by focusing on the fact that the Nautical Bottom and the rheological transition are identical in muddy areas.

Without measuring the rheological transition, the safety of a vessel, maneuvering in a muddy navigational area, cannot be estimated or confirmed.

The concept of 'mud', as used in this context, refers to estuarine mud, a concentration in water of mainly cohesive sediment, some organic matter and a smaller fraction of coarser, non-cohesive sediment (silt and sand) [1].

Influenced by tide and increasing width of the river, mud settles on the seabed or the riverbed in ports and fairways.

The behaviour of ships in muddy navigation areas, especially with reduced under keel clearances, changes substantially. Guillaume Delefortrie in his doctoral thesis [2] has thoroughly researched this influence on the behaviour of a 6000 TEU and a 8000 TEU container carrier.

He reports however a major unsolved problem: what exactly is the Nautical Depth in muddy navigation areas, and how can it be measured directly and continuously: "*Finally the search for better survey techniques in muddy navigation areas should not be closed. It would be very useful if the rheological characteristics of the mud layer, and particularly the rheological transition, could be measured in a continuous way, as both echo sounding results and density values are only a surrogate to indicate the position of the rheological transition. [2, p. 12.6]"*

The significance of this quote with regard to the definition of the Nautical Bottom in muddy navigational areas, is highlighted by reading it next to the PIANC definition of Nautical Bottom: *"The Nautical Bottom is the level where the physical contact with a ship's keel causes either damage or unacceptable effects on controllability and manoeuvrability"* [3]

Is the rheological transition in mud to be regarded and defined as the equivalent Nautical Depth?

There is no doubt that this is the case. In what follows, arguments are developed and illustrated. Furthermore, and most importantly, the existing (recently developed) survey techniques to measure this rheological transition already are operational and will be discussed.

2 THE GEL POINT

2.1 IN THE LABORATORY

The settling process of estuarine mud passes through different phases. E.A. Toorman [1] researches the process and carries out settling experiments: in Fig. 1 the water – mud interface relative height position is represented against the settling time in days. The experiment starts with a homogenized water mud column. Phases 1 and 2 are fluid, the phase 3 is not fluid.

In this phase 3, the cohesive sediment particles, under the influence of van der Waals forces and electrostatic forces, have formed a network structure: the gel point has been reached: see Figure 1.

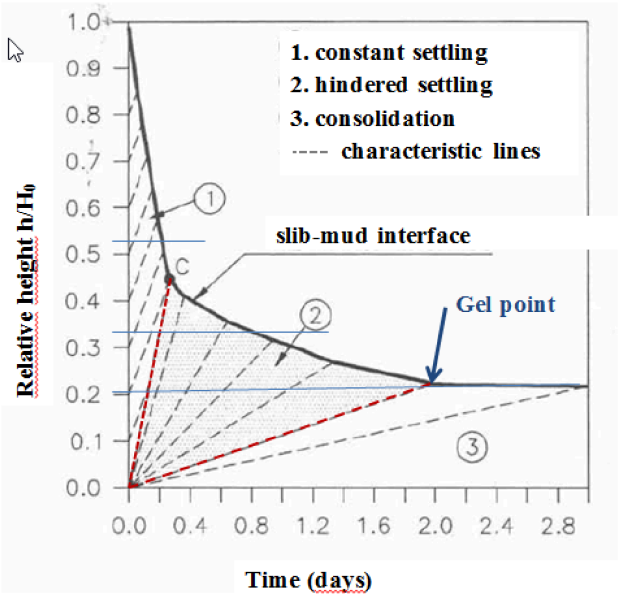

Figure 1. Settling curve (mud-water interface evolution) and characteristic (iso-density) lines. (adapted)

The 3rd phase is a soil marked by significant shear stress σ'[1] [4]. The gel point separates fluid mud from solid mud.

The same experiment, carried out with a constant feed of mud particles, would result in the situation as represented in Fig. 2. The gel point will slowly rise, but, unlike in the original experiment, all three phases would be present simultaneously and continuously.

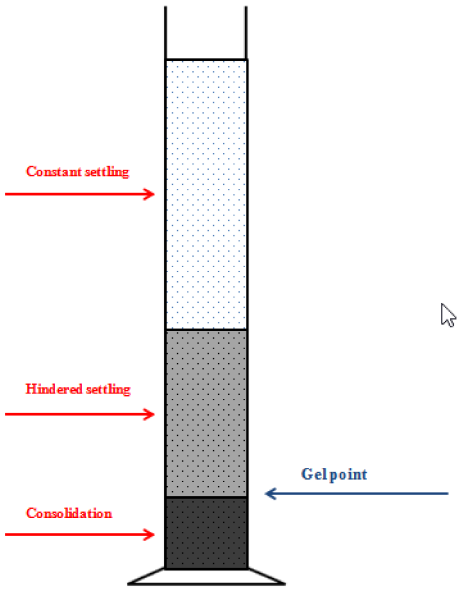

Figure 2. Profile generated during continuous/ cyclical feeding with mud particles as in estuaries.

In an estuarine mud layer, continuously or cyclically fed by settling mud particles, a gel point exists. It is situated at the interface of the fluid mud layer (hindered settling phase) and the consolidating mud layer.

2.2 IN SITU

In the presence of mud, the in situ depth measurements with dual frequency acoustic survey methods – Figure 3 Zeebruges – reveal the first two phases as in Figure 2: constant settling phase (above the 210 kHz echo) and hindered settling phase (below the 210 kHz). The 33 kHz reflection generally is unstable and unreliable when fluid mud is involved: there apparently exists no clear reflector for the 33 kHz signal. In general, the transition level from the hindered settling phase to the consolidation phase is situated in between the 210 and 33 kHz reflections.

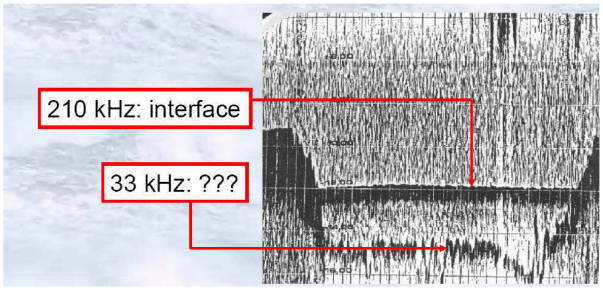

Figure 3. In situ profile (CDNB, Port of Zeebruges)

A following example is the Port of Emden: the blue line represents the water – fluid mud interface, generated by the 210 kHz echo, the red line the echo of the 15 kHz echo.

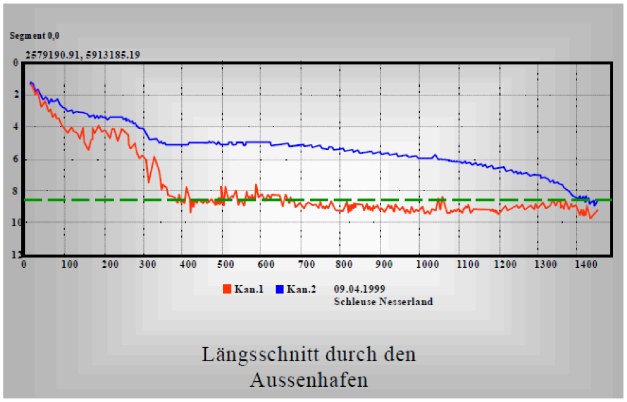

Figure 4. Longitudinal section outer port Emden [5]

It is a persistent and ongoing problem that the position of the 33 kHz echo in the mud, or of any low frequency, is not stable, but depends on echo sounder settings and on the surveyors' skill, both subjective parameters.

Furthermore and as a consequence, the physical reality connected to the level of the 33 kHz echo is confuse, unknown and unrelated to the position of the gel point.

On the other hand the fact itself that there exists a difference between the 210 kHz reflector and the 33 kHz

reflector, measured at the same location, is always sufficient evidence for the presence of a fluid mud layer.

2.3 GEL POINT AND DENSITY

The gel point can be considered the equivalent for mud, as the temperature of 0° C is for water: above 0° C there is water, below 0° C there is ice and nothing in between.

All over the world at this moment, densities are being used to identify the gel point. This is basically incorrect. The density at the gel point is strongly influenced by the sand content. With each variation of the sand content corresponds a different density for the gel point. Since the sand content in any port or fairway varies continuously form location to location, density is to be ruled out as a parameter to measure the depth of the gel point.

3 THE RHEOLOGICAL TRANSITION

3.1 THE 'FREEZING' OF MUD

The physical reality of the concept 'gel point' at the interface between fluid mud and solid mud, may seem to be rather abstract, but can easily be visualized: see Fig. 5.

The photo is taken in the DEME harbour on the left bank of the river Scheldt. The harbour is exposed to the tide, which makes this photo possible: at low tide both the fluid mud and the consolidating mud are visible at the same moment.

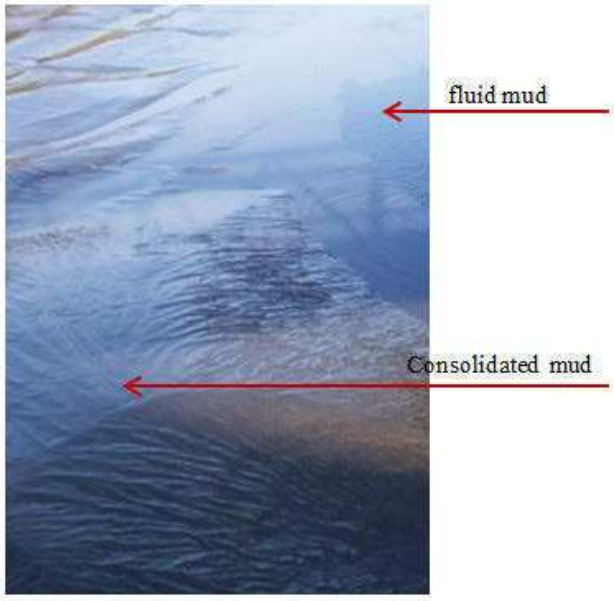

Figure 5. DEME harbour Antwerp, left bank river Scheldt

Visual observations confirm the presence of a fluid (smooth surface) and a soil (rough and undulating surface). There is no evidence of a third element, an eventual intermediate phase between them: the transition is abrupt and shows the physical reality of the gel point, which is the 'freezing' point of mud.

As a consequence, the gel point phenomenon generates a physical separation between two phases in the mud layer: the liquid state and the solid state, or a low viscosity phase and a high viscosity phase as reported by Kerckaert, Malherbe and Bastin already in 1985 [6]. Moreover, it was observed that in the transition between the two phases, the viscosity parameters do change drastically.

The conclusions at that time were based upon laboratory measurements – dynamic viscosity, initial rigidity or yield stress – of Zeebrugge mud. Although in situ measurements of viscosity are very difficult to achieve, later developments made it possible to measure yield stress depth profiles.

3.2 YIELD STRESS

The yield stress depth profile in fig. 6 [7] is a representative sample of – literally – hundreds of profiles measured in the Port of Zeebrugge.

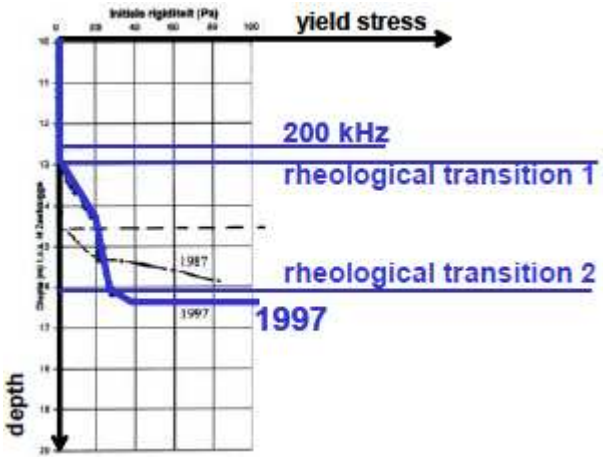

Figure 6. Yield stress depth profile, Zeebrugge [6]

Again, the profile reflects the situation as showed in Fig. 2 and Fig. 3: no yield stress in the constant settling phase (above the rheological transition 1, which is the earlier mentioned mud – water interface), low viscosity in the hindered settling phase (between the rheological transitions 1 and 2), high viscosity in the consolidation phase (below the rheological transition 2).

The yield stress depth profile reflects the three phase settling situation but, in contrast to the situation reflected by the acoustical survey methods, the gel point is accurately identifiable.

While just below the water-mud interface – the 1st transition –, the rheological properties of the mud are hardly different from those of water, it is undeniable that the 2nd transition is from a low viscosity area to a high viscosity area. The transition is also very drastic: the yield stress increases very quickly with the depth. This

depth is the transition between fluid mud and solid or 'frozen' mud.

3.3 OTHER RHEOLOGICAL PARAMETERS

During individual trials of the Rheocable in the laboratory of Flanders Hydraulics Research at Antwerp, the relation shear stress – shear rate at different depths in the Sediment Test Tank (STT) was measured [8]. In Fig. 7, some of these relations have been visualized.

The STT was, among other things, used to test different survey methods in an environment of classic mud layers: see Fig. 2 and Fig. 3. Estuarine mud from the river Scheldt was used for these tests.

The drastic change (discontinuity) of the viscosity in the mud – in terms of dynamic and kinematic viscosity parameters - between the level of -85 cm and -95 cm is striking. The drastic change of the yield stress at shear rate 0 (1/s) between the same depth levels is also evident.

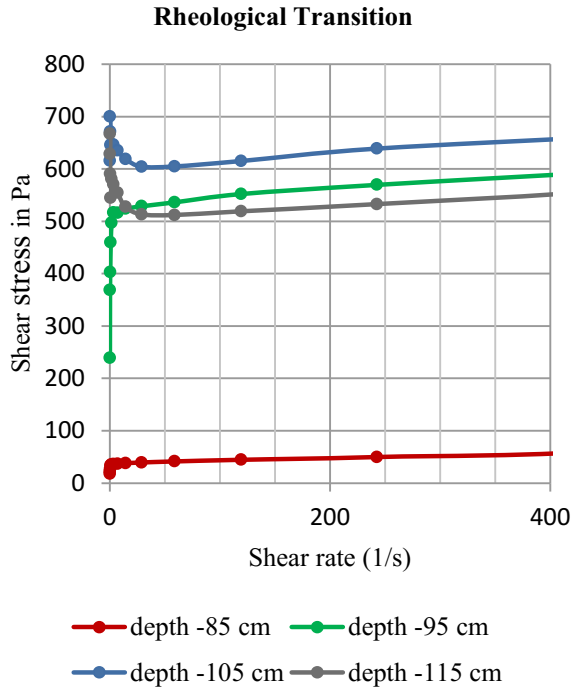

Figure 7. Shear stress/shear rate in the STT

This transition was not only observed in the laboratory, where the conditions for sample taking, for measurements and for observations are optimal. In situ measurements in many different locations, with different survey methods, have confirmed, directly or indirectly, the presence of this drastic change in the viscosity parameters, i.e. the presence of a true rheological transition.

All viscosity parameters do change drastically at the gel point level in the estuarine mud layers: this is called the rheological transition (and this transition occurs in all estuarine mud layers).

4 A SHIP'S BEHAVIOUR

4.1 IN A MUD-FREE ENVIRONMENT

A reduction in under keel clearance (squat), reduced effectiveness of the propeller(s) and the rudder, increasing stopping distances and stopping time, increasing diameter of turning circles: these are the shallow water effects related to the interaction between ship and seabed. [9]

With the exception of the squat, these effects are caused by the reduced effectiveness of the propeller(s): the flow of water to the propeller becomes severely hindered (throttled) with decreasing under keel clearance. As a consequence, rudder forces are equally reduced producing the effects as mentioned.

Ultimately, with the under keel clearance reduced to zero, the vessel, in contact with the hard surface (sand or rock) of the bottom, will be immobilized: the friction between the ship's keel and the bottom is overpowering.

In this case, the definition of the Nautical Bottom is not a problem, nor its detection by survey techniques.

4.2 IN THE PRESENCE OF MUD

4.2 (a) In the Laboratory

The behaviour of a ship in the presence of a fluid mud layer has been thoroughly researched by G. Delefortrie [2]. This work is based upon multiple captive manoeuvring tests in Flanders Hydraulics Research shallow water tank, with a model of a 6000 TEU container carrier, a 8000 TEU container carrier and a bulk carrier.

Figure 8 summarizes very well the influence of fluid mud on the ship's behaviour: on top of the effect caused by the interaction ship-hard bottom (see preceding paragraph 4.1), a ship's behaviour is additionally affected – slowed down – by the presence of a fluid mud layer in the speed range from 2 to 6 knots, a speed range very commonly applicable within harbours.

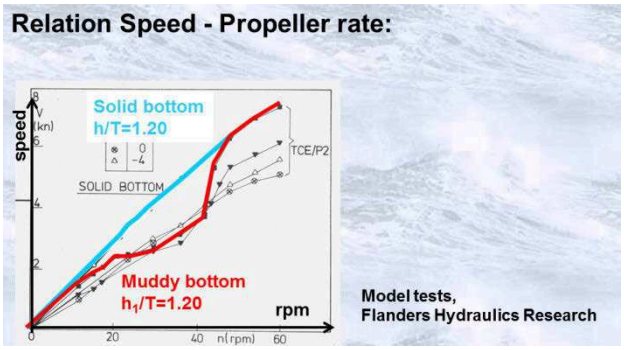

Figure 8. Influence of fluid mud layer [2]

The definition of the Nautical Bottom in the test towing tank is not a problem, nor it's detection: it is the bottom of the towing tank.

Supposing the rheological transition would be accepted – quod non at this moment – to coincide with the Nautical Bottom, would it be safe than to transfer the test results to the in situ reality, without additional correction factors with regard to this Nautical Bottom concept?

4.2 (b) In situ

In the test tank, exactly as in situ, there are two interfaces: the interface water – fluid mud equivalent – and the interface fluid mud equivalent – solid bottom.

This second interface in the test tank (fluid mud / solid bottom) is a very extreme transition and, although not a rheological one but a fluid/solid one, it is similar to the rheological transition in the in situ mud layers.

Furthermore, from the point of view of fluid mechanics, the high viscosity mud phase does resist flowing much more than the low viscosity phase, the propeller's efficiency degenerates accordingly and induces the same kind of effects as described in paragraph 4.1.: reduced effectiveness of the propeller(s) and the rudder, increasing stopping distances and stopping time, increasing diameter of turning.

The scale of these effects, however, may be somewhat less pronounced because the high viscosity mud does flow eventually while solid soil doesn't. Anyway, the laboratory test results can be expected to be on the safe side as compared to the real situation.

5 SHZ VLAANDEREN 18 TRIALS [10]

In the period 1986 – 1988, a series of trials were carried out with SHZ 'Vlaanderen 18'. These have been reported on many occasions and one particular trial is extremely relevant and has raised a lot of interest in the maritime community. Delefortrie [2] reports it as follows: *An occasional full scale trial that deserves to be mentioned is when the ship navigated at slow speed in contact with the probable rheological transition level, situated at a density of 1.20 ton/m³. The crew of the ship thought the vessel would decelerate quickly due to contact with the highly viscous mud layer, but the opposite occurred. The ship kept navigating at slow speed and not even the reversed propellers or bow thrusters were able to stop the vessel. A disaster could be avoided in extremis by decreasing the draught of the vessel.*

The vessel sailed with an under keel clearance of quasi zero, relative to the rheological transition level. Propeller and rudder effectiveness were reduced to zero, but the vessel didn't stop when in contact with the high viscosity mud.

In comparison to the vessel's contact with the mud-free (sandy/rocky) bottom, the friction forces between the ship's keel and the high viscosity mud are too small to reduce the ship's speed immediately.

This situation is extremely critical: a vessel, without steering capacity, without propeller capacity, unstoppable, retaining its original speed from time of first contact with the high viscosity mud….The consequences could be very damaging, not only for the vessel itself, but also for nearby vessels, quay walls, sluices, bridges…*The Nautical Bottom is the level where the physical contact with a ship's keel causes either damage or unacceptable effects on controllability and manoeuvrability* [3]

The situation described – a vessel navigating with zero under keel clearance relative to the rheological transition – fits perfectly the PIANC definition of the Nautical Bottom

6 SURVEYING THE NAUTICAL BOTTOM

Without the availability of operational survey techniques to measure the rheological transition, it would be useless to introduce the rheological transition as the Nautical Bottom in muddy navigational areas.

Above mentioned survey techniques, however, do exist, and are operational for some time now. Their specifications are public, but these are not the object of this paper: only a synopsis is provided.

The following instruments are perfectly capable to detect the rheological transition.

Remark: derived parameters such as density, viscosity and others are not taken into consideration by the authors, only the capability for locating the level of the rheological transition.

6.1 PRICK PROBES

6.1 (a) MIR – Jan De Nul Group

This instrument is a rebuilding of the Rheometer [11], introduced by Haecon nv in the eighties (the company is no longer active). It is a single point rheometric profiler, measuring the resistance encountered by a small propeller when lowered in the water and the mud layers.

6.1 (b) Graviprobe – dotOcean nv

This instrument is a free fall penetrometer, measuring the accelerations/deceleration when passing through the water and mud layers.

6.1 (c) Rheotune – Stema Systems BV

It uses the tuning fork response in the water and mud layers when lowered.

6.1 (d) Acceleroprobe - THV Nautic (prototype)

This probe uses the measurement of acceleration/ deceleration of a falling (streamlined) body in the water to detect the depth of the rheological transition. It is integrated in the Rheocable equipment

6.2 CONTINUOUS SURVEY METHODS

6.2 (a) Rheocable – THV Nautic

A heavy object is towed behind a survey vessel. If the vessel would stop the object would slowly sink into the solid mud. Within a given velocity window, usually between 1 to 5 knots, the high viscosity of the solid mud generates a tension in the towing cable pulling the object out of the solid mud, where it stays on the solid/fluid mud interface. A pressure sensor attached to the object measures the water depth. A resistivity cable trailing behind the object verifies if the cable is on the solid mud and not floating above it.

7 CONCLUSIONS

The following steps have led to the conclusion that the Nautical Bottom coincides with the rheological transition:

1. In an estuarine mud layer, continuously or cyclically fed by settling mud particles, a mud gel point always exists.

2. The gel point phenomenon generates a physical separation between two phases in the mud layer: the liquid state and the solid state, or a low viscosity phase and a high viscosity phase.

3. All viscosity parameters do change drastically at the gel point level in the estuarine mud layers: this is called the rheological transition.

4. This rheological transition is a physical reality in all estuarine mud layers.

5. A vessel navigating with zero under keel clearance relative to the rheological transition is out of control. Therefore - in accordance with the PIANC definition - the rheological transition is identical to the Nautical Bottom

6. Instruments, based on different techniques, are available and operational to measure the rheological transition.

Without the use of the under keel clearance to the rheological transition as a parameter, no exact estimation of a ship's safety, navigating in a muddy area, can be obtained. This involves important risks: the safety of the ship on one side, a (to) heavy maintenance dredging budget on the other side. In the present state of affairs, these risks are perfectly avoidable.

8 REFERENCES

1. Toorman, E.A. (1992). Het mechanisch gedrag van slib in estuaria, *Water, tijdschrift over de waterproblematiek*, nr. 66, pp. 159-167

2. Delefortrie, G. (2007). *Manoeuvring Behaviour of Container Vessels in Muddy Navigation Areas,* PhD thesis, Ghent University.

3. PIANC (1997). Approach channels – A guide for design, *Final report of the joint Working Group PIANC and IAPH, in cooperation with IMPA and IALA. Supplement to PIANC Bulletin, No. 95,* 108 pp.

4. Verruijt, A. (2004). *Soil Mechanics*, Delft University of Technology.

5. Wurpts, R. (2003). Bestimmung der Nautische Sohle durch Anwendung rheologische Parameter – 15 Jahre Erfahrung mit fluid mud, *Hansa International Maritime Journal,* Volume 140, 10, pp. 74 – 79.

6. Kerckaert, P.; Malherbe, B.; Bastin, A. (1985). Navigation in muddy areas – the Zeebrugge experience, , *Bull. Perm. Int. Assoc. Navig. Congr*. 59(48), pp. 127-135

7. Vantorre, M.; Laforce, E., Delefortrie, G. (2006). A novel methodology for revision of the nautical bottom, Seminar: *Flanders, a maritime region of knowledge*,(MAREDFlow) p.15-34. (http://hdl.handle.net/1854/LU-345084, consulted 2nd of October 2015).

8. Claeys, S.; De Schutter, J.; Mostaert, F.; Van Hoestenberghe, T. (Apr-2011). Individual trials of in-situ rheological based instruments in the Sludge Test Tank. Rheocable & Accelero probe. Version 2_0. *WL Rapporten, 751-1a*. Flanders Hydraulics Research: Antwerp, Belgium.

9. Bole, A. G.; Dineley, W. O.; Nicholls, C. E., (2011). *The Navigation Control Manual*, Routledge (New-York), second edition, 216 pp.

10. Vantorre, M., (1990). *Meetvaarten met sleephopperzuiger Vlaanderen XVIII te Zeebrugge (1986–1988), interpretatie der meetwaarden en vergelijking met modelproeven*, Rijksuniversiteit Gent, Dienst voor Scheepsbouwkunde, Diensten van de Vlaamse Executieve – Openbare Werken en Verkeer, Bestuur der Waterwegen en van het Zeewezen, Waterbouwkundig Laboratorium Borgerhout.

11. Van Craenenbroeck, K.; Vantorre, M. (1992). Navigation in muddy areas: establishing the navigable

depth in the port of Zeebrugge, *Terra et Aqua: International Journal on Public Works, Ports and Waterways Developments* 47: 3-12.

9 AUTHORS' BIOGRAPHIES

Peteralv Brabers is since 1996, the managing director of Demco NV, a company performing marine geophysical surveys: Aquares and Rheocable. He holds a Ph. D. in mining engineering and was from 1981 to 1986 teaching and research assistant at the KUL-Leuven. His previous experience includes also project management and development of new geophysical techniques for Geosurvey NV, a Belgium based geophysical company.

Marcus Druyts is since 2001 managing director of MDCE bvba, a company involved in dredging consultancy, development of new sounding equipment – Rheocable – and tools for the dredging industry. He holds a M. Sc. Degree in naval architecture, Ghent University and has a career in the dredging industry: Baggerwerken Decloedt NV (Deme). From 1991 to 2001 he was operations manager for the capital and maintenance dredging activities on the Belgian Coast.

4th MASHCON, Hamburg - Uliczka et al. (eds) - © 2016 Bundesanstalt für Wasserbau ISBN 978-3-939230-38-0 (Online)
DOI: 10.18451/978-3-939230-38-0_9

NUMERICAL SIMULATION OF THE SHIP BOTTOM INTERACTION OF DTC CONTAINER CARRIER FOR DIFFERENT KEEL CLEARANCE IN PURE SWAY MOTION

R He, **Z Z Zhang, X Z Wang** and **D K Feng,** School of Naval Architecture and Ocean Engineering, Huazhong University of Science and Technology, P. R. of China

SUMMARY

In this paper, numerical simulations were performed to study the hydrodynamic behavior of DTC container carrier under the same conditions with the experimental set up and operation conditions. In order to predict ship motion with larger amplitude, overset grid generation technology was used during the simulation. For ship-bottom interaction, the mean running sinkage and trim are major concerns during the Planar Motion Mechanism (PMM) test as well as forces and moment measurement. Therefore, the 3DOF module is applied in the numerical simulation. The heave and pitch motions are predicted by solving the equations of motions on each time step based on the hydrodynamic forces obtained from the solver. A good correspondence between the measured and simulated result is noted, indicating that forces and moments on the ship are well predicted. In the second stage, a set of systematic computations is carried out to study the ship-bottom interaction with different depth. The forces and moments on the hull with varying water depth are predicted and explained.

NOMENCLATURE

B	Beam (m)
Cfx	Coefficient of non-dimensional surge force
Cfy	Coefficient of non-dimensional sway force
Cmz	Coefficient of non-dimensional yaw moment
D	Depth (m)
Fr	Froude number based on L_{pp} (-)
Fr_{crit}	Critical value of Froude number (based on water depth) accounting for blockage(-)
h	Water Depth (m)
L_{pp}	Length between perpendiculars (m)
L_m	Length of the ship model (m)
$O_0x_0y_0z_0$	Earth-bound reference system
$Oxyz$	Ship-bound reference system
$O'x'y'z'$	Horizontal bound towing carriage System
p	Roll velocity (rad/s)
q	Pitch velocity (rad/s)
r	Yaw velocity (rad/s)
t	Time (s)
T	Time period (s)
Tm	Mean draft (T)
u	Longitudinal velocity component (m/s)
v	Lateral velocity component (m/s)
v_{max}	Maximum lateral velocity component(m/s)
w	Vertical velocity component (m/s)
y_{max}	Maximum lateral position (m/s)
β	Drift angle (deg)
φ	Roll angle (deg)
θ	Pitch angle (deg)
ψ	Course angle (deg)
AP	Aft Perpendicular
CG	Centre of Gravity
DTC	Duisburg Test Case
FP	Fore Perpendicular
UKC	Under Keel Clearance
▽	Displacement (m^3)

1 INTRODUCTION

Nowadays, Computational Fluid Dynamics (CFD) is being used as an efficient design tool to predict the maneuvering characters of a ship. Increasing ship sizes in all dimensions and optimizations in the design and maintenance of waterways, request clearer understanding of the interaction between a ship hull and the bottom of the waterways helps to improve the maneuvering performance and increase the security of operation. Therefore, ship-bottom interaction is significantly important for the navigation. Particularly in restricted water the interaction can be stronger, and the problem may also be crucial for the waterways and harbor design. Due to these facts, ship-bottom interaction has been the focus in many ways for a long time. In general, most of the investigations still rely on empirical formula, experimental tools as well as numerical simulations, among which the first two types are more widely used. In this article, the planar motion mechanism (PMM) simulation is employed using an in-house RANS solver.

Table 1. Effect of depth restrictions[1]

Definitions	Ratio	Depth restrictions
Deep water	$h/T_m>3.0$	No effect
Medium deep water	$1.5<h/T_m<3.0$	Noticeable
Shallow water	$1.2<h/T_m<1.5$	Very significant
Very shallow water	$h/T_m<1.2$	Dominates the behavior

In shallow water, the clearance under the vessel becomes smaller, resulting in an increase of the current loads due to the blockage effect. The ratio of water depth to draft is used to evaluate the depth restrictions. Table 1 shows the details of effect of depth restrictions.

Among several methods for maneuvering characters prediction, PMM tests are the most commonly accepted approaches.
However, the tests contain several disadvantages; (1) the expensive test facilities and sophisticated experimental settings; (2) considerable scale effect resulting from the impossibility in practice to achieve Froude number and Reynolds number similarities simultaneously; (3) limitations in obtaining details of flow fields around the ship. CFD based maneuvering prediction methods significantly manage to resolve these problems as the viscous effects
are very important for accurate maneuvering prediction.
SIMMAN2008 [2] and SIMMAN2014 maneuvering workshop benchmarks the prediction characters of ship maneuvering using both system-based and CFD-based methods. Broglia [3] demonstrated the capability of CFD prediction for dynamic PMM simulations of KVLCC1/KVLCC2 with appendage. KumarPatel [4] investigated the shallow water effect on the wave pattern using a commercial Rans solver starccm+. Liu [5] extends a new 6DOF module and simulate the oblique towing tests, while the shallow water effect is also taken into account. These studies showed that CFD can improve the modeling of ship hydrodynamics. Sakamoto [6] and Yoon [7] present the benchmark CFD validation measurements for surface combatant 5415, both experiment and simulation results are mathematically formulated by Fourier series method to obtain expressions of the hydrodynamic derivatives.
In this paper computations are presented for the ship-bottom interaction in a small UKC. The CFD results are shown to accurately match the experimental results. Blockage effects and scale effects are known issues when carrying out model tests for shallow water but these effects can be efficiently quantified with CFD.
Furthermore, a series of systematic computations with a wide range of UKC are presented to provide more extensive knowledge about the ship-bottom interaction.

2 BENCHMARK DESCRIPTION

The model ship used for this research is the Duisburg Test Case (DTC) [8][9] container ship, which is a 14,000 TEU capacity container ship developed by Institute of Ship Technology, Ocean Engineering and Transport Systems for research purpose, including the benchmarking and validation of numerical method. The Planar Motion Mechanism tests include both static test and dynamic tests that have been executed with a scale model of DTC container ship in the Towing Tank for Maneuvering in Shallow Water at Flanders Hydraulics Research, Antwerp Belgium.
The geometric characteristics of the DTC model are presented in [9] The length between perpendiculars is 3.984m with a scale factor 1/89.11. The DTC container ship was equipped with a twisted rudder with a costa bulb, and with a pitch-fixed five-bladed propeller. The geometries of both hull and appendage are illustrated in Figure 1. For the dynamic PMM simulations, the ship has prescribed lateral velocity in pure sway motion and rotation velocity around Z axis as well as lateral velocity in pure yaw motion. Table 2 lists the principal dimensions of the vessel for the model used in the PMM tests. In the benchmark test, static draft and dynamic PMM tests have been performed, for both test two model speed are tested. It should be noted that only detailed test data of pure sway and pure yaw are given by the experiments.

Table 2. Principal Dimensions of vessel

Ship parameter		Full Scale	Model Scale
Scale	λ	1	89.11
Lpp	m	355	3.984
B	m	51	0.572
d	m	14.5	0.163
∇	m^3	173.925	0.2458

Figure 1. DTC Hull Form

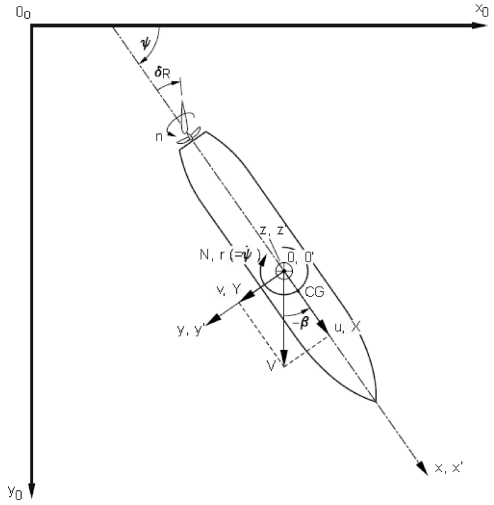

Figure 2. PMM test coordinate system

The coordinate system utilized for PMM test is given by Figure 2 [9] Two coordinate system are used in the experimental test, $O_0x_0y_0z_0$ represents the earth-fixed coordinate system and be used for towing carriage, Oxyz is the ship-fixed coordinate system, and center is at mid-point of the ship (0.5Lpp from AP to FP). O'x'y'z' is used during experimental test and thus also during ship hydrodynamics simulation based upon model test. In the ship-fixed coordinate system, x axis follows from stern towards bow direction, y axis follows from middle towards starboard, z axis follows from the waterline towards the keel.
During the pure sway test, the ship axis is always parallel along with the velocity direction of the free-steam, the longitudinal speed u takes a constant value, while the sway position y, sway velocity v and sway acceleration $\dot{v}$ as a function of time.

$$\begin{cases} y = y_{max}cos(\omega t) \\ v = -v_{max}sin(\omega t) \\ \dot{v} = -\dot{v}_{max}cos(\omega t) \end{cases} \quad (1)$$

where $\omega_{sway} = 2\pi/T$ is the angular frequency of sway motion, v_{max} is the maximum sway velocity, and $\dot{v}_{max}$ is the maximum sway acceleration.

3 RANS SOLVER

3.1 DYNAMIC OVERSET

The overset grid technique is adopted to simulate dynamic ship motion and grid refinement, the overset grid technique provides the ability of separate grids independently moving without restrictions. The in-house overset software os-grid written by Fortran is used to obtain the grid connectivity information. For the dynamic PMM simulation in this paper, the relative position between overset grids change very time step, requiring regeneration of the grid connectivity information in every step time. While simulation starts, flow variables (velocity, force, pressure, density function) exchange information between the RANS solver and the overset solver at every time step. Firstly, the RANS solver computers the basic flow parameter, and then os-grid searches for the point located in the overlapping domain. Secondly, the forces and moments will transmit to the inner grid, as well as the motions predicted by the first step. Flow parameter in the inner grid finishes its iteration and send the flow information back to the outer grid by os-grid. By repeating the process every time step, the RANS solver can finish the PMM test trim and sinkage prediction.

Unlike the general overset grid assembly software SUGGAR [10], os-grid can only handle with structured grids and lacks the capability for generating the grid connectivity information in parallel computers. Since the generation of the grid connectivity information on structured grid is much more fast than on an unstructured grid, the time spent on the exchange of information is acceptable. But the promotion of the efficiency will be an important part of the future work. Serial and parallel performance of the code is still being investigated and improved and will not be discussed in this paper.

3.2 GOVERNING EQUATIONS

The viscous flow is represented by the non-dimensional incompressible unsteady Reynolds-Averaged Navier-Stokes (URANS) equations coupled with the time-averaged continuity equation:

$$\begin{cases} \frac{\partial \bar{u}_i}{\partial t} + \bar{u}_j \frac{\partial \bar{u}_i}{\partial x_j} + \frac{\partial \bar{p}}{\partial x_i} - \frac{1}{Re}\frac{\partial^2 u_i}{\partial x_j \partial x_j} - \frac{\partial}{\partial x_j}\left(-\rho \overline{u_i' u_j'}\right) = 0 \\ \frac{\partial \bar{u}_i}{\partial x_i} = 0 \end{cases} \quad (2)$$

Where $\bar{u}_i$, $\bar{u}_j$, $\bar{p}$ denote the average velocity, pressure, respectively. $-\rho\overline{u_i' u_j'}$ denotes the Reynolds stresses, u_i' represents the fluctuating velocity in time.

In addition, the two-equation shear stress transport (SST) model is employed to close the RANS equations:

$$\begin{cases} v_t = \frac{k}{\omega} \\ \frac{\partial k}{\partial t} + \left(U_j - \sigma_k \frac{\partial v_t}{\partial x_j}\right)\frac{\partial k}{\partial x_j} - \frac{1}{R_k}\nabla^2 k + s_k = 0 \\ \frac{\partial \omega}{\partial t} + \left(U_j - \sigma_\omega \frac{\partial v_t}{\partial x_j}\right)\frac{\partial k}{\partial x_j} - \frac{1}{R_\omega}\nabla^2 \omega + s_\omega = 0 \end{cases} \quad (3)$$

The control equations adopted cell-centered finite differential. The discretization of time terms in implemented by 2nd Euler backward difference scheme. In eq.3, the discretization of convective terms is implemented by 2nd upwind differences scheme and for the diffusive fluxes central differences are applied.

3.3 MANEUVERING SIMULATION

A motion of five degrees of freedom (5 DOF) was adopted in the simulation. The rigid-body equations described in eq.4 written in a hybrid coordinate system have determined the motions excepting roll.

$$\begin{cases} X = m[\dot{u} - rv + wq - x_G(q^2 + r^2) + z_G\dot{q}] \\ Y = m(\dot{v} + ru + z_G qr + x_G\dot{r}) \\ N = I_z\dot{r} + mx_G(\dot{v} + ur) \end{cases} \quad (4)$$

Where u, v and w are the surge, sway and heave velocity in the longitudinal, lateral and vertical directions of the earth-fixed coordinate system, respectively. $\dot{u}$, $\dot{v}$ are accelerations. q and r are the angular velocity rotations around the axes x and axes z, respectively. $\dot{q}$ and $\dot{r}$ are the pitch and yaw accelerations, respectively. x_G, z_G are the location of the center of gravity of the vessel. I_z are the mass and moment of inertia of the model.

3.4 COMPUTATIONAL DOMAIN AND GRIDS

The computational domain for benchmark test study is made up by various boundaries as follows: inlet plane in front of the bow, outlet plane behind the tail, no-slip conditions are applied on the hull, relative-frame no-slip conditions are applied for both the bottom and side. The domain extend from xmin = -Lpp to xmax = 3Lpp on axis x, from ymin = -3.5m to ymax = 3.5m on axis y and from zmin = -0.196 to zmax = 0.2Lpp on axis z, respectively.

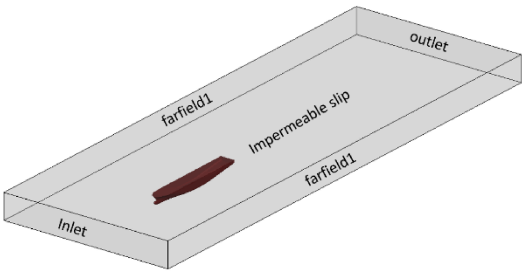

Figure 3. Solution domain and boundary conditions

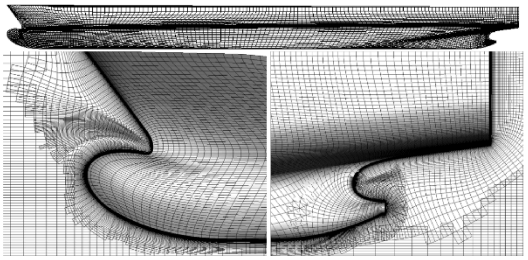

Figure 4. Overset grid near the bulb, stern and in gap between ship and bottom

The grids were generated by Pointwise for different UKC, with h/T = 1.2 representing very shallow water, h/T = 1.5 representing shallow water, h/T = 3 representing middle deep water and h/T = 10 representing deep water. There are two different grid blocks for each set: inner grid for hull, outer grid for background. With the dynamic overset technology, the inner grid topology around the hull for the four water depths was the same, the outer grid topology are similar except for the water depth between the keel and bottom. The inner grid is generated with a hyperbolic grid generator using C-type topology. In this study, no wall function is used, the minimum size of the grid cell for boundary layer should be refined to 10e-6 as the SST $k-\omega$ turbulence model was adopted and maximum y+ value around the hull is less than 1. The outer grid is generated using H-type grid topology. The total number of grid points is 4.1M.

3.5 GRID SENSITIVITY INVESTIGATION

To investigate the sensitivity of the results to the grid resolution, three sets of grids with 2.3M, 4.1M and 9.7M are used in the preliminary study. The grid densities are systematically vary as a refinement ratio 1.4 at each directions. A comparison of resistance coefficient is shown in Table 3, the inlet velocities of various are at 0.599m/s and 0.872m/s respectively. As can be seen, there is lightly difference between the medium and fine meshed and the computation values of resistance are in good agreement with the experimental values. Thus, the medium mesh with about 4.1M is selected as the final grid in the PMM simulation.

Table 3. A comparison of coefficient of resistance of the DTC at different Fr values

V (m/s)	Coefficient of total resistance at different Fr values (10e-3)		
	Coarse mesh(2.3 M)	Medium mesh (4.1 M)	Fine mesh (9.7M)
5.99	6.82	6.79	6.78
8.72	7.30	7.28	7.28

4 RESULTS AND ANALYSIS OF HYDRODYNAMIC DERIVATIVES

4.1 NON-DIMENSIONALISED OF PARAMETERS

All the fluid variables are transmitted to a non-dimensional form with respect to the advancing velocity of ship u, the ship length *Lpp* and the fluid density ρ. The relations between non-dimensional parameters and dimensional ones can be seen in the following equations.

$$time, t^* = t\left(\frac{u}{Lpp}\right)$$

$$position,\ x^* = \frac{x}{Lpp}$$

$$velocity, v^* = \frac{v}{u}$$

$$acceleration, \dot{v}^* = \frac{v}{u^2}$$

$$force, F^* = \frac{F}{0.5\rho u^2 Lpp^2}$$

$$Moment, M^* = \frac{M}{0.5\rho u^2 Lpp^3}$$

$$Pressure, p^* = \frac{pLpp}{\rho u}$$

4.2 PURE SWAY MOTION

Comparisons between numerical simulation results and experimental results will be presented for the resistance coefficient Cfx, sway resistance coefficient Cfy, yaw moment coefficient Cmz, as well as the sinkage and trim. Test 2016_C and Test 2016_D have the same under-keel-clearance (UKC) and motion frequency, but the inlet velocity u is different. The pure sway test can be used to determine derivatives of $Y_{\dot{v}}$ and $N_{\dot{v}}$, as well as the Y_v and N_v. However, Y_v and N_v can also be determined from the static PMM test, and results through static test are more accurate and convenient to obtain in general.

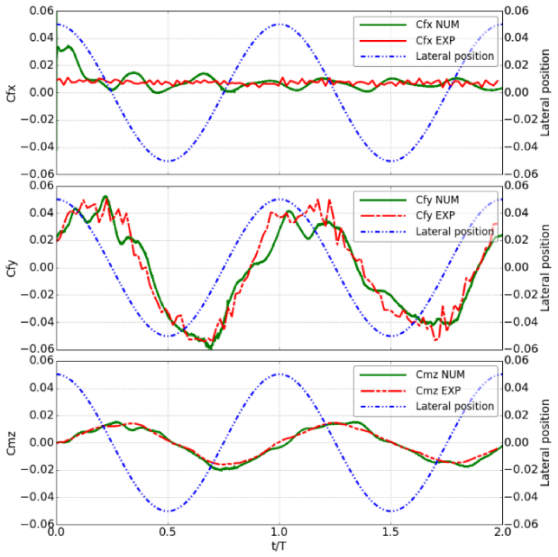

Figure 5. Time-history of coefficient of force and moment over 2 periods for DTC in pure sway motion, free to heave and pitch (u=0.599m/s)

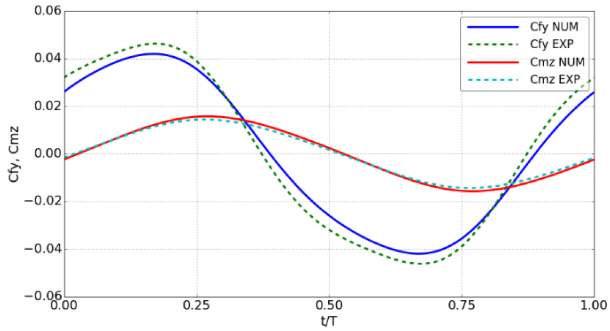

Figure 6. Time-history of coefficient of force and moment over 1 period for DTC in pure sway motion, free to heave and pitch (u=0.599m/s)

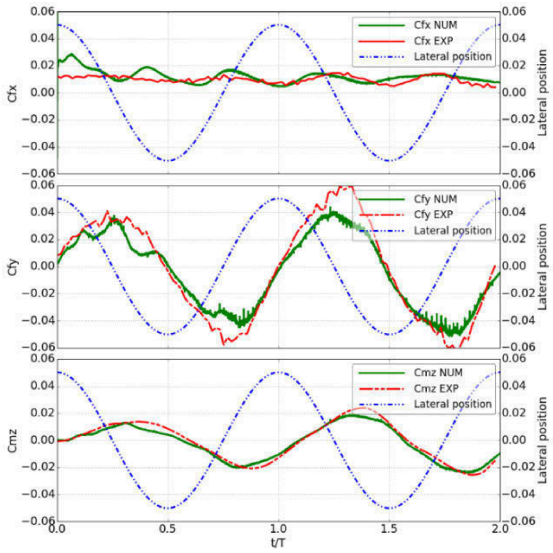

Figure 7. Time-history of coefficient of force and moment over 2 periods for DTC in pure sway motion, free to heave and pitch (u=0.872m/s)

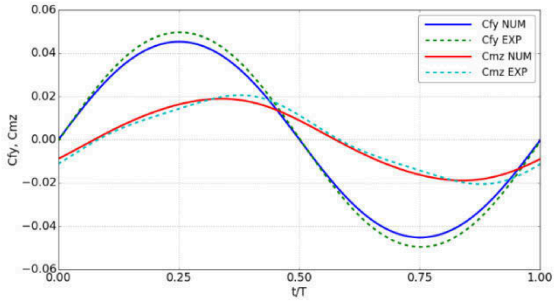

Figure 8. Time-history of coefficient of force and moment over 1 period for DTC in pure sway motion, free to heave and pitch (u=0.872m/s)

For each force and moment, the results are presented as non-dimensional time history type. Figure 5 and Figure 7 show the CFD pure sway test compared with the experimental test of resistance coefficient Cfx, total lateral force coefficient Cfy and yaw moment coefficient Cmz for Test 2016_C and Test 2016_D, respectively. In these figures, the raw curve from the simulation in two motion cycles has been used for analysis. Figure 6 and Figure 8 are also the Cfy and Cmz comparisons, only for the curves have been fitted using Fourier series, for both the simulation and experimental results.

Table 4. Hydrodynamic derivatives value for the pure sway motion

	u=0.599m/s			u=0.872m/s		
	EFD	CFD	E%	EFD	CFD	E%
Y_v	-0.2186	-0.2585	18.2	-0.7154	-0.6555	8.3
N_v	-0.1214	-0.1329	9.4	-0.2975	-0.2487	16.4
$Y_{\dot{v}}$	-0.1461	-0.1186	18.8	0.0066	0.0016	75.3
$N_{\dot{v}}$	0.0075	0.0110	46.7	0.1092	0.0864	20.9

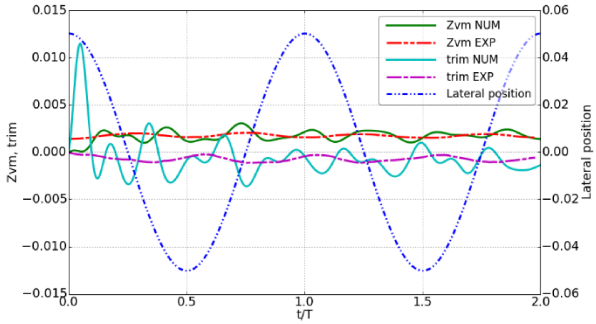

Figure 9. Time-history of mean sinkage and trim over 2 periods for DTC in pure sway motion (u=0.599m/s)

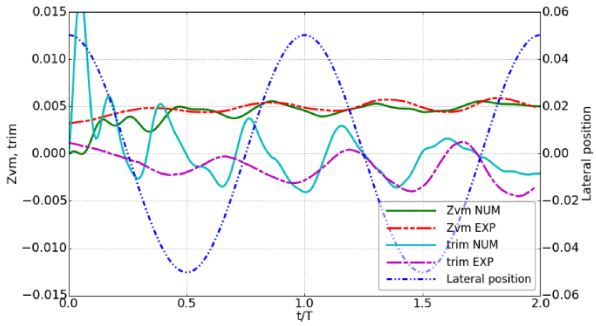

Figure 10. Time-history of mean sinkage and trim over 2 periods for DTC in pure sway motion (u=0.872m/s)

Figure 9 shows the comparison of the motion tendency of sinkage and trim with respect to non-dimensional time. Results for both sinkage and trim are almost the same after the simulation get stable. In common with comparison in Figure 5 - Figure 10, using simulation for pure sway shows high feasibility, accuracy and acceptable time consumption. The overall trend shows that the computational results agree well with the experimental data. It implies that the numerical simulation of pure sway test can be an alternative option to the experiment. Normally, $Y_{\dot{v}}$ is negative, but it increases to a positive value when the velocity gets close to the critical velocity, and the value is very close to zero, thus E% errors of the derivative $Y_{\dot{v}}$ get larger.

4.3 SYSTEMATIC COMPUTATIONS

In the previous sections, the ship-bottom interaction in very shallow water has been studied for four benchmark test cases. The comparison included resistance, lateral forces and yaw moment, and provided sinkage and trim. However, the trend with respect to various UKC is not clear. More over in the real situation, specifically during the motion in the harbor, the ship-bottom interaction often takes place in a complex situation with different UKC. Therefore, it would be worthwhile to study the ship-bottom interaction from a more general perspective.
The systematic computations were performed applying the same motion as in the preliminary benchmark case study, and the results will be reported as follows.
By using overset method, the grid topology around the hull for the four water depths was the same. The difference is the overset region between the bottom and the hull, as shown in Figure 11.

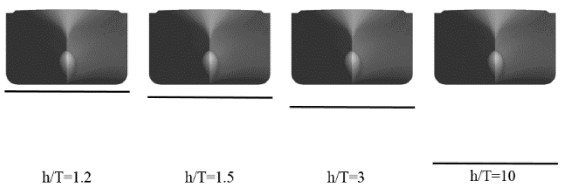

Figure 11. Different water depth considered in the systematic computations

Table 5. Matrix of simulation conditions for systematic computations

Conditions	Pure Sway				
Test no.	C	D	E	F	G
h/T_m	1.2	1.2	1.5	3.0	10
Speed(m/s)	0.599	0.872	0.872	0.872	0.872
Fr	0.096	0.139	0.139	0.139	0.139
Re (10e-6)	2.381	3.463	3.463	3.463	3.463
ymax(m)	0.2	0.2	0.2	0.2	0.2
Drift Angle(deg)	6.004	4.132	4.132	4.132	4.132
T(s)	20	20	20	20	20

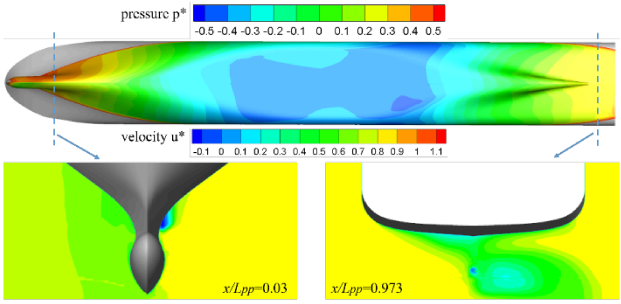

Figure 12. Pressure distributions on the bottom of DTC and velocity distributions on two slices in simulation case D (h/T = 1.2)

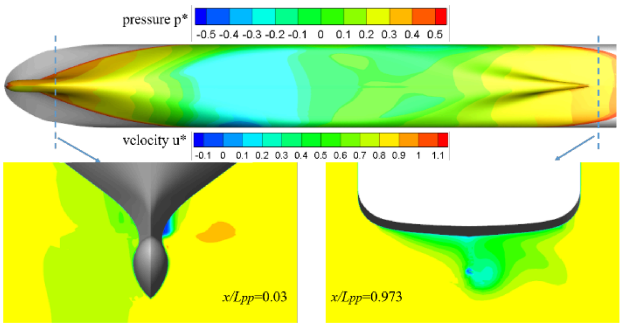

Figure 13. Pressure distributions on the bottom of DTC and velocity distributions on two slices in simulation case E(h/T = 1.5)

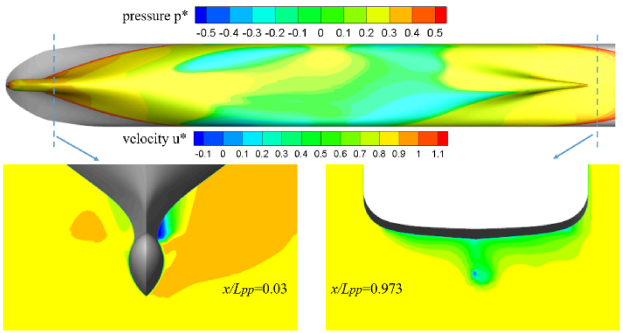

Figure 14. Pressure distributions on the bottom of DTC and velocity distributions on two slices in simulation case F (h/T = 3.0)

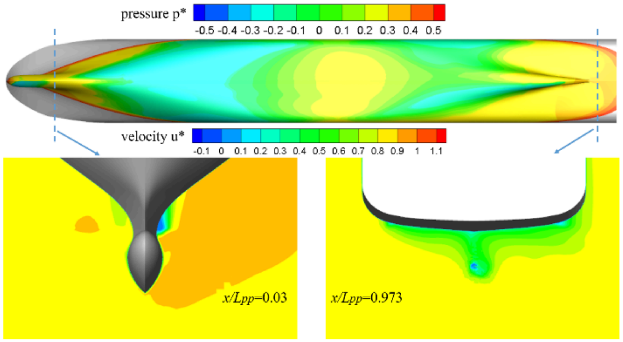

Figure 15. Pressure distributions on the bottom of DTC and velocity distributions on two slices in simulation case G (h/T = 10)

Figure 12, Figure 13, Figure 14 and Figure 15 show the pressure distributions on the keel and the averaged axial velocity at two slices along the longitudinal direction.
In case D (Figure 12), the suction peak (i.e. negative pressure region) is located at the middle of the bottom. Therefore there is an additional resistance, tending to increase the lateral force and the sinkage. For the velocity distributions on the slice at x/lpp = 0.973, there is a clear hook-shape pattern.
In contrast with case D, in case E (Figure 13) the negative pressure region on the middle-body is moving to the fore-body and the value of the pressure is increased over the entire bottom. Furthermore, the pressure difference is reduced at the bow.
As in case F (Figure 14) and case G (Figure 15), there is a positive pressure region located at the middle of the

ship. The velocity distributions on the slice located at the bulb and stern show the same characteristics.
The tendency of Cfy and Cmz for ratio h/Tm is shown in Figure 16, and the tendency of the non-dimensional sinkage and trim for ratio h/Tm is shown in Table 6.

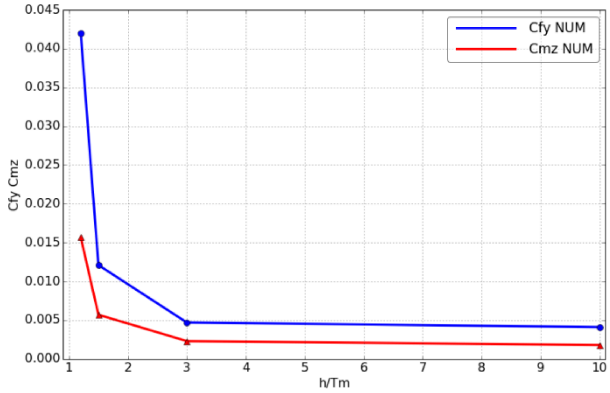

Figure 16. Tendency of Cfy and Cmz for ratio h/Tm

Table 6. Matrix of simulation results for systematic computations vs. expriments

Test no.	D exp	D	E	F	G
Zvm*(10e-3)	-4.833	-4.855	-3.012	-1.139	-0.489
Trim*(10e-3)	-1.464	-1.039	-1.424	-0.900	-0.786

5 CONCLUSIONS

The paper includes Planar Motion Mechanism (PMM) test results produced using CFD and compares with experimental data. It also discusses the hydrodynamic derivation from the simulated PMM results and compares them with the values from the test. These results show good agreement in pure sway cases, some discrepancy is observed, which may be attributed to the complex motion. The predicted pressure distribution on the hull and on the surface in one motion period was used to explain the lateral force and yaw moment acting on the hull. There was also a good correspondence between the two sets of PMM simulations both for trim and sinkage, despite for the difference in Cfy as mentioned above. However, the difference of lateral force Cfy between the simulation results and experimental results with the smallest UKC was relatively large and needs further studying. A detailed error analysis in both computations and measurements should be of great value.
Based on the benchmark validation study, an investigation about PMM simulations with different UKC was made. In the investigation, the forces and moments in the variation were predicted. Furthermore, the axial wake fields and the axial velocity contours on the slices along the longitudinal direction illustrated the ship-bottom interaction with varying UKC. In this way, resulting trends of the systematic computations could be explained. The forces and moments all decreased as the UKC was increased, and the changes on the forces were most significant. The sinkage and trim also decreased as the UKC was increased, while for the change was relatively small.

6 ACKNOWLEDGEMENTS

The authors thank Flanders Hydraulics Research and the Maritime Technology Division, Ghent University, Belgium, for providing the ship-bottom interaction benchmark test data.

7 REFERENCES

1. PIANC (1992). Capability of Ship Manoeuvring Simulation Models for Approach Channels and Fairways in *Harbours: Report of Working Group No. 20 of Permanent Technical Committee II*.

2. Stern, F.; Agdrup , K. (2008). SIMMAN 2008 workshop on verification and validation of ship maneuvering simulation method. *Proceedings of SIMMAN 2008 workshop on verification and validation of ship maneuvering simulation methods*, Lyngby, Denmark.

3. Broglia, R.; Muscari, R.; Di Mascio, A. (2008). Numerical simulations of the pure sway and pure yaw motion of the KVLCC1 and 2 tanker. *Proceedings of SIMMAN 2008 workshop on verification and validation of ship maneuvering simulation methods*, Lyngby, Denmark.

4. Patel, P..K.; Premchand, M. (2015). Numerical Investigation of the Influence of Water Depth on Ship Resistance. *International Journal of Computer Applications* 116: pp. 10-17

5. Liu, X.; Wan, D. (2015). Numerical Simulation of Ship Yaw Maneuvering in Deep and Shallow Water. *The Twenty-fifth International Offshore and Polar Engineering Conference*, Hawaii, USA.International Society of Offshore and Polar Engineers: pp. 21-26

6. Sakamoto, N.; Carrica, P. ; Stern, F. (2012). URANS simulations of static and dynamic maneuvering for surface combatant: part 1. Verification and validation for forces, moment, and hydrodynamic derivatives. *Journal of Marine Science and Technology* 17: pp. 422-445. doi:10.1007/s00773-012-0178-x

7. Yoon, H.; Simonsen, C.; Benedetti , L.; Lon-go, J. ; Toda, Y. ; Stern, F. (2015). Benchmark CFD validation data for surface combatant 5415 in PMM maneuvers–Part I: Force/moment/motion measurements. *Ocean Engineering* 109: pp. 705–734. doi:10.1016/j.oceaneng.2015.04.087

8. el Moctar, O.; Shigunov, V.; Zorn, T. (2012). Duisburg Test Case: Post-panamax container ship for benchmarking. *Ship Technology Research* 59: pp. 50-64.

9. Eloot, K.; Vantorre, M.; Delefortrie, G.; Lataire, E. (2016). Running Sinkage and Trim of the DTC Container Carrier in Harmonic Sway and Yaw Motion: Open

Model Test Data for Validation Purposes. *Fourth International Conference on Ship Manoeuvring in Shallow and Confined Water (MASHCON): Ship - Bottom Interaction*, 23-25 May 2016, Hamburg, Germany.

10. Noack, R. (2005). SUGGAR: a general capability for moving body overset grid assembly. *17th AIAA Computational Fluid Dynamics Conference*, Toronto, Ontario, Canada.

8 AUTHORS BIOGRAPHIES

Ran He is a research student, pursuing Ph.D., in School of Ocean Engineering, Huazhong University of science and technology. His area of research is Numerical study of surface ship maneuvering.

Zhiguo Zhang holds the position of Professor School of Ocean Engineering, Huazhong University of science and technology. He has more than 20 years' experience in teaching and research related to Naval Architecture and Ocean Engineering. His major fields of interest are ship maneuvering and motions, propeller performance and ocean wave-structure interaction.

Xianzhou Wang is a lecturer and research fellow in School of Ocean Engineering, Huazhong University of science and technology. He obtained his Ph.D. in Ocean Engineering. His research interests are nonlinear dynamical fluid structure interaction systems applications in ocean and ship system control.

Dakui Feng is a lecturer and research fellow in School of Ocean Engineering, Huazhong University of science and technology. He obtained his Ph.D. in Ocean Engineering. His area of interest is ship hydrodynamics, ocean wave-structure interaction and wind engineering.

4th MASHCON, Hamburg - Uliczka et al. (eds) - © 2016 Bundesanstalt für Wasserbau ISBN 978-3-939230-38-0 (Online)
DOI: 10.18451/978-3-939230-38-0_10

RANS-BASED NUMERICAL SIMULATION OF CAPTIVE MODEL TESTS IN SHALLOW WATER FOR THE DTC CONTAINER CARRIER

Y Liu, School of Naval Architecture, Ocean and Civil Engineering, Shanghai Jiao Tong University, Shanghai, China
Z J Zou, School of Naval Architecture, Ocean and Civil Engineering, State Key Laboratory of Ocean Engineering, Shanghai Jiao Tong University, Shanghai, China; Collaborative Innovation Center for Advanced Ship and Deep-Sea Exploration, Shanghai, China
L Zou, School of Naval Architecture, Ocean and Civil Engineering, Shanghai Jiao Tong University, Shanghai, China

SUMMARY

In very shallow water, the effect of depth restriction is very significant and dominates ship manoeuvrability. In this paper, numerical simulations of the viscous flow around a bare hull of the DTC container carrier manoeuvring in shallow water are conducted at model scale using the CFD software STAR CCM+. RANS-based simulations of static drift and pure sway tests at 20% UKC and two forward speeds are carried out considering the dynamic sinkage and trim as well as the tank wall effect. The hydrodynamic forces acting on the hull, as well as dynamic sinkage and trim are predicted and discussed. Compared with the model test data, time histories of the forces and moments obtained from numerical simulations show satisfactory agreement, while some discrepancies are found in the dynamic sinkage and trim simulations.

NOMENCLATURE

a	Surface area (m^2)
b	Breadth of ship (m)
B	Width of tank (m)
F	External body force (N)
H	Depth of water of tank (m)
I	Identity matrix (-)
p	Pressure (N/m^2)
R_T	Total resistance (N)
S_m	Blockage factor (-)
T	Ship's even keel static draft (m)
tr	Transpose of the matrix (-)
v	Velocity (m/s)
v_g	Mesh grid velocity (m/s)
V	A cell of volume (m^3)
Y+	Dimensionless wall distance (-)
α	Volume fraction (-)
Γ	Viscous stress (N/m^2)
μ_{eff}	Sum of the laminar μ and turbulence viscosities μ_t (N s/ m^2)
ρ	Density of water (kg/m^3)
DFBI	Dynamic Fluid Body Interaction
RANS	Reynolds-averaged Navier Stokes
UKC	Under-Keel Clearance

1 INTRODUCTION

A ship manoeuvring in restricted waters usually experiences much larger hydrodynamic forces than in unrestricted waters due to the hydrodynamic interaction between the ship and the bottom/bank of the waterway. This hydrodynamic interaction has detrimental influence on ship manoeuvrability and may result in marine accidents such as collision or grounding. The ship experiences dynamic sinkage and trim (squat), notably in very shallow waters, due to the hydrodynamic forces acting on the hull. In addition to the squat, shallow water flows are influenced by various factors such as free surface elevation, tank wall blockage, ship speed, bank geometry, unsteady flow features, water depth, etc. Therefore, to ensure a safe navigation it is of great importance to accurately predict the hydrodynamic force acting on the ship by taking the shallow water effect into account.

Traditionally, model tests, full scale trials and theoretical and semi-theoretical methods are used to predict the squat and the hydrodynamic force acting on a manoeuvring ship [1, 2]. Among several methods for manoeuvring prediction, static or dynamic planar motion mechanism (PMM) test is one of the most commonly used approaches. Captive model tests were executed and the shallow water effect on ship manoeuvring was discussed [3, 4]. Some free-running tests in shallow water were also presented [5, 6]. Furthermore, programs based on slender-body theory were used to model the hydrodynamic flow around ships in shallow water [7, 8].

Nowadays, with the rapid development of computer technique and Computational Fluid Dynamics (CFD) method, CFD-based numerical prediction of the hydrodynamic forces has become possible. Ship manoeuvring predictions by solving unsteady Reynolds-averaged Navier Stokes (RANS) equations have been presented in SIMMAN 2008 Workshop [9]. In addition to the deep water manoeuvres, SIMMAN 2014 Workshop also focused on ship manoeuvring in shallow water [10]. In the past, there were many studies regarding the simulation of static manoeuvres [11, 12] while the unsteady manoeuvres were not covered, the situation has been changed recently [5, 13-14]. Free-running tests such as zigzag and turning manoeuvres were numerically studied in reference [5]. Captive model tests were numerically simulated for different drift angles, water depth to draft ratios and ship speeds [15-18]. As presented by these investigations, shallow water effect can be simulated by CFD but still without enough accuracy, especially in the very shallow water condition with below 20% UKC.

To further investigate the interaction between a ship and the bottom of a shallow waterway, this paper uses the benchmark cases of a DTC container carrier, which are provided by Flanders Hydraulics Research (FHR) and Ghent University [19] for the 4th Conference on Manoeuvring in Shallow and Confined Water (MASHCON2016). The benchmark model tests contain harmonic yaw and harmonic sway tests with the DTC at 20% UKC. In this paper, numerical simulations of the viscous flow around the DTC bare hull manoeuvring in shallow water are conducted at model scale using the CFD software STAR CCM+. RANS-based simulations of the static drift and pure sway tests at 20% UKC are carried out considering the dynamic sinkage and trim as well as the side walls of the towing tank as in the model tests. The effect of free surface elevation on the hydrodynamic forces is included by using the Volume of Fluid (VOF) method. The numerical results are compared with the benchmark data and the hydrodynamic characteristics of ship-to-bottom interaction are analyzed.

2 MATHEMATICAL FORMULATION

The governing equations are RANS equations which are closed by modeling the Reynolds stress tensor using SST *k-ω* turbulence model. Mean flow quantities near the wall are simulated according to an all Y+ wall treatment where blended wall function is adopted. This approach is flexible because of its ability to handle a range of local mesh refinement levels near the wall. Cells with low Y+ values are assumed to be properly resolved such that no wall treatment is necessary, while cells of Y+>30 are treated as in the logarithmic region. Simulation of the viscous flow around the DTC hull is obtained through a finite volume discretization of the numerical domain. A VOF method is employed to capture the position of the phase interface between water and air. Equations are solved as an uncoupled system using a segregated flow solver which employs a SIMPLE algorithm for pressure-velocity coupling.

2.1 COORDINATE SYSTEMS

Considering the feature of the ship motion, three Cartesian coordinate systems are established, as shown in Fig.1. Definitions of the coordinate system are identical to those of the model tests in reference [19]. O_0-$X_0Y_0Z_0$ is the earth-fixed coordinate system. O-XYZ is the body-fixed coordinate system whose origin locates at the intersection of water plane, central longitudinal plane and mid-ship section plane, with X-axis pointing to the bow and Y-axis pointing to the starboard. The reference coordinate system O_1-$X_1Y_1Z_1$ maintains a static position during the heave, pitch or yaw motion. It coincides with the body-fixed coordinate system at rest. Reference coordinate system is used in the present simulations and also in computing the ship hydrodynamics.

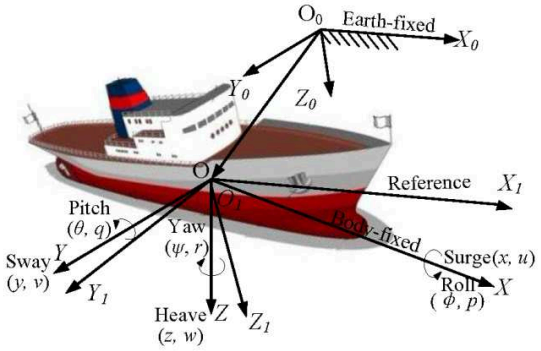

Figure 1. Coordinate systems in the simulation

2.2 GOVERNING EQUATIONS

The Navier-Stokes equations are given in the integral form as:

$$\frac{d}{dt}\int_V \rho dV + \oint_A \rho(\boldsymbol{v}-\boldsymbol{v_g})\cdot d\boldsymbol{a} = 0 \quad (1)$$

$$\frac{d}{dt}\int_V \rho \mathbf{v} dV + \oint_A \rho \mathbf{v} x(\boldsymbol{v}-\boldsymbol{v_g})\cdot d\boldsymbol{a} = -\oint_A p\,\mathbf{I}\cdot d\boldsymbol{a} + \oint_A \boldsymbol{\Gamma}\cdot d\boldsymbol{a} + \int_V \mathbf{F} dV \quad (2)$$

The terms on the left hand side of Eq. (2) are the transient and convective flux terms respectively. Pressure gradient, viscous flux and body force terms are given on the right hand side.

The complete stress tensor for a turbulence flow invokes the Boussinesq approximation such that:

$$\boldsymbol{\Gamma} = \mu_{eff}[\nabla \boldsymbol{v} + \nabla \boldsymbol{v}^{tr} - \tfrac{2}{3}(\nabla\cdot\mathbf{v})\mathbf{I}] \quad (3)$$

Turbulent viscosity is used to model the Reynolds stress tensor as a function of mean flow quantities so that the governing equations are closed.

A finite volume method (FVM) is used to discretize the flow domain as a finite number of control volumes (CVs) corresponding to computational grid cells. The formulation is with second-order accuracy in space and in time.

2.3 VOF INTERFACE CAPTURING

The air-water interface at the free surface is captured using the VOF method. VOF assumes a common velocity and pressure field for all phases within a single CV, and monitors the phase fraction. The governing equations for mass and momentum continuity in a single-phase flow are thus solved for an equivalent fluid whose physical properties (density and laminar viscosity) are a function of the constituent phase's properties and volume fractions within each CV. This is often known as the volume-fraction method. The transport of volume fraction is described by an additional conservation equation:

$$\frac{d}{dt}\int_V \alpha_i dV + \oint_A \alpha_i(\boldsymbol{v}-\boldsymbol{v_g})\cdot d\boldsymbol{a} = 0 \quad (4)$$

3 NUMERICAL METHOD

3.1 SHIP MODEL

The geometry of DTC is shown in Fig. 2.

Figure 2. DTC geometry

In order to analyze the shallow water effect, FHR conducted captive model tests under 20% UKC as the very shallow water condition. L_{pp} is 355m and the designed draft T is 14.5m. The breadth of ship b is 51m. Other main particulars of the ship can been found in [20]. The dimension of FHR shallow water towing tank is 68.5m in effective length, 7.0m in width and 0.5m in maximum water depth. Sinkage and trim of DTC were free in the test, while roll of the hull was fixed.

3.2 COMPUTATIONAL DOMAIN AND GRIDS

The influences of tank side walls, squat, ship speed, drift angle, water depth are investigated in present computations. Both deep and shallow water simulations are conducted, their corresponding water depth to draft ratio are 10 and 1.2 respectively. Only straight-ahead and static drift motions are simulated in the static captive model tests under 20% UKC. For pure sway tests, two different forward speeds (Fr=0.096 and 0.139) under 20% UKC are considered. The corresponding Froude depth number Fr_h are 0.433 and 0.630. The amplitude and period of sway motion are 0.2m and 20s, respectively. Investigations of the effects of tank side walls and squat are conducted for the higher speed case (Fr=0.139).

Two domain widths are considered. The narrow domain width has the same value as in the towing tank, i.e. $1.757L_{pp}$, while the larger width is $5L_{pp}$. As shown in Fig. 3, the computational domain for all shallow water simulations extends $3.5L_{pp}$ from outlet plane to the A.P., $1.5L_{pp}$ from inlet plane to the F.P.. The bottom of the domain is determined according to the water depth considered. The boundary conditions shown in Fig. 3 are: velocity inlet for inlet plane, outflow for outlet plane, no slip condition for ship hull and slip condition for side walls. For the deep water case, slip condition on the bottom is used. In shallow water, however, the effect of the boundary layer on the bottom greatly influences the flow in the gap between the ship and the bottom, so a moving no-slip condition is used on the bottom.

An unstructured predominantly hexahedral mesh is applied in the computation. The grid is refined towards the free surface and the hull. Orthogonal prismatic cells are generated next to hull and bottom surface to improve the accuracy of the flow resolution. Prism layer is not used on the bottom surface in deep water case, where blockage effect is minor. Though different grids are used for simulating different captive model tests, the grid sizes around the hull keep the same to minimize the influence of the grid fitness [16]. The grids consist of approximately 2.0M cells for the lower speed case (Fr=0.096). The Y+ values are below 15. To avoid the negative volume during morphing (see Section 3.3), coarse grid is generated for higher speed and non-zero drift angle cases, which is about 1.5M cells. The Y+ values are below 70. The grid structure around the ship and the bottom in shallow water is shown in Fig.4. The free surface, bow, stern as well as bottom parts are refined during mesh generation.

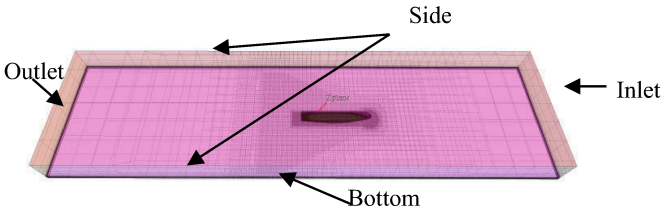

Figure 3. Computational domain and boundary with tank side walls in shallow water

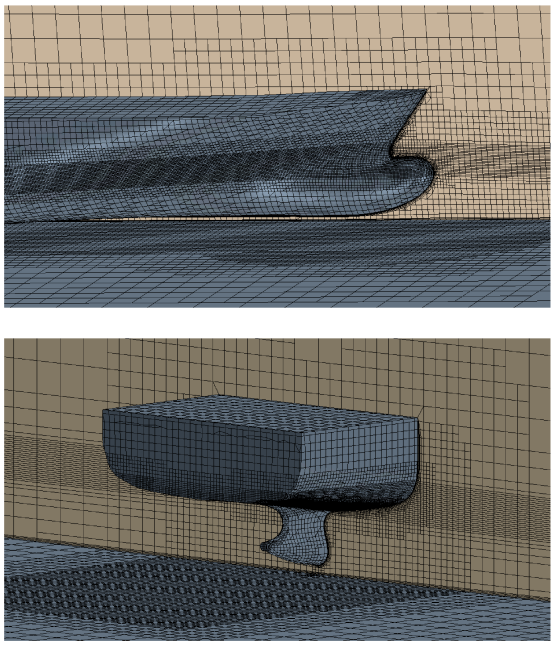

Figure 4. Mesh structure around ship and bottom in shallow water

3.3 DFBI MODULE

Dynamic Fluid Body Interaction (DFBI) module involves actual displacement of mesh vertices, which can model the motion of rigid bodies in six degrees of freedom (6-DOF) within the fluid system. 6-DOF Solver and 6-DOF Motion Solver model are then activated and used to compute the resultant fluid forces, gravitational forces and moments acting on the body caused by all influences, and solve the governing equations of rigid body motion to find its new position and orientation.

DFBI Translation and Rotation and DFBI morphing are used in this paper. The difference between these two

modules is that the former involves the whole mesh moving, while the latter uses control points and their associated displacements to generate an interpolation field throughout the region, which can then be used to displace the actual vertices of a mesh. "Six Dof Body" boundary and "Six Dof Body plus Displacement" are selected in DFBI morphing motion to trace the vertices on this boundary. User defined functions are written and added to the Field Function to define the additional specified displacement superposed in the 6-DOF body motion. All the simulations are carried out on a shared-memory workstation with 16 CPU cores (Intel XEON @ 2.60GHz).

4 RESULTS AND DISCUSSIONS

4.1 SIMULATIONS OF STATIC CAPTIVE MODEL TESTS IN DEEP AND SHALLOW WATER

4.1 (a) Validation of straight ahead test in deep water

In order to evaluate the accuracy of the numerical method, deep water case is simulated by two motion modules, i.e. DFBI Translation and Rotation and DFBI morphing. During all the simulations, sinkage and trim are free. The total resistance R_T of DTC hull under straight-ahead conditions is obtained and compared with the experimental data [20]. Table 1 shows the comparison between the CFD results and experimental data (EFD) at Re=8.054×10^6 and Fr=0.192, where "E%D" denotes the relative error.

Table 1. Resistance results in deep water

Case*	R_T (N)	E%D (%)*
EFD	24.14	(-)
DFBI Translation and Rotation	25.146	4.1665
DFBI morphing	25.09	3.9373

* Ship model scale 1: 59.407
* E%D = (CFD-EFD)/ EFD×100%

From Table 1, it can be seen that both of these two numerical methods over-predict the resistance, but their relative errors are small and DFBI morphing method is slightly better. Because the method of DFBI Translation and Rotation cannot solve the near wall problem when considering squat, DFBI morphing method is selected for the following computations.

4.1 (b) Validation of static drift test in shallow water

In this section, straight-ahead ($\beta = 0°$) and static drift ($\beta = 2.5°$) motions are numerically simulated under 20% UKC. Modeling static drift motion in shallow water is more difficult comparing to the deep water case due to the blockage effects, and it is much more time-consuming. Fig. 5 shows the computed transient oscillation and the convergence of sinkage and trim in $\beta = 0°$case, where non-dimensional trim is obtained by dividing the difference in vertical position at the fore and aft perpendiculars by $L_{pp.}$ It can be seen that both sinkage and trim converge to an approximate constant value.

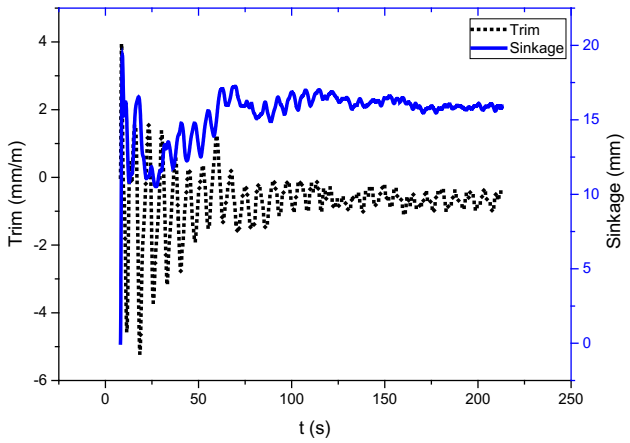

Figure 5. Transient oscillation and convergence of sinkage and trim in $\beta = 0°$ case

Table 2 shows the computed results of sinkage and trim, as well as the relative error compared with the experimental data at Fr=0.139 (Fr_h=0.630). The error of trim is much larger than that of sinkage. More investigations are needed to find out the reason. When the drift angle turns to nonzero, both sinkage and trim are increased. Compared to the experimental data, the increase ratios of computational value are much smaller. Moreover, CFD computations under-predict the sinkage and trim under static drift ($\beta = 2.5°$) conditions and sinkage under straight-ahead ($\beta = 0°$) condition, but over-predict the trim under straight-ahead ($\beta = 0°$) condition.

Table 2. Results and errors of sinkage and trim

Case*	Squat		E%D (%)	
Unit	Trim (mm/m)	Sinkage (mm)	Trim (%)	Sinkage (%)
EFD-$\beta = 0°$	-0.3886	16.4508	(-)	(-)
CFD-$\beta = 0°$	-0.6540	15.9327	68.3	-3.15
EFD-$\beta = 2.5°$	-2.0207	18.1347	(-)	(-)
CFD-$\beta = 2.5°$	-0.7118	16.9858	-64.77	-6.335

* Ship model scale 1: 89.11

4.2 SIMULATIONS OF HARMONIC SWAY MODEL TESTS IN SHALLOW WATER

Pure sway tests are simulated with 0.05Hz frequency and 0.2m oscillation amplitude as shown in Fig. 6. The ship has a constant forward speed U along the towing tank and a periodically varying lateral displacement. The simulation starts when the hull position locates at tank centerline, while the experiment data is started to record when the hull turns to maximum lateral sway. In order to compare with the experiment directly, the computation in the first quarter of period is ignored. Furthermore, release time and ramp time in the computations are up to 20s to allow some time for the fluid flow to initialize.

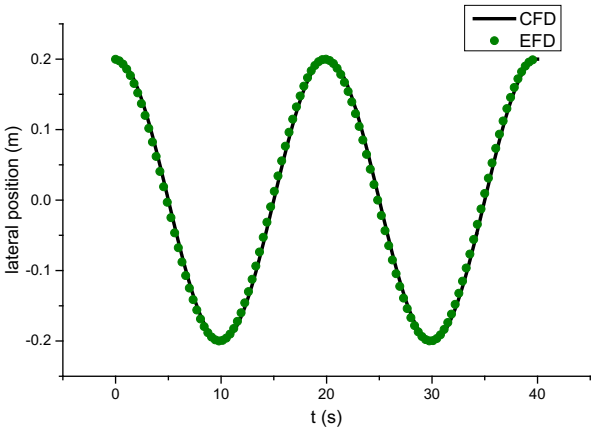

Figure 6. Pure sway (model scale 1: 89.11)

4.2 (a) Fr_h=0.63

In order to discuss how the squat and tank side walls affect the hydrodynamic forces in shallow water, four different cases are numerically simulated at Fr_h=0.63.The case definition and parameters are summarized in Table 3. Two domain widths and blockage factors S_m are listed there. Two kinds of ship states are considered. Dynamic ship squat is numerically simulated as model tests while fixed ship has zero sinkage and trim.

Table 3. Cases definition and parameters

Case No.	Domain	$^*S_m$	State	Sinkage	trim
1	wide	0.024	fixed	0	0
2	bank	0.069	fixed	0	0
3	wide	0.024	squat	dynamic	dynamic
4	bank	0.069	squat	dynamic	dynamic

$^*S_m = (b \times T)/(B \times H)$

Fig. 7-Fig. 9 show the hydrodynamic forces and moments of these four cases, as well as the comparison with the experimental data. These figures show that the hydrodynamic forces and moments obtained for Case 4 are the most accurate ones compared to the experimental data. When both ship squat and tank side walls are ignored (Case 1), the amplitudes of lateral force and yaw moment decrease by more than 50% compared with the results of Case 4. When comparing the results of Case 2 and Case 3 with those of Case 4, the amplitude of hydrodynamic forces and moment of Case3 is quantitatively larger than those of Case 2. It means that the squat plays a more important role in affecting hydrodynamic forces than the blockage effect by the tank side walls. In Case 4, CFD prediction gives the best results but still there are discrepancies. It under-predicts lateral force while over-predicts yaw moment at peak values.

Fig. 10 and Fig. 11 show the dynamic sinkage and trim during pure sway in 2 periods. For Case 4, the same trends of the sinkage and trim are predicted qualitatively as in the tests, but with some error in value. Case 4 has a relative better trend than Case 3 since the time when the sinkage and trim value reaches extreme points in Case 4 basically coincides with experiment data. Nevertheless, the sinkage is much under-predicted compared with EFD data. The large errors in computations are probably caused by the coarse grid or the increased complexity of the flow. The experimental investigations do not show a fully steady state of ship's sinkage and trim neither. Since the error and uncertainty of the model test data are not available, it is difficult to draw any conclusion so far.

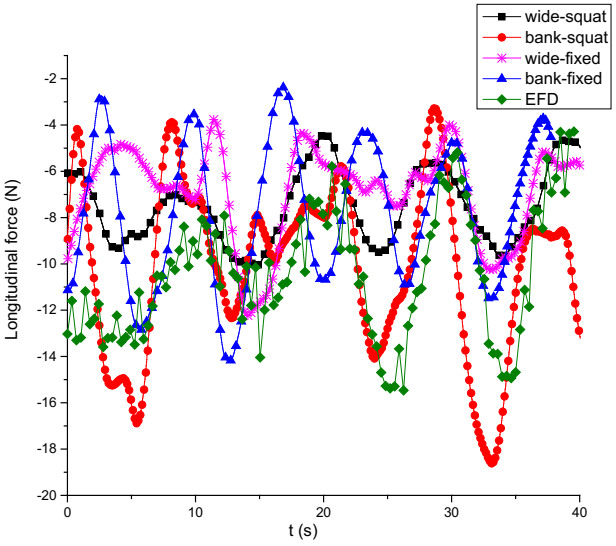

Figure 7. Time history of longitudinal force (Fr_h=0.63)

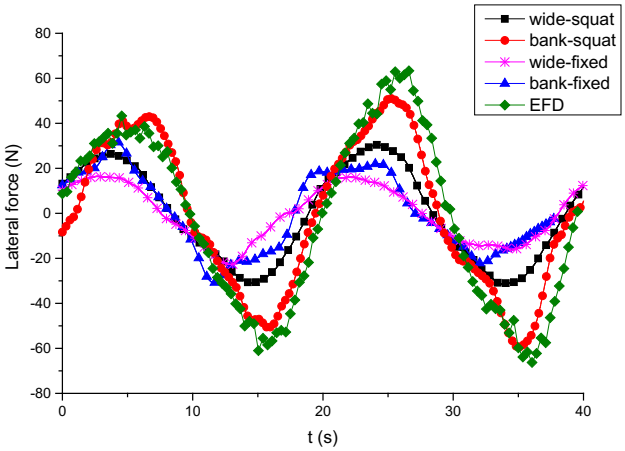

Figure 8. Time history of lateral force (Fr_h=0.63)

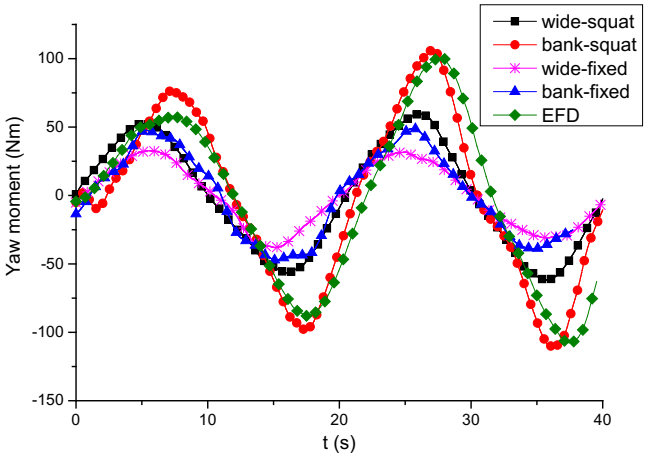

Figure 9. Time history of yaw moment (Fr_h=0.63)

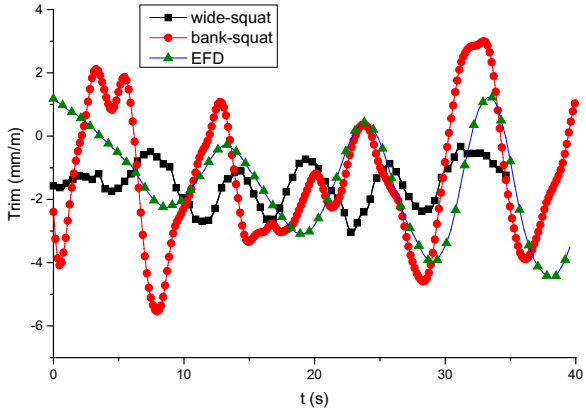

Figure 10. Time history of trim (Fr_h =0.63)

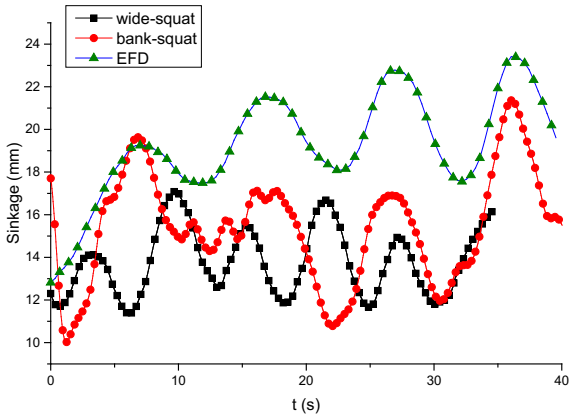

Figure 11. Time history of sinkage (Fr_h =0.63)

Fig. 12 shows the pressure contours on the hull at three successive motion phases: maximum lateral displacement to port (180°), central position of the tank (270°), and maximum lateral displacement to starboard (360°). Only Case 4 is considered for the comparison with lower Fr case to be discussed below. A strong port-starboard asymmetry of the pressure is observed on the hull according to Fig.12.

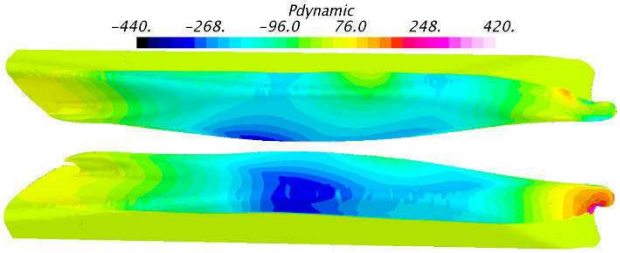

(a) Maximum lateral displacement to port (180°)

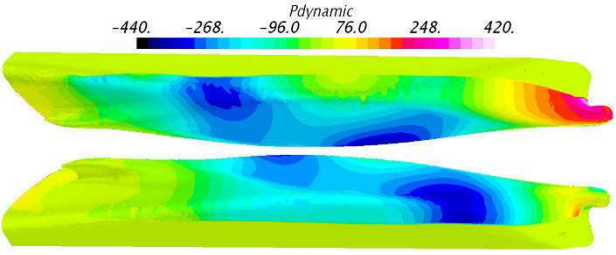

(b) Central position of the tank (270°)

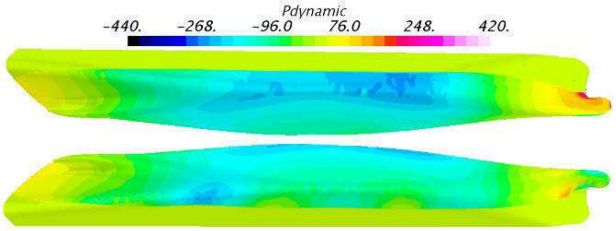

(c) Maximum lateral displacement to starboard (360°)

Figure 12. Pressure contours at three successive motion phases (Fr_h =0.63)

4.2 (b) Fr_h=0.433

As shown in the last subsection, the tank side walls and squat have tremendous influences on the hydrodynamic characteristics in shallow water, so for pure sway case at Fr_h=0.433, only the conditions of Case 4 are considered in the computations.

The hydrodynamic forces and moment, as well as squat compared with EFD data are shown in Fig. 13-Fig. 17. The time histories of computed and measured lateral force and yaw moment are in good agreement. Although there are some discrepancies between computed and measured longitudinal force, sinkage and trim, their trends are reasonable to some extent. All the peak values are smaller than those of Fr_h=0.63, which means in addition to squat and tank side walls, ship speed is another important factor affecting the ship-bottom interaction.

Fig. 18 shows pressure contours on the hull at three successive motion phases: maximum lateral displacement to port (180°), central position of the tank (270°), and maximum lateral displacement to starboard (360°). Compared to the higher Fr_h, the whole pressure on the hull decreases. The pressure distribution of each phase shows slight differences.

Fig. 19 gives the vorticity contour from the port/starboard side view at two different ship velocities. Strong asymmetric bilge vortices around the hull are generated by the interactions with the side wall and bottom. When the ship speed increases, vorticity system looks similar but the strength is larger. Fig.12, Fig.18 and Fig 19 reveal the complexity of the turbulent flow in the pure sway motion in shallow waters.

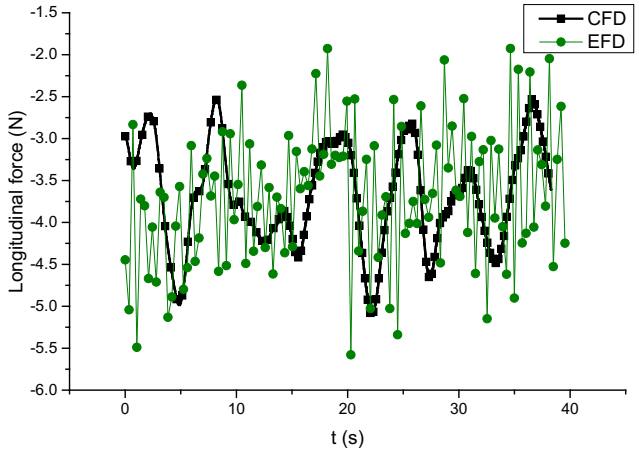

Figure 13. Time history of longitudinal force (Fr_h=0.433)

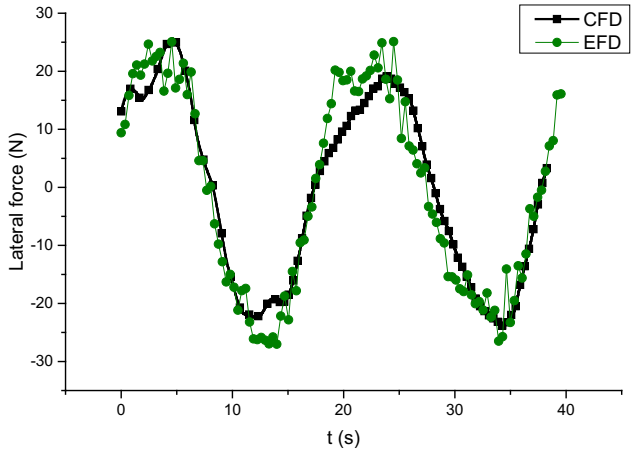

Figure 14. Time history of lateral force (Fr_h =0.433)

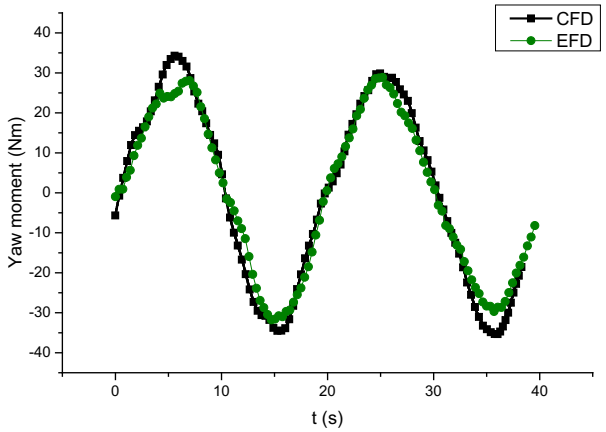

Figure 15. Time history of yaw moment (Fr_h =0.433)

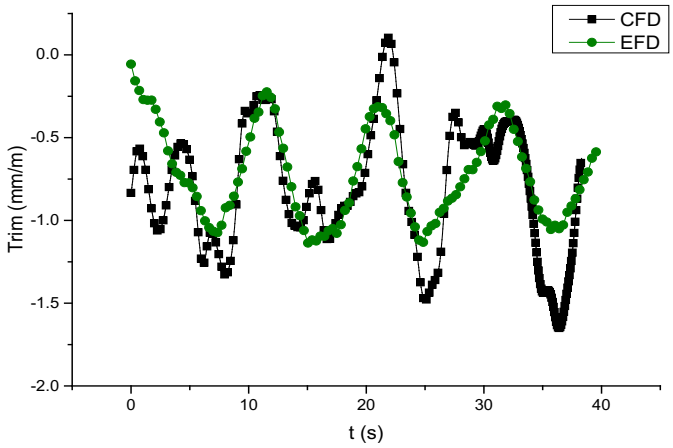

Figure 16. Time history of trim (Fr_h =0.433)

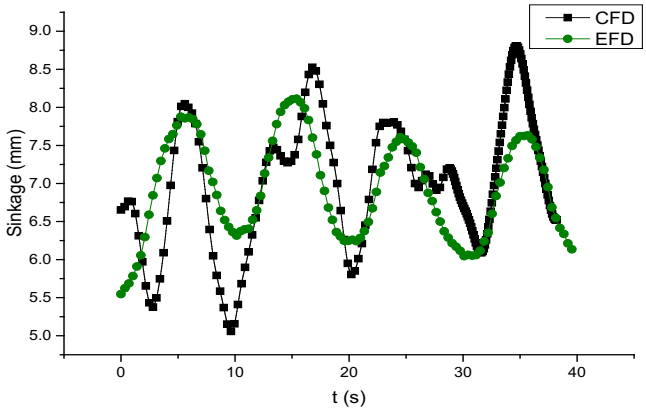

Figure 17. Time history of sinkage (Fr_h =0.433)

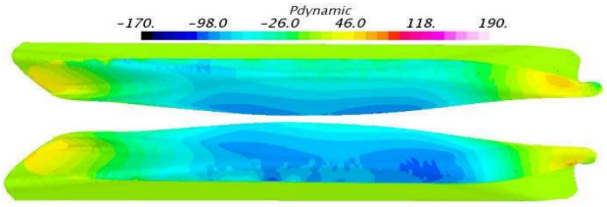

(a) Maximum lateral displacement to port (180°)

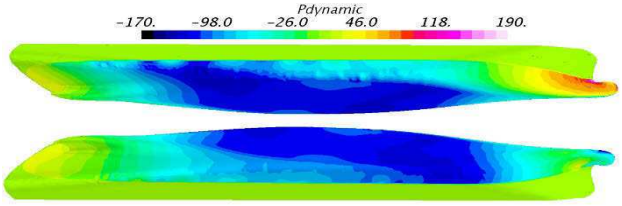

(b) Central position of the tank (270°)

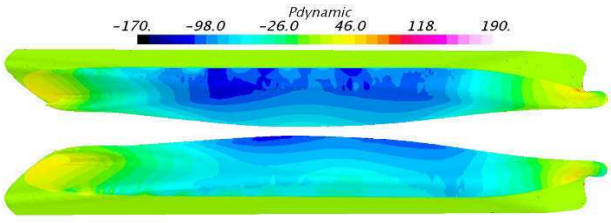

(c) Maximum lateral displacement to starboard (360°)

Figure 18. Pressure contours at three successive motion phases (Fr_h =0.433)

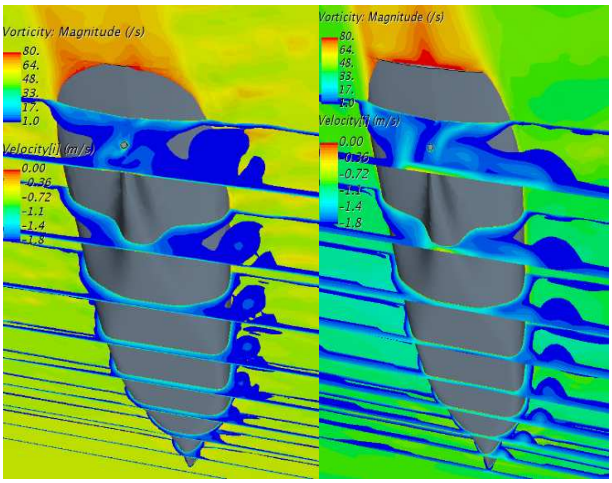

(a) Maximum lateral displacement to port (180°)

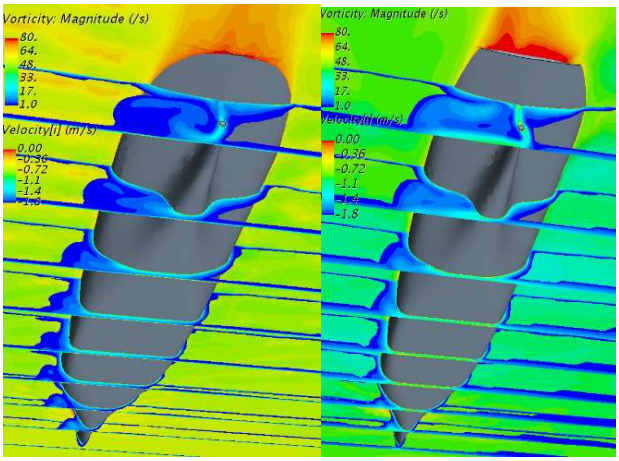

(b) Central position of the tank (270°)

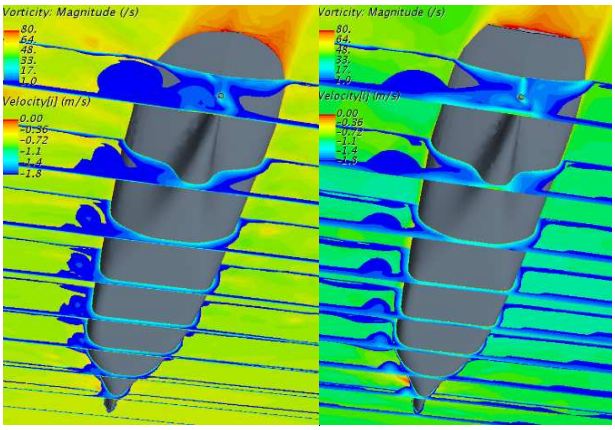

(c) Maximum lateral displacement to starboard (360°)

Figure 19. Cross sections colored with vorticity magnitude at three successive motion phases. Free surface colored with velocity (Left: Fr_h =0.433 Right: Fr_h =0.63)

5 CONCLUSIONS

In this paper, RANS-based simulations of the static drift and pure sway tests of a DTC model at 20% UKC are carried out considering its dynamic sinkage and trim, as well as the effects of tank side walls at two forward speeds with Fr_h=0.63 and Fr_h=0.433. DFBI morphing method is adopted to simulate the dynamic sinkage and trim. The hydrodynamic forces acting on the hull, dynamic sinkage and trim under these conditions are predicted and discussed.

The numerical method applied in the present paper is validated by comparing the predicted resistance with EFD data in deep water. For shallow water computations, the squat, tank wall and ship speed are shown to be important and the results indicate that those factors greatly influence the transverse force, dynamic sinkage and trim. When considering tank side bank and ship squat, CFD prediction gives the best results compared with EFD data but still there are slight discrepancies. It under-predicts lateral force while over-predicts yaw moment at peak values with higher Fr number. Moreover, Details of simulated flow field, such as pressure distribution and vorticity around the hull are given to explain the hydrodynamic characteristics.

However, the computed sinkage and trim do not match the experimental data very well, especially at higher Fr number where the sinkage is under-predicted. Reasons for the discrepancies are still not clear. More studies are needed to investigate the error and to further improve the accuracy in the computations.

6 ACKNOWLEDGEMENTS

This work is supported by the National Natural Science Foundation of China (Grant No: 51309152).

7 REFERENCES

1. Briggs, M.J. (2006). *Ship squat predictions for ship/tow simulator.* DTIC Document.

2. Ankudinov, V.; Daggett, L.; Huval, C.; Hewlett, C. (1996). Squat predictions for manoeuvring applications. *Seventh International Conference on Marine Simulation and Manoeuvrability (MARSIM),* Copenhagen, Denmark.: pp.467-495.

3. Maimun, A.; Priyanto, A.; Muhammad, A.; Scully, C.; Awal, Z. (2011). *Manoeuvring prediction of pusher barge in deep and shallow water.* in *Ocean Engineering*. pp. 1291-1299. doi: 10.1016/j.oceaneng.2011.05.011.

4. Eloot, K.; Marc, V.; Delefortrie, G. (2006). Prediction of ship manoeuvrability of an 8000 TEU containership in deep and shallow water: mathematical modelling and captive model testing.

International Conference on Marine Simulation and Ship Manoeuvring (MARSIM), Terschelling, The Netherlands. pp.3-1.

5. Carrica, P.M.; Mofidi, A.; Eloot, K.; Delefortrie, G. (2016). Direct simulation and experimental study of zigzag maneuver of KCS in shallow water. *Ocean Engineering* 112: pp. 117-133. doi: 10.1016/j.oceaneng.2015.12.008.

6. Tonelli, R.; Quadvlieg, F. (2015). New Benchmark Data for Manoeuvring in Shallow Water Based on Free Running Manoeuvring Tests Including Uncertainty of the Results. *Thirty-fourth International Conference on Ocean, Offshore and Arctic Engineering (OMAE),* St. John's, Newfoundland, Canada.

7. Gourlay, T.P. (2014). ShallowFlow: A Program to Model Ship Hydrodynamics in Shallow Water. *Thirty-third International Conference on Ocean, Offshore and Arctic Engineering (OMAE),* San Francisco, California, USA. pp.V01AT01A018-V01AT01A018.

8. Tuck, E. (1966). Shallow-water flows past slender bodies. *Journal of Fluid Mechanics* 26(01): pp. 81-95. doi: 10.1017/S0022112066001101.

9. SIMMAN (2008). *Workshop on Verification and Validation of Ship Manoeuvring Simulation Methods*, Copenhagen, Denmark.

10. SIMMAN (2014). Workshop on Verification and Validation of Ship Manoeuvring Simulation Methods, Copenhagen, Denmark.

11. Van Hoydonck, W.; Eloot, K. (2014). Shallow water CFD computations for SIMMAN 2014. *Workshop on Verification and Validation of Ship Manoeuvring Simulation Methods (SIMMAN),* Copenhagen, Denmark.

12. Böttner, C.-U.; Kastens, M.; Hirata, N.; Wasserbau, B.F. (2014). Contribution to numerical Test Cases in shallow water conditions. *Workshop on Verification and Validation of Ship Manoeuvring Simulation Methods (SIMMAN),* Copenhagen, Denmark.

13. Liu, X.; Wan, D. (2015). Numerical Simulation of Ship Yaw Maneuvering in Deep and Shallow Water. *Twenty-fifth International Offshore and Polar Engineering Conference (ISOPE),* Kona, Hawaii, USA.

14. Liu, X.; Fan, S.; Wang, J.; Wan, D. (2015). Hydrodynamic Simulation of Pure Sway Tests with Ship Speed and Water Depth Effects. *Twenty-fifth International Offshore and Polar Engineering Conference (ISOPE),* Kona, Hawaii, USA.

15. Simonsen, C.; Stern, F.; Agdrup, K. (2006). CFD with PMM test validation for manoeuvring VLCC2 tanker in deep and shallow water. *International Conference on Marine Simulation and Ship Manoeuvring (MARSIM),* Terschelling, The Netherlands.

16. Toxopeus, S.; Simonsen, C.; Guilmineau, E.; Visonneau, M.; Xing, T.; Stern, F. (2013). Investigation of water depth and basin wall effects on KVLCC2 in manoeuvring motion using viscous-flow calculations. *Journal of Marine Science and Technology* 18(4): pp. 471-496. doi: 10.1007/s00773-013-0221-6.

17. Koop, A. (2015). Shallow Water Current Loads on a LNG Carrier Using CFD. *Thirty-fourth International Conference on Ocean, Offshore and Arctic Engineering (OMAE),* St. John's, Newfoundland, Canada. American Society of Mechanical Engineers.

18. Toxopeus, S.L. (2013). Viscous-flow calculations for KVLCC2 in deep and shallow water. *Fourth International Conference on Computational Methods in Marine Engineering (MARINE),* Netherlands. Springer: pp.151-169.

19. Eloot, K.; Marc, V.; Guillaume, D.; Evert, L. (2016). Running Sinkage and Trim of the DTC Container Carrier in Harmonic Sway and Yaw Motion: Open Model Test Data for Validation Purposes. *Fourth International Conference on Ship Manoeuvring in Shallow and Confined Water (MASHCON): Ship - Bottom Interaction,* Hamburg, Germany (to be published).

20. Moctar, O.E.; Shigunov, V.; Zorn, T. (2012). Duisburg Test Case: Post-panamax container ship for benchmarking. *Ship Technology Research* 59(3): pp. 50-64. doi: 10.1179/str.2012.59.3.004.

8 AUTHORS' BIOGRAPHIES

Yi Liu holds the current position of PhD student at School of Naval Architecture, Ocean and Civil Engineering, Shanghai Jiao Tong University. Her previous experience includes numerical studies on the ship manoeuvring in restricted waters, etc.

Zaojian Zou holds the current position of full professor at School of Naval Architecture, Ocean and Civil Engineering, Shanghai Jiao Tong University. He is responsible for teaching and research on marine hydrodynamics. His previous experience includes PI of some projects on manoeuvring and control of ships and other marine vehicles. He was a member of the 22nd, 23rd, 25th and 26th ITTC MC.

Lu Zou is a lecturer at School of Naval Architecture, Ocean and Civil Engineering, Shanghai Jiao Tong University. Her major research interest is in the ship manoeuvring in confined waters, as well as Verification and Validation of CFD simulations.

4th MASHCON, Hamburg - Uliczka et al. (eds) - © 2016 Bundesanstalt für Wasserbau ISBN 978-3-939230-38-0 (Online)
DOI: 10.18451/978-3-939230-38-0_11

INVESTIGATION OF SHIP-BANK, SHIP-BOTTOM AND SHIP-SHIP INTERACTIONS BY USING POTENTIAL FLOW METHOD

Z-M Yuan and **A Incecik,** Department of Naval Architecture, Ocean and Marine Engineering, University of Strathclyde, UK

SUMMARY

The authors were inspired by the benchmark model test data in MASHCON [1, 2] and carried out some numerical studies on ship-bank, ship-bottom and ship-ship interactions based on potential flow method in the last few years. In the confined waterways, many researchers question the applicability of the classical potential flow method. The main objective of the present paper is to present some validations of the 3D boundary element method (BEM) against the model test data to exam the feasibility of the potential method in predicting the hydrodynamic behaviour of the ships in confined water. The methodology used in the present paper is a 3D boundary element method based on Rankine type Green function. The numerical simulation is based on the in-house developed multi-body hydrodynamic interaction program MHydro. We calculate the wave elevations and forces (or moments) when the ship is manoeuvring in shallow and narrow channel, or when the two ships is travelling side by side or crossing each other. These calculations are compared with the benchmark test data, as well as the published CFD results. Generally, the agreement between the present calculations and model test and CFD results are satisfactory, which indicates that the potential flow method and developed program are still capable to predict the hydrodynamic interaction involved in ship-bank, ship-bottom and ship-ship problem.

1 INTRODUCTION

Ships manoeuvring in confined waterways is continuously a topic with both academic and practical interests. As the water depth becomes small, the fluid is compressed to pass through the bottom of the vessel with larger velocity than the fluid velocity in deep water. The change of the fluid velocity could modify the pressure distribution. The negative pressure distributed on the bottom of the vessel could induce a very large suction force, which attracts the ship to sink towards the bottom of the waterway. Meanwhile, the pressure distribution on the bow of the ship is different from that on the stern, which leads to the wave-making resistance and pitch moment. When the water depth becomes very small, or the forward speed increases, the wave-making resistance, sinkage and trim can achieve a very large value. As the resistance increases, the ship's speed loss is inevitable. Meanwhile, due to the large sinkage and trim, the advancing ship would have the risk of grounding. Moreover, if the bank effect is taken into consideration, the shallow water problem becomes even worse. Due to narrow gap between the bank, bottom and ship, the fluid velocity could be very large. If the banks are not symmetrical, the fluid velocity in the portside and starboard of the ship will be different, which could result in different pressure distribution, and hence leads to a suction force attracting the vessel moving towards the bank. Due to the non-symmetrical pressure distribution, there also exist a yaw moment which makes the ship deviate from its original course and causes the collision. For these reasons, the ships manoeuvring in shallow and narrow channel has attracted extensive interests from the researchers.

In order to estimate the ship-bank, ship-bottom and ship-ship interactions, the most reliable approach is by experimental measurement. The experimental method is extremely critical in the early years when the computer is not capable to conduct large amount of calculation. The only reliable way to predict hydrodynamic interactions relies on the model test due to the complexity of the geometry of the 3D ships. The numerical method is only available when the computers are capable to solve the very large matrix. But the early version of the numerical programs to predict the hydrodynamic problem is mainly based on 2D method, or so-called strip theory. Beck et al. [3], Tuck [4-6], Newman and Tuck [7], Yaung [8] and Gourlay's [9] proposed approaches based on the slender ship assumption. The limitation of this 2D method is very obvious. The predictions are not accurate due to the 3D effects. And also, it cannot estimate the wave-making resistance due to the assumption that the x- component of the normal vector is small on the whole body surface including bow and stern areas. In order to predict the hydrodynamic interactions accurately, the 3D potential flow method has been used nowadays, which benefits from the improvement of the computer capacity. From the published results and validations [10, 11], it can be found that the 3D potential flow method can general provide a satisfactory estimation. However, the publications of using 3D potential flow method to investigate the confined water problem are still quite limited. One of the reason is the lack of the validations due to the limited model test data. The complexity of free surface condition is another reason which prevents it from being widely used. In some publications, the free surface is treated as a rigid wall. This will of course affect the accuracy of the calculations, since the wave elevation on the free surface in confined waterways could be much larger than that in open water. The limitation of the potential method lies in the assumption of ideal flow, which neglects the viscus effects. That is the reason why many researchers are still not confident about the potential flow method and doubt its reliability in confined water calculations. From this

point of view, the CFD method seems to be the perfect method to solve the ship-bank, ship-bottom and ship-ship problem. It is true that CFD programs are capable to investigate many complex hydrodynamic problems. But it is also a fact that CFD programs require highly on the computational power. Even through there are some successful examples of using CFD programs to predict the hydrodynamic problems involved in the confined waterways [12, 13], the large amount of computational time is still a problem which prevents it from being widely used in the practice.

In order to carry out parameter studies to find out the factors which determines the hydrodynamics in confined waterways, potential flow theory is still an effective method due to its acceptable calculation time. Before extending potential flow method to predict the ship-bank, ship-bottom and ship-ship problems, a rigorous validation should be conducted to verify its reliability. The main objective of the present paper is to present some validations of the 3D boundary element method (BEM) against the model test data to exam the feasibility of the potential method in predicting the hydrodynamics involved in ship-bank, ship-bottom and ship-ship problems. Since 2009, the International Conference on Ship Manoeuvring in Shallow and Confined Water has successfully attracted the researchers to deal with the hydrodynamics involved in confined waterways. And during these conferences, Ghent University in cooperation with the Flanders Hydraulics Research (FHR) published extensive benchmark model test data related to various topics, including bank effects (Antwerp, May 2009), ship-ship interaction (Trondheim, May 2011) and ship behaviour in locks (Ghent, June 2013). Based on these model test data, the validations of applying potential flow method to predict the ship-bank, ship-bottom and ship-ship problems will be carried out in the present paper.

2 MATHEMATICAL FORMULATION

2.1 THE BOUNDARY VALUE PROBLEM OF SHIP-BANK AND SHIP-BOTTOM PROBLEM

When a ship advances at constant speed in calm water, it will generate steady waves and induce the so-called wave-making resistance. It is assumed that the fluid is incompressible and inviscid and the flow is irrotational. A velocity potential $\varphi_T = ux + \varphi$ is introduced and φ satisfies the Laplace equation $\nabla^2\varphi = 0$

$$\nabla^2\varphi = 0 \qquad \text{in the fluid domain} \tag{1}$$

Following Newman [14], the nonlinear dynamic free-surface condition on the disturbed free surface can be expressed as

$$u\frac{\partial\varphi}{\partial x} + \frac{1}{2}\left[\left(\frac{\partial\varphi}{\partial x}\right)^2 + \left(\frac{\partial\varphi}{\partial y}\right)^2 + \left(\frac{\partial\varphi}{\partial z}\right)^2\right] + g\zeta = 0, \quad on\ z = \zeta(x,y) \tag{2}$$

The kinematic free-surface condition is

$$u\frac{\partial\zeta}{\partial x} - \frac{\partial\varphi}{\partial z} + \frac{\partial\varphi}{\partial y}\frac{\partial\zeta}{\partial y} + \frac{\partial\varphi}{\partial x}\frac{\partial\zeta}{\partial x} = 0, \quad on\ z = \zeta(x,y) \tag{3}$$

The first approximation is based on the linear free surface conditions on the undisturbed water surface. By neglecting the nonlinear terms in Eq. (2) and (3), we can obtain the linear classic free surface boundary condition

$$u^2\frac{\partial^2\varphi}{\partial x^2} + g\frac{\partial\varphi}{\partial z} = 0, \text{ on the undisturbed free surface} \tag{4}$$

For the ship-to-ship with same forward speed problem, the body surface boundary condition can be written as

$$\frac{\partial\varphi}{\partial n} = u\cdot n_1, \quad \text{on the wetted body surface} \tag{5}$$

where $\vec{\mathbf{n}} = (n_1, n_2, n_3)$ is the unit normal vector inward on the wetted body surface of Ship_a and Ship_b. The boundary condition on the sea bottom and side walls can be expressed as

$$\frac{\partial\varphi}{\partial n} = 0, \qquad \text{on } z = -h \text{ and side walls} \tag{6}$$

Besides, a radiation condition is imposed on the control surface to ensure that the waves vanish upstream of the disturbance.

2.2 THE BOUNDARY VALUE PROBLEM OF SHIP-SHIP PROBLEM

In order to deal with the different forward speeds, we propose a new uncoupled method. The potential φ can be divided into two components

$$\varphi = \varphi_a + \varphi_b \tag{7}$$

φ_a is the potential produced by the case that Ship_a is moving with u_a while Ship_b is stationary. According to the linear theory, it satisfies the Laplace equation. The boundary value problem for φ_a can be written as

$$\begin{aligned}
&\nabla^2\varphi_a = 0, \quad \text{in the fluid domain}\\
&\frac{\partial\varphi_a}{\partial n} = u_a\cdot n_1, \quad \text{on wet body surface of Ship_a}\\
&\frac{\partial\varphi_a}{\partial n} = 0, \quad \text{on wet body surface of Ship_b}\\
&u_a^2\frac{\partial^2\varphi_a}{\partial x^2} + g\frac{\partial\varphi_a}{\partial z} = 0, \quad \text{on undisturbed free surface}\\
&\frac{\partial\varphi_a}{\partial n} = 0, \quad \text{on sea bottom and side walls}
\end{aligned} \tag{8}$$

Similarly, the φ_b is defined as the potential produced by the case that Ship_b is moving with u_b while Ship_a is stationary. The boundary value problem for φ_b can be written as

$$
\begin{aligned}
&\nabla^2\varphi_b = 0, \quad \text{in the fluid domain} \\
&\frac{\partial\varphi_b}{\partial n} = u_b \cdot n_1, \quad \text{on wet body surface of Ship\_b} \\
&\frac{\partial\varphi_b}{\partial n} = 0, \quad \text{on wet body surface of Ship\_a} \\
&u_b^2\frac{\partial^2\varphi_b}{\partial x^2} + g\frac{\partial\varphi_b}{\partial z} = 0, \quad \text{on undisturbed free surface} \\
&\frac{\partial\varphi_b}{\partial n} = 0, \quad \text{on sea bottom and side walls}
\end{aligned}
\tag{9}
$$

φ_a and φ_b can be obtained by solving the boundary value problem in Eq. (8) and (9). The details about how to discretise the boundaries numerically by using the 3D Rankine source method can be found in Yuan et al. [15]. The same procedure will be applied in the present study.

3 VALIDATIONS AND DISCUSSIONS

The above theory is applied in our in-house developed 3D BEM program MHydro to investigate the ship-bank, ship-bottom and ship-ship problems. The convergence study for MHydro can be found in Yuan et al. [16].

3.1 VALIDATION OF SHIP-BANK INTERACTION

3.1 (a) Ship model and test matrix

The ship model used in ship-bank and ship-bottom problem is a very large crude oil carrier (referred as KVLCC2 hereafter). The main particulars of the KVLCC2, designed by MOERI, in model scale with scale factor 1/75 are shown in Table 1. The model tests of bank and bottom effects are conducted at Flanders Hydraulics Research (FHR), and the measurement data, as well as the CFD results used in the present paper is published by Hoydonck, et al. [17]. The towing tank at FHR is 88 *m* (length) × 7 *m* (breadth) × 0.5 *m* (depth). The towing tank is equipped with a double bank configuration along the full length of the tank. An overview of the towing tank with banks is shown in Figure 1.

Table 1. Main particulars of KVLCC2 (model scale)

Length (L) (m)	4.2667
Breadth (B) (m)	0.773
Draft Amidships (T) (m)	0.2776
Longitudinal CoG (XG) (m)	0.1449
Vertical CoG (KG) (m)	0.2776
Displacement (m^3)	0.741
Block coefficient	0.8098

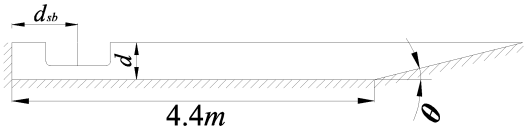

Figure 1. Cross section of the tank geometry, where d_{sb} is the distance between the ship and vertical bank, d is the water depth and $tan(\theta) = 1 / 4$.

In the present study, we only present the results of the ship model without consideration of propulsion.) is 0.055.
Table 2 lists the test matrix of the cases without propulsion. Case 1- Case 3 has the same water depth (d), while the distance between the ship and the vertical wall (d_{sb}) is different. Therefore, this set of cases are used to represent the ship-bank interaction. Case 3- Case 5 has the same d_{sb}, while the water depth is different. Therefore, this set of cases are used to represent the ship-bottom interaction. In Case 1- Case 5, the Froude number F_n ($F_n = u/\sqrt{gL}$) is 0.055.

Table 2. Test matrix of the cases without propulsion.

Test case	d_{sb} (m)	d_{sb}/B	d (m)	d/T
Case 1	0.5175	0.67	0.3744	1.35
Case 2	0.5866	0.76	0.3744	1.35
Case 3	0.9731	1.26	0.3744	1.35
Case 4	0.9731	1.26	0.416	1.5
Case 5	0.9731	1.26	0.3051	1.1

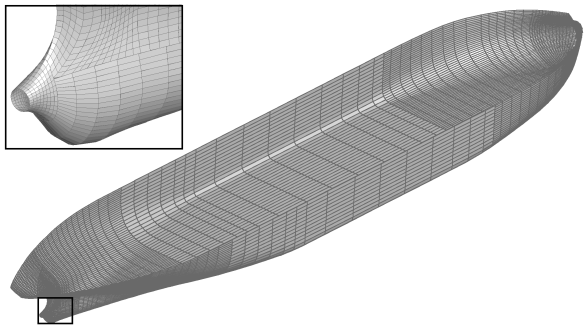

Figure 2. Mesh distribution on wet body surface of KVLCC2. There are 8,080 panels distributed on the body surface.

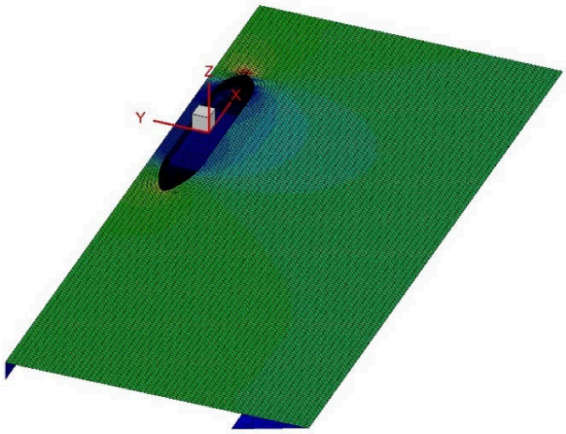

Figure 3. The coordinate system and panel distribution on the computational domain of Case 1. There are 27,060 panels distributed on the entire computational domain: 8,080 on the body surface of body surface, 17,700 on the free surface, and 1280 on the side walls. The computational domain is truncated at L upstream and 2L downstream. The contour of this figure illustrates the wave elevations on the free surface of Case 1.

Figure 3 shows the panel distribution and wave elevation of Case 1. It should be noted that in the present study, there are 100 panel distributed at per ship length ($\Delta x / L$). The panel size (let's say Δx) is small enough to capture the wave property for most of the speed range. However, in the present study, the water depth d and the forward speed u are both very small. According to Kim's finding [18], the ratio of $\Delta x / \lambda$ should be less than 0.1 in order to restrain the numerical dispersion and damping. As the speed of the vessel is $0.356 m/s$, the corresponding wave length produced the ship is about 0.08 m. It means $\Delta x / L$ should be at least 500, and this is very difficult to realize in the present constant panel method. It can be expected that the wave elevations, especially in the far field, will be underestimated by the present program.

3.1 (b) Validation of wave elevations

Figure 5 compares the wave elevations obtained from different methods. The wave gauge is located $0.02m$ away from the vertical bank. It can be observed that the agreement between the present predictions and the experimental measurements is generally satisfactory. There are some fluctuations of the results obtained from URANS solver by using a first-order time discretization, which are the un-expected phenomenon since the first-order scheme with more numerical damping is expected to be more stable. It seems that the second-order scheme can eliminate these spikes. But in all of the 3 cases, the CFD programs overestimate the wave elevation in the trough, while the present MHydro underestimates the trough of the wave profile.

As explained above, these underestimations are mainly due to the insufficient panel size, which introduce the numerical damping and suppressed the wave elevation. There are two approaches to eliminate the numerical damping. The first approach is to minimize the panel size (according to the speed of the present case studies, $\Delta x / L$ should be at least 500).

The other approach is to use the high-order boundary element method (HOBEM). It can be observed from Figure 4 that as the distance between the ship and bank increases, the underestimations become more noticeable. This is an expectable error due to the numerical damping. However, it can be concluded that the potential flow method is still a reliable way to predict the wave elevations in the gap between the ship and bank when the bank effects are significant. The accuracy of the prediction relies on the panel size and forward speed.

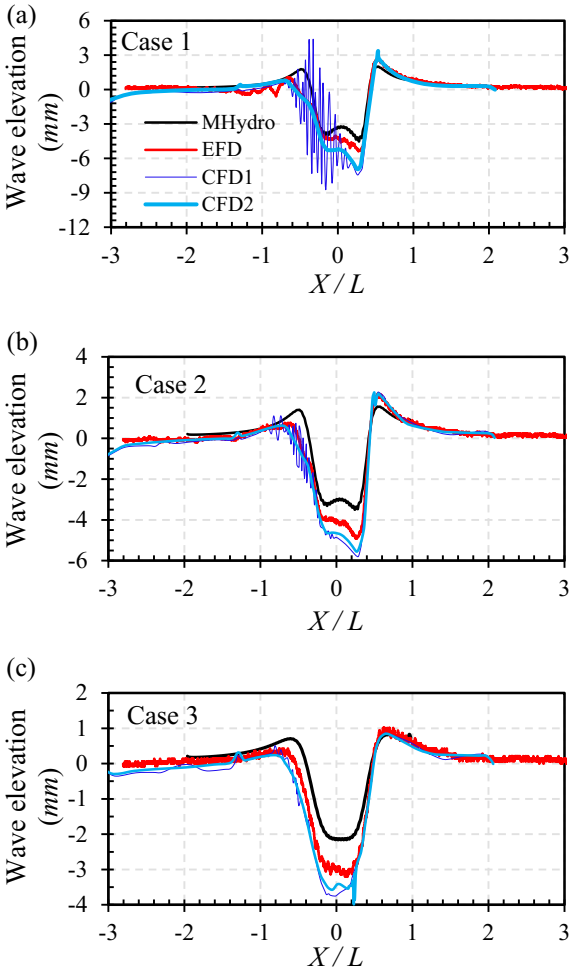

Figure 4. Results of wave elevation at different d_{sb} obtained from different programs. (a) Case 1; (b) Case 2; (c) Case 3. MHydro is the present potential flow program based on 3D Rankine source panel method; EFD represents the model test results from Hoydonck et al. [17]; CFD1 represents the results obtained by an incompressible, unsteady, Reynolds-averaged Navier-Stokes (URANS) solver by using a first-order time discretization; CFD2 represents the results obtained by URANS solver by using a second-order time discretization.

Figure 5 compares the wave elevation at different d_{sb}. It can be found as the gap becomes smaller, the wave trough increases dramatically. Due to the existence of the bank, the flow is squeezed to pass through the narrow gap with high velocity. According to Bernoulli equation, there exist a very large negative pressure in the body surface close to the bank, and positive pressure on the bank. The modification of the pressure distribution induce these troughs in the gap. As the gap becomes smaller, the wave trough will become large correspondingly. However, in the other side of the ship, the sloped bank is far away from the ship. As a results, the pressure distribution is not symmetrical. That is the reason of the suction forces and yaw moments, which will be presented later.

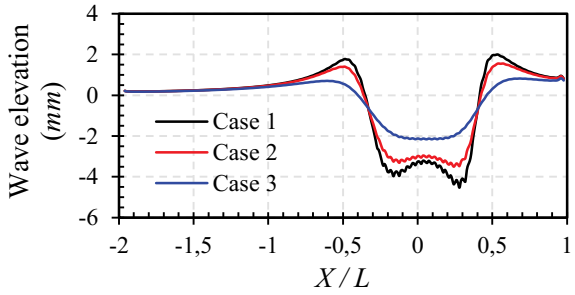

Figure 5. Results of wave elevation at different d_{sb} obtained from MHydro.

3.1 (c) Validation of the forces (or moments)

Figure 6 compares the results of forces (or moments) at different ratio of d_{sb} / B from different programs. With regard to the lateral forces and roll moments, the present results from MHydro agrees with the experimental results well.

Compared with the other CFD programs, the present potential flow program shows even better predictions. However, the sign of the yaw moment predicted by MHydro is incorrect compared to the EFD and other CFD results.

This problem of the adverse sign is also encountered by Ropes, which is also a BEM program based on potential flow method. The reason for this false estimation may attribute to the ignorance of the lifting forces due to the non-symmetrical flow. Therefore, in order to estimate yaw moment correctly, the so-called Kutta condition must be imposed to the trailing edge in the wake region.

It can also be concluded from Figure 6 (a) and (b) that as the ratio of d_{sb} / B becomes smaller, the lateral forces and roll moments will increase rapidly.

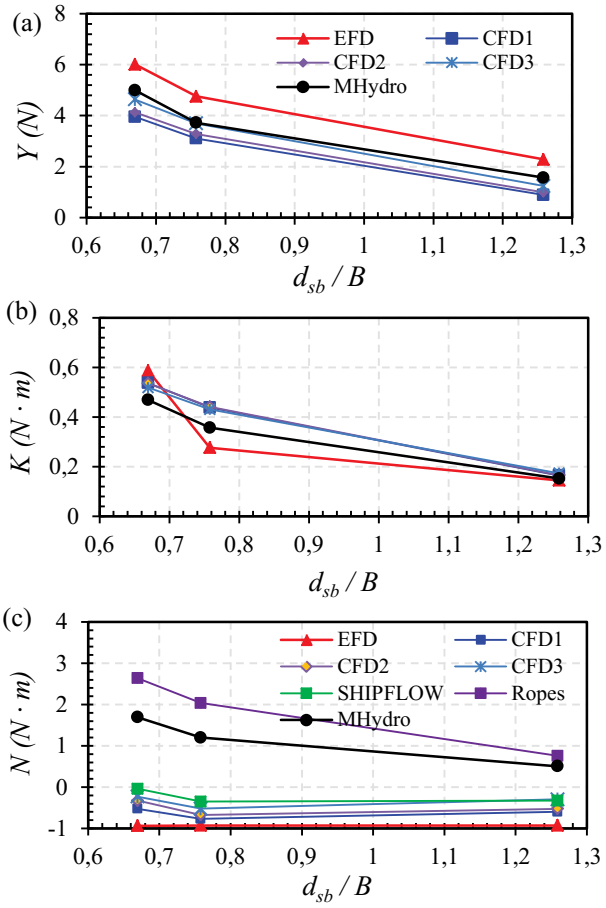

Figure 6. Comparison of forces (or moments) at different ratio of d_{sb} / B from different programs. (a) Lateral forces; (b) roll moments; (c) yaw moment. The definitions of EFD, CFD1, CFD2 and MHydro are the same as Figure 4. CFD3 is a viscous-flow CFD code that solves multiphase (unsteady) incompressible flows with the RANS equations, complemented with turbulence closure models, cavitation models and volume-fraction transport equations for different phases [19]; SHIPFLOW is a steady state CFD software which contains a RANS solver XCHAP based on the finite volume method with variables collocated at cell centers [12]; Ropes is a 3D potential flow program based on the double-body assumption. All the results apart from those from MHhydro are provided by Hoydonck et al. [17].

3.2 VALIDATION OF SHIP-BOTTOM INTERACTION

Case 3 – Case 5 illustrates the ship-bottom interaction. The comparisons of the wave elevation in Figure 7 and Figure 8 show similar information as the ship-bank interaction problem. Generally, the potential flow method is capable to predict the wave elevations when the ships are advancing in shallow water. Because of the numerical damping due to the insufficient panel size, the wave

trough is underestimated. It can also be found in Figure 8 that as the water depth decrease, the wave elevation could increase significantly.

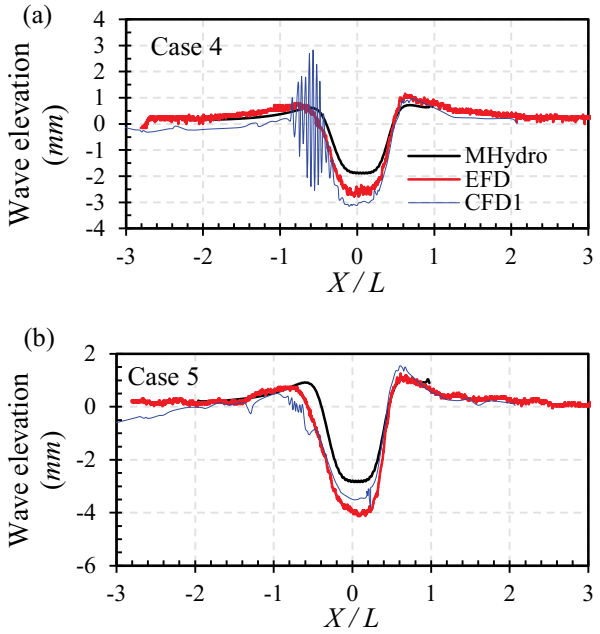

Figure 7. Results of wave elevation at different *d* obtained from different programs. (a) Case 4; (b) Case 5.

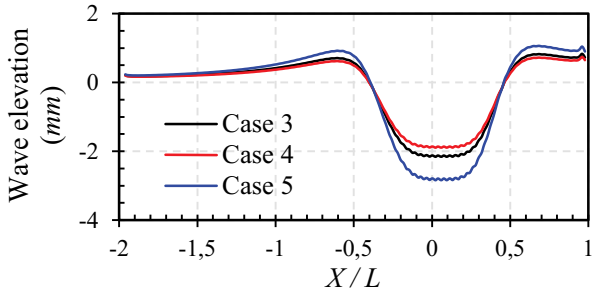

Figure 8. Results of wave elevation at different water depths obtained from MHydro.

The comparisons of the forces and moments in Figure 9 show similar information as the ship-bank interaction problem. With regard to the lateral forces and roll moments, the present results from MHydro agrees with the experimental results well. Compared with the other CFD programs, the present potential flow program show even better predictions in some degree. However, the sign of the yaw moment predicted by MHydro as well as Ropes is incorrect compared to the EFD and other CFD results. As explained above, this may due to the lifting force which is neglected in the present study.

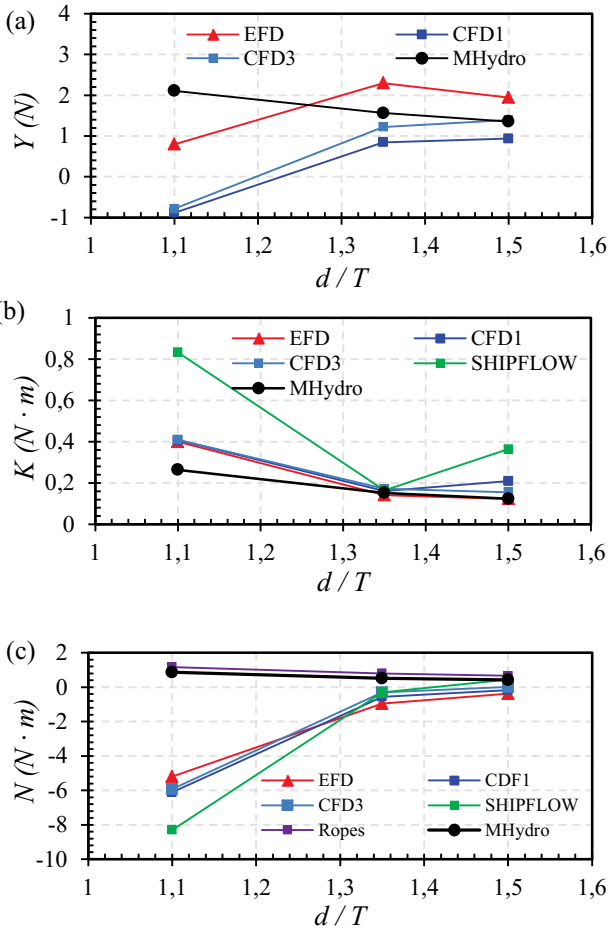

Figure 9. Comparison of forces (or moments) at different distance *d* from different programs.

3.3 VALIDATION OF SHIP-SHIP INTERACTION

3.3 (a) Validation of wave elevations

The model tests for ship-to-ship with the same forward speed were carried out at the same tank described above. The model test data is published and provide by Lataire et al. (2009). The ship models involved includes a KVLCC2 (as described above and it is referred as Ship_a) and an Aframax tanker model (Ship_b) with scale factor 1/75. The main dimension of the Aframax model is 3.085 *m* (length) × 0.56 *m* (breadth) × 0.1 *m* (draft). The test condition (Test 1) is shown below: the water depth is 0.374 *m*, the speed of the ships is 0.237 *m/s*, the transverse and longitudinal distance between two ships is 0.9995 *m* and 0 *m* respectively. In the numerical simulation, there are 14,040 panels (8,080 on KVLCC2 and 6,020 on Aframax) distributed on the body surface, 13,875 panels distributed on the free surface, 760 panels distributed on the control surface. The free surface is truncated at $1.5L_a$ upstream and $3L_a$ downstream, where L_a refers to the ship length of KVLCC2 model.

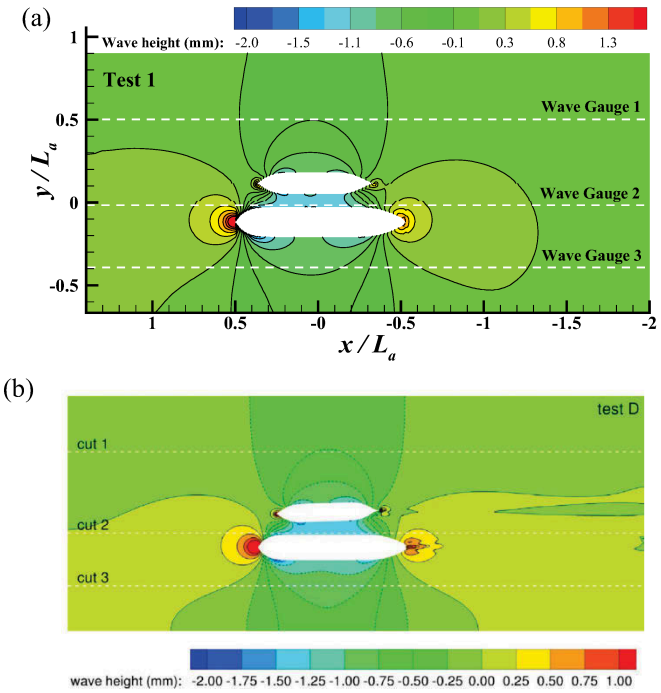

Figure 10. Wave patterns of Test 1. (a) Present calculation; (b) CFD results from Zou and Larsson [12].

The wave pattern of Test 1 obtained from MHydro is shown in Figure 10 (a) and the CFD results [12] are shown in Figure 10 (b). The label 'test D' in the right-top of Figure 10 (b) corresponds to test conditions of Test 1 in the present study. Generally, a very good agreement has been obtained between these two programs. Only very small discrepancies can been found in the stern areas of both ships, which is due to the influence from the propeller. In the present calculation based on the potential flow theory, the influence from the propeller has been neglected.

Figure 11 shows the wave profiles measured from three wave gauges. The present results from MHydro and CFD results from SHIPFLOW [12] are also presented. The positive x values represent the upstream part of the domain. It can be found from these figures that the present predictions agree with the measurements and CFD results very well at wave gauge 1 and 3. At wave gauge 2, the present method under-estimates the wave elevation between the two ships. But it matches the CFD method very well, which indicates that viscous effects on the wave elevation are very small. These waves will account for the so-called wave-making resistance.

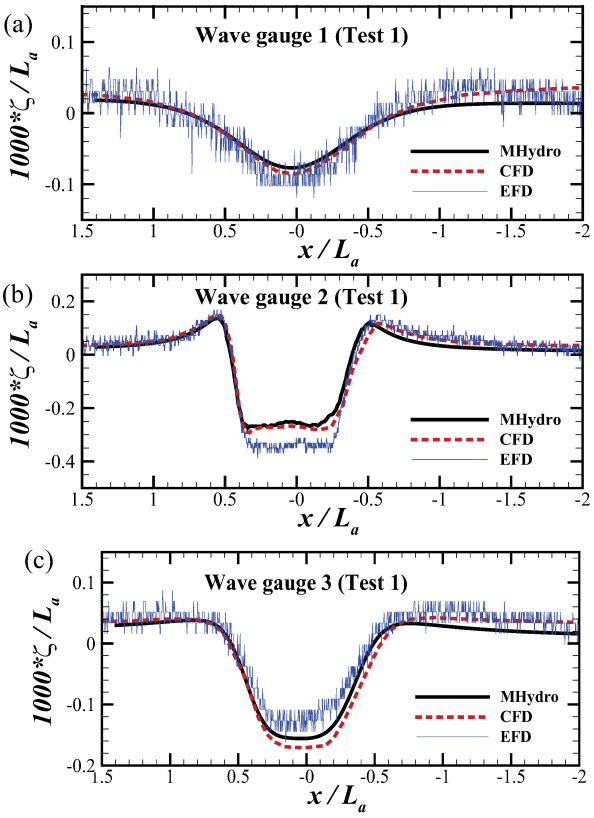

Figure 11. Wave profiles of Test 1. (a) Wave gauge 1; (b) wave gauge 2; (3) wave gauge 3.

3.3 (b) Validation of wave elevations

In order to validate the present method and numerical program, another simulation is performed to investigate the ship-to-ship with different forward speeds problem. The model tests used here were carried out by Vantorre, et al. [20] at the same tank as mentioned in ship-bank interaction test. They installed an auxiliary carriage alongside the main carriage to achieve a different towing speed. They performed a comprehensive test programs based a series of ship models. In the present study, two Esso Osaka models (referred as Model C and Model E hereafter) with scale factor 1/75 are selected to validate the developed method. The main particulars of Model C and Model E in full scale can be found in Table 3.

Table 3. Main particulars of Model C and Model E

	Model E	Model C
Length *(m)*	$L_a = 286.8$	$L_b = 298.8$
Breadth *(m)*	$B_a = 46.8$	$B_b = 37.8$
Draft *(m)*	$T_a = 15.53$	$T_b = 13.5$
Block coefficient	$C_{Ba} = 0.816$	$C_{Bb} = 0.843$

In the model test, Model E was towed by the main carriage at centre line ($y = 0$) of the tank, while Model C was towed by the auxiliary carriage. The transverse distance is $dt = B_b + 0.5B_a$ and the water depth h is $18.63m$. The forward speed of Model E is 8 knots in full scale, and

Model E was overtaken by Model C at the speed of 12 knots. Figure 12 is the computational domain of the numerical model. The reference coordinate system is fixed on Model E.

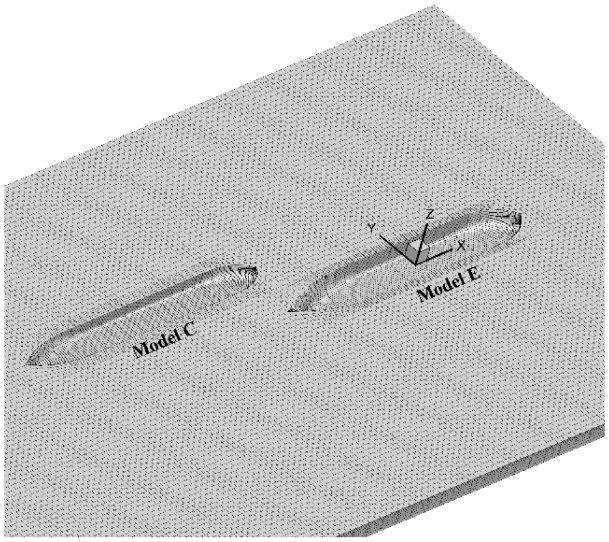

Figure 12. The computational domain of the numerical model. There are 23,840 panels distributed on the entire computational domain: 1,200 on the body surface of Model C, 1,040 on the body surface of Model E, 20,640 on the free surface and 960 on the side walls. The computational domain is truncated at L_b upstream and $3L_b$ downstream, referred to the upstream ship.

The force and moment acting on Model E in shallow water are shown in Figure 13. The experimental results are due to Vantorre, et al. [20]. The numerical predictions are obtained by solving the boundary value problem in Eq. (8) and (9). It is worthwhile to note that while the general behavior of the experimental curves is predicted fairly well, the peak sway force is substantially overestimated, particularly when Model C is "off the shoulder" of Model E. One possible reason could be the neglect of the rudder in the numerical model. It can also be found from Figure 13 (a) that the calculated wave-making resistance agrees with the experimental measurement very well. The latter one represents the total resistance including the viscus component. It indicates that due to the hydrodynamic interaction between the two ships, the resistance from the pressure integration contributes dominantly to the total resistance even in the low forward speed condition. This is different from the single vessel case [21].

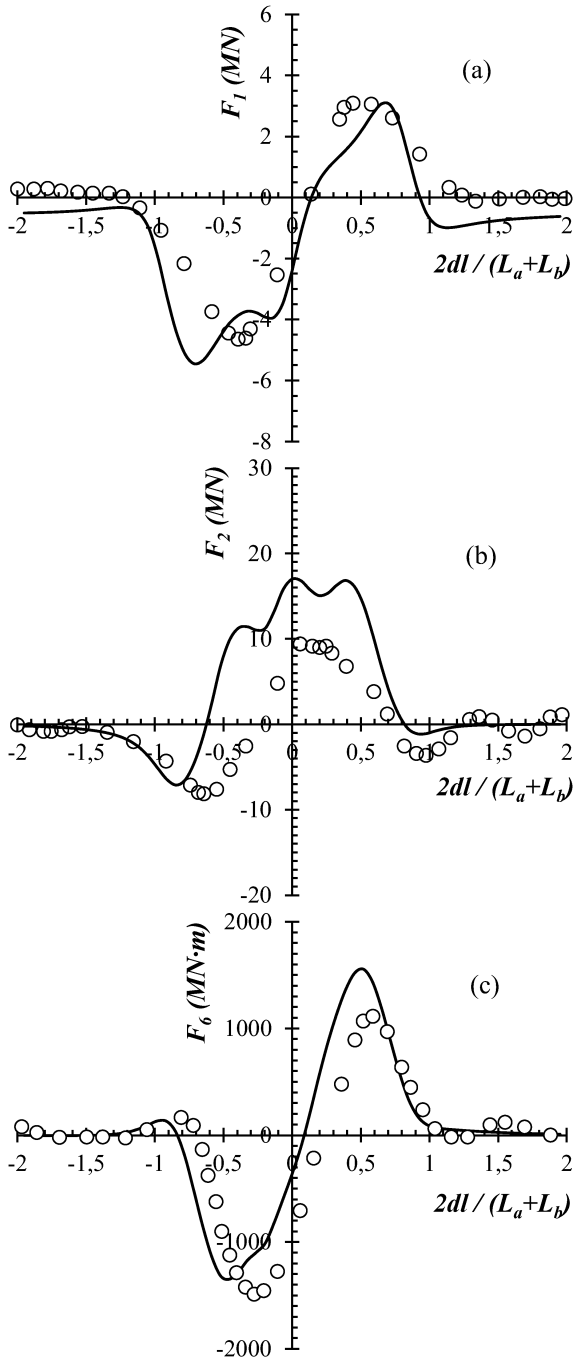

Figure 13. (a) The resistance, (b) the sway force and (c) the yaw moment acting on Model E overtaken by Model C. The negative x values denote that Model C is in the downstream side of Model E. As Model C moves to the upstream side, the x values become positive. ○, experiment, Vantorre, et al. [20]; –, the present prediction from MHydro.

4 CONCLUSIONS

In the present study, we present many case studies which include the problems of ship-bank, ship-bottom and ship-ship interaction. The results of the present study are calculated by potential flow program. Through the comparisons to the experimental measurements and CFD calculation, we can come to the following conclusions:

1) The potential flow method is a reliable way to predict the wave elevation when the bank and bottom effects are significant. The accuracy of the prediction relies on the panel size and forward speed. As for the very low forward speed cases, the potential flow method underestimates the wave trough due to the insufficient panel distributed on the free surface;
2) Compared with the CFD programs, the present potential flow program shows even better predictions in predicting the lateral forces and roll moments in the confined waterways. However, because of the neglecting of the lifting forces due to the non-symmetrical flow, the potential flow method fails to predict the sign of the yaw moment. In order to estimate yaw moment correctly, the so-called Kutta condition must be imposed to the trailing edge in the wake region.
3) The potential flow method is able to predict the wave elevation of ship-ship problem. The forces or moments predicted by potential flow method have a good agreement with the model test results.

5 ACKNOWLEDGEMENTS

The work reported in this paper was performed within the project "Energy Efficient Safe Ship Operation (SHOPERA)" funded by the European commission under contract No. 605221. The authors thank Maxim Candries and Evert Lataire at Ghent University, Wim Van Hoydonck at Flanders Hydraulics Research, for support and allowing us to use their model test data for validations.

6 REFERENCES

1. Lataire, E., M. Vantorre, and G. Delefortrie, Captive model testing for ship to ship operations, in *MARSIM 2009*. 2009: Panama City, Panama.

2. Vantorre, M., G. Delefortrie, and F. Mostaert, Behaviour of ships approaching and leaving locks: Open model test data for validation purposes. Version 3_0. WL Rapporten, WL2012R815_08e. Flanders Hydraulics Research and Ghent University - Division of Maritime Technology: Antwerp, Belgium. 2012.

3. Beck, R.F., J.N. Newman, and E.O. Tuck, Hydrodynamic forces on ships in dredged channels. *Journal of Ship Research*, 1975. 19(3): p. 166–171.

4. Tuck, E.O., A systematic asymptotic expansion procedure for slender ships. *Journal of Ship Research*, 1964. 8: p. 15–23.

5. Tuck, E.O., Shallow water flows past slender bodies. *Journal of Fluid Mechanics*, 1966. 26: p. 81–95.

6. Tuck, E.O., Sinkage and trim in shallow water of finite width. *Schiffstechnik*, 1967. 14: p. 92–94.

7. Tuck, E.O. and J.N. Newman, Hydrodynamic interactions between ships, in *Proceedings of 10th Symposium on Naval Hydrodynamics*. 1974: Cambridge, MA, USA. p. 35-70.

8. Yeung, R.W. and W.T. Tan, Hydrodynamic interactions of ships with fixed obstacles. *Journal of Ship Research*, 1980. 24(1): p. 50-59.

9. Gourlay, T., Slender-body methods for predicting ship squat. *Ocean Engineering*, 2008. 35(2): p. 191-200. doi:10.1016/j.oceaneng.2007.09.001.

10. Yuan, Z.M., et al., Ship-to-Ship Interaction during Overtaking Operation in Shallow Water. *Journal of Ship Research*, 2015. 59(3): p. 172-187. doi: 10.5957/JOSR. 59.3.150004.

11. Yao, J.-x. and Z.-j. Zou, Calculation of ship squat in restricted waterways by using a 3D panel method. *Journal of Hydrodynamics*, *Ser. B*, 2010. 22(5): p. 489-494. doi: 10.1016/S1001-6058(09)60241-9.

12. Zou, L. and L. Larsson, Numerical predictions of ship-to-ship interaction in shallow water. *Ocean Engineering*, 2013. 72: p. 386-402. doi:10.1016/j.oceaneng.2013.06 .0 15.

13. Sakamoto, N., R.V. Wilson, and F. Stern, Reynolds-Averaged Navier-Stokes Simulations for High-Speed Wigley Hull in Deep and Shallow Water. *Journal of Ship Research*, 2007. 51(3): p. 187-203.

14. Newman, J.N., Linearized wave resistance, in International Seminar on Wave resistance. 1976: Tokyo.

15. Yuan, Z.M., A. Incecik, and L. Jia, A new radiation condition for ships travelling with very low forward speed. *Ocean Engineering* 2014. 88: p. 298-309. doi:10.1016/j.oceaneng.2014.05.019.

16. Yuan, Z.M., A. Incecik, and A. Day, Verification of a new radiation condition for two ships advancing in waves. *Applied Ocean Research* 48, 2014: p. 186-201. doi:10.1016/j.apor.2014.08.007.

17. Hoydonck, W.V., et al., Bank Effects for KVLCC2, in *World Maritime Technology Conference*. 2015: Rhode Island, USA.

18. Kim, Y., D.K.P. Yue, and B.S.H. Connell, Numerical dispersion and damping on steady waves with forward speed. *Applied Ocean Research*, 2005. 27(2): p. 107-125. doi:10.1016/j.apor.2005.11.002.

19. Vaz, G., F.A.P. Jaouen, and M. Hoekstra, Free Surface Viscous Flow Computations. Validation of URANS Code FRESCO, in *28 th International*

20. Vantorre, M., E. Verzhbitskaya, and E. Laforce, Model test based formulations of ship–ship interaction forces. *Ship Technology Research*, 2002. 49: p. 124-141.

21. Schultz, M.P., Effects of coating roughness and biofouling on ship resistance and powering. *Biofouling*, 2007. 23(5-6): p. 331-41.
doi:10.1080/ 089270107014619 74.

7 AUTHORS' BIOGRAPHIES

Zhi-Ming Yuan holds the current position of lecturer in hydrodynamics at University of Strathclyde. His research interests mainly lie in the theoretical and numerical analysis of the hydrodynamic performance of the ship and offshore structures

Atilla Incecik is a Professor of Offshore Engineering and Associate Deputy Principal at Strathclyde University. His current research includes development of dynamic load and response prediction tools for the design and installation of floating offshore platforms and marine renewable energy devices; seakeeping of marine vehicles; and low carbon shipping.

4th MASHCON, Hamburg - Uliczka et al. (eds) - © 2016 Bundesanstalt für Wasserbau ISBN 978-3-939230-38-0 (Online)
DOI: 10.18451/978-3-939230-38-0_12

CFD SIMULATION OF PMM MOTION IN SHALLOW WATER FOR THE DTC CONTAINER SHIP

G Deng, A Leroyer, E Guilmineau, P Queutey, M Visonneau and **J Wackers,** METHRIC, LHEEA/UMR 6598 CNRS, Ecole Centrale de Nantes, France

SUMMARY

This paper is devoted to the validation exercises with the ISIS-CFD code, our in house finite volume RANSE (Reynolds Averaged Navier-Stokes Equation) solver, conducted for the test cases proposed for the 4th MASHCON conference (International Conference on Ship Manoeuvring in Shallow and Confined Water). CFD simulations have been performed for the 4 different pure yaw and pure sway test cases under shallow water condition. Predicted results are compared with the measurement data provided by FHR (Flanders Hydraulic Research).

1 INTRODUCTION

CFD can be considered as a mature tool now for steady state ship hydrodynamic applications such as resistance in calm and deep water. Predictions which are accurate enough can be obtained with reasonable resources even for fully appended hulls, both for model and for full scale in a routine design procedure. However, for applications with unsteady flow such as PMM (Planar Motion Mechanism) motion, more validation works need to be done before we can consider CFD as a reliable tool for those applications. International workshops devoted to ship maneuvering simulation have been organized in 2008 and 2014 (SIMMAN 2008 and SIMMAN 2014, Workshop on Verification and Validation of Ship Maneuvering Simulation Methods). Due to limited submissions with CFD approach, assessment is difficult to make. Simulation of PMM motion in shallow water is a challenging task. As flow separates under shallow water condition, especially with PMM motion, physical modeling error due to turbulence modeling could be more important. From numerical point of view, handling ship PMM motion in shallow water with confined side wall is a difficult task. Overset grid approach is more flexible to handle ship motion in such configuration. However, as conservation property cannot be ensured with overset, ensuring a good numerical accuracy is a very difficult task, especially when the mesh is highly stretched. Mesh deformation approach can provide a better numerical accuracy compared with overset approach. But it can only be used when the ship motion amplitude is small. Computation for the 4 test cases proposed by the MASHCON conference (Eloot, 2016 [3]) will be performed with the latest version of our in house flow solver ISIS-CFD including overset approach, also available in the commercial software FINE™/Marine in the coming 5.1 release.

2 NUMERICAL APPROACH

The ISIS-CFD flow solver developed by our team is a finite volume code supporting control volume of arbitrary shape. Turbulent flow is simulated by solving the incompressible Reynolds-averaged Navier-Stokes equations (RANS). The flow solver is based on finite volume method to build the spatial discretization of the transport equations. The velocity field is obtained from the momentum conservation equations and the pressure field is extracted from the mass conservation constraint, or continuity equation, transformed into a pressure-equation. In the case of turbulent flows, additional transport equations for modeled variables are discretized and solved using the same principles. The gradients are computed with an approach based on Gauss's theorem. Non-orthogonal correction is applied to ensure formal first order accuracy. Second order accurate result can be obtained on a nearly symmetric stencil. Inviscid flux is computed with a piecewise linear reconstruction associated with an upwinding stabilizing procedure which ensures a second order formal accuracy when flux limiter is not applied. Viscous fluxes are computed with a central difference scheme which guarantees a first order formal accuracy. We have to rely on mesh quality to obtain a second order discretization for the viscous term. Free-surface flow is simulated with a multi-phase flow approach. Incompressible and non-miscible flow phases are modeled through the use of conservation equations for each volume fraction of phase/fluid. Implicit scheme is applied for time discretization. Second order three-level time scheme is employed for time-accurate unsteady computation. Velocity-pressure coupling is handled with a SIMPLE like approach. Ship free motion can be simulated with a 6 DOF module. Some degree of freedom can be fixed as well. An analytical weighting mesh deformation approach is employed when free-body motion is simulated. Additionally the overset approach is also implemented recently for the numerical PMM tests. It will be employed in one of the test cases in the present study. Several turbulence models ranging from one-equation model to Reynolds stress transport model are implemented in ISIS-CFD. Most of the classical linear eddy-viscosity based closures like the Spalart-Allmaras one-equation model, the two-equation k-ω SST model by Menter [2], for instance are implemented. More sophisticated turbulence closures like an explicit algebraic stress model (EASM) [1] are also implemented in the ISIS-CFD solver. The EASM model is employed in the present study. Wall function is implemented for two-equation turbulence model.

Overset approach has been implemented recently in the ISIS-CFD code. A distance based cell blanking procedure with high parallel efficiency is implemented. Data exchange between different domains is handled with a second order least squared interpolation procedure. Adaptive grid refinement procedure has been adapted to overset approach in such a way that user can apply an adaptive grid refinement such that mesh size near the overset interface is nearly the same in different overlapping domain.

3 RESULTS AND DISCUSSIONS

The test case simulated in this paper is described in [3]. It concerns the DTC container carrier in model scale with a scale factor of 89.11 and 20% UKC shallow water condition. Water depth is 0.195m. The width of the towing tank (7.0m) is taken into account in the computation. The bare hull configuration (without rudder, propeller and bilge keel) is simulated. There are two test cases with pure yaw motion and two test cases with pure sway motion. Test cases A and B concern a pure yaw motion with a period of 25s and yaw amplitude of 15 degrees. Model speed is 0.599m/s and 0.872m/s respectively. The maximum sway motion is about 0.62m and 0.9m respectively. Test cases C and D concern pure sway motion with a period of 20s and sway amplitude of 0.2m. Model speed is the same as case A and B respectively.

Mesh management is a critical issue for shallow water computation. To ensure a good numerical accuracy, single domain computation with mesh deformation is the best choice. Our mesh deformation approach has been recently adapted for shallow water computation such that mesh deformation in the XY plane near the bottom wall in shallow water configuration is free. With this special implementation, all test cases can be simulated with single domain using mesh deformation. To better handle ship heave and pitch motion with mesh deformation approach, the mesh is generated with the ship model located at a prescribed sinkage position. The prescribed sinkage value for the low and high speed cases are 8mm and 23mm respectively. According to our experiences [4], for shallow water computation, it is preferred to use low Reynolds number model at the hull, and wall function at the bottom wall. This gives a mesh with about 8.2M and 9.2M cells for the low and high speed respectively. For case B, due to high maximum sway motion (about 0.9m over half tank width of 3.5m), mesh deformation is too severe. We also attempt to use the newly developed overset approach for this computation. An overlapping domain containing the hull with outer boundaries located at about 0.3Lpp is generated. It contains about 3.5M cells. The background grid containing about 2M cells is employed to simulate the towing tank. To avoid numerical difficulty related to overset approach as much as possible in this first attempt with overset approach for shallow water application, viscous layer is not inserted at the bottom wall. Moreover, wall function approach is employed at the hull in order to reduce CPU time. Ship heave and pitch motions in the overlapping domain are still handled with mesh deformation, while mesh rigid motion is applied for yaw and sway motions.

Table 1. Results for Resistance Computation

Case	u(m/s)	Rt(N)	Trim(mm/m)	Sink(mm)
A	0.599	3.35	-0.31	5.25
B1	0.872	9.48	-0.41	15.8
B2	0.872	9.60	-0.43	19.1

To initialize the computation with PMM motion, a resistance computation is performed first. Ship resistance, trim and sinkage results for these computations are shown in table 1. Case B1 is performed with single domain, while case B2 is performed with overset approach. Overset approach over predicts ship resistance, trim and sinkage by 1.2%, 4.9% and 21% respectively compared with single domain approach. Based on our experiences with similar configuration [4], ship resistance predicted with wall function is smaller compared with the result obtained with low Reynolds number model. Hence, the over prediction of ship resistance with overset is not due to the use of wall function. Inspection of the numerical result obtained with overset approach reveals that when the ship advance in the numerical tank, water level near the inlet decreases by about 2mm compared with the expected calm water level. This unexpected result must be due to the fact that with overset approach, mass conservation cannot be ensured. As the simulated water level is lower, resistance and sinkage are over predicted. Only trim and sinkage results are reported in [3]. The measurement trim angle is about -0.4mm/m for both speeds. CFD prediction agrees well with the measurement data for this quantity except for the case with low speed. Measurement values for sinkage are 5.1mm and 16.5mm respectively for both speeds. At high speed, the predicted sinkage is only 0.7mm smaller than the measurement value. In relative value, it is only 4.4% smaller. Taken into account measurement uncertainty; we consider that CFD prediction for sinkage with single domain is accurate., Over estimation by 16% observed with overset approach is due to simulated water level in numerical tank as mentioned above. The comparison with the measurement data suggests that the single domain computation provides good prediction for trim and sinkage, while correction should be made based on the simulated water level when using overset approach..

As ship resistance measurement data are not available, to give an indication on numerical uncertainty for hydrodynamic force, comparison of ship resistance for the DTC container ship in deep water is shown in figure 1. The measurement data are provided in [5]. Computations have been performed with the k-ω SST turbulence model with a grid containing about 1M cells

on half domain. For all speeds, ship resistance is under predicted by less than 2%. Grid independent study has been performed for the highest speed v=1.668m/s (with Fr=0.218). The later results are also given in table 2. The error shown in this table is the difference between the measurement result (31.83N) and the CFD prediction, while numerical uncertainty is the difference between the CFD result and the extrapolated CFD prediction (30.658N) with observed order of convergence (p=1.95). Such convergence behavior is a typical result obtained with our solver for such verification and validation exercise for a conventional hull form. Predicted resistance becomes smaller than the measurement value when we refine the grid. This is a well-known default of linear turbulence model. CFD prediction can be improved by using a more accurate turbulence model such as the non-linear EASM model. More validations in shallow water on the hydrodynamic forces as well as ship trim and sinkage including the results obtained with our code can be found in [4].

Table 2. Grid dependency study for Fr = 0.218.

Nb. cells	Resistance (N)	Error	Uncertainty
400K	32.27	-1.38%	5.3%
1025K	31.53	0.94%	2.8%
2071K	31.21	1.95%	1.8%

Measurement data at Fr = 0.218: resistance = 31.83N

Restarting from the resistance computation, a time accurate unsteady simulation with prescribed PMM motion is performed. For case A with pure yaw motion, a small time step with 2500 time steps per period is necessary to ensure numerical stability. Time step is larger for case C and D with pure sway motion (1000 time steps per period). 20 non-linear iterations per time step are performed. With 64 cores, one time step takes about 100s wall clock time. A typical computation takes about 10 days. The CPU time with overset approach is similar.

Comparison with measurement results for heave and pitch motion as well as longitudinal and lateral forces, roll and yaw moments for different cases are shown in figures 2 to 9. For verification purpose, imposed sway motion, v velocity and yaw motion are also shown in the figures. Forces and moments are given in the horizontal-bound towing carriage coordinate system as described in [3]. Solid lines are CFD predictions, while symbol lines are measurement data. Averaged Reynolds number and Froude number based on ship length are 2.28×10^6 and 0.0958 respectively for the case with low speed, and 3.23×10^6 and 0.139 respectively for the case with high speed.

Restarting from the resistance computation, a time accurate unsteady simulation with prescribed PMM motion is performed. For case A with pure yaw motion, a small time step with 2500 time steps per period is necessary to ensure numerical stability. Time step is larger for case C and D with pure sway motion (1000 time steps per period). 20 non-linear iterations per time step are performed. With 64 cores, one time step takes about 100s wall clock time. A typical computation takes about 10 days. The CPU time with overset approach is similar.

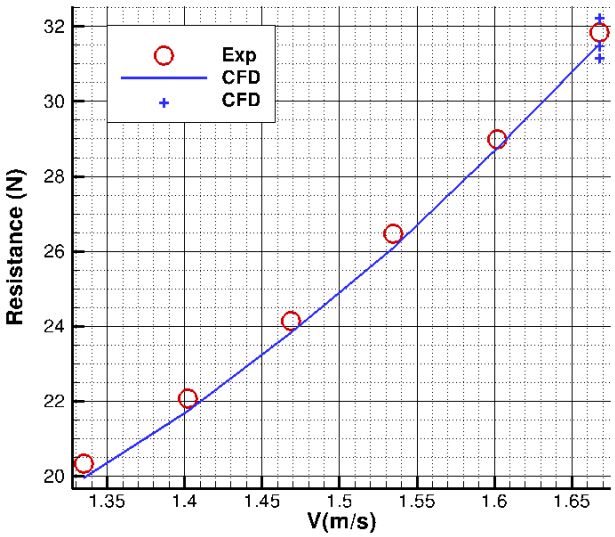

Figure 1. Deep water resistance prediction.

Comparison with measurement results for heave and pitch motion as well as longitudinal and lateral forces, roll and yaw moments for different cases are shown in figures 2 to 9. For verification purpose, imposed sway motion, v velocity and yaw motion are also shown in the figures. Forces and moments are given in the horizontal-bound towing carriage coordinate system as described in [3]. Solid lines are CFD predictions, while symbol lines are measurement data. Averaged Reynolds number and Froude number based on ship length are 2.28×10^6 and 0.0958 respectively for the case with low speed, and 3.23×10^6 and 0.139 respectively for the case with high speed.

Case A (figure 2 and 3) is a pure yaw motion at low speed. Sinkage is under predicted by about 0.5mm. Trim angle is also slightly under predicted. Taking into account measurement and numerical uncertainty, it can be considered that ship motion is correctly predicted. Measurement data for longitudinal force is very noisy (figure 3). To allow a better comparison, smoothed measurement data is also plotted. It can be seen that the predicted longitudinal force agree well with the smoothed measurement data. The predicted lateral force is quite different from the measurement data. First order amplitude is almost 3 times smaller than the measurement value. Such huge discrepancy is not consistent with the good agreement observed for the yaw moment. Moreover, lateral forces are correctly predicted for the cases with pure sway motion. We believe that there might be a measurement data processing problem for the lateral force for this test case.

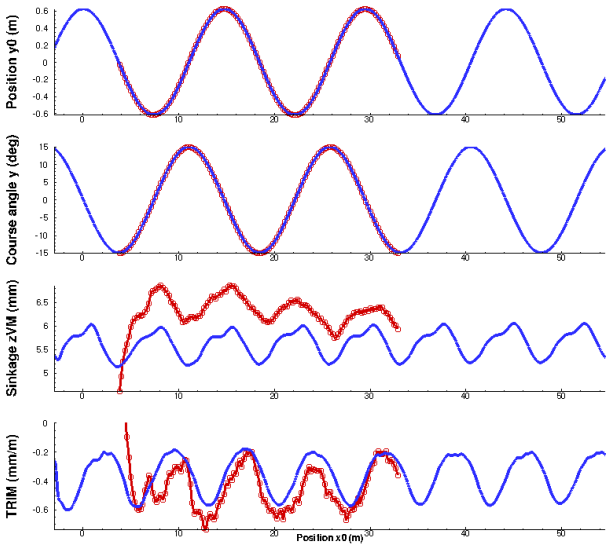

Figure 2. Motions for case A

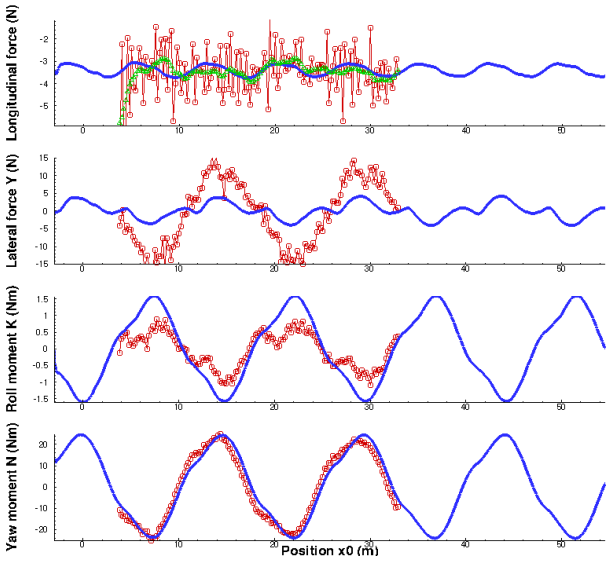

Figure 3. Forces and moments for case A

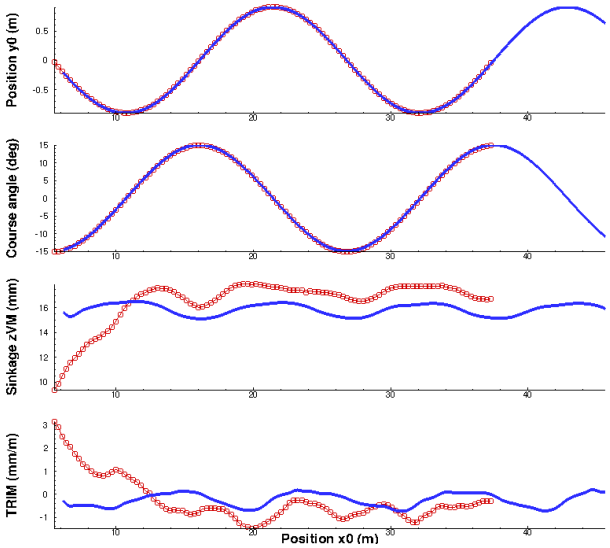

Figure 4. Motions for case B

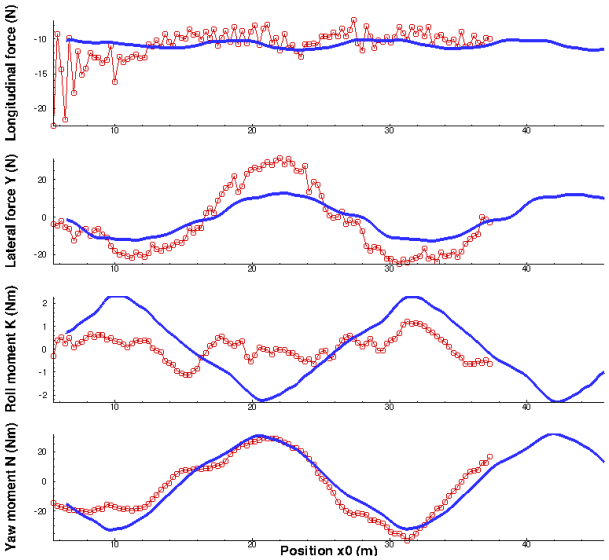

Figure 5. Forces and moments for case B

Case B (figures 4 and 5) is a pure yaw motion with high speed. We fail to obtain plausible result with overset approach for this case. Results shown in figures 4 and 5 are also obtained with single domain approach with mesh deformation. Predicted heave motion is about 1mm smaller compared with the measurement data with very small fluctuation. Pitch angle is very small. Longitudinal force is almost constant. It agrees well with the measurement data. As for case A, amplitude of the lateral force is under predicted by about 50%. However, yaw moment is in much better agreement. As for case A, roll moment amplitude is also higher in the CFD computation. But it remains very small compared with the yaw moment.

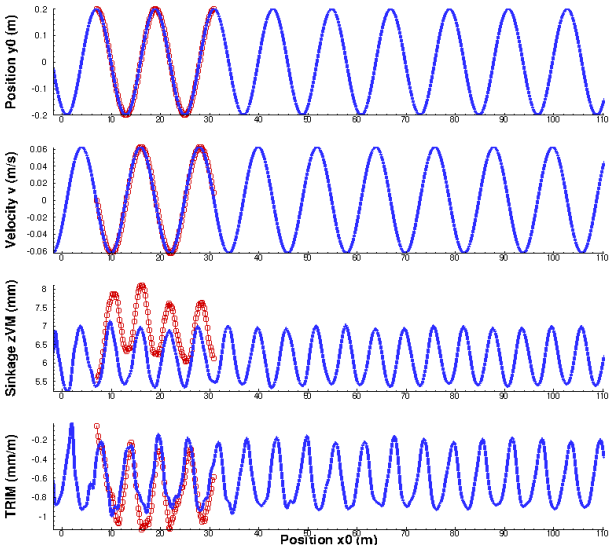

Figure 6. Motions for case C

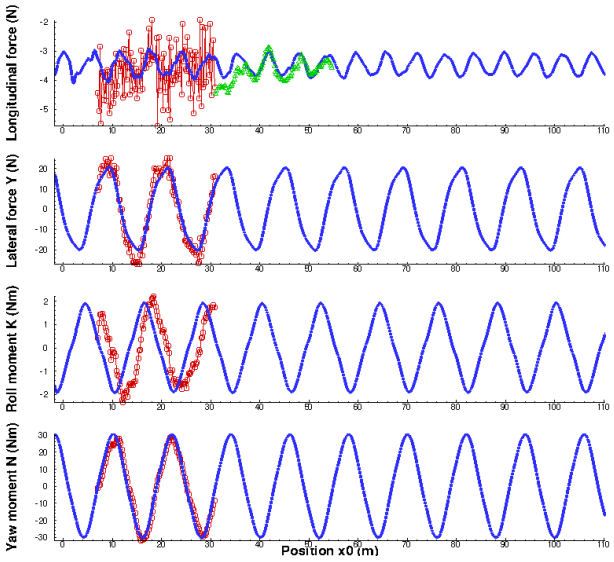

Figure 7. Forces and moments for case C

Case C (figure 6 and 7) is a pure sway motion at low speed. Predictions for trim and sinkage are similar for case A. Measurement data for longitudinal force is also very noisy. It varies from -6N to -2N, while CFD prediction varies from -4N to -3N only. As for case A, smoothed measurement data is also plotted to allow a better comparison. CFD prediction agrees well with the smoothed measurement data (shifted to the right for better comparison). Unlike for case A, good agreement is observed for lateral force. Force amplitude is under predicted only by about 15% rather than by 3 times. Roll and yaw moments are also correctly predicted, although a phase lag is observed for the roll moment.

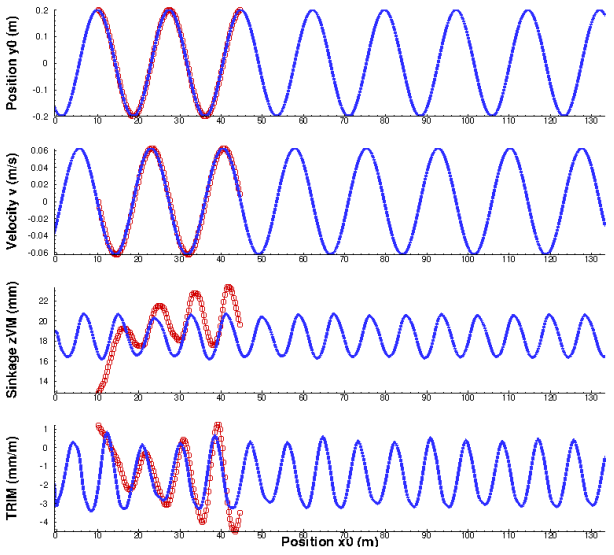

Figure 8. Motions for case D

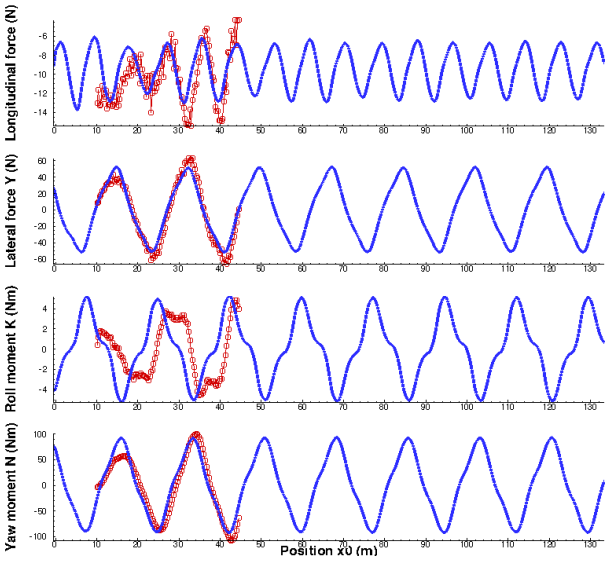

Figure 9. Forces and moments for case D

Case D (figures 8 and 9) is a pure sway motion at high speed. CFD computation aims at predicting fully established stat with quasi periodic result. Measurement data were recorded only for the first 2 periods after the acceleration due to limited length of the towing tank. Figure 8 shows that due to the transitional effect during the acceleration period, ship trim and sinkage are far from the expected quasi periodic behavior. For this reason, it is difficult to compare the CFD prediction with measurement. Nevertheless, the predicted trim and sinkage are about the same magnitude as observed in the measurement. Similar behavior is observed for force and moments shown in figure 9..To better validate CFD computation, a transitional flow simulation with exactly the same motion laws applied during the acceleration period as in the measurement could be more useful. Unfortunately, those motions laws are not specified in [3]. Another interesting alternative is to perform CFD simulation corresponding to arm rotating basin.

4 CONCLUSIONS

The 4 test cases proposed for the MASHCON conference with PMM pure yaw and pure sway motion for the DTC carrier in shallow water have been computed with the ISIS-CFD flow solver. Good agreement is observed for ship motions, forces and moments in general except for lateral force for pure yaw motion. All computations have been performed with single domain approach using mesh deformation. When ship motion amplitude becomes larger, alternatives such as overset approach are needed for such simulation. Such simulations will be investigated in future studies.

5 ACKNOWLEDGEMENTS

This work was granted access to the HPC resources under the allocation 2015-2a1308 made by GENCI (Grand Equipement National de Calcul Intensif). The authors are in debt to K. Eloot et al. for providing the experimental data.

6 REFERENCES

1. Deng, G.; Queutey, P.; Visonneau, M. (2005). Three-Dimensional Flow Computation with Reynolds Stress and Algebraic Stress Models. Engineering *Turbulence Modelling and Experiments 6*, W. Rodi and M. Mulas eds. Elsevier, pp. 389-398..

2. Menter, F.R. (1993). Zonal two-equations k-ω turbulence models for aerodynamic flows. *AIAA Paper* 93-2906.

3. Eloot, K.; Vantorre, M.; Delefortrie, G.; Lataire, E. (2016). Running Sinkage and Trim of the DTC Container Carrier in Harmonic Sway and Yaw Motion: Open Model Test Data for Validation Purposes. *Fourth International Conference on Ship Manoeuvring in Shallow and Confined Water (MASHCON): Ship - Bottom Interaction*, 23-25 May 2016, Hamburg, Germany.

4. Mucha, P.; Deng, G.; Gourlay, T. ; Moctar O. el (2016). Validation Studies on Numerical Prediction of Ship Squat and Resistance in Shallow Water. *Fourth International Conference on Ship Manoeuvring in Shallow and Confined Water (MASHCON): Ship - Bottom Interaction*, 23-25 May 2016, Hamburg, Germany.

5. Moctar, O. el; Shigunov, V.; Zorn, T. (2012). Duisburg Test Cases: Post-Panamax Container Ship for Benchmarking. *Ship Technology Research, Schiffstechnik* Vol. 59, No. 3.

7 AUTHORS' BIOGRAPHIES

Ganbo Deng holds a research position in the METHRIC group of LHEEA at Ecole Centrale de Nantes, France. His main activities concern CFD code development and application for hydrodynamic. His recent activities concern overset development.

Alban Leroyer holds an associate professor position in the METHRIC group of LHEEA at Ecole Centrale de Nantes, France. His main activities concern FSI simulation.

Emmanuel Guilmineau holds the current position of Researcher at CNRS (French National Center for Scientific Research). He is responsible for the study of turbulence models.

Patrick Queutey holds the current position of Researcher at CNRS (French National Center for Scientific Research). He is at the head of the METHRIC team (Turbulent Modelling of Incompressible Flows at High Reynolds Number).

Michel Visonneau , born in France in 1957. He obtained the Engineer's diploma in 1980 from Ecole Nationale Supérieure de Mécanique (now Centrale Nantes) and the diploma of Advanced Naval Architecture from ENSM in 1981. In 1985, he got the PhD of Fluid Dynamics and Heat Transfer of University of Nantes and entered the "Centre National de la Recherche Scientifique (CNRS)" as Research Scientist. He was the head of the CFD department of the Fluid Mechanics Laboratory (ECN) from 1995 to 2011. In 2001, he got the Research Habilitation Diploma. He holds the position of Research Director within CNRS from 2006. His main research topics are Computational Fluid Dynamics (CFD), Ship Hydrodynamics and Turbulence Modeling for high Re flows. In 1991, he got the 2nd Cray Prize for CFD and was awarded 30th Georg Weinblum Memorial Lecturer (2007-2008) in 2007.

Jeroen Wackers holds a research position in the METHRIC group of LHEEAat Ecole Centrale de Nantes, France. He is responsible for the study of adaptive grid refinement.

Squat

4th MASHCON, Hamburg - Uliczka et al. (eds) - © 2016 Bundesanstalt für Wasserbau ISBN 978-3-939230-38-0 (Online)
DOI: 10.18451/978-3-939230-38-0_13

DEVELOPMENT OF A SQUAT FORMULA BASED ON NUMERICAL CALCULATIONS

A Gronarz, DST – Development Centre for Ship Technology and Transport Systems, Duisburg, Germany

SUMMARY

Many different formulae for the estimation of the squat exist, but they do not cover a real wide range of variables describing the hydrodynamic details of the flow situation. Based on an extensive series of numerical calculations using the shallow water code BESHIWA, the squat of an idealized ship including variations of length, breadth, draught, block coefficient, speed, water depth, channel width and the slope of the bank has been calculated.
The new approach is using a base formula over the Froude depth number which is fitted to the numerical results for the idealized standard ship of 100 m length, 10 m breadth and 3 m draught. The value of this base curve is scaled to the project ship size and corrected by considering different influence factors for the variables of the calculations as B/L, T/L, CB, B/W and the slope. The new formula proves to be a universal tool for all applications, e.g. the implementation in simulator software.

NOMENCLATURE

B	Breadth (m)
CB	Block coefficient (-)
Fnh	Froude depth number
h	Water depth (m)
KB	Breadth factor (-)
KC	Block coefficient factor (-)
KL	Length factor (-)
KM	Slope factor (-)
KT	Draught factor (-)
KW	Channel width factor (-)
L	Length (m)
m	Slope of the bank x/y (-)
T	Draught (m)
V	Velocity (m/s)
W	Channel width (m)
W'	Reduced channel width (m)
Wm	Mean channel width (m)
x	x-coordinate of ship hull (m)
y	y-coordinate of ship hull (m)
y	Position in the channel (%)
yPt	Distance from the centerline of the ship to the port shoreline (m)
yStb	Distance from the centerline of the ship to the starboard shoreline (m)
z	Squat (sinkage midships) (m)
λ	Scale between test ship and real ship (-)

1 INTRODUCTION

A simulator software for the calculation of the own ship's behavior should ensure that every possible situation is handled with satisfactory results. The squat behavior can be either stored in a data base or it can be computed by a formula, taking into account or considering all or most imaginable. The installation of the new inland waterway simulator SANDRA at the DST as well as the availability of an appropriate software entailed to this project. A formula to replace the rather simple approach, based on a quadratic speed dependency of a maximum squat should be developed for the simulator.

As an institute with special dedication to shallow water hydrodynamics, the main question was: How does the squat change with speed and water depth? Additional variables are the ships parameters as length *L*, breadth *B*, draught *T*, block coefficient *CB* and the parameters of the waterway as width *W*, the slope *m* of the bank and the Position *y* of the ship in the channel.

2 THE SOFTWARE "BESHIWA"

The numerical code BEShiWa (Boussinesq Equations for Ship Waves), which has been developed in the DST, uses a Boussinesq-approach [1, 2] to calculate the generation and propagation of waves in shallow water. The dynamic sinkage and trim of the ship is fully regarded. Thereby it is suitable for the planned squat calculations.
In Figure 1 the wave patterns generated by a ship running through channels of different width are shown.

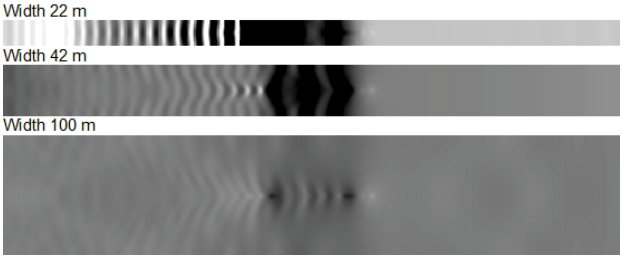

Figure 1. Density plots of wave patterns at constant speed in canals of different width

A full calculation of all elements of the multidimensional matrix consisting of the variables *V, h, L, B, T, CB, W, m* and *y* with say 7 steps per variable would need nearly 5 million cases. To make the project manageable, a simplification strategy was followed:

- Deeply investigate the speed and the water depth
- Use the length for scaling the results
- Check the dependencies of the other variables and develop functions to handle the alterations

In the end, about 300 cases have been calculated for the final development of the formula.

3 THE IDEALIZED SHIP

Disregarding changes due to differences of *L, B, T* and *CB,* a basic ship with standard main dimensions was defined:

L	100 m
B	10 m
T	3 m
CB	0.75

For the primary calculations standard conditions for the other variables have also been specified:

h	6 m
W	240 m
V	4.6 m/s = 16.6 km/h (*Fnh*=0.6)
m	0 (vertical wall)
y	50% (Centerline of the channel)

As the main focus for the calculations in BeShiWa is given to the displacement distribution, but the section data have to be given as input, automatisms have been developed to generate ships with different *CB*.
They are identical in bow and stern and have a varying parallel midship length. The displacement distribution is shown in Figure 2.

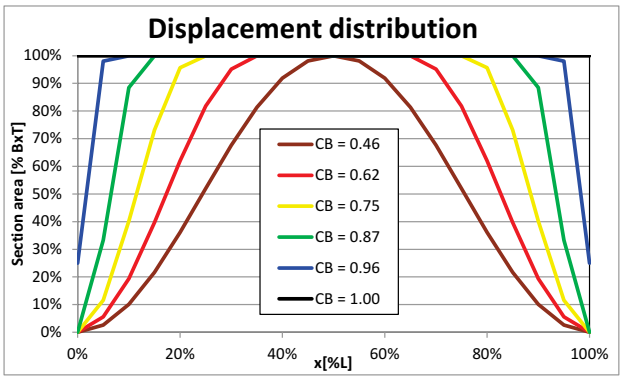

Figure 2. Displacement distribution of test ship

The sections in Figure 3 have a flat bottom, a bilge radius dependent on the block coefficient and a vertical side following a waterline similar to the displacement distribution. Besides the complicated variation in *CB*, the ship modifications due to *B* and *T* have been done by simple scaling of *x* and *y*.

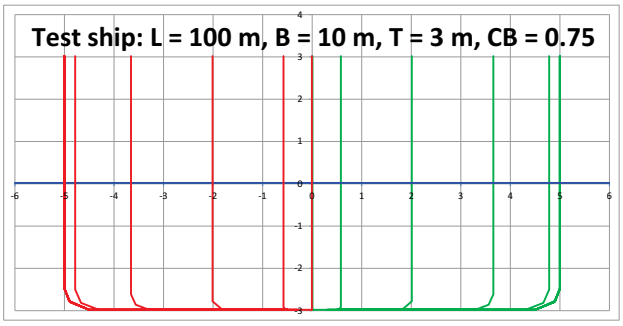

Figure 3. View of sections

4 THE BASIC FORMULA

The most important parameter for the squat is the speed. It would be appropriate for deep water calculations to use this for the generation of a formula but the second important influence is the water depth and it has also a major impact.
The Froude-depth number *Fnh* covers both influences in a single value. After several unsuccessful attempts with both *V* and *h* this dependency was chosen for the regression. This implies a failure in deep water which can be treated by a lower limitation of *Fnh* to 0.2.
In Figure 4 the basic formula (1) for the test ship in default conditions (see chapter 3) is compared to the calculations with BeShiWa.

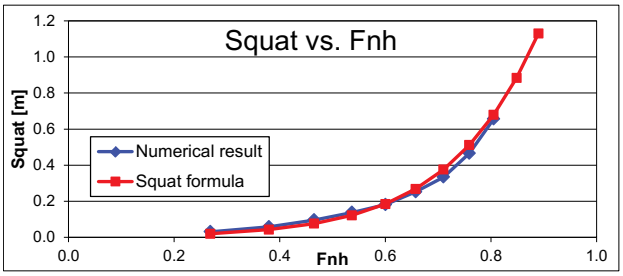

Figure 4. Basic formula for the default case

$$z = 0.0065 \cdot e^{5.2 \cdot Fnh} + 0.95 \cdot Fnh^6 - 0.065 \qquad (1)$$

As the squat for the test ship with *L* = 100 m is calculated for the same speed and water depth conditions as the target length, the squat can be scaled up or down using a length factor *KL* (2).

$$KL = \lambda = \frac{L}{100} \qquad (2)$$

5 FURTHER DEPENDENCIES

All other dependencies are used as changes to the default case and not as absolute values. A green line which intersects with the curves always at the ordinate 1 marks the basic condition in the figures. For stability reasons polynomials will be avoided. To prevent unsafe extrapolation limits for the correction factors are given in the following.

5.1 BREADTH

With the dimensions L and B of the test ship the default value for the breadth factor *KB*=1 (3), Figure 5 is at *B*/*L*=0.1.

$$KB = 16 \cdot \left(\frac{B}{L}\right)^{1.17}, \quad 0.25 < KB < 4 \qquad (3)$$

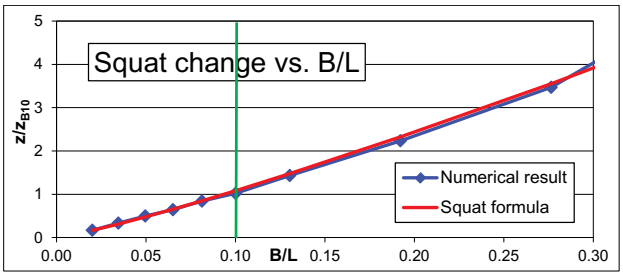

Figure 5. Breadth factor *KB*

5.2 DRAUGHT

The draught variation was calculated with constant speed *V* and water depth *h*, consequently constant *Fnh*. For different water depth the squat change was always the same for varying *T/L*. Compared to the handling of the breadth, the draught is also related to the length to achieve a result of 1 for the default ship. The outcome for the *KT* is shown in Figure 6 and the equation (4) below.

$$KT = 38.3 \cdot \frac{T}{L} - 0.15\,,0.25 < KT < 4 \qquad (4)$$

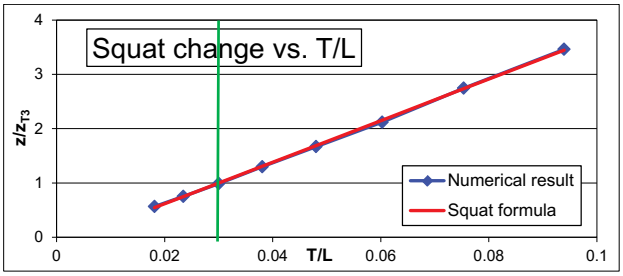

Figure 6. Draught factor *KT*

5.3 BLOCK COEFFICIENT

For unknown reasons the numerical results for the CB-variation were not as good as the others. But a clear tendency can be seen. Equation (5) and Figure 7 give the results.

$$KC = 0.07 \cdot \left(\frac{CB}{0.75}\right)^6 + 0.93\,,0.5 < CB < 0.9 \qquad (5)$$

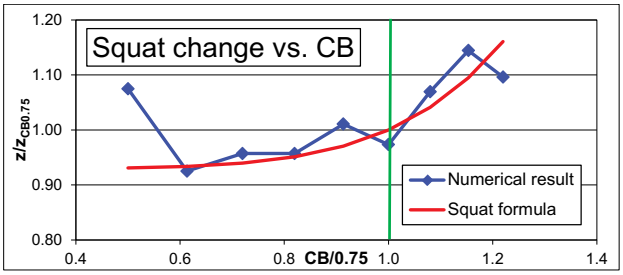

Figure 7. Block coefficient factor *KC*

5.4 CHANNEL WIDTH

On the basis of the default channel width of 240 m, which is close to infinite width, the calculations have been carried out with decreasing width. The comparison with the formula is given in Figure 8 and equation (6).

$$KW = 42 \cdot \left(\frac{B}{W}\right)^2 + 0.93\,,1 < KW < 6 \qquad (6)$$

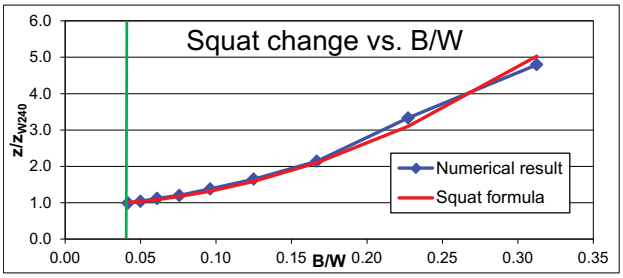

Figure 8. Channel width factor *KW*

5.5 CHANNEL SLOPE

For evaluation purposes the slope should be independent from the channel width. Therefore, a mean channel width *Wm* is defined, which is measured at half depth. This means, that the channel cross section area *Wm·h* is always constant for all slopes *m*.
Several calculations have been carried out varying *m*, *Wm* and *Fnh* to detect the dependencies regarding the squat. As regards the results of the increase of squat due to the bank slope a reasonable formula (7) has been developed which takes into account all influences as shown in Figure 9.

$$KM = 1 + 1.2 \cdot m^2 \cdot Fnh^{11} / \left(\frac{Wm}{L}\right)^{2 \cdot Fnh}\,,1 < KM < 4 \qquad (7)$$

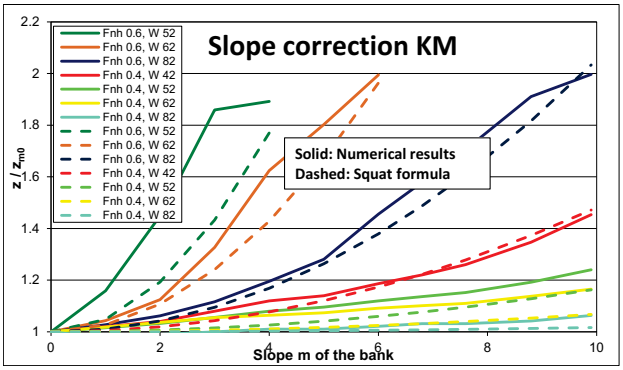

Figure 9. Slope factor *KM*

5.6 ECCENTRICITY OF THE SHIP

For this parameter no calculations have been carried out, however a procedure is proposed to handle this influence. A half circle over the width of the channel may be used to estimate a reduced channel width *W'* which increases the squat due to the eccentricity of the ship. The estimated approach is shown in Figure 11 and equation (8)

$$W' = W \cdot \sqrt{1 - \left(1 - 2 \cdot \frac{yPt}{yStb}\right)^2} \qquad (8)$$

To take this effect into account *W'* should be used in section 5.4 instead of *W*.

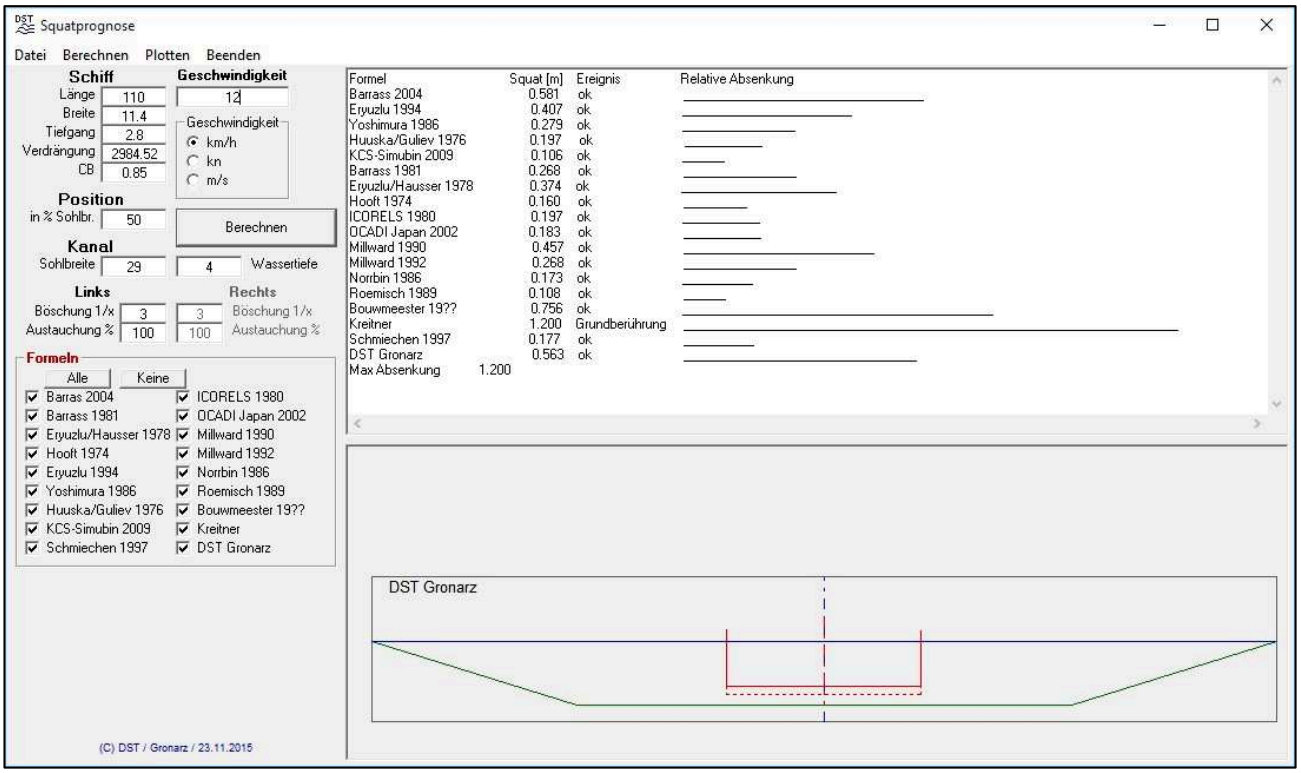

Figure 10. Squat prediction program

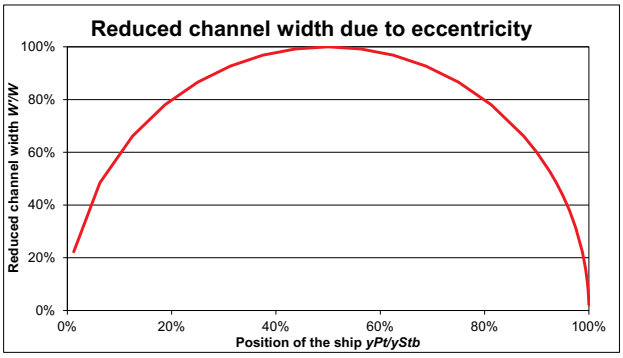

Figure 11. Reduction of W due to eccentricity

5.7 FINAL FORMULA

Based on the estimated squat z for the basic ship in default conditions the squat including all influences can be calculated by multiplying all correction factors to z as shown in equation (9).

$$z_{Final} = z \cdot KL \cdot KB \cdot KT \cdot KC \cdot KW \cdot KM \quad (9)$$

It is recommended to limit the squat to a value of e.g. *T/2* to avoid extrapolation errors and to indicate grounding if z increases *h-T*.

6 COMPARISON WITH OTHER FORMULAE

The evaluation of a squat formula can be either made by full scale results or by comparison with other existing formulae. The full scale comparison would be the best but the main problem is the availability of results for inland vessels considering a broad variety of influencing parameters.

As there are many formulae existing [3, 4] it is interesting to check both the new approach and the other published estimations regarding their behavior with varying input parameters. A software has been programmed which includes most of the recent published squat formulae and which is able to compute their results both for a single case and for a systematic variation of one parameter only. Figure 10 shows an example for a special scenario which is used as default case (boundary conditions see in the screenshot) for all following calculations. The selected speed of 12 km/h is higher than allowed for loaded vessels in German channels but gives a better impression of the capabilities of the different formulae than the lower one of 8 km/h.

The results of these systematic calculations are presented below. Comments to the results are placed above the figure. The results of the approach presented in this paper are always marked with a fat red line.

The variation of the **water depth *h*** in Figure 12 shows an increasing squat for all formulae. Barras 2004 predicts a significant squat for deep water but has a simply linear dependency with *h*. Kreitner and Bouwmeester calculate the most steep shallow water influence. All results are limited by the grounding condition.

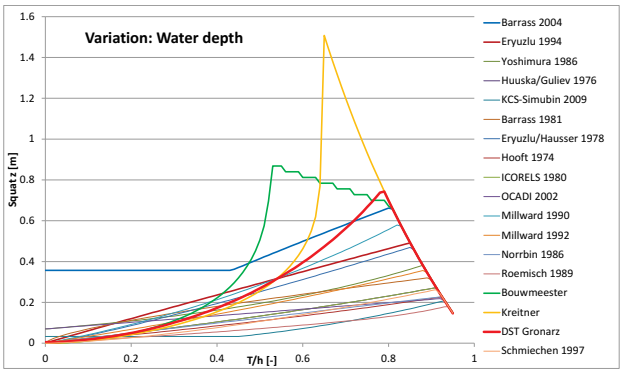

Figure 12. Variation: Water depth

The variation of the **speed *V*** in Figure 13 (here given in km/h as standard in inland navigation) is present in all examples, but with a different development. They are all limited by z=h-T, here 1.2 m, except of Bouwmeester, which has an internal limit below.

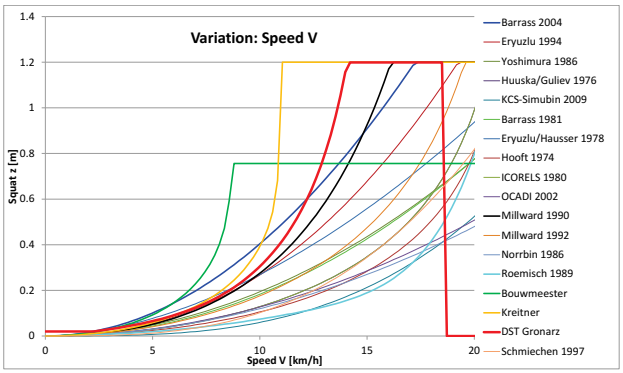

Figure 13. Variation: Speed

The variation of the **length *L*** in Figure 14 is not an input variable in several attempts. This should be linear at minimum as Millward 1990, but realistic is a nonlinear behavior as estimated by most formulae.

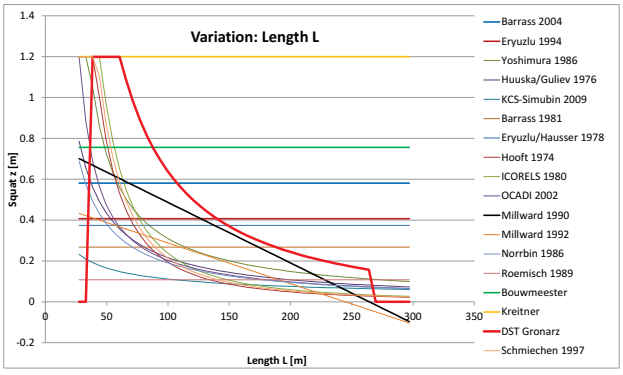

Figure 14. Variation: Length

The variation of the **breadth *B*** in Figure 15 is not an input variable in several attempts. This should be linear at minimum as Millward 1990, but realistic is a nonlinear behavior as estimated by most formulae. Barras 1981 fails completely because he estimates a decreasing squat with increasing beam.

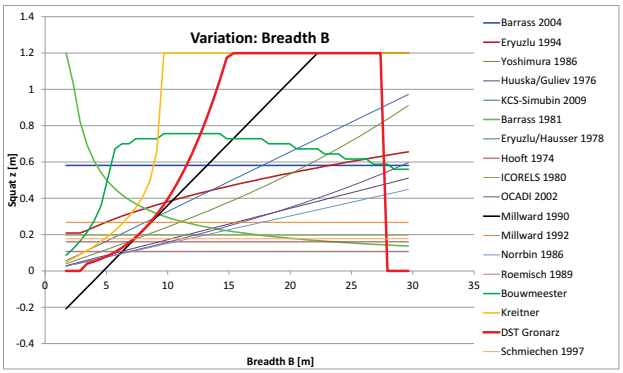

Figure 15. Variation: Breadth

The variation of the **draught *T*** in Figure 16 is obviously overestimated by Kreitner and disregarded by many other formulae. The rest of the graphs show a more or less linear dependency, all limited by the grounding condition.

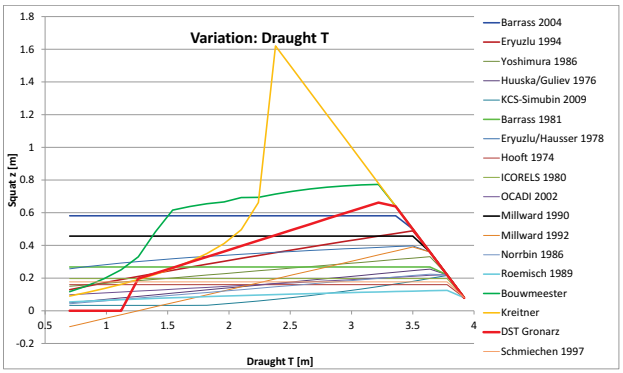

Figure 16. Variation: Draught

The variation of the **block coefficient *CB*** in Figure 17 is missing in some formulae or linear in the other ones. Kreitner is out of discussion because he predicts grounding at this speed, compare Figure 13. Only the new approach forecasts a nonlinear behavior which seems to be obvious.

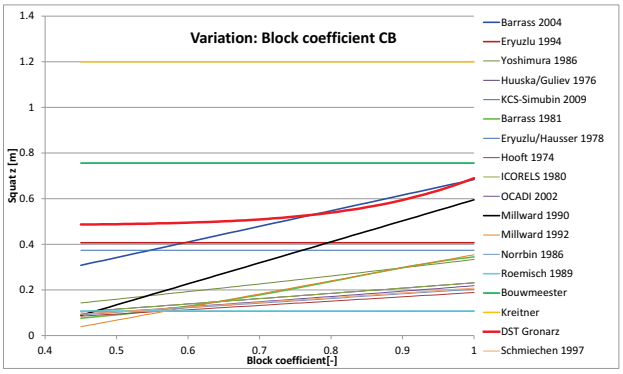

Figure 17. Variation: Block coefficient

The variation of the **channel width *Wm*** in Figure 18 is handled only by some authors. There are great differences about the magnitude of the squat and the behaviour with changing *W*. A reason for that may be that some formulae are designed only for unrestricted water.

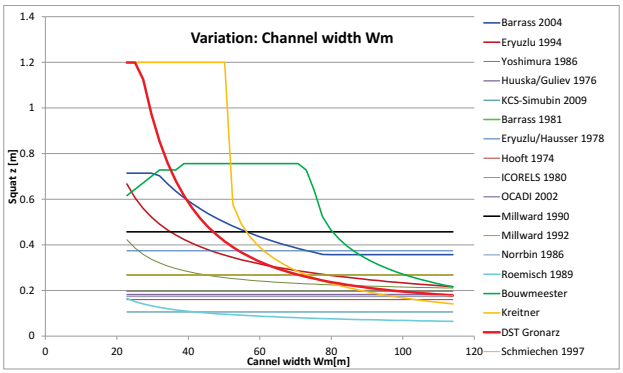

Figure 18. Variation: Channel width

The variation of the **bank slope *m*** in Figure 19 is disregarded by most formulae. There should be a decrease with steeper walls because the proximity of the bank to the bilge decreases. In this respect Bouwmeester fails and only Eryuzlu 1994 and DST Gronarz calculate a dependency however with different shape.

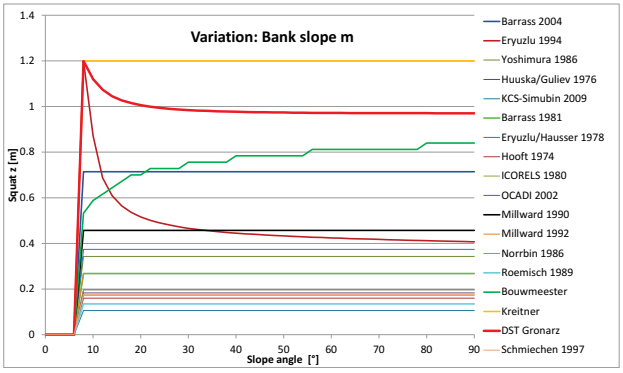

Figure 19. Variation: Bank slope

The variation of the **lateral position *y*** in Figure 20 is only calculated by the new approach presented in this paper. Even if the data are not based on calculations but on realistic assumptions the results seem to be acceptable because observations have shown that the proximity of a wall at one side increases the squat. Model tests or numerical calculations might substantiate this proposal.

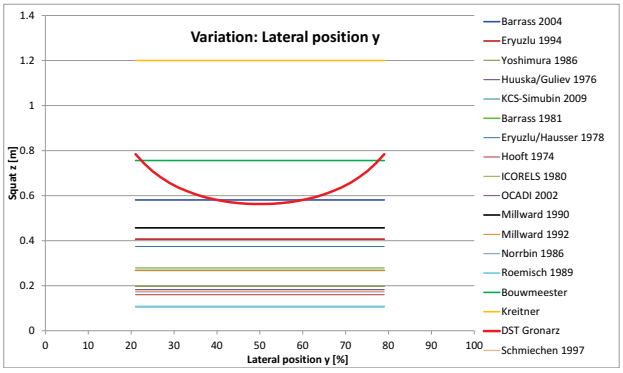

Figure 20. Variation: Lateral position

7 TRIM

Although the numerical results deliver also a trim of the ship, no estimation formula will be generated, because the calculations have been carried out for the resistance case. As most applications need the trim for the self-propelled ship, the trim based on the resistance is not only imprecise to use but sometimes completely wrong.
For seagoing ships on deep water it is known that with increasing block coefficient ($CB > 0.6 - 0.7$) the trim changes from stern down to bow down. On open water the difference between trim in resistance and propulsion is rather small.
Otherwise inland waterway vessels, which sail on restricted and shallow water, behave in a different way as it is known very well from model tests in the DST. Because of the normally large block coefficients they trim always bow down in resistance tests. In propulsion condition the stern mostly trims down due to the suction of the propeller at the bottom which creates a low pressure field at the stern.
To avoid misunderstandings and misinterpretations a trim estimation is omitted in this paper. In addition, the influence of the longitudinal centre of buoyancy is disregarded because it affects mainly the trim.

8 CONCLUSIONS

- A new formula (additional to the big number of formulae by different authors) has been developed based on systematic calculations with a software specially dedicated to the flow around ships in shallow and restricted waters.
- The new approach is based on the dependency on the Froude depth number *Fnh*, calculated for a default ship.
- Other dependencies like L, B, T, CB, W, slope and eccentricity are treated as correction factors for the basic formula.
- The new approach is compared with several existing ones and fits well into their results.
- The formula presented in this paper is the unique one which covers all important influences.
- This makes it recommendable as a module to be used in simulators.

Constraints:

- Only the sinkage *z* is considered – the trim is not investigated.
- The formula predicts the squat for the resistance case. In self-propulsion the result might be slightly higher due to the propeller suction at the bottom.
- The results for infinite water depth might not be correct because *Fnh* is zero in that case. It is recommended to limit the water depth to $5 \cdot T$ to overcome this problem.

9 REFERENCES

1. Henn, R. (2008). Entstehung und Ausbreitung von Schiffswellen in Binnen- und Küstengewässern. *Dissertation, University Duisburg-Essen (in German)*

2. Jiang, T. (2001). Ship Waves in Shallow Water, *Fortschrittsberichte VDI, Reihe 12, Nr. 466, VDI Verlag, Düsseldorf (in German)*

3. Briggs, M. (2006). Ship Squat Predictions for Ship/Tow Simulator. *US Army Corps of Engineers*

4. Eloot, K.; Vantorre, M. (Eds.) (2009). International Conference on Ship Manoeuvring in Shallow and Confined Water: Bank Effects, *R.I.N.A. Proceedings*

10 AUTHOR'S BIOGRAPHY

Andreas Gronarz holds the position of a research engineer at the DST. Since his employment 30 years ago he is working in the field of manoeuvrability of ships, especially in shallow and restricted waters. With the installation of the inland waterway simulator SANDRA he is responsible for the mathematic modeling and the operation of the simulator. The successful execution of several nautical studies on inland waterway increased his experience in the assessment of inland navigation.

4th MASHCON, Hamburg - Uliczka et al. (eds) - © 2016 Bundesanstalt für Wasserbau ISBN 978-3-939230-38-0 (Online)
DOI: 10.18451/978-3-939230-38-0_14

SQUAT IN BERTHED SHIP – PASSING SHIP INTERACTION FOR RESTRICTED WATER CASES

S P Denehy, AMC Search Ltd, Australia
J T Duffy, D Ranmuthugala and **M R Renilson**, Australian Maritime College, Australia

SUMMARY

This paper presents a study on berthed ship – passing ship interaction for two different channel widths using physical model scale physical experiments and Computational Fluid Dynamics (CFD). The interaction forces and moment and the sinkage of the berthed ship were measured for the two different channel widths. In order to determine the effect that the additional blockage caused by the berthed ship had on the squat of the passing ship, the squat was also measured under the same conditions as in the ship interaction scenarios, but without the presence of berthed ship. The two restricted water cases were replicated in model scale using 3D inviscid double body CFD simulations and validated against experimental results. The CFD models were run with the passing ship fixed in the static level trim condition as well as with the passing ship fixed at the running sinkage and trim condition measured from the physical model scale experiments to determine whether the latter would improve correlation with the experimental results.

NOMENCLATURE

AMC	Australian Maritime College
B	Beam (m)
BD_N	Near bank offset distance (m)
BD_F	Far bank offset distance (m)
Fr_h	Froude depth number $\left(Fr_h = U/\sqrt{gh}\right)$
g	Gravitational constant (9.81 m/s^2)
h	Water depth (m)
L_B	Berthed ship length between perpendiculars (m)
L_C	Characteristic length ($L_C = \frac{L_P+L_B}{2}$) (m)
LCG	Longitudinal centre of gravity
L_P	Passing ship length between perpendiculars (m)
MTB	Model Test Basin
N	Yaw moment (N)
N'	Non-dimensional yaw moment (-)
PD	Passing ship position $\left(\text{PD} = \frac{\text{x}}{\text{L}_\text{C}}\right)$
S	Lateral separation, centreline to centreline (m)
T	Draft (m)
U	Passing ship speed (m/s)
UKC	Under keel clearance
x	Longitudinal coordinate of passing ship's centre of gravity from berthed hip's centre of gravity (m)
X	Surge force (N)
X'	Non-dimensional surge force (-)
Y	Sway force (N)
Y'	Non-dimensional sway force (-)
ρ	Water density (kg/m3)
∇_B	Berthed ship displacement (m3)
∇_C	Characteristic ship displacement $\nabla_C = \frac{\nabla_P+\nabla_B}{2}$) (m3)
∇_P	Passing ship displacement (m3)
θ	Trim angle (degrees)

1 INTRODUCTION

Berthed ship motions induced by the interaction effects of a passing ship can cause excessive mooring forces and interrupt loading/unloading procedures. Extreme cases of berthed ship - passing ship interaction have resulted in damage to vessels and mooring infrastructure, injury and even death to personnel. To ensure safe and efficient port operation, it is essential to understand the interaction between berthed and passing ships.

In order to accurately predict the berthed ship motions and mooring loads due to the passing ship, the interaction forces and moments must first be accurately predicted. There are a number of empirical methods [1, 2] that can be used to predict the berthed ship - passing ship interaction forces and moments. These methods are mostly based on results from laterally unrestricted cases, where the effect of the banks is negligible. Past work, including some conducted by the current authors [3-6], has shown that the increase in blockage due to banks has a significant effect on the magnitude and form of the interaction forces and moments and should be accounted for when predicting the interaction effects.

This study presents results from physical scale model experiments of berthed ship - passing ship interaction of bulk carriers conducted at the Australian Maritime College's (AMC) Model Test Basin (MTB) facility. The interaction forces and moments imparted on the berthed ship were measured for two restricted water bathymetries. The model tests were conducted with a berthed bulk carrier being passed by an identical bulk carrier on a parallel heading. Two near bank arrangements were tested; a wide channel, where the bank effects are negligible [7], as well as for the case where a bank was placed close to the berthed ship, resulting in significant bank effects. The tests were conducted at four passing ship speeds from Fr_h 0.15 to 0.25. In addition to the surge force, sway force and yaw moment, the sinkage at the LCG and the trim angle experienced by the berthed ship

during the interaction scenario were also measured. The sinkage at the LCG and the running trim angle of the passing ship were measured during the interaction scenarios as well as under the same conditions but without the berthed ship in order to quantify the effects of the additional blockage from the berthed ship on the squat of the passing ship.

Results from the physical scale model experiments were used to quantify the interaction forces and moments and sinkage and trim angle and also used to validate CFD simulations using an inviscid double body model. Past authors [8-10] have shown that this method can accurately predict the interaction forces and moments for certain cases. The bathymetry for the two cases tested in the physical scale model experiments was replicated in the CFD models. The CFD models were run with the passing ship fixed in the static trim condition as well as with the passing ship fixed with the running sinkage and trim angle measured in the physical scale model experiments to determine whether this would improve the correlation between the CFD predictions and the experimental results.

The work presented in this paper is part of a larger study to develop a technique to rapidly predict the interaction forces and moments on a berthed ship due to a passing ship in restricted waterways. The aim of this study is to use a validated CFD model to predict the interaction forces and moments for a wide range of cases to form a matrix of data to develop the new simplified technique.

2 PHYSICAL SCALE MODEL EXPERIMENTS

A series of physical scale model experiments were conducted at the AMC's MTB facility to measure the interaction forces and moments experienced by a berthed ship due to a passing ship for two bathymetry arrangements. The sinkage at the LCG and the running trim angle (squat) experienced by the passing ship and the sinkage at the LCG and the trim angle of the berthed ship were measured in the region in which interaction effects can be felt by the berthed ship (two ship lengths forward and aft of the berthed ship [11]). The passing ship squat measurements from the interaction scenarios were then compared to squat measurements, in the same bathymetry arrangement, with the berthed ship removed to quantify the effect the additional blockage of the berthed ship has on the squat of the passing ship.

The test program used in the physical scale model experiments is given in Table 1. The bathymetry arrangement and sign convention used in the experiments and CFD simulations are shown in Figure 1. The forces and moments were measured about the berthed ship's longitudinal centre of gravity (LCG). The LCG was located $0.475L_B$ aft of the forward perpendicular.

The tests were conducted at low passing ship speeds typical of real life scenarios. For such cases the free surface effects can be considered negligible [11]. The water depth to draft ratio was 1.20 for all conditions.

The passing ship's path was parallel to the berthed ship's centreline, with a $2.50B$ lateral separation between the berthed and passing ship's centrelines (S). The vertical surface piercing banks were positioned parallel to the passing and berthed ship's centerlines. The near bank (portside of berthed ship) and far bank (starboard side of the passing ship) for Conditions 1 and 3 were equally spaced $8.25B$ from the passing ship's path (see Figure 1). For Conditions 2 and 4, the near bank was $3.04B$ to the portside and the far bank was $8.25B$ to the starboard side from the passing ship's path.

Table 1. Test program for physical scale model experiments test program

Condition	Passing ship speed	Lateral separation	Near bank offset	Far bank offset
	Fr_h	S	BD_N	BD_F
1	0.17 – 0.23	$2.50B$	$8.25B$	$8.25B$
2	0.17 – 0.23	$2.50B$	$3.04B$	$8.25B$
3	0.17 – 0.23	-*	$8.25B$	$8.25B$
4	0.15 – 0.23	-*	$3.04B$	$8.25B$

Note * - No berthed ship

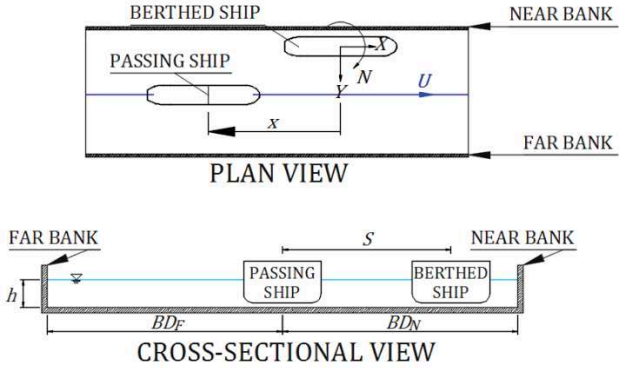

Figure 1. Schematic view of bathymetry arrangement and sign convention

The physical scale model experiments were conducted using 4m MarAd F series bulk carriers [12]. This would represent a 1:71 scale to represent a 300m cape class vessel. The passing ship was fitted with a turbulence stimulation wire fitted at 5% L_P [13]. The berthed and passing ship models were ballasted to a static even keel draft of 0.22m. The pitch radius of gyration for the berthed and passing ship models were $0.24L_B$ and $0.24L_P$ respectively. A body plan view of the ship models used in the experiments and CFD simulations are shown in Figure 2. To reduce modelling and meshing requirements, a bulk carrier hull form with a simplified skeg arrangement was used in the CFD predictions (shown in red in Figure 2). Huang and Chen [14] has shown that the form and magnitude of the interaction forces and moments are not greatly influenced by the hull form, how-

ever, the effect that the simplified hull geometry has on the interaction forces and moments has not be quantified in this study.

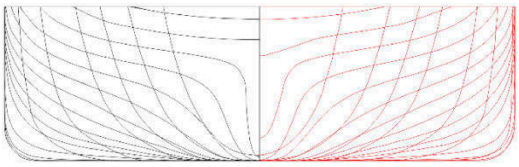

Figure 2. Left (black): body plan of MarAd F Series [12] used in the physical scale model experiments. Right (red): hull form used in the inviscid double body numeric simulation.

2.1 TEST PROCEDURE

The passing ship was accelerated from rest to a predetermined constant speed before reaching the region that affects the berthed ship (two ship lengths fore and aft of the berthed ship's LCG) [11]. The passing ship speed was kept constant until the effects on the berthed ship were negligible. For the passing ship the following were measured passing ship speed, sinkage at the LCG and running trim angle. For the berthed ship the following were measured: interaction surge force, sway force, yaw moment, sinkage at the LCG and trim angle. All measurements were sampled at 200Hz. An uncertainty analysis was conducted for each instrument used within the experiments, employing a similar method to that presented by Duffy [15].

2.2 EXPERIMENTAL RESULTS AND DISCUSSION

The results from the experiments were filtered using a 4th order low pass Butterworth filter with a 0.12Hz cut off frequency. The interaction forces and moments were non-dimensionalised by the formulae:

$$X' = \frac{X}{\rho g \nabla_C {Fr_h}^2} \quad (1)$$

$$Y' = \frac{Y}{\rho g \nabla_C {Fr_h}^2} \quad (2)$$

$$N' = \frac{N}{\rho g \nabla_C L_C {Fr_h}^2} \quad (3)$$

The time domain results are presented against the non-dimensional passing ship position (PD) where,

$$PD = \frac{x}{L_C} \quad (4)$$

and x is the coordinate of the passing ship's LCG relative to the berthed ship's LCG. Hence, when the passing ship is adjacent the berthed ship at $x = 0$ and $PD = 0$.

The peak to peak interaction surge force, sway force and yaw moment experienced by the berthed ship due to the passing ship are shown in Figure 3. Due to the size of the data point markers required, the uncertainty bars presented are somewhat obscured. The increase in the surge force, and the reduction in the sway force and yaw moment due to the smaller near bank offset is consistent with past findings [3-6].

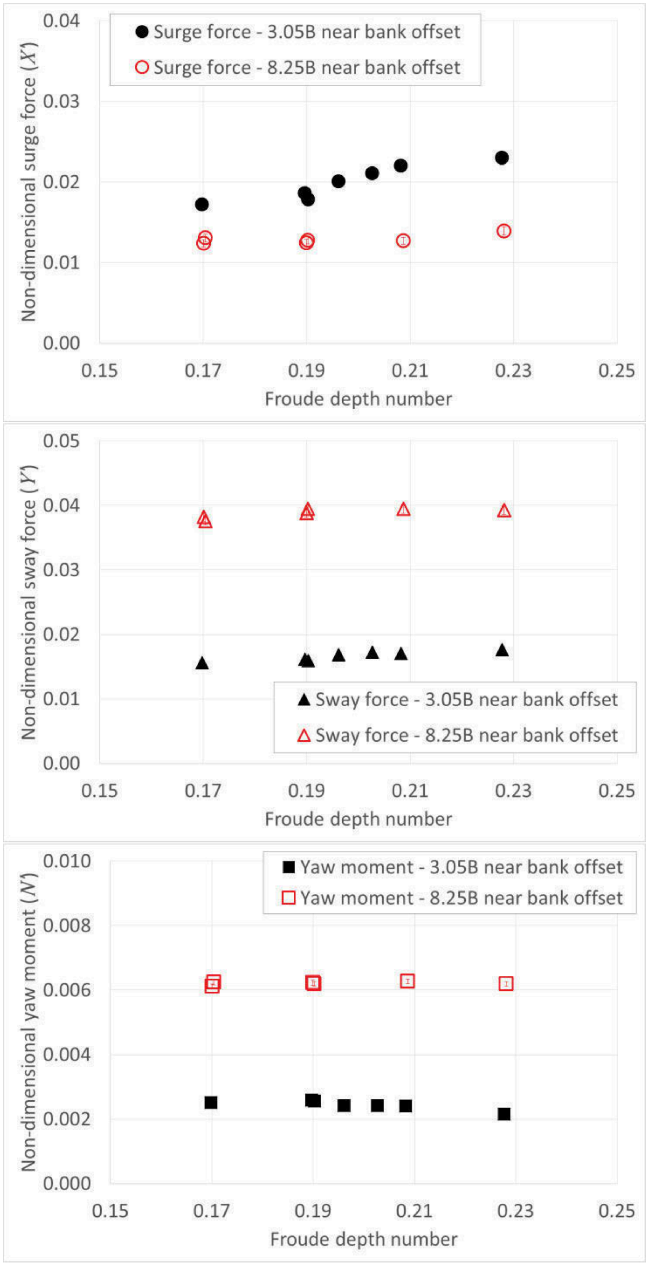

Figure 3. Peak to peak surge force (top), sway force (middle) and yaw moment (bottom) for Conditions 1 and 2 showing the effect of near bank offset distance.

Figure 4 shows the sinkage and trim angle experienced by the berthed ship due to the passing manoeuvre as a function of the passing ship position at the passing ship speed of $Fr_h = 0.23$. The uncertainty in the sinkage at LCG and trim angle measurement is shown in grey and light red/pink in Figure 4.

The maximum berthed ship sinkage at the LCG occurred when the berthed and passing ships were approximately adjacent. The maximum berthed ship trim angle occurred when the passing ship was half a ship length aft and forward of the berthed ship ($-0.5PD$ and $+0.5PD$).

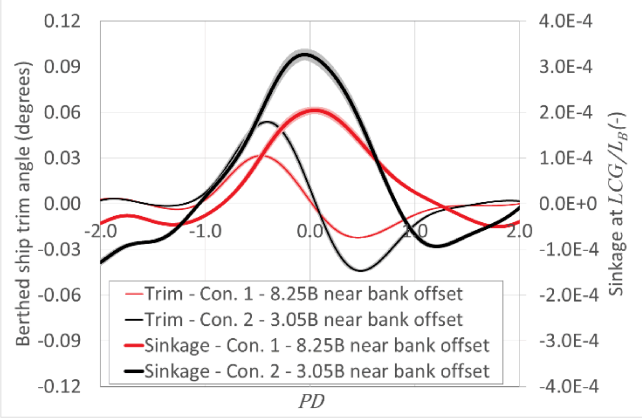

Figure 4. Berthed ship sinkage at LCG and trim angle measured in Conditions 1 and 2 as a function of passing ship position (*PD*).

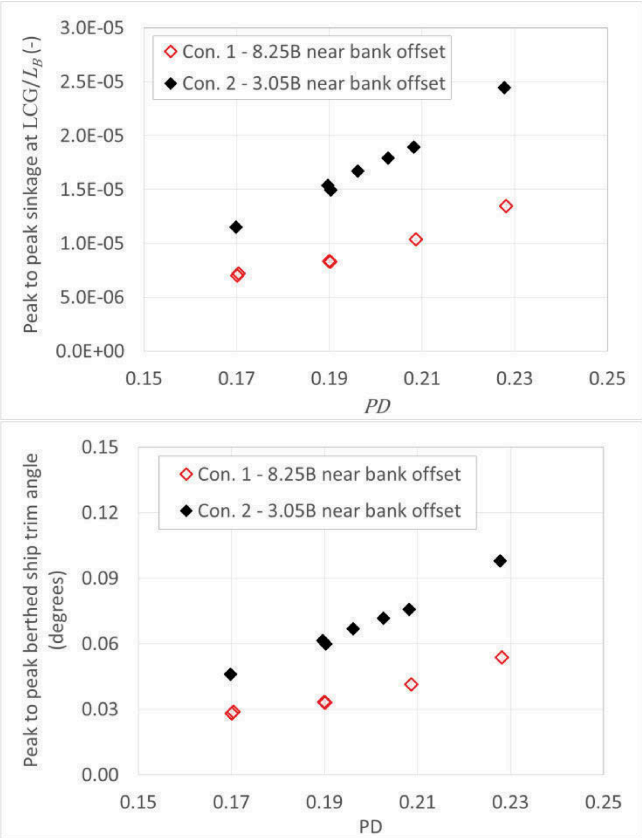

Figure 5. Peak to peak berthed ship sinkage at LCG (top) and trim angle (bottom) easured in Conditions 1 and 2 as a function of passing ship speed.

The peak to peak berthed ship sinkage at the LCG and the trim angle for Conditions 1 and 2 are shown in Figure 5. The measured sinkage at the LCG and the trim angle for the berthed ship increased as passing ship speed increased. The reduction of the near bank offset distance increased both the sinkage at the LCG and the trim angle of the berthed ship. It should be noted, however, that the sinkage at the LCG and the trim angle experienced by the berthed ship due to the passing ship was small. The maximum heave experienced by the berthed ship was 0.6% of the berthed ship's draft and the maximum peak to peak trim angle of the berthed ship was only 0.098 degrees.

No unsteady effects were observed in the passing ship sinkage at the LCG and the running trim angle due to the presence of the berthed ship in either bathymetry arrangement. It should be noted that the experimental results presented here are for the water depth to draft ratio of 1.20. The additional blockage due to the berthed ship would have been greater in shallower cases and should be investigated further in order to determine if it has any dynamic effects on the passing ship.

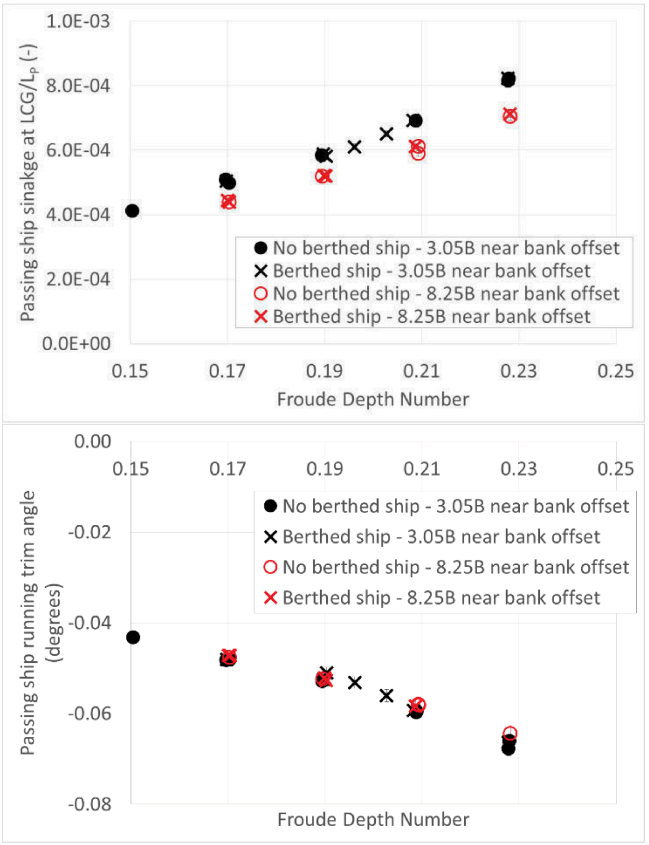

Figure 6. Passing ship average sinkage at the LCG (top) and trim angle (bottom) measured in Conditions 1 - 4 as a function of passing ship speed.

Figure 6 shows the average heave and running trim angle of the passing ship for Conditions 1 – 4 as a function of the passing ship speed. Again, due to the data point size, the uncertainty bars are hard to see in Figure 5. The additional blockage of the berthed ship did not increase the passing ship's sinkage at the LCG or the trim angle in either bathymetry case. The reduction of the near bank offset increased the heave of the passing ship but had

little effect on the measured trim angle. It should be noted that the measured trim angle of the passing ship was very low, below 0.1 of a degree.

3 CFD SIMULATIONS

The interaction forces and moments on the berthed ship were predicted for four cases using an inviscid double body CFD simulation model developed within the software Star CCM+© [16]. The CFD predictions were conducted at model scale. Remery [11] observed that at the low passing ship speeds (commonly seen in berthed ship – passing ship interaction), due to the lack of Kelvin type wave pattern the free surface and viscous effects could be ignored, while still accurately predicting the interaction forces and moments imparted on the berthed ship. This method has been successfully implemented by others [8-10] with good correlation achieved against compatible experimental data.

The CFD predictions in this study were conducted using a six degree of freedom implicit unsteady solver. The berthed and passing ship models were constrained in six degrees of freedom. To achieve the double body method the dimensions of the physical scale model experiments were replicated in the CFD model and mirrored about the free surface. The domain was discretized using a hexahedral mesh. An overset mesh was used to model the passing ship. The longitudinal ends of the domain boundaries were modelled as a velocity inlet and a pressure outlet. In order to verify the CFD model, a time step and mesh convergence study was conducted. The mesh used in the CFD model had a base size of 0.08m. The mesh in Case 1 & 3 ($8.25B$ near bank) and Case 2 & 4 ($3.04B$ near bank) consisted of approximately 2.3 and 2.1 million cells, respectively. The time step used in the CFD model was 0.125 seconds. Details of the CFD model can be found in Denehy et al. [17, 18].

The test program for the CFD simulations is shown in Table 2. Cases 1 and 2 were conducted with the passing ship fixed in the static draft condition (i.e. at an even keel draft of 0.220m) for the bathymetry in Conditions 1 and 2 [17, 18]. Cases 3 and 4 were conducted with the passing ship fixed in the running sinkage and trim position measured in the physical scale model experiments. The CFD predictions were conducted at the passing ship speed of $Fr_h = 0.23$.

As with the experiments, the water depth to draft ratio for all CFD cases was 1.20.

Table 2. Test program for CFD simulations

Case	Near bank offset	Far bank offset	Passing ship		
			Speed	Draft at LCG	Trim angle
	BD_N (-)	BD_F (-)	Fr_h (-)	T (mm)	θ (deg)
1	$8.25B$	$8.25B$	0.23	$0.303B$	0.00
2	$3.05B$	$8.25B$	0.23	$0.303B$	0.00
3	$8.25B$	$8.25B$	0.23	$0.306B$	-0.06
4	$3.05B$	$8.25B$	0.23	$0.307B$	-0.06

3.1 CFD RESULTS AND DISCUSSION

The interaction forces and moments were filtered using a 4th order 0.12Hz cut off frequency Butterworth filter. The interaction surge force, sway force and yaw moment were non-dimensionalised using equations (1), (2) and (3), respectively, while the passing ship position was non-dimensionalised using equation (4). The non-dimensional interaction forces and moments from the CFD predictions from Cases 1 – 4 are compared to the measured non-dimensional interaction forces and moments from the experimental Conditions 1 and 2 in Figure 7 for the passing ship speed of $Fr_h = 0.23$. The uncertainty in the interaction force and moment measurements is shown in grey and light red/pink in Figure 7.

The percentage difference between the peak positive and peak negative interaction forces and moments between the experiments and CFD predictions can be seen in Table 3.

Surge force prediction

For the near bank offset of $8.25B$, the peak negative surge force, occurring around $-0.5PD$, was predicted fairly accurately in both Case 1 & 3 by the CFD models (within 8%). The positive peak surge force, occurring around $0.5PD$, was over predicted by the CFD models (Case 1 & 3). For the $3.04B$ near bank offset, Cases 2 & 4, the peak surge force values were over predicted by the CFD models. The over prediction was greater for the case with the passing ship fixed in the running sinkage and trim angle condition.

From the non-dimensional surge force (X') in Figure 7a, it can be seen that the experimental surge force was increased by approximately 65% by the reduction in the near bank offset. The increase in the predicted surge force from the CFD was 82% and 80% for the fixed static draft level trim condition (Case 1 & 2) and the fixed running sinkage and trim angle (Case 3 & 4), respectively.

Sway force prediction

For the $8.25B$ near bank offset, the even keel CFD model predicted the experimental sway force very well, agreeing within 6% of the experimental measurement. The peak positive sway force, occurring around $0.0PD$, was

over predicted by the CFD model with the passing ship fixed in the running sinkage and trim angle by 24.6%. The level keel CFD model tested correlated very well with the sway force in the 3.04*B* case, within 5% of the experiments.

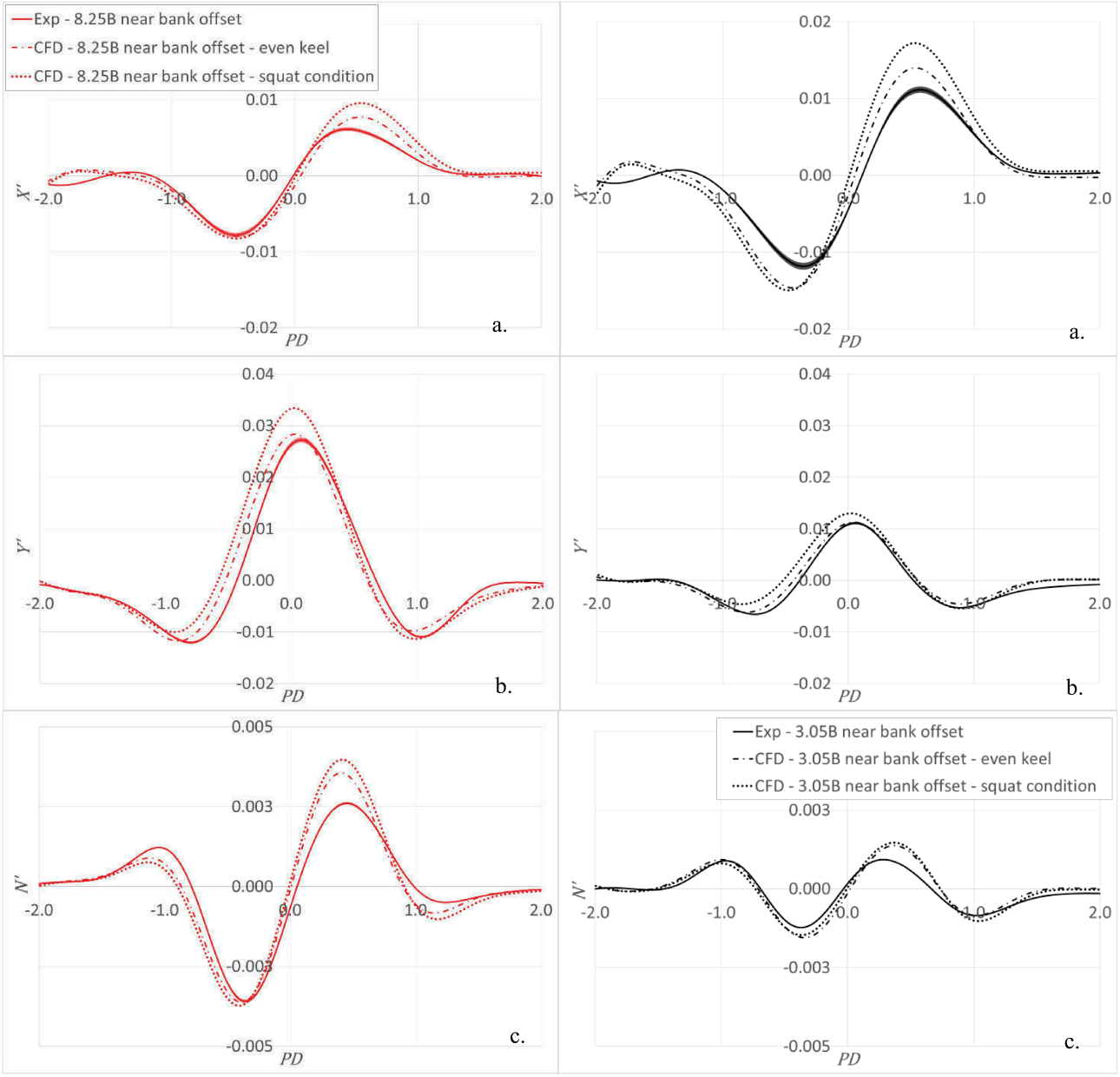

Figure 7. Comparison of the non-dimensional interaction surge force (X'), sway force (Y') and yaw moment (N') from physical scale model experiments and the inviscid double body CFD simulations.

Table 3. Percentage difference of the peak positive and peak negative interaction forces and moments of CFD prediction from the experimental results (+percentage indicates an over estimation, - percentage indicates under estimation)

		X'		Y'		N'	
		Peak - %	Peak + %	Peak - %	Peak + %	Peak - %	Peak + %
Case 1	8.25*B* - Level static draft	4.3	27.7	-0.8	5.9	2.4	38.6
Case 2	3.04*B* - Level static draft	26.0	27.9	-4.7	3.4	28.4	51.5
Case 3	8.25*B* - Using measured sinkage and trim angle	7.7	58.6	-4.1	24.6	5.6	55.1
Case 4	3.04*B* - Using measured sinkage and trim angle	28.9	57.5	-15.7	19.7	21.6	61.0

From Figure 7b the reduction in the near bank offset reduced the sway force (Y') by 55% in the experimental measurements and 57% and 58% for the CFD predictions with the passing ship fixed with static level trim and fixed in the running sinkage and trim angle configuration respectively for the passing ship at a speed of $Fr_h = 0.23$.

Yaw moment prediction

For the $8.25B$ near bank offset case, the initial peak positive yaw moment was under predicted by CFD model in Case 1 & 3. The CFD predicted peak negative yaw moment, occurring around -$0.4PD$, correlated well with the experimental results, within 6%. The peak positive yaw moment, occurring around $0.4PD$, and the second peak negative yaw moment, occurring around $1.2PD$, was over predicted by the CFD model. For the $3.04B$ near bank offset case the CFD model correlated poorly with the experimental results using both the fixed and measured sinkage and trim cases as seen in Figure 7.

The yaw moment (N') was reduced by 65% in the experimental case by the reduction in the near bank offset for the passing ship speed of $Fr_h = 0.23$, as seen in Figure 7c. The CFD models predicted a reduction of 59% and 62% due to the reduction in near bank offset for the passing ship fixed in the level static trim case and fixed at the running sinkage and trim angle case, respectively.

In general, the predictions from the CFD model with the passing ship fixed in the even keel condition correlated very well with the experimental sway force. More work is required to better model the surge force and yaw moment. Modelling the passing ship fixed at the running sinkage and trim angle based on the experiment results in general reduced the agreement with the experimental results. Hence, further investigation into the CFD prediction technique is required to determine why this is the case.

4 CONCLUDING REMARKS

A series of physical scale model experiments were conducted at AMC'S MTB facility to measure the interaction forces, moments, sinkage and trim on a berthed ship and the sinkage and trim on a passing ship for two different channel widths at a water depth to draft ratio of 1.20.

The reduction in the near bank offset significantly increased the surge force and reduced the sway force and yaw moment. The passing ship was shown to cause a very small change in sinkage and trim on the berthed ship. The berthed ship sinkage at the LCG and trim angle was increased as passing ship speed increased. The additional blockage caused by the presence of the berthed ship did not affect the squat of the passing ship for the cases tested.
Simulations using the CFD model generally agreed reasonably well with the experimentally measured sway forces, however the agreement with the experimentally measured surge force and the yaw moment was poor.
Modelling the passing ship fixed at the sinkage and running trim based on the experimental results reduced the agreement with the experimentally measured forces and moment.

5 REFERENCES

1. Flory, J. (2002). The Effect of Passing Ships on Moored Ships. *Prevention First 2002 Symposium*, California State Lands Commission.

2. Kriebel, D.; Seelig, W.; Eskijian, M. (2005). Mooring loads due to parallel passing ships. *Naval Facilities Engineering Service Center*, Port Hueneme, California, USA,

3. Denehy, S.P.; Duffy, J.T.; Ranmuthugala, D.; Renilson, M.R. (2014). Influence of restricted water on the time domain interaction forces and moment on a berthed ship due to a passing ship. *Australian Journal of Civil Engineering, ,* Vol 12, No. 1, pp. 53 – 66.

4. Duffy, J.T.; Webb, G. (2003). Berthed Ship - Passing Ship Interaction: A Case Study for the Port of Newcastle. *Coasts & Ports Australasian Conference 2003*, Auckland, New Zealand.

5. Flory, J.; Fenical, S. (2010). Quay Wall Influence on Passing-Ship Induced Mooring Loads. *Ports: 2010: Buiding on the Past*, *Respecting the Future*, ASCE.

6. van der Molen, W.; Moes, J.; Swiegers, P.B.; Vantorre, M. (2011). Calculations of Forces on Moored Ships due to Passing Ships. *2nd International Conference on Ship Manoeuvring in Shallow and Confined Water: Ship to Ship Interaction*, Trondheim, Norway

7. Lataire, E.; Vantorre, M.; Vandenbroucke, J.; Eloot, K. (2011). Ship to Ship Interaction Forces During Lightering Operations. *2nd International Conference on Ship Manoeuvring in Shallow and Confined Water: Ship to Ship Interaction*, Trondheim, Norway.

8. Pinkster, J.A.; Pinkster, H.J.M.; (2014). A fast, user friendly, 3-D potential flow program for the prediction of passing vessel forces. *2014 PIANC World Congress*, San Francisco, USA.

9. Bunnik, T.; Toxopeus, S. (2011). Viscous Flow Effects of Passing Ships in Ports. *Proceedings of the ASME 2011 30th International Conference on Ocean, Offshore and Artic Engineering*, Rotterdam, The Netherlands.

10. van der Hout, A.J.; de Jong, M.P.C. (2014). Passing Ship Effects in Complex Geometries and Currents. *PIANC World Congress*, San Francisco, USA.

11. Remery, G.F.M. (1974). Mooring Forces Induced by Passing Ships. *Proceedings of the 6th annual Offshore Technology Conference*, Dallas, Texas, USA.

12. Roseman, D.P. (ed.) (1987). The MarAd systematic series of full form ship models. *Society of Naval Architects and Marine Engineers Publications*.

13. International Towing Tank Conference (ITTC), (2002). *Recommended Procedures and Guidelines: Model Manufacture Ship Models, 7.5-01-01-01*.

14. Huang, E.T.; Chen, H.C. (2006). Passing Ship Effects on Moored Vessels at Piers. *Proceedings Prevention First 2006 Symposium*, Long Beach, California, USA.

15. Duffy, J.T. (2008). *Modelling of Ship-Bank Interaction and Ship Squat for Ship-Handling Simulator*. Thesis for Doctorate of Philosophy, University of Tasmania, Launceston, Australia.

16. Star CCM+ User Manual, www.cd-adapco.com/products/star-ccm%C2%AE, first accessed 01/01/2014.

17. Denehy, S.P.; Duffy, J.T.; Renilson, M.R.; Ranmuthugala, D. (2015). Channel width effects on berthed ship - passing ship interaction from experiments and CFD predictions. *2015 MARSIM Conference*, Newcastle, UK.

18. Denehy, S.P.; Duffy, J.T.; Renilson, M.R.; Ranmuthugala, D.; (2015). Restricted water effects on berthed ship – passing ship interaction. *2015 Coast and Ports Conference*, Auckland, New Zealand.

6 AUTHORS' BIOGRAPHIES

Shaun Denehy is a Research Engineer employed within the AMC Search Ltd. He mainly works within the AMC's Towing Tank and Model Test Basin Facilities conducting research and commercial consultancy projects. He is also a part-time PhD candidate. His research focuses on berthed ship – passing ship interaction in restricted water. He has several publications in this area which can be found at "https://rmdb.research.utas.edu.au/public/rmdb/q/indiv_detail_warp_trans/24666#research-tab-5".

Jonathan Duffy holds the current position of Deputy Director (Research) (National Centre for Maritime Engineering and Hydrodynamics)/Research Engineer/Senior Lecturer at the Australian Maritime College, a specialist institute of the University of Tasmania. He is responsible for coordinating research for the National Centre for Maritime Engineering and Hydrodynamics and lecturing Naval Architecture subjects. His previous experience includes work in the field of ship hydrodynamics; including prediction of ship behaviour in shallow and restricted water and prediction of berthed ship motions and mooring loads due to passing ships, waves, wind and current.

Martin Renilson holds the current position of adjunct Professor at the Australian Maritime College. He established the Ship Hydrodynamics Centre at the Australian Maritime College in the mid-1980s, was director of the Australian Maritime Engineering Cooperative Research Centre, and then Head of Department of Naval Architecture and Ocean Engineering. He then spent six years as Technical Manager for Hydrodynamics at DERA/QinetiQ in the UK. He has a significant research interest in ship maneuvering, particularly in restricted waters.

Dev Ranmuthugala holds the current position of Director, Ports and Shipping at the Australian Maritime College. He has also served as Head of Maritime Engineering and Vessel Operations over the past 20 years. Prior to joining AMC, he worked as a marine engineer and in the design and sales of piping systems. His research includes: experimental and computational fluid dynamics to investigate the hydrodynamic characteristics of underwater vehicles, behaviour of submarines operating near the free surface, stability of surfaced submarines, towed underwater vehicle systems, and maritime engineering education.

4th MASHCON, Hamburg - Uliczka et al. (eds) - © 2016 Bundesanstalt für Wasserbau ISBN 978-3-939230-38-0 (Online)
DOI: 10.18451/978-3-939230-38-0_15

IMPACT OF BANKS ON SHIP SQUAT

E Lataire, Ghent University, Belgium
G Delefortrie, Flanders Hydraulics Research, Belgium
M Vantorre, Ghent University, Belgium

SUMMARY

In a restricted channel the hydrodynamic behaviour of a sailing vessel is affected by both the vertical and horizontal boundaries. The restricted space underneath and alongside a vessel has a noticeable influence on both the running sinkage and trim of a vessel, also known as squat. A different bank geometry will obviously change the available space around the vessel. To assess these influences an extensive model test program has been carried out in the *Towing Tank for Manoeuvres in Shallow Water* (cooperation *Flanders Hydraulics Research – Ghent University*) in Antwerp, Belgium. The tests were performed with 11 different ship models (both seagoing as inland vessels) along 25 different bank geometries and cross section areas. Systematic model tests were carried out along vertical quay walls, constant sloped banks (from full depth to free surface) and banks with a submerged sloped part and a horizontal submerged area (semi submerged banks). Also rectangular cross sections with a range of widths and water depths were tested in the towing tank. During the model tests the models were free to heave and trim and the running sinkage was measured at four discrete positions of the ship model (fore-aft / starboard-port side). In this article the executed model tests are described and the impact of different bank geometries on the squat of the vessel is discussed. The change in squat for different slopes of the bank as well as the bank type (quay wall/surface piercing) and cross section areas is shown.

NOMENCLATURE

A_M	Midship section area (m²)
B	Breadth of ship (m)
C_B	Block coefficient (-)
C_M	Midship coefficient $A_M/(BT)$ (-)
Fr_h	Froude number based on water depth h (-)
h	Water depth (m)
L_{PP}	Length between perpendiculars (m)
L_{OA}	Length over all (m)
m	Blockage ratio (-)
Re	Reynolds number (-)
T	Draft (m)
V	Velocity (m/s)
V_{ship}	Ship's velocity (m/s)
δV	Return flow (m/s)
W	Width of the cross section (m)
W_h	Width of the section at full water depth (m)
x	Longitudinal position from FPP (m)
y	Lateral position from the centre line (m)
y_{infl}	Influence width (m)
y_{small}	Closest distance between ship and bank (m)
z_{VA}	Running sinkage at the aft perpendicular (mm)
z_{VF}	Running sinkage at the fore perpendicular (mm)
z_{VM}	Running sinkage at the midship (mm)
δ	Thickness of the boundary layer (m)
λ	Scale factor (-)
θ_V	Running trim (m/m)
ξ	Coefficient of the mathematical model (-)
ν	Kinematic viscosity (m²/s)
Ω	Canal cross section area (m²)
APP	Aft perpendicular
FPP	Fore perpendicular
FHR	Flanders Hydraulics Research
LNG	Liquefied Natural Gas
RoRo	Roll on/Roll off
UKC	Under Keel Clearance

Subscripts:

m	at model scale
M	at midship
s	at full scale

1 INTRODUCTION

The dynamic under keel clearance of a sailing ship is affected by the changed pressure distribution around the ship's hull. As a consequence the ship will move vertically downwards and will mostly trim as well due to the asymmetry between the fore and aft part of the ship. This phenomenon is commonly referred to as squat. The magnitude of this squat is affected by different parameters, among which the ship's speed, the propulsion of the ship and the available water depth. These effects have already been the subject of numerous literature e.g. [1].

Figure 1. Ship and water at rest (1.1), return flow induced free surface water level depression (1.2), the sailing ship displacing the same volume of water as in 1.1 but having less under keel clearance (1.3).

In open and unrestricted conditions, the water displaced by a sailing vessel can travel almost without restriction underneath and along the ship's hull. In more shallow sailing conditions this water will rather be deviated around the hull, due to the limited space available between the ship's keel and the bottom of the waterway. This will result in higher velocities of the return flow travelling along the hull. This return flow will generate a pressure drop around the ship (Bernoulli's principle) and because of that, the free surface of the water will go down compared to the situation at rest. As such, the running sinkage or squat of a vessel should not be interpreted as an increase in the draft of the vessel but rather as a local decrease of the water depth around the ship.

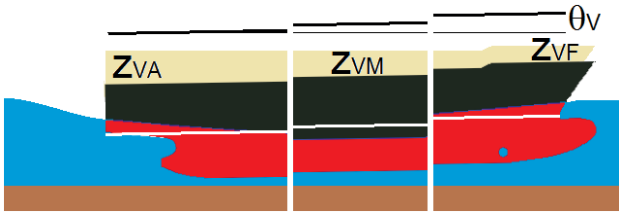

Figure 2. Two pairs of parameters to express the running sinkage: sinkages at the fore and at the aft perpendiculars (z_{VF} ; z_{VA}), or trim (θ_V) and mean sinkage z_{VM}.

In fact not only the water depth, but the entire cross section of the navigation channel affects the pressure distribution and the resulting squat. In general a more confined area will lead to larger squat for a given speed. In this article the attention will be put on the horizontal boundaries of a canal or fairway on the ship's squat. The effect of the bank geometry on the squat will be discussed based on an analysis of the database of captive model tests that have been carried out in the Towing Tank for Manoeuvres in Shallow Water at Flanders Hydraulics Research (FHR).

Banks with varying geometries are frequently built into this towing tank to investigate ship-bank interactions. The test results used for the present paper are acquired in the frame of different projects. As such a database is acquired with model tests with as much as 11 different ship models and about 25 different bank geometries. The database consists of more than 14 000 different test conditions (ship, draft, water depth, bank geometry, relative position, drift angle, speed, propeller action). A limited selection of these model tests has been made public as benchmark data in [2].

The running sinkage can be expressed as either the combination of the mean sinkage and the trim or as the sinkage at the fore and aft perpendiculars. The latter will be used in this article with a positive sign convention in case of a downwards motion.

2 MODEL TESTS

2.1 TOWING TANK

The model tests under consideration are a selection of the model tests performed over the last 10 years in the fully automated towing tank at FHR. A technical overview of this facility can be found in [3]; its main dimensions are listed in Table 1.

Table 1. Main dimensions of the towing tank at FHR

Total length	87.5 m
Useful length	68.0 m
Width	7.0 m
Maximum water depth	0.50 m

2.2 SHIP MODELS

Tests have been carried out with eleven different ship models of about 4m long (2 container carriers, 4 tankers, 3 RoRo-vessels, 1 inland vessel, 1 Wigley hull), some of them at different loading conditions. Detailed information on the ships' hulls is available in [4], the properties of the four ship models, used in this article, are shown in Table 2.

Table 2. Main properties of the ship models

		KVLCC2	***T0H***	***LNG***	***RoRo***
λ	[ ]	*75*	*75*	*70*	50
Lpp	[m]	4.267	2.210	3.809	3.800
L_{OA}	[m]	4.448	2.316	4.000	4.060
B	[m]	0.773	0.296	0.594	0.620
T_M	[m]	0.277	0.178	0.157	0.148
C_B	[ ]	0.81	0.85	0.77	0.62

2.3 BANK GEOMETRIES

In present article only a selection of tests in a steady state regime condition are considered to check the influence of the bank geometry on the running sinkage of the vessel. Therefore, the installed cross section did not change in geometry for a significant amount of ship lengths (at least six ship lengths) before the ship model decelerates or another bank geometry initiates. When two geometries are installed consecutively in the tank, the transition zone of one bank to another is constructed in such a way to create a smooth change in geometry, this is to avoid abrupt and long lasting transition effects.

In the past tests have been carried out with surface piercing banks (a constant slope from the bottom of the towing tank up to the highest water level tested, Figure 3) and semi submerged banks (a sloped under water part in

combination with a horizontal submerged part). In present examples, only surface piercing banks are considered. The slope of the surface piercing banks is expressed as the ratio between the rise and run (Figure 3) with a normalised rise (a run/rise ratio of zero is a vertical wall). In Table 3 the width at the bottom of the cross section (W_h) is added.

Table 3. Slopes and full width of different installed banks

run/rise	0	0	0	0	0	0	0
W_h (m)	0.812	0.966	1.314	1.933	3.865	4.400	6.330
run/rise	0	1	3	3	4	5	8
W_h (m)	7.000	4.200	4.200	5.730	4.400	4.030	4.030

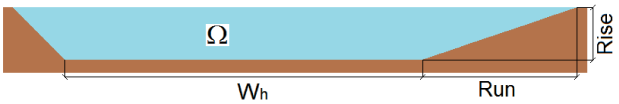

Figure 3. Definition of the dimensions of the cross section: run, rise, W_h and cross section area Ω.

2.4 WATER DEPTH

The tests are carried out at a range of shallow to very shallow water depths. For most ships this is a water depth to draft ratio of 2.00, 1.35 and 1.10 but for the ship model of a RoRo vessel as many as eleven different water depths were systematically tested.

2.5 POSITION, VELOCITY AND PROPELLER

The relative lateral distance between a ship model and a bank can be defined in different ways. The most straightforward method is by referring to the earth bound coordinate system of the towing tank itself. In most combinations, tests are carried out at about 5 different lateral positions to be able to understand the influence of the lateral position and bank effects.

Forward speeds are tested systematically from 8 to 12 knots (full scale). In very shallow water tests at a lower (less than 8 knots full scale) forward speed are added while in more deep water higher speeds (more than 12 knots full scale) were added to the test program. All the tests under consideration were captive motion tests. As such any propeller rate can be imposed on the ship model.

2.6 MEASUREMENTS

During captive manoeuvring tests, the ship model is forced to follow a predetermined trajectory applied by the towing carriage. The ship model is rigidly connected to the planar motion mechanism except for the vertical motions (heave and pitch). The running sinkages are measured at four positions on the vessel (bow-stern/port-starboard).

The forces acting on the ship model, the rudder and the propeller are measured as well as the propeller rate and the rudder angle. In some cases wave gauges were mounted at different locations in the towing tank to capture the water level variations.

3 RESULTS AND DISCUSSION

3.1 CANAL WIDTH AND CROSS SECTION AREA

In [5] results are shown of a tanker (KVLCC2) sailing in a rectangular cross section with a wide range of width and water depth combinations (Figure 4).

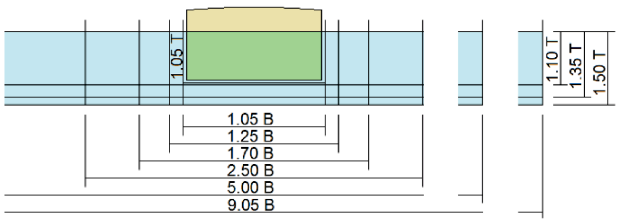

Figure 4. Rectangular cross sections in which the KVLCC2 was tested [5].

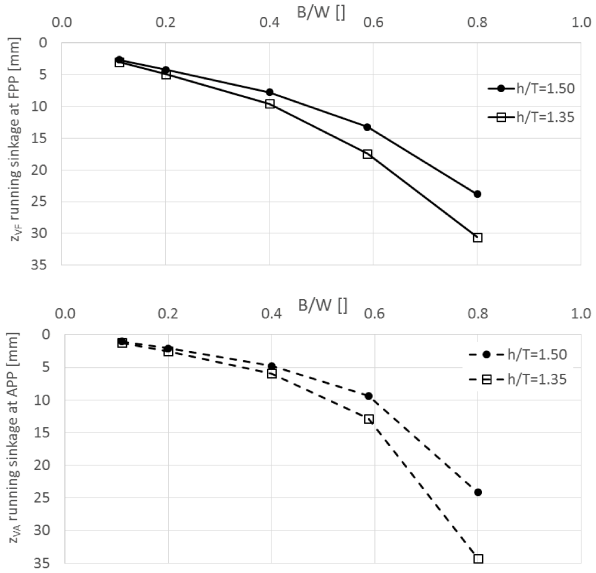

Figure 5. The running sinkage of the KVLCC2 at 6 knots (full scale) in a range of rectangular cross sections and two water depths.

In Figure 5 the running sinkage at the fore and aft perpendicular is plotted for this ship model sailing at a speed according to 6 knots full scale in rectangular cross sections with a width of 125, 170, 250, 500 and 905% of the ship's beam and an initial water depth of 135 and 150% of the draft. All captive tests in this figure are performed with the ship on the centre line of the cross section and with a propeller rate according to the self-propulsion propeller rate at 6 knots in open water. Because of the increased sinkage in very shallow waters, the tests at h/T=1.10 are not included because these were not possi-

ble in the narrow sections at 6 knots and hence no systematic comparisons could be made.

The difference in sinkage is significant when the most open test section (towing tank walls) is compared with a test section only 25% wider than the ship's breadth. In the first case the maximum sinkage is (scaled to full scale) 0.20 m and as much as 1.80 m in the narrow section for the ship sailing under the same conditions (6 knots, centre line, h=1.50T).

In Figure 6 the sinkage is plotted to the blockage ratio (ratio between the midship section area A_M and the cross section area of the canal Ω), an exponential correlation can be observed. Since the tests in both water depths are on the same correlation, the impact of shallower water depth seems to be the same as a more narrow canal (when the change results in the same cross section area). The dashed and full line in Figure 6 are both an exponential function and only added for the interpretation of the figure. In [6] the equivalent blockage m_{eq} was introduced, in a future publication the correlation between the running sinkage and this m_{eq} will be covered in detail.

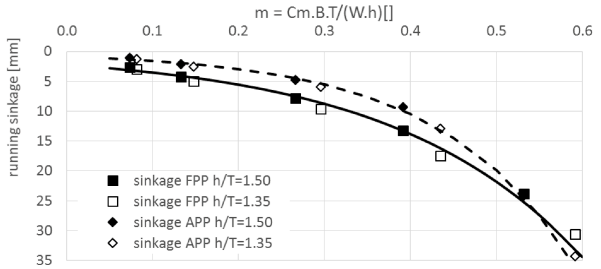

Figure 6. The running sinkages plotted to the blockage ratio m for the KVLCC2 at 6 knots in the different tested rectangular cross sections.

3.2 LATERAL POSITION

In Figure 6 all plotted test results were carried out with the ship model sailing on the centre line of the cross section, hence the distance between ship and port side bank equals the distance between ship and starboard bank. In Figure 7 only tests in the rectangular cross section with a width of 5.0B at a water depth of 1.5 T are plotted. This means that all six tests in this figure are carried out at the same blockage ratio but an increase of running sinkage can be observed when sailing more eccentric (or closer to one bank) in the section. The value y is the lateral distance from the symmetry line of the section while y_{small} is the closest distance between ship and bank wall. At the side closest to the bank the return flow must be higher to evacuate the water in the smaller space available. As a consequence the pressure drop increases along with the running sinkages.

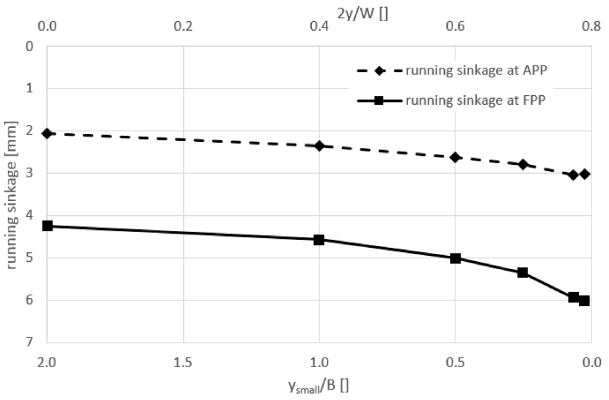

Figure 7. KVLCC2 towed according to 6 knots full scale in a rectangular cross section 5Bx1.5T at six different lateral positions.

A bank will only affect the pressure distribution on the hull if the distance between ship and bank is sufficiently small. As a result, a value for the ship-bank distance can be defined that can be considered as the boundary between open and restricted water. If the ship-bank distance exceeds this value, no (significant) influence of the bank on the ship's sinkage (and more global, her manoeuvrability) will be observed. Therefore systematic model tests were carried out with a modest sized ship model of a tanker which is about half as long as a common ship model at FHR (Table 2).

A systematic database was constructed with this ship model being towed in the towing tank (without extra banks installed) at a range of forward speeds, water depths and lateral positions. In Figure 8 the tests at one forward speed (1.00 m/s) and water depth (1.35T) are plotted for 11 lateral positions.

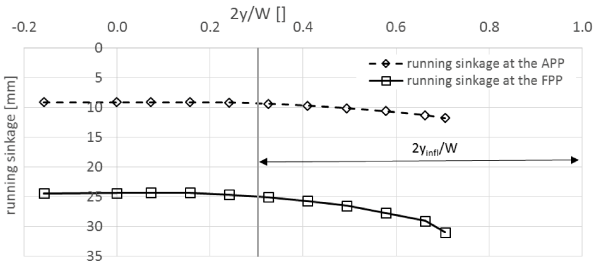

Figure 8. T0H in the towing tank at a water depth 1.35T and towed at 1.00m/s.

For the first five lateral positions the difference in sinkage is less than 1%. Therefore it is assumed that these tests are not influenced by the presence of the tank walls. When sailing closer to the port side tank wall the sinkage increases and this is ascribed to the influence of this wall on the hydrodynamic pressure distribution on the model's hull. The bank has thus a lateral reach which depends on the water depth and forward speed [7]:

$$y_{infl} = B(5Fr_h + 5) \quad (1)$$

In other words, a ship sailing at a distance larger than y_{infl} from the closest bank will not be affected by this bank and thus the ship will act as sailing in open (but possibly shallow) water.

3.3 RUN/RISE RATIO OF THE BANK

A common manmade canal often has an isosceles trapezoid as cross section geometry. The deepest section as the navigable area (fairway) and two equally sloped banks at both sides. In Figure 10 a ship model of an LNG carrier is towed with the ship's flat of side above the toe of three different sloped banks. Again, the slope of the bank is expressed as the run to rise ratio with a normalised rise, for a rise according to one unit these banks need 3, 5 and 8 horizontal units (Figure 9).

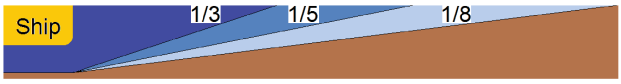

Figure 9. Ship's side above the toe of the three different sloped banks

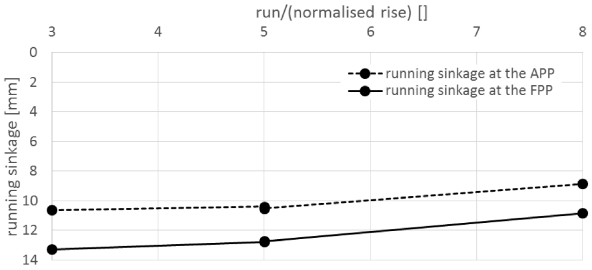

Figure 10. Model of an LNG carrier towed according to 12 knots full scale towed with the port side above the toe of the port side bank for three different bank slopes.

The steeper the bank the more the ship squats, however in these examples it is not easy to separate the influence of the bank slope because a gentler sloped bank will (in this data set) also result in a lower blockage ratio and, as mentioned before, a lower blockage ration will also result in less squat.

3.4 WATER DEPTH

For the RoRo ship model more tests than at three water depths were carried out. These series consists out of tests carried out in the towing tank without extra banks installed, at a range of forward speeds (6, 8, 10 and 12 knots according to full scale) and at three lateral positions (y = 0.00, 2.06 and 2.50m). In Figure 11 the tests at 8 knots (according to full scale) and at lateral position y = 2.500 m (in the 7.0 m wide towing tank) are plotted.

In this figure the increase in running sinkage from deep to shallow water can be observed. However, the running sinkage at the aft perpendicular decreases again for under keel clearances of less than 20% (or T/(h-T) greater than 5). This unexpected behaviour is ascribed to the influence of the boundary layer which is developed along the ship's hull and keel.

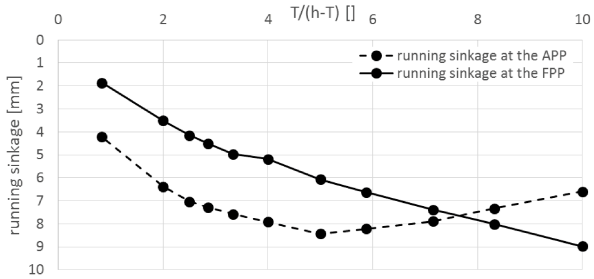

Figure 11. Running sinkage at a wide range of water depths for a RoRo ship model at 8 knots (full scale) and lateral position 2.50 m in the towing tank.

3.5 INFLUENCE OF THE BOUNDARY LAYER

When model tests are scaled according to Froude's law then the boundary layer in the model test will always be relatively thicker than at full scale. This is because fluids of more or less the same viscosity are used on both model scale and full scale (water). The velocity and ship length are both smaller on model scale than on full scale and therefore the Reynolds number will always be (much) smaller on model scale than on full scale. A major consequence of this is the thicker boundary layer on model scale compared to full scale (and relative to the ship length).

$$Re_m < Re_s \tag{2}$$

$$\frac{V_m Lpp_m}{\nu_m} < \frac{V_s Lpp_s}{\nu_s} \tag{3}$$

For reasons of simplicity the viscosities of fresh water and seawater are assumed to be equal, so

$$V_m Lpp_m < V_s Lpp_s \tag{4}$$

$$\frac{V_s}{\sqrt{\lambda}} \frac{Lpp_s}{\lambda} < V_s Lpp_s \tag{5}$$

or

$$\lambda^{1.5}\, Re_m = Re_s \tag{6}$$

The thickness of the boundary layer at the aft body of the vessel can be calculated according to [8] and Prandtl & Von Karman's momentum law. The boundary layer thickness is defined as the locus of points where the velocity parallel to the plate reaches 99 per cent of the external velocity and is calculated with the skin friction law (assuming a turbulent flow along the plate):

$$\delta = 0.16 \frac{x}{\sqrt[7]{Re}} \tag{7}$$

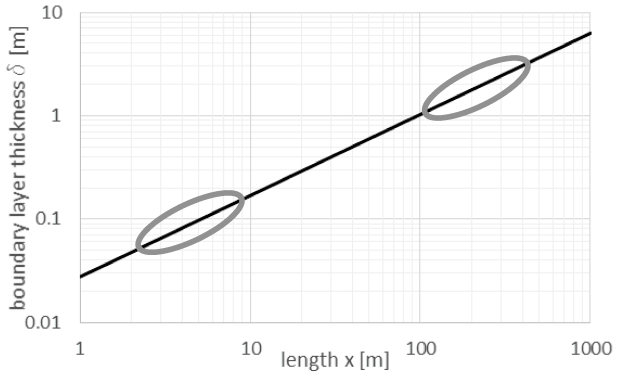

Figure 12. The boundary layer thickness for a wide range of lengths x at a constant Froude number Fr(x)=0.08

This boundary layer develops along the hull with the longitudinal position x (with origin at the forward perpendicular and the axis directed towards the stern). The boundary layer is thus thinner at the first half of the vessel compared to her second half, hence the influence being much more significant on the sinkage at the aft compared to the sinkage at the fore perpendicular. The influence of the boundary layer extends the boundaries of the layer itself. In Figure 12 the boundary layer thickness is plotted to the length x and with a constant (x-dependent) Froude number $\left(V/\sqrt{g.x} = 0.08\right)$. For a ship model the boundary layer (at the aft) is about 0.10m while the boundary layer for the same but full scale ship (at the same Froude number) is about 2.0m thick.

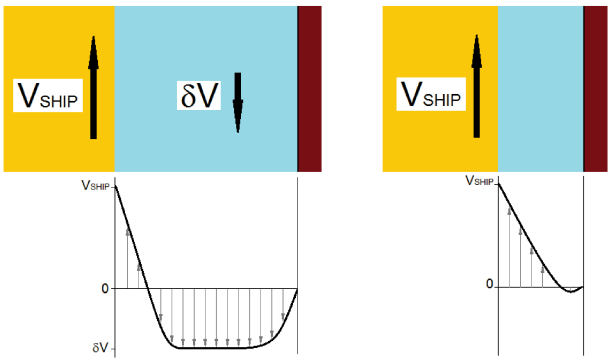

Figure 13. Velocity profile between the ship and bottom or bank.

The viscosity of the water results in water being stuck to the ship, bank and bottom (hence the presence of a boundary layer). This means that the water close to the ship (or bank or bottom) will not be able to evacuate and generate a return flow (Figure 13). Therefore the space available for the return flow is smaller and the influence of the boundary layer will extend its own thickness (by definition reaching 99% of the outer speed). Similar conclusions can be drawn from the other tests (at other lateral positions or forward speeds) as plotted in Figure 11.

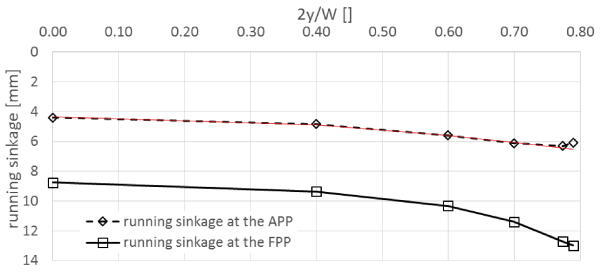

Figure 14. Running sinkage at different lateral positions for the KVLCC2 ship model at 8 knots (full scale) and water depth 1.35T.

Another example of the boundary layer influence is shown in Figure 14, where the running sinkage is plotted for the KVLCC2 towed in the 5.00B wide cross section and a water depth of 1.35T. The two most eccentric model tests were carried out at a distance between the vertical wall and ship as small as 0.050 m and 0.020 m. At the forward perpendicular an increase in sinkage is observed when the ship model is towed closer to the quay wall, but at the aft perpendicular the pace of increase decreases (the plotted red line is proportional to $\left(\frac{2y}{w}\right)^2$) and the running sinkage z_{VA} even decreases being towed at a distance of 0.020 m compared to being towed under the same conditions but at 0.050 m from the installed vertical wall. Now looking back at Figure 7 the same can be observed for the running sinkage at the aft for the position closest to the bank.

It should be noted that the boundary layer influence will only occur at full scale at even more extreme conditions since the boundary layer thickness is relatively smaller at full scale compared to model scale. For example, the ratio of the boundary layer thickness for a 4 m long ship model (δ_4=0.08m) to a 400 m long full scale ship (δ_{400}=3.06m) (as in Figure 12) is 37 and thus smaller than the scale (λ=100). In [4] a mathematical model is introduced which takes into account the influence thickness of the boundary layer on the hydrodynamics on both the ship model as well as the full scale vessel.

4 CONCLUSIONS

A sailing displacement ship will generate a deformation of the free surface in the vicinity of the vessel (and generate waves). Close to the ship the (average) free surface level will drop and as a consequence, the ship will have a vertical displacement (often in combination with a trim), commonly known as ship squat.

Within the boundaries of the reach of the banks, defined by the influence width y_{infl}, the entire bathymetry of the cross section will influence the running sinkage of the ship. Both the horizontal boundary (bank) as the vertical boundary (bottom) has a similar effect on the squat. A steeper bank will also result in a higher magnitude of the running sinkages compared to a less steep bank slope.

The viscosity of the water will influence the squatting behaviour of the ship when sailing very close to the bottom or bank. Because of the scale effects, this influence is more pronounced on model scale than at the full scale vessel.

5 REFERENCES

1. Briggs, M.J ., Vantorre, M., Uliczka, K., Debaillon, P., 2009. Prediction of Squat for Underkeel Clearance. *Handbook of Coastal and Ocean Engineering.* Edited by: Young C Kim (California State University, Los Angeles, USA)

2. Lataire, E.; Vantorre, M.; Eloot, K., (2009). Systematic Model Tests on Ship-Bank Interaction Effects, *Ship Manoeuvring in Shallow Water with Ship-Bank Interaction Effects. In International Conference on Ship Manoeuvering in Shallow and Confined Water: Bank Effects 2009*, Antwerp, Belgium

3. Delefortrie, G.; Geerts, S.; Vantorre, M. (2016). The Towing Tank for Manoeuvres in Shallow Water. *MASHCON 2016*, Hamburg, Germany.

4. Lataire, E. (2014) Experiment Based Mathematical Modelling of Ship-Bank Interaction, *PhD thesis*, Ghent University, Ghent.

5. Lataire, E.; Vantorre, M. ; Delefortrie, G. (2012). A Prediction Method for Squat in Restricted and Unrestricted Rectangular Fairways. *Ocean Engineering*, 55, pp.71–80.
dx.doi.org/10.1016/j.oceaneng.2012.07.009

6. Lataire, E., Vantorre, M. & Delefortrie, G., (2015). Longitudinally Directed Bank Effects. In *MARSIM 2015*. Newcastle.

7. Lataire, E.; Vantorre, M.; Laforce, E.; Eloot, K.; Delefortrie G.; (2007). Navigation in Confined Waters: Influence of Bank Characteristics on Ship-Bank Interaction. P*roceedings of the 2nd International Conference On Marine Research And Transportation*, Ischia, Naples, Italy

8. White, F.M. (2003). *Fluid Mechanics Third Edit.*, McGraw-Hill, Inc.

6 AUTHORS' BIOGRAPHIES

Evert Lataire is currently assistant at the division of Maritime Technology at Ghent University. He has made a PhD on the topic of bank effects mainly based upon model tests carried out in the shallow water towing tank of FHR. His ten year experience includes research on ship manoeuvring in shallow and confined water such as ship-ship interaction, ship-bottom interaction and ship-bank interaction

Guillaume Delefortrie is expert nautical research at Flanders Hydraulics Research. He is in charge of the research in the Towing Tank for Manoeuvres in Shallow Water (cooperation Flanders Hydraulics Research – Ghent University) and is secretary of the 27th and 28th ITTC Manoeuvring Committee.

Marc Vantorre, naval architect, is full senior professor of marine hydrodynamics and head of the Maritime Technology Division at Ghent University, Belgium. His research focuses on ship behaviour in shallow and confined waters, mainly in close co-operation with Flanders Hydraulics Research in Antwerp. He is member of PI-ANC Working Groups and former member of the ITTC Manoeuvring Committee.

4th MASHCON, Hamburg - Uliczka et al. (eds) - © 2016 Bundesanstalt für Wasserbau ISBN 978-3-939230-38-0 (Online)
DOI: 10.18451/978-3-939230-38-0_16

VALIDATION STUDIES ON NUMERICAL PREDICTION OF SHIP SQUAT AND RESISTANCE IN SHALLOW WATER

P Mucha, University of Duisburg-Essen, Federal Waterways Engineering and Research Institute (BAW), Germany
G Deng, École Centrale de Nantes (ECN), France
T Gourlay, Curtin University, Australia
O el Moctar, University of Duisburg-Essen, Germany

SUMMARY

A validation study on numerical prediction of ship squat and resistance in shallow water is presented. Two methods based on the solution of the Reynolds-averaged Navier-Stokes (RANS) equations, a Rankine Panel Method and a method based on slender-body shallow water theory were applied and explored in terms of reliability and performance. Validation studies relied on comparison with model experiments for Post-Panmax container ship Duisburg Test Case (DTC), Panmax Kriso Container Ship (KCS) and Kriso Very Large Crude Carrier (KVLCC) 2. It was found that all methods are generally capable of predicting midship sinkage with good accuracy, while the boundary element methods (BEM) yield larger deviations in higher Froude depth number regimes, especially in predicting trim. For very shallow water ship flows, resistance predictions with viscous flow solvers were shown to be sensitive to turbulence modelling, near-wall treatment and the boundary condition on the tank bottom. In shallow water lifting ship flows, consideration of squat was found to be crucial for accurate computation of transverse forces and yaw moments.

NOMENCLATURE

B_{WL}	Waterline breadth (m)
C_B	Block coefficient (-)
F_{nh}	Froude depth number (-)
g	Gravitational acceleration constant (m/s²)
G	Rankine source
h	Water depth (m)
L_{pp}	Ship length between perpendiculars (m)
m	Ship mass (m)
n	Face normal vector (-)
N	Hydrodynamic yaw moment (Nm)
q	Source strength
Re	Reynolds number (-)
R_T	Total ship resistance (N)
S	Control volume surface area (m²)
$S(x)$	Sectional area (m²)
S_w	Wetted surface area (m²)
t	Time (s)
T	Stress tensor (N/m²)
T	Ship draft (m)
U	Ship speed (m/s)
u^*	Nondimensional wall velocity (-)
v	Velocity vector (m/s)
V	Volume (m³)
x	Longitudinal ship coordinate (m)
x_G	Longitudinal center of gravity (m)
X	Longitudinal hydrodynamic force (N)
y	Transverse ship coordinate (m)
y^+	Nondimensional wall distance (-)
y_g	Transverse center of gravity (m)
Y	Transverse hydrodynamic force (N)
z	Sinkage (mm)
β	Drift angle (°)
ζ	Free-surface elevation (m)
ϑ	Trim (1/60°)
λ	Scale factor (-)
ν	Kinematic viscosity (m²/s)
ρ	Density of water (kg/m³)
ξ	Relative distance of sources (m)
ϕ	Velocity potential (m²/s)

1 DEFINITIONS

Under-keel clearance (UKC) is the distance from the ship keel at T to the vertical flow restriction at water depth h, valid for a Cartesian coordinate system located at the calm water level (Figure 1). Here, ship squat is defined as the decrease of UKC in response to pressure variations along the ship hull underway, which cause the ship to adjust her dynamic floating position in terms of a vertical translation (sinkage) and a rotational displacement in pitch mode of motion (trim), accompanied by a change of the ambient free-surface water level. Sinkage z is given positive downwards and trim ϑ positive aft-down in arc minutes [1/60°]. In straight ahead motion, ship Resistance R_T equals the negative longitudinal hydrodynamic force X.

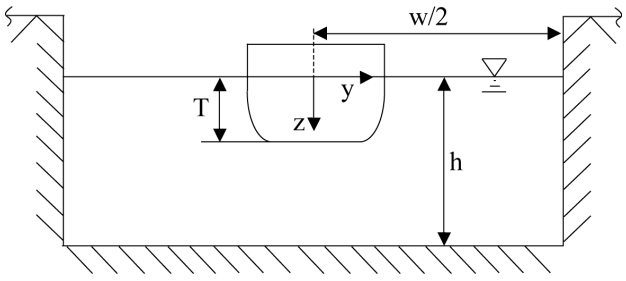

Figure 1. Coordinate systems and definitions for squat predictions in shallow water tanks

2 INTRODUCTION

The prediction of ship squat in shallow water has become an issue of renewed relevance for the hydrodynamic community, as port and waterway administrations face the challenge of growing ship sizes and request ship motion predictions to adapt accessibility to ports and waterways, or to regulate ship operation. Knowledge of shallow water induced added hydrodynamic forces is relevant for maneuvering and minimum power requirement prediction, especially in light of a more strict regulatory framework regarding environmental protection. Over the past three decades, numerical methods based on potential flow theory have been established as efficient tools for ship hydrodynamic analyses, including the application to squat prediction. Yet, the advance of numerical methods based on the solution of the Navier-Stokes equations - benefitted by a substantial increase in computational power - has enabled extended insight into shallow water ship flows. There are theoretical and experimental grounds to anticipate that the effects of turbulence and viscosity in such flow regimes are more dominant than in deep water, challenging the application of inviscid methods. This conflict is aggravated by the predominate investigation of model ship flows to establish a common basis for validation through comparison with experiments, because viscous effects are overbooked in lower Reynolds number regimes. For the particular problem of squat prediction the significance of these aspects was confirmed in the PreSquat workshop [1]. PreSquat aimed at benchmarking capabilities of available numerical methods for squat prediction through comparison with model experiments with the DTC container ship. With additional test cases added, this work drew upon the main findings of the workshop. Special attention was referred to the challenges involved in RANS-based predictions, addressing turbulence modelling, near-wall and free-surface treatment and consideration of rigid body motions.

3 CANDIDATE SHIPS AND TEST CASES

Main particulars of the candidate ships DTC, KCS and KVLCC2 are given in Table 1. No-full scale representations of these ships exist. They have been designed for the particular purpose of experimental hydrodynamic analyses and generation of benchmark data for comparison with numerical methods. Figure 2 presents lines plans (not drawn to scale). Geometries are publicly available online [2], [3].

3.1 MODEL EXPERIMENTS

Model experiments were performed in the shallow water tanks of the Development Centre for Ship Technology and Transport Systems (DST) in Duisburg, Germany, and the Bulgarian Ship Hydrodynamic Center (BSHC) in Varna, Bulgaria. Both facilities operate their tanks with actual desired water depths and do not need to install so-called *false bottoms*.

3.1 (a) DTC and KCS

Towed model tests with DTC, appended with a rudder, were carried out at DST for the PreSquat workshop at h/T=1.143. Captive maneuvering tests in shallow water with KCS in bare hull condition were carried out at DST in the framework of research project [4]. Both models were tested at scale 40 at various water depths. KCS was investigated in different setups at h/T=1.2 and h/T=1.3 at four different forward speeds in the range of Froude depth numbers $F_{nh} = U/\sqrt{gh}$ from 0.27 to 0.68. The models were free to sink and trim, but otherwise constrained. Sinkage was measured by means of laser plates at positions ahead and behind amidships at $L_{pp}/2$. Static trim of the models was zero. DST's towing tank is 200m long and 10m wide. In both experimental setups the towing force point of attack was chosen as to ensure that no additional trim moment was induced. Vertical centers of gravity lay sufficiently below the waterline.

3.1 (b) KVLCC2

Captive maneuvering tests in shallow water were performed with a scale model (λ=45.714) of KVLCC2 at BSHC at h/T=1.2 in the framework of the SIMMAN workshop. Trim and sinkage were measured with wired potentio-meters attached to the model at positions ahead and behind amidships at $L_{pp}/2$. Static trim was zero. BSHC's towing tank is 200m long and 16m wide.

Table 1. Main particulars of candidate ships

	L_{pp} [m]	B_{WL} [m]	T [m]	C_B [-]	x_G [m]	S_w [m²]
DTC	360	51.0	14.0	0.66	-0.56	21560
KCS	230	32.2	10.0	0.64	-2.18	8992
KVLCC2	320	58.0	20.8	0.81	11.14	27194

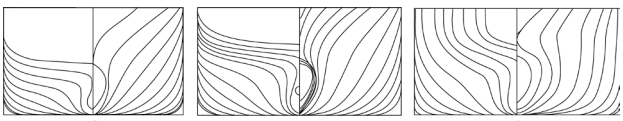

Figure 2. Lines plans of candidate ships DTC, KCS and KVLCC2 (from left to right; not drawn to scale).

4 NUMERICAL METHODS

The aim of the study was to assess the reliability of RANS-based methods for resistance and squat prediction in shallow water and involved sensitivities to turbulence modelling, near-wall treatment and boundary conditions, while a more general interest existed in the performance of BEMs and the computational cost compared to the field methods. While the prediction of pressure-dominated midship sinkage was expected to be accurate with simplified flow models, the problem of accurate resistance prediction –which is itself affected by squat –

was expected to require a fine resolution of near-wall ship flows. Wall functions (WF) are commonly applied in routine computations in industrial applications to economize on computational resources and have been shown to yield good results for resistance prediction in unrestricted waters [5]. However, their application to shallow water ship flows is questionable. Here, computations were performed with both WFs and Low-Reynolds number (LRN) near-wall treatment, integrating the flow equations down to the wall. A Neumann-type boundary condition is usually applied to the tank bottom, imposing zero face-normal velocity (slip wall). However, in ship flows with small UKC a boundary layer may develop and inflicting zero face-tangential velocity (no-slip wall) would yield the physically consistent boundary condition. Field methods draw upon the numerical solution of the Navier-Stokes equations. General mass and momentum conservation equations are formulated in integral notation

$$\frac{\partial}{\partial t}\int_V \rho \, \mathrm{d}V + \int_S \rho \mathbf{v} \, \mathrm{d}S = 0 \quad (1)$$

$$\frac{\partial}{\partial t}\int_V \rho \mathbf{v} \, \mathrm{d}V + \int_S \rho(\mathbf{v}\mathbf{v}) \cdot \mathbf{n} \, \mathrm{d}S = \int_S \mathbf{T} \cdot \mathbf{n} \, \mathrm{d}S + \int_V \rho \mathbf{b} \, \mathrm{d}V \quad (2)$$

where **v** denotes the fluid velocity vector, **n** is the normal vector of S, which represents the area of the surface of control volume (CV) V, **T** denotes the stress tensor and **b** a vector representing a force per unit mass. The transport of turbulent momentum is considered by introducing time averaging and fluctuating terms of the flow quantities to the equations, with yet to be introduced approximations for the resulting stress tensor. Forces acting upon the ship hull are obtained by integrating the pressure and shear stresses over the ship's surface allowing for a separate analysis of pressure and friction resistance.

4.1 RANS-METHOD A

Method A refers to the ISIS-CFD solver [6], developed at ECN and available as part of the FINE™/-Marine computing suite [7]. The solver is based on the Finite Volume (FV) method to constitute the spatial discretization of the transport equations. Grids can be completely unstructured, and CVs with an arbitrary number of arbitrarily-shaped faces are accepted. Pressure-velocity coupling relies on Rhie and Chow Semi-Implicit Method for Pressure-Linked Equations (SIMPLE) [8]. Free surface flow is modelled with the Volume of Fluid (VoF) approach. The two-equation $k\omega$-SST model and the two-equation Explicit Algebraic Stress Model (EASM) were applied in the present study for turbulence modelling [9]. Near-wall CV composition was chosen in accordance with the targeted nondimensional wall distance $y^+ = u^* y/\nu$, where $u^* = \sqrt{\tau/\rho}$ with wall shear stress τ and the distance from the wall to the first interpolation grid point y. Kinematic viscosity is ν. In case of application of the LRN approach, y^+ was targeted equal to or less than one. In case of applying WFs, y^+ was targeted to be ten or greater. The technique included for the modelling of rigid body motions in six degrees of freedom followed the descriptions by [10]. Time-integration of Newton's law for ship motions was combined with analytical weighted or elastic analogy grid deformation to adapt the computational mesh. A parallelized, anisotropic and automatic grid refinement algorithm with dynamic load balancing was implemented and controlled by flow-related criteria. The height of the computational domain was about 0.5*Lpp*, extended 1.6*Lpp* in upstream direction and 2.2*Lpp* in downstream direction of the hull. The mesh was generated with the unstructured hexahedral mesh generator Hexpress™ [11]. Prismatic layers were built around the ship hull boundary. A far field boundary condition was applied at the inlet and outlet boundaries. A slip wall condition was applied to the side wall. A pressure boundary condition was applied to the top boundary. Due to port-starboard symmetry of the bare hull ship models, the question arose whether only half of the fluid domain could be modelled and a Neumann boundary condition in the plane of symmetry could map the solution onto the domain image. From a theoretical standpoint, possible occurrence of flow separation, vortex shedding and associated asymmetries in the shallow water ship flow would make modelling of the entire domain mandatory. An associated sensitivity study in preparation of the application of method A showed negligible effects on predictions of resistance and squat and thereafter, advantage was taken in the application of method A of the mentioned symmetry boundary condition.

4.2 RANS-METHOD B

Method B refers to the application of the commercial solver STARCCM+ [12]. The flow equations are discretized using the FV-method. Here, hexahedral control volumes were arranged in an unstructured fashion. The discretization scheme was of second order using central differences. On the surface of the ship prismatic cells were used. A SIMPLE algorithm [13] was used for segregated solution of the velocity-pressure coupling problem. The free surface was modelled using VoF-method and a High-Resolution Interface Capturing (HRIC) scheme to achieve tracking of sharp interfaces between water and air [14]. The applied turbulence model was $k\omega$-SST [15]. Near-wall grid resolution depended on the wall treatment approach and targeted y+. One ship length upstream from the bow a velocity inlet boundary condition was set, specifying flow velocity, turbulent kinetic energy and dissipation rate. An outlet boundary condition was set two to four ship lengths downstream, where the pressure is given directly, a zero-gradient condition is fulfilled and velocities are found from the arithmetic average of neighboring cells. Inflow on these types of boundaries can be considered in terms of the normal component of boundary recirculation. The width of the numerical tank equaled the width of the tank from the model test facilities for the respective test case, i.e. no symmetry condition was

applied in the midship plane. Free-slip conditions were chosen for the tank side walls. specifying zero face-normal velocity components. Bottom cells were assigned the velocity of the undisturbed flow in the no-slip setup. The numerical grid was locally refined in the UKC region, in the stern region and around the free water surface according to the HRIC scheme. Near the outlet boundary the grid was coarsened to provide damping of the downstream propagating ship waves. The domain extended about half a ship length into the air-phase above the ship. Compared to deep water resistance computations, attention needed to be given to the modelling of relative motions between the ship and the tank restrictions. In unrestricted flow, it is possible to take advantage of moving reference frames and resulting motions of the entire domain according to the coupling of fluid forces from the numerical solution and rigid body equations of motion. This approach involves the additional solution of a space conservation equation, but no deformation of CVs (mesh morphing). In shallow water, application of mesh morphing or overset grids is mandatory to model relative motions between the hull and tank bottom. In method B trim and sinkage were modelled with mesh morphing and two different methods to couple the flow and rigid body equations of motion. The first method is the one of the transient solution of the coupled flow and rigid body equations of motion found from Newton's law, hereafter called free motion approach. The second method uses quasi-steady hydrostatic balancing, where the rigid body is released stepwise based on prescribed increments of sinkage and trim. The methods were studied in terms of performance and accuracy.

4.3 BE-METHOD C

Method C is the Rankine Panel Method GLRankine, developed by GL [16], [17]. GLRankine predicts steady ship flows in potential flow regime using nonlinear boundary conditions. Rankine sources are used to model the ship flow and appropriate boundary conditions are satisfied to define the strengths of the point sources. Following the assumption of inviscid, incompressible and irrotational flow, a velocity potential Φ exists, which has to satisfy the Laplacian (3) in the fluid domain and the boundary conditions on the body wetted boundary and free surface (4), on the channel bottom and walls (5) and on the free surface (6)

$$\Delta\Phi = 0 \tag{3}$$

$$(\nabla\Phi - \mathbf{U}) \cdot \mathbf{n} = 0 \tag{4}$$

$$\nabla\Phi \cdot \mathbf{n} = 0 \tag{5}$$

$$\frac{\zeta}{g} = \mathbf{U}\nabla\Phi - \frac{1}{2}|\nabla\Phi|^2 \tag{6}$$

In (3-6) **U** is the ship velocity vector and ζ the free surface elevation. An unstructured triangular grid is used on the submerged ship surface and a block-structured quadrilateral grid is employed on the free surface. Rankine sources are distributed following the desingularization method. Channel boundaries can be modeled either directly, using triangular panels, or employing image sources for rectangular channel cross sections. The Laplacian is satisfied by the formulation of the potential

$$\Phi(\mathbf{x}) = \sum_{j=1}^{n} q_j G(\mathbf{x}, \xi_j) \tag{7}$$

where $G(\mathbf{x}, \xi_j)$ is a Rankine source of strength q_j and ξ_j denotes the source location points. Upon the determination of the potential and the pressure at each panel, found from Bernoulli's equation, forces acting on the ship hull are available through integration and used to determine iteratively the dynamic trim and sinkage from hydrostatic balancing. Upon determination of the new ship position and orientation, the dynamic boundary condition is used to find the new free-surface elevation, waterline and grid positions. The numerical algorithm is described in detail in [17].

4.4 BE-METHOD D

Method D refers to ShallowFlow, a code for predicting ship squat, developed at the Centre for Marine Science and Technology (CMST) at Curtin University. It is based on slender-body shallow theory [18], [19]. The method uses linearized hull and free-surface boundary conditions. A ship moving in a shallow rectangular canal is modelled as a line of sources and sinks, where the leading-order disturbance velocity potential valid for a ship-fixed coordinate system follows from

$$(1 - {F_{nh}}^2)\frac{\partial^2\Phi}{\partial x^2} + \frac{\partial^2\Phi}{\partial y^2} = 0 \tag{8}$$

subject to the inner boundary condition

$$\frac{\partial\Phi}{\partial y} = \pm\frac{U}{2h}S'(x) \text{ on } y=0_{\pm} \tag{9}$$

and the far-field conditions that $\frac{\partial\Phi}{\partial x}$ and $\frac{\partial\Phi}{\partial y}$ vanish sufficiently far from the ship ($y \to \pm\infty$), where *S'(x)* is derivative of the hull cross-sectional area with respect to *x*. Here, the shallow-water equations are solved by Fourier-transform of (8) subject to (9), whereupon the following expression for the pressure is obtained

$$p(x,y) = -\frac{\rho U^2}{4\pi h\sqrt{1-{F_{nh}}^2}}\int_{-\infty}^{\infty} i\overline{S'(k)}\frac{\cosh(\sqrt{1-F_{nh}^2}k[y-0.5w])}{\sinh(0.5\sqrt{1-F_{nh}^2}kw)}e^{-ikx}\,dk \tag{10}$$

where *w* is the width of the canal. The so-determined potential is used to find the hydrodynamic pressure and compute the vertical force and trim moment hydrostatically. The method is described in detail in [20].

5 VALIDATION STUDY

Uncertainty analysis of results generated by RANS-methods followed the ITTC recommendation [21]. Resistance, sinkage and trim were determined on grids of various resolutions to investigate the sensitivity of the solution to spatial discretization. The error ratio $E\%=100(D-S)/D$ compares the experimental data D to the simulation result S . Where applicable, order of discretization error p was determined.

Table 2. Overview of simulation cases for DTC

Setup	WF-SLIP	LRN-SLIP	LRN-WF
Hull	WF	No-slip	No-slip
Bottom	Slip	Slip	WF
CVs	$1.5\cdot10^6$	$3.09\cdot10^6$	$3.05\cdot10^6$

WF: wall function; SLIP: slip wall BC; LRN: Low-Reynolds number approach

Table 3. Grid sensitivity study, DTC simulations with RANS-A WF-WF *kω*-SST

	R_T [N]	z [mm]	ϑ [1/60°]
Experiment	29.39	11.800	-0.600
$0.86\cdot10^6$ CVs	27.04	13.815	0.792
$1.77\cdot10^6$ CVs	26.92	13.796	0.756
$3.20\cdot10^6$ CVs	27.00	13.787	0.732
Extrapolation	-	13.771	0.708*
Order	-	1.9	0.32

* Second-order assumed

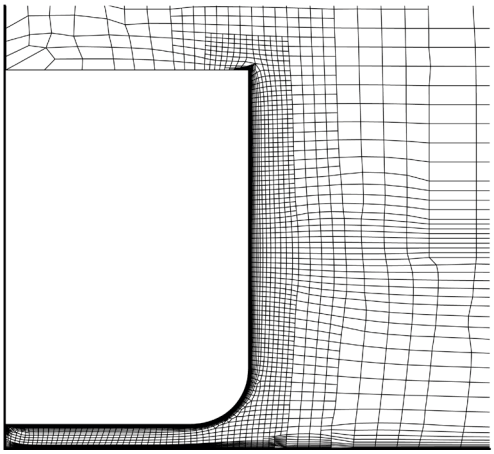

Figure 3. Typical mesh composition at midship section (KCS) in the LRN-WF setup, generated with method A

5.1 DTC

Simulations of the DTC model tests were performed with RANS-method A as a submission of ECN to the PreSquat workshop. Results for application of BE-method D for the DTC were reproduced from the PreSquat workshop, while computations with method C were performed in the framework of this paper. A detailed validation study of both methods with a focus on different container ship shapes is given in [22]. Consistent with the strategy of investigation, Table 2 summarizes the simulation setups with the different near-wall treatments under scrutiny. Figure 3 shows a typical grid composition in the LRN-WF setup at the midship section. A typical computation with $3\cdot10^6$ CVs using 24 cores of Intel E5472 processors took about one day of physical time. A grid dependency study was performed at U=0.791 m/s ($k\omega$-SST model) and is summarized in Table 3. Resistance did not show monotonic convergence, but the difference between results was small. Monotonic convergence was observed for sinkage with almost second-order discretization error. Estimated uncertainty for sinkage was $0.2p$. The observed order of convergence for the trim angle was too small (p=0.32) for extrapolation and was therefore carried out with assumed second order. Reliable uncertainty estimation as suggested by [21] is generally difficult, but from experience results are believed to be within 10% confidentiality. All remaining computations with method A were performed with the medium grid density. Figure 4 shows the comparison of experimental and computational results with respect to Table 2. Deviations in resistance prediction were observed for the WF-SLIP setup. Results were under-estimated by about 3-5%. Divergence at the two highest speeds occurred due to severe grid deformation as a consequence of unsuitable mesh composition. Applying WFs instead of a slip boundary condition at the bottom wall lead to a further improvement of results in terms of an increase in resistance by about 1-2%, except for the case with the lowest speed. Finally, turbulence modelling was crucial. The predicted resistance with the EASM model was about 3-5% higher than with the $k\omega$-SST model and in better agreement with experimental results. The effect was more dominant in the lower speed regime. The maximum difference between the limiting cases of applying the $k\omega$-SST model with WF-SLIP setup and EASM model with LRN-WF setup was 8.3%, valid for U=0.632 m/s. However, at the highest speed the LRN-WF setup and computation with the EASM model yielded still more than 5% difference to the experimental result. Sensitivity to turbulence modelling and tendency for under-prediction of resistance is likely to rest with occurrence of flow separation in the aft ship. RANS-based field methods are known to fail in resolving such flow phenomena with required accuracy. Validation with experimental data is required for extended assessment of the accuracy of both turbulence models employed in the present study. Table 4 provides the predicted friction resistance available from the ITTC 57 [23] formula and computations with the EASM model.

Friction resistance prediction was less sensitive to different near-wall treatment and to turbulence modelling. Hence, only results from LRN-WF/EASM cases are presented. Over the entire speed range friction resistance was about 20% higher than the ITTC 57 formula, challenging straightforward application of the friction correlation line for extrapolation procedures in shallow water.

Table 4. Predicted friction resistance for DTC by method A and ITTC 57

U [m/s]	R_F (ITTC) [N]	R_F (RANS-A) [N]	$E\%$
0.475	5.35	6.35	-18.69
0.632	8.98	11.06	-23.16
0.791	13.51	16.62	-23.02
0.949	18.82	23.07	-22.58
1.027	21.74	26.15	-20.29

Unlike for resistance, sinkage (Figure 5) was not observed to be sensitive to different near-wall treatment or to turbulence modelling. In the lower speed range RANS-method A showed over-prediction of sinkage compared to experiments and BE-method D, while for higher speeds agreement becomes fairly good. Both BEMs showed increasing deviations to experimental results with increasing speed. Better performance was observed for nonlinear method C compared to slender-body theory method D. A typical computational setup for the Rankine Panel method C comprised between $1.0 \cdot 10^4$ and $1.8 \cdot 10^4$ panels. Computations were performed on an ordinary desktop PC (2.4GHz, 4GB RAM) and took between one and four hours, depending on the Froude depth number and convergence criteria. With similar computational resources results from method D are readily available within minutes. The case with the lowest speed was not run with method C due to divergence in the overall computational setup. Treatment of low forward speeds requires small panel sizes and high computational effort. These challenges could be circumvented with double-body simulations, which were omitted here. In the lower speed regime, slender-body theory (method D) with linearized hull and free-surface conditions yield good agreement with experiments and the Rankine Panel method C using nonlinear boundary conditions. As F_{nh} increases above 0.6, method D significantly under-predicted the sinkage. This was referred to the increasing importance of nonlinear effects at all speeds in narrow canals, or at high speed in wide canals. Predicted trim angles (Figure 5) were very small (less than one arc minute), which has to be taken into account in the discussion of relative comparison errors.
These observations were consistent with the established notion that sinkage is dominating in the subcritical speed regime $U < \sqrt{gh}$, i.e. midship sinkage is an order of magnitude greater than the difference between sinkage at the fore and aft perpendicular. The trend of the experimentally determined trim angle does not correspond to the anticipated quadratic dependence on forward speed. Both BEMs predicted a strong bow-down trim increasing with increasing forward speed.

5.2 KCS

Further investigations were conducted with KCS at h/T=1.2 and h/T=1.3. Results for KCS and method C for the case at h/T=1.3 were taken from a previous study [24].

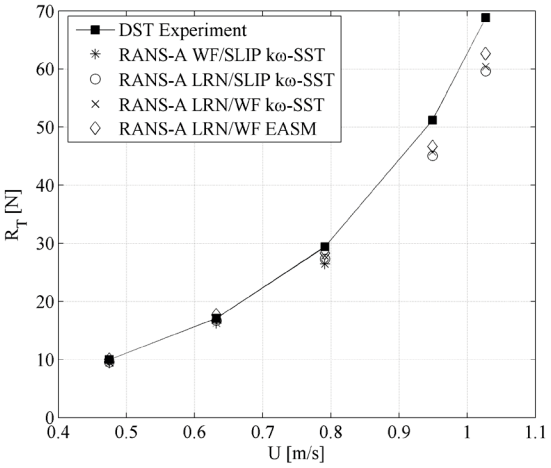

Figure 4. Overview of resistance for DTC predictions in comparison of RANS-method A and DST experiment

Method A is applied in the LRN-WF/EASM setup using medium resolution grids similar to the DTC cases. Results for method B and h/T=1.3 are reproduced from [24]. Here, a WF-SLIP setup was applied in good agreement with experimental results in terms of resistance and sinkage. Hydrostatic computations in preparation of RANS-method A gave a different x_G for the static zero trim floating condition than available from the model test (0.04014m instead of 0.0545m). This adjustment was found to have little effect on resistance and sinkage, but improved the observed agreement in trim with experiments and RANS-method A. In the new computational setup, the tank bottom was modelled as a moving no-slip wall according to descriptions in 4.2. A grid sensitivity study led to the choice of a similar medium grid resolution ($4.4 \cdot 10^6$ CVs). Computations were carried out with the actual free motion approach and the iterative hydrostatic balancing routine. The quasi-steady approach was found to be six times faster than the transient resolution of the fluid-body coupling problem. Results differed by less than 2%. In a High Performance Computing (HPC) environment with 64 cores a computation using hydrostatic balancing took between six and eight hours until a converged trend of resistance, trim and sinkage was observed. The efficient application of this approach required careful choice of sinkage and trim increments and relaxation parameters. The stepwise hydrostatic balancing mitigates the well-known shock effect - i.e. divergence of the numerical solution due to severe rigid body motions in the initializing process of the solution - but is only suitable for steady or weakly unsteady flow problems. Resistance predictions for KCS at both water depths are depicted in Figure 6. For the case at h/T=1.3 both RANS-methods performed similar and yield fairly good agreement with model experiments. Consistent with the findings of the previous section, resistance prediction with method A in the LRN-WF/EASM approach yield slightly better results compared to the WF-WF/$k\omega$-SST setup of method

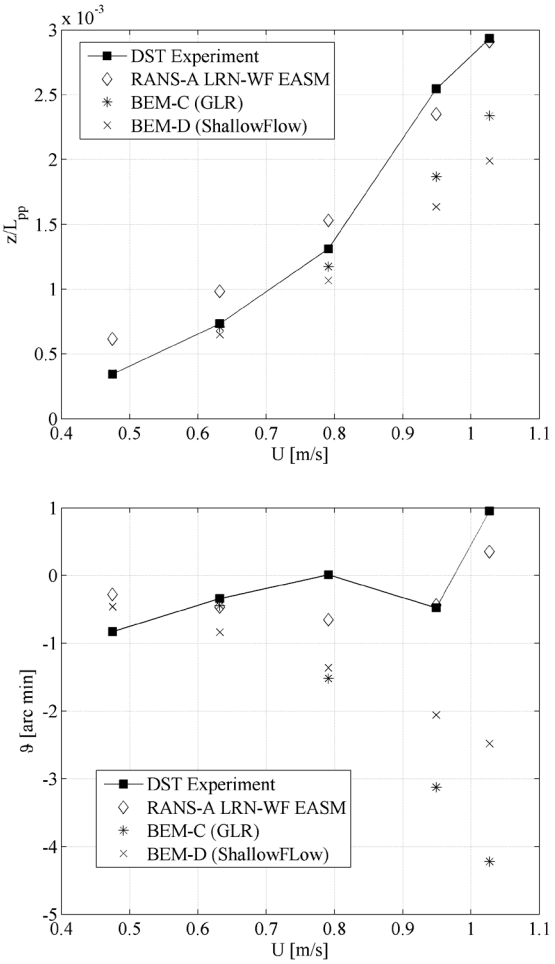

Figure 5. Overview of squat predictions for DTC in comparison of RANS-method A, BEMs and DST experiment

B. The case at U=0.98 m/s laid slightly outside this trend. Observed deviations between computations and experiments on one hand, and between different computational setups on other hand were generally smaller in the case study at h/T=1.3 compared to h/T=1.2. In light of reduced UKC and the experience gained in previous investigations, no effort was made to generate computational setups other than LRN-WF for the case at h/T=1.2. Within the present study, grids generated with RANS-method A and B following LRN setups feature 50% to 100% more CVs than grids for WF cases. A grid sensitivity study for method B is presented in Table 5. For resistance and sinkage the difference between computed results from different grids is very small, but did not show monotonic convergence. The trim angle predicted with the finest grid was more than twice the value of the other computations, but generally still small. No attempt was made to perform Richardson extrapolation and discretization error. Remaining computations were performed on the medium size grid. Resistance predictions from RANS-methods and experiments agreed well at lower forward speeds and gave larger deviations as forward speed increased. At the highest speed deviations between RANS-A and experiment on one hand, and RANS-A (EASM) and RANS-B ($k\omega$-SST) on other hand were larger than in the DTC study. Findings for both sinkage and trim predictions (Figure 7) were reencountered for the KCS test cases. RANS-methods gave a bow-down trim close to experimental predictions, except for method B at the two lowest forward speeds. BEMs under-predicted sinkage and over-predicted trim in the higher forward speed regime. The Rankine Panel method C was again seen to be closer to model test results at F_{nh}>0.6. The overall more bow-down trim predictions of BEMs encountered in investigations with DTC and KCS were referred to the neglect of viscous boundary layer thickening towards the stern. Hull pressure is characterized by deep low-pressure regions at the forward and aft shoulders. If the centroid of this vertical force is ahead of the longitudinal center of floating position, the ship will trim bow-down, and vice versa. Dynamic trim is governed by the difference between large quantities, the downward force at the forward and aft shoulder, and the upward force at the bow and stern. Small changes in hull shape, or submerged volume, will change the balance between each of these, which is discussed for squat of various container shapes in [22]. In light of higher Reynolds-numbers in full-scale ship flows BEMs are expected to show improved agreement when compared to full-scale measurements. For model scale ship flows, systematic studies in conjunction with experience in running the method might be translated into empirical corrections for sinkage and trim, as demonstrated in [22].

Table 5. Grid sensitivity study, KCS simulations with RANS-B LRN-WF $k\omega$-SST, h/T=1.2, U=0.82 m/s

	R_T [N]	z [mm]	ϑ [1/60°]
Experiment	12.53	10.96	-1.429
$4.4 \cdot 10^6$ CVs	10.22	10.38	-1.175
$6.9 \cdot 10^6$ CVs	10.13	10.10	-1.488
$12.5 \cdot 10^6$ CVs	10.23	10.30	-1.191
Extrap.	-	-	-
Order	-	-	-

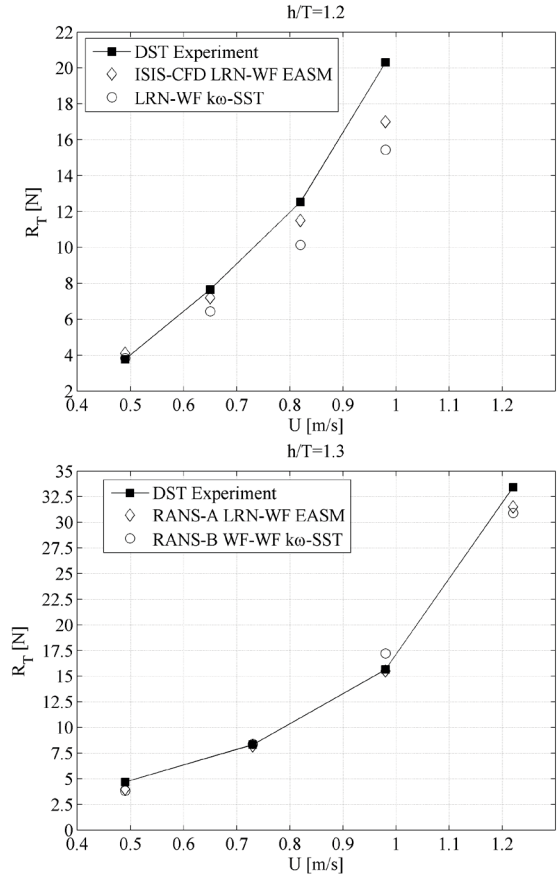

Figure 6. Overview of resistance predictions in comparison of RANS-methods and DST experiments, KCS at h/T=1.3 and 1.2

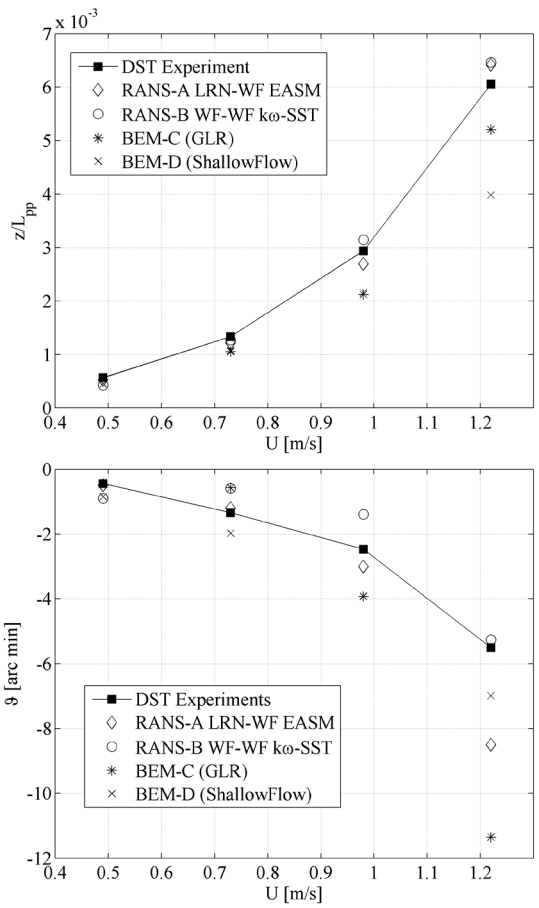

Figure 7. Overview of squat predictions for KCS in comparison of numerical methods and DST experiment, h/T=1.3

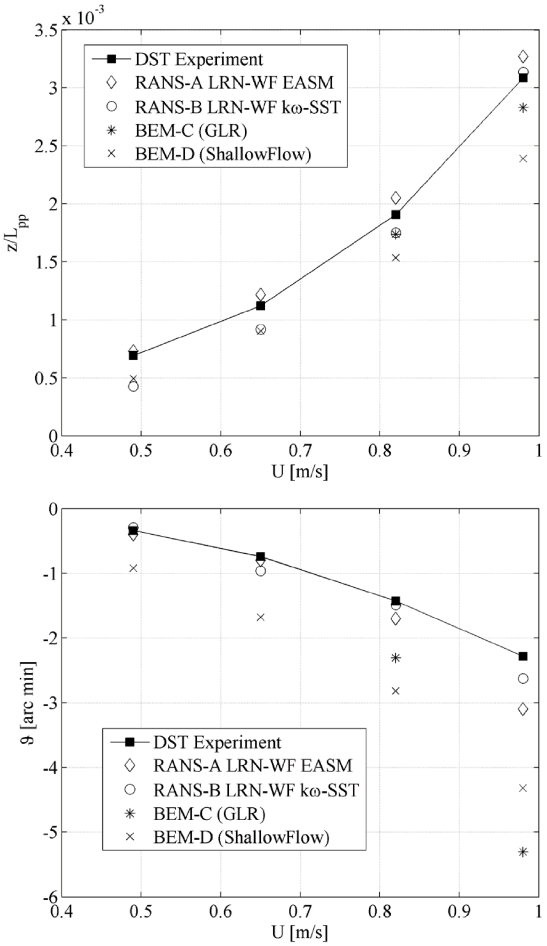

Figure 8. Overview of squat predictions for KCS in comparison of numerical methods and DST experiment, h/T= 1.2

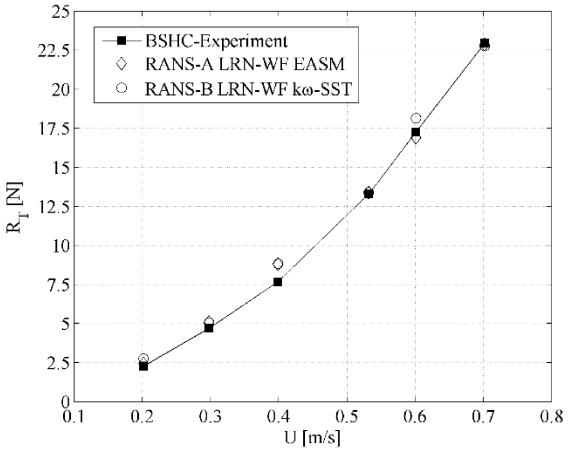

Figure 9. Overview of resistance predictions for KVLCC2 in comparison of RANS-methods and BSHC experiments, h/T= 1.2.

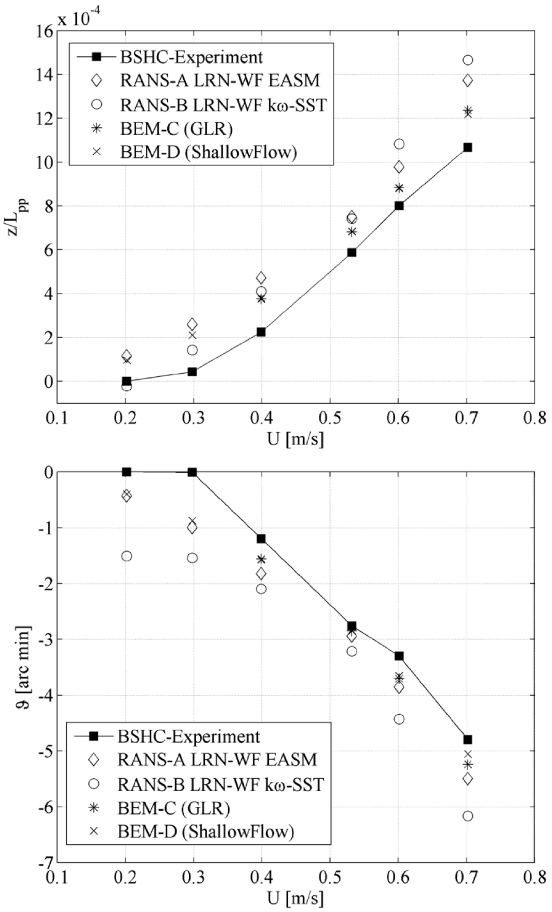

Figure 10. Overview of squat predictions for KVLCC2 in comparison numerical methods and BSHC experiments, h/T= 1.2.

5.3 KVLCC2

Numerical methods were applied to simulate the BSHC model tests with KVLCC2, which represented a different kind of ship model compared to the container ships. It was towed in an overall lower Froude depth number range. Resistance predictions by RANS-methods A and B were in good agreement with experimental results in the entire speed range (Figure 9), owing to the generally lower Froude depth number regime compared to the investigations with the containerships. All methods predicted a similar trend bow-down trim, but with deviations between 20-50% in magnitude, where the relative comparison error is larger at low forward speeds. Significant deviations between RANS-methods and BEMs at the highest forward speed were observed for midship sinkage predictions (Figure 10). Moreover, an offset between all computational and experimental results was observed over the entire speed range.

6 INFLUENCE OF SQUAT IN LIFTING FLOWS

Finally, KCS was investigated at h/T=1.3 (U=0.98 m/s) at three different drift angles with RANS-method B using the medium size grid. The objective was to assess the influence of squat on hydrodynamic forces *X, Y* and moment *N*, valid in a ship-fixed Cartesian coordinate system located at amidships and commonly used in influence of squat on hydrodynamic forces *X, Y* and moment *N*, valid in a ship-fixed Cartesian coordinate system located at amidships and commonly used in

maneuvering simulations (*x*-axis points in the ship's forward direction, *y*-axis to starboard, *z*-axis downwards). Two kinds of computations were performed; one with fixed floating position and one with trim and sinkage free using quasi-steady hydrostatic balancing. Roll motion was constrained. Simulated sinkage was close to experimental results, while the bow-down trim was greater by 40%. In general, squat is significantly greater compared to the straight ahead run at the same speed. With the ship drifting at an angle of 12°, sinkage almost doubled, while the bow-down trim became almost five times greater. While the simulation considering squat gave results for *Y* and *N* of less than 10% deviation compared to experiments (Table 6), the constrained motion simulation under-predicted *Y* and *N* almost by 50%. For the smallest drift angle of 4° deviations were only moderate (Figure 12). Longitudinal force *X* is 24% higher for the CFD prediction including squat, and 64% higher with the ship being fixed.

Table 6. Comparison of transverse forces and yaw moments for KCS at β=12°, U=0.98 m/s, h/T=1.3 between experiment and different computations with RANS-B LRN-WF *kω*-SST

	X [N]	*Y* [N]	*N* [Nm]	*z* [mm]	*ϑ* [1/60°]
Exp.	-9.88	414.00	726.80	31.17	-15.70
Free	-12.31	443.12	804.82	31.51	-22.19
Fixed	-16.26	227.13	335.53	-	-

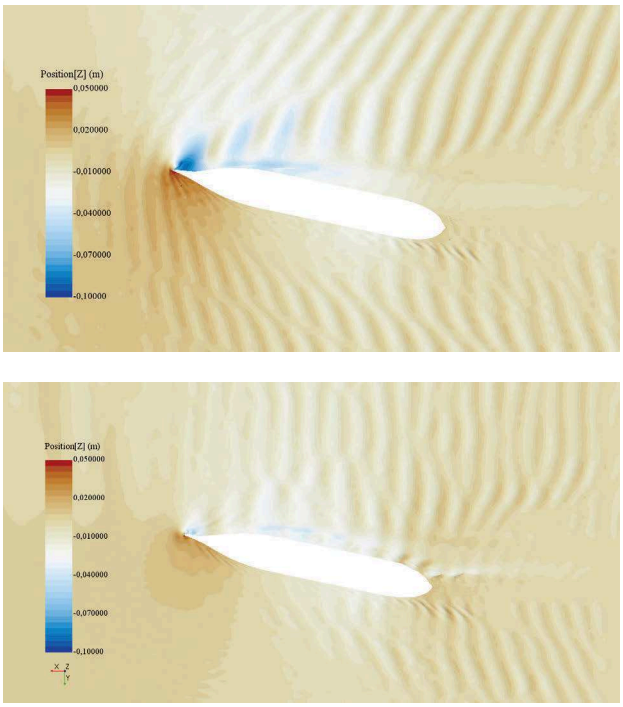

Figure 11. Comparison of free-surface elevation around KCS at β=12°, U=0.98 m/s for simulations with free and fixed sinkage and trim.

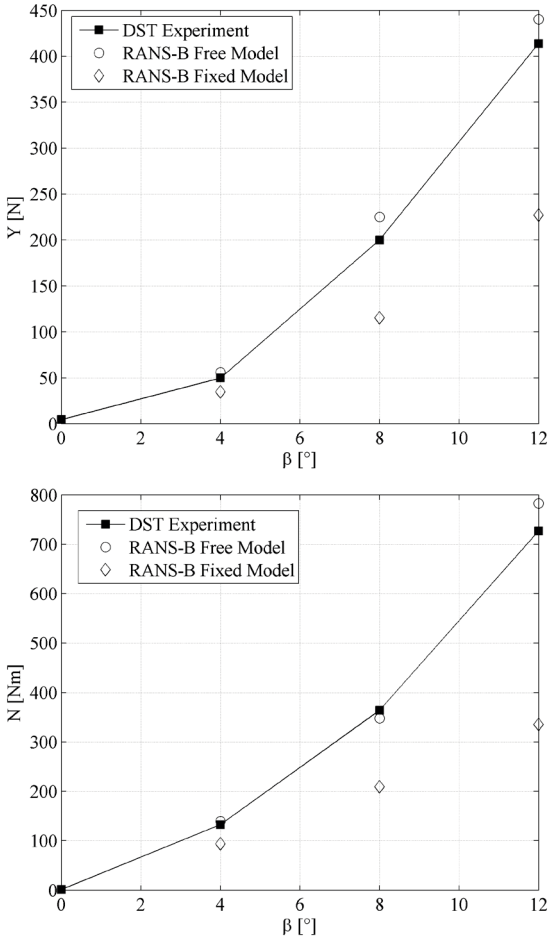

Figure 12. Comparison of transverse forces and yaw moments for KCS at β=12°, U=0.98 m/s between experiment and different computations with RANS-B LRN-WF *kω*-SST

Figure 11 provides insight into the local flow field around the KCS in terms of the free-surface elevation.
The massive bow-down trim resulted in a large difference in the water level in the bow area between the wind- and leeward sides. The different water levels induced an increase of transverse force *Y* - the point of attack in such lifting flows generally lays in the fore ship area - and yaw moment *N*. In the constrained motion simulation with fixed UKC the difference in water levels is significantly smaller. Such force contributions are anticipated to be proportional to $\rho g \Delta\zeta_l$, integrated over the ship length, where $\Delta\zeta_l$ is the local water level difference. The effect is anticipated to amplify with increasing F_{nh}. In light of the considerable magnification of ship squat in lifting flows, such scenarios should be taken into consideration in UKC management, as the approach of ports might involve maneuvers in which ships might attain drift angles. Besides, results emphasized the requirement of considering squat in shallow water captive maneuvering tests used to derive hydrodynamic coefficients for maneuvering prediction.
In this context, the influence of drifting on the roll mode of motion remains to be investigated, as the low-pressure

field along the bilge on the windward side of the ship might induce hydrodynamic roll moments and affect lateral forces.

7 CONCLUSIONS

A validation study on numerical prediction of ship squat and resistance in shallow water was performed with two methods based on the solution of the Reynolds-averaged Navier-Stokes (RANS) equations, a Rankine Panel Method and a method based on slender-body shallow water theory. Validation studies relied on comparison with experimental data for the well-known candidate ships DTC, KCS and KVLCC2 at various water depths, speeds and drift angles. All methods were shown to be capable of predicting midship sinkage with good accuracy at low and moderate forward speeds. BEMs yield larger deviations in higher Froude depth number regimes, especially in predicting trim. Deviations in trim predictions were found to be larger than for midship sinkage. In general, it is desirable to perform repeatability studies in experimental investigations to supplement validation exercises for numerical methods. For BEMs available model test data might serve as a basis for introducing empirical corrections to account for systematic errors in model scale investigations, which are believed to stem from neglecting viscous flow effects. Both BEMs under scrutiny represent a time-efficient tool for squat predictions in shallow water. Viscous flow computations on the basis of the solution of the RANS-equations offer accurate, but expensive squat predictions. For very shallow water ship flows (h/T<1.2), application of simplified models for near-wall treatment at the ship hull and tank bottom results in significant under-prediction of resistance. The EASM turbulence model performed generally better than the $k\omega$-SST model. At high speeds, where flow separation is likely to be present, resistance in very shallow water condition with such RANS-methods is still under-predicted. In shallow water lifting ship flows, consideration of squat was found to be crucial for accurate computation of transverse forces and yaw moments, which is important for maneuvering predictions.

8 ACKNOWLEDGEMENTS

The authors acknowledge collaboration with model test facilities DST and BSHC in the framework of the PreSquat and SIMMAN workshops. Andreas Gronarz of DST kindly provided model test data for the KCS. Alexander von Graefe and Vladimir Shigunov of DNV GL consulted in running GLRankine. The contribution of Nour Yahfoufi of Université Pierre et Marie Curie to computations related to RANS-method A are acknowledged.

9 REFERENCES

[1] Mucha, P.; el Moctar, O.; Böttner, C.U. (2014). Technical note: PreSquat - Workshop on Numerical Prediction of Ship Squat in Restricted Waters. *Ship Technology Research - Schiffstechnik.* 61(3): pp. 162-165.

[2] El Moctar, O.; Shigunov, V.; Zorn, T. (2012). Duisburg Test Case: Post-panamax container ship for benchmarking. *Ship Technology Research - Schiffstechnik.* 59(3), pp. 50-64.

[3] http://simman2014.dk/ship-data/, called 12/10/2015.

[4] Gronarz, A.; Broß, H.; Mueller-Sampaio; C., Jiang, T., Thill, C. (2009). SIMUBIN - Modellierung und Simulation der realitaetsnahen Schiffsbewegungen auf Binnenwasserstraßen (in German). *Report 1939 B*. Development Centre for Ship Technology and Transport Systems (DST).

[5] Larsson, L.; Stern, F.; Bertram, V. (2003). Benchmarking of Computational Fluid Dynamics for Ship Flows: The Gothenburg 2000 Workshop. *Journal of Ship Research* 47(1): pp. 63-81.

[6] Queutey, P.; Visonneau, M. (2007). An interface capturing method for free-surface hydrodynamic flows. *Computers and Fluids* 36: pp. 1481–1510.

[7] Numeca (2015.): *FINE™/-Marine User Guide*.

[8] Rhie C. M.; Chow W. L. (1983). Numerical Study of the Turbulent Flow Past an Airfoil with Trailing Edge Separation. *AIAA Journal* 21(11): pp. 1525-1535.

[9] Deng, G.B.; Visonneau, M. (2005). Three-dimensional Flow Computation with Reynolds Stress and Algebraic Stress Models. *Engineering Turbulence Modelling and Experiments* 6: pp. 389-398.

[10] Leroyer, A.; Visonneau, M. (2005). Numerical methods for RANSE simulations of a self-propelled fish-like body. *Journal of Fluids and Structure*s 20: pp. 975–991.

[11] Numeca. (2015.): *Hexpress™ User Guide*.

[12] Cd Adapco. (2015). *STARCCM+-User-Guide 10.06.009.*

[13] Caretto, L.S.; Gosman, A.D.; Patankar, S.V.; Spalding, D.B. (1972). Two calculation procedures for steady, three-dimensional flows with recirculation. *Proceedings of the 3rd International Conference on Numerical Methods Fluid Dynamics*.

[14] Ferziger, J.; Peric, M. (1996). *Computational Methods For Fluid Mechanics*. Springer.

[15] Menter, F.R. (1994). Two-Equation Eddy-Viscosity Turbulence Models for Engineering Applications. *AIAA Journal* 32(8): pp. 1598-1605.

[16] Söding, H.; von Graefe, A.; el Moctar, O.; Shigunov, V. (2012). Rankine source method for seakeeping predictions. *Proceedings of the 31st Interantional Conference on Ocean, Offshore and Arctic Engineering*, OMAE2012-83450.

[17] Von Graefe, A. (2015). *A Rankine source method for ship-ship interaction and shallow water problems.* Ph.D. Thesis, University of Duisburg-Essen.

[18] Tuck, E.O. (1966). Shallow water flows past slender bodies. *Journal of Fluid Mechanics* 26: pp. 81-95.

[19] Tuck, E.O. (1967). Sinkage and trim in shallow water of finite width. *Schiffstechnik* 14: pp. 92-94.

[20] Gourlay, T.P. (2014). ShallowFlow: A Program to Model Ship Hydrodynamics in Shallow Water. *Proceedings of the ASME 33rd International Conference on Ocean, Offshore and Arctic Engineering*, OMAE2014-23291.

[21] ITTC (2008). *Recommended Guidelines and Procedures 7.5-03-01-01: Uncertainty Analysis in CFD Verification and Validation Methodology and Procedures.* http://ittc.info, called 12/10/2015.

[22] Gourlay, T.; Jeong, H.H.; Mucha, P.; Uliczka, K. (2015). Sinkage and Trim of Modern Container Ships in Shallow Water. *Proceedings of the Australasian Coasts and Ports Conference*, Auckland, New Zealand.

[23] ITTC (2011). *Recommended Guidelines and Procedures 7.5-02-02-01: Resistance Tests.* http://ittc.info, called 12/10/2015.

[24] Mucha, P.; el Moctar, O. (2014). Numerical Prediction of Resistance and Squat for a Containership in Shallow Water. *Proceedings of the 17th Numerical Towing Tank Symposium*, Marstrand, Sweden.

10 AUTHORS' BIOGRAPHIES

Philipp Mucha is a doctoral student and research assistant at the University of Duisburg-Essen (UDE) and Federal Waterways Engineering and Research Institute (BAW) in Germany. His research deals with ship maneuvering in restricted waters and application of numerical methods in ship hydrodynamics.

Ganbo Deng is a Senior Research Fellow at LHEEA (Hydrodynamics, Energetics, Atmospheric Environment) laboratory, École Centrale de Nantes, France. He works on software development for RANSE solvers with the finite volume approach for marine applications.

Tim Gourlay is a Senior Research Fellow at the Centre for Marine Science and Technology (CMST), Curtin University. He undertakes research and consulting work in ship under-keel clearance for ports in Australia and internationally. This work typically includes theoretical development, software development, UKC management guidelines, port liaison and full-scale validation trials.

Ould el Moctar is Professor for Ship Technology and Hydrodynamics at UDE and Managing Director of the Institute for Ship Technology, Ocean Engineering and Transport Systems (ISMT) at UDE. He heads the board of DST.

4th MASHCON, Hamburg - Uliczka et al. (eds) - © 2016 Bundesanstalt für Wasserbau ISBN 978-3-939230-38-0 (Online)
This paper: joint © 2016 Fisheries and Oceans Canada DOI: 10.18451/978-3-939230-38-0_17

WATER LEVEL FORECASTS AND SQUAT CALCULATION FOR THE TRAVERSE DU NORD

S Mercier and **B Cayer,** Corporation des pilotes du Bas Saint-Laurent, Canada
D Lefaivre, Fisheries and Oceans Canada / Maurice Lamontagne Institute, Canada
G Sauvé, Innovation maritime, Canada
A D'Astous, Fisheries and Oceans Canada / Maurice Lamontagne Institute, Canada

SUMMARY

Vessels with drafts of up to 15.5 m call into the port of Quebec on a regular basis, using the crest of the tide to transit a 16.6 nautical mile (M) long, 12.5 m dredged channel. The average tide in the channel is 5.5 m. Readings from tide gauges located above, below and in the dredged channel are available via AIS or the internet. The Canadian Hydrographic Service (CHS) uses an accurate mathematical model called *SPINE* (*Système de Prévision et d'Interpolation des Niveaux d'Eau* - Water Level Forecast and Interpolation System) to forecast water levels that include tidal predictions, the St. Lawrence River flow, and atmospheric forcing. The Canadian Coast Guard has published a squat table and under-keel clearance requirements for the Traverse du Nord by which all ships must abide. A web-based solution called the Tide Windows Module was developed by Innovation maritime for the Corporation des pilotes du Bas Saint-Laurent to give its pilots a tool to manage under-keel clearance, which incorporates the Canadian Coast Guard UKC requirements, real-time water levels and forecasts, ship's draft, beam and speed.

1 INTRODUCTION

The port of Quebec is situated at the head of the St. Lawrence River estuary in Canada. The average tide height in the harbour is 4.9 m. Downstream from the harbour exists a 16.6 nautical mile (M) long dredged channel with a maintained depth of 12.5 m called the Traverse du Nord (hereinafter the "Traverse"). It presents an average tide of about 5.5 m at the Saint-François tide station (Figure 1). Real-time tide gauge readings for locations above, below and in the middle of the dredged channel are available via AIS or the internet.

The Canadian Hydrographic Service (CHS) issues water level forecasts that include tidal predictions, with the influence of fresh water flow from the St. Lawrence River and the atmospheric forcings. These forecasts are provided through an application called SPINE (Système de Prévision et d'Interpolation des Niveaux d'Eau - Water Level Forecast and Interpolation System) which uses the results of a one-dimensional numerical model of water levels and flows. In the presence of strong weather systems, it is not uncommon to see variations of up to 0.80 m between the predicted tidal level and the actual water level.

Figure 1. Quebec and the Traverse du Nord

Vessels with drafts of up to 15.5 m call safely into the port of Quebec on a regular basis, using the crest of the tide to transit through the 12.5 m dredged channel. In order to have a better control of the safety margins, the CPBSL developed, together with its partners, a "Tide Windows Module" that uses the tide gauge readings, CHS's SPINE forecasts, vessel beam, draft and speed, as well as the specific squat table based on the "Eryuzlu with beam" model and safety and manoeuvrability margins published by the Canadian Coast Guard.

$$S = 0{,}181 \cdot \sqrt{T \cdot b} \cdot \left(\frac{V}{\sqrt{g \cdot T}} \right)^{2{,}269} \cdot \left(\frac{T}{H} \right)^{0{,}994}$$

Equation 1. Eryuzlu with beam

The processed information is available to the pilot and captain via a user-friendly, secured web application which can be adapted to vessels of different beams and drafts, and adjusted for different transit speeds.

2 THE FIVE INGREDIENTS

2.1 THE TRAVERSE DU NORD

The Traverse (Figure 2) is located on the St. Lawrence River. It is 16.6 M long, 305 m wide with a maintained depth of 12.5 m and consists of three legs with 9 degrees between each of them (033° x 10', 024° x 3.1' and 033° x 3.6'). Its western limit is 15 M downstream from Quebec City.

The average tide at Saint-François is 5.5 m whereas at the western limit of the Traverse, only five miles away, the average tide is 30 cm less.

The natural depth of the Traverse prior to dredging was between 7 m and 8 m for approximatively 50% of its length and between 10 m and 20 m for the remainder. The Traverse is not considered a confined canal as the horizontal limits outside the dredged channel do not impede water flow [1]. The coastline is situated at more than one quarter mile from the channel limits for most of its length. It is considered restricted because of the water depth available.

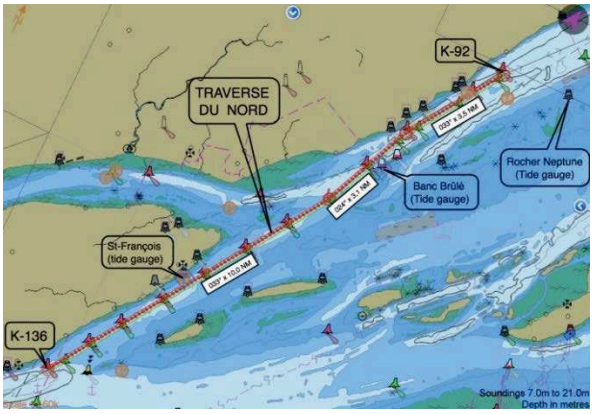

Figure 2. Traverse du Nord

2.2 THE SHIPS

Vessels calling the port of Quebec, that warrant careful UKC management, are mostly Suezmax crude oil tankers (Figure 3) and Capesize bulk carriers measuring up to 294 m in length, with beams between 48 m and 52 m and with drafts of up to 15.5 m.

Figure 3. Typical Capesize vessel in Quebec City

2.3 THE SQUAT MODEL

The formula used by the Canadian Coast Guard in the Traverse, to estimate vessel squats, is "Eryuzlu with beam" (Equation 1), as determined by Morse and Simard [2], to offer the best performance possible. It is thus designed to be used within the following parameters:

- Merchant vessel for which Cb = 0.80 and static draft is 8.13 m to 20.32 m;
- Vessel without significant trim (less than 10%);
- Vessel sailing alone, with SOG of 4 to 17 knots;
- No external forces (waves, wind, etc.) affecting the vessel during the trip;
- Relatively straight channel of unrestricted width and uniform depth;
- Channel no deeper than 37.5 m, with a water depth–to-draft ratio between 1.1 and 3.0;
- Vessel travelling in the central part of the channel, given that squat may increase if the vessel gets significantly closer to shore.

Using these parameters, the *UKC for the Traverse* table (Table 1) is then computed from the equation for the mariner where he only needs to input in the table the speed and beam of the vessel, as these variables have the most impact the squat predictions at a level above critical value (>5%). The safety/manoeuvrability margin is based in part on the PIANC manoeuvrability requirement and on a safety margin that account for the different variables whose impact are individually below critical values.

Table 1. UKC for the Traverse

Vessel Beam Not Exceeding (m)	Vessel Speed Not Exceeding (knots)							
	7	8	9	10	11	12	13	14
Required Under-Keel Clearance (m)								
31	0.86	0.95	1.06	1.17	1.38	1.60	1.84	2.09
34	0.87	0.97	1.08	1.20	1.41	1.64	1.89	2.15
37	0.89	0.98	1.10	1.22	1.44	1.68	1.93	2.20
40	0.90	1.00	1.11	1.25	1.47	1.72	1.97	2.25
43	0.91	1.01	1.13	1.27	1.50	1.75	2.01	2.29
46	0.92	1.03	1.15	1.29	1.53	1.78	2.05	2.34
49	0.93	1.04	1.17	1.32	1.56	1.81	2.09	2.38
52	0.94	1.05	1.18	1.34	1.58	1.85	2.13	2.42
Estimated Squat (m)								
31	0.25	0.34	0.45	0.56	0.70	0.84	1.00	1.18
34	0.27	0.36	0.47	0.59	0.73	0.88	1.05	1.23
37	0.28	0.37	0.49	0.62	0.76	0.92	1.09	1.28
40	0.29	0.39	0.51	0.64	0.79	0.95	1.14	1.33
43	0.30	0.40	0.52	0.66	0.82	0.99	1.18	1.38
46	0.31	0.42	0.54	0.68	0.84	1.02	1.21	1.42
49	0.32	0.43	0.56	0.71	0.87	1.05	1.25	1.47
52	0.33	0.44	0.57	0.73	0.90	1.08	1.29	1.51
Safety/Manoeuvrability Margin (m)								
	0.61	0.61	0.61	0.61	0.69	0.76	0.84	0.91

The comparison of predicted squat and measured (OTF-GPS technology using the Canadian Coast Guard's GPS network (accuracy of 5 cm @ 95%)) squat for 12 ships ranging from 294 m long container vessels and Suezmax tankers to smaller Handysize bulkers transiting in the St. Lawrence waterway was studied in [3-5], extracts of which are presented in Figure 4 and in Table 2.

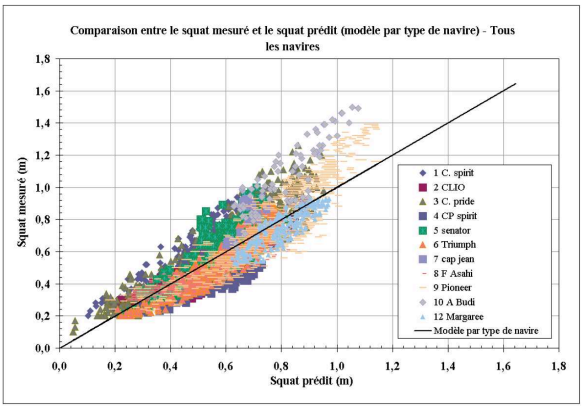

Figure 4. Predicted vs observed Squat

Table 2. Performance of the squat model used by the CCG UKC tables

Vessel Type	Coefficient of Determination (-)	Bias *E* (m)		Relative Bias *ER* (%)	
		Mean	Standard Deviation	Mean	Standard Deviation
All	0.60	0.15	0.17	28	33
Container Ships	0.62	0.25	0.15	47	30
Bulk Carriers	0.78	0.07	0.12	13	26
Tankers	0.68	0.04	0.14	10	24

An overall tendency to slightly overestimate the squat (Figure 5) was observed, with a mean deviation of 4 cm and a standard deviation of 14 cm in the case of Suezmax tankers, the area's most critical vessels.

2.4 THE HYDRODYNAMIC MODEL

The hydrodynamic model has been documented by Lefaivre et al. [6, 7]. It is a one-dimensional model applied to the St. Lawrence River from Montreal to Saint-Joseph-de-la-Rive, near Baie-Saint-Paul to forecast water levels in support of CHS activities. At the upstream end, the model uses the forecasted flows at Montreal from Lake Ontario outflow, the Ottawa River and other smaller tributaries to the St. Lawrence River. The atmospheric forcing is added to the tidal forecast at the downstream boundary. In the model domain, at the tidal stations in the Traverse (Rocher Neptune, Banc Brûlé, Saint-François, Saint-Jean), the model forecasts are assimilated to the last observation on a 15-minute schedule. The forecasted values of the water levels are available at every 3 km of the navigational channel, updated every 15 minutes with the observations made at the 4 stations in the area, using the forecasted wind influence for the next 48 hours and the forecasted St. Lawrence River flow for the next 30-day period.

- The St. Lawrence River is modelled from Montreal to Saint-Joseph-de-la-Rive;
- From unidirectional flow regime at Montreal to an almost symmetrical tidal cycle up to Saint-Joseph-de-la-Rive;
- Uses forecasted flows at Montreal from Lake Ontario outflow, the Ottawa River and other smaller tributaries;

- Atmospheric forcing added to the tidal forecast at the downstream boundary;
- Hourly forecasted wind intensity;
- Added values (positive of negative) at Saint-Joseph-de-la-Rive for the next 48 hours;
- Model forecasts assimilated to the last observation on a 15-minute schedule;
- Forecasted values of the water levels available at every 3 km of the navigational channel.

2.5 THE COMMUNICATION PROTOCOL

All tide gauges are sending their data through UHF or a cellular modem every 3 minutes. The data is sent at least twice, with a 20-second delay to implement validation, in order to ensure availability and limit problems due to collisions on UHF channels.

Installations throughout the St. Lawrence River receive the UHF data and convert it in IP data packets which are then retransmitted via commuted phone lines (128 and 56 kbs) to the Quebec server, then retransmitted via CHS intranet (DFOnet) to ODINS servers in Ottawa and Sidney, BC.

Other tide gauges, especially downstream of Saint-Joseph-de-la-Rive, transmit their data via cellular modems directly to the Ottawa and Sidney servers through the internet.

All the raw data is only available through DFO intranet (DFOnet), so SOAP (Simple Object Access Protocol) web services are used as bridges to access predictions, observations from the tide gauges, and forecast from SPINE. Those three services (PRED, OBS and SPINE) are accessible on the WDS (Windows Deployment Services) server via internet. Predictions and observations are linked to specific stations whereas forecasts are accessed via locations specified by longitude and latitude. Those services are called by the pilot's internet application website server (Figure 5).

The HTML web application running on tablets and phones can access the data through RESTful web services running on the pilot's website server. The results of a RESTful (Representative State Transfer) call can include multiple calls to CHS Web services which are less verbose, pre-validated and compressed. This helps mitigate problems with slow cellular connections or bad reception and reduce bandwidth. They are also required since SOAP services are not accessible via JavaScript queries, so the HTML application cannot access the CHS SOAP Web services directly.

It is important to note that the Tide Windows Module is a web-based application and not a native application.

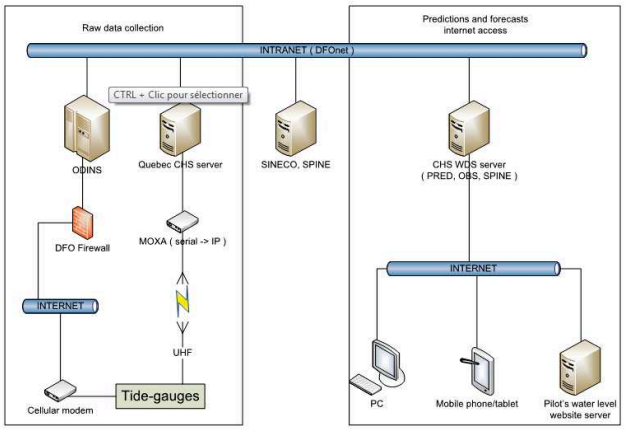

Figure 5. Data flow and process

3 THE TIDE WINDOWS MODULE

Every CPBSL pilot carries a Portable Pilot Unit (PPU) that consists of a tablet equipped with a state-of-the-art and sophisticated navigation software getting information from the ship's equipment, and supported by its own high precision GNSS (Global Navigation Satellite System) receiver. Pilot's tablet can also access the internet via 3G or any other better network. Cellular coverage on the St. Lawrence River approaches 95%. This allows web-based tools to be custom-developed for and used by pilots to manage predicted and forecasted water levels and the corresponding under-keel clearance.

As stated earlier, variations of up to 80 cm can be observed between predicted and actual water levels. The prudent mariner would benefit from knowing in advance when such variations are to occur. In Figure 7, taken from an actual event, the red curve is the predicted tide, as published, the black curve shows the actual tide gauge reading, whilst the green dotted line represents the SPINE corrected forecast. Note how fast the prudent mariner can lose 50 cm. One can also observe a shift of phase, particularly visible at low tide, from about 15:00 to 15:30. In this case, from the mariner's point of view, *the tide just kept falling!*

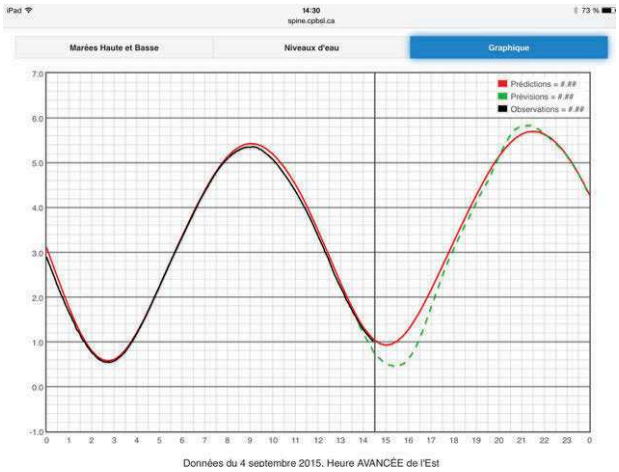

Figure 6. Tide prediction, reading and forecast

3.1 TIDE OPTIONS

The Tide Windows Module offers the pilot the following options:

- Simple high and low tides for 11 locations in the area;
- Tabular or graphic displays (Figure 6), featuring predictions, SPINE forecasts and actual readings of tide gauges;
- Ship's particulars' entries;
- Actual Tide Windows Module.

3.2 USING THE TIDE WINDOWS MODULE

To this day, the most important part of the pilot's job is to look out the bridge windows. So, one has to be extra careful when giving him another window to look at. From the beginning of the project, special attention was given to keep the Tide Windows Module as simple and user-friendly as possible, so that all the functionalities are a couple of clicks away, in order to keep the pilot's attention on the job at hand: the safe and efficient conduct of the vessel.

By feeding the ship's particulars (ship's beam, draft and speed) into the *Ships Information* dialogue box (Figure 7), and taking in consideration the channel's depth, the module will compute, using the UKC table, the water level required to proceed in the Traverse at the expected transit speed. In this case, UKC should be no less than 1.31 m and water level, no less than 4.31 m. The user can then switch to the graphic display (Figure 8) of the Tide Windows Module and assess, by observing the meeting points of the proper tide forecast curves and the shaded area, his earliest entry time for an upriver transit (red K-92 curve at 13:05) in the Traverse, as well as his exit time at the western limit of the Traverse (blue K-136 curve, at 16:05).

In this case, the vessel would have had 3 hours to transit the 16.6 M Traverse at 10 knots on the afternoon tide, from an earliest entry time of 13:05 at buoy K-92 to the latest exit time of 16:05 at buoy K-136. Note that the morning tide did not offer sufficient tide height to transit in these conditions. It can be seen at a quick glance that the appropriate curves either barely exceed the shaded area or are well inside that area, indicating inadequate water levels for safe transit.

If the pilot reduces the expected transit speed from 10 to 7 knots (Figure 9), he would be required to maintain 0.93 m UKC and then only need a water level of 3.93 m. As the transit speed is lowered, so is the shaded area on the graphic (Figure 10). The vessel could now enter the Traverse safely at about 12:45 (red K-92 curve) and exit at 16:45 (blue K-136 curve), giving it 4 hours to transit, either to accommodate other deep draft traffic or giving the vessel more operational flexibility. In that case, taking into acount the expected flood current, it could even have transited during the night tide between 01:10 and 03:30, as the required levels are met at every tide station over a long enough time period.

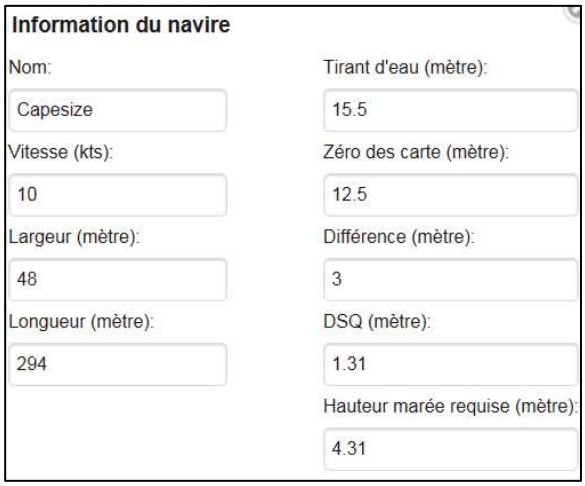

Figure 7. Ships Information dialog box

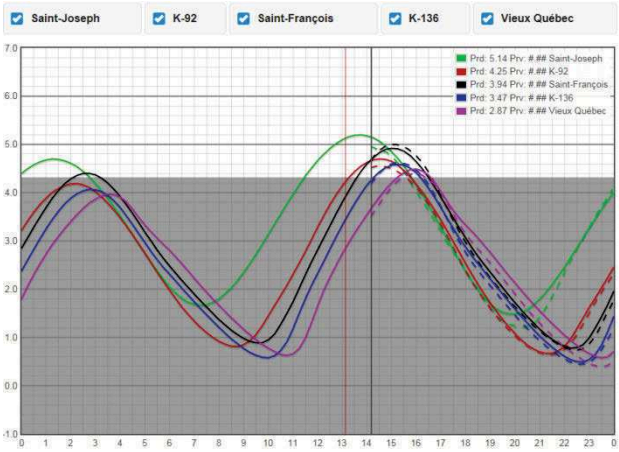

Figure 8. Water level curves

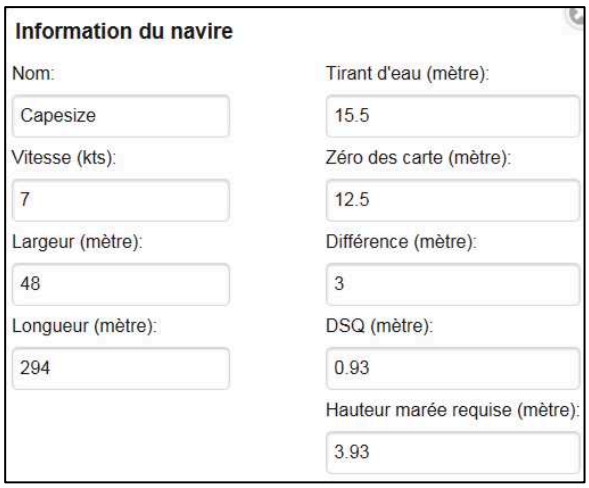

Figure 9. Ships Information dialog box

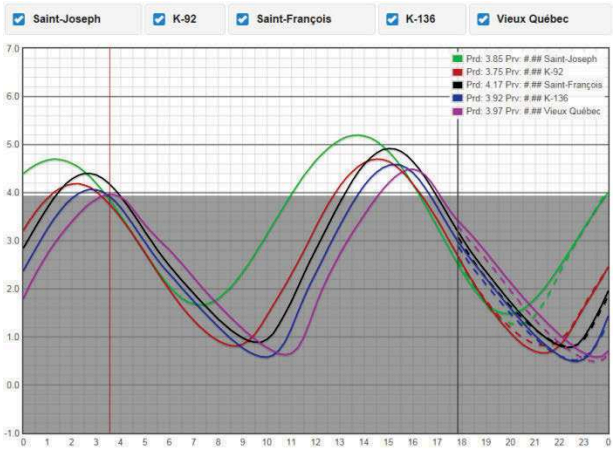

Figure 10. Water level curves

4 CONCLUSIONS

The Tide Windows Module was developed with the Canadian Coast Guard e-Navigation Strategy in mind. High-quality government data was customized by professional third parties to the specific needs of an end user.

The module offers the pilot a user-friendly tool to plan, manage and monitor the water levels and the under-keel clearance necessary for the safe and efficient transit through the Traverse du Nord.

Finally, in Chapter 2, five basic ingredients were mentioned for developing the module. A sixth was left out on purpose, e.g. the people. People from various organizations, with multiple backgrounds, among which navigation, oceanography, software design and communication technologies, brought together their expertise and knowledge to make this project a success. Their collective work is now in the hands of pilots, helping to make the St. Lawrence a safer and more efficient waterway.

5 ACKNOWLEDGEMENTS

We would like to express our greatest appreciation to Mr. Samir Gharbi for his valuable and constructive help in the research of information for the present publication.

6 REFERENCES

1. PIANC (2014). Harbour Approach Channels Design Guidelines. *Report No. 121-2014*.

2. Morse, B.; Simard, L. (1991). La détermination du dégagement sous quille. *Research Rep.*, Canadian Coast Guard, Fisheries and Oceans, Canada.

3. Gharbi, S. Delage, P.-L (2012). Squat Modelling for Merchant Vessels Transiting the St. Lawrence Waterway. *Research Report. Canadian Coast Guard, Fisheries and Oceans Canada*.

4. Gharbi, S. (2007). Squat of deep draft ships in St. Lawrence Waterway. *Summary Rep.*, Canadian Coast Guard, Fisheries and Oceans Canada.

5. Beaulieu, C.; Gharbi, S.; Ouarda, T. B.; Seidou, O. (2009) Statistical approach to model the deep draft ships' squat in the St. Lawrence Waterway. *Journal of Waterway, Port, Coastal, and Ocean Engineering* 135(3), 80-90. (doi:10.1061/(ASCE)WW.1943-5460.0000003).

6. Lefaivre, D., Hamdi, S., Morse, B. (2009). Statistical analysis of the 30-day water level forecasts in the Saint-Lawrence River. *Marine Geodesy*, pp. 30-41.

7. Lefaivre, D., D'Astous, A. & Matte, P. (2015). Hindcast of Water Level and Flow in the Saint-Lawrence River over the 2005–2012 period. *Submitted for publication.*

7 AUTHORS' BIOGRAPHIES

Simon Mercier is a master mariner and the President of the Corporation des pilotes du Bas Saint-Laurent. Before becoming a marine pilot, he served on merchant ships from 1985 to 2000.

Bernard Cayer has been serving as a pilot at the Corporation des pilotes du Bas Saint-Laurent since 1985. During his career, he has been involved with all aspects of tidal windows and UKC, electronic navigation (Pilot Portable Units) as well as the simulator of the Maritime Simulation and Resource Centre.

Germain Sauvé holds the current position of Software Analyst at Innovation maritime. He is managing and developing software projects related to electronic navigation, real-time simulation, electronic design and mobile applications. His previous experience includes research projects in medical analysis web portals, electronic design of GPS and communication systems for the marine industry, mechanical monitoring system and human machine interface running mobile device and Estimated Time of Arrival on the St. Lawrence software.

Denis Lefaivre holds the current position of research scientist at Fisheries and Oceans Canada. He is responsible for issuing ocean forecasts for the Gulf of St. Lawrence, Canada, and specifically developing water level forecasts for the St. Lawrence River.

Alain D'Astous holds the current position of research assistant at Fisheries and Oceans Canada. He is responsible for implementation and operation of ocean forecasts for the Gulf of St. Lawrence, Canada, and of water level forecasts for the St. Lawrence River.

4th MASHCON, Hamburg - Uliczka et al. (eds) - © 2016 Bundesanstalt für Wasserbau ISBN 978-3-939230-38-0 (Online)
DOI: 10.18451/978-3-939230-38-0_18

APPLICABILITY OF ARTIFICIAL NEURAL NETWORKS TO SQUAT PREDICTION OF VERY LARGE AND ULTRA LARGE CONTAINER VESSELS BASED ON MEASUREMENTS ON THE ELBE ESTUARY

B Reiter and **T Albers**, von Lieberman GmbH, Germany
F Treuel, Hamburg University of Technology, Germany
H Jansch, Federal Waterways Engineering and Research Institute, Germany

SUMMARY

An artificial neural network approach to squat prediction was implemented and the results were analyzed. Several artificial neural networks were created and trained on data for 15 voyages of very large and ultra large container vessels that were obtained during a measurement campaign concerned with the dynamic response of vessels on approach to and departure from the port of Hamburg. The artificial neural network was able to reproduce the training data with an accuracy better than +/- 0.30 m. Training the network on a partial dataset and testing it on a different voyage resulted in lower accuracy, with values diverging up to 0.50 m.

NOMENCLATURE

AP	Aft perpendicular
BOA	Beam over all (m)
cb	Block coefficient (-)
FP	Fore perpendicular
GNSS	Global Navigation Satellite System
GPS	Global Positioning System
LOA	Length over all (m)
RPM	Revolutions per minute (1/min)
Stw	Speed through water (m/s)
VDR	Voyage data recorder

1 INTRODUCTION

Artificial neural networks are a family of mathematical models within the framework of machine-learning models. They are based on a number of interconnected units, so-called neurons, which can be trained and subsequently used to classify or approximate arbitrarily large datasets. With recent advances in computer hard- and software their use has become near ubiquitous. Examples include, among many others, image recognition, biometrics, disease forecasting [1], prediction of estuarine salinity, stock market prediction [2], load forecasting for power grids [3], autonomous vehicle control and genome sequencing [4].

Ship squat is an effect that is nonlinearly dependent on a number of environmental circumstances. Since artificial neural networks have been used successfully to approximate similarly nonlinear relationships, their application to squat-prediction should be possible.

To achieve high levels of accuracy and reliability with these models a large and comprehensive amount of training data is required. During a measuring campaign for the German Federal Waterways and Shipping Administration (WSV) in cooperation with the Federal Waterways Engineering and Research Institute (BAW) concerning the behavior of large container vessels during their passage of the Elbe estuary Consulting Engineers von Lieberman collected a large amount of data pertaining to these voyages. These data are used as a basis for training several artificial neural networks and for evaluation of their performance as predictors for ship-squat.

2 DATA

2.1 DESCRIPTION OF COLLECTED DATA

During the measurement campaign data for 21 voyages of different types of vessels were collected. The vessels were selected from 7 classes relevant for the current traffic on the Elbe River. For most of these classes, two outbound voyages and one inbound voyage were surveyed. Among these classes were five classes with a vessel length larger than 300 m. This study concentrates on these vessels. Table 1 shows an overview of the classes with major dimensions.

Table 1. Classes of vessels

Class name	LOA [m]	BOA [m]
C335	335	42.8
C347	347	45.2
C366	366	51.2
C396	396	53.6
C400	400	58.6

Due to operational constraints, one outbound and two inbound voyages were observed for the C347-class.
The data collected on each voyage included

- GNSS and GPS position measurements of 6 antennae that were attached to the vessels (4 GNSS antennae, 2 GPS antennae) and recorded positions with a frequency of 2 Hz and 1 Hz respectively
- Salinity and water flow measurements, measured from a convoying vessel with a frequency of about 1 Hz
- VDR recordings of operational parameters (rpm, wind measurements, rate-of-turn etc.)

- Vessel dimensions and hydrodynamic parameters as described in the stability book (draught-dependent measures, derivatives and coefficients)
- Precise determination of actual freshwater draught

After thorough validation tests, all time-dependent variables were interpolated to 2 Hz and an equal timestamp to achieve data consistency and useable time series was applied.
Based on this data collection, additional parameters, such as vessel speed and heading, heel, trim and change of draft and trim were calculated and included in the database.

2.2 SELECTION OF DATA USED FOR NEURAL NETWORK DESIGN

Due to different reception conditions, GNSS post processing did not always result in positions of an adequate quality for a reliable analysis. Possible causes for this include atmospheric effects, local sources of electromagnetic interference or segments of the voyage with limited availability or unfavorable constellations of visible satellites resulting in lower quality observations. Because the measurements were made on a moving vessel, individual measurements could not be repeated to improve the quality. This made it necessary to limit the datasets that were used for training and analysis of the artificial neural networks to a subset of the collected data. Therefore, only database records with 4 or more available antennae of sufficient quality for position and attitude determination were used.

Of similar importance was limiting the data used for training to parameters that were not correlated to the variables that were to be predicted, i.e. squat at the forward and aft perpendiculars. This necessitated exclusion of e.g. the under-keel-clearance that was obtained from the dataset.

To avoid training the network to recognize only certain classes of ships, variables that varied discretely with those classes, e.g. ship length and beam, were also excluded from the training sets. With the perspective of possible future use for immediate squat forecasting aboard the vessel an effort was made to consider only variables that were both readily available to the ships command crew and characteristic for influencing squat behavior.

The variables selected for training were
- Position along river
- Course over Ground
- RPM
- Rudder angle
- Width of swept track
- Speed through water
- Trim angle
- Heel angle
- Water depth
- Water body cross section
- Draft or $c_{B,}$ alternatively

From these variables a number of combinations were tried as input parameters for the network.

Only data sections where all selected variables were recorded were used for inclusion in the input data. Timespans where vessel interaction and mooring took place were excluded from the data as well.

All of the above led to a significant decrease in available data points, resulting in a total of slightly over 500,000 from originally 835,000 data points, amounting to roughly 60% of the recorded data, which formed the basis for network training and analysis. While these are considerably less data than originally collected, it is still a large enough amount to expect artificial neural networks with a good performance as a predictor. Figure 1 shows a sample of the data consisting of the parameters speed through water, trim and squat at FP for a segment of the voyage, plotted against river kilometers. The visible gaps in the data are a result of either vessel encounters or reception problems.

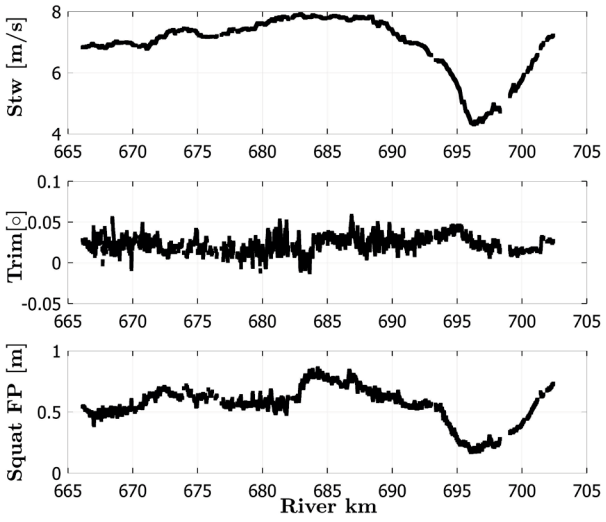

Figure 1. Squat results (sample) obtained during campaign

3 NETWORK ARCHITECTURE, TRAINING AND MODEL SELECTION

3.1 INTRODUCTION TO ARTFICIAL NEURAL NETWORKS

Since a lot of material is available on the basic concepts of artificial neural networks, only a brief introduction is provided. A more in-depth introduction can be found e.g. in [5].
An artificial neural network consists of nodes, so-called neurons, which are usually organized in different layers. Numerical values are passed between these nodes

according to specific rules that define the network architecture. Each node has an activation function that determines its output based on the value of the input. The inputs to a node are assigned weights and bias functions that are changed during the training phase to optimize the network's output to achieve an accurate representation of the training data. The layers are called hidden layers if all inputs and outputs to and from these layers are only to other layers of the network, as opposed to external inputs or outputs of values.

Observed errors between the predicted outcome and the provided training outcome are used to adjust the weights and biases during the next iteration. Several algorithms have been developed for this purpose. After a stopping criterion is reached, training is considered to be finished. If a division of the available data into a training set and a test set was made before training began, the network's performance as a predictor can be estimated by analyzing the error that it produces using the test set.

A commonly used type of artificial neural network is a feed-forward network. In this network architecture, the values resulting from each layer are passed along to the next layer, and each sample of the dataset is treated as independent of previous or following samples.

Another type of network are recurrent neural networks. In this type of network, node values or outputs that were obtained from the network can be fed back into the network or into network layers as additional inputs that augment the samples by conveying information about the state of the network during application to the current or previous samples of the dataset. This makes it possible to use the network for the analysis of time-series, including the analysis of time-lagged effects of input parameters. To further illustrate this distinction, the treatment of RPM in the two network types is given as an example. In the regular feed-forward network, the RPM value for one sample, i.e. the collection of data for one timestep, is passed from the input layer to the hidden layer. In the hidden layer, an output is calculated based on these values and the weights and activation functions of the neurons and passed on to the neurons of the output layer. The neurons of the output layer calculate the final output for this timestep from these values. Intermediate values or the final result of this timestep do not influence the treatment of the next sample. Consequently, in this type of network, squat is only being influenced by the current RPM-value. In a recurrent network, these steps are identical, but in addition to the input based on the measured data, the outputs of the hidden layer or the final results for one timestep can be stored and used as additional input variables for subsequent samples. This way, previous RPM values can influence the result for a later sample. Other network types include e.g. networks where the number of nodes per layer is not fixed but adjusted during training.

3.2 NETWORK ARCHITECTURE

The artificial neural network used in this study was a simple two-layer feed-forward artificial neural network created using Neural Network Toolbox of MATLAB [6]. It consisted of one hidden layer and one output layer. The hidden layer consisted of neurons with a hyperbolic tangent sigmoid transfer function. The number of neurons on the hidden layer was kept constant during training, but several networks with a different number of neurons on the hidden layer were trained as a basis for a comparison between them. The output layer consisted of two output neurons with a linear transfer function. The outputs of these two neurons were selected to be squat at FP and AP, respectively.
The training algorithm used was the MATLAB default Levenberg-Marquardt backpropagation algorithm with validation based early stopping.

3.3 NETWORK TRAINING

For training the neural network, different approaches were used. The first approach involved training of the neural network on a dataset including all voyages. The datasets for each training session were split into three subsets, the training, validation and test set. Splitting was done randomly to create sets with a previously specified sample percentage.
For the second approach, subsets of vessels were created that contained only voyages of vessels belonging to one class. This was done to arrive at conclusions as to whether networks trained on subsets can be used to make predictions about different subsets and if networks that were trained on two voyages for one vessel type could be used to arrive at better predictions for the third voyage than networks trained on datasets including different vessel classes. The datasets were split in a way similar to the divisions for the first approach. Additional testing was performed using data not included in the initial selection.
For all approaches the training data were normalized in a preprocessing stage to span the interval [-1, +1] to improve training performance and avoid numerical errors.

3.4 MODEL SELECTION

In terms of artificial neural networks, model selection describes the process of evaluating which one of several trained artificial neural networks produces the best results with regard to the test data. This includes comparisons between networks of different sizes, the use of different input parameters and different training runs. In this study, several networks with different numbers of neurons in the hidden layer were tested. In addition, different combinations of input variables were used for training. Evaluation of the artificial neural networks was performed by comparing the results of the network with measured squat data. To avoid overfitting the network to the training data, an upper limit for the hidden layer was

set at 15 neurons. Using less than 10 neurons resulted in a decrease in accuracy with no apparent improvement in generalization of the network to out-of-sample data. The input parameters were chosen to give as adequate a representation of possible influences as possible. The inclusion of the vessels' position along the river, for instance, was selected to address possible localized phenomena that were not covered by the other variables, such as river bottom structure or influences of river tributaries.The best results on the training set were obtained from a network with 10 hidden nodes and all input parameters mentioned in 2.2.

4 RESULTS

The study yielded mixed results. While on the one hand a good approximation of the observed data was possible using the artificial neural network approach, the use for predictions on different inputs than those used for training resulted in moderate to large errors.

Figure 2 shows a section of the comparison between measured and predicted ship squat at FP for the network that was trained using all but 15% randomly selected data for training. The differences in this section of the data are between 0.05 m and 0.10 m. Figure 3 shows a histogram of the differences between predicted and measured squat at FP for the whole dataset. As can be seen, most differences have a magnitude between +0.30 m and -0.30 m, with the majority lying between +0.10 m and -0.10 m.

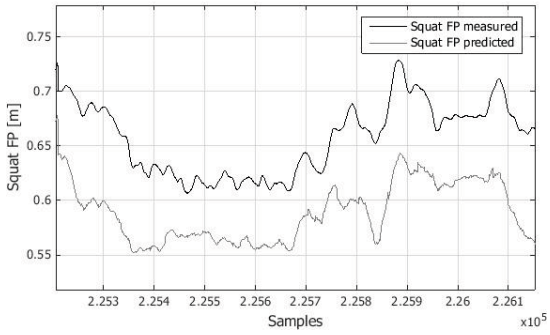

Figure 2. Comparison measured vs. predicted squat FP

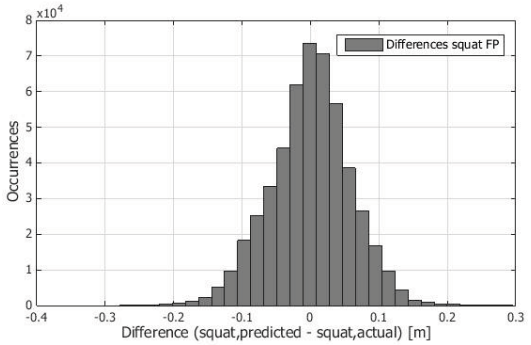

Figure 3. Differences between predicted and measured squat FP

Figure 4 shows the squat prediction of a network trained on data for two voyages of the C400 class for the third voyage of this class in comparison to measured squat data. The differences in this section of the comparison show a wider spread than the differences in figure 1, in a range between 0.00 m and 0.25 m. In Figure 5, the histogram for these differences shows a spread of the differences that is about equal to the spread visible in figure 2, but with a different distribution. While squat is underestimated for only a few data points and only up to -0.15 m, a marked overestimation of the actual squat is evident, with a considerable percentage of values more than 0.20 m up to 0.50 m larger than the observed values. Similar results were obtained for different classes and inter-class comparisons.

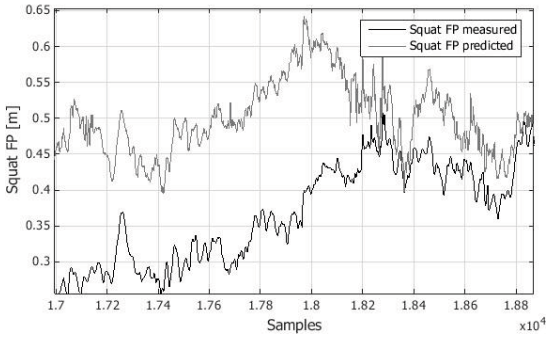

Figure 4. Comparison measured vs. predicted squat FP, C400

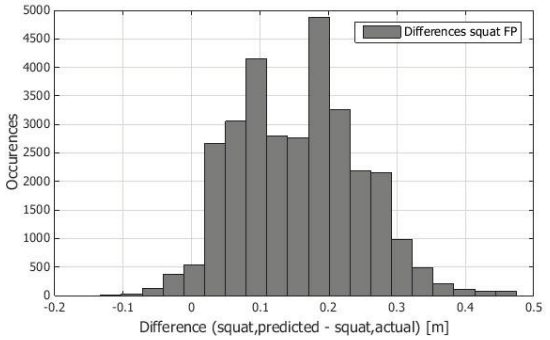

Figure 5. Differences between predicted and measured squat FP, C400

5 DISCUSSION OF RESULTS

One cause for the failure to accurately predict squat for voyages other than those on which the network was trained were parameters with values outside of the range on which the network was trained. For example, vessels with drafts larger or smaller than the drafts included in the training data showed squat behavior that differed markedly from the squat predicted by the network.

Another possible cause for the failure to accurately predict squat may have been a non-optimal choice of input parameters, by neglecting other influences on squat behavior, such as e.g. immersed ship cross-section or different ship specific parameters.

6 OUTLOOK

To further investigate the applicability of artificial neural networks in the context of squat prediction a number of additional approaches to network design should be tried. One approach the authors plan to pursue is the use of recurrent artificial neural networks in order to cover possible time-delayed influences. Additionally, different selections or other combinations of input parameters will be considered and their influence investigated, e.g. the use of Froude-numbers.

Other possible avenues of research include different network architectures with additional layers or only partially connected layers, separate networks for squat prediction at the individual perpendiculars or using several networks for prediction and averaging their outputs.

The inclusion of different types of vessels in the future is also desirable. However, this would be dependent on the procurement of an adequately large database containing possible training data for individual ship types. A first step in this direction could be testing the models on data acquired for bulk-freighters in the context of the squat-study this paper is based upon. However, the cb-values of those ships lie far outside the values that were available for training the container vessel model, which makes a direct applicability of the model for those vessel types rather unlikely.

After a sufficiently accurate artificial neural network model has been found, knowledge discovery techniques for neural networks could be utilized. A first approach could involve gradually reducing the input parameters until a good prediction is still possible, in order to determine the main factors influencing the prediction of squat behavior in the context of these artificial neural networks.

7 CONCLUSIONS

While this study highlighted some of the difficulties of using artificial neural networks for the prediction of ship squat, the authors remain optimistic about the potential of this family of machine learning models. With the artificial neural networks that were created and trained during this study, Squat prediction with an accuracy of 0.5 m could be achieved in a large number of cases. This kind of accuracy must be considered insufficient for practical applications; it is however an encouraging result considering the simplicity of the model used in this study. Further refinement of the network type, architecture and input parameters is expected to improve prediction accuracy.

8 REFERENCES

1. Amato, F.; López, A.; Peña-Méndez, E.M.; Vaňhara, P.; Hampl, A.; Havel, J. (2013). Artificial neural networks in medical diagnosis. *Journal of applied biomedicine* 11.2: pp 47-58. doi: 10.2478/v10136-012-0031-x.

2. Vui, C.S.; Soon, G.K.; On, C.K.; Alfred, R.; Anthony, P. (2013). A review of stock market prediction with Artificial neural network (ANN). *International Conference on Control System, Computing and Engineering (ICCSCE)*, Penang, Malaysia, IEEE: pp. 477-482.

3. Park, D.C.; El-Sharkawi, R.J.; Marks II, R.J.; Atlas, L.E.; Damborg, M.J. (1991). Electric load forecasting using an artificial neural network. *IEEE Transactions on Power Systems* 6.2: pp. 442-449.

4. Wu, C. H.; McLarty, J. W. (eds.)(2012). *Neural networks and genome informatics*. Vol. 1. Elsevier Science

5. Hastie, T.; Tibishirani, R.; Friedman, J. (2009). *The Elements of Statistical Learning*. Springer-Verlag New York.

6. MATLAB and Neural Network Toolbox Release 2013a. (2013) *The MathWorks Inc., Natick, Massachusetts*

9 AUTHORS' BIOGRAPHIES

Dr.-Ing. Thorsten Albers is Head of the Department of River and Coastal Engineering and member of the Management Board at Consulting Engineers von Lieberman. He is responsible for project management and works as a consultant for GIZ and World Bank in the field of coastal zone management in Southeast Asia.

Hanne Jansch, Dipl.-Ing. (FH), currently holds the position of Research Engineer at the Federal Waterways Engineering and Research Institute (BAW), Hamburg Office, Germany. She conducts investigations into ship/waterway interaction for the coastal department; within the Waterways and Shipping Administration project for determining dynamic response of vessels in fairways, she is responsible for the quality control. Her previous experiences include field measurements such as offshore and onshore surveys worldwide.

Berthold Reiter, Dipl.-Ing. (TU), currently holds the position of project engineer at Consulting Engineers von Lieberman GmbH, Hamburg, Germany. He is responsible for data analysis and GIS applications with a focus on hydraulic engineering.

Frederik Treuel, Dipl.-Ing. (TU), is a Research Associate at Hamburg University of Technology (TUHH), Hamburg, Germany. As a graduated civil engineer he is responsible for project management and performance of R&D projects in coastal engineering.

4th MASHCON, Hamburg - Uliczka et al. (eds) - © 2016 Bundesanstalt für Wasserbau ISBN 978-3-939230-38-0 (Online)
DOI: 10.18451/978-3-939230-38-0_19

APPLICATION OF POTENTIAL FLOW METHODS TO SHIP SQUAT IN DIFFERENT CANAL WIDTHS

T Gourlay, Curtin University, Australia
E Lataire, Ghent University, Belgium
G Delefortrie, Flanders Hydraulics Research, Belgium

SUMMARY

This paper presents a comparison of numerical methods with model test results for squat (sinkage and trim) of a 1:75 KVLCC2 model in the Flanders Hydraulics Research towing tank, at a range of rectangular canal widths and depths. The numerical methods are the *Linear-2D* and *Nonlinear-1D* methods in *ShallowFlow*, the *Double-Body* method in *HullWave* and the *Rankine-Source* method in *GL Rankine*. Analysis of the model tests showed that in the narrowest canals, mass flux past the ship was not conserved, nevertheless it appears that the *Nonlinear-1D* method may give good results for the narrowest canals. The *Linear-2D* method was found to give good results in the widest canal, particularly at the shallowest water depth. The *Rankine-Source* method was found to give good results for the widest canal, particularly at high speed. The *Double-Body* method was found to give quite consistently good results across all conditions.

NOMENCLATURE

AP	Aft perpendicular
B	Ship beam (m)
$b(x)$	Local ship waterline breadth (m)
C_B	Block coefficient based on L_{PP} (-)
F_h	Froude depth number (-)
FP	Forward perpendicular
g	Gravitational acceleration = 9.806 m/s^2
h	Water depth (m)
L_{PP}	Length between perpendiculars (m)
r	Radial distance from source (m)
$S(x)$	Local ship cross-section area (m^2)
s_{mid}	Midship sinkage (m)
T	Ship draft (m)
U	Ship speed (m/s)
w	Rectangular canal width (m)
X	=0 at start of canal test section, positive in direction of ship travel
x	=0 at transom, positive forward (m)
y	=0 on centreline, positive to port (m)
z	=0 at keel, positive upward (m)
λ	scale factor (-)

1 INTRODUCTION

Ships operate in different types of shallow-water areas where they are at risk of grounding due to squat, heel and wave-induced motions. Shallow-water areas might be open shallow water (such as Torres Strait), dredged channels (such as most approach channels across continental shelves) or canals with surface-piercing banks (such as river ports or inland waterways). The main focus of this paper is to work towards being able to predict ship squat accurately in any bathymetry.

Model tests are necessarily conducted in tanks with surface-piercing banks, so that dredged channels and open water cannot be simulated at model scale. For these cases, ideally a numerical method is used that has been validated against model test data in more restricted waterways. Typically the numerical method may be a potential flow method, a Computational Fluid Dynamics (CFD) method, or an empirical method. In this paper four potential flow numerical methods are considered.

The model test program considered here is unique in providing comprehensive measured squat results at six different canal widths. These model test results are ideal for validating numerical methods over a range of canal widths. The tests were done in a simple rectangular cross-section, which is realistic for locks, but not for river ports or inland waterways. Therefore numerical methods should also be assessed against model test results with realistic sloping bank conditions, such as [12, 15].

2 MODEL TESTS

2.1 EXPERIMENTAL PROGRAM

The hull considered here for model tests and numerical analysis is the KVLCC2 hull [8, 13]. This research hull, developed by Korea Research Institute of Ships and Ocean Engineering (KRISO) is representative of a Very Large Crude Carrier (VLCC).

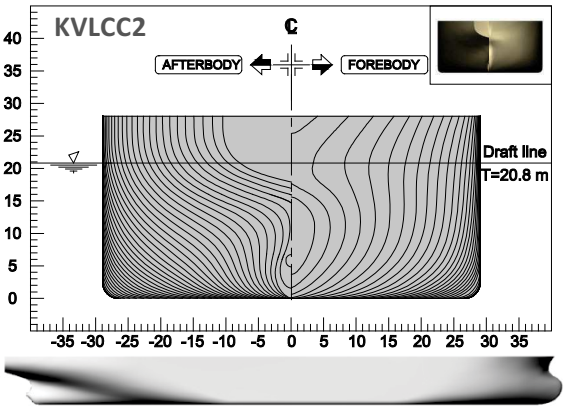

Figure 1. Body plan (top) and profile (bottom) of KVLCC2 hull

Model tests were undertaken in June 2010 in the Towing Tank for Manoeuvres in Shallow Water (cooperation Flanders Hydraulics Research – Ghent University) [1] on a 1:75 scale model of the KVLCC2. The tests are described in [9]. Principal particulars of the model and full-scale hull are shown in Table 1.

Table 1. Principal particulars of the KVLCC2 hull at model-scale and full-scale

	Model-scale	Full-scale
λ	75.0	1.0
L_{PP}	4.267m	320.0m
B	0.773m	58.0m
T	0.277m	20.8m
C_B	0.810	0.810

The towing tank has a length of 88m and width of 7.00m. This width is 9.05 times the model beam (i.e. w/B=9.05). By using a 30m-long vertical wall parallel to the tank walls, this width could be reduced to simulate successively narrower rectangular canals. At each canal width, various water depths were tested, as shown in Table 2.

Table 2. Model test combinations of canal width and water depth

Canal parameter	Values model-tested
w/B	1.05, 1.25, 1.70, 2.50, 5.00, 9.05
h/T	1.05 (only for w/B=1.05)
	1.10, 1.35, 1.50 (all widths)

A range of ship speeds was undertaken for each canal configuration, as described in [9].

2.2 WAVE PROFILE OBSERVATIONS

The ship model was towed at a constant forward speed in the rectangular cross sections at different widths and water depth combinations (Table 2, Figure 2). At sub-critical speed conditions the water displaced by the sailing vessel has to flow under and along the vessel. This results in a return flow directed opposite to the sense of the motion of the vessel. A consequence of this return flow is a high flow velocity relative to the ship and hence a low pressure region on the ship's hull (Bernoulli's principle) which results in a decrease of the water level around the vessel. This is the cause of the running sinkage (or squat).

Based on the conservation of mass, the lower the water depth and/or the smaller the canal width the faster this return flow will be. However, the canal was open at both inlet and outlet, so water from the outer section could freely flow in and out of the test section during a test run. This was specifically observed for the most confined cross sections, in which the full ship model acts like a piston, pushing the water out of the canal section. This effect has previously been observed and predicted by potential-flow theory at high speed [5], but in this case it appears that it may be affected by boundary-layer friction. The resulting wave system travels towards the far end of the towing tank, reflects and enters the test section again. The assumption of a mass conservation within the smaller cross section is no longer valid.

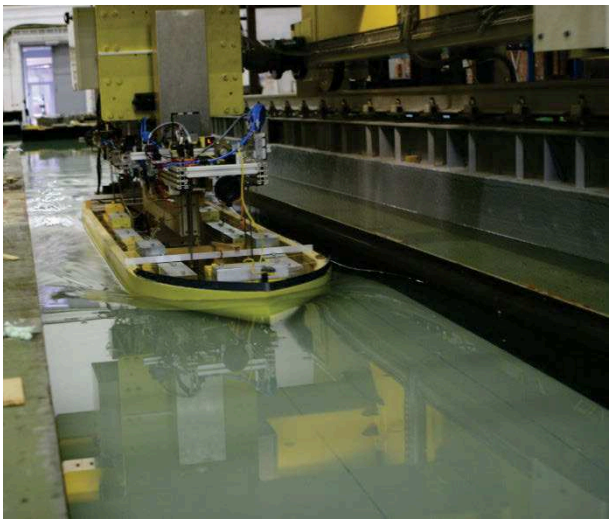

Figure 2. KVLCC2 model during an experiment.

During the model tests five wave gauges registered the water surface at five discrete positions in the towing tank (Figure 3). Two at the longitudinal centre of the installed rectangular cross section, one at starboard (wave gauge 1) and the other at port side (wave gauge 5) of the ship. Two wave gauges were positioned at the outlet of the test section, of which one was in the extended test section (wave gauge 4) and the other behind the starboard side wall (wave gauge 2). The final wave gauge was positioned in the extension of the centreline of the installed cross section but 15m away from the outlet (wave gauge 3).

The wave registrations at these wave gauges will be compared for five model tests. All tests are carried out at the same forward speed (6 knots full scale) and at the same water depth (h=1.50T). This water depth was selected because of the large availability of test results, however the observations are valid for all water depths tested. The lateral position of the ship model was always on the centreline of the installed cross section.

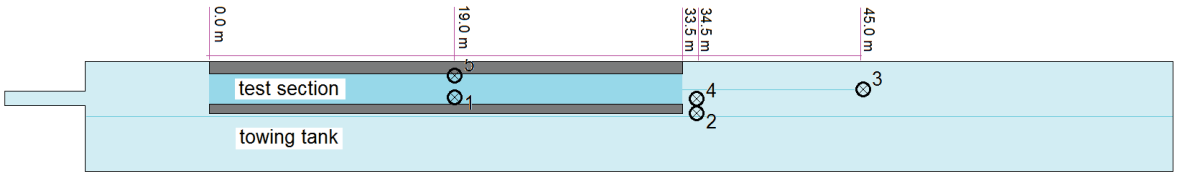

Figure 3. Positions of the wave gauges in the towing tank

The registration of the wave gauges 1 and 5 are plotted to the longitudinal position of the midship of the ship model in the cross section in Figure 4. Different observations can be made. The first peak of the water level (X is about 7m) is caused by the acceleration of the ship model. This acceleration results in a leading wave running through the tank at the critical speed. The wave height increases with decreasing canal width. After this wave has passed the wave gauges, the water level returns to its initial position (X=15m) and when the ship passes wave gauges 1 and 5 a clear water level drop is visible (17m<X<21m) which results in the squat of the ship. When the ship has passed, the water level returns to the initial water level except for the two smallest test sections (w=1.25B and 1.05B). For the latter the water level in the cross section is lower than the initial water level for a longer period of time.

The wave registration at the outlet of the test section (Figure 5) shows again the water level increase because of the acceleration of the ship model (5m<X<15m) but there is a second, longer water level increase when the ship is at position X=20m until the ship is at the end of the installed section (X=33m). This is caused by the previously described piston effect caused by the ship. The more confined the cross section the more water is pushed out and the higher the water level increases. This is almost absent in the 5.00B wide cross section but easily discernible in all the smaller cross sections. The ship only decelerates when it is entirely out of the installed cross section and as such the water level drop when she passes the wave gauges is again clearly visible (33m<X<37m).

Figure 4. Wave registrations for two wave gauges at 5 different cross section widths

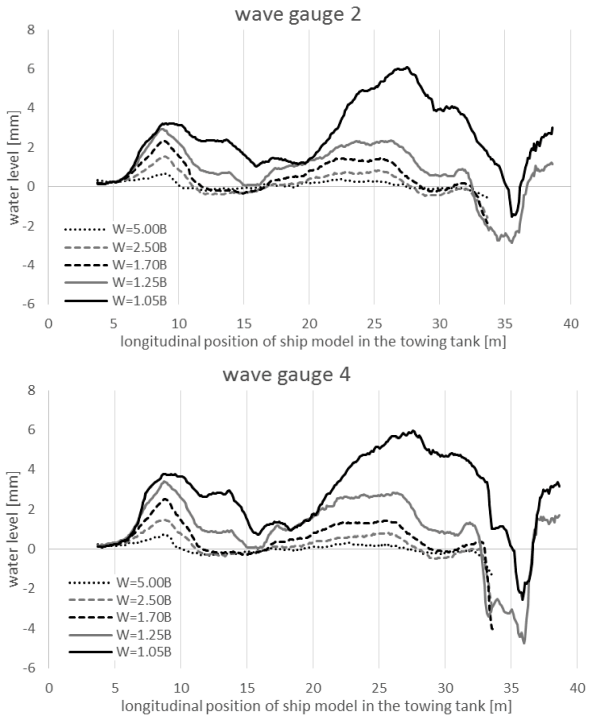

Figure 5. Wave registrations for two wave gauges at the outlet of five different cross section widths

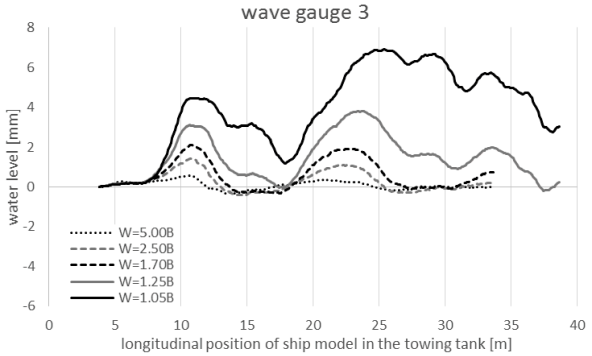

Figure 6. Wave registrations at the open section of the towing tank

Wave gauge 3 is positioned further away from the test section under consideration and the ship model stopped long before it reaches this gauge. In Figure 6 the water level increase because of the acceleration phase can be observed again (8m<X<15m). From X=18m a water level increase is observed which can be linked to the piston effect. This results in a long wave because the water level increases while the ship model is travelling through the canal section and at the same time pushing water out of the canal section. If the water level would have been measured for a longer period of time (after the model test terminated) then a water level drop would be observed. This long wave bounces back at the end of the towing tank and enters the cross section at the outlet again. Obviously, after some time the water level in the entire tank returns to its initial level.

3 NUMERICAL METHODS

3.1 LINEAR-2D METHOD

The *Linear-2D* method is the slender-body shallow-water theory of Tuck for rectangular canals [14]. Each hull cross-section is represented by a vertical line source with source strength proportional to the rate of change of section area, as shown in Figure 7.

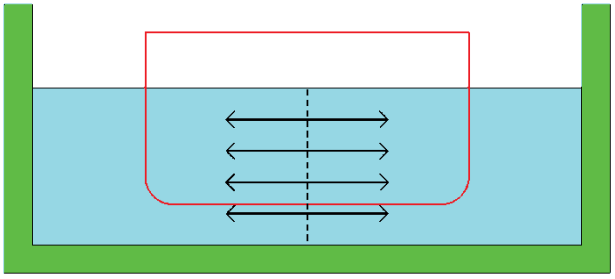

Figure 7. *Linear-2D* method. Each hull section is represented as a vertical line source, with strength proportional to the rate of change of section area.

The wall boundary conditions on the outside of the canal are correctly applied, but the method does not take account of the nonlinear blockage effect of the ship in the canal. The sources are assumed to lie on the hull centreline, rather than on the outside of the ship as done in the panel methods.

Flow speeds are averaged in the vertical direction, incorporating the shallow-water assumption. Therefore this is a two-dimensional method, with flow speeds varying longitudinally and transversely. The slender-body assumption is that ship beam and draft are small relative to ship length. This infers that flow disturbance velocities are small relative to the ship speed, and free surface slopes are small. Quadratic and higher-order terms in disturbance velocities and free-surface slope are therefore neglected. The method is implemented in the CMST in-house code *ShallowFlow*, as described in [4].

For this and the other methods, all calculations were done at full scale. Since potential-flow methods were used, there is no scale effect on any of the dimensionless output quantities.

An IGES file of the KVLCC2 was obtained from the SIMMAN workshop [13]. This was imported into MAXSURF software and used to develop offsets at 50 evenly-spaced sections from the transom to the front of the bulb, and 11 evenly-spaced waterlines from the keel to the design waterline. The hull offsets are shown in Figure 8.

ShallowFlow uses hull section areas and waterline breadths as input. Section areas were calculated using Simpson's rule, with correct treatment of the bilge radius along the parallel midbody. Section areas and waterline breadths used for the KVLCC2 are shown in Figure 9.

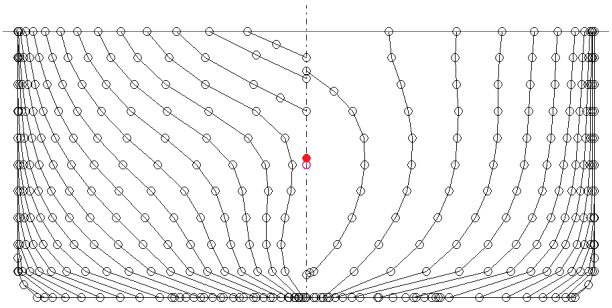

Figure 8. KVLCC2 offsets (circles) used to develop *ShallowFlow* and *HullWave* hull files

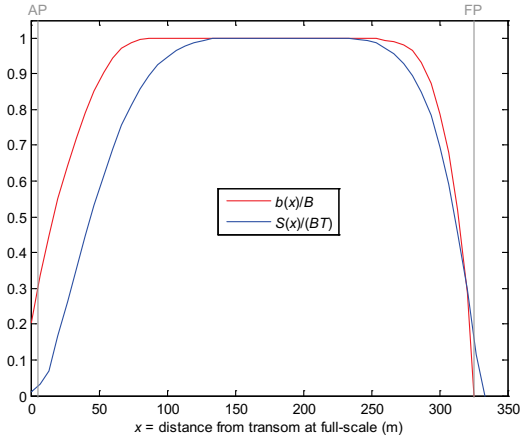

Figure 9. Section area and waterline breadth curve for KVLCC2, as input to *ShallowFlow*

All run times given here were on an Intel i7-940 2.93 GHz processor with 12 GB of RAM. Run time for the Linear 2D method was 3.8s to do a total of 200 speeds for a single bathymetry.

3.2 NONLINEAR-1D METHOD

The *Nonlinear-1D* method is the hydraulic theory described in [6], designed for narrow canals. This solves the mass conservation and Bernoulli equations, with constant flow velocity assumed across each canal cross-section, as shown in Figure 10.

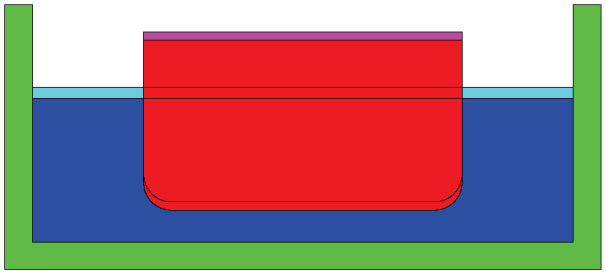

Figure 10. *Nonlinear-1D* method. Pink shows static floating position, red shows squatted position. Light blue shows static free surface, dark blue shows actual free surface.

Horizontal and vertical velocity components are neglected, and the longitudinal flow velocity is assumed constant across each cross-section. The water cross-section area (dark blue area shown in Figure 10) is calculated allowing for the squat of the ship and the changed free surface height, approximating the ship as wall-sided at the waterline. Therefore this is a one-dimensional, but highly nonlinear, method.

The *Nonlinear-1D* method is implemented in *Shallow-Flow* and uses the same hull input files as the *Linear-2D* method described above. Run time for this method was 292s to do a total of 200 speeds for a single bathymetry.

3.3 DOUBLE-BODY METHOD

The *Double-Body* method is developed in this article. It is an extension of the method commonly used for ships in deep water, and less commonly for ships in shallow open water.

For a ship in deep water, the double-body method involves reflecting the submerged ship hull about the static free surface, so as to model the free surface as a rigid wall, as shown in Figure 11.

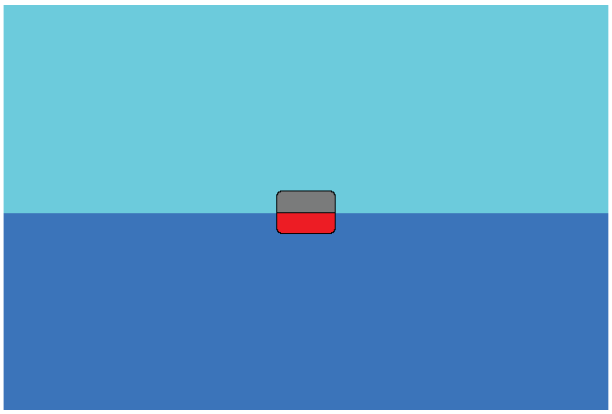

Figure 11. Double-body method for a ship in deep water (stern view). Submerged hull shown in red, image hull shown in grey.

The double-body method is commonly used to approximate the flow field around ships at low speed in deep water. The approximation can be exploited in model testing, by using a double-body of the ship in a recirculating water flume or wind tunnel (see e.g. [10]).

For a ship in open shallow water a double-body method using an infinite vertical array of ship reflections was developed [11], as shown in Figure 12. In this article the method is extended to model a ship in a shallow canal with vertical walls, by using an infinite array of horizontal and vertical reflections, as shown in Figure 13.

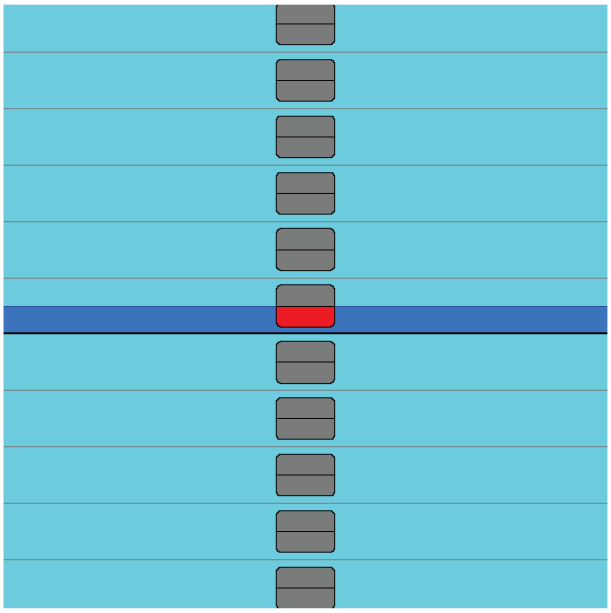

Figure 12. Double-body method for a ship in shallow open water (stern view). Submerged hull shown in red, image hulls shown in grey.

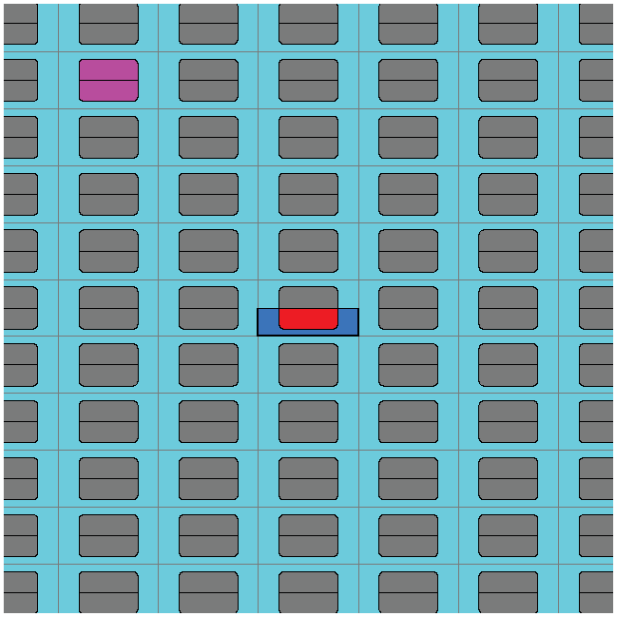

Figure 13. Image system stretching to infinity for ship in a shallow rectangular canal (stern view). Submerged hull shown in red. Image hulls shown in grey. Example image hull shown in pink as used in Figure 15.

Other than the horizontal reflections, the analysis goes over unchanged from that described in [11]. A standard Hess and Smith panel method [7] is used, implemented in CMST's submarine hydrodynamics code *HullWave* [2]. Although *HullWave* is written to model Havelock sources, it can be run in Rankine source mode by removing the Havelock free-surface correction terms.

HullWave requires a hull surface mesh as input. Because of the computational intensity of the *Double-Body*

method, a relatively coarse mesh of 868 panels was used, as shown in Figure 14. Convergence testing showed that sinkage and trim were well-converged with this number of panels.

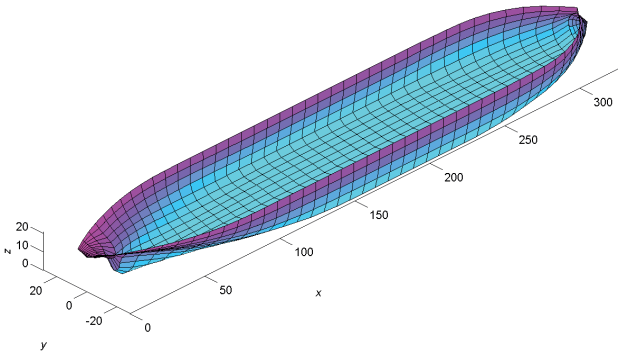

Figure 14. 868-panel surface mesh (434 panels port side) used for *HullWave* calculations. Hull meshed up to static waterline.

Each hull panel is considered to be a source of uniform source density. The wall boundary condition is applied at the null point of each panel, as described in [7]. This includes contributions from the submerged hull as well as all of the hull reflections shown in Figure 13 (theoretically out to infinity). For the meshed hull shown in Figure 14 this results in a 434 x 434 matrix equation for the 434 unknown source densities on the port side of the hull.

The method was tested first in shallow open water (Figure 12), where it was found to agree with [14] for a slender hull, and give slightly higher sinkage than [14] for the KVLCC2 hull, as expected. Convergence was rapid with vertical reflections for the shallow-open-water case.

For the shallow-canal case, convergence is slower and can be assessed as follows. Consider the radius vector from an image source panel to a hull receiver panel, as shown in Figure 15.

Due to the symmetry, transverse and vertical velocity contributions from diagonally opposite hull images quickly tend to cancel out for distant hull images. No such cancellation occurs for longitudinal velocities, due to the ship's fore-aft asymmetry. Radial velocities are $O(1/r^2)$, so longitudinal velocities are $O((1/r^2)(L_{PP}/r))$. Summing the contributions from all hull images is $O((1/r^2)(L_{PP}/r)(2\pi r\, dr))$, which is convergent as $r \to \infty$.

Run time for the *Double-Body* method was 25 minutes for a single bathymetry. A single run gives the results for all speeds, due to the quadratic speed dependence.

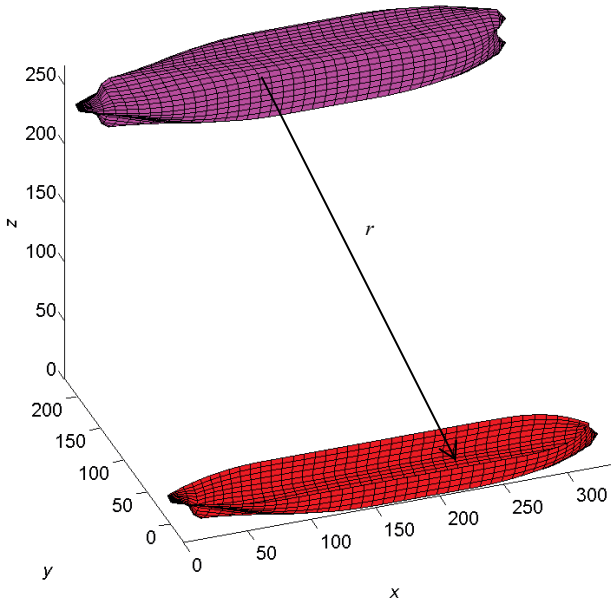

Figure 15. Radius vector from source panel on image hull (pink) to receiver panel on actual submerged hull (red), distance *r*. See also Figure 13.

3.4 RANKINE-SOURCE NUMERICAL METHOD

The *Rankine-Source* method is implemented in *GL Rankine* [16] using Rankine source patches on the hull and free surface, and exact hull and free-surface boundary conditions.

GL Rankine uses an input STL file and automatically generates a hull surface mesh, based on input mesh size parameters. The surface mesh generated by *GL Rankine* and used for these calculations is shown in Figure 16.

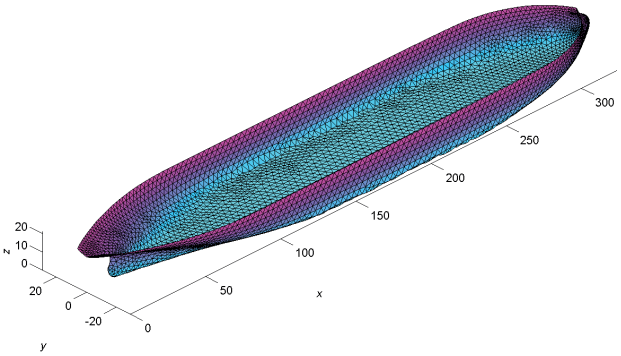

Figure 16. 7936-panel surface mesh (3968 panels port side) used for *Rankine-Source* calculations. Hull meshed up to static waterline.

These calculations were run by CMST under an academic license supplied by DNV GL. Run times were in the order of 1 minute for each ship speed in each bathymetry.

4 RESULTS AND DISCUSSION

Comparisons between the four potential-flow methods and model test results are shown in Appendix A for midship sinkage and Appendix B for dynamic trim. Ship speed is non-dimensionalized using the Froude depth number:

$$F_h = \frac{U}{\sqrt{gh}} \quad (1)$$

Most of the model tests were done with propeller operating at the self-propulsion point (labelled "Self-prop."). For w/B = 9.05, tests were also done with the propeller fixed (labelled "Towed"). We can see that the self-propelled model tends to have larger midship sinkage and less bow-down trim than the towed model, which is in line with comparisons for container ships [3].

Some of the tests involved very low speed, at which the Rankine-Source method has difficulty resolving the very short wavelengths produced. Therefore converged results for the Rankine-Source method could not be obtained in all cases. The other methods are shown for all cases.

As discussed in Section 2.2, mass flux past the ship was not conserved in the model tests for w/B = 1.05 and 1.25. We see that measured trim is bow-up for these model tests, with water being pushed ahead of the ship and a wave trough trailing behind the ship. The numerical methods all assume conservation of mass flux past the ship, so these comparisons are not fair comparisons. Further numerical and/or experimental work are required in order to make fair comparisons between theory and experiment for the narrowest canals. Qualitatively speaking, we may say that the effect of having non-constant mass flux may be to cause a bow-up trim and decrease the sinkage. We may infer that the *Nonlinear-1D* method is likely to give the most accurate sinkage predictions for the narrowest canals.

For w/B = 1.70 and 2.50, the *Nonlinear-1D* and *Double-Body* methods are close to the measured sinkage results, while the *Linear-2D* and *Rankine-Source* methods significantly under-estimate the sinkage. It was expected that the *Rankine-Source* results would be larger than the *Linear-2D* results and closer to the *Double-Body* results, so further work will be done in future on the *Rankine-Source* method in narrow canals. The ship-piston effect on the measured results is diminishing at this canal width, which results in a measured trim that changes sign, but which is still small compared to the numerical methods for w/B = 1.70.

The case w/B = 5.00 is the "cross-over" point for the *Linear-2D* and *Nonlinear-1D* methods. For narrower canals, the *Nonlinear-1D* method gives larger sinkage (because of the nonlinearity) and is closer to the model test results; for wider canals the *Linear-2D* method gives larger sinkage (because it predicts higher flow speeds near the ship) and is closer to the model test results. At this canal width, all four potential methods give similar sinkage predictions, which under-estimate the measured sinkage at this canal width. The *Linear-2D* and *Double-Body* methods give similar trim predictions, which are very close to the measured results for $F_h < 0.4$, but under-predict at higher speeds. The *Rankine-Source* method gives generally larger bow-down trim than the *Double-Body* and *Linear-2D* method here, and is further from the model tests at h/T = 1.10 but closer at h/T = 1.35.

For w/B = 9.05, the *Linear-2D*, *Double-Body* and *Rankine-Source* methods all give similar sinkage for $F_h < 0.4$, and all are close to the model test results. The predictions are smaller than the self-propelled model results by 15%, 13% and 13% respectively at F_h = 0.43, and 21%, 22% and 16% respectively at F_h = 0.50. The *Rankine-Source* method again predicts larger bow-down trim than the *Linear-2D* and *Double-Body* methods. All of these methods give trim predictions which are close to the measured results, with differences comparable to the difference between towed and self-propelled models.

5 CONCLUSIONS

- An extensive set of model test results for the KVLCC2 has been used to validate four potential-flow methods over a range of rectangular canal widths and depths.
- The most restricted model tests showed that mass flux past the ship was not conserved, so that fair comparisons could not be made between the model tests and numerical methods. The effect was most noticeable on trim, because water builds up in front of the model, causing the bow to rise (this is also observed when entering a lock). Further numerical and/or experimental work are required to better understand this effect.
- Despite the above, it appears that the *Nonlinear-1D* method may give good estimates of midship sinkage in narrow canals ($w/B \leq 2.5$). It is inappropriate for wide canals with $w/B > 5.0$, due to the 1D assumption being violated.
- The *Linear-2D* method gives good results for wide canals with $w/B > 5.0$, although an empirical correction is desirable, especially at high speeds. This method is inappropriate for narrow canals with $w/B < 5.0$, due to the linear flow assumption being violated.
- The *Rankine-Source* method gives good results for wide canals, especially at higher speeds when the *Linear-2D* method under-predicts the midship sinkage. Unexpectedly-low sinkage results were obtained for the *Rankine-Source* method in narrow canals, and further work will be done on this topic.
- The *Double-Body* method gave quite consistently good results across all canal widths.

6 ACKNOWLEDGEMENTS

Alexander von Graefe provided assistance with installing, running and convergence testing GL Rankine software. Scott Ha provided assistance with KVLCC2 hull modelling.

7 REFERENCES

1. Delefortrie, G.; Geerts, S.; Vantorre, M. (2016). The Towing Tank for Manoeuvres in Shallow Water. *MASHCON 2016*, Hamburg, Germany.

2. Gourlay, T.P.; Dawson, E., (2015). A Havelock-source panel method for near-surface submarines. *Journal of Marine Science and Application* 15(3), 215-224.

3. Gourlay, T.P.; Ha, J.-H.; Mucha, P.; Uliczka, K. (2015). Sinkage and trim of modern container ships in shallow water. *Proc. Coasts and Ports*, Auckland, 15-18 September 2015.

4. Gourlay, T.P. (2014). ShallowFlow: A program to model ship hydrodynamics in shallow water. *Proc. 33rd International Conference on Ocean, Offshore and Arctic Engineering (OMAE 2014)*, June 8-13, San Francisco, USA.

5. Gourlay, T.P. (2001). The supercritical bore produced by a high-speed ship in a channel. *Journal of Fluid Mechanics* 434, 399-409.

6. Gourlay, T.P. (1999). The effect of squat on steady nonlinear hydraulic flow past a ship in a channel. *Schiffstechnik* 46, 217-222.

7. Hess, J.L.; Smith, A.M.O. (1964). Calculation of nonlifting potential flow about arbitrary three-dimensional bodies. *Journal of Ship Research* 8(2), 22-44.

8. Kim, W.J.; Van, S.H.; Kim, D.H. (2001). Measurement of flows around modern commercial ship hulls. *Experiments in Fluids* 31, 567-578.

9. Lataire, E.; Vantorre, M.; Delefortrie, G., (2012). A prediction method for squat in restricted and unrestricted rectangular fairways. *Ocean Engineering* 55, 71-80.

10. Lee, S.-J.; Kim, H.-R.; Kim, W.-J.; Van, S.-H. (2003). Wind tunnel tests on flow characteristics of the KRISO 3,600 TEU containership and 300K VLCC double-deck ship models. *Journal of Ship Research* 47(1), 24-38.

11. Martin, H.; Puls, D. (1986). Vertical forces, trim moments and changes of draught and trim of ships in shallow water. *Schiffbauforschung* 25(3), 155-159.

12. Mucha, P.; el Moctar, O. (2014). PreSquat - Numerische Vorhersagen von dynamischem Squat in begrenzten Gewässern, *Bericht F005/2014*, Institut für Schiffstechnik, Universität Duisburg-Essen.

13. SIMMAN 2014 (2014). Workshop on Verification and Validation of Ship Manoeuvring Simulation Methods, Copenhagen, Denmark, December 8 -10. www.SIMMAN2014.dk

14. Tuck, E.O. (1967). Sinkage and trim in shallow water of finite width. *Schiffstechnik* 14, 92–94.

15. Uliczka, K.; Kondziella, B.; Flügge, G. (2004). Dynamisches Fahrverhalten sehr großer Containerschiffe in seitlich begrenztem extremen Flachwasser, *HANSA*, 141.

16. von Graefe, A. (2014). A Rankine source method for ship-ship interaction and shallow water problems, *Ph.D. thesis*, University of Duisburg-Essen.

8 AUTHORS' BIOGRAPHIES

Tim Gourlay is a Senior Research Fellow at the Centre for Marine Science and Technology, Curtin University. He undertakes research and consulting work in ship under-keel clearance for ports in Australia and internationally. This work typically includes theoretical development, software development, UKC management guidelines, port liaison and full-scale validation trials.

Evert Lataire is currently assistant at the division of Maritime Technology at Ghent University. He has made a PhD on the topic of bank effects mainly based upon model tests carried out in the shallow water towing tank of FHR. His ten year experience includes research on ship manoeuvring in shallow and confined water such as ship-ship interaction, ship-bottom interaction and ship-bank interaction

Guillaume Delefortrie, naval architect, is expert nautical research at Flanders Hydraulics Research. He is in charge of the research in the Towing Tank for Manoeuvres in Shallow Water, development of mathematical models based on model tests and is secretary of the 27th and 28th ITTC Manoeuvring Committee.

APPENDIX A: MIDSHIP SINKAGE COMPARISONS

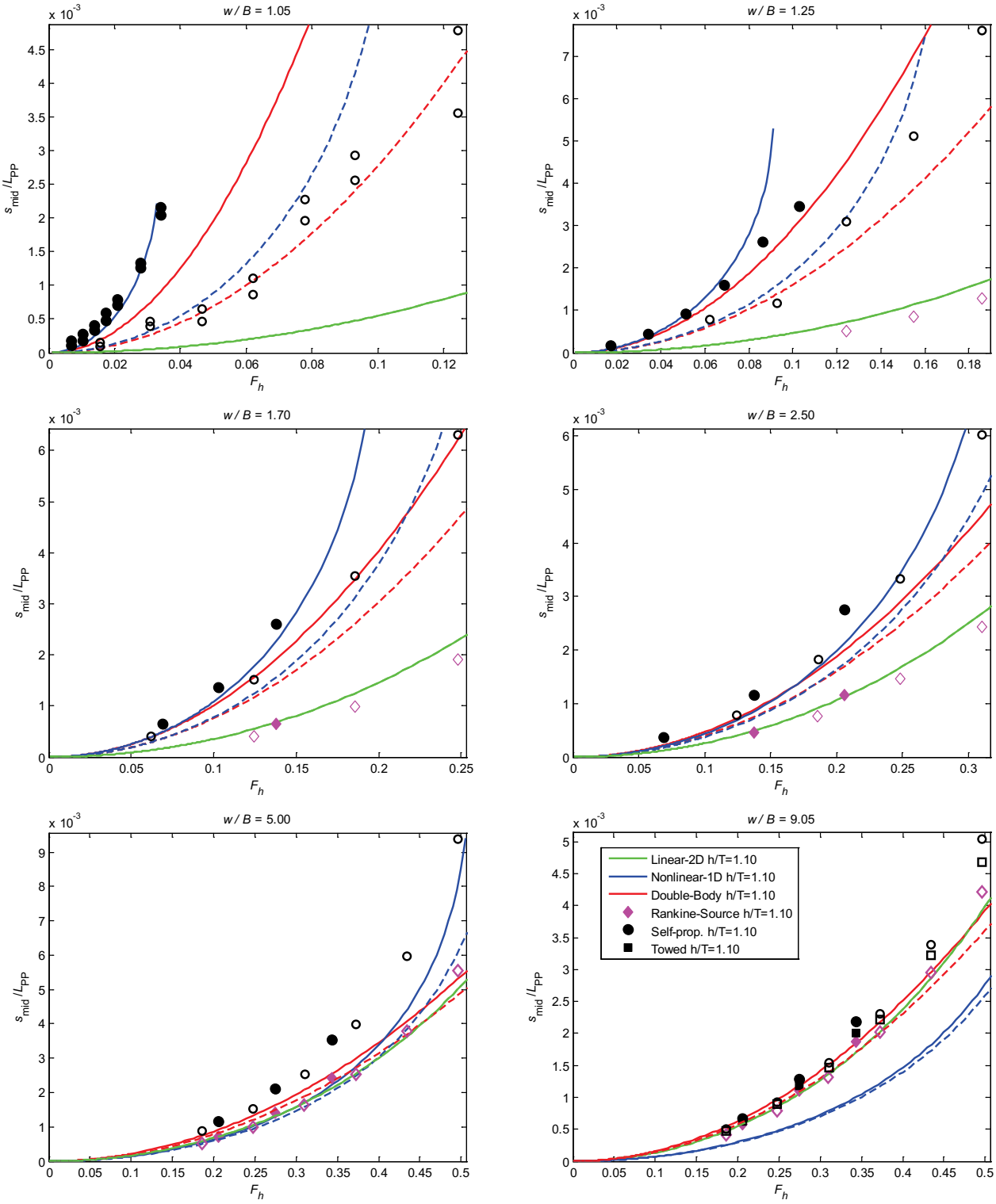

Figure A1. Midship sinkage predictions and model test results for KVLCC2 in rectangular canals of increasing *w*/*B* ratio. The same legend applies to all subplots. Dashed lines and unfilled markers are corresponding results for *h*/*T*=1.35. The *Linear-2D* results for both water depths are almost coincident.

APPENDIX B: DYNAMIC TRIM COMPARISONS

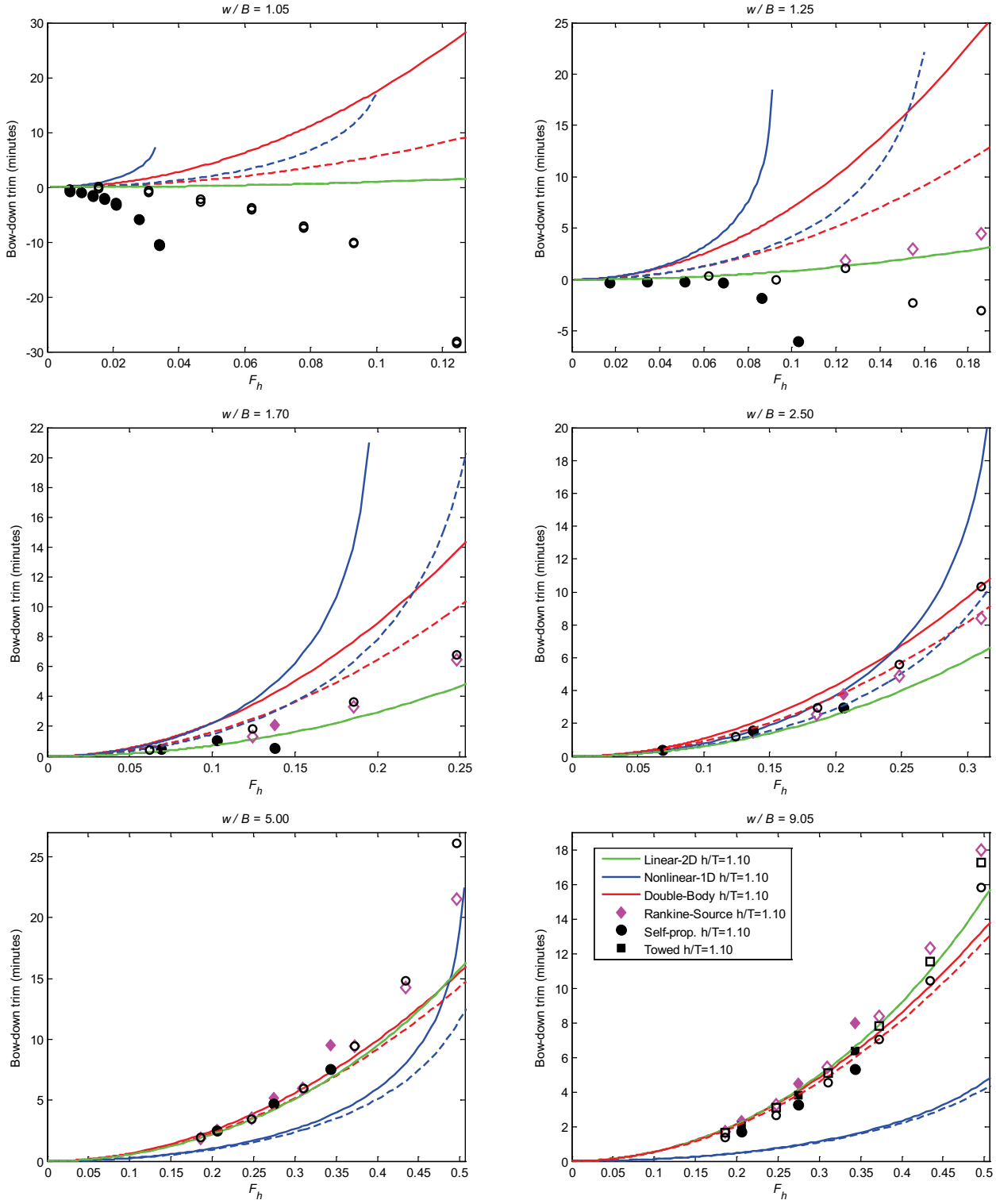

Figure B1. Dynamic trim predictions and model test results for KVLCC2 in rectangular canals of increasing *w*/*B* ratio. The same legend applies to all subplots. Dashed lines and unfilled markers are corresponding results for *h*/*T*=1.35. The *Linear-2D* results for both water depths are almost coincident.

Ship-Bank and Ship-Ship Interaction Effects

4th MASHCON, Hamburg - Uliczka et al. (eds) - © 2016 Bundesanstalt für Wasserbau ISBN 978-3-939230-38-0 (Online)
DOI: 10.18451/978-3-939230-38-0_20

PROGRESS ON REAL-TIME PREDICTION OF SHIP-SHIP-SHORE INTERACTIONS BASED ON POTENTIAL FLOW

J A Pinkster, PMH bv, The Netherlands

SUMMARY

A prediction method for ship-ship and ship-shore interaction forces and moment is being developed based on 3-dimensional double-body potential flow. The application of the prediction method is for the purpose of training marine personel on real-time ship manoeuvring simulators for, among others, manoeuvring in ports. To this end a fast accurate prediction method is developed that can be used to model complex port geometries and ship manoeuvres without the penalty of excessive computation times. An existing 3-d flow model is extended to include the option of multi-domains which allows considerably more complex port modelling while keeping the computational load within bounds. To this end the code is run on a desk-top computer fitted with a fast, multi-core GPU which result in a considerable computational speed gain. Examples are given of the application of the multi-domain method. Where appropriate, results of computations are compared with results of the conventional computations which do not make use of the multi-domain option. Finally, an example is given showing that there are realistic cases for which the multi-domain method for computing interactions is probably the only practical option.

1 INTRODUCTION

Ship-ship and ship-shore interactions are part of the disturbances of which the effects on manoeuvring ships in ports are investigated by means of real-time ship simulators. In most simulators ship-ship and ship-shore interactions are included by interpolation of look-up tables of forces and moments on the vessels which have been computed off-line using potential flow methods or, increasingly, CFD methods. Vantorre et al [1] developed empirical models of ship-ship interaction effects for real-time use on manoeuvring simulators based on an extensive set of model tests. In most cases, such interaction forces and moments are treated as external effects acting on the mathematical ship model used in the ship simulator i.e. the interaction model is separate from the mathematical ship model.

The present day trend is to generate ship interactions by computing such effects in real time based on the solution of appropriate hydrodynamic equations taking into account the hull forms of the vessels, the instantaneous position and velocity components of the ships while also taking into account the local port geometry, see [2],[3],[4]. In order for such computations to be useful, the hydrodynamic equations need to be solved sufficiently fast and to deliver sufficiently accurate results on the interaction forces and moments acting on the vessels.

For fast computation of interaction effects of ships in ports the so-called double-body model seems appropriate. The flow is three-dimensional but bounded between the horizontal bottom and equally horizontal mean free surface. The double-body flow model assumes that the speed of the ships is sufficiently low so that the free-surface effect can be neglected. For typical moderate speeds of large ships in ports, it has been shown that the effects of passing ships on large moored vessels are accurately predicted by the computations based on the double-body assumption, see Talstra and Bliek [5]. Until a number of years ago, very few systematic experimental investigations were carried out which could be used to establish the accuracy of predictions of interactions between sailing ships. Results of such investigations, see, for instance [1], are a good basis for evaluation of numerical prediction methods such as the double-body flow method described in this paper.

In its simplest form, the double-body potential flow model predicts interaction effects assuming the ships to be non-lifting bodies. Extensions taking into account lift effects have been investigated in recent years and may find their way into real-time interaction computations in due course. Koning-Gans et al [6]. investigated a double-body potential flow model including lift effects. Bunnik and Toxopeus & Bunnik [7], using a CFD-based code, gave some insight in the effect of the drift angle of the sailing ship on the forces on a moored vessel.

While the quantitative accuracy of the computed interactions between sailing ships is still not well established, it is clear that the most important characteristics of interaction effects seem to be reasonably well predicted even without the inclusion of lift effects. This contribution will be restricted to the non-lifting body version of the double-body flow model.

In order for the computional procedure to be practically useable on a real-time maneuvering simulator, the interaction computations must have a sufficiently fast update rate. An update rate of 2-5 Hz for close maneuvres of overtaking /passing ships seems adequate when there is a high probability of an almost immediate occurrence of a collision. An update rate of 0.3-1 Hz could apply for a vessel carrying out a gentle maneuver such as an approach to a quay or into a lock. There are a number of factors influencing the update rate. The first of these is the complexity of the modelling of ships and port geometry. The more detailed and extensive the modelling, the longer the computation times. Secondly, the sophistica-

tion of the code and the platform used for the computations. Code needs to be optimized and parallelised using all available computing cores of a machine. More computing cores increase the update rate if the code is suitably parallelized.

In a previous paper [4] an approach based on real-time computation of interaction forces using the double-body potential flow model was discussed. The fluid equations were solved based on a Rankine source distribution over zero-order panels describing the wetted surfaces of the vessels and surrounding port geometry. The code is parallelized and the linear equations in the unknown source strengths were solved based on the no-leak condition at the panel centres using a fast Graphical Processing Unit (GPU) which nowadays has up to about 3000 single precision computing cores. All equations were valid for a single fluid domain with constant water depth. In some cases the measured bathymetry of a harbor or channel is used to develop a port panel model. Due to the large number of panels involved special measures have to be taken to retain the necessary update rate for simulator use. It was clear that at the present time GPUs are an affordable means to significantly reduce computation times.

In this contribution this model is extended to include multi-domains i.e. fluid domains each modelling a specific part of the port area with it's own water depth and using features such as symmetry planes to reduce computational load and increase accuracy. By such means a straight vertical quay or a channel with vertical, parallel sides need not be modelled by panels. In this way areas with different water depth are modelled without the necessity to apply panels to the harbor floor. The domains are connected through matching boundaries at which normal velocity and potential are equated in order to assure continuity of the flow conditions through the domains. These matching boundaries involve a limited number of additional panels.

In the following a short introduction is given regarding the double-body flow model and the multi-domain approach.

After the theoretical overview a first example illustrating the accuracy of the matching boundary for the case of forces on a moored vessel due to a passing vessel at a constant water depth will be given. Results of passing vessel forces will be compared for the case with and without a matching boundary around the moored vessel.
A second example illustrates the flexibility in modeling the case of a vessel moored in a so-called pocket, a local increase in water depth to accommodate a deeper draft vessel at lower tide levels. Results will be shown of the forces due to a passing container vessel.
Finally a novel application of the multi-domain concept will be that of a vessel sailing through the matching boundary, for instance, from open water through a narrow channel. Results will be shown which illustrate possibilities and problems with such cases.

2 DOUBLE-BODY POTENTIAL FLOW

The complete model includes the possibility to apply multi-domains. In each domain the theoretical aspects reviewed in the following section apply.

2.1 THEORETICAL BACKGROUND

The computational method is based on 3-d potential theory assuming double-body flow i.e. no free surface deformations and a rigid bottom. The fluid is assumed to be inviscid, incompressible and irrotational. This means that no viscous effects are present in the computed results on forces and moments. The numerical solutions to the flow equations are found based on the boundary element method in which all models, including port geometry are modeled by means of lower order panels.

The vessels are assumed to either lie stationary or sail along an arbitrary track at constant or variable speed in the horizontal plane. The effects of yaw rotations and drift angles are included. Even though the motions of vessels are restricted to three degrees of freedom (surge, sway, yaw), the forces on the vessels are computed for all 6 degrees of freedom.

The numerical model is similar to that described by Korsmeyer et al [8] in that it is based on 3-dimensional potential flow. For the double-body flow model, the potentials describing the flow are based on the Rankine source formulation taking into account restricted water depth and a rigid still water level. To this end the Rankine source formulation needs to be modified to take into account the zero normal velocity which is applicable at both the still water level and the bottom of the waterway. This implies that sources are mirrored an infinite number of times about both the free surface and the bottom. For this code use is made of the formulation given by Grue and Biberg [9]. The infinite mirror series is replaced by a polynomial representation thus making the computations less demanding in terms of time.

2.1 (a) Multi-domain

First the concept of a domain will be clarified. Figure 1 shows docks alongside a channel (A) consisting of three docks B, C and D, each with different water depths with transition slopes between the areas with different water depths.

Shown in the Figure are vessels moored in the docks. The disturbance due to a passing ship propagates into the docks resulting in forces acting on the moored vessels thus generating motions, and forces in mooring lines and fenders.

In conventional double-body flow computations, only one water depth would apply (i.e. the largest water depth), in this case the water depth in the channel (A). The water depth in B, C and D would have to be modelled by a distribution of horizontal panels over the bottom.

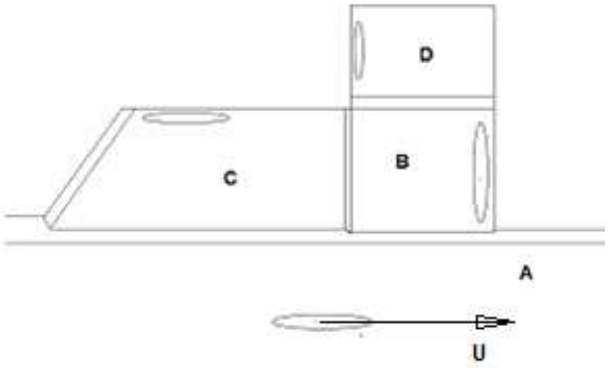

Figure 1. Layout of a port with 4 domains with different water depths.

This could result in a very large number of panels to describe the geometry of the dock and channel adequately. Instead, the port and the sea area are divided in a number of domains, each with their own water depth. That means that when considering the flow within a domain, the potential equations describing the flow would be based on that water depth thus avoiding the necessity of distributing panels over the bottom. Because the domains are separated i.e. sources within a domain have no direct influence on field points in another domain, use can also be made of such features as vertical symmetry planes within each of the domains. A vertical plane of symmetry about which sources on the bodies in the particular domain are reflected creates a perfect reflecting boundary thus avoiding the necessity of panelization of that particular part of the boundary. Symmetry planes are often standard in 3-d codes but only one such construction can be used at a time.

Even though such boundaries stretch infinitely in both directions, their direct influence is now restricted to the particular domain in which they are defined. In this case there are 4 domains i.e. A, B, C and D and each could have a vertical quay section modelled that way. An interesting extension is the ability to make use of double-symmetry planes to model channels with parallel vertical sides, see Newman [10]. In this paper an example is given in which use is made of the double-symmetry approach.

In order to obtain the proper flow in the port and the docks, it must be ensured that the domains are properly connected, i.e. the flow across the boundaries between the domains must be continuous with respect to the momentum flux and mass flow. This is achieved by equalizing the potential and the normal velocities on vertical boundaries between the domains. These vertical boundaries are virtual in that they do not represent physical structures but only serve to ensure the proper flow between the domains. The position of the boundaries is relatively arbitrary but are best chosen so that the other, physical boundaries within a domain can be represented by panels which do not extend below the water depth of that domain. An example is shown in Figure 2 with the location of the boundaries between domain A and domain B as well as between domain B and domain D. This shows that, for instance, the slope between B and D is modelled by panels in domain B. Likewise, the slope between A and B is modelled by panels in A.

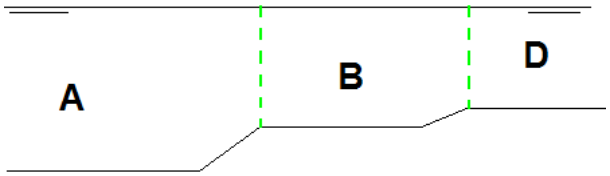

Figure 2. Location of matching boundaries between domains.

How are these boundaries modelled? At these 'matching boundaries', or interfaces between the domains, conditions of equal potential and normal velocity are to be imposed. This is made possible by modelling the interfaces by panels of identical number and size on both sides of the interface. The panels of the interfaces between domains are in a back-to-back situation with positive normal of the two parts of the matching boundary directed into each domain. In the computations the normal velocities and potential at the colocation points of the matching boundary panels belonging to a domain are determined using only the sources within the same domain. Likewise, the normal velocities and pressures on the corresponding panels of the matching boundary belonging to the adjacent domain are computed based on sources in that adjacent domain. An example involving 4 different domains is shown in Figure 3 in which the matching boundaries or interfaces are the checkered parts. The checkering is due to the fact that these panels are in the same location with different normal directions. The hidden surface algorithm gets confused! In the following the equations on the basis of which the flow through the domains and the forces on the moored vessels will be solved, will be discussed.

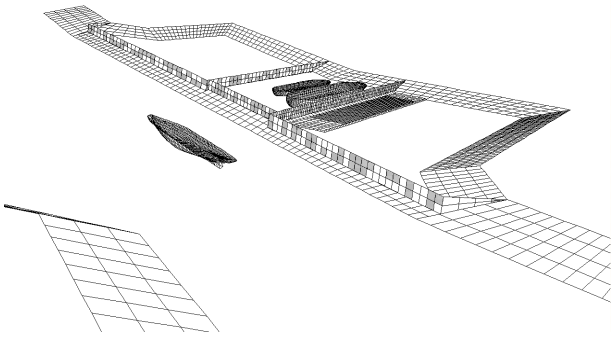

Figure 3. Matching boundaries in a complex port geometry.

The system of equations is arranged so that the port geometry may be subdivided into a number of interconnected domains with in each domain zero or one or more moored vessels.

Assume a passing vessel in the first domain. This means that vessels not moored in the first domain will not 'feel' the disturbance due to te passing vessel directly, but in an indirect manner due to the flow through the interfaces between the domains into the domain in which the particular vessel is moored.

The hydrodynamic equations for the flow within a domain containing moored vessels are given below.

The additional equations for the boundary conditions between the domains are then given. Together equations for the no-leak conditions on each domain (excluding the interfaces) and for all vessels combined with the boundary conditions at the interfaces (equal pressure on both sides and continuity of normal velocity) lead to a set of linear equations in the unknown source strengths which are solved using standard methods.

2.1 (b) Flow equations

The 3-d panel method involves a homogeneously distributed Rankine source on each zero-order panel describing both the ships, port geometry and matching boundaries between domains. Within each domain the potential function ϕ which is dependent on the earth-bound coordinates X,Y,Z and time t containing all information on the flow is the sum of the potentials due only to sources in that domain. At each time step the unknown source strengths are solved based on the no-leak boundary condition at the center of each panel of fixed port structures and sailing vessels in that domain and the boundary conditions valid for the matching boundaries connecting the flow to other domains.

The no-leak condition on panels describing the vessels and panels of fixed port structures may be formulated in terms of the velocity component normal to the target panel as follows:

$$\frac{\partial \phi}{\partial n} = V_n \tag{1}$$

in which:

$$V_n = 0 \tag{2}$$

for fixed port structures and:

$$V_n = (\overline{U} + \overline{r} \times \overline{x}) \cdot \overline{n} \tag{3}$$

for a vessel sailing at speed $\overline{U}$ and rate of yaw rotation $\overline{r}$. The location of a point of the hull is $\overline{x}$ relative to the vessel axes and the normal vector to the hull is $\overline{n}$. The positive normal direction is pointing out of the body into the fluid.

In order to assure the correct transfer of fluid impuls between domains the boundary conditions at the matching boundary between two domains require the normal velocity on both sides of the boundary to be continuous and the potential to be equal. This is achieved by modelling a matching boundary by two identical sets of source panels, one set for each of the two sides of the boundary. The panels are arranged in a back-to-back situation i.e. the side of the matching boundary belonging to a domain has the positive normal direction into the fluid of that domain, see Figure 4.

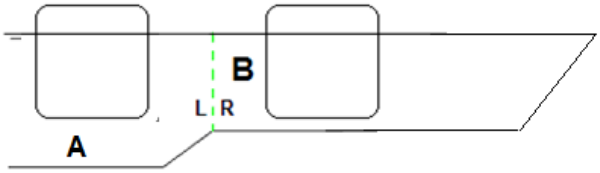

Figure 4. Left and right side of a matching boundary

For the normal velocity at a matching boundary the following requirement applies for each pair of back-to-back panels:

$$\frac{\partial \phi}{\partial n_L} = -\frac{\partial \phi}{\partial n_R} \tag{4}$$

or:

$$\frac{\partial \phi}{\partial n_L} + \frac{\partial \phi}{\partial n_R} = 0 \tag{5}$$

For the potential the following applies:

$$\phi_L - \phi_R = 0 \tag{6}$$

The last two equations require that the normal velocity and potential with index *Left* or *Right* be evaluated based on the sources in the relevant domain.

For the panels on ships and fixed port structures, excluding matching boundaries, the no-leak condition of Equation 1 is applied. For panels on the matching boundaries Equation 5 and Equation 6 are applied.

The number of unknown source strengths is equal to the total sum of panels in all domains including panels on ships, port structures and matching boundaries. The number of linear equations which have to be solved at each time step is equal to the number of unknowns. A large number of influence functions relating a source to a field point will be zero. This will be the case for all combinations where the source is not in the same domain as the field point.

Based on the solutions for the source strengths, the forces and moments acting on the vessels can be computed. The reader is referred to Pinkster [11] for further details of the method of solution of the unknown source strengths when applying matching boundaries in 3-d diffraction computations.

2.1 (c) Hydrodynamic forces

Forces are determined based on the following equation assuming the unit normal $\overline{n}$ pointing out of the body into the fluid:

$$\overline{F} = -\iint_S p\overline{n}dS \tag{7}$$

The pressure p follows from Bernoulli's equation in which the potential ϕ and it derivatives are given relative to an earth-fixed system of axes:

$$p = -\rho\frac{\partial\phi}{\partial t} - \tfrac{1}{2}\rho|\overline{\nabla}\phi|^2 \tag{8}$$

The first term on the right-hand side of this equation is the instationary pressure component including added mass effects. The second term is the pressure drop due to the square of the fluid velocity sometimes referred to as the Bernoulli pressure term. The potential contains contributions from all vessels or bodies, moving or otherwise, in the fluid domains.

In the code the equations for the interaction forces between ships as derived by Xiang & Faltinsen [12] have been implemented. The equations apply to deep or shallow water and take into account arbitrary motions of the vessels.

3 APPLICATION OF DOMAINS

In the following some examples will be given of the application of the domain concept to ship interaction problems. The following cases will be treated:

- Forces on a moored vessel due to a passing vessel
- Passing vessel forces on a tanker moored in a pocket
- Forces on a vessel entering and passing through a narrow channel or lock

In the first and third cases the forces on the vessel will be computed for two cases i.e. using the conventional approach based on a single water depth without and with application of the domain approach. Comparison of the results are intended to illustrate that the results are essentially the same which will indicate that the flow between the domains is modelled correctly.

The second case is added to illustrate the flexibility of the domain approach to analyse unusual cases which cannot be modelled easily otherwise.

In the examples two different ship models are used, a container vessel and a tanker. The main particulars of the vessels are given in Table 1.

Table 1. Main particulars of the vessel

		Container	Tanker
L_{pp}	m	230.0	257.0
Beam	m	32.2	36.8
Draft	m	10.8	15.7
Displacement	m^3	52030	118800
No. of panels	-	828	792

3.1 FORCES ON A MOORED VESSEL DUE TO A PASSING VESSEL

The layout for the conventional case and the case with application of two domains is shown in Figure 5 and Figure 6. The symmetry boundary modelling the vertical quay wall is coloured light blue withing the domain of the moored vessel and grey outside. This is to denote that both parts of the symmetry boundary are declared separately for each domain. In this case they are declared in the same plane to form a continuous, straight vertical quay.

The same container vessel is used both as the moored vessel and the passing vessel, see Table 1. This is a container vessel with a displacement of 52030 m^3. The passing speed is 8 kn and the passing distance is 100 m measured from centreline to centreline. The water depth amounted to 15 m. The moored container vessel centreline is 20 m from the vertical quay.

A rectangular matching boundary measuring 400 m along the vertical quay at a distance of 50 m from the quay was modelled as shown in Figure 6. The location of the matching boundary is relatively arbitrary but is also used in the second example in which the effect of a pocket is included.

The inner and outer vertical matching boundaries are each modelled by 100 panels. These are arranged in two sides perpendicular to the quay at distances of +200 m and -200 m from midship of the moored tanker and one side parallel to and 50 m from the quay.

Figure 5. A vessel moored against a vertical quay and a passing vessel.

The panels on the matching boundary are relatively large. This is possible because the flow gradients are relatively low some distance away from the passing or moored ship.

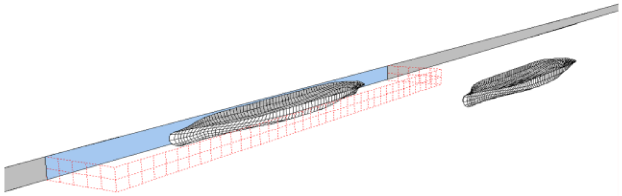

Figure 6. A vessel moored against a vertical quay in a domain surrounded by a matching boundary (red dotted line) and a passing vessel in a second domain.

The computed surge force, sway force and yaw moment on the moored container vessel are shown in Figure 7 for both cases. The results are shown to be almost identical confirming that the matching boundary between the vessels is fully transparent.

In this example the waterdepth in both domains was the same so that the effectiveness of the matching boundary could be established.

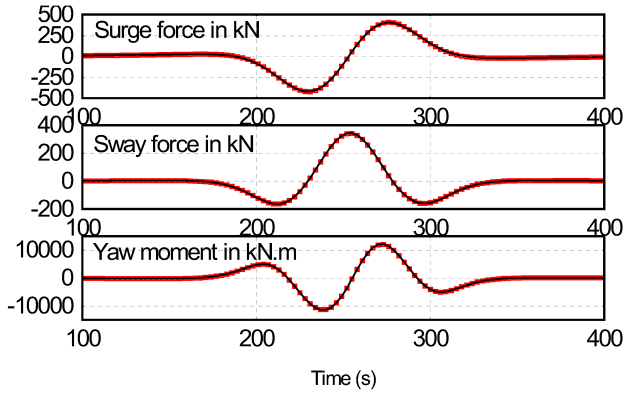

Figure 7. Forces and yaw moment on the moored vessel. Results with application of domains in red. Other results in black. . Surge force positive forward, Sway force positive to port, Yaw moment positive, bow to port.

3.2 PASSING EFFECTS ON A VESSEL MOORED IN A POCKET

An extension to the aforegoing example is to apply the domain split to the case of a tanker moored in a pocket with a greater waterdepth than in the channel through which the passing vessel is sailing. The layout of the matching boundary is the same as in the first case except that a pocket is modelled in the domain around the moored vessel. The water depth in the pocket amounted to 20.0 m while the water depth outside the pocket amounted to 15.0 m. The layout is shown in Figure 8.

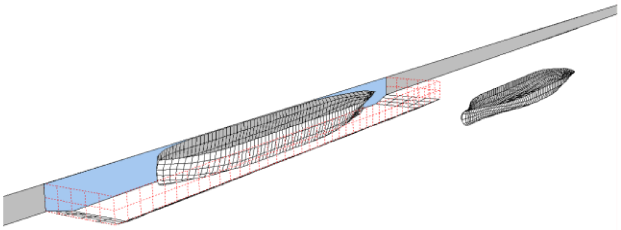

Figure 8. A tanker moored in a pocket surrounded by a matching boundary.

Figure 8 shows the matching boundary (dotted red lines) around the pocket and the pocket side which are modelled as a slope between the water depths of 20 m and 15 m. In this case the moored vessel is a tanker of 118800 m^3 displacement. The passing vessel is again the container vessel. Dimensions of both vessels are given in Table 1. The passing speed is 8 kn and the passing distance between the centrelines of the vessels is 100 m. The moored vessel centreline is 20 m from the vertical quay. The results of the computations are shown in Figure 9.

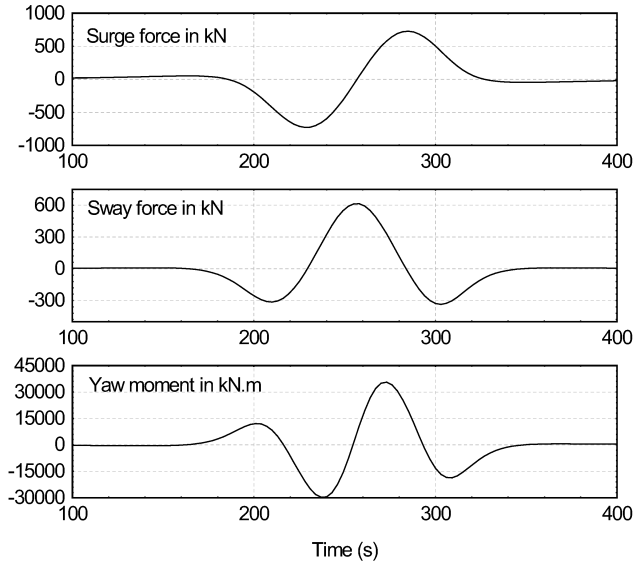

Figure 9. Passing vessel forces on a tanker moored in a pocket.

The overall characteristics of the forces and moment on the moored tanker are similar to the case of a vessel moored to a vertical quay and with the same waterdepth as the channel in which the passing vessel is sailing as shown in Figure 7. The forces and moment are however, generally higher for this case since the moored vessel is larger. A large part of the increased interaction force is related to the gradients of the pressure field generated by the passing vessel acting on the larger volume of the moored vessel.

As the passing vessel closes in on the moored vessel, the surge force on the moored vessel draws the vessel backwards. This reverses to a forward-directed force when the passing vessel passes the midship of the moored vessel.

The peak in the lateral force on the moored vessel is reached when the vessels are abreast and is directed to port, towards the passing vessel.

The yaw moment is positive (bow to port) early in the manoeuvre then changes sign when the bow of the passing vessel is level with the stern of the moored vessel, tending to draw bow and stern towards each other.

This trend reverses as the passing vessel sails past the midship of the moored vessel.

For this case no comparison is made with another method since this is not a case which can be easily modelled using a single water depth. Modelling this layout would require the basic water depth to be equal to the 20.0m water depth in the pocket and the area with a water depth of 15.0 m would need to be modelled with a very large number of horizontal panels.

3.3 FORCES ON A TANKER SAILING THROUGH A NARROW CHANNEL

The last case is that of a vessel entering a 500m long narrow channel (or open lock) with a width of 60m from open water leading to the exit also into open water. The water depth in the open water parts and the channel were equal to 20m.

For this case the focus is on the forces on the sailing vessel. Navigation through restricted channels presents special problems for the vessel since transient forces associated with entering a channel of restricted width and bank suction effects become important. Also the dynamic properties of the vessel are affected by the waterway restrictions. For this reason attention is also paid to added mass effects during the channel transit.

The computations were carried for two cases i.e. for the first case the channel is modelled using panels for the vertical sides and a single domain not requiring matching boundaries.

For the second case use is made of three domains. The first open area is the first domain which is modelled by panels representing vertical quays to either side of the channel entrance. This domain is connected to the second domain, the channel by a matching boundary. At the exit side the channel domain is connected to the domain of the open area by a second matching boundary. A plan view of the vessel entering the narrow channel from open water is shown in Figure 10.

Figure 10 shows the vessel, which is the same tanker used in the last example, entering the channel from open water. The black lines represent the vertical quays at almost right-angles to the channel centreline at the entrance and the exit and also the vertical sides of the 500m long and 60m wide waterway.

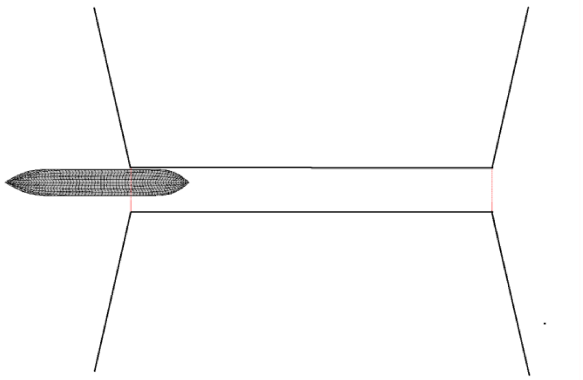

Figure 10. Plan view of a tanker entering a narrow channel from open water.

The vessel is shown 10.0m off-centre of the channel centreline. The beam of the vessel is 36.6 m. This means that the clearance between the port side of the vessel and the quay amounted to 1.7 m. This is an extremely small clearance associated more with a vessel entering a lock than traversing a channel. It is however, important to investigate the robustness of the computational procedure for such extreme cases.

For the computations the vessel speed was set at a constant value of 1 m/s. The track was parallel to the channel axis.

The panel model used to compute the forces on the vessel without making use of the domain concept is shown in Figure 11.

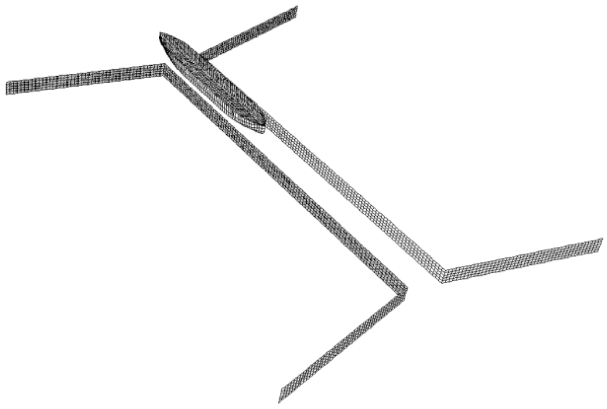

Figure 11. Channel sides modelled by panels.

The total number of panels used to model the channel amounted to 1900, of which 1000 panels were devoted to the 500 m long parallel quays.

The corresponding model developed using three connected domains is shown in Figure 12 and in Figure 13.

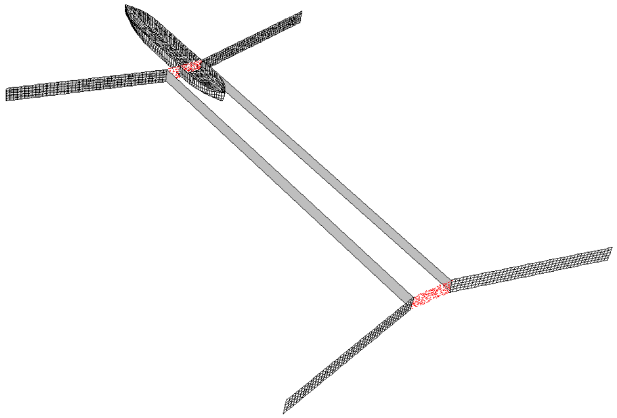

Figure 12. Channel sides modelled by double-symmetry. Matching boundaries at entrance and exit to the channel.

In Figure 12 and Figure 13 the channel sides are shown as a single grey panel. This represents the double-symmetry boundaries about which the potentials are mirrored in order to achieve the no-leak condition for all points of the channel sides. The matching boundaries at the channel entrance and exit are shown in red dots. Each matching boundary is modelled with 330 panels. The total number of additional panels for the matching boundaries amounted to 4 x 330 = 1320 which is 120 more than used for the model shown in Figure 11.

A detail of the intersection of the vessel with the matching boundary is shown in Figure 13. In Figure 13 it is seen that the matching boundary extends through the vessel model. No modifications are made to the matching boundary at any point.

The vessel panel model is cut at the intersection between vessel and matching boundary.

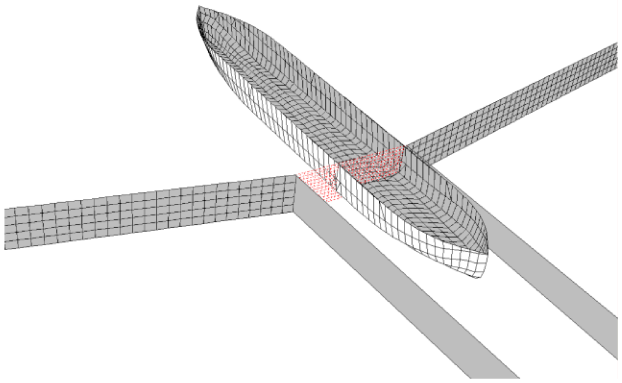

Figure 13. Detail of the matching boundary at the channel entrance and the intersection with the panel model of the ship.

Panels which are cut by the matching boundary are re-modelled into parts which are in one of the two domains on either side of the matching boundary depending on the location of the collocation point of the panel sections relative to the matching boundary.

This approach means that at each step the panel model of the vessel is modified in the vicinity of the matching boundary. It may be that a vessel is crossing more than one matching boundary at the same time. This is also taken into account in the computational procedure.

The results of the computations for this case are shown in Figure 14 through Figure 16.

The vessel starts with the midship located 300 m from the channel entrance. As can be seen, the added mass values start to rise and when the vessel is completely in the channel are about double the open water values. As the vessel leaves the channel values drop back down to the open water levels. Higher added mass values indicate that it will be more difficult to change a manoeuvre in the channel than outside of it.

The results in the figures show that when the vessel is completely in the channel, the difference between the methods amounts to 15-20% for the surge added mass. Predictions for the sway and yaw added mass values are almost the same for both methods.

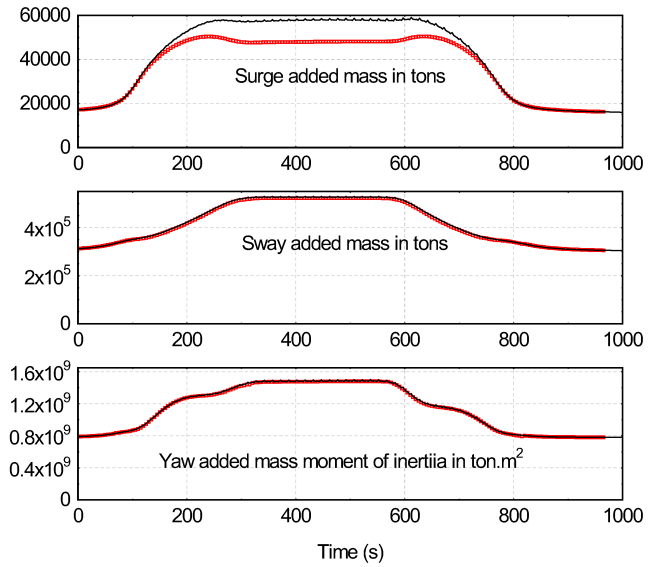

Figure 14. Added mass of the vessel. Domain results in red. Panel model results in black.

Another important component of the forces on the vessel are those due to the fluid pressure drop which occurs when the fluid velocity increases. This is the second term in Equation 8, sometimes referred to as the Bernoulli term. Results of computations of these force components are shown in Figure 15.

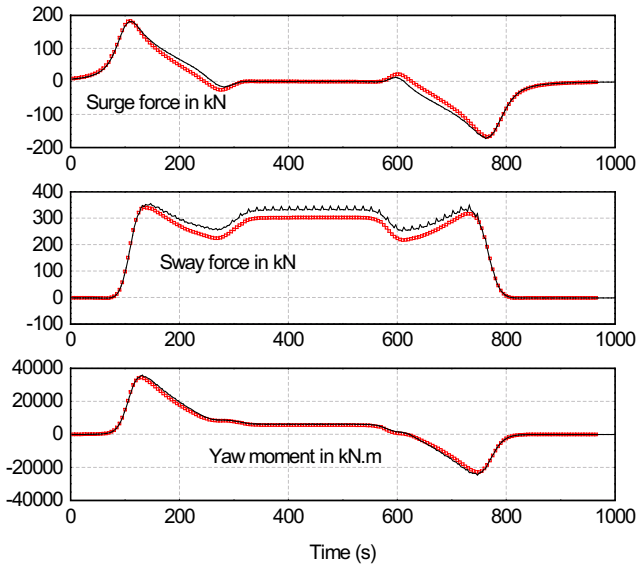

Figure 15. Bernoulli pressure term contribution to the forces and yaw moment on the vessel. Domain results in red. Panel model results in black. Surge force positive forward, Sway force positive to port, Yaw moment positive, bow to port.

Results shown in Figure 15 for this component of the surge force indicates that as the vessel approaches and enters the channel a forward-directed force is generated sucking, as it were, the vessel into the channel. When the vessel is in the channel the surge force drops to zero. This in keeping with, or in line with double-body potential flow theory. Since there is no viscosity, no shear forces are generated and no flow separation occurs leading to zero longitudinal force under constant conditions i.e. without significant effects from the channel entrance or exit. As the vessel exits the channel a resistance increase occurs tending to slow the vessel down in this phase. It should be remembered that this term is one of the two main force components arising from Equation 8.

The transverse force shown in Figure 15 indicates a force value which rises to about 300 kN when the vessel has fully entered the channel. Some variations are shown entering and exiting the channel. The transverse force is directed to port (positive value) as can be expected from the bank suction phenomenon.

The yaw moment acting on the vessel as it enters the channel is directed bow to port. As the vessel proceeds into the channel the port-directed moment decreases but stays at a non-zero positive value for most of the time. As the vessel approaches the exit the yaw moment becomes directed to starboard and drops back to zero when the vessel has cleared the channel. The behaviour of the yaw moment is in keeping with a bank suction force to port on, at first, the bow, and finally the stern.

The overall comparison between the results of both computational methods agree quite well with the domain method results being slightly lower for the sway force when the vessel is fully in the channel.

Finally, the total surge force, sway force and yaw moment on the vessel are examined. The total forces include inertia related terms arising from the pressure Equation 8. The total forces and yaw moment are shown in Figure 16.

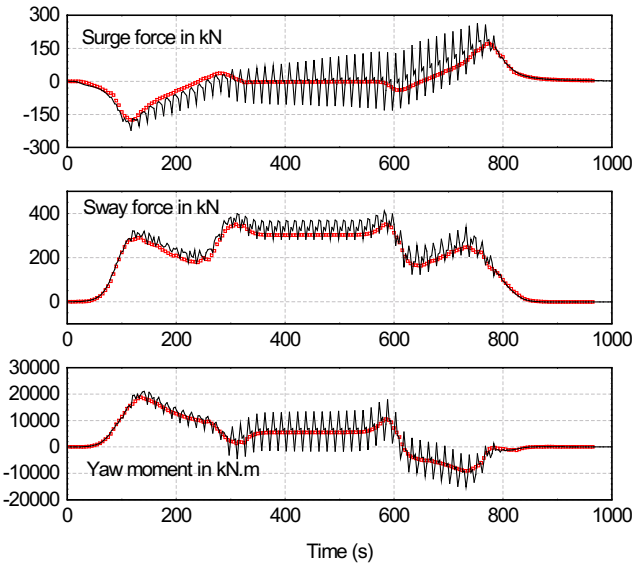

Figure 16. Total forces and yaw moment. Domain results in red. Panel model results in black.

In Figure 16 the differences in the results of the computed forces and yaw moment are quite remarkable. The results based on application of the panel modelling of the channel (solid black line) show distinct spikes. The results found by application of the domain approach combined with the double-symmetry modelling of the channel are, in contrast, quite regular and smooth throughout the simulation.

It is noted that the total surge forces shown in Figure 16 is different from the component of the Bernoulli pressure term shown in Figure 15. At the entrance of the channel the total surge force shows a resistance increase while the Bernoulli term predicts a resistance reduction. The difference is due to the unsteady (first) term in the pressure of Equation 8. This term is related to the rate of change of the surge added mass on approaching the channel entrance. The increasing added mass reflects the kinetic energy in the fluid being increased by the vessel. The reaction to this is the increase in resistance. This increase is sufficient to overcome the negative resistance due to the Bernoulli term.

On average, both methods of computation of the hydrodynamic forces agree reasonably well however, in a real time application of forces with strong fluctuations to a dynamic simulation of ship manoeuvres may lead to unstable simulation results and are as such undesirable.
The cause for the fluctuations in the forces and yaw moment are related to the fact that the source panels on the

vessel are sliding past the source panels of the channel sides. This results in what might be termed a 'cobblestone effect' in the results. This can only be reduced effectively by increasing the number of panels on both the vessel and the channel sides. This is, however, detrimental with respect to the computation effort and is also undesirable. Slight fluctuations are also seen in the added mass terms in Figure 14 and the Bernoulli pressure force terms shown in Figure 15 for the method using panels on the channel sides. These effects magnified in the total forces since the inertia term contribution, which is related to the added mass terms, is based on differentiation with respect to time.

Due to the fact that in the domain approach no panels are used to model the channel sides, the cobblestone effect is absent.

The results show that the multi-domain approach, which makes it possible to apply the double-symmetry model to the channel while leaving the entrance and exit to the channel open, is an attractive alternative. All the more so since it also allows water depth differences between the domains to be easily modelled as well.

4 CONCLUSIONS

In this paper multi-domain method for the prediction of ship-ship interactions based on the double-body potential flow equations was introduced. Comparative computations were carried with the domain method and the conventional method based on constant waterdepth and using only panels to model port geometry. Results show that for the classic case of passing vessel effects on a ship moored alongside a vertical quay, the predictions for forces on the moored vessel are almost identical.
The domain method was subsequently applied to the case of a vessel moored in a pocket alongside a vertical quay for which the conventional method is less suitable due to the extreme large number of panels needed to model the channel floor outside the pocket.

Finally, comparative computations were carried out for the case of a tanker sailing off-centre through a narrow channel. Results of added mass agreed reasonably well as well as the force components based on the velocity-dependent part of the pressure (Bernoulli pressure term). It was shown that, for a vessel passing closely to a vertical quay in the narrow channel, the conventional method based on modelling the channel sides by means of panels, extreme spikes appeared in the force records due to a 'cobblestone' effect related to the proximity of the panels of ship and channel.

Due to the use of the double-symmetry option to model the channel, this cobblestone effect is not present in the domain method.

There are some aspects which have not been addressed in this paper:

- Computation times have not been discussed. At this stage of the development the most important aspects are the accuracy and consistency of the results. Computations are carried using a GPU to speed up computations but the code has not been fully optimized.
- Potential flow computations of passing ship effects on moored ships have been correlated with model test results and found to be reliable for typical harbour speeds of large ships. [4]. For the ship-ship interaction problem, few comparisons have been made between computed and experimental results. This will be part of the future effort with respect to the development and the evaluation of the present method.

5 REFERENCES

1. Vantorre, M.; Verzhbitskaya, E.; Laforce, E. (2002). Model Test Based Formulations fo Ship-Ship Interaction Forces. *Ship Technology Research* Vol. 49, pp 124-141.

2. Sutulo, S; Guedes Soares, C.; Otzen, J.F. (2012). Validation of Potential-Flow Estimation of Interaction Forces Acting upon Ship Hulls in Parallel Motion*, Journal of Ship Research*, Vol.56, No.3, pp 139-145. SNAME

3. Lindberg, O.; Bingham, H.B.; Engsig-Karup, A.P.; Madsen, P.A. (2012). Towards Realtime Simulation of Ship-Ship Interaction*. 27th International. Workshop on Water Waves and Floating Bodies*. Kopenhagen.

4. Pinkster, J.A.; Bhawsinka, K. (2013). A real-time simulation technique for ship-ship and ship-port interactions. *28th International Workshop on Water Waves and Floating Bodies*. L'Isle sur la Sorgue, France

5. Talstra, H; Bliek, A.J. (2014). Loads on moored ships due to passing ships in a straight harbor channel. *PIANC World Congress*, San Francisco.

6. Koning Gans, H. J. de; Huijsmans, R.H.M.; Pinkster, J.A. (2007). A Method to Predict Forces on Passing Ships under Drift. *9th International Conference on Numerical Ship Hydrodynamics*, Ann Arbor, Michigan.

7. Bunnik, T.; Toxopeus, S. (2011). On the modeling ofpassing ship effects, *26th International Workshop onWater Waves and Floating Bodies,* (IWWWFB 2011),Greece.

8. Korsmeyer, F.T.; Lee, C.-H.; Newman, J.N. (1993). Computation of Ship Interaction Forces in RestrictedWaters, *Journal of Ship Research*, Vol. 37, No. 4, pp 298-306

9. Grue, J.; Biberg, D. (1993). Wave Forces on MarineStructures with small speed in water of restricted depth, *Applied Ocean Research* 15, pp 121-135

10. Newman, J.N. (1992). The Green function for potentialflow in a rectangular channel. *Journal of Engineering Mathematics* 26: 51-59

11. Pinkster, J.A. (2011). A multi-domain approach in 3-d diffraction calculations. *30th International Conference on Ocean, Offshore and Arctic Engineering*, Rotterdam.

12. Xiang, X.; Faltinsen,O.M. (2010). Maneuvering of Two Interacting Ships in Calm Water, *11th International Symposium on Practical Design of Ships and Other Floating Structures*, Rio de Janeiro.

6 AUTHOR'S BIOGRAPHY

J. A. Pinkster is a graduate of Delft University of Technology and he obtained a PhD from the same university in 1980. He worked at MARIN, Wageningen from 1970-1990 and subsequently became Professor of Ship Hydromechanics in the Marine Technology Department of Delft University. He retired from Delft in 2006 and has since then been active in consultancy for the marine community and in the development of new methods of analysis for ships and offshore structures.

4th MASHCON, Hamburg - Uliczka et al. (eds) - © 2016 Bundesanstalt für Wasserbau ISBN 978-3-939230-38-0 (Online)
DOI: 10.18451/978-3-939230-38-0_21

PASSING SHIPS INTERACTION IN THE OIL TERMINAL OF SÃO SEBASTIÃO (BRAZIL): AN APPLIED STUDY TO DEFINE THE OPERATIONAL LIMITS

F Ruggeri and **R A Watai,** Argonáutica Engineering & Reseach, Brazil
E A Tannuri, Numerical Offshore Tank of the University of São Paulo (TPN-USP), Brazil

SUMMARY

The passing ship effect in a moored vessel is a well-known problem discussed in the literature that involves harbour operations. The consequences of these interactions are dynamic loads in the mooring system that can exceed the design values and lead to severe accidents as, for example, the one occurred with the Yusho Regulus and Coal Hunter ships in Santos port (Brazil). This paper presents the application of a numerical method for the evaluation of mooring loads due to passing ship problems in São Sebastião port (TEBAR), which is one of the most important oil terminals in Brazil. The specific operation studied is a Ship-to-Ship transfer considering several vessels (VLCC-VLCC, VLCC-Suezmax), a condition where no simplified regressions is available to estimate the passing ship forces. Therefore a Rankine Panel Method (RPM) is applied to evaluate these effects. The forces computed by means of the panel method are applied in the mooring integrity analysis code (MeDuSa) to verify the maximum loads, which are then compared to design criteria so as to define the maximum operational conditions. The mooring arrangement, cable properties, fender etc. are determined by following OCIMF STS recommendations, as well as the Q88 form available for the design vessels.

1 INTRODUCTION

In a near future, the exploration and transportation of Brazilian pre-salt layer petroleum will demand a large number of support, transport and offloading vessels in order to supply all operations, increasing waterway and port traffic and consequently the chances of berthed ship-passing-ship interaction events.

Consequently, the berthed ship -passing ship interaction prediction is very important for the safety of waterways, port facilities and open sea operations that can be critical if the ships are sailing close to each other and/or through a constrained channel, in which wall effects may increase those interactions, justifying a specific study.

In the past, model scale tests were commonly performed for estimating the hydrodynamic loads involved in such a problem. The reference [1] presented an extensive passing ship experimental campaign in which several arrangements relating distance, ship size and speed were investigated. Other experimental results may be found in [2], [3] and [4], among others. However, this approach is a very costly way to study the phenomena, especially if the number of distinct setups/operations is large.

In this sense, some researchers were motivated to create empirical regressions that can be extended for other conditions as may be observed, for example, in [4] that provides expressions for estimating forces and moments based on model tests data with series 60 ships in shallow water, which may be useful for simple hand calculations or for use in spreadsheet predictions. Other empirical regressions are also proposed in [5] and [6].

Another approach, based on mathematical models, is presented in [7], which applied the slender body theory for evaluating the interaction effects involved in the passing ship problem. This method, however, is limited to simple and slender hull forms and might not be properly applied in situations involving large oil carriers, such as the ones used in Oil & Gas operations.

The advances in computational capability and numerical methods allowed the continuous improvement of mathematical models for hydrodynamic problems. The reference [8] presented calculations considering two identical and parallel Wigley hulls using RANSE CFD method (RNG k-ε turbulence model) and compared the results with the potential flow boundary elements method (BEM) proposed by [9], demonstrating a good agreement between both solutions. The reference [10] presented numerical solutions and validations for conditions involving non-zero ship drift angle obtained via the CFD code ReFRESCO and a 3D BEM, in which the authors conclude that for drift angle higher than 7.5 degrees, the CFD is a better option to be applied. For zero drift angles, however, fortunately the 3D BEM is a sufficient method for the problem, providing efficient solutions in terms of computational time.

The present paper presents briefly the formulation of the 3D BEM code developed in the Numerical Offshore Tank of the University of Sao Paulo (TPN-USP) used to solve the passing ship problem. The code was compared in [11] to empirical expressions proposed by [4], the strip body theory method presented by [7] and experimental data obtained by model tests carried out in the State of São Paulo Institute for Technological Research (IPT), presented in [12].

The numerical method is then applied to compute the hydrodynamic forces in the case of a berthed ship-to-ship operation in São Sebastião Port (Brazil), one of the most important oil terminals in Brazil, illustrated in Figure 1. For this specific operation, no simplified regression is available considering 3 vessels (2 of them only separated by pneumatic fenders), and a 3D BEM numerical model

was applied to evaluate the berthed ships - passing ship interaction forces.

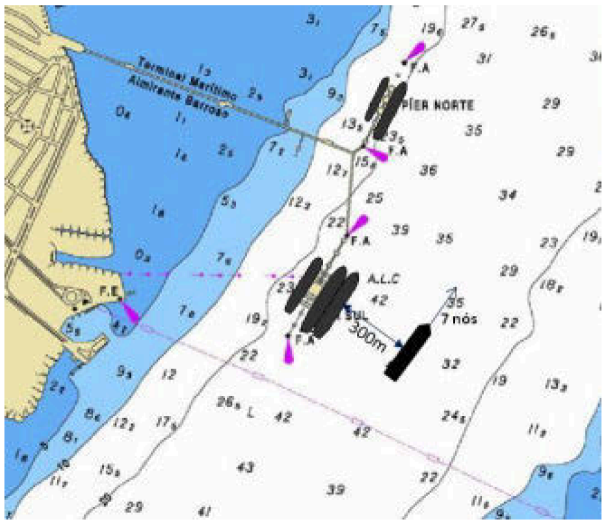

Figure 1. STS operation in the berth and a passing vessel along the channel

After the hydrodynamic loads are computed in each vessel, the mooring integrity is evaluated using the MeDuSa code, also presented, that considers the dynamic loads due to passing ships, current and wind forces. The last two forces (current and wind) are computed using CFD, taking into account the "shadow effect" due to the proximity of the STS vessels, and providing the forces in each vessel independetly.

2 MATHEMATICAL MODEL

2.1 HYDRODYNAMIC MODEL FOR THE CALCULATION OF THE PASSING SHIP INTERACTION LOADS

The procedure used to estimate the forces and moments originated by the problem of a ship passing on the side of a berthed ship may be also treated by means of the double body potential flow. Under the hypothesis of incompressible and irrotational flow, and inviscid, isotropic and homogeneous fluid, the velocity vector field $\vec{V}$ is assumed conservative and, therefore, may be written as the gradient of a scalar potential function φ, as presented in equation (**1**), therefore the continuous equation is replaced by the Laplace equation (**2**) in volume Ω.

$$\vec{V} = \nabla\varphi \tag{1}$$

$$\nabla^2\varphi = 0 \text{ in } \Omega \tag{2}$$

Following [13] and [14], the free surface effects were not considered, since its influence was assumed small upon the low Froude number values evaluated.

Within this scope, the appropriate boundary conditions for determining the potential flow are described by the impermeability condition (**3**) and (**4**) on the lateral walls, bottom and ships wetted surfaces, and a zero flux equation (**5**) at the mean water level $z = 0$, as follows:

$$\frac{\partial\varphi}{\partial n} = 0 \text{ on the captive ship surface, domain bottom and lateral walls} \tag{3}$$

$$\frac{\partial\varphi}{\partial n} = \vec{U}\cdot\vec{n} \text{ on the passing ship surface} \tag{4}$$

$$\frac{\partial\varphi}{\partial z} = 0 \text{ at } z = 0 \tag{5}$$

where $\vec{n}$ and $\vec{U} = (-U,0,0)$ are the normal vectors of the ships wetted surfaces and the ship forward speed vector, respectively.

Through the use of the Green's Second Identity, the volume problem may be rewritten in terms of a boundary formulation expressed by the second type Fredholm integral equation (**6**).

$$\iint_{\partial\Omega}\left[\left(\frac{1}{r}+\frac{1}{r'}\right)\frac{\partial\varphi}{\partial n} - \varphi\frac{\partial}{\partial n}\left(\frac{1}{r}+\frac{1}{r'}\right)\right]d\partial\Omega = 2\pi\varphi \tag{6}$$

in which $1/r$ is the Rankine source and $\partial\Omega$ is the boundary surface. The source image is assumed in order to avoid the above free surface discretization and guarantee the no-flux condition in the z=0 plane.

A three-dimensional Boundary Element Method (BEM), developed in TPN-USP, is then used to solve the boundary value problem specified. By the use of this method, the wetted surfaces of the ships, the lateral walls and the bottom are subdivided into a set of N quadrilateral panels with N collocation points. Moreover, the velocity potential, normal vectors etc. are assumed as constant values over each panel, leading to the so called Low Order Boundary Elements Method, firstly presented by [15]. An example of a typical panel mesh is illustrated in Figure 2.

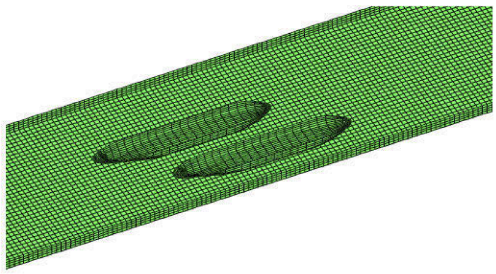

Figure 2. Example of a panel mesh with the two ships, domain bottom and lateral walls

By applying the collocation method, the integral equation (6) is discretized in equation (16), and the velocity potential determined by the solution of a linear system of N equations,

$$2\pi\varphi_i + \sum_{j=1}^{N}\varphi_j\iint_{S_j}\frac{\partial}{\partial n_j}\left(\frac{1}{r_{ij}}+\frac{1}{r_{ij}'}\right)dS_j = \sum_{j=1}^{N}\frac{\partial\varphi_j}{\partial n_j}\iint_{S_j}\left(\frac{1}{r_{ij}}+\frac{1}{r_{ij}'}\right)dS_j \tag{7}$$

where the indexes $i = 1,2,3...N$ and j denote to collocation and source panels, respectively, and S_j is the surface of the panel j.

Once the velocity potentials for each panel of the berthed ship are determined, the hydrodynamic pressure is evaluated through the use of the Bernoulli's equation (8), in which the time derivative term is evaluated by means of a centered difference scheme. Notice that the quadratic velocity term was neglected since the disturbance velocities were assumed small. The hydrostatic restoration term is neglected since it is assumed that the induced roll, pitch and heave are small (which is also in accordance to the double body model) and it is balanced by the gravitational forces.

$$p = -\rho \frac{\partial \varphi}{\partial t} \tag{8}$$

in which ρ is the density of water.

Hence, the hydrodynamic forces and moments are obtained by simply pressure summation over the panel collection for each body, as presented in expressions (9) and (10), respectively.

$$\vec{F}^{\,t+\frac{\Delta t}{2}} = -\rho \sum_{J=1}^{N_c} \frac{\left(\varphi_j^{t+\Delta t} - \varphi_j^{t}\right)}{\Delta t} \vec{n}_j A_j \tag{9}$$

$$\vec{M}_o^{\,t+\frac{\Delta t}{2}} = -\rho \sum_{J=1}^{N_c} \frac{\left(\varphi_j^{t+\Delta t} - \varphi_j^{t}\right)}{\Delta t} \vec{n}_j \wedge \vec{r}_{jo} A_j \tag{10}$$

where A_j is the area of the panel j, N_c is the set of panels which belong to the captive ship and the index O is the pole from which the moment is calculated.

The linear system of equations resultant from equation (7) is solved for discrete time steps Δt as the passing ship advances, since the relative positions between the vessels change during the calculations. Consequently, the coefficients that multiply the velocity potential and its normal derivative, which are expressed by the two surface integrals in equation (7), must also be recalculated and the influence matrix inverted at each instant of time t. This procedure is responsible for most of the consumption of time and computational memory during the simulations and, therefore, only the quantities involving panels from different ships, in which the relative distance changes, were updated.

The convergence of the meshes was checked by comparing the forces in x and y directions, as well as the moment in z using the results obtained with three different meshes for the ships with an increasingly number of panels (511, 1022 and 2044). Through this analysis it was possible to set the number of panels of each ship to 1022 , since the results obtained with the two most dense meshes did not present significant differences.

An example of a typical panel mesh used for all the simulations is illustrated in Figure 3.

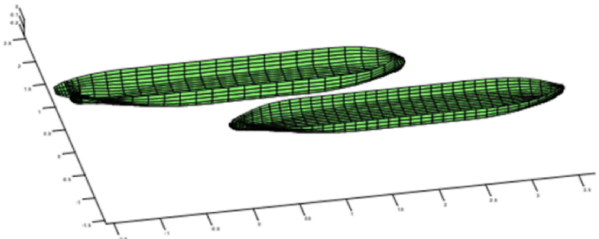

Figure 3. Example of a panel mesh disregarding domain bottom and lateral walls

2.2 MOORING ANALYSIS SOFTWARE (MEDUSA®)

The MeDuSa software for mooring analysis can perform static, quasi-static and dynamic analysis. The static and quasi-static solutions are based on a linearization procedure therefore the solution is fast, allowing the simulation of thousand of environmental conditions, while the dynamic one is based on Cummins equation requiring more computational time. The static analysis is applied to define the critical conditions to be studied in more details using the dynamic one. This methodology will be discussed in details in a future work.

The first step of the mooring analysis is to compute the pretension of each individual line keeping the balance of the vessel, which is performed using a linear optimization model since the problem is usually hyper static. The objective function is to reduce the sum of all cables pretension (11), under the equilibrium constraints in the longitudinal, transversal directions and the moment, described in equations (12), (13) and (14), respectively. In these equations N_i and N_f are the number of cables and fenders, (x_{i0}, y_{i0}) or (x_{j0}, y_{j0}) are the fairleads coordinates, (X_{CG}, Y_{CG}, Z_{CG}) the vessel center of gravity position, θ_{i0} is the mooring line angle, F_i is the cable pretension, F_j the fender forces in transversal directions and F_j^* the friction forces in the fenders. The constraint (15) is used to guarantee that the fenders only "push" the vessel, constraint (16) is used to define the range of allowed pretensions in the cables (usually based on the winch capacities) and (17) is used to define the limits of friction forces.

$$min \sum_{i=1}^{N_i} F_i \tag{11}$$

$$\sum_{i=1}^{N_i} F_i \cos\theta_{i0} + \sum_{i=1}^{N_f} F_j^* = 0 \tag{12}$$

$$\sum_{i=1}^{N_i} F_i \sin\theta_{i0} + \sum_{j=1}^{N_f} F_j = 0 \tag{13}$$

$$\sum_{i=1}^{N_i} F_i[\sin\theta_{i0}\,(x_{i0}-X_{CG})-\cos\theta_{i0}(y_{i0}-Y_{CG}) - \sum_{i=1}^{N_f} F_j^*\,(y_{j0}-Y_{CG}) + \sum_{i=1}^{N_f} F_j\,(x_{j0}-X_{CG}) = 0 \quad (14)$$

$$F_j > 0, j = 1,2,\dots N_f \quad (15)$$

$$F_{refmin} < F_i < F_{refmax}, i = 1,2,\dots N_i \quad (16)$$

$$-\mu_{max}F_j \le F_j^* \le \mu_{max}F_j, j = 1,2,\dots N_f \quad (17)$$

After the pretensions are computed the linear static solution is computed based on Hooke's law (18), considering the linearized cable elongation (19), where $(\Delta x_i, \Delta y_i, \Delta z_i)$ are the fairlead motions, which can be computed from the rigid body motions $(X_1, X_2, X_3, X_4, X_5, X_6)$=(surge,sway,heave,roll,pitch,yaw) using equation (20), assuming a linearization hypothesis.

$$F_i = K_i \Delta l_i \quad (18)$$

$$\Delta l_i = \frac{1}{l_0}(\Delta x_{i0}\Delta x_i + \Delta y_{i0}\Delta y_i + \Delta z_{i0}\Delta z_i), \quad i = 1,2,\dots N_i + N_f \quad (19)$$

$$\begin{Bmatrix}\Delta x_i\\ \Delta y_i\\ \Delta z_i\end{Bmatrix} = \begin{Bmatrix}X_1\\ X_2\\ X_3\end{Bmatrix} + \begin{Bmatrix}X_5(z_{i0}-Z_{CG}) - X_6(y_{i0}-Y_{CG})\\ X_6(x_{i0}-X_{CG}) - X_4(z_{i0}-Z_{CG})\\ X_4(t_{i0}-Y_{CG}) - X_5(x_{i0}-X_{CG})\end{Bmatrix} \quad (20)$$

Therefore the additional cable forces (in relation to the pretension) can be computed from the rigid body motions, the 6 variables to be solved. The forces in each cable or fender can be decomposed in forces and moments in the 6 DoF. The sum of all cable forces provides an equivalent stiffness matrix $[K_t]_{6X6}$ and the environmental forces acting in the vessel are defined by a vector $\{F\}_{6X1}$. The linear system (21) is then solved to compute body motions and after that the cables/fender elongation. If the cable forces are negative or the fender forces positive (considering the pretensions computed previously) the cable/fender contribution to the stiffness matrix is eliminated and the solution recomputed.

$$[K_t]_{6X6}\{X\}_{6X1} = \{F\}_{6X1} \quad (21)$$

The procedure is summarized in Figure 4.

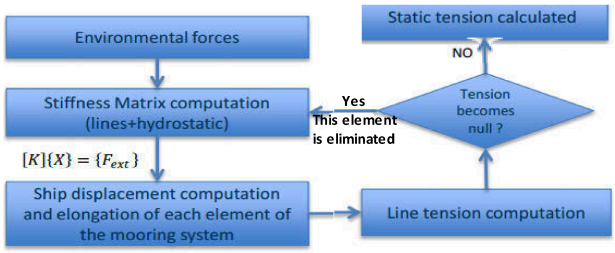

Figure 4. Summary of the linear mooring model.

The non-linear solution considering the "real" fender/cable curves ($K_i = K_i(\Delta l_i)$) can also be computed assuming the linearized solution as the initial point in order to simplify the convergence. The dyamic solution can also be computed based on Cummins equation from the pretension values, as described previously. However the computation time rate is about 1:100 considering the static (quasi-static) and dynamic approach, therefore only for some critical conditions the dynamic approach is applied. The wave model will not be described since the studied terminal is sheltered from waves.

The wind and current coefficients were evaluated using CFD models to compute the forces in each vessel, considering the "shadow" effect, for two different loading conditions (VLCC-starboard-loaded/VLCC-portside-ballast and VLCC-starboard-ballast/VLCC-portside-loaded), assumed as the most critical from the operational point of view. Some examples of exposed areas assumed for CFD computations can be seen in Figure 5 and Figure 6. An example of the pressure field obtained can be seen in Figure 7.

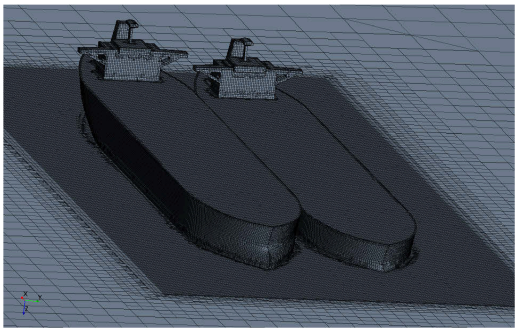

Figure 5. Exposed wind surface for wind forces computation using CFD.

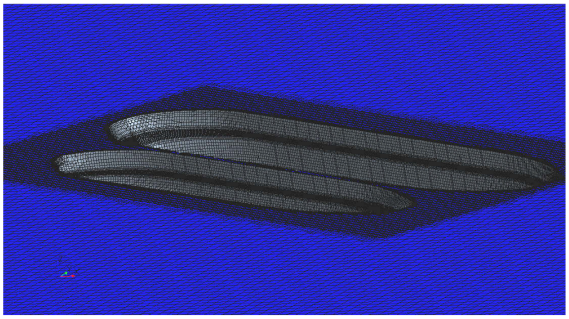

Figure 6. Exposed current surface for current forces computation using CFD.

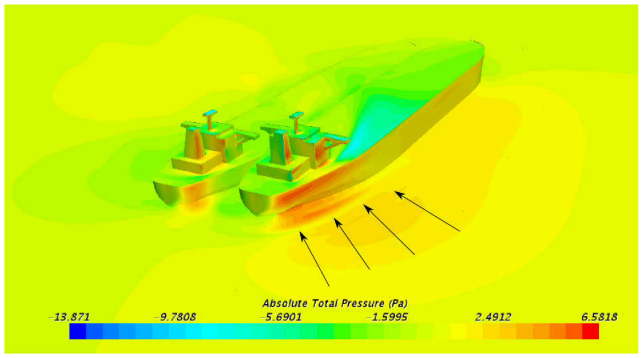

Figure 7. Pressure field in STS simulations using CFD.

The forces are non-dimensional following OCIMF recommendations and some examples of wind coefficients regarding both vessels can be verified in Figure 8, where it can be verified that the forces acting in the vessel in the shadow region are considerably smaller. A similar behavior is verified for current forces.

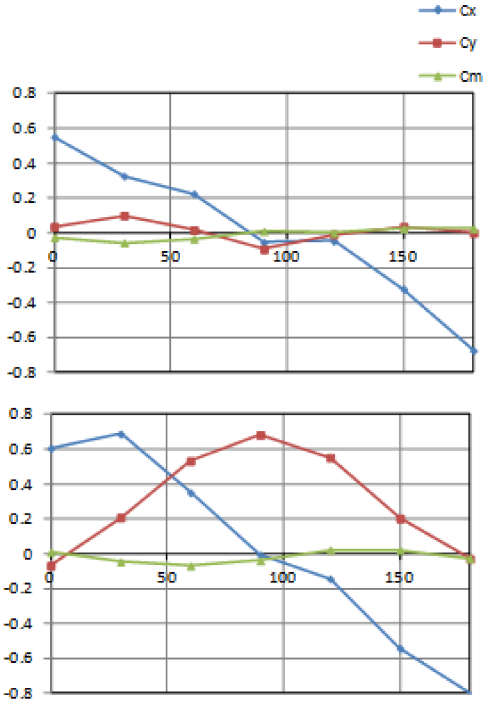

Figure 8. Wind coefficients for both vessels in STS simulation (bottom-exposed in ballast and top-shadow region loaded).

3 CASE STUDY

The methodology discussed in the previous sections is now applied to the analysis of limiting operational conditions of a mooring system of two ships in ship-to-ship arrangement berthed at the PP1 of the São Sebastião Oil Terminal (TEBAR). The TEBAR is located in the São Sebastião Channel, defined by the land and the São Sebastião Island. The natural navigation channel is approximately 800m wide and more than 24m deep, as indicated in the Figure 9.

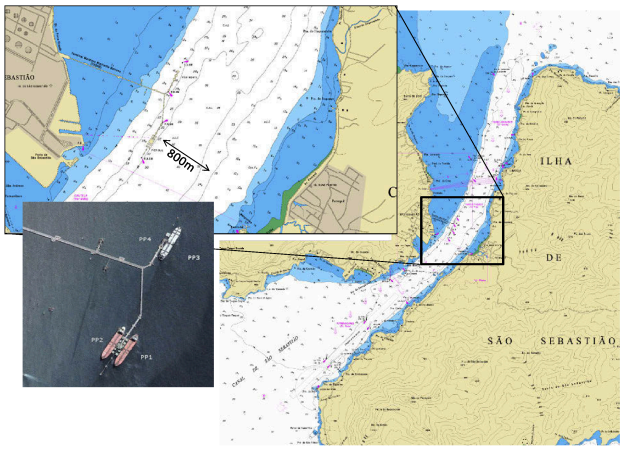

Figure 9. São Sebastião Terminal Location and Channel Dimension

In order to optimize the oil exportation logistics, Petrobras (the Brazilian oil state company) and its subsidiary Transpetro (owner of the Terminal) intends to perform a ship to ship (STS) oil transfer in the external berth (PP1), involving VLCC´s and Suezmax´s classes tankers.

Analyses of different aspects of these operations have been carried out by the University of São Paulo and the company Argonautica Engineering & Research. The analyses include an updated bathymetry, current measurements campaign, hydrodynamic flow modelling, fast and real time manoeuvring simulations, different mooring arrangements, prediction of the loads in the terminal equipments, cables and structures, definition of environmental window and availability of the operation in general.

Besides the analysis of the ship-to-ship operation itself, an additional concern of the Maritime Authority is the possible restrictions that the STS operations might bring to the navigation along the channel, as illustrated in Figure 10. As may be observed in the figure, the ships must navigate along the channel in order to reach the anchorage area in the north and hence any additional restriction in the navigation speed or safe distance to the oil terminal must be properly evaluated.

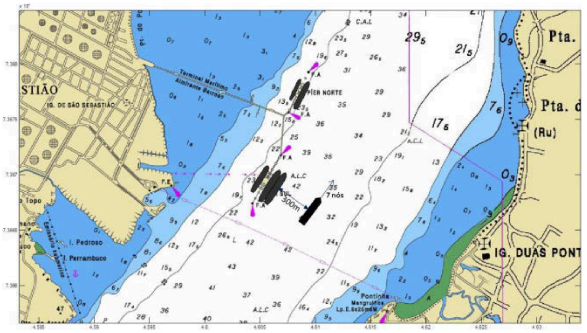

Figure 10. STS operation in the berth PP1 and a vessel along the channel

The critical case is represented when two VLCC vessels are berthed in STS configuration, and a VLCC tanker in full load condition is navigating along the channel. The main characteristics of the vessels considered in the present study are presented in the **Table 1**.

Table 1. VLCC mains characteristics

VLCC Characteristics	Ballasted	Full Loaded
Displacement (ton)	143920	347937
Draft (m)	10.0	22.3
Total Length LOA (m)	332	
Length Bet. Perp. LBP (m)	320	
Beam (m)	58	
Depth (m)	31	
Lateral Windage Area(m^2)	7673	3744
Frontal Windage Área (m^2)	1833	1132

The analyses were performed by considering not only the passing ship loads, but also including the effects introduced by current and wind. At TEBAR, the current velocity along the channel may reach up to 4 knots, and an extensive monitoring campaign and hydrodynamic model has been performed in order to predict the current close to the berths. The current flow is aligned to the central axis of the channel, going to NE or SW as indicated in the Figure 11.

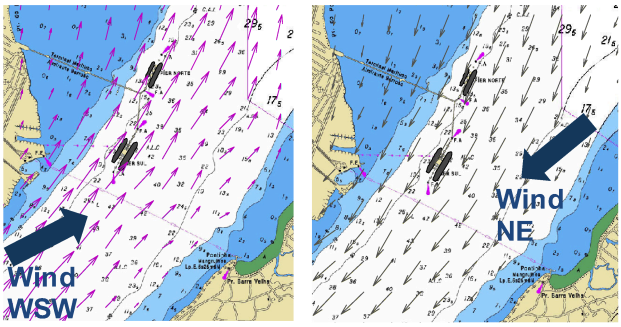

Figure 11. Current flow in the Terminal: (left) NE; (right) SW

The wind direction is mainly NE, but some strong wind gusts can be verified from WSW direction, reaching up to 40 knots. Therefore, in order to perform a conservative analysis, wind is assumed to come from the same direction as the current flow, as indicated in the Figure 11.

The mooring arrangement is defined following the OCIMF STS Guide recommendations, using 42mm diameter steel wire and 121ton maximum breaking load (MBL). A 55% MBL is adopted as failure criterion of the lines whereas for the fenders the maximum allowed compression loads are considered. Figure 12 shows the mooring arrangement and indicates the number of each type of mooring lines.

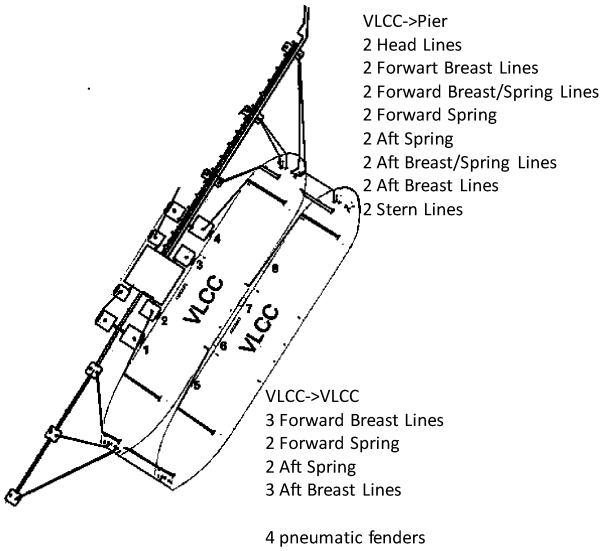

Figure 12. Mooring Arrangement for 2 VLCC in STS configuration

Firstly it is discussed the evaluation of the mooring loads in a 1-year operation, with no passing vessel along the channel. In this analysis, it was observed that the critical lines are the spring lines connecting the vessels and the aft breast line between the quay and the inner vessel. The maximum extreme load observed in these 1-year environmental conditions was 40% of the line MBL. Analogous analysis concerning the prediction of maximum loads was also performed for the pier structure and inland equipment (Figure 13), indicating that the loads on these structures reached 45% of the maximum dimensioning load of the dolphins.

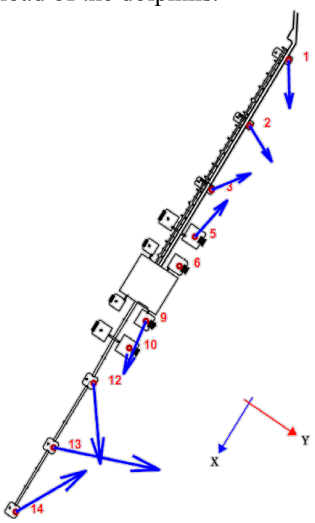

Figure 13. Loads in the pier and equipments

The limiting environmental conditions are obtained by exhaustive calculation of the loads in the mooring lines, structures and equipments, in which several current and wind values are taken into account. Figure 14 shows the results, in which the red markers indicate a combination of wind and current speed that induces a non-admissible load, whereas the green ones indicate safe conditions. The blue line indicates the limiting environmental conditions for the scenario disregarding the passing ship

effect, which illustrates that for safe conditions the current and wind must be lower than 2.8knots and 30knots, respectively.

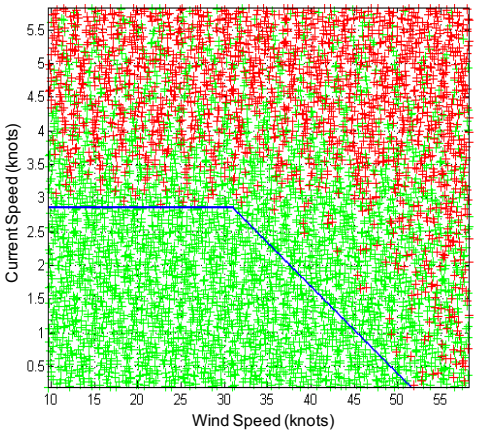

Figure 14. Maximum environmental conditions for VLCC-VLCC STS operation

Now, results considering the extra loads induced in the mooring system by a full-loaded VLCC navigating at 7knots along the channel are discussed. This ship speed was informed by the Maritime Authority as being a common ship navigation velocity at the port channel.
In this analyses, the 3 vessels are modelled using the Rankine Panel Method aforementioned, and the forces in each moored vessels are obtained and used as input data to MeDusA® software, which is applied for the mooring load calculations.

Results of the interaction forces induced by the passing ship on the berthed ones at the quay are presented in Figure 15, where it may be noticed that the forces reach relatively high values of 22tonf and 75tonf for distances between the vessels of 200m and 300m, respectively.

By applying these interaction loads on the mooring system of the ships, the maximum environmental conditions could be re-evaluated as shown in Figure 16 for the ship distance between the vessels of 300m. As may be observed, results show that when considering the 300m distance, the new current speed limit was slightly reduced from 2,8knots to 2,75knots. This small change is considered to be within the limits of uncertainty of the prediction technique.

The same calculation was done for the smaller passing ship distance, and the limit current speed was reduced, thus increasing the restrictions to the STS operations at the berth.

As a final recommendation, the study indicated that the STS operation can be carried out and the navigation along the channel is not affected, as soon as the vessel maintains a minimum distance of 300m to the vessels in the berth and keeps the maximum speed of 7 knots.

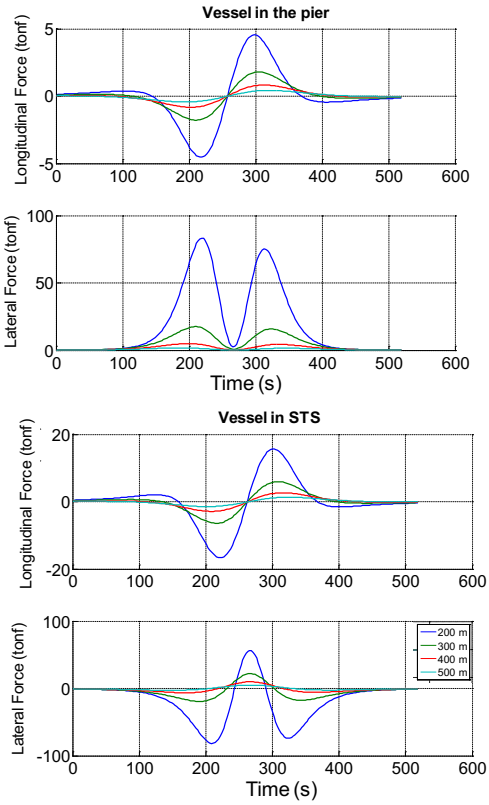

Figure 15. Hydrodynamic interaction forces

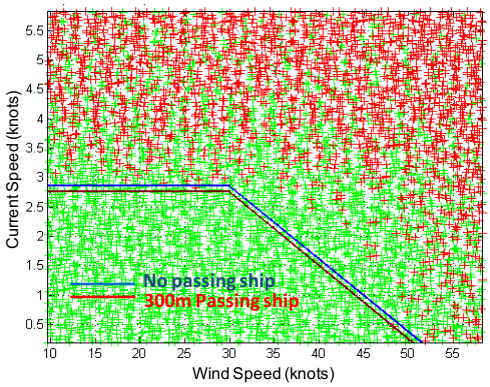

Figure 16. Maximum environmental conditions for VLCC-VLCC STS operation for the passing ship case

4 CONCLUSION

The application of a numerical method for the evaluation of mooring loads due to passing ship problems in São Sebastião Port (TEBAR) was presented in this paper. The specific condition studied is the passing ship problem involving a VLCC vessel navigating along the port channel and two other ones arranged in a ship-to-ship configuration at one of the port quays.

The analyses were performed by calculating the passing ship interaction forces by means of a Boundary Elements method. These forces were then imposed as input data on MeDuSa® software, which was responsible for the calculation of the loads on the mooring lines and fenders.

Besides, current and wind loads were also taken into account.

The results were focused on the definition of limiting environmental conditions to the ship-to-ship operations at the port quay, which were determined for scenarios with and without the influence of the VLCC navigating along the channel.

Results have shown that the VLCC navigating at the port channel at 7 knots in a distance shorter than 300 m was responsible for the imposition of a restrictive condition of current speed for the STS operations. Moreover, the results have also illustrated that as soon as the navigating vessel maintains a minimum distance of 300m to the vessels in the berth and keeps the maximum speed up to 7 knots the STS operations are not significant affected.

5 ACKNOWLEDGEMENTS

Authors gratefully acknowledge Petrobras for allowing the publication of the results. Third author acknowledge the CNPq by the research grant (process 308645/2013-8).

6 REFERENCES

1. Remery, G.F.M. (1974). Mooring Forces Induced by Passing Ships, *Offshore Technology Conference*.

2. Delefortrie, G. ; Vantorre, M. ; Cappelle, J. ; Ides, S. (2012). The Effect of Shipping Traffic on Moored Ships. *10th International Conference on Hydrodynamics*, October 1 - 4, St. Petersburg, Russia.

3. Duffy, J.T. ; Denehy, S. ; Ranmuthugala, D ; Renilson, M.R. (2013). The effect of berth blockage on berthed ship - passing ship interaction. *Conference Proceedings, 3rd International Conference on Ship Manoeuvring in Shallow and Confined Water*, 3-5 June, Ghent, Belgium, pp. 237-247.

4. Kriebel, D. ; Seelig, W. ; Eskijian, M. (2005). Mooring loads due to parallel passing ships. *Naval Facilities Engineering Service Center*, Port Hueneme, California, USA.

5. Flory, J. (2002). The Effect of Passing Ships on Moored Ships, *Prevention First 2002 Symposium*, California State Lands Commission, USA.

6. Varyani, K.S. ; Vantorre, M. (2006). New Generic Equations for Interaction Effects on a Moored Containership Due to a Passing Tanker. *Journal of Ship Research*, Vol. 50, No. 3.

7. Wang, S. (1975). Dynamic effects of ships passage on moored vessel, *Journal of Waterways*, *Harbours and Coastal Engineering Division*.

8. Yang, H. ; Wu, B.S. ; Miao, Q.M. ; Xiang, X. ; Berg, T.E. ; Kuang, X.F. (2011). Study on the Effects of Unsteady Ship to Ship Interaction by CFD Method. *2nd International Conference on Ship Manoeuvring and Confined Water: Ship to Ship Interaction*.

9. Xiang, X. ; O.M. Faltinsen. (2010). Manoeuvring of two interacting ships in calm water, *PRADS*, Rio de Janeiro, Brazil

10. Bunnik, T. ; Toxopeus, S. (2011). Viscous Flow Effects of Passing Ships in Ports. *Proceedings of the ASME 2011 30th International Conference on Ocean, Offshore and Arctic Engineering OMAE2011*, Roterdam, The Netherlands.

11. Watai, R.A. ; Ruggeri, F. ; Tannuri, E. A. ; Weiss, J. (2013). Evaluation of empirical and numerical methods on the prediction of hydrodynamic loads involved in the passing ship problem, *3rd International Conference on Ship Manoeuvring in Shallow and Confined Water*, 3-5 June, Ghent, Belgium, p. 167-175.

12. Araujo, M.F.B.P. ; Pereira, A.A.P. ; Carmignotto, M.A.P. ; Weiss, J.G.M. ; Gandara, M.A. (2011). Mooring Loads Induced by other Ships in Navigation Channels. *XXII COPINAVAL – IPIN,* Buenos Aires, Argentina.

13. Korshmeyer, F.T. ; Newman, J.N. (1993). Computational of Ship Interaction Forces in Restricted Waters, *Journal of Ship Research*.

14. Pinkster, J.A. (2004). The Influence of a Free Surface on Passing Ship Effects, *Int. Shipbuilding Prog.*, 51, no. 4.

15. Hess, J.L. ; Smith, A.M.O. (1964). Calculation of nonlifting potential flow about arbitrary three-dimensional bodies, *Journal of Ship Research*.

16. Varyani, K.S. ; Krishnankutty, P. (2006). Modification of ship hydrodynamic interaction forces and moment by underwater ship geometry. *Ocean Engineering*, Vol. 33, pp. 1090-1104.

7 AUTHORS' BIOGRAPHIES

Felipe Ruggeri, M.Sc, Mr. Ruggeri has graduation and M.Sc degrees from the Naval Architect and Ocean Engineering Department of the University of São Paulo (USP) in 2010 and 2012, respectively, and is a Ph.D candidate developing the thesis entitled as "A Numerical Method for Non Linear Analysis of the Dynamics of Marine Systems under Gravity Waves and Current". From 2008 to 2015, he worked as a research engineer at the Tanque de Provas Numérico of USP developing projects on green ship designs, high speed vessels for crew transportation and also design of logistic hubs for the Pre-Salt layer in Brazil. Mr. Ruggeri is one of the founders and director of ARGONAUTICA

ENGINEERING AND RESEARCHES where he has been mainly involved in the conduction of fast-time simulations for maneuvering analysis and development of innovative numerical tools to improve operational safety and efficiency of ports, which includes, for example, the development of ReDRAFT® (Real Time Draft) and MeDuSa® (Mooring Design Tool) software.

Rafael de Andrade Watai, Ph.D, Dr. Watai is graduated (2010) and Doctor of Sciences (2014) in Naval Architect and Ocean Engineering by the University of São Paulo (USP). From 2006 to 2014 he worked as a researcher at the Tanque de Provas Numérico of USP, participating on research projects of marine structures for oil exploration, mainly involved in mooring system designs, development of hydrodynamic numerical tools and model tests conduction and specification. Dr. Watai is one of the founders and director of ARGONAUTICA ENGINEERING AND RESEARCHES where he has been actively involved in the implementation of computational hydrodynamic tools for seakeeping analysis of floating bodies, hydrodynamic interaction problems induced by the passing ships effect and also for breakwater efficiency predictions.

Eduardo Aoun Tannuri, Associate Professor at the Department of Mechatronics Engineering, Escola Politécnica, University of São Paulo (EPUSP), and one of the coordinators of the Numerical Offshore Tank (TPN). Member of ITTC Maneuvering Committee. Works on Dynamic Positioning (DP) Systems applied to offshore vessels and platforms, Maneuvering and Sea-keeping time-domain simulation codes development and application and Experimental analysis of floating structures. He coordinates several R&D projects in the area of offshore oils&gas exploration, maritime and river navigation and port development.

4th MASHCON, Hamburg - Uliczka et al. (eds) - © 2016 Bundesanstalt für Wasserbau ISBN 978-3-939230-38-0 (Online)
DOI: 10.18451/978-3-939230-38-0_22

PARAMETRIC STUDY OF A MODIFIED PANEL METHOD IN APPLICATION TO THE SHIP-TO-SHIP HYDRODYNAMIC INTERACTION

S Sutulo and **C Guedes Soares,** Instituto Superior Técnico, Universidade de Lisboa, Portugal

SUMMARY

Properties of a new modification of the potential flow algorithm developed by the authors and called "dihedral panel method" are studied in application to the ship-to-ship interaction problem. The method uses quadrilateral dihedral panels with constant source density distributed. The non-penetration condition is satisfied in the integral sense over each panel using Gauss cubature formulae with various numbers of nodes. Numerical investigation was carried out for the case of a parallel overtaking manoeuvre modelled as a kinematic pseudo-simulation with output of the surge and sway forces and of the yaw moment. Responses for Gauss formulae with 1, 4 and 7 nodes per any triangular subpanel were compared with those obtained with the classic Hess and Smith algorithm demonstrating, at equal overall number of panels, better accuracy of the new method especially when an increased number of Gauss nodes is used.

NOMENCLATURE

L	Ship length, m
M	"Field" point
$\mathbf{n}$	Outer unity normal
N	Yaw moment, kNm
p	Pressure, Pa
P	Source point
r	Angular velocity of yaw, rad/s; or dis tance, m; or Gauss formula order
S	Wetted surface, m^2
t	Time, s
$\mathbf{V}$	Local velocity of surface point, m/s
$\mathbf{V}_{Ci}$	Velocity of origin of i th body, m/s
$\mathbf{V}_I$	Induction velocity, m/s
x, y, z	Coordinates in body frame, m
X	Surge force, kN
Y	Sway force, kN
ρ	Density of water, t/m^3
σ	Single layer density, m/s
ξ, η, ζ	Coordinates in fixed frame, m
ϕ	Velocity potential, m^2/s

1 INTRODUCTION

Ability to predict hydrodynamic interaction effects occurring during manoeuvring of surface displacement ships is rather important for adequate modelling of the ship's reactions in the bridge simulators and importance of the latter for appropriate training of human operators necessary for safe navigation is evident. Importance of mathematical modelling of this kind of forces is especially high due to the simple fact that full-scale training of this kind is impossible because of safety and economic considerations.

There were many publications on hydrodynamic interaction and a rather comprehensive review can be found in [9]. Regarding some later developments, the perfect-fluid formulation which includes wave effects including those stemming from oncoming sea waves was proposed and handled by Yuan et al. [11]. Also, direct application of CFD methods for RANS equations is becoming more and more popular, sea [3] as an example.

As dangerously close manoeuvres are mostly performed in slow speed, it is often acceptable to exploit the so-called Havelock hypothesis [1] stating that the hydrodynamic interaction is mainly caused by inertial hydrodynamic loads rather reliably estimated within the double-body potential flow model. Of course, the Havelock hypothesis does not hold when the velocities of the interacting ships are not sufficiently low and the wavemaking effects may become tangible especially in shallow water [5]. It is rather difficult to establish exact limits of the applicability of the waveless flow model as, for instance, the Froude number can be based on various linear distances even in the deep water case. In particular, if the Froude number based on the ship length is quite small (i.e. of the order 0.05–0.1) it may become quite large if one of the interacting ships is crabbing, which is possible when e.g. a tractor tug is interacting with a large assisted vessel, and its breadth must be considered as the characteristic length. Moreover, the characteristic length can be based on the distance between the ship hulls and indeed definite influence of the free-surface effects is always observed when the lateral clearance is of the order of 1m in full scale.

Viscosity is in general less important as viscous effects are much more localized but these also can be expected to be significant at large drift angles when developed separation of the flow happens but no definite conclusions on this matter can be drawn at present.
However, in spite of the mentioned limitations, the double-body potential flow interaction model often gives reasonable predictions and is unique from the viewpoint of absence of kinematic limitations i.e. it can be applied online at any mutual position and motion of the interaction bodies. The "curse of dimension" associated with the interaction problem is not always well understood but becomes evident in view of the fact that for a system of two unconnected bodies in 2D motion the overall number of state variables completely defining their position and

motion is 12 of which only 3, i.e. position and heading of one of the bodies, will not affect the hydrodynamic interaction loads. The simple fact that the interaction loads depend on 9 independent kinematical parameters practically exclude any possibility of preliminary computations or experiments [10] which would result in a sufficiently complete database for further online estimation of interaction forces and moments. All existing methods of this kind are based on incomplete experimental designs and cannot supply credible predictions in all situations.
At the same time, the double-body potential flow model can be applied in online simulations with sufficient speed and without necessity of any preliminary computations. During last several years such a model was developed by the authors and under their supervision at the Centre for Marine Technology and Ocean Engineering at the University of Lisbon [6–9], [12–16].

This model was based from the beginning on the well-known Hess and Smith panel method [2] and the primary in-house code was developed in Fortran 90 for the case of deep water or shallow water with constant depth [6]. The number of arbitrarily moving interacting bodies was also arbitrary although most of the computations were carried out for two interacting ships. The Fortran version was later extended to embrace the case of uneven bottom with arbitrary bathymetry [12–16]. At the same time, to facilitate fusion with the offline manoeuvring simulation program [7], the version only applicable to a flat seabed was recoded in C++ and that code was later extended to include propellers modelled with disks of sinks [8].
While in general the codes based on the Hess and Smith method produced quite satisfactory results, they showed also some visible uncertainty in predicting the surge interaction force. Such an imperfection of the Hess and Smith algorithm had already been known and was probably related to some peculiarities of the method caused by the fact that the quadrilateral panels were shifted to intersect the original hull surface introducing additional error to the integral loads. To fight this, Söding [4] proposed another variant of the panel method which he named "patch method" based on flat triangular and, where possible, quadrilateral panels forming an inscribed polyhedron. These panels serve only for fulfilling the non-penetration condition averaged over each panel while the induction velocities are coming from sub-surface point sources. This method typically gives more accurate results but in practice operating triangular elements is less convenient for ship forms and additional uncertainty is introduced by the applied desingularization presuming some subsurface submergence depth for the point sources.

The authors have undertaken an attempt to develop a panel method allegedly combining advantages of Hess and Smith's and Söding's approaches. This method is based on non-flat quadrilateral dihedral panels each constituted of two flat triangular subpanels. The distributed source density is assumed constant over each panel i.e. equal for the both subpanels which determines substantial difference from methods directly based on triangular panels. Induction from each subpanel is computed using the Hess and Smith formulae but collocation at a single point at a panel is here impossible as two different normals are associated with each of them. This predetermined application of the integral collocation using Gauss cubature formulae over each subpanel.

This paper presents brief description of the new panel method and results of its application to the prediction of interaction forces and moments obtained with various numbers of Gauss nodes on each subpanel compared also with results obtained with the classic Hess and Smith method.

2 PROBLEM FORMULATION AND MAIN RELATIONS

2.1 FORMULATION

The general formulation of the interaction problem is identical to that already presented in earlier publications by the authors and will only be briefly outlined here.

1. Unbounded perfect fluid is considered containing the plane $O\xi\eta$ is considered to which the axis $O\zeta$ is perpendicular and the ξ-, η- and ζ-axes form a right-hand Cartesian frame fixed in space. As the gravity is not involved, the orientation of the frame can be arbitrary but in application to surface ships it is natural to assume that the ζ-axis is oriented vertically downwards and its positive half corresponds to the actual water volume.
2. Present are N arbitrary moving in the horizontal plane doubled bodies with wetted surfaces $S_i, i = 0,\ldots,N-1$ all symmetric with respect to the plane $O\xi\eta$ intersecting them along the waterlines.
3. A body frame $C_i x_i y_i z_i$ is associated with each S_i so that the axes $C_i z_i$ remain always parallel to $O\zeta$ and the planes $C_i x_i y_i$ coincide with $O\xi\eta$. In the case of a ship hull each axis $C_i x_i$ lies in the centerplane of the hull and is directed from stern to bow while the axis $C_i y_i$ is directed to the starboard.
4. The instantaneous position of each body is described by the position vector $\mathbf{r}_{Ci}$ connecting O with C_i and its motion—with the velocity $\mathbf{V}_{Ci}$ and the angular velocity of yaw r_i.

It is assumed that the flow is completely described by the absolute velocity potential $\phi(\xi,\eta,\zeta,t)$ such as $\Delta\phi = 0$ over all the fluid volume; $\frac{\partial\phi}{\partial\zeta} = 0$ on the plane $O\xi\eta$;

$\frac{\partial \phi}{\partial n} = \mathbf{V} \cdot \mathbf{n}$ on S_i, where $\mathbf{n}$ is the outer unity normal, and $\mathbf{V}$ is the local velocity of a point on S_i depending on $\mathbf{V}_{Ci}$ and r_i. When the flow potential is known, the induced velocity is computed as $\mathbf{V}_I = \nabla \phi$.

2.2 SOLVING EQUATIONS

The primary integral equation for the source (single layer) density σ is:

$$2\pi\sigma(M) + \int_{S^+} \sigma(P) \frac{\partial G(M,P)}{\partial n_M} \mathrm{d}S(P) = f(M), \qquad (1)$$

where $M(\xi,\eta,\zeta)$ and $P(\xi',\eta',\zeta')$ are the points on S^+, which is the part of S for $\zeta > 0$; $f(M) = \mathbf{V}(M) \cdot \mathbf{n}(M)$ and the Green function is

$$G(M,P) = \frac{1}{r} + \frac{1}{\bar{r}}, \qquad (2)$$

where

$$\left.\begin{matrix} r \\ \bar{r} \end{matrix}\right\} = \sqrt{(\xi - \xi')^2 + (\eta - \eta')^2 + (\zeta \mp \zeta')^2}\ . \qquad (3)$$

Collocation methods solving the equation (1) presume the following steps:

1. The actual wetted surface S^+ is approximated with some surface $\tilde{S}$ which can be easily partitioned into n non-intersecting panels S_i: $\tilde{S} = \bigcup_{i=0}^{n-1} S_i$ In the case of the Hess and Smith method, first, the panels are formed and then they are united into $\tilde{S}$ representing a set of not necessarily connected flat quadrilaterals. In the dihedral method $\tilde{S}$ is an inscribed polyhedron whose facets are organized in pairs forming quadrilateral dihedral panels S_i.
2. On each panel the source density is approximated with some chosen shape functions depending on a number of parameters. In the both Hess and Smith and dihedral methods a 1-parameter constant density distribution is assumed.
3. Each panel serves also as a platform for satisfying discretely the equation (1). In the Hess and Smith case it is satisfied locally at one control point (usually the centroid) per panel. In the dihedral method each panel has two different normals and it is not possible to keep the same approach. The non-penetration condition is then satisfied in the integral sense for the whole panel.

As result, in the dihedral method the equation (1) can be re-written in the following semi-discretized form:

$$\begin{aligned} &2\pi\sigma_i S_i + \sum_{j=0, \neq i}^{n-1} \sigma_j \int_{S_i} \mathrm{d}S(M) \int_{S_j} \frac{\partial G(M,P)}{\partial n_M} \mathrm{d}S(P) \\ &= \int_{S_i} f(M)\,\mathrm{d}S(M), \quad M \in S_i, \quad i = 0,\ldots,n-1. \end{aligned} \qquad (4)$$

The set above must be solved with respect to the densities σ_i. After that, the induced velocities and the potential can be found as

$$\begin{aligned} \mathbf{V}_I(M) &= \sum_{j=0}^{n-1} \sigma_j \int_{S_j} \nabla_M G(M,P)\,\mathrm{d}S(P), \\ \phi(M) &= \sum_{j=0}^{n-1} \sigma_j \int_{S_j} G(M,P)\,\mathrm{d}S(P). \end{aligned} \qquad (5)$$

The pressure can then be calculated with the Bernoulli integral:

$$p(M) = \rho\left[-\frac{\Delta\phi(M)}{\Delta t} + \frac{1}{2}\left(\mathbf{V}^2(M) - \mathbf{V}_p^2(M)\right)\right], \qquad (6)$$

where $\mathbf{V}_p = \mathbf{V}_I - \mathbf{V}$, and the force and moment acting on a body are:

$$\mathbf{F} = -\sum_k \int_{S_k} p\,\mathbf{n}\,\mathrm{d}S; \quad \mathbf{M} = -\sum_k \int_{S_k} p\,\mathbf{r} \times \mathbf{n}\,\mathrm{d}S, \qquad (7)$$

where summations are only performed over the panels belonging to the body in concern.

All integrals over the panel S_j in the formulae above are calculated analytically using the formulae suggested by Hess and Smith with appropriate asymptotic simplifications at larger distances while the integrals over S_i or S_k are computed numerically, separately for each subpanel, with the Gauss integration formulae for triangles [17].
For any suitable function $g()$ the integral over each subpanel S_Δ is represented as

$$\int_{S_\Delta} g(M)\mathrm{d}S(M) \approx S_\Delta \sum_{k=1}^{m} w_k g(M_k), \qquad (8)$$

where m is the number of Gauss nodes M_k and w_k are the corresponding weights. Correspondence between the order of the Gauss formula r and the number of nodes is given by:

r	1	2	3	5
m	1	3	4	7

The nodes of the second-order formula are located not inside the triangle but on its sides which makes this case unsuitable for the method applied. Also, it is clear that

the first-order Gauss formula with the node at the centroid of the triangle and with unity weight is nothing else then application of the average value theorem.

3 NUMERICAL INVESTIGATION

3.1 OBJECTIVES AND SCENARIO

The aim of the present study is testing the new potential flow dihedral panel method in application to the ship-to-ship interaction in overtaking manoeuvre using Gauss integration of various order. Also, performance of the new algorithm should be compared with the already well validated Hess and Smith method.

The scenario presumes kinematical simulation of the parallel motion of two identical vessels. The hull form corresponds to the "tanker" shape used in [9] was taken as basis but transformed to match the particulars of the *S-175* container ship: $L = 175\text{m}$, $B = 25.4\text{m}$, $T = 9.5\text{m}$, $\nabla = 40842.6\text{m}^3$. The lateral distance between the centerplanes remained constant and equal to 38m which corresponds to the distance between the sidewalls 12.6m. The overtaking ship (Ship 1) was advancing with 6kn while the target ship to be overtaken (Ship 2) had the speed of 4kn. The overtaking simulation started when Ship 1 was 300m behind Ship 2 and ended when it was 300m ahead. The output was represented by time histories of the forces of surge, sway and yaw represented, however as functions of the relative longitudinal shift

$$\xi_s' = \frac{2(\xi_{C1} - \xi_{C2})}{L}. \tag{9}$$

The value $\xi_s' = -1.0$ corresponds to the situation when the midship of Ship 1 is abreast with the stern of Ship 2 while $\xi_s' = +1.0$ means it is abreast the stem.

3.2 GRID OF PANELS

All computations were performed with 2 grids: (1) coarse grid with 172 panels per hull and (2) a fine grid with 558 panels per hull. The panelled hull is shown in Figure 1. In addition, the computations with the Hess and Smith method were carried out for even finer grid with 1258 panels per hull.

It can be seen that the grids are not perfect in the sense that they do not represent a polyhedron without gaps. This is caused by the fact that the initial set of the hull offsets was subdivided into 5 sub-bodies with different number of contour points on each of them. This inequality was kept in the transformed hull representation. Although it can be noticed that some panels are definitely non-plane, their dihedral nature is not clearly demonstrated because of absence of the dividing diagonals on the sketch.

3.3 RESULTS

Numerical results in form of responses for the surge and sway interaction forces and for the yaw moment are shown in Figures 2 and 3 for the coarse grid and in Figures 4–5 for the finer grid.

Besides the responses obtained with the dihedral code with various order of the Gauss integration formulae, every plot contains also the response obtained with the classic Hess and Smith algorithm which had been validated by the authors earlier [6], [9]. In general, it must be

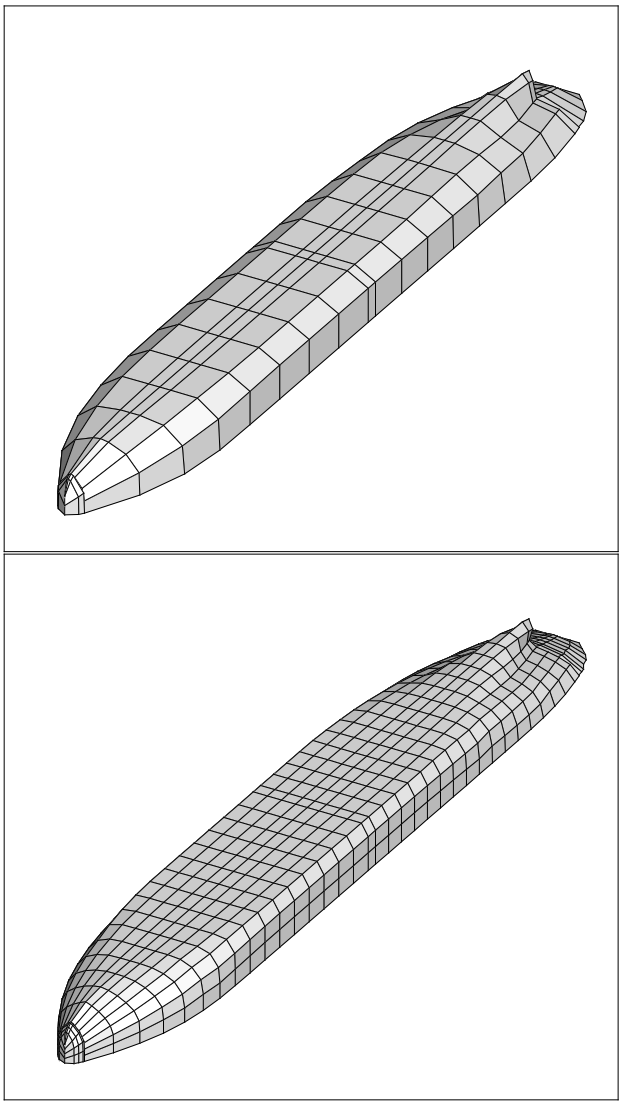

Figure 1. Panel grids used in computations

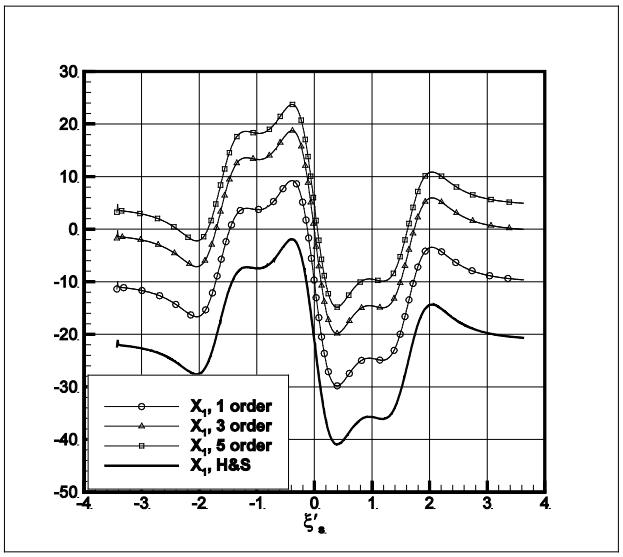

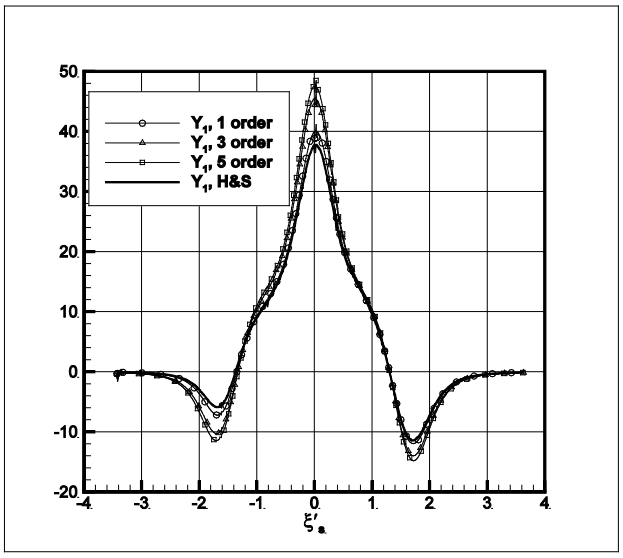

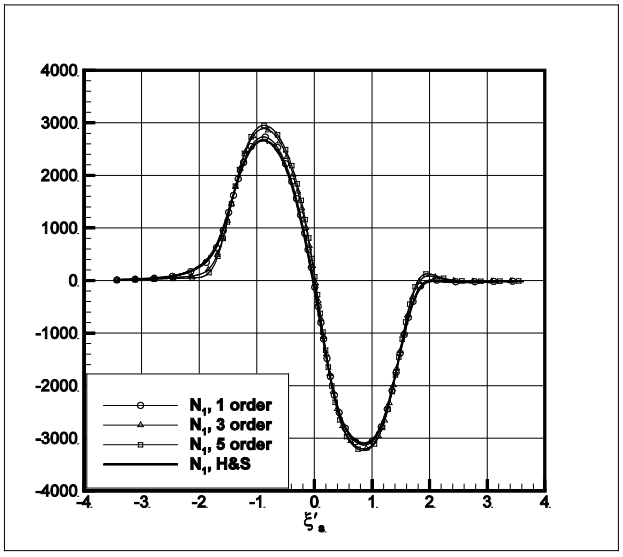

Figure 2. Interaction forces and moment responses for Ship 1 and coarse grid

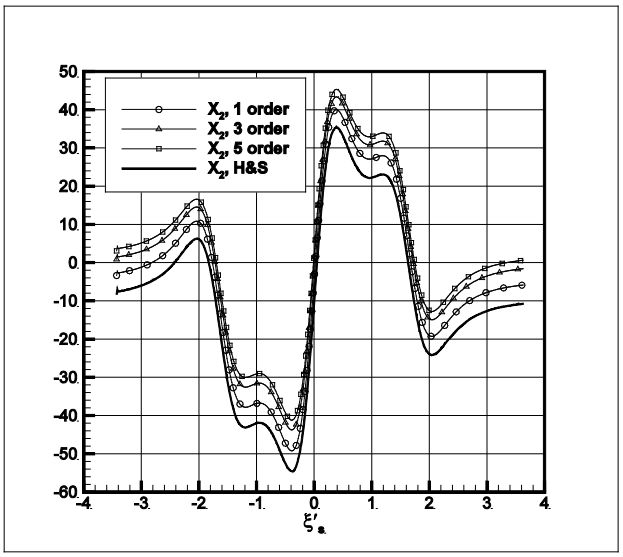

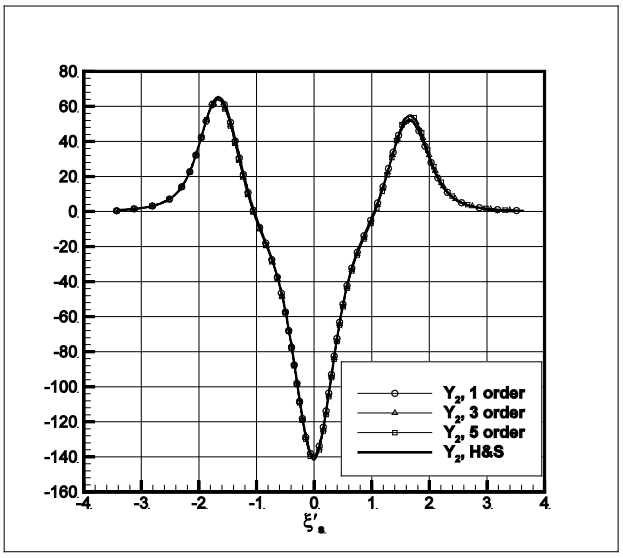

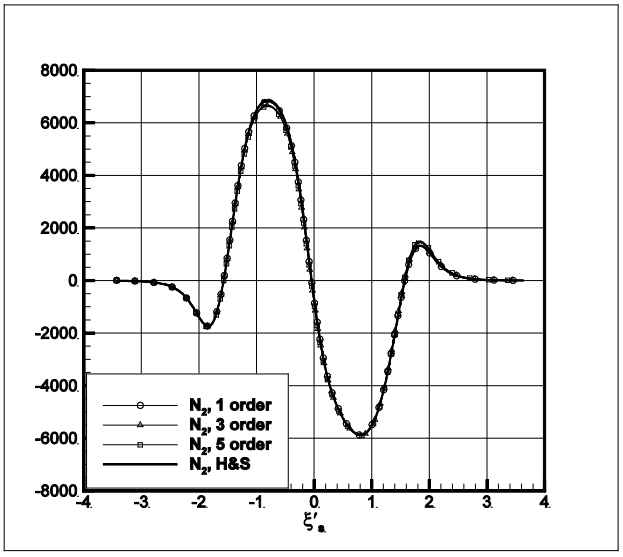

Figure 3. Interaction forces and moment responses for Ship 2 and coarse grid

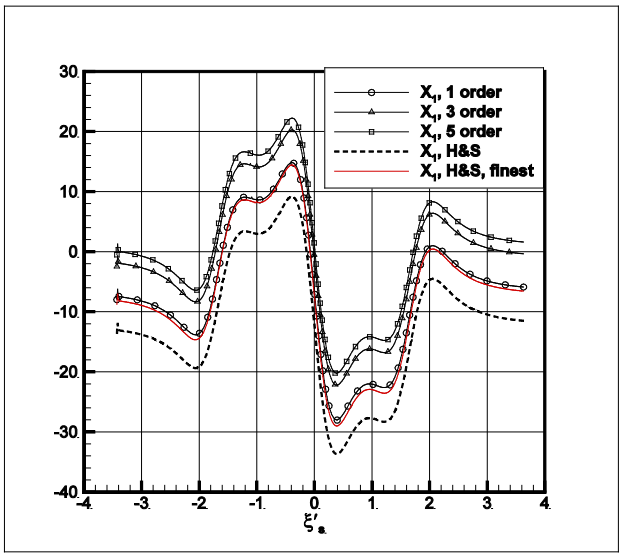

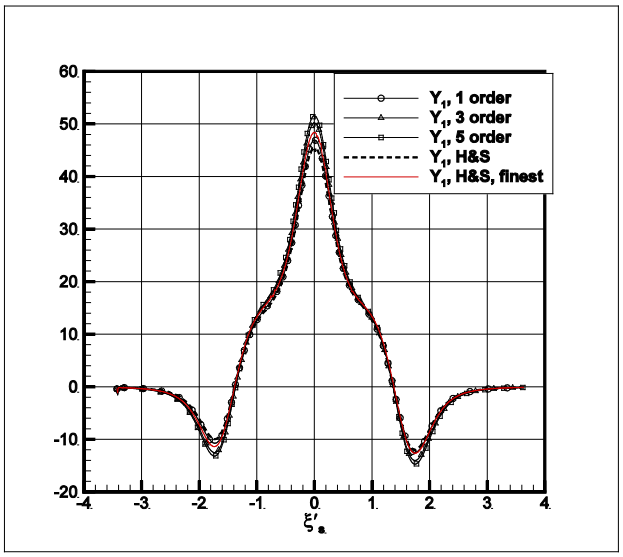

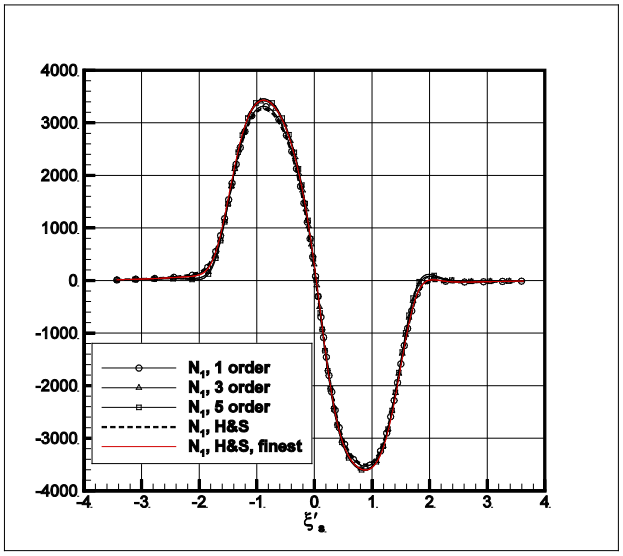

Figure 4. Interaction forces and moment responses for Ship 1 and fine grid

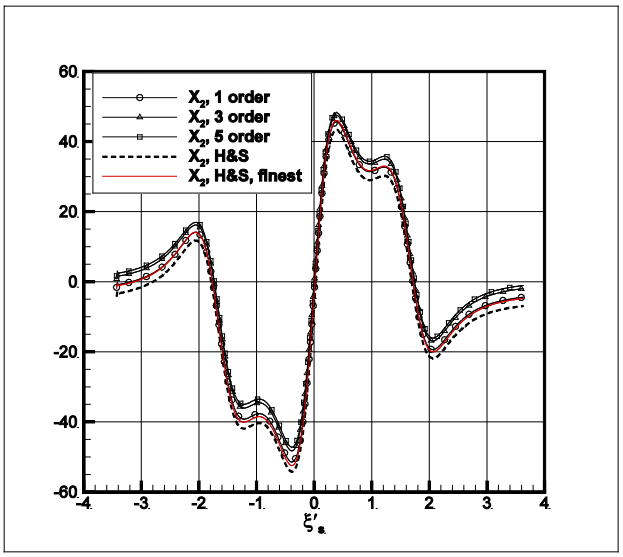

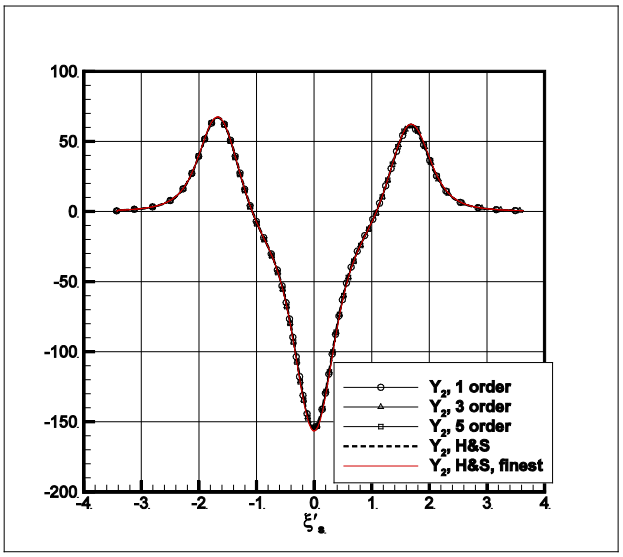

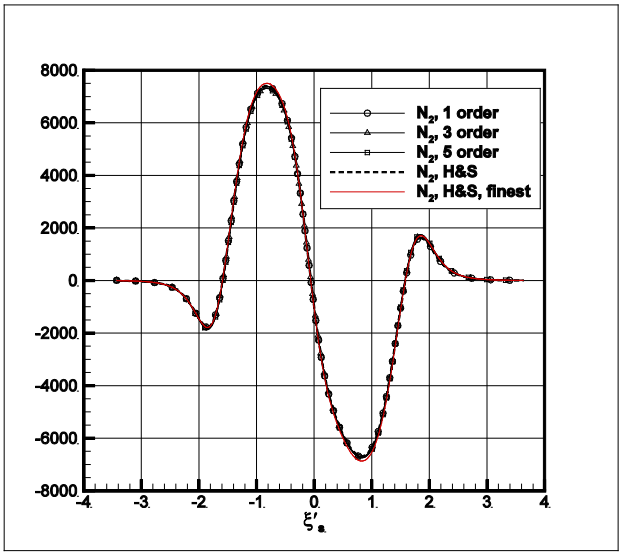

Figure 5. Interaction forces and moment responses for Ship 2 and fine grid

understood that no one of the shown responses represents "true" or "exact" values although some judgement can be made. The most pronounced influence of the collocation method is observed for the surge interaction force, especially on the overtaking vessel. Here it is evident that the results provided by the Hess and Smith method certainly are not dependable as the surge interaction force must change its sign in course of the overtaking manoeuvre and with the Hess and Smith method it does not happen at all. The situation is already substantially improved with the dihedral first-order variant but seemingly most consistent results are obtained with 3rd and 5th order formulae.

The difference between the results obtained with various methods is much smaller for the sway force and yaw moment especially for Ship 2 where it can be practically neglected. For Ship 1, however, it is possible to note that the peak values (both global and local) depend on the method non-negligibly: the relative difference between the peak values of the suction sway force reaches more than 25 percent and even more than 100% for the initial repulsion peak. This deserves some attention as the estimates obtained with simpler methods are non-conservative.

Differences in the integrated loads obviously are caused by variations in the pressure distribution as can be illustrated by Figure 6 where snapshots of this distribution are shown for the Hess–Smith and dihedral methods. Although the pressure differences may seem insignificant, they are quite sufficient to produce significant difference in the estimated surge forces.

As could be expected, the influence of the method and of the Gauss order becomes much weaker when a finer grid is used although this influence is still significant for the surge force. Considering the trends in the behaviour of the data it can be concluded that even with the finest grid the accuracy of the Hess and Smith method is comparable with that of the dihedral method with coarser grids and 1st-order Gauss integration.

At the same time, it was noticed that the dihedral method is substantially slower at a given number of panels as the necessity of at least two computations of normal components of the induced velocities for each panel instead of only one required by the Hess and Smith method increases accordingly the time required for formation of the induction matrix. In the case of the 3rd and 5th-order Gauss scheme the corresponding time augmentation factor becomes 8 and 14 respectively.

4 CONCLUSIONS

The following conclusions can be drawn on the basis of the study performed:

1. The new variant of the potential flow algorithm based on dihedral panels has confirmed its applicability for studying ship-to-ship interaction problems.
2. Comparison of the numerical results obtained with the new method with those produced by the classic Hess and Smith algorithm has demonstrated potential superiority of the former in terms of accuracy, especially at small number of panels.
3. The surge interaction force turned out the most sensitive to the method, integration parameters and number of panels in the grid, so that application of the Hess and Smith algorithm can even result in qualitatively wrong estimates.
4. At the same time, the dihedral method may at present seem too slow for online real-time simulations and can only be immediately recommended for benchmark and validation computations.

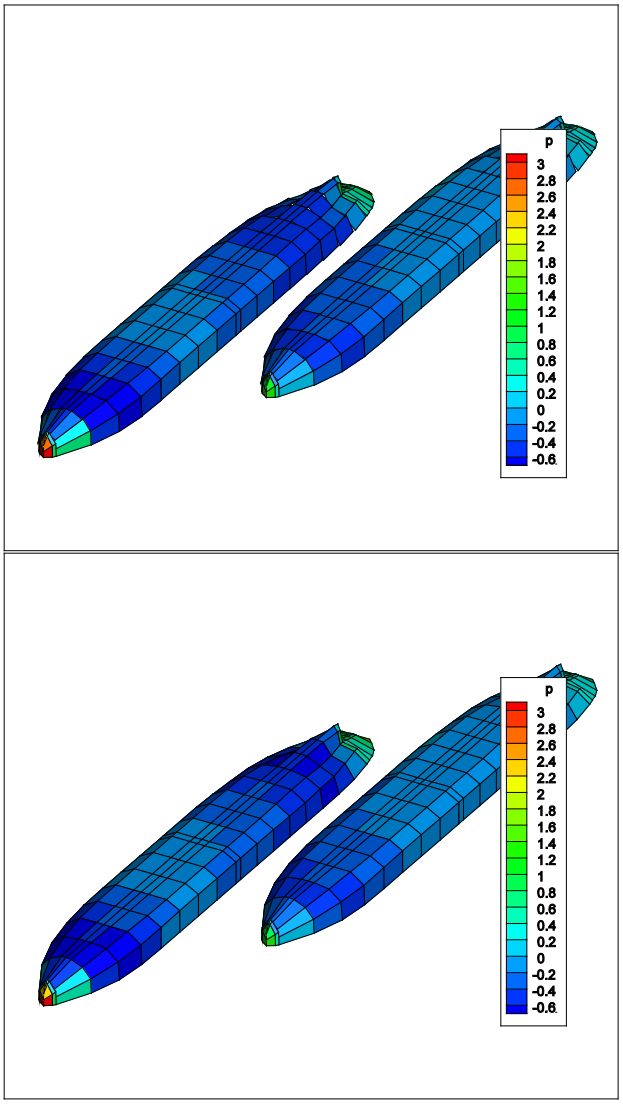

Figure 6. Pressure distribution: top – Hess and Smith method, bottom – 5-order dihedral method; the overtaking vessel is on the left

Regarding the last conclusion, the method has some reserves for increasing its speed. In particular, integrated induction on each subpanel from distant panels represented asymptotically by point sources can be computed not with the Gauss scheme but using analytic formulae proposed by Söding [4] which not only can promise faster computation but also somewhat better accuracy.

5 ACKNOWLEDGEMENTS

This work was performed within the project "Energy Efficient Safe Ship Operation (SHOPERA)" funded by the European Commission under contract No.605221.

6 REFERENCES

1. Abkowitz, M.A., Ashe, G.M., Fortson, R.M. (1976) Interaction effects of ships operating in proximity in deep and shallow water, *Proceedings of the 11th Symposium on Naval Hydrodynamics,* London, UK, March 28–April 02, London–New York, 1977, pp. 671–691.

2. Hess, J.L., Smith, A.M.O. (1967) Calculation of Potential Flow About Arbitrary Bodies, *Progress in Aeronautical Sciences*, Vol.8, pp. 1–137.

3. Nikushchenko, D., Zubova, A. (2015) Hydrodynamic interaction phenomena investigations during the ship overtaking maneuver for marine related simulators with the use of CFD methods, MARSIM 2015: International Conference on Ship Manoeuvrability and Maritime Simulation, Newcastle University, United Kingdom, 8–11 September 2015, Paper 3-4-3, 13p.

4. Söding, H. (1993) A Method for Accurate Force Calculations in Potential Flow, *Ship Technology Research*, 40, pp. 176–188.

5. Söding, H., Conrad F. (2005) Analysis of Overtaking Manoeuvres in a Narrow Waterway, *Ship Technology Research* 52, pp. 189–193.

6. Sutulo S., Guedes Soares C. (2008) Simulation of the Hydrodynamic Interaction Forces in Close-Proximity Manoeuvring, *Proceedings of the 27th Annual International Conference on Offshore Mechanics and Arctic Engineering (OMAE 2008),* Estoril. Portugal, 15–19 June 2008, Paper OMAE2008-57938, 10p.

7. Sutulo S., Guedes Soares C. (2009) Simulation of Close-Proximity Maneuvers Using an Online 3D Potential Flow Method, *Proceedings of International Conference on Marine Simulation and Ship Manoeuvrability MARSIM 2009*, Panama City, Panama, 17–20 August 2009, pp. M-9-1–M-9-10.

8. Sutulo S., Guedes Soares C. (2012) Hydrodynamic interaction forces on ship hulls equipped with propulsors, *Proceedings of the 31th Annual International Conference on Offshore Mechanics and Arctic Engineering (OMAE 2012),* Rio de Janeiro, Brasil, 6–11 June 2012, Paper OMAE2012-84181, 10p.

9. Sutulo S, Guedes Soares C., Otzen J. (2012) Validation of potential-flow estimation of interaction forces acting upon ship hulls in parallel motion, *J. Ship Research* 56, pp. 129–145.

10. Vantorre, M., Verzhbitskaya, E., Laforce, E. (2002) Model Based Formulations of Ship-Ship Interaction Forces, *Ship Technology Research* 49, pp. 124–140.

11. Yuan, Z.-M., Incecik, A., Dai, S., Alexander, D., Ji, Ch.-Y., Zhang, X. (2015) Hydrodynamic interaction between two ships travelling or stationary in shallow waters, *Ocean Engineering* 108, pp. 620-635.

12. Zhou, X., Sutulo, S., Guedes Soares C. (2012) Ship Hydrodynamic Interaction Forces in Restricted Waters, In: *Maritime Engineering and Technology,* C. Guedes Soares, Y. Garbatov, S. Sutulo, T.A. Santos, (Eds.), Taylor & Francis Group, London, UK, 2012, pp. 241-252.

13. Zhou X., Sutulo S., Guedes Soares C. (2012) Computation of Ship Hydrodynamic Interaction Forces in Restricted Waters using Potential Theory*, J. Marine Sci. Appl.* 11, pp. 265–275.

14. Zhou, X.-Q., Sutulo, S., Guedes Soares, C. (2015) Simulation of hydrodynamic interaction forces acting on a ship sailing across a submerged bank or an approach channel, *Ocean Engineering* 103, pp. 103–113.

15. Zhou, X-Q., Sutulo, S., Guedes Soares, C. (2014) Computation of Ship-to-Ship Interaction Forces by a Three-Dimensional Potential-Flow Panel Method in Finite Water Depth, *J. Offshore Mech. Arct. Eng*. 136, pp. 041301-1—041301-8

16. Zhou, X., Sutulo, S. and Guedes Soares, C. (2015) Analysis of the numerical errors in the application of the 3D moving patch method to ship-to-ship interaction in shallow water, In: *Maritime Technology and Engineering,* Guedes Soares, C. & Santos T.A. (Eds.), Taylor & Francis Group, London, UK, pp. 973-984.

17. Zienkiewicz, O.C., Morgan, K. (2006) *Finite elements and approximations*, Dover Publications, Inc., Mineola, N.Y.

7 AUTHORS' BIOGRAPHIES

Serge Sutulo holds the current position of Researcher at the Centre for Marine Technology and Ocean Engineering (CENTEC) and of Adjunct Associate Professor at IST. He is responsible for research and teaching in the field of Ship Manoeuvrability and Dynamics of Marine Craft. His previous experience includes various theoretical and experimental studies in the mentioned area.

C. Guedes Soares is President of CENTEC and holds position of Full Professor at IST. He is supervising multiple research projects in various areas and has worked in many fields of Ship Hydrodynamics, Naval Architecture, Sea Dynamics, Applied Reliability Theory and Risk Analysis.

4th MASHCON, Hamburg - Uliczka et al. (eds) - © 2016 Bundesanstalt für Wasserbau ISBN 978-3-939230-38-0 (Online)
DOI: 10.18451/978-3-939230-38-0_23

SHALLOW WATER AND INTERACTION EFFECTS IN ECDIS REAL-TIME MOTION PREDICTION SYSTEM

A Ozersky and **E Rogozhina,** Transas Technologies, Russia

SUMMARY

Modern ECDIS systems are often equipped with optional motion prediction system. Often such prediction systems do not calculate influence of shore and bottom profile, ship-ship and ship bank interaction and some other effects. Problems that must be solved during the implementation of a motion prediction system for shallow water manoeuvring go beyond engineering aspects of such system. Depths and other chart-acquired data should be automatically analysed to form the optimal environment for further calculations. Algorithms for motion prediction must be much faster than real-time simulation algorithms, considering that each relatively long predicted trajectory must be fully re-calculated every few seconds. To achieve the required performance, simplified mathematical models are suggested, analysed and partially validated using experimental data. Results from a bridge simulator installation of the prediction system demonstrated its potential use in education and manoeuvring in restricted and shallow waterways.

NOMENCLATURE

Q	Generalised velocity vector $[u \quad v \quad w \mid p \quad q \quad r]^T$	
P	Resultant forces vector $[X \quad Y \quad Z \mid K \quad M \quad N]^T$	
η	Generalised coordinate vector $[x \; y \; z \; \phi \quad \theta \quad \psi]^T$	
U	Body-fixed linear velocity $[u \quad v \quad w]^T$	(m/s)
W	Body-fixed angular velocity $[p \quad q \quad r]^T$	(rad/s)
F	Force in body-fixed coordinates $[X \quad Y \quad Z]^T$	(N)
L	Moment about body-fixed centre $[K \quad M \quad N]^T$	(N m)
μ	Position vector of a point $[x \quad y \quad z]^T$	(m)
Θ	Inclination Euler angles $[\phi \quad \theta \quad \psi]^T$	(rad)
μ_c	Vector of ship centre of gravity	(m)
D	Generalised inertia matrix 6×6	
D_R	Rigid-body inertia matrix 6×6	
D_A	Fluid Added Mass and Inertia matrix 6×6	
J_1	Euler angle rotation matrix 3×3	
J_2	Euler attitude transformation matrix 3×3	
I_0	Inertia tensor 3×3	(kg m^2)
I	Identity matrix 3×3	
S_s	Skew-symmetric matrix 3×3	
Ω	Square matrix of generalised velocities 6×6	
m	Mass of ship	(kg)
ρ	Density of water	(kg/m^3)
g	Gravity acceleration	(m/s^2)
∇	Volumetric ship displacement	(m^3)
L_{pp}	Ship length between perpendiculars	(m)
B	Ship breadth	(m)
T	Ship draught	(m)
C_B	Block coefficient	
h	Water depth	(m)
Fn	Length Froude number	
Fh	Depth Froude number	
H_w	Pressure measured in meters of water of water gauge	(m)
S	Area of pressure field zone	(m^2)
α	Bottom incline angle	(rad)
C_{BL}	Channel blockage factor	
l_{tr}	Transversal distance to boundary	(m)
C_{CFD}	Cross flow drag coefficient	
n_p	Propeller revolutions	(s^{-1})
γ_R	Apparent wind angle	(rad)
C_{XH} C_{YH} C_{NH}	Hull hydrodynamic coefficients	
C_{XA} C_{YA} C_{NA}	Hull aerodynamic coefficients	
ECDIS	Electronic Chart Display and Information System	
VTS	Vessel Traffic Systems	
DOF	Degree of Freedom	
AIS	Automatic Identification System	
HDI	Hydrodynamic Interaction	
UKC	Under Keel Clearance	

1 INTRODUCTION

Factors such as the increase in marine transport traffic and the growth of ships' dimensions create difficulties in ship handling and increase the probability of unexpected challenging situations which can affect safe navigation in congested waterways. The human factor is one of the most important which affects navigation safety. Reliable prediction of ship manoeuvrability may need water restrictions and other ship interactions under complicated environmental conditions to be taken into account, such as wind, waves or strong current. This may avoid collisions with obstacles or with the banks of narrow waterways.

Modern navigation systems are often equipped with a ship motion prediction system. These systems calculate

the future ship trajectory, considering the ship's motion model and some assumptions about steering commands. Assumptions on the steering commands can be rather simple (e.g. rudder and telegraph will be always in the same position as they are now), or very complex as defined by the ship's pre-defined route or manoeuvring plan.

The outcome of the prediction depends on the quality of the ship motion model, the number of effects covered by the model and the quality of the input data including environmental information.

Prediction systems can be used as a part of an ECDIS system, as a part of an onboard route/manoeuver planning tool, or as a part of an educational or simulation system. There are many examples of such systems including, for instance, prediction of manoeuvring indices in Nomoto's equation and sailed rudder angle from AIS data [1], prediction systems with complex manoeuver planning tools, actual manoeuvring limits and area estimation [2, 3], fuzzy algorithm of collision avoidance in shallow confined waterway [4]. In 2010-2011, the prediction system based on the ship mathematical model was also implemented in Transas Navi-Sailor for the Stena Germanica III passenger ship. The system employed a 6DOF ship model used for navigational training and considered ship controls state, weather and water depth. It was found that ignoring interaction effects may confuse operators and potentially lead to wrong decisions.

In this paper, a prediction system that in addition to usual deep-water simulation considers shallow and restricted water effects, hydrodynamic and mechanical interaction with nearby objects and propeller wash interaction will be described. An overview of the human-machine interface between the system and its users and will be also provided.

2 DATA SOURCES FOR SHIP MOTION PREDICTION

The primary data for the prediction system are orders and the actual state of the ship's rudders, engines and thrusters.

Ship-bank and ship-ship hydrodynamic interaction effects require additional information sources to estimate influence on ship trajectory. For ship-bank interaction forces, such information sources are usually high quality S-57 charts or other official charts available for an area. Charts of required quality are sometimes not included in chart folios and can be received from local port authorities. Available 2D chart data is converted into the 3D environment and then analysed to predict ship-bank interaction forces.

For ship-ship interaction forces, it is necessary to obtain information about another ship manoeuvres and plans. If two ships and shore stations can be connected using e-Navigation digital channels, then the information exchange can be more complete, as shown in figure 1. The information can include a motion model of another ship or even the complete online trajectory prediction calculated by the target ship's ECDIS or VTS system.

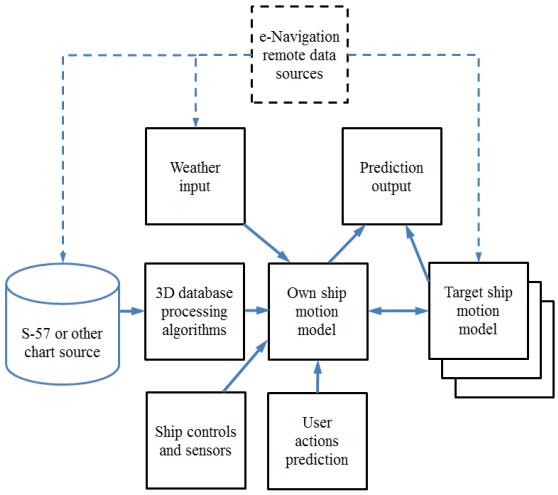

Figure 1. Information exchange in prediction system. Dashed lines represent future potential for e-Navigation systems.

Other information vital for online trajectory prediction is weather conditions. While weather information at the ship position can be acquired using the ship's own sensors, the information along the future trajectory is usually not known and should be estimated. The estimation can be made either as constant (e.g. constant wind value along the future trajectory) or using some simplified predictions (e.g. simplified wind shadowing algorithms if 3D models of surrounding area and ships are available). Sometimes this information can be pre-calculated using shore computers, as shown in [5]. In the future, when e-Navigation tools and cheap arrays of sensors will become widely available, such information could also be delivered online from shore VTS systems.

3 PREDICTOR MATHEMATICAL MODEL DESCRIPTION

3.1 COORDINATE FRAMES AND NOTATIONS

The following Cartesian coordinate frames are used to determine the position and orientation of a ship in 6 DOF, as shown in figure 2:

- Earth-fixed inertial reference frame $X_0Y_0Z_0$ with O_0 origin in a certain fixed point
- Body-fixed moving frame XYZ with C origin in the ship centre of gravity
- Local frame $X_lY_lZ_l$ fixed to the equilibrium state with C origin. Axis obtained by translating $X_0Y_0Z_0$ earth-fixed coordinate system parallel to itself until its origin coincides with the origin of the body-fixed coordinate system.

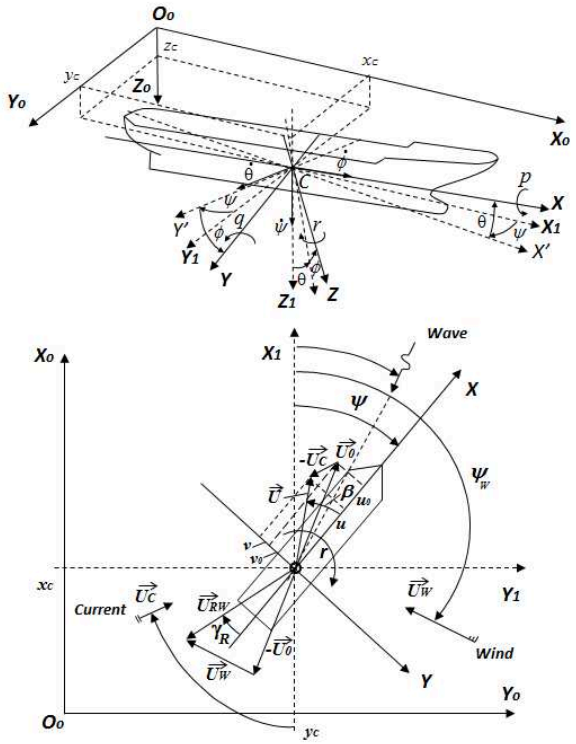

Figure 2. Coordinate frames and sign conventions.

The earth fixed coordinate system $X_0Y_0Z_0$ is used to describe the ship trajectory and orientation. The ship's motion and forces acting on the ship are described in the body-fixed coordinate frame XYZ.

3.2 SHIP MOTION EQUATIONS

Kinematic equations of motion for linear and angular velocities in compact form are as follows [6].

$$\begin{aligned} \dot{\mu_C} &= J_1(\Theta)U \\ \dot{\Theta} &= J_2(\Theta)\mathrm{W} \end{aligned} \tag{1}$$

Here $\mu_C = [x_C, y_C, z_C]^T$ are the coordinates of the centre of gravity in body-fixed reference frame, $J_{1\,3\times3}$ and $J_{2\,3\times3}$ denote transformation matrixes between Local and body-fixed reference frames. J_1 is Euler angle rotation matrix, J_2 is Euler angle attitude transformation matrix.

The ship dynamic equations of motion based on Newton's 2nd law of motion written in a compact matrix-vector form in the body-fixed reference frame according to [7] are:

$$D\dot{Q} + \Omega D Q = P \tag{2}$$

Here P denotes total vector of external forces, D is the generalised inertia matrix defined as the sum of rigid-body inertia matrix $D_{R\,6\times6}$ and fluid Added Mass and Inertia matrix $D_{A\,6\times6}$, which determines the kinetic energy of the surrounded fluid. Ω is the square matrix of generalised velocities, which can be written as a combination of skew-symmetric matrixes S_S for linear and rotational velocities.

$$D = D_R + D_A \tag{3}$$

$$D_R = \begin{bmatrix} m\,I & -m\,S_S(\mu_C) \\ m\,S_S(\mu_C) & I_0 \end{bmatrix} \tag{4}$$

$$\Omega = \begin{bmatrix} S_S(\mathrm{W}) & 0 \\ S_S(U) & S_S(\mathrm{W}) \end{bmatrix} \tag{5}$$

Where m is the ship mass, $I_{3\times3}$ is the identity matrix and $I_{0\,3\times3}$ is the inertia tensor. The matrix products of ΩD in equation (2) gives Coriolis and Centripetal terms. The matrix-vector equation (2) forms the six scalar equations and together with the kinematic equations (1) gives a complete equations system to be solved for ship 6DOF motion simulation. The system can also be supplemented by a propulsor-engine dynamics equation.

Solution of the equation (2) yields ship velocities Q in body-fixed reference frame. The ship's trajectories and location η are obtained by integrating the kinematic equations (1) over time.

In the predictor model the set of ship motion equations can be calculated for 300 seconds in advance with the maximum integrational time step equal to 1 second. The motion model can be easily adapted to lower DOF simulation by excluding the corresponding DOF from the equations.

3.3 EXTERNAL FORCES

The total external vector P includes buoyancy force, restoring and damping moments, the mechanical interaction and hydrodynamic forces in calm water as well as various environmental exciting forces due to wind, currents, waves shallow water effect, interaction with other ships, etc.

3.3 (a) Hull hydrodynamic Forces

The general structure of hydrodynamic force components of the ship hull for arbitrary motion in horizontal plane is considered as the sum of two non-linear functions of drift angle and yaw rate. The hydrodynamic coefficients are non-dimensionalised using density of water ρ, the reference area $L_{pp}T$, the reference length L_{pp}, squared linear velocity U^2 and squared generalised velocity $U^2 + r^2 L_{pp}^2$.

$$\begin{bmatrix} X_H \\ Y_H \\ N_H \end{bmatrix} = \frac{\rho}{2} L_{pp} T \left(\begin{bmatrix} C_{XH}\left(v,u,Fn,\frac{h}{T}\right) \\ C_{YH}\left(v,u,\frac{h}{T}\right) \\ L_{pp}C_{NH}\left(v,u,\frac{h}{T}\right) \end{bmatrix} U^2 + \begin{bmatrix} C_{XH}\left(v,u,r,\frac{h}{T}\right) \\ C_{YH}\left(v,u,r,\frac{h}{T}\right) \\ L_{pp}C_{NH}\left(v,u,r,\frac{h}{T}\right) \end{bmatrix} \left(U^2 + r^2 L_{pp}^2\right) \right) \tag{6}$$

The first parts are referred to as longitudinal force $C_{XH}\left(u,v,Fn,\frac{h}{T}\right)$, lateral force $C_{YH}(u,v,\frac{h}{T})$ and yawing moment $C_{NH}(u,v,\frac{h}{T})$ coefficients caused by pure drift motion. The second parts $C_{XH}\left(v,u,r,\frac{h}{T}\right)$, $C_{YH}(u,v,r,\frac{h}{T})$ and $C_{NH}(u,v,r,\frac{h}{T})$ express the corresponding compo-

nents arising from both yaw rate and drift. The coefficients also depend on load conditions. The shallow water effect is taken into account by means of the multiplicative exponential functions of relative depth $^{h}/_{T}$. These functions are individually applied to the hydrodynamic derivatives as ratios of shallow to deep water values in order to scale the hydrodynamic coefficients [8, 9].

The hydrodynamic coefficients can be derived from approximations proposed by Krylov State Research Centre [8], MMG group [10] as well as from model basin measurements performed in rotating arm facilities and planar motion mechanisms or can be precomputed using CFD methods. The system identification technique on the basis of full-scale trials is also applied. Therefore, a particular ship model can be adjusted according to any trial data available for a given ship.

In the mathematical model the above-mentioned coefficients are represented as multi-dimensional surfaces of draft, trim angle, drift angle, generalised trajectory curvature and $^{h}/_{T}$ ratio. An example of the total lateral force coefficient in deep water is presented in figure 3.A.

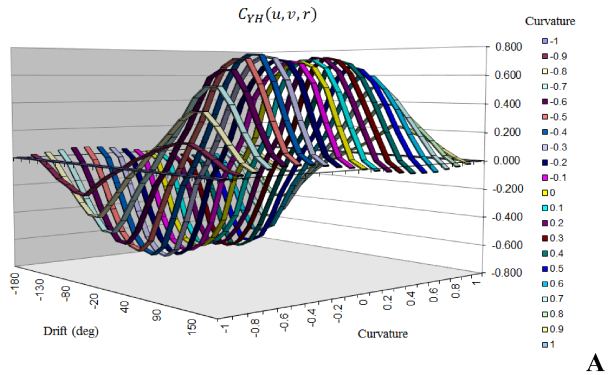

A

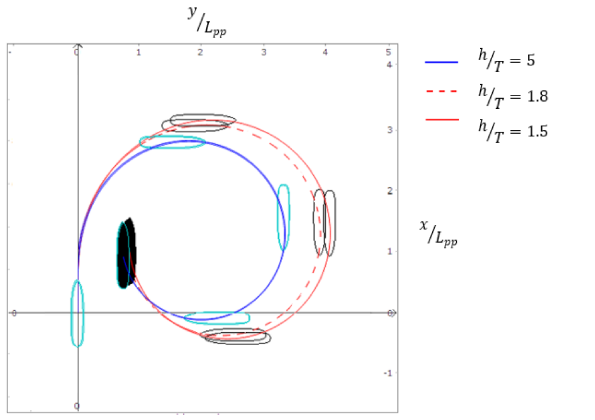

B

Figure 3. A – Total sway force coefficient referred to squared generalised velocity. B – Comparison of the predicted trajectories of turning circle with rudder angle 35° at different h/T.

The mathematical model of ship motion at shallow water also accounts for increasing inertial added masses and damping forces with decreasing water depth.

An example of simulation results of turning circle maneuvers both in deep and shallow water for the model described below in Table 1 is presented in figure 3.B with relative depths $^{h}/_{T}$ equal to 5, 1.8 and 1.5.

3.3 (b) Rudder and Propeller Forces

The rudder is considered as a low aspect ratio wing influenced by propeller induced flow and hull wake flow which gives flow-straightening effects. The forces and moments induced by the rudder are characterized by lift and drag coefficients, the rudder deflection angle and the actual slipstream and freestream areas with the corresponding effective velocities over the rudder. The rudder hydrodynamic coefficients are also functions of $^{h}/_{T}$ ratio.

The hydrodynamic forces induced by the propeller are computed using the common representation of propeller thrust and torque coefficients given in four quadrants versus a modified advanced coefficient, in order to cover all possible combinations of axial and rotational motions for arbitrary manoeuvres.

The influence of the shallow water on the propeller action is considered indirectly by changing the thrust deduction factor and wake fraction. The change of the lateral force on the rudder is considered to be dependent on the propeller operating conditions and, consequently, on the flow speed behind the propeller.

3.3 (c) Wind Forces

The wind model provides the continuous increase of the natural wind with the height above the sea level. The profile of the true wind is correlated with the Beaufort scale and determined by the average wind velocity given for the standard height of 10 metres. Wind forces and moments acting on the moving ship are computed from the apparent wind profile which is considered as a superposition of the uniform approaching $-\vec{U}_s$ and gradient $\vec{U}_a$ flows.

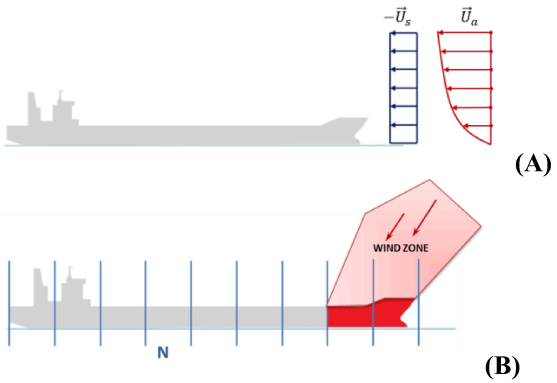

(A)

(B)

Figure 4. A – profiles of wind gradient flow and relative flow. B – Container ship exposed to the wind local load at bow.

Non dimensional wind force coefficients C_{XA}, C_{YA}, C_{NA} given for the entire range of apparent wind angle γ_R obtained from wind-tunnel tests or from known approximations are used according to [11].

The model also allows consideration of the apparent wind non-uniformity and gusts impact over the hull length. The underwater hull is divided into *N* sections as shown at figure 4.B; for each section the apparent wind profile is computed. The wind additional forces are predicted from the areas of the sections exposed to the local wind load.

3.3 (d) Current Forces

The current model is quite similar to wind force calculation. The current model allows the ship's motion to be modelled in complex hydrographic conditions: bends of river beds and channels, port approaches within the port areas with tidal currents, channel junction areas, etc.

The current is considered as a stationary flow with given velocity distribution in horizontal and vertical directions. The current vector interpolated by the local speed and direction is set at certain reference points on a chart, accounting for variables in depth current.

Forces and moments due to current computed in the body fixed reference frame are represented by two components. The first component as a part of the total current force on the hull depends on the mean current velocity $\overline{U}_c$ calculated over the ship hull.

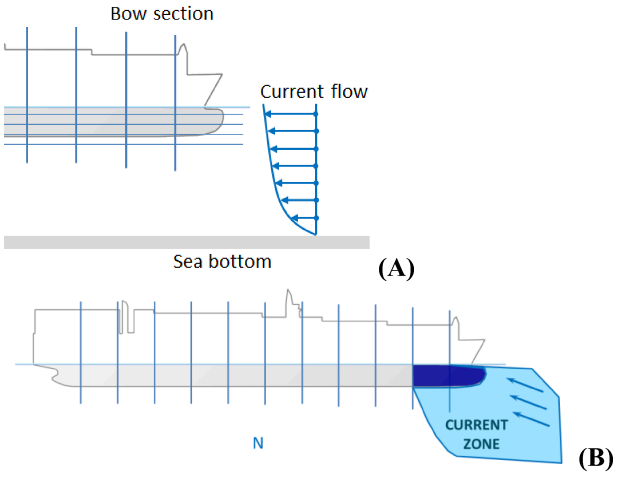

Figure 5. A – profile of current gradient flow. B – Cruise ship exposed to the current local load at bow.

The second component calculates the non-uniformity of the transversal local current speed $v_c(x)$ along the ship length. The additional sway force and yaw moment can be written as follows:

$$Y_c = -\frac{\rho}{2}\int_{-L/2}^{L/2} T(x)C_{CFD}(x)(v_c(x)-\overline{v_c}) \cdot |v_c(x)-\overline{v_c}|\,dx \quad (7)$$

$$N_c = -\frac{\rho}{2}\int_{-L/2}^{L/2} T(x)C_{CFD}(x)(v_c(x)-\overline{v_c}) \cdot |v_c(x)-\overline{v_c}|x\,dx \quad (8)$$

where $T(x)$ is variable draft along the hull, $C_{CFD}(x)$ is cross flow drag coefficient.

3.3 (e) Hydrodynamic Interaction Forces

Ship-to-ship and ship-to-bank effects modelling is based on taking into account the pressure field induced by other moving ships or pressure field modification in the vicinity of channel walls, moored ship, short pier, inclined bottom, under water shoals and jetties.

In order to provide accelerated-time computations the pressure distribution about the moving ship is approximated by simple geometrical zones. Positive pressure zones are located forward and aft, low pressure zone are located amidships. Each zone is represented in the ship motion model data by two semicircles of a given radius and a location centre. The aft zone also includes a sector of circle which reflects the low pressure wake field as well as the propeller action effect.

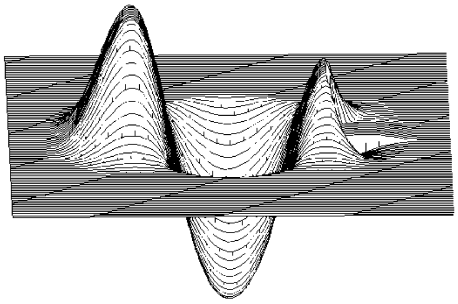

Figure 6. The example of pressure field induced by a river-sea ship.

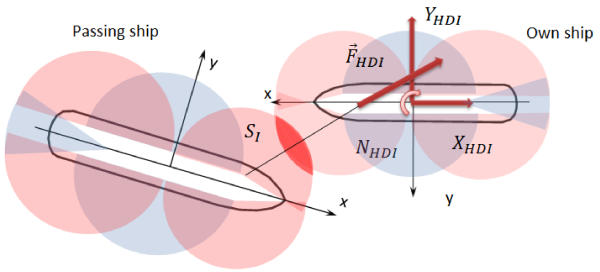

Figure 7. HDI forces computational scheme.

Excessive pressure induced by the moving ship is approximate in the motion model as pressure in metres of water gauge related to the corresponding geometrical zone.

The resultant pressure field H_w in point with coordinated $\mu\,(x, y)$ considered as a sum of the following components.

$$H_w(\mu) = H_w(Fn, \mu) + H_w(v, r, \mu) + H_w{}^{wake}(u, v, r, n_p) \quad (9)$$

Here n_p is propeller revolutions.

The first one corresponds to straight ahead or astern motion and depends on hull geometry and Froude number Fn. Maximum values of water gauge height H_w corresponds to a zone origin and then steady decrease from the origin to the zone periphery. The second component reflects the influence of drift and yaw rate on the pressure field, taking into account relative transversal speed distribution in a lateral direction. The third component considers wakeflow and the main propeller induced jet.

An example of water gauge height H_w distribution in body fixed reference frame for pressure field induced by a river-sea ship running straight ahead at constant speed in calm unrestricted water is shown on figure 6.

For computation of HDI forces, loop searches for geometrical intersection between each of the own ship zones S_{own} and each of the other passing ships' zones $S_{passing}$ are performed. If intersection area S_I^i is found the force F_{HDI} is applied from the passing ship to own ship along the line linked by two origins of the corresponding intersected zones (figure 7).

$$F_{HDI} = S_{own} \bigcap_{i}^{N} S_{passing} \left[\rho g \int_{S_I^i} \left(H_w(\mu_I^i) \right) ds \right] \quad (10)$$

Here N denotes a number of the intersected zones and μ_I^i is a centre of the intersected area.

The total HDI longitudinal X_{HDI} and transversal Y_{HDI} forces are obtained by projecting F_{HDI} to the corresponding axis. For yawing moment N_{HDI} computation the point of force application is considered to be in the intersection of the line linked two origins and the ship centre plane.

To define the influence of waterways conjunctions on hydrodynamic forces, the vicinity of the ship is divided by longitudinal and transversal cross-sections to regular mesh with rectangular cells. Each cell with lateral and transversal indexes i, j has area S^{ij} and centre point $\mu_{ij}^G = \left[x_{ij}^G, y_{ij}^G, z_{ij}^G\right]^T$ In the centre point of each cell at every computational time step the water gauge height H_w^{ij}, water depth h^{ij}, shortest distances to boundaries, etc. are received from the map and translated to body-fixed frame XYZ.

The pressure field in each cell determined by the water gauge height H_w^{ij} is corrected by influencing function f_{BI} of the local Froude number with respect to water depth Fh^{ij}, local water depth ratio $h^{ij}/_T$, local sea bottom incline angle α_i, local channel blockage factor C_{BL}^i and local transversal distance to boundary l_{tr}^{ij}.

The influencing dependencies were empirically obtained and validated on the basis of an integrated theoretical and empirical approach using numerical analysis and the results of specially designed small scale self-propelled ship model tests [12, 13].

Hydrodynamic bank interaction forces are determined as the difference between forces in unrestricted and constrained conditions. Below are formulas for transversal force Y_{BI} and yawing moment N_{BI}.

$$Y_{BI} = \rho g \left(\sum_i \sum_j sign\left(y_{ij}^G\right) \left(H_w^{ij} \cdot f_{BI}\left(Fn, Fh^{ij}, h^{ij}/_T, \alpha_i, C_{BL}^i\right) S^{ij} - H_w^{ij} S^{ij} \right) \right) \quad (11)$$

$$N_{BI} = \rho g \left(\sum_i \sum_j x_{ij}^G\, sign\left(y_{ij}^G\right) \left(H_w^{ij} \cdot f_{BI}\left(Fn, Fh^{ij}, h^{ij}/_T, \alpha_i, C_{BL}^i\right) S^{ij} - H_w^{ij} S^{ij} \right) \right) \quad (12)$$

The mathematical model also takes into account the influence of jets induced by other ships' propulsors. A jet from an external propeller or a thruster is modelled as a layer of local current.

It is important to note that this rough approach was developed as a compromise between accuracy and the computation speed appropriate for faster than real time computations. The model can be tuned to comply with basin experiments or with more advanced computational methods.

3.3 (f) Squat Forces

For accelerated time usage of the predictor, squat computations are based on the various simple empirical formulas used in practice, such as Romisch, Tothill, Barrass and the others [14]. During previous years Transas had performed analysis of the various empirical formulas used in marine practice and test measurements from the numerous sources and had developed sinkage and trim formulation for simulator real time use [15]. While such methods often over-predict squat, for better coincidence with real squat measurements or advanced time consuming computations the sinkage and trim formulation can be adopted for the particular ship model, by means of individual coefficients.

Squat parameters in the predictor are represented as precomputed data set. Considering that another squat formula, results of CFD experiments, model basin or full-scale measurements can be entered as a source for squat database for a ship model.

At each computational time step, bow sinkage and stern sinkage in metres are computed from current speed, depth and channel profile. Further on the base of precomputed data of buoyancy coefficient and restoring pitching moment versus relative submergence and pitch

the vertical force and pitching moment from the squat effect are computed and implemented into model.

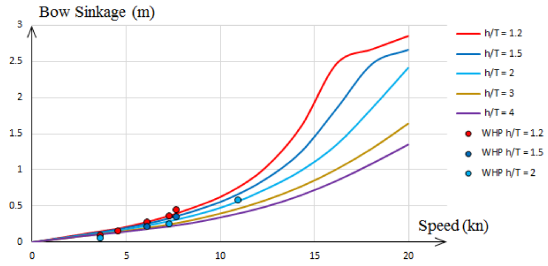

(A)

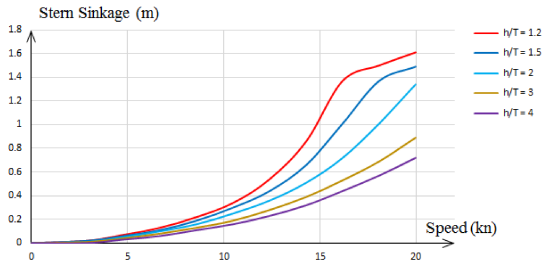

(B)

Figure 8. Bow (A) and stern sinkage (B) in metres versus speed.

In figure 8 the simulation results of squat bow and stern sinkages on shallow water are shown according to the Romisch prediction method for the model of container ship used in the bridge simulator exercise described below. Ship parameters are listed in table 1. These predicted results of the bow sinkage are compared with data from wheelhouse posters of similar containerships scaled according to the ship dimensions.

Table 1. Main Particulars of Container ship

Displacement, ∇, m^3	32921.8
L_{pp}, m	190
B, m	30
T (full load), m	8.5
Engine Diesel, MW	17.3
Propeller	FPP
Maximal speed, kts.	20.1

3.4 ANALYSIS OF 3D BOTTOM SURFACE

Conversion of 2D electronic chart data into 3D bottom outline is performed automatically using triangulation, as shown on the figure 9. The depth and height marks, together with isobaths and some other map objects are treated as input. The output of triangulation is a set of 3D points connected with lines, together forming a mesh made of triangles.

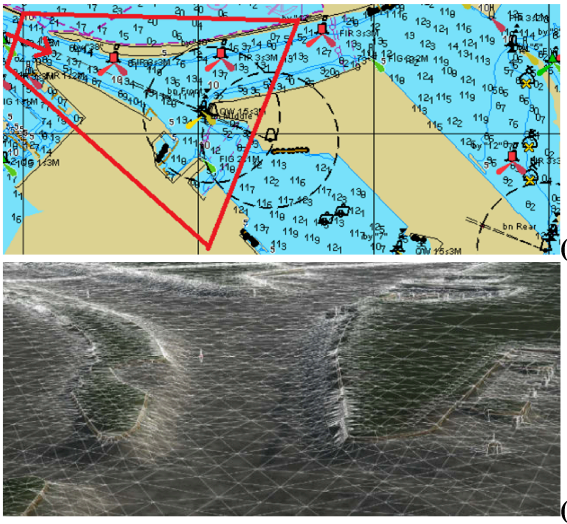

(A)

(B)

Figure 9. Example of automatic conversion from S-57 chart (A) into 3D surface (B). The red trapezoid on the left shows the field of view of the 3D picture.

This mesh comes through additional processing to identify parameters important for ship-bank interaction:

- average depth near ship
- distances to banks
- channel profile
- 3D surface shape to evaluate ship-bank interaction forces
- water flow restriction coefficient, which can also be interpreted as channel blockage factor.

The water way parameters required from the electronic chart are refreshed in the motion model's body-fixed reference frame every second or every time when ship position changes more than 0.1 of its length.

4 MODEL VALIDATION

The kinematic parameters and trajectories of ship-to-ship and ship-to-bank interaction were validated by specially designed model experiments [12, 13].

In order to distribute some particular results of model basin measurement onto the collection containing ships of varied types and dimensions, similarity criteria have been proposed [12] and an algorithm of the automated selection of model pairs has been developed. The satisfaction of the criteria enables the required geometric and dynamic similarity between small scale self-propelled test-tank models and full scale mathematical ship models in similarly investigated conditions.

4.1 SHIP-TO-SHIP HYDRODYNAMIC INTERACTION

Below is an example illustrating a comparison of behaviour of the ship mathematical models with the tank-test experimental results for similar models and navigational conditions for the overtaking manoeuvre on crossing courses.

In the simulated test the Container ship model also used in the predictor experiment below, sailing initially ahead by 0.6L, is overtaken by the Car Carrier ship.
The main particulars of the model used in the comparative tests are displayed in table 2.

Table 2. Main Ship particulars and test conditions

	Transas		Experiment	
Model	Container ship	Car carrier	TCH	CPT
∇, m^3	32921.8	68217.4	0.96 10^{-3}	1.73 10^{-3}
L_{pp}, m	181.5	228.9	0.477	0.592
B, m	30	36.2	0.094	0.12
T, m	8.5	10.88	0.0385	0.048
Initial x_c, m	155.07	-20.74	0.4	-0.05
Initial y_c, m	370.08	250.18	1.19	0.81
Course, deg	-7.74	-6.09	-9.57	-7.53
Speed, m/s	8.07	9.82	0.6	0.73
$h/_T$	5.87	4.59	5.97	4.79
Fn	0.19	0.21	0.28	0.3
Fh	0.36	0.44	0.4	0.48

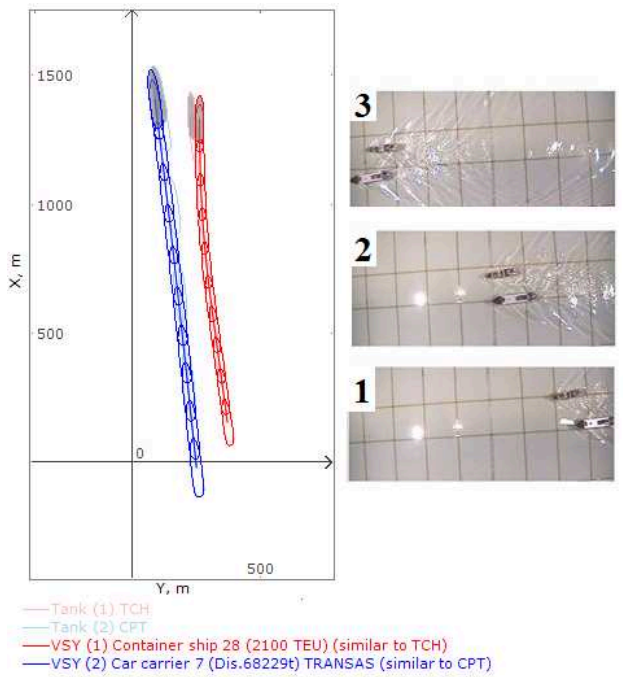

Figure 10. Comparison of the simulated trajectories for overtaking manoeuvre against model basin measurements for similar models.

The trajectories of the mathematical models shown in figure 10 obtained in this test are in qualitative agreement with the trajectories recorded in the tank test for the pair of models satisfying the similarity criteria.

4.2 HYDRODYNAMIC FORCES INDUCED BY PASSING SHIPS

The ship motion model was validated by a comparison with published results from passing ship model test for the open water case. It is known that the passing-ship-induced forces and moments can produce large motion responses of the moored ship, causing it to move along and away from the pier. These motions can damage cargo hoses, loading arms, gangways and ramps.

Figure 11 shows a comparison of the calculated external loads on the moored tanker induced by the passing tanker with the experiment [16]. The speed of the passing tanker is 7 knots; distances between the passing tanker and the moored tanker are 30, 60 and 120 metres, measured board to board. Path and course of the passing tanker were parallel to the moored tanker.

Loads on the moored tanker are related to the position of the passing tanker relative to the moored tanker.
The comparison with Remery's results are good enough: the shapes of the plots are almost identical, the values for peak and trough values for X, Y, and N predicted by the ship motion model are all essentially the same as those measured and predicted by Remery.

Table 3. Ship particulars for interaction comparison.

	Transas		Experiment (scale 1 : 60)	
	Moored Vessel	Passing Vessel	Moored Vessel	Passing Vessel
Ship type	Tanker	Tanker	Tanker	Tanker
∇, m^3	104000	131000	118800	129600
L_{pp}, m	239	270	257	250
B, m	44	49.9	36.8	40.4
T, m	12.2	12.2	15.7	15.2
$h/_T$	1.15	1.15	1.15	1.15
C_B	0.81	0.8	0.8	0.85

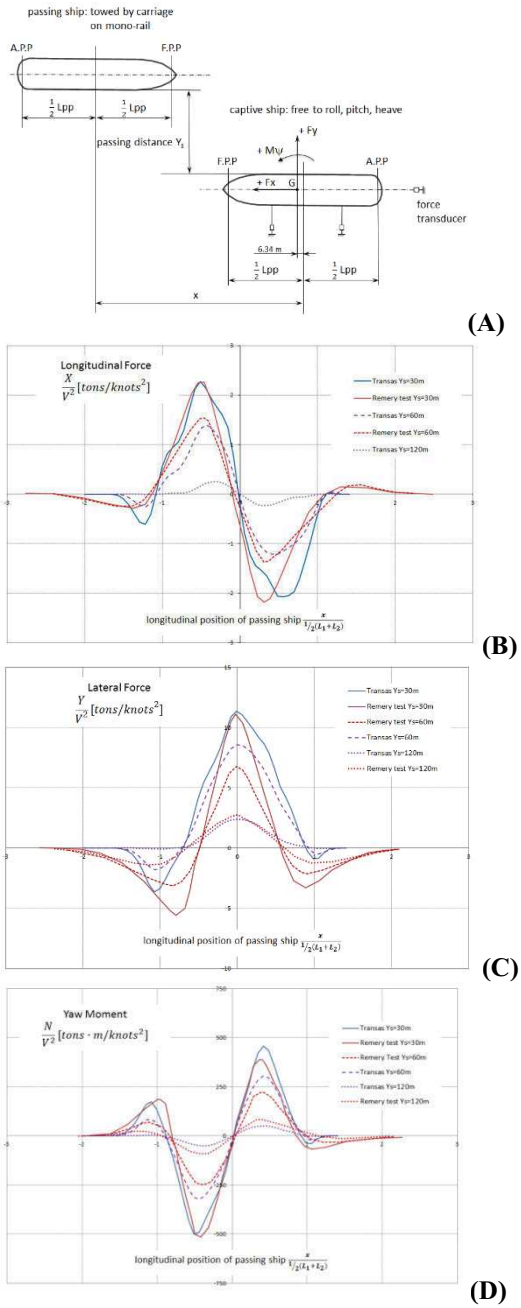

Figure 11. A – Test set-up for force measurement on captive vessel (according to [16]). B, C, D – Forces induced by passing ship.

5 REPRESENTATION OF THE PREDICTED TRAJECTORY

The predicted trajectory data contains the following information, which can be important for an operator:

- predicted ship positions over pre-set period of time
- possibility of grounding or mechanical interaction along the trajectory
- UKC along the trajectory
- magnitude of interaction forces along the trajectory.

This information can be important for proper ship handling if some of these parameters are close to critical. Also, a set of trajectories can be generated depending on the following expectations:

- all controls will be left as they are now
- rudder will ordered hard to port (starboard)
- rudder will ordered hard to port (starboard) and full speed ahead will be ordered
- full thruster power will be applied to port (starboard)
- full speed astern will be ordered with or without additional steering.

All these options form a space of potential manoeuvres available to the operator, and it could be useful to display some or all of them to make decision making more reliable. However, if all these options will be used simultaneously the user will be overloaded with information and that will prevent decision-making.
Trajectories of other vessels can also be represented in different ways:

- keeping existing course and speed
- keeping existing rate of turn and speed
- use trajectory received from external sources (e.g. e-Navigation).

In figure 12 the example of predicted trajectory representation is shown. The purple dashed line represents ship position at which UKC is below the given limit or hydrodynamic interaction forces will be higher than the available rudder capabilities. The three trajectories shown in the figure 12 represent the full range of ship manoeuvring capabilities. The default assumption that rudder order will remain the same for next few minutes is represented as central black trajectory, while red and green trajectories represent assumptions that hard to port or starboard order will be executed.

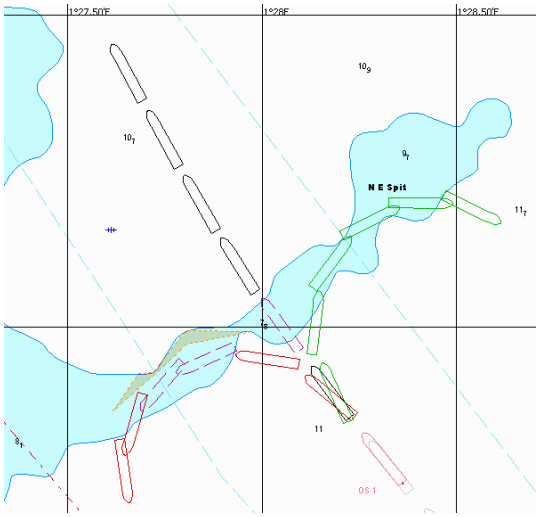

Figure 12. Representation of predicted trajectory.

6 SIMULATION EXPERIMENT

An experiment was conducted in a simulated Transas NTPro environment to analyse the efficiency of the motion prediction system's support for emergency navigational situation analysis and on-board decision making.
The simulated situation is shown in figure 13. The simulated ship is about to enter the narrow part of the channel after the turn, but the ship moving in the same direction experiences a rudder jam and becomes grounded at the northern entrance to the channel

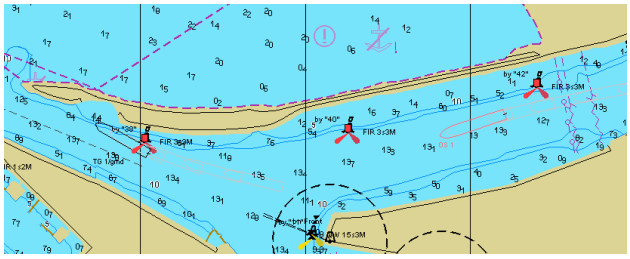

Figure 13. Simulated manoeuvre: ship TG1 (left, black) is grounded during turn, ship OS1 (right, red) is approaching the turn. At 1:10000 scale.

In every simulation experiment, a participant was operating OS 1 ship while authors controlled all other ships. . Before the simulation participant was instructed to make the safest decision in a potentially dangerous situation that will happen during the training session, as shown in figure 12. Some trainees were professional mariners, while others were naval architects without ship handling experience. All trainees had 20 minutes introductory training to get used to ship manoeuvring characteristics. The result of each simulation session was estimated as one of three possible cases: collision with channel boundary or other vessel, soft grounding or safe manoeuvre.

Table 4. Results of simulation experiment

	Prediction of own ship	
	Predictor (1st attempt)	None (2nd attempt)
Manoeuvring result (group of 3 naval architects)		
Collison with boundary or vessel	2	1
Soft grounding	1	0
Safe passage	0	2
Average time for safe passage case, min	n/a	9:15
Manoeuvring result (group of 3 mariners)		
Collison with wall or vessel	0	0
Soft grounding	0	1
Safe passage	3	2
Average time for safe passage case, min	16:55	13:36

Though the number of participants was relatively small, some preliminary conclusions could be suggested after analysis of trajectories and results of these experiments:

- Use of the advanced predictor for skilled users forced them to decrease speed in advance and proceed in a safer way, thus reducing the possibility of rough errors.
- Unskilled trainees gain more from their previous experience than from the use of advanced navigation tools.

7 CONCLUSIONS

- The developed mathematical model allows fast-time simulation of ship motion considering shallow water effects and simplified model of hydrodynamic interaction between ship and its environment.
- Access to high precision and up-to-date navigational charts is essential for prediction considering mechanical and hydrodynamic interaction.
- Different representation forms of predicted trajectory may provide additional information about future manoeuvre.
- Usage of motion prediction tool is useful for skilled mariners to evaluate and control ship behaviour. Such tools may become even more useful if prediction exchange between different ships in the area is available.
- Future research can be focused on precision enhancement of the model and on enhancing prediction representation. Additional simulated experiments will provide more information about the optimal amount of information provided by a prediction tool.

8 ACKNOWLEDGEMENTS

The authors would like to thank the engineers and mariners who helped and participated in simulation experiments: Alexander Sosonkin, Mikhail Andrianov, Andrey Vasiliev, Alexey Antonov, Petr Sobolev, Dmitry Shilkin, Ivan Cheryrbok, Alexey Vasiliev.

9 REFERENCES

1. Nakano, T.; Hasegawa, K. (2013). An Attempt to Predict Manoeuvring Indices Using AIS Data for Automatic OD Data Acquisition. *International Workshop of Next Generation Nautical Traffic Models*, Delft, The Netherlands.

2. Baldauf, M.; Mehdi, R.; Deeb, H.; Schröder-Hinrichs, J. U.; Benedict, K.; Krüger, C.; Fischer, S.; Gluch, M. (2015). Manoeuvring areas to adapt ACAS for the maritime domain. *Scientific Journals of the Maritime University of Szczecin* No.43 (115): pp. 39–47.

3. Benedict, K.; Gluch, M.; Kirchhoff, M.; Schaub, M.; Fischer, S.; Baldauf, M. (2015). Innovative simulation

tools for learning & teaching ships dynamic and investigation of manoeuvring capabilities. *MARSIM2015*, Newcastle, UK.

4. Son, N. S.; Furukawa, Y. (2009). Study on the algorithm of collision avoidance for large container in shallow confined waterway. *International Conference on Ship Manoeuvring in Shallow and Confined Water: Bank Effects*, Ghent, Belgium, R.I.N.A.: pp. 113-120.

5. Wijhe van, H. J.; Janssen, W. D.; Blocken, B. (2015). Wind loads on ships in a complex environment. *MARSIM2015,* Newcastle, UK.

6. Fossen, T. I. (2011). *Handbook of Marine Craft Hydrodynamics and Motion Control*. John Wiley & Sons Ltd.: p. 575.

7. Lerner, D. M.; Lukomskiy, Y. A.; Mikhaylov, V. A.; Nornevskiy, B. I.; Petrov, Y. P.; Popov, O. S.; Shleyer, G. E. (1979). *Control of marine moving objects [Upravlenie morskimi podvizhnyimi ob'ektami]*, Shipbuilding [Sudostroenie], Leningrad: p. 271.

8. Voytkunskiy, Y. I., Ed. (1985). *Handbook on ship theory [Spravochnik po teorii korablya] Vol. III*, Shipbuilding [Sudostroenie], Leningrad: p. 544.

9. Vantorre, M. (2001). Manoeuvring coefficients for a container carrier in shallow water: an evaluation of semi-empirical formulae. *Mini Symposium on Prediction of Ship Manoeuvring Performance*, Tokyo, Japan: pp. 71-81.

10. Yoshimura, Y.; Masumoto, Y. (2012). Hydrodynamic database and manoeuvring prediction method with medium high-speed merchant ships and fishing vessels. *MARSIM2012*, Singapore.

11. Brix, J., Ed. (1993). *Manoeuvring technical manual*, Seehafen-Verlag, Hamburg: p. 266.

12. Ankudinov, V. K.; Filippov, I. I.; Sobolev, P. K. (2006). Modeling Of Ship Motions In Restricted Channels On Marine Simulators. *MARSIM2006*, Terschelling, The Netherlands.

13. Sobolev, P. K. (2015). *Basin modeling of ships motion [Basseynovoe modelirovanie dvizheniya sudov]*, Elmore, Saint-Petersburg, Russia: p. 304.

14. Briggs, M. ; Uliczka, K.; Vantorre, M.; Debaillon, P. (2010) Prediction of Squat for Underkeel Clearance. In: *Handbook of Coastal and Ocean Engineering*, Kim, Y. C., Ed., World Scientific, New Jersey: Chapter 26, pp. 723-774.

15. Daggett, L.; Hewlett, C.; Ankudinov , V.; Filippov, I.; Ponomarev, V.; Rogozhina, E.; Shilkin, D. (2009). Application of latest ship maneuvering technology and ship hydrodynamics modeling to the expansion of the panama canal – working out operation procedures and techniques. *MARSIM2009*, Panama City, Panama.

16. Remery, G. F. (1974). Mooring Forces Induced by Passing Ships. *Offshore Technology Conference*, Dallas, Texas: pp. 349-363.

10 AUTHORS' BIOGRAPHIES

Ekaterina Rogozhina holds the current position of senior expert at Transas Technologies. She is responsible for research in the area of hydrodynamic modelling.

Alexander Ozersky holds the current position of section manager at Transas Technologies. He is responsible for algorithm development in the area of hydrodynamic modelling.

4th MASHCON, Hamburg - Uliczka et al. (eds) - © 2016 Bundesanstalt für Wasserbau ISBN 978-3-939230-38-0 (Online)
DOI: 10.18451/978-3-939230-38-0_24

SIMULTANEOUS SHIP-TO-SHIP INTERACTION AND BANK EFFECT ON A VESSEL IN RESTRICTED WATER

A Y Sian, A Maimun and **Y Ahmed,** Marine Technology Centre, Universiti Teknologi Malaysia, Malaysia
Rahimuddin, Universitas Hasanuddin, Indonesia

SUMMARY

The present study investigates the hydrodynamic interaction between two vessels, an LNG tanker and a container ship, advancing in parallel in the close proximity of a bank using an unsteady Reynolds-averaged Navier-Stokes (URANS) simulation. The study focused on the simultaneous effect of ship-ship interactions and the presence of the bank in the vicinity. Computations were carried out for the following various scenarios: (1) single ship bank effect, (2) two-ship interaction and (3) simultaneous effect of the bank and the presence of a nearby ship. Through a comparative CFD analysis, this study reveals the behaviours of the hydrodynamic forces and moments acting on the vessels and the changes in the flow field when the bank effect and ship-ship interaction complement each other. Apart from the CFD simulation, model tests were carried out for validation purposes. The overall results of the numerical simulation showed fairly good agreement with the experiment, though there was a high validation comparison error in some cases, indicating challenges in CFD prediction.

NOMENCLATURE

α	Bank slope (-)
B	Ship's breadth (m)
C_B	Block coefficient (-)
D	Experimental data value (-)
Fn	Froude number [$U/\sqrt{(gL)}$]
g	Acceleration of gravity (ms^{-2})
h	Water depth (m)
L_{pp}	Length between perpendiculars (m)
N	Yaw moment (Nm)
N'	Non-dimensional yaw moment (-)
o	Earth bound coordinate system (-)
ρ	Density of water (kg/m^3)
T	Ship's draft (m)
T_1	Draft of LNG ship (m)
T_2	Draft of S60 ship (m)
U	Ship's speed (ms^{-1})
X	Longitudinal force (N)
X'	Non-dimensional longitudinal force (-)
x, y, z	Coordinates in body axes (m)
Y	Sway force (N)
Y'	Non-dimensional sway force (-)
$y+$	Non-dimensional wall distance (-)
y_b	Distance from the ship's centreline to the toe of the bank (m)
y_b/B	Distance from the ship's centreline to the toe of the bank over the ship breadth ratio (-)
y_{ss}	Lateral distance between midship (m)
y_{ss}/B	Lateral distance between midship over the ship breadth ratio (-)

1 INTRODUCTION

During the last decade, vessel size has been increasing to meet the demands of trade. Larger liquefied natural gas (LNG) carriers can meet the demand of energy. As a consequence, larger vessels are increasingly influenced by waterway restrictions, which are further aggravated by the increase in marine traffic.

Features of restricted water, such as the presence of a sea bottom, the presence of a bank or the presence of other ships, can influence the behaviour of a vessel in operation, increasing the risk of marine disasters. Ship-to-ship interaction, for instance, can cause a ship to alter course. The forces from the interaction often draw ships together, resulting in a possible collision. Vessels operating in the close proximity of banks or lateral boundaries, however, may experience a lateral force and yaw moment, known as the bank effect, attracting the vessel to the bank because of asymmetric flow around the ship. The causes of these phenomena lie in the changes in the delicate balance of the pressure forces acting on a moving ship.

All of these hydrodynamic phenomena adversely modify the ship's manoeuvring behaviour. Thus, these hydrodynamic interactions have become important to consider for safe navigation, especially in restricted water, where vessels interact and experience hydrodynamic forces from shallow water, the bank effect, interaction between ships or a combination of these.

Information regarding all factors affecting the hydrodynamics effect in restricted water is vital for the safety of navigation. For this to be possible, the hydrodynamic forces between ships and the bank in restricted water should be properly understood. The realistic estimation and quantification of the hydrodynamics forces from the interaction in advance is important to the ship operator before the hydrodynamics forces lead to a disastrous event.

There have been a number of studies on the hydrodynamic behaviour of ships in restricted water, and they presented an important fundamental understanding to these phenomena. However, few studies have taken into account the simultaneous effects of shallow water, the bank

effect and ship-to-ship interactions, all which are linked in practice in restricted waters.

Most of the investigations of the interaction are on the bank effect or ship-ship interactions alone. Norrbin [1,2] experientially investigated the bank effects and obtained empirical expressions for the bank-induced lateral force and yaw moment for three different bank configurations, a vertical bank, a vertical submerged bank and a slope bank. Li et al. [3] extended the works of Norrbin [1,2] and focused on the bank effect in extremely shallow water ($h/T < 1.2$).

Vantorre et al. [4] performed a model test program on bank effects using a vertical surface-piercing bank and proposed empirical formulae for predicting the ship-bank interaction forces. Mathematical models for the estimation of the hydrodynamic forces, moment and ship sinkage by a sloped surface piercing bank and a bank with a submerged platform were given by Lataire and Vantorre [5].

Zou at al. [6] performed CFD analyses on a low-speed KVLCC2 tanker in a canal characterized by surface piercing banks. Zou and Larsson [7] provided a physical explanation of the bank effects in confined water.

Varyani et al. [8] and Varyani et al. [9] published empirical formulae to predict the sway force and yaw moment of a two-ship encounter and overtaking in a channel. Vantorre at al. [10] performed model tests with an auxiliary carriage installed in a towing tank to study the case of a ship meeting and overtaking. Varyani and Vantorre [11] presented semi-empirical generic models for calculation of the interaction forces acting on a moored ship based on slender body theory and experiments.

Lataire et al. [12] proposed mathematical models for the prediction of the surge force, sway force and yaw moment during a lightering manoeuvre. Zou and Larsson [13] conducted CFD computations on the ship-to-ship interaction in a lightering operation.

Fewer studies had considered the problems of the combined bank effect and ship interaction. Korsmeyer et al. [14] presented a three-dimensional panel method for the analysis of ship interactions applicable to a fluid domain bounded by irregular surfaces. Kijima and Yasukawa [15] examined the behaviour of hydrodynamic forces and the moment when two ships meet and overtake each other in a narrow water channel with vertical side walls using slender body theory. Kijima et al. [16] extended the study to the case of two ships in the proximity of a bank wall with semi-circle shape breakwater, a circular pier and an oval shaped pier. Kijima and Furukawa [17] discussed the effect of the ship's speed ratio for the case of ships running closely in the proximity of a bank wall with semi-circle shape breakwater and a circular pier.

The details of these hydrodynamic problems are worth examining further. The present work tries to gain insight into the interaction of ship-bank and ship-ship in shallow water and reveal the effect of various factors affecting the interaction. The focus of this study will be on vessel manoeuvring behaviour influenced by hydrodynamic interactions due to the bank effect and interaction with another ship nearby in restricted shallow water.

2 MODEL TESTS

2.1 TEST FACILITIES

The experiments in this study were conducted in the towing tank at the Marine Technology Centre (MTC) of Universiti Teknologi Malaysia (UTM). The tank has a total length of 120 m, a width of 4 m and a depth of 2.5 m. The towing carriage, equipped with a planar motion mechanism (PMM), can tow the ship models at speeds up to 5 m/s.

2.2 SHIP MODELS AND BANK GEOMETRIES

Two ship models have been used in this model test program. The main dimensions of the models are listed in Table 1. The primary ship model is a Tenaga Class LNG carrier scaled by a factor of 1:112. The performance and geometric properties of this specific model were published by Sian et al. [18] and Maimun et al. [19].

The secondary ship model used is an L_{pp} =2.534 m standard Series 60 C_B=0.7 hull form. The model was a single-screw merchant ship hull. This hull form is a classical model for ship hydrodynamics research with experimental data available in the literature. The body plans of both models are shown in Figures 1 and 2.

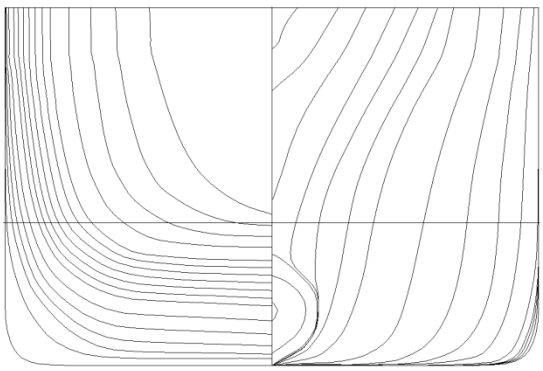

Figure 1. Body plan of the LNG carrier.

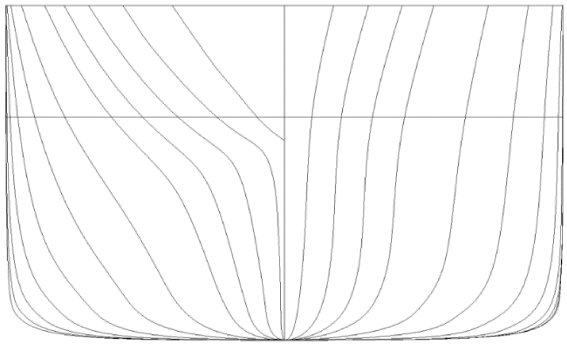

Figure 2. Body plan of the Series 60 model.

A 20-m shallow water platform was installed in the towing tank to investigate the shallow water effect. To investigate the bank effect, the bank of the submerged platform type was installed on top of the shallow water platform. The bank model composed a slope of 1/5, with a height of 0.08 m and a horizontal submerged part.

Table 1. Ship model dimensions

	LNG model	S60 model
Ship length, L_{pp}	2.375 m	2.534 m
Breadth, B	0.371 m	0.362 m
Draft, T	0.099 m	0.110 m
Block coefficient	0.746	0.7

2.3 MODEL TEST CONDITIONS

Water was drained from the tank to achieve the desired water height-to-LNG model's draught ratio of $h/T_1 = 1.2$, 1.4 and 1.6 during the test. The primary LNG model was attached to the computer controlled planar motion mechanism (PMM). The model was allowed to have pitch and roll but was restrained in the surge, sway and yaw motions. Two load cells were installed at the mechanical connectors.

The S60 model was mounted with a fixed frame at the towing carriage's working platform, allowing for the test of two ships travelling in parallel with no speed differences. The position of the working platform was flexible, allowing for lateral adjustment. The model was rigidly connected to the towing carriage. Thus, all motion of the model was restrained. No measurement was taken from the secondary model.

Both models were tested in an even keel without a rudder and propeller attached (Figure 3). The transversal position of the LNG ship model can be adjusted via a computer-controlled PMM, while the transversal position of second ship models can be manually adjusted by shifting the working platform.

The forces and moments on the LNG were measured with two strain gauge type load cells. The results presented in this study were obtained by averaging the measurements over the steady state conditions in the model tests for a distance of 1 to 2 ship lengths, which were usually achieved after the ships travels for a distance of 2 to 5 ship lengths.

It must be noted that the h/T_1 ratio is computed based on the draft of the primary LNG model (0.099 m). Despite the best effort of the authors to perform the study with two models with identical size, the S60 model has approximately 10% extra ship draft at 0.110 m. At the $h/T_1 = 1.2$ condition, the gap beneath the model is essentially narrower for S60. For the S60 model, the water depth condition at $h/T_1 = 1.2$ is equal to $h/T_2 = 1.10$.

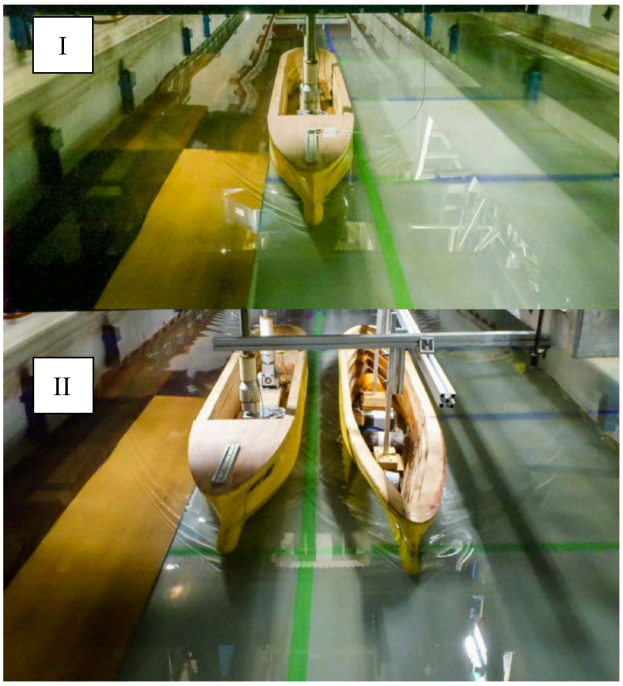

Figure 3. Captive model tests in the towing tank. I – Test on the bank effect in the shallow water condition and II – test on the two ships and bank effect.

2.4 CONVENTIONS AND REGISTRATION

The conventions and registration used in the tests are illustrated in Figure 4.

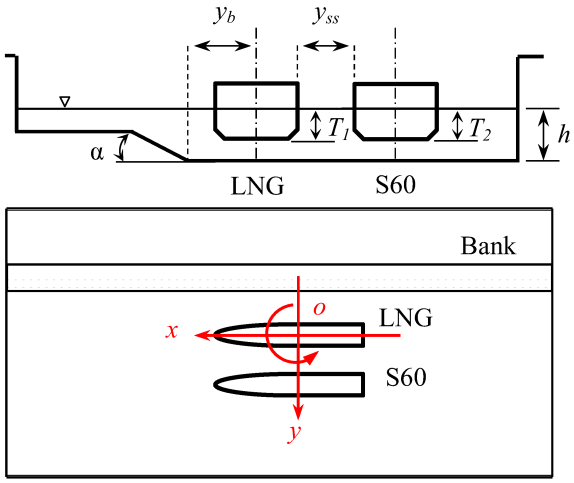

Figure 4. Test conventions and registrations.

2.5 NON-DIMENSIONALIZATION

The longitudinal force, sway force and yawing moment were non-dimensionalized using the following equations:

$$X' = \frac{X}{\frac{1}{2}\rho L^2 U^2} \quad (1)$$

$$Y' = \frac{Y}{\frac{1}{2}\rho L^2 U^2} \quad (2)$$

$$N' = \frac{N}{\frac{1}{2}\rho L^3 U^2} \quad (3)$$

3 NUMERICAL METHOD

3.1 GENERAL REMARKS

The hydrodynamic interactive forces and free surface flow in this study were examined using the general purpose CFD solver Fluent V15. The code solves incompressible unsteady Reynolds-averaged Navier-Stokes (URANS) computations by the finite volume method (FVM). The turbulence model used is the shear-stress transport (SST) $k-\omega$ model. The free surface in the CFD computations was tracked with the volume of fluid (VOF) model.

3.2 GRID GENERATION

The computational grids are generated by ICEM CFD by entirely using a structural grid approach. Some care has been taken in creating the grid. Finer grids are distributed at the region of the free surface and surrounding the ship hulls to resolve the flow gradients and to provide greater resolution about the free surface interface. The size of the first grid point away from ship hull was at approximately $y+ = 50$, with 20 cells within the boundary layer to capture the detailed fluid property. The number of grid points used was approximately 2 million.

3.3 COMPUTATIONAL DOMAIN AND BOUNDARY CONDITIONS

Calculations were performed at the model scale. The computational domain was made up by seven boundaries: the hull surface, flow pressure inlet, flow pressure outlet, top, bottom and two side walls. A schematic diagram indicating the computational domain is given in Figure 5.

The dimensions of the hulls, tank bottom and two side walls of the domain correspond to the exact experiment set up in the towing tank. The length of the numerical towing tank was 11.5 m, and the ships were located 1.3 ship lengths of the slightly longer S60 model behind the flow inlet and flow outlet at the aft of the two ship models at a distance of 2.3 ship lengths of S60.

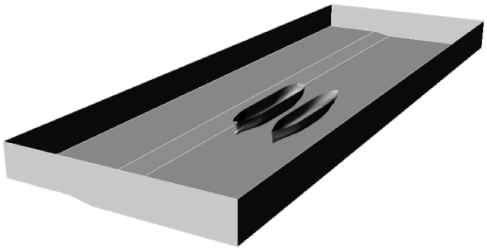

Figure 5. Overview of the computational domain.

Smooth walls and the no-slip condition were imposed for the hulls. The bank geometry and towing tank's wall were implemented as a moving wall to model the relative motion between the ground and ship model. A translational velocity identical to the flow inlet was imposed on the moving wall.

3.4 COMPUTATIONAL SETUP

The SIMPLE-Consistent algorithm was used for pressure-velocity coupling. The gradient discretization of the variables in the flow conservation equations was performed using the least squared cell-based method. Variables including the volume fraction, turbulent kinetic energy, dissipation rate and specific dissipation rate were discretized in time using the bounded second order implicit time integration transient formulation.

The pressure staggering option (PRESTO!) scheme was used for pressure interpolation in the discretization of the momentum equation, and the second-order upwind method was used for density interpolation in the discretization of the continuity equation. The turbulent kinetic energy and specific dissipation rate were discretized using the second-order upwind scheme. The volume fraction was discretized by the compressive scheme.

Simulations were performed with the free surface, and the ship models were fixed at an even keel for all cases. Simulations were performed in a time accurate manner to capture the unsteady flow features during hydrodynamic interactions, should they exist. The total physical time of 90 seconds was computed with the step size of 0.01 s.

Convergence was monitored by ensuring the ships' body forces and moments were stable. The convergence of each time step was to ensure that the residuals scaled by the initial imbalance of equations dropped three orders of magnitude, which was typically achieved in approximately 10-15 iterations during simulations. The simulation results were obtained by averaging the flow quantities over its statistical steady state.

The computations were conducted on a shared-memory type workstation. The computations employed four processors (3.6 GHz) and a total of 32 GB of 1600 MHz

DDR3 RAM. The computing time for each case required approximately 40 hours.

4 RESULTS AND DISCUSSION

4.1 CFD VALIDATION

The predicted sway force and yaw moment induced by the presence of the bank on the LNG were compared with the experimental data in Figure 6. The published bank effect formulations of Norrbin (1985) and Vantorre et al. (2002) for the sway force and yaw moment prediction were used to compare these values with the hydrodynamic force and moment in the current research.

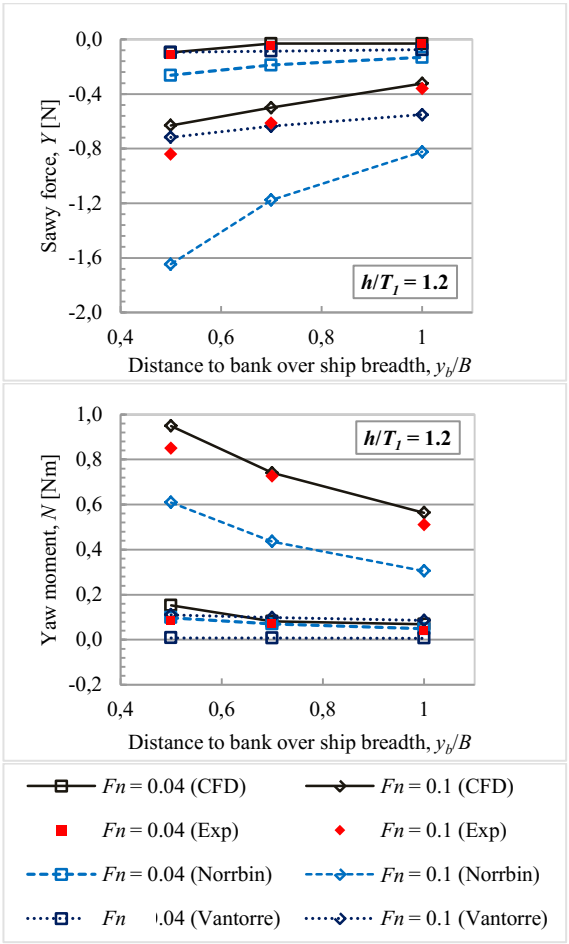

Figure 6. Sway force and yaw moment induced by the bank on the LNG at h/T_1 = 1.2 from the CFD analysis, the experiment, and the formulations of Norrbin (1985) and Vantorre et al. (2002).

For the ship-bank interaction, the agreement of the computed results and experiment measurement is generally satisfactory, with small deviations. The general tendency of the hydrodynamic force and moment by the experiments is well captured.

In general, CFD tends to under-predict the sway force and over-predict the yaw moment. The sway force of the LNG model is predicted with an average error at 16.21%*D*, the largest error being 30.46%*D* under-predicted and 0.91%*D* over-predicted. The yaw moments are all over-predicted, with an average error of 32.37%*D*, the largest error being 78.71%*D*.

The formulation of Norrbin [2] and Vantorre [10] over-predicted the sway force and yaw moment compared to the CFD model, as expected. The ship models used by Norrbin [2] and Vantorre [10] were tankers with a higher block coefficient compared to the LNG carrier in this research. Moreover, the expressions of Norrbin [2] were developed for a vertical submerged bank, whereas the formulations of Vantorre [10] were developed for a sloped surface piercing bank. Both bank models resulted in a higher blockage in the navigation channel compared to the bank model used in this research.

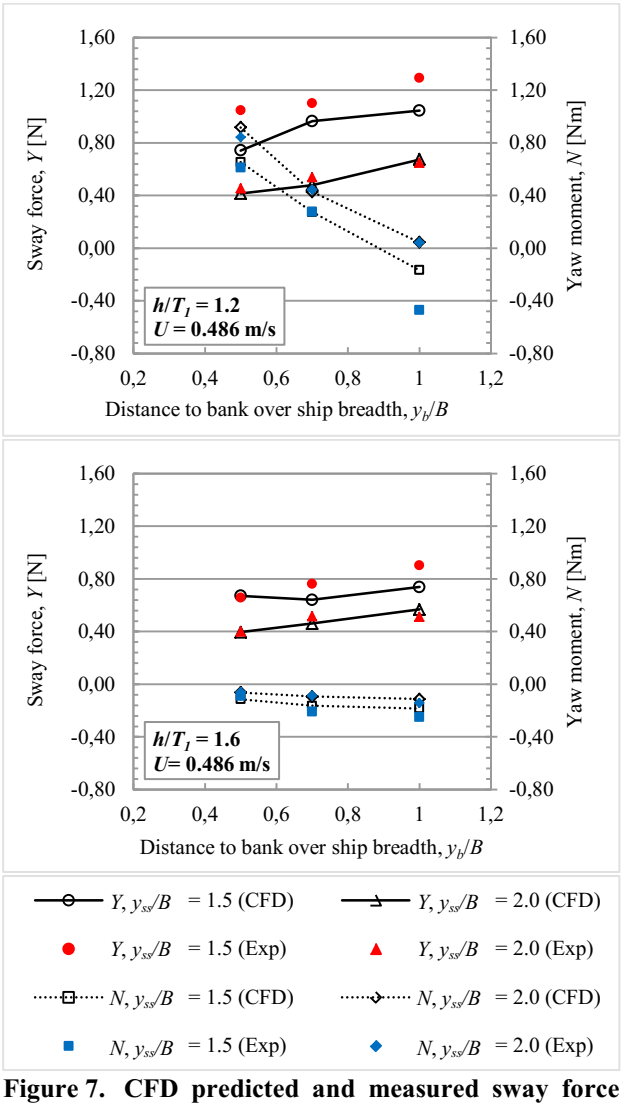

Figure 7. CFD predicted and measured sway force and yaw moment acting on the LNG ship model from simultaneous ship-bank and ship-ship interaction.

The predicted forces and moment in the simultaneous ship-bank and ship-ship interaction are compared with the experimental results in Figure 7. The sway forces are generally under-predicted, whereas the yaw moments are

over-predicted. The sway forces are predicted at an average error of 11.91%D, the largest error being 10.93%D over-predicted and 29.08%D under-predicted. The yaw moments are predicted at an average error of 16.43%D, the largest error being 27.52%D over-predicted and 64.49%D under-predicted. The changes in the sign for the yaw moment at h/T_1 = 1.2, y_b/B = 1 and y_{ss}/B = 1.5 are successfully captured in the CFD computation. The overall computational results are encouraging, and the general tendency of the hydrodynamic force and moment by the experiments is well captured.

4.2 SHIP-BANK INTERACTION

Figure 8 shows the computed Y' and N' acting on the LNG model travelling in a straight course along the bank in shallow water for a wide range of Froude numbers and ship-bank distances. The interaction clearly shows where the model experiences a sway force, attracting the model to the bank, and the yaw moment pushed the ship bow away from the bank.

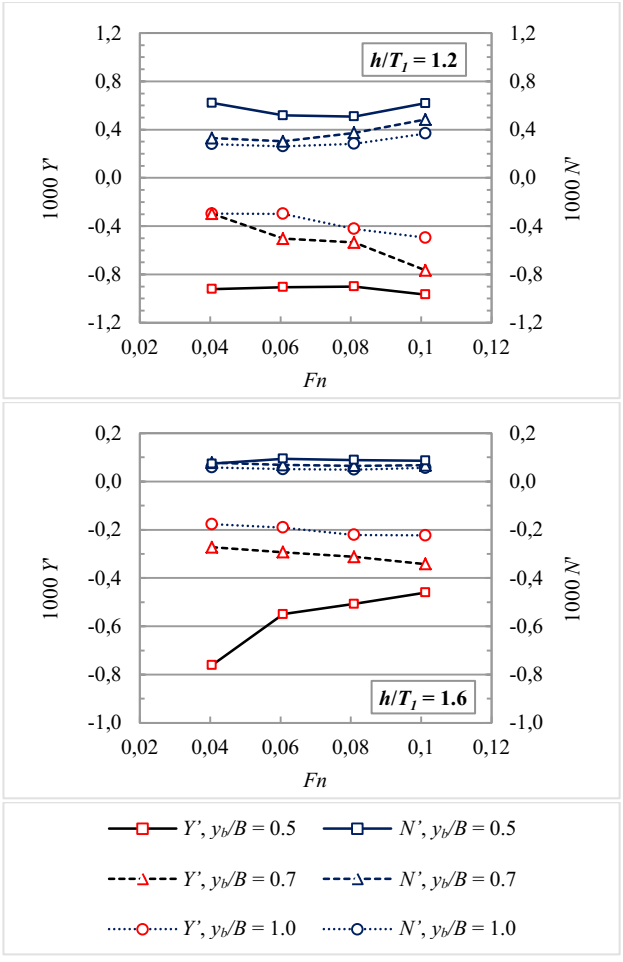

Figure 8. Computed Y' and N' induced by the bank on the LNG model.

The force and moment coefficients are made non-dimensional by the square of the ship speed. The curves obtained in the plots of the forces and moments over different Froude numbers indicate that the forces and moment are not proportional to the speed squared, especially at h/T_1 = 1.2. Straight horizontal lines should be obtained instead of a direct square proportion relationship.

Both the sway force and yaw moment are intensified at a lower h/T_1 ratio. This is particularly the case for the yaw moment where a dramatic increment is observed when h/T_1 approaches 1.2. The forces and moment are noticeably greater at a lower bank distance over the ship breadth ratio. The magnitude of the yaw moment is generally weaker compared to the sway force in the ship-bank interaction.

The expected transition of the sway force direction at an extremely low h/T ratio, as reported by Duffy [20] and Li et al. [3], was not demonstrated, probably because of the limited h/T_1 condition tested, with 1.2 being the extreme water depth.

The test in a water depth of less than h/T_1 = 1.2 or a ship closer to the bank at y_b/B less than 0.5 could not proceed without grounding the ship model.

4.3 SHIP-SHIP INTERACTION

The interaction of the two ships moving along parallel paths in shallow water is presented in this part. The problem considered here is limited to two approximately similar size vessels, the LNG model and S60, moving at a constant velocity with the midships aligned. Experimental data are not available for this part. Thus, only the numerical result presented. Figure 9 shows the predicted Y' and N' acting on LNG and S60 for several ship-ship distances at Fn = 0.04 and 0.1 and h/T_1 = 1.2 and 1.6.

The interaction force and moment acting on the models were greater as the distances between the two ships decreased. Given that the gap between the ships becomes narrow at a lower y_{ss}/B, a more pronounced pressure drop was expected because of the accelerated flow. Therefore, a larger interactive sway force and yaw moment should be noted.

A higher magnitude of the sway force and yaw moment can be seen acting on the LNG at lower h/T_1 ratio, except at h/T_1 = 1.2, with a short distance between the two ships, where the magnitude decreased.

The numerical simulations have captured the effect of the reduction of the sway force, followed by changes in the force direction at small lateral distances between the ships, as reported by Fonfach et al. [21]. This is particularly the case for the LNG model at y_{ss}/B = 1.5 and h/T_1 = 1.2. More of such sway force reduction phenomena are found in S60 because of its deeper ship draft.

At Fn = 0.04, the sway force changed from negative to positive, indicating that the force acting on the model changed from an attraction force to a repulsion force.

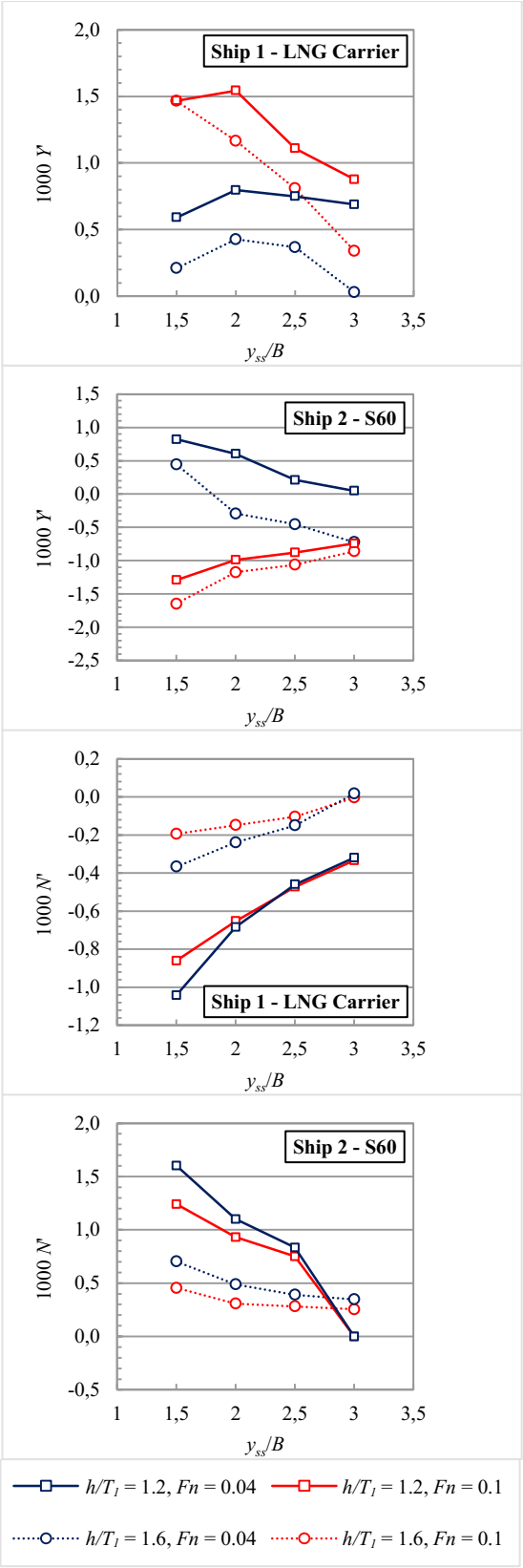

Figure 9. Computed *Y'* and *N'* induced on the LNG due to the interaction with the S60 ship model as a function of the lateral distance between the midships over the ship breadth ratio.

However, such a transition of the force direction was not seen in the LNG model. Such force transition phenomena have been reported by Duffy [20] and Li et al. [3] when the critical h/T ratio exceeds 1.10.

4.4 SIMULTANEOUS SHIP-BANK AND SHIP-SHIP INTERACTION

The interaction of two ships moving along parallel paths in the vicinity of the bank is presented in this part. The situation considered in the present study is where the LNG carrier model travel parallel with the S60 ship model at her port side and the submerged sloped bank at her starboard side.

Figure 10 shows the computed free surface elevations for a single ship in the shallow water condition, a single ship interacting with the bank, two ships interacting and a ship simultaneously interacting with the bank and the second ship at Fn = 0.1, y_b/B = 1.0 and y_{ss}/B = 1.5. The wave profiles along the hull are shown in Figure 11.

As seen in Figure 10, wave crests located at the zones of the high pressure at the ship bow are detected well by the CFD simulation. A great region of wave crests can be observed upstream of the ships, which could be attributed to stagnation.

A higher wave elevation and a greater region of wave crests upstream were observed in the case of simultaneous ship and bank interaction compared to the other two, which are responsible for the significant increase in the longitudinal force. Two peaks of the elevated water were observed between the bows of the two ships, which seem to be responsible for the bow out yaw moment induced on the two ships model.

Moving downstream, a wave trough attributed to Bernoulli's effect was observed over the length of the vessels. Careful observation shows the presence of two dips in the middle of the two ship models, which produce the attractive force between the two ships. In general, the free surface pattern between the two ships was similar for the two-ship interaction and the simultaneous bank and two-ship interaction, although the wave trough of the latter was more pronounced, indicating a stronger suction between the two ships.

An instantaneous snapshot of the free surface wave pattern at the starboard side of the LNG model during the experiment is shown in Figure 12. The computational results reproduce the trough and crest at the starboard and astern of the LNG model, very similar to the experimental results, and suggest that the wave elevation is well predicted by the CFD method.

A strong asymmetry of the free surface was observed in the ship-bank interaction cases. The wave trough at the starboard, followed by the wave crest astern of the starboard, suggests the presence of a lower pressure region

than the port side. A bow out yaw moment induced by the presence of the bank is expected because of the imbalance of the pressure field. This structure of the free surface at the starboard remains in the simultaneous ship-bank and two ship interactions, but there are distinct differences in the magnitude of wave elevation observed. The wave trough, followed by the wave crest, is noticeably more pronounced in the simultaneous two ship and bank interaction.

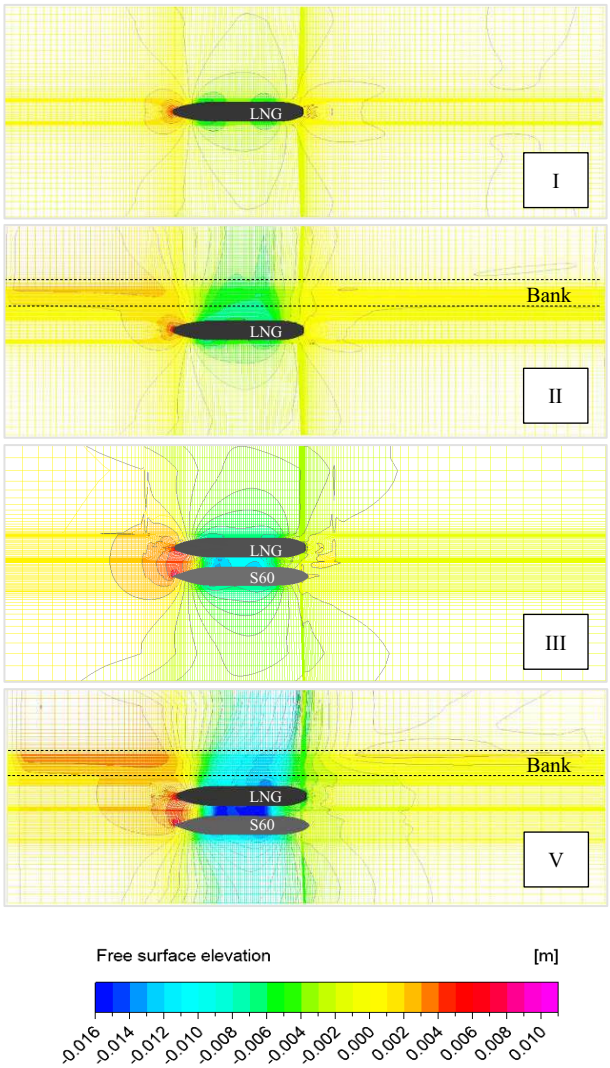

Figure 10. Computed free surface wave pattern at h/T_1 = 1.2. I – LNG model, II – LNG model with bank at the starboard, y_b/B = 1.0, III- Two-ship interaction, y_{ss}/B = 1.5, V- simultaneous two ship and bank interaction, y_b/B = 1.0, y_{ss}/B = 1.5.

The predicted X', Y' and N' for the conditions of ship-bank interactions, two-ship interactions and simultaneous ship-bank and ship-ship interactions at h/T_1 = 1.2, 1.4 and 1.6 are given in Figure 13. Comparing the ship-bank interaction and the ship-ship interaction, the magnitudes of X', Y' and N' from the ship-ship interaction alone were always greater than the magnitude induced by the ship-bank interaction alone.

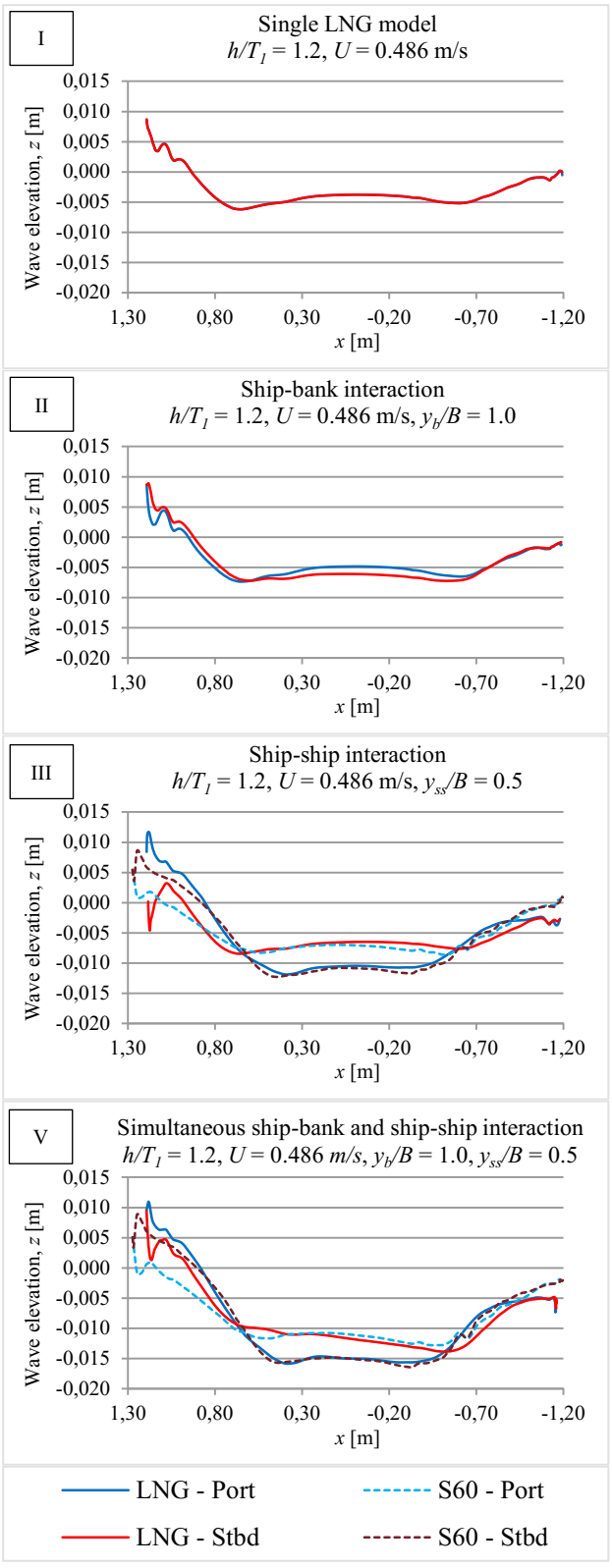

Figure 11. Computed wave profile along the hull at h/T_1 = 1.2. I – LNG model, II – LNG model with bank at the starboard, y_b/B = 1.0, III – two-ship interaction, y_{ss}/B = 1.5, V – simultaneous two ship and bank interaction, y_b/B = 1.0, y_{ss}/B = 1.5.

As discussed earlier, on the LNG carrier, the ship-bank interaction gives a negative Y' and positive N', whereas

the ship-ship interaction gives a positive *Y'* and negative *N'*.

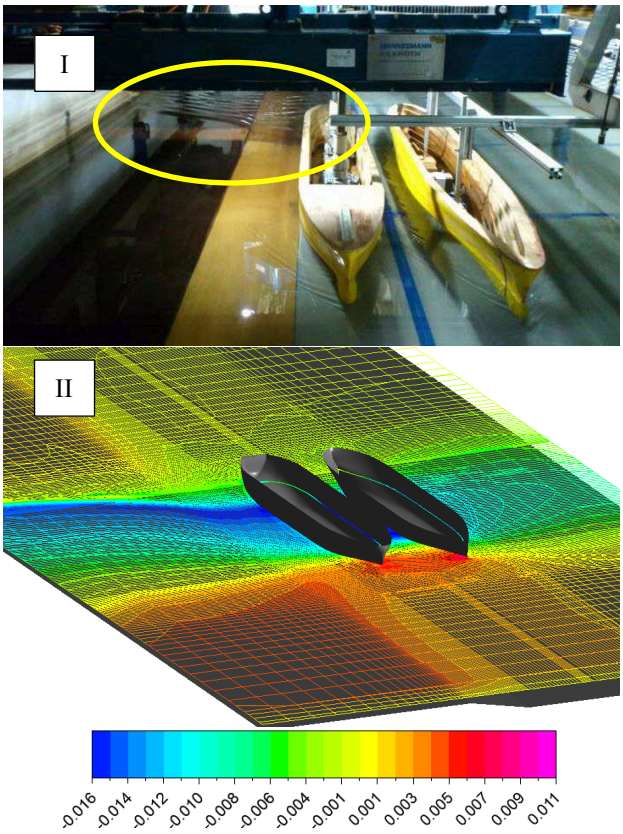

Figure 12. Comparison of the free surface wave pattern between the experimental and computational results, h/T_1 = 1.2, y_b/B = 0.5, y_{ss}/B = 1.5, *Fn* = 0.1. I – Experiment (the circle indicates a wave trough followed by a wave crest due to presence of the bank), II – CFD.

From Figure 13, it can be seen that the simultaneous ship-bank and ship-ship interactions resulted in a higher magnitude of *X'* compared to the magnitude from the ship-bank interaction or the ship-ship interaction alone, while the *Y'* and *N'* from the simultaneous ship-bank and ship-ship interactions were in the range of the two peak values from the bank or ships' interaction alone. *X'* increased rapidly between h/T_1 = 1.2 and 1.4 but dropped between h/T_1 = 1.4 and 1.6. For a specific distance from the bank, the magnitude of *X'* increased with shorter distances between the two ships.

Comparing the *Y'* and *N'* of the ship-bank interaction, the ship-ship interaction and simultaneous ship-bank and ship-ship interaction are all at their equal ship-ship or ship-bank distances at y_b/B = 1.0 and y_{ss}/B = 1.5. The resemblance of the *Y'* and *N'* direction in the simultaneous ship-bank and ship-ship interaction with the ship-ship interaction proved that the ships' interaction has more influence on the LNG compared to the bank effect. This conclusion agrees well with Kijima et al. [16], though different ships and bank models were used compared to the present paper.

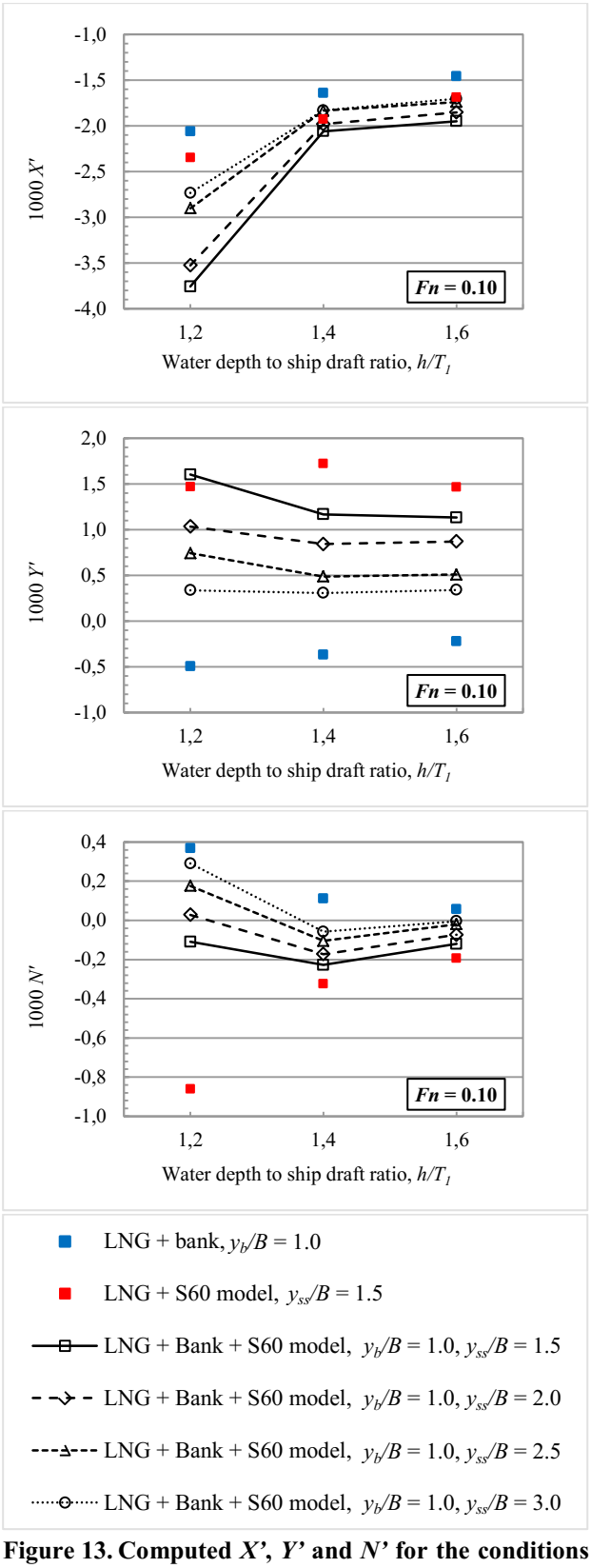

Figure 13. Computed *X'*, *Y'* and *N'* for the conditions of ship-bank interaction, two ship interaction and simultaneous bank and two ship interaction.

As seen in Figure 13, at a specific ship-bank distance at y_b/B = 1.0, a larger influence of the ship-ship interaction can be seen on *Y'*, where the LNG is attracted to the S60

model at y_{ss}/B lower than 2.0. At y_{ss}/B = 2.5, the resultant effect of the bank and ships interaction resulted in *Y'* being close to zero. At y_{ss}/B = 3.0, *Y'* acts in a different direction, and a higher influence of the bank effect can be seen where the LNG is attracted to the bank.

N' behaves in a different way compared to *Y'*. At a specific ship-bank distance at y_b/B = 1.0, the negative *N'* acted on the LNG for all cases at h/T_1 = 1.4 and 1.6, indicating that the influence of the ship-ship interaction is dominant and the ship bow swings toward the bank. At h/T_1 = 1.2, however, a positive *N' is* seen in all cases except at y_{ss}/B = 1.5.

Preliminary computations have indicated the sway forces and yaw moments from the ship-bank interaction and the ship-ship interaction seem to superpose and counteract each other, but these effects will require further investigation.

5 FUTURE WORKS

It has been shown that computations on simultaneous ship-bank and ship-ship interactions yield results that are in good agreement with the measured data. In all cases, the results presented were for two ships moving at a zero speed difference and zero longitudinal distances without a rudder and propeller. In addition, ship motion such as sinkage and trim were not included. Additional investigations on the influence of these factors are needed for a more realistic understanding of ships and bank interactions in restricted waters.

6 CONCLUSIONS

This paper presented an investigation of the hydrodynamic interaction between two vessels, an LNG tanker and an S60 container ship, advancing in parallel in close proximity of submerged sloped bank in restricted shallow water. Computations conducted for various scenarios, including (1) the single ship bank effect, (2) the two-ship interaction and (3) the simultaneous effect of the bank and the presence of a nearby ship, have provided deeper insight into the hydrodynamics of simultaneous ship-ship and ship-bank interaction.

The CFD model successfully simulated the wave pattern, and the computed results show fairly good agreement with the experimental data. The correlation between the experimental and computed results indicated adequately reliable estimates of the hydrodynamic interaction forces and moment obtained. Changes in the flow field on the ships when the bank effect and ship-ship interaction complement each other were also revealed.

The main conclusions are as follows:

- The combination of the ship-bank and ship-ship interactions resulted in a higher longitudinal force compared to ship-ship or ship-bank interactions alone.
- At a fixed ship-bank and ship-ship distances, the presence of the second ship has more influence compared to the bank effect.
- The interaction effects are amplified at a low water depth.
- The sway forces and yaw moments from the ship-ship interaction and the ship-bank interaction acted on a ship from the opposite direction and offset each other. The magnitude of the simultaneous ship-bank and ship-ship interaction lie between the values of the ship-bank interaction and the ship-ship interaction.

7 ACKNOWLEDGEMENTS

The presented work is supported by the Marine Technology Center (MTC) and Centre for Information and Communication Technology (CICT) in Universiti Teknologi Malaysia.

8 REFERENCES

1. Norrbin, N. (1974) Bank effects on a ship moving through a short dredged channel, *10th ONR Symposium on Naval Hydrodynamics*, Cambridge.

2. Norrbin, N. (1985) Bank clearance and optimal section shape for ship canals, *26th PIANC International navigation Congress*, Brussels.: pp. 167-178.

3. Li, D. Q.; Leer-Andersen, M.; Ottoson, P.; Tragardh, P. (2001). Experimental investigation of bank effects under extreme conditions. *Proceedings of Practical Design of Ships and Other Floating Structures (PRADS)*, Shanghai, China.: pp. 541-546.

4. Vantorre, M.; Delefortrie, G.; Eloot, K.; Laforce, E. (2003). Experimental investigation of ship-bank interaction forces. *Proceedings of The International Conference on Marine Simulation and Ship Maneuverability (MARSIM)*, Kanazawa.: pp. 311-319.

5. Lataire, E.; Vantorre, M. (2008). Ship-bank interaction induced by irregular bank geometries. *Proceedings of 27th Symposium on Naval Hydrodynamics*, Seoul, Korea.

6. Zou, L.; Larsson, L.; Delefortrie, G.; Lataire, E. (2011). CFD prediction and validation of ship-bank interaction in a canal. *Proceedings of the Second International Conference on Ship Manoeuvring in Shallow and Confined Water: Ship to Ship Interaction*. 18-20 May. Trondheim, Norway.: pp. 413-422.

7. Zou, L.; Larsson, L. (2013). Confined Water Effects on the Viscous Flow around a Tanker with Propeller and

Rudder. *International Shipbuilding Progress*. 60: pp. 309-343.

8. Varyani, K. S.; McGregor, R. C.; Krishnankutty, P.; Thavalingam, A. (2002). New Empirical and Generic Models to Predict Interaction Forces for Several Ships in Encounter and Overtaking Manoeuvres in a Channel. *International Shipbuilding Progress*. 49(4): pp. 237-262.

9. Varyani, K. S.; Thavalingam, A.; Krishnankutty, P. (2004). New Generic Mathematical Model to Predict Hydrodynamic Interaction Effects for Overtaking maneuvers in Simulators. *Journal of Marine Science and Technology*. 9: pp. 24-31.

10. Vantorre, M.; Verzhbitskaya, E.; Laforce, E. (2002). Model Test Based Formulations of Ship-Ship Interaction Forces. *Ship Technology Research*. 49: pp. 124-137.

11. Varyani, K. S.; Vantorre, M. (2006). New Generic Equation for Interaction effects on a Moored Containership Due to a Passing Tanker. *Journal of Ship Research*. 50(3): pp. 278-287.

12. Lataire, E.; Vantorre, M.; Delefortrie, G.; Candries, M. (2012). Mathematical Modelling of Forces Acting on Ships during Lightering Operations. *Ocean Engineering*. 55: pp. 101-115.

13. Zou, L.,; Larsson, L. (2013). Numerical Predictions of Ship-to-Ship Interaction in Shallow Water. *Ocean Engineering*. 72: pp. 386-402.

14. Korsmeyer, F. T.; Lee, C. H.; Newman, J. N. (1993). Computation of Ship Interaction Forces in Restricted waters. *Journal of Ship Research*. 37(4): pp. 298-306.

15. Kijima, K.; Yasukawa, H. (1984) Manoeuvrability of Ships in Narrow Waterway. *J Soc Nav Archit Jpn*. 156: pp. 25-37.

16. Kijima, K.; Furukawa, Y.; Qing, H. (1991). The Interaction Effects between Two Ships in the Proximity of Bank Wall. *Trans. Of the West-Japan Society of Naval Architects*. 81: pp. 101-112.

17. Kijima. K.; Furukawa. Y. (1994). A ship manoeuvring motion in the proximity of pier. *Proceedings of the International Committee on Manoeuvring and Control of Marine Craft (MCMC)*. Southampton.: pp. 211-222.

18. Sian, A. Y.; Maimun, A.; Priyanto, A.; Ahmed, Y. M.; Nakisa, M.; Rahimuddin. (2014). Numerical Investigation for Resistance Characteristics of LNG Carrier. *Jurnal Teknologi*. 67(9): pp. 101-107.

19. Maimun, A.; Priyanto, A.; Rahimuddin; Sian, A. Y.; Awal, Z. I.; Celement, C. S.; Nurcholis; Waqiyuddin, M. (2013). A Mathematical Model on Manoeuvrability of a LNG Tanker in Vicinity of Bank in Restricted Water. *Safety Science*. 53: pp. 34-44.

20. Duffy. J. T. (2002). *Prediction of bank induced sway force and yaw moment for ship handling simulator*. Australian Maritime College, Australia.

21. Fonfach, J. M. A.; Sutulo, S.; Soares, C. G. (2011). Numerical study of ship-to-ship interaction forces on the basis of various flow models. *Proceedings of the Second International Conference on Ship Manoeuvring in Shallow and Confined Water: Ship to Ship Interaction*, Trondheim, Norway.: pp. 137-146.

9 AUTHORS' BIOGRAPHIES

A. Y. Sian is currently a Ph.D. student at the Marine Technology Centre, Universiti Teknologi Malaysia. He received his BSc (Maritime Technology) from Universiti Malaysia Terengganu, Malaysia. His research interests include manoeuvring in shallow water, bank effects and ship-to-ship interactions.

A. Maimun is a Professor at the Marine Technology Centre, Universiti Teknologi Malaysia. He received his BSc in 1983, MSc in 1985 and Ph.D. from Strathclyde University, Glasgow, in naval architecture and ocean engineering. His research interests include ship dynamic stability, ship simulator, seakeeping, manoeuvring, offshore structures dynamics and fast craft design.

Y. Ahmed is currently a senior lecturer at Universiti Teknologi Malaysia, Malaysia. He received his Ph.D. from Alexandria University, Egypt. His research interests include ship hydrodynamics and computational fluid dynamics (CFD).

Rahimuddin is currently a lecturer at Universitas Hasanuddin, Indonesia. He obtained his Ph.D. from Universiti Teknologi Malaysia.

4th MASHCON, Hamburg - Uliczka et al. (eds) - © 2016 Bundesanstalt für Wasserbau ISBN 978-3-939230-38-0 (Online)
DOI: 10.18451/978-3-939230-38-0_25

NUMERICAL MODELLING OF PROPELLER-INDUCED FLOW VELOCITIES ON EMBANKMENTS

S Leschka, DHI Deutschland GmbH, Germany
B Xu and **L Yde,** DHI Water & Environment (S) Pte. Ltd., Singapore
O Stoschek, DHI Deutschland GmbH, Germany
J Best, Hamburg Port Authority AöR, Germany

SUMMARY

To support maintenance works of the Bubendey embankment in the Port of Hamburg, DHI set up a computational fluid dynamic (CFD) model to calculate flow velocities on embankments. The model has been calibrated and validated successfully with the help of in-situ measurements, performed by DHI in September 2014. The numerical model is comprised of the exact embankment geometry as well as a parameterized ship propeller. The results have been compared to the results of standard design guidelines [1]. The model leads to lower flow velocities on the embankment compared to available standard methods. It proved its potential in supporting embankment design by leading to less conservative and, thus, more economic design parameters.

1 INTRODUCTION

Ship-induced waves and propeller jets are important loads to be considered for embankment design in ports. Existing design guidelines such as [1] provide empirical formulae which result in high safety values. Flow velocities in a propeller jet for example can be estimated based on simplifying assumptions leading to standardized cases. According to [1], there are four standard cases, which distinguish whether there is a rudder present to split the propeller jet or not and how the dispersion area of the jet is constrained. Here, only vertical quay walls are considered laterally or downstream of the propeller jet.
The estimates are used to determine material characteristics such as rock sizes for safe embankment design. To date, such estimates are on the very conservative side [2]. Increasing ship sizes and thus increasing sizes of bank protection raise the demand of reviewing embankment design methods with the aim to still guarantee safe embankment design but also providing a more economical solution for harbor planners.
Propellers and their interaction with rudders cause complex flow fields in the stern region of a ship. Water is drawn in, accelerated and discharged downstream, propelling the vessel forward. The discharge of water contains high kinetic energy, a turbulent flow and is referred to as propeller jet. The phenomenon comprises velocity components in axial, tangential and radial direction. They can be assessed making use of empirical approaches, physical experiments and numerical modelling.

1.1 EMPIRICAL APPROACHES

Propeller jets have been systematically investigated during the last decades, e.g. in [3] and [4]. [5] describes the flow velocities in the jet with the help of generated thrust, torque and advance velocity of the vessel. The thrust coefficient in particular is dependent on the propeller type [6], which can be parameterized with the help of the pitch ratio H_S/D_p. [7] ascertained K_T for a range between 0.6 and 1.4 and found that the difference of the thrust coefficient is in the order of 100 % for free propellers and even higher for conducted propellers. The velocity distribution in the propeller jet has been described through the axial momentum theory by [3]. The maximum velocity can be calculated according to [8].
The influence of the rudder has been investigated for example in [8], showing that the propeller jet is split into two streams; one is directed upwards to the water surface and the other is directed downwards to the seabed. The maximum jet velocity at the bottom has been described in [9] in dependence of the pitch ratio and a coefficient, which is dependent on whether a rudder is present or not and if the propeller is ducted. Velocity decay with increasing distance and the vertical velocity distribution has been described in [11, 12].

1.2 NUMERICAL MODELLING

In detailed 3-dimensional (3D) numerical modelling (CFD), the following three approaches are often applied to model propeller-induced jets:

- **Sliding Mesh Model**: The computational domain is separated into two domains, a rotor mesh that follows the propeller and a stator mesh that covers the remaining model domain. The sliding grid approach is a transient method where the rotor mesh actually rotates with respect to the stator mesh. The interaction between the rotor and stator are thus fully resolved. This requires a sliding grid interface between the rotor and stator domains to transmit the flow variables across the coupled patches. The sliding mesh approach provides full details of unsteady flow features of propellers.
- **Multiple Reference Frame Approach (MRF)**. Steady-state formulation where the rotor domain

and stator domain are fixed with respect to each other and different reference frames are used in the rotating and stationary parts (momentum equation is modified with Coriolis and centrifugal forces in the rotating reference frame). It allows taking into account the effect of the rotation of the propeller, although no transient rotor-stator interaction is included.

- **Momentum Source Model (MSM)**: Constructed with the purpose of describing the effect of the propeller adequately through a computationally efficient model. The momentum equations include a body-force term which can be used to model the effects of a propeller without resolving the detailed blade flow [13].

The methods have been extensively compared in [14]. The results reveal that propeller characteristics such as the diameter have minor influence on bed velocities compared to parameters such as ship velocity, under keel clearance or rudder angle. Detailed numerical investigations of rudder-propeller interaction showed that as long as the radial variation in axial and tangential momentum generated by the propeller is included, the influence of the unsteady propeller flow can be removed and steady calculations can be performed to evaluate the influence of the propeller on the rudder [15]. Therefore, MSM has been used in this study.

1.3 OUTLINE OF THE STUDY

In this study, the comparison of 3D numerical model results with field measurements is presented for three cases. The measurements are described in section 2. The numerical model setup is given in section 3. This is followed by a result presentation and discussion, setting it into relation with empirical approaches.

2 FIELD MEASUREMENTS

The measurements took place at the Bubendey embankment in Hamburg during one week in September 2014. A sketch of the embankment is given in figure 1.

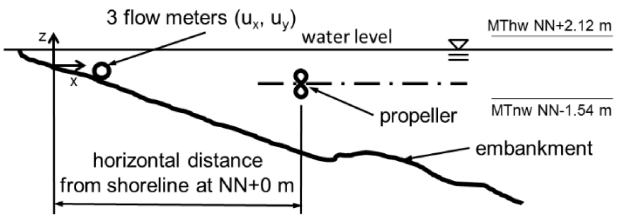

Figure 1. Cross-section of embankment (modified from [16]).

The slope of the embankment was determined to be ~ 1:3 through measurements and surveying. The tug boat "Schleppko" was placed at the embankment in an angle of ~ 90° to the embankment and a pontoon was deployed next to it in order to support the position of the vessel. It features a 500 kW engine. The propeller diameter is 1.72 m. The pitch ratio is 0.661. Figure 2 provides an impression of the scene.

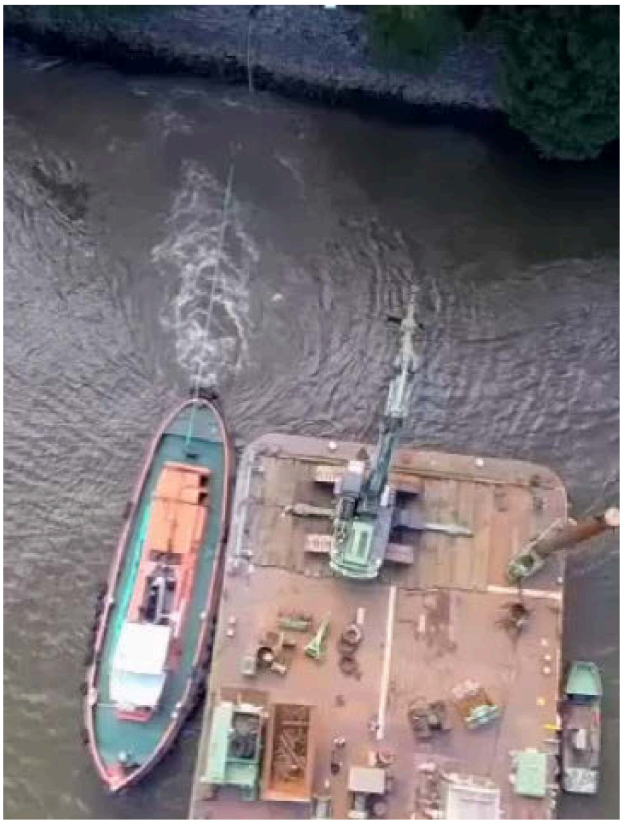

Figure 2. Aerial view of measurements at Bubendey embankment with tug boat "Schleppko" and pontoon.

A slight diversion of the propeller jet towards the left is noted, before the jet enters the shore. It originates from river flow and tide-induced currents. In order to exclude these ambient currents from the measured data, each test was enclosed by two periods of "zero" measurements which took place before and after each test and in which the propeller was not rotating. Thus, the two "zero" measurements only contained the ambient currents. To estimate the magnitude of ambient currents during the period of each propeller test, measurement results have been linearly interpolated over the time between both enclosing "zero" measurements so that the influence of the ambient currents on the propeller test data could be reduced to a large extent.

The measurement conditions considered in this study, including the averaged ambient currents measured at the velocity sensors, are summarized in table 1.

Each propeller test was conducted for a period of three to five minutes.

Scenario 1 has been used to calibrate the numerical model. The scenarios 2 and 3 serve for model validation. 6 velocity sensors have been placed at the propeller axis as well as aside. Three sensors measured the velocity component towards the embankment and three sensors measured the components parallel to the embankment.

The coordinates of the velocity sensors are given in table 2.

Table 1. Measurement conditions.

Scenario	1 Calibration	2 Validation	3 Validation
date	16/9/2014	17/9/2014	19/9/2014
start time	10:56	11:36	0.42
water level [-mNN]	1.42	1.38	1.45
propeller axis level [-mNN]	-0.38	-0.34	-0.32
atmospheric pressure [-hPa]	1019	1019	1012
engine capacity [-%]	50	25	70
rounds/minute [--]	250	192	275
distance from shoreline [-m]	16.55	16.95	16.53
ambient current speed [m/s]	0.16	0.10	0.07

Table 2. Velocity sensor coordinates.

Velocity sensor	x [-m]	y [-m]	z [-mNN]
VS1	1.47	1.80	-0.289
VS2	1.29	-2.19	-0.247
VS3	1.39	-0.06	-0.270

The origin of the coordinate system has been set at the intersection of the shoreline and the propeller axis, when the water level is at NN+0m. The datum NN also provides the vertical reference of the coordinate system (see figure 1).
Figure 3 presents the measured velocities in x direction in sensor VS3, located close to the propeller axis.

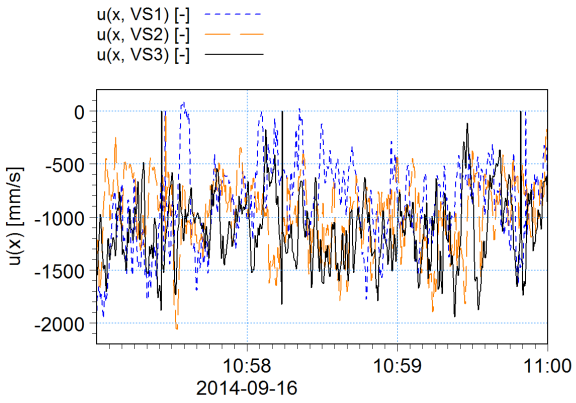

Figure 3. Measured velocity components perpendicular to embankment.

Data reveal high turbulent oscillations, which are in the order of the mean value. This pronounces the importance of considering these fluctuations in further analysis.
While pressures have been measured with 16 pressure sensors distributed along the embankment, the obtained values reveal high sensitivity of the water level fluctuations. The hydrostatic pressures exceeded the dynamic pressures by a factor in the order of 10^2.

3 NUMERICAL SETUP

3.1 OPENFOAM

All CFD simulations are carried out using OpenFOAM ® [17]. CFD simulations have been performed applying the solver simpleFoam. It is based on a steady state Reynolds Average Navier-Stokes (RANS) solver. In a RANS solver, basic equations are averaged and closed by a turbulent closure model that models the effect from turbulence on the mean flow. The result of this approach is that in the momentum equation averaged scales appear as the Reynolds stress tensor. The eddy viscosity hypothesis relates the turbulent stresses to the velocity gradients of the mean flow. The modelling is then reduced to the specification of the eddy or turbulent viscosity (exchange coefficient for momentum) in terms of the local turbulence in the flow.
Preliminary tests showed the importance of the turbulence model in propeller induced flow models. It influences the velocities close to the embankment up to the first order. In this project the k-ε model has been applied. The turbulence quantities k and ε at slope and rudder have been approximated using the corresponding wall functions, whereas zero gradient conditions have been applied at the free flow patches right, left, offshore and top. The turbulence intensity has been estimated to be 10 %, which is in the typical range of high turbulent cases with rotating machinery. The asymmetric body force with axial and tangential components (MSM) was implemented in the numerical solver. The advance coefficient is defined by

$$J = \frac{U_0}{nD_p} \tag{1}$$

where U_0 is the speed of advance, n is the number of propeller revolutions and D_p is the propeller diameter. The thrust coefficient is expressed by

$$C_T = \frac{8K_T}{\pi J^2} \tag{2}$$

with

$$K_T = \frac{T}{\rho n^2 D_p^4}, \tag{3}$$

in which ρ is the water density and T is the thrust. The torque coefficient is expressed by

$$K_Q = \frac{Q}{\rho n^2 D_p^5} \tag{4}$$

with the torque Q. For further details it is referred to [18].

3.2 NUMERICAL DOMAIN AND MESH

The numerical domain and mesh are shown in figure 4.

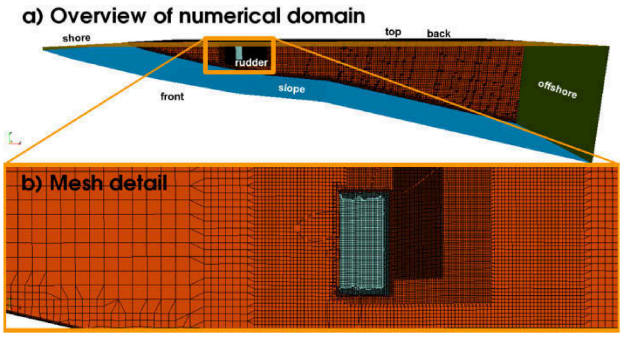

Figure 4. Exemplary computational mesh scene.

The domain extends over 30 m of the embankment length and 43.45 m from the propeller disk into the river. It domain included the exact embankment shape as well as the exact rudder geometry of the tug boat. The ship hull was neglected in the model.

A parametric mesh was created using the snappyHexMesh utility, which forms part of the OpenFOAM ® package. The snappyHexMesh utility generates 3D meshes containing hexahedra (hex) and split-hexahedra (split-hex) automatically from triangulated surface geometries in stereo lithography (STL) format. The mesh has been refined around the rudder and the momentum source field. It approximately conforms to the surface by iteratively refining the intermediate mesh and morphing the resulting split-hex mesh to the surface. The mesh was shrank back from specified surfaces (here from the embankment and the rudder) and additional cells have been inserted resulting in well specified layers. Mesh conversion has been tested by assessing the maximum flow velocity in relation to the cell height at the embankment slope. The deviation between the chosen and the next finer mesh is less than 1 %.The final mesh consisted of approximately 3.0 million cells: The cell height at the embankment slope was 0.01 m.

3.3 BOUNDARY CONDITIONS

The top patch of the numerical domain has been set at the position of the water level. It is noted that the free surface has not been modelled. Thus, the propeller induced water level variations and the rise of water surface close to the shore have been neglected for the sake of simplification and faster model convergence. Thus, slip conditions have been imposed. At the offshore boundary, the so called pressureInletOutletVelocity condition together with the totalPressure condition for pressure have been applied so that water can leave and enter the domain. At the lateral boundaries front and back, the velocity condition inletOutlet has been paired with the fixed pressure value condition. At the bottom, velocities have been set equal to zero and pressures follow the zero gradient condition. In order to account for the sizes of the rocks lying on the embankment slope, the so called nutURoughWallFunction has been applied, allowing incorporating the roughness height of 0.03 m.

3.4 SIMULATION MATRICES

As part of the calibration process, sensitivity tests have been performed, varying the MSM parameters by 10 % each. An overview is given in table 3.

Table 3. Simulation matrix for calibration. The modified values are marked as bold.

scenario	s1.0	s1.1	s1.2	s1.3	s1.4
K_T	0.837	0.837	0.837	0.837	**0.921**
K_Q	0.029	**0.032**	0.029	0.029	0.029
U_0	5.902	5.902	5.902	**6.493**	5.902
J	0.824	0.842	**0.906**	0.842	0.842

The scenarios represent flow fields induced by the tug boat running with 50% of its engine capacity. Scenario s1.0 comprises of original calculated values making use of equations (1) to (4), whereas scenarios 1.1 to 1.4 include the parameter variations. The validation cases are summarized in table 4.

Table 4. Simulation matrix for validation.

scenario	s2	s3
K_T	0.837	0.837
K_Q	0.029	0.029
U_0	5.902	5.902
J	0.824	0.842

In scenario 2, the tug boat runs with 25 % of its engine capacity. In scenario 3, it runs with 70 %.

4 RESULTS

Velocity and pressure data have been analyzed. As total pressure measurements showed high sensitivity to the water level fluctuations during the tests and the CFD model was setup without tracking of the free surface, pressure data has been discarded from the comparisons.
The numerical model calculates averaged values and does not provide information on velocity fluctuations occurring during propeller propulsion. Therefore, the numerically achieved velocities have been compared with averaged measured velocity data. However, as measurements reveal dynamic variations lying in the order of the averaged velocities, they cannot be neglected. In order to maintain the relation between averaged values and fluctuations, the measured fluctuations have been transferred to the numerical results using the relations for the velocities u

$$\frac{u_{i,j,min}}{u_{m1,j,min}} = \frac{u_{i,j,avg}}{u_{m1,j,avg}} = \frac{u_{i,j,max}}{u_{m1,j,max}}. \quad (5)$$

$i = \{1.0, 1.1, 1.2, 1.3, 1.4, 2, 3\}$ indicates the scenario number, $j = \{x, y\}$ the direction of the velocity component, min stands for minimum values, max for maximum values and $m1$ marks measured values during the measurement with 50 % engine capacity. It should be noted that this relation has been adopted for the validation simulations with 25 and 70 % engine capacity, too. x is the direction normal to the embankment (see also figure 1) and y is the parallel direction.

4.1 CALIBRATION

The measured and simulated velocities normal and parallel to the embankment due to a propeller jet caused by the tug boat running with 50 % of its engine capacity are presented in figure 5.

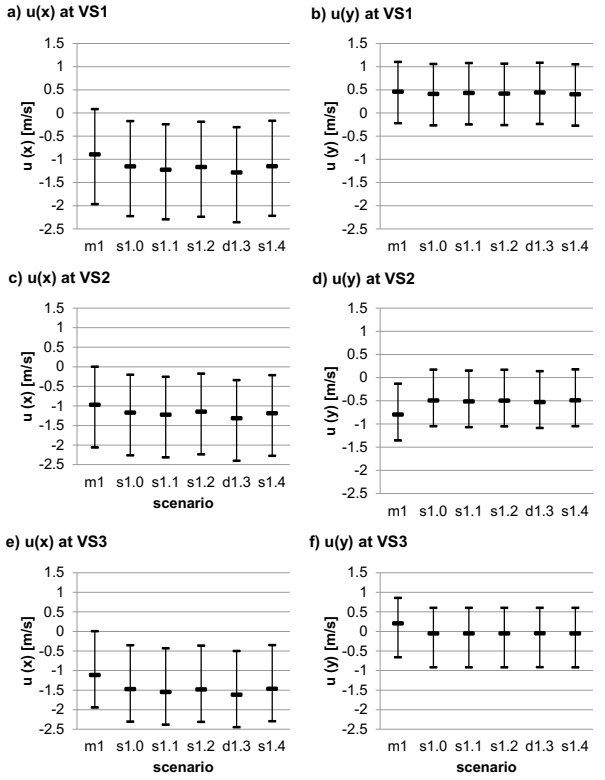

Figure 5. Measured and simulated averaged velocities (calibration with 50 % engine capacity). For m1, the black line spans between the minimum and the maximum measured values, which has been transferred to the simulations s1.0 to s1.4 (see equation (5)).

All numerically achieved velocities exceed the averaged measured velocities towards the embankment (see figures 5.a), c) and e)). The velocity component parallel to the embankment is underestimated (see figures 5.b) and d)), except near the propeller axis (see figure 5.f)). As expected, the velocities are highest near the propeller axis and normal to the embankment. There, the parallel velocity component is comparably small. Scenario s1.3 (increase of U_0) leads to the most conservative results.

Compared to the high fluctuations, the simulated velocities are well within the range of measured velocities. Taking into account these fluctuations and then comparing the maximum velocities normal to the embankment near the propeller axis, the originally derived MSM parameters (scenario s1.0) lead to a deviation of 18 %. The agreement is still good and the numerical model provides results lying on the conservative side. The original parameters of calibration scenario s1.0 have therefore been applied to the validation simulations.

4.2 VALIDATIONS

The calibrated MSM parameter set has been applied to the simulations aiming to reproduce the situations with 25 % and 50 % engine capacities.

4.2 (a) 25 % engine capacity

The measured and simulated velocities normal and parallel to the embankment due to a propeller jet caused by the tug boat running with 25 % of its engine capacity are presented in figure 6.

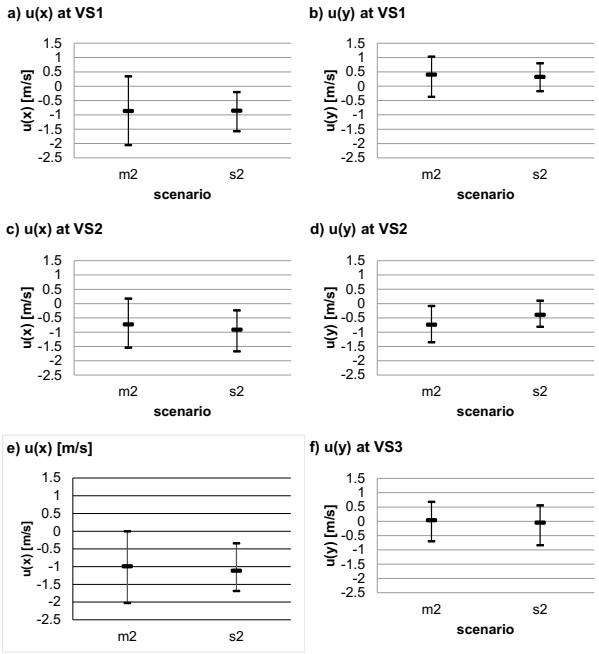

Figure 6. Measured and simulated velocities (validation with 25 % engine capacity). For m2, the black lines span between the minimum and the maximum values. For s2, the black line represents the fluctuation range transferred from the measurement m1 (see equation (5)).

For the velocity component normal to the embankment, the deviation in the outer sensors take values of 1 and 26 % (see figure 6.a) and c), respectively). At the middle sensor, the deviation in maximum velocities is 12 % (see figure 6.e)), whereas the numerically derived value exceeds the measured values. The deviations of the

components parallel to the embankment are slightly higher, especially at the positions of the outer sensors (see figure 6.b) and d)). It can be assumed that the main reason for this deviation lies in the real position of the propeller axis during the measurement. Although the tug boat has been moored at embankment and pontoon, motions could not totally be suppressed. As a consequence, the propeller jet did not hit the embankment at the position of sensor VS3. Nevertheless, the numerical model still provides conservative values.

4.2 (b) 70 % engine capacity

The measured and simulated velocities normal and parallel to the embankment due to a propeller jet caused by the tug boat running with 70 % of its engine capacity are presented in figure 7.

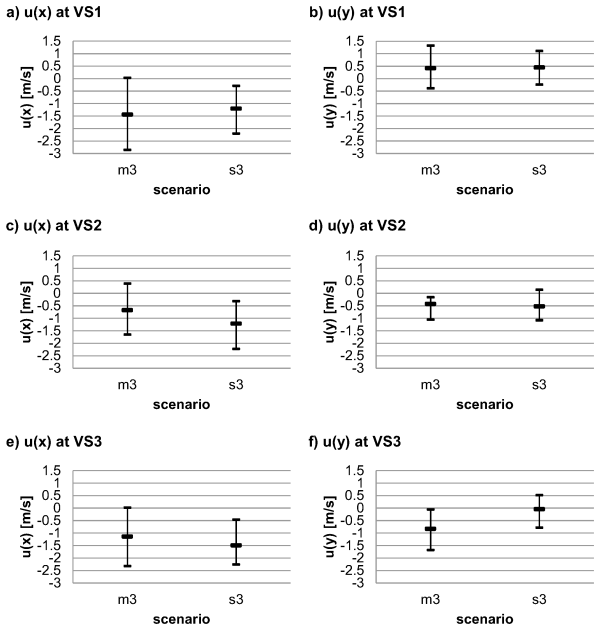

Figure 7. Measured and simulated velocities (validation with 70 % engine capacity). For m2, the black lines span between the minimum and the maximum values. For s2, the black line represents the fluctuation range transferred from the measurement m1 (see equation (5)).

As in the previous comparison (m2 vs. s2), the deviations for velocity components parallel to the embankment are higher than for the components normal to the embankment. This deviation is predominantly governed by the real position of the propeller axis during the measurements. The normal components are underestimated by 17 and overestimated by 81 % (see figure 7.a) and c)), which confirms the observation of the propeller axis. Near the propeller axis, the maximum normal velocities are overestimated by 31 %.
Acceptable agreements for the validation cases have been noted. The numerical model derives conservative values for maximum velocities near the propeller axis in all scenarios.

4.3 COMPARISON WITH GBB STANDARD METHOD

The method considers the propeller parameters diameter D, the factor of applicable propeller rotation rate, the thrust coefficient K_T, design propeller rotation rate and the induced initial velocity U_0. Furthermore, the design pitch ratio H_S/D_p has to be specified. For the here used tug boat, H_S/D_p = 0.661. A differentiation is made between unducted and ducted propellers. Maximum velocities on the embankments are determined based on four standard situations, which are

- **Standard situation 1 (no splitting of the jet)**: Propeller without a middle rudder located behind it; the jet is restricted by the depth of the water but there are no lateral limits to the dispersion of the jet,
- **Standard situation 2 (jet splitting)**: Unducted propeller with a middle rudder located behind it; jet splitting is limited by the depth of the water but no laterally,
- **Standard situation 3 (jet splitting)**: Unducted propeller with a middle rudder located behind it; additional lateral limitation of jet dispersion (by quay wall),
- **Standard situation 4 (no jet splitting)**: Ducted propeller (also with a middle rudder) or unducted propeller without a middle rudder located behind it; dispersion of the jet is limited vertically in the direction of propagation (e.g by a quay wall).

The here investigated situation compares to standard situation 2. The situation is depicted in figure 8.

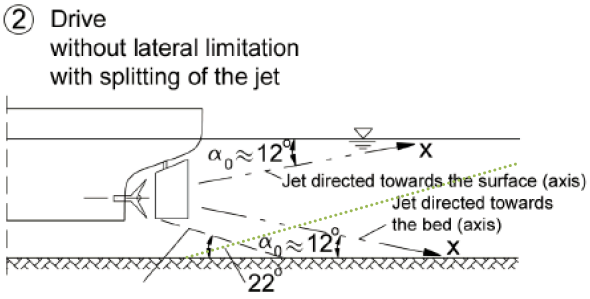

Figure 8. Standard jet dispersion situation 2 (modified from [1]). The green dotted line indicates the idealized slope of the Bubendey quay.

Detailed information on the procedure of determining maximum velocities on the embankment can be taken from [1].

The comparison between CFD and GBB results for all investigated scenarios are given in figure 9.

The velocities have been extracted from the CFD results in a distance of 0.03 m, which is in the range of the equivalent sand grain roughness height [19]. The mean diameter of the rocks on the embankment is 0.1 m. In all cases, the velocities derived with the CFD model fall below the GBB values. The maximum velocities are given in figure 10 and table 4.

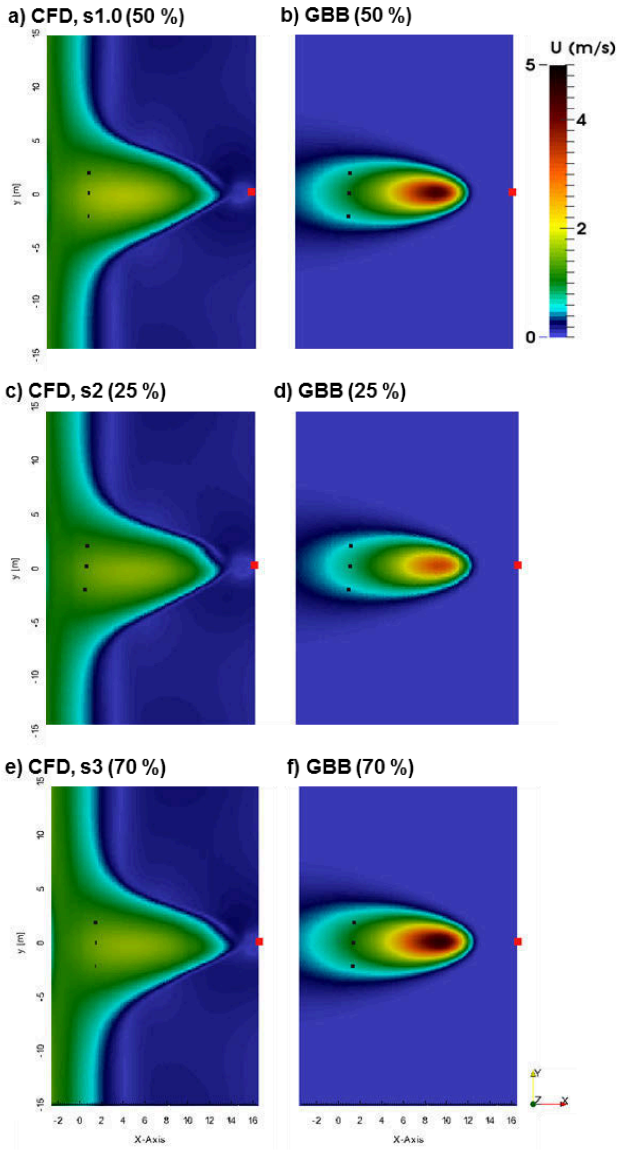

Figure 9. Velocities on the embankment (left: CFD results, right: GBB method) for engine capacities of 25, 50 and 70%. The black dots mark the position of the velocity sensors. The red dot marks the position of the propeller.

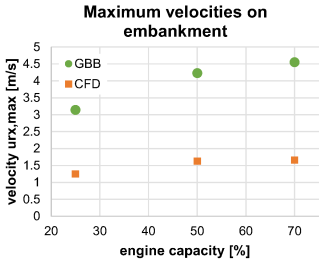

Figure 10. Maximum velocities on embankment after CFD and GBB methods.

Table 4. Maximum velocities on embankment after CFD and GBB methods.

Engine capacity	CFD	GBB
25 %	1.25 m/s	3.14 m/s
50 %	1.63 m/s	4.23 m/s
70 %	1.66 m/s	4.55 m/s

Maximum velocities on the embankment derived by CFD take values between 36 and 40 % smaller than the GBB values. It should be noted that standard situation 2 in [1] considers a horizontal bottom. A slope as found in this application case would deflect the propeller jet upwards. This is not accounted for by the GBB method. When applying the GBB method to a slope as done in this study, the (real) slope is located within the (idealized) undeflected propeller jet, which results in higher velocities. The deviation between CFD and GBB results originates from the high generalization in [1].

5 SUMMARY AND CONCLUSIONS

In this study, a CFD model has been calibrated with the help of in-situ measurements on Bubendey embankment in Hamburg, Germany in September 2014. The model has been validated with the help of two independent data sets originating from the same measurement campaign.
The modelled results are in good agreement with the measurements. It is equally important to point out that the model leads to conservative values.

The results have been compared to the standardized GBB method [1]. For the here tested configurations, CFD results are well below 50 % of the GBB values. The main reason for this deviation originates from the high degree of generalization in the GBB method. For example, the method does not account for the embankment slope. Another reason may have its origin in the measurements used to derive the empirical relations in GBB and to calibrate/validate the CFD model. On one hand, the field measurements comprise of uncertainties, e.g. due to propeller axis orientation during the measurements. From these measurements, mean velocity and its turbulent variation have been obtained. On the other hand, it could not be clarified by the authors if the maximum or the mean value in a propeller jet formed the basis for the GBB standard.

The CFD approach applied in this work has proven to be efficient and economical alternative for embankment design, because it is able to account for local conditions such as embankment slopes.

6 ACKNOWLEDGEMENTS

The authors thank Michel Kopiske (TU Braunschweig) for his contribution regarding the correct application of the GBB method and on measurement data review.

7 REFERENCES

1. BAW (2010). Principles for the Design of bank and Bottom Protection for Inland Waterways, *Bulletin no. 88 of the Federal Waterways Engineering and Research Institute*, Karlsruhe, Germany.

2. PIANC (2015). Guidelines for protecting berthing structures from scour caused by ships, *Report no. 180 of MARCOM WG 48*, Brussels, Belgium.

3. Albertson, M.L.; Dai, Y.B.; Jensen, R.A.; Rouse, H. (1950). Diffusion of a submerged jet. *Transactions of the American Society of Civil Engineers (ASCE)*, (Paper no. 2409) 115: pp. 639-697.

4. Lam, W.; Hamill, G.A.; Song, Y.C.; Robinson, D.J.; Raghunathan, S. (2011). A review of the equations used to predict the velocity distribution within a ship's propeller jet. *Ocean Engineering* 38: pp. 1-10.

5. Steward, D.P.J. (1992). *Characteristics of a ship screw wash and the incluence of a quay wall proximity*. PhD thesis, Queen's University, Belfast/UK.

6. Hamill, G.A.; Johnson, H.T.; Steward, D.P.J. (1995). Estimating the velocity in a ship's propeller Wash. *PIANC Bulletin*, Edinburgh/Scottland, S9.

7. Froehlich, D.C.; Shae, C.C.; Damigella, R.J. (1998). Screwed-Up Riprap: Sizing Rock Riprap to Resist Propeller-Induced Erosion. XII(3). *PB Technote*, PB Network.

8. Blaauw, H.G.; van de Kaa, E.J. (1978). Erosion of bottom and sloping banks caused by the screw race of manoeuvring ships. In *Proc. of the 7th International Harbour Congress* (also Paper no. 202, Delft Hydraulics), Antwerp/Belgium, July 1978.

9. Fuehrer, M.; Roemisch, K. (1977). Effects of modern ship traffic on inland- and ocean waterways and their structures. In *Proc. Of the XXIV. PIANC Congress, Section 1-3*, Leningrad/Soviet Union.

10. Verheij, H.J. (1983). The stability of bottom and banks subject to the velocities in the propeller jet behind ships. *7th International Harbour Congress (also Paper no. 303, Delft Hydraulics)*, Antwerp/Belgium, April 1983.

11. Hamill, G.A.; McGarvey, J.A. (1996). Design for propeller action in harbours. In *Proc. of the 25th International Conference on Coastal Engineering*, Orlando/Florida.

12. Sumer, B.M.; Fredsoe, J. (2002). *The Mechanics of Scour in the Marine Environment*. World Scientific.

13. Hough, G.R.; Ordway, D.E. (1964). The Generalized Actuator Disc. *TAR-TR 6401*, Therm Advanced Research, Inc., Ithaca, New York.

14. DHI (2015). Sediment Re-suspension and Seabed Scour Induced by Ship-Propeller Wash. *Draft Final Report no. 61800151-1*, 18/02/2015, Singapore, Syke/Germany.

15. Phillips, A.; Furlong, M.; Turnock, S.R. (2010). Accurate capture of rudder-propeller interaction using a coupled blade element momentum-RANS approach. *Ship Technology Research (Schiffstechnik)* 57: pp. 128-139.

16. Heinrich Weseloh Straßen- und Tiefbau GmbH (2014). Bubendeyufer Böschungsinstandsetzung Teil 1 Achse 401, *Technical drawing on bottom scanning data 25/07/2014, Station 0+144,000, profile no. 61.3.9*, 9/12/2015.

17. The OpenFOAM Foundation (2011). OpenFOAM-The Open Source CFD Toolbox. *User Guide*, http://www.openfoam.org, last accessed: 23/12/2015.

18. Paterson, E.G.; Wilson, R.V.; Stern, F. (2003). General-purpose parallel unsteady RANS ship hydrodynamics code: CFDSHIP-IOWA. *Report no. 432*, Nov. 2003, IIHR, University of Iowa, Iowa City.

19. Adams, T.; Grant, C.; Watson, H. (2012). A Simple Algorithm to Relate Measured Surface Roughness to Equivalent Sand-grain Roughness. *International Journal of Mechanical Engineering and Mechatronics* 1(1): pp. 66-71.

8 AUTHORS' BIOGRAPHIES

Stefan Leschka holds the position of a senior project engineer and project manager at DHI Deutschland GmbH, Germany. He is responsible for coastal engineering projects on advanced 2D and 3D wave modelling, involving fluid-structure interaction and sediment transport. His previous experience includes wave studies in ports and modelling of floating structures, such as breakwaters and moored ships.

Xu Bin holds the position of a senior CFD engineer at DHI Singapore. He is responsible for developing CFD solutions in relation to these topics including

hydrodynamics, sediment transport and ecological processes in industrial, coastal and marine environments. He is further involved in the development of new CFD technology. His experience includes the analysis of outfall structures, intake structures, etc.

Lars Yde holds the position of the Chief Engineer and is head of the detailed hydrodynamic modelling group in DHI Singapore. He is responsible for all refined hydrodynamic modelling in DHI Singapore. His previous experiences include the modelling of propeller-induced sediment re-suspension.

Oliver Stoschek holds the position if the head of the hydrodynamic and coastal engineering department in DHI Germany. He has focused his work on the studies of currents, scours, sediment transport, thermal re-circulation studies, conceptual design of intake/discharge structures and ship movement in coastal regions as well as coastal protection measures.

Jann Best studied Civil Engineering specialized in Coastal Engineering and Marine Works. Currently, he is Senior Project Manager at the Hamburg Port Authority and responsible for Infrastructure Projects and this Research Project.

4th MASHCON, Hamburg - Uliczka et al. (eds) - © 2016 Bundesanstalt für Wasserbau ISBN 978-3-939230-38-0 (Online)
DOI: 10.18451/978-3-939230-38-0_26

BANK EFFECTS MODELLING IN REAL-TIME MANOEUVRING SIMULATIONS

R Redondo, R Atienza, I Trejo, I Verdugo and **J R Iribarren,** Siport21, Spain

SUMMARY

Navigation in restricted waters or within a fairway with asymmetrical banks might be exposed to additional "undesirable" external forces. The forces produced by bank effects can reach considerably high values and therefore bank effects should be included in manoeuvring models. Modelling of bank effects can be performed by using specific numerical models which can be used to obtain the six degrees of freedom hydrodynamic forces over the vessel hull. Those forces are then used to estimate the bank coefficients of the numerical model of the vessel for a specific fairway-vessel configuration which can be used as input parameters in real-time manoeuvring simulators. An example of the beneficial use of bank effects to keep a vessel within the fairway with reduced usage of vessel rudder, as performed by Pilots in real manoeuvres, is explained within the paper. Nevertheless, using bank effects (i.e. using the yaw moment created by bank effects to turn at the bends) should only be performed by trained and very experienced Pilots or Masters, as suction/repulsion forces can reach values higher than those the vessel rudder is able to compensate.

NOMENCLATURE

B	Vessel's beam (m)
w	Width of the channel (m)
h	Mean depth of the channel (m)
β	Blockage parameter (-)
α	Asymmetry parameter (-)
μ	Moment multiplication factor (-)
u	Vessel's forward speed (m/s)
v	Vessel's lateral speed (m/s)
UKC	Under Keel Clearance
CFD	Computational Fluid Dynamics
ROPES	Research on Passing Effects of Ships
MARIN	Maritime Research Institute Netherlands
PIANC	The World Association for Waterborne Transport Infrastructure
CEDEX	Centro de Estudios y Experimentación de Obras Públicas

1 INTRODUCTION

Navigation in restricted waters or within a fairway with asymmetrical banks might be exposed to additional "undesirable" external forces due to an asymmetry on the flow surrounding the vessel on her movement. The forces produced by bank effects over the vessels can reach considerably high values and therefore bank effects should be included in manoeuvring models both for port design and training and education of Pilots and Masters.

Modelling of bank effects can be performed by using specific numerical models which can be used to obtain the hydrodynamic forces over the vessel hull. Those forces are then used to estimate the bank coefficients of the numerical model of the vessel for a specific fairway-vessel configuration which can be used as input parameters in real-time manoeuvring simulators.

As any external force, bank effects usually force the vessel to use her manoeuvring means (rudders and propellers) to compensate the deviation from the desired track produced by the force.

Sometimes, in port design processes these effects are not taken into account and afterwards a safety margin is included in the fairway width in order to avoid its occurrence. At least some estimation on bank effects should always be done to be sure if it is really relevant. Nevertheless the bottom configuration of some areas does not allow the designer to avoid bank effects, therefore it should be properly modelled so that minimizing the effects or using them in favour of the vessels can be considered.

In general terms bank effects produce undesired forces and under a new fairway/harbour/port design the aim is to reduce these effects by increasing the channel width.

Nevertheless there are certain bottom configurations where it is very difficult to reduce or minimize bank effects at reasonable costs, as in those very shallow flatland areas (just some 3 to 5 meters depth below sea level), like river deltas or estuaries where no navigational channel is present and therefore a complete artificial dredged fairway has to be done. In those cases the costs are directly proportional to the width of the fairway, meanwhile bank effects are indirectly proportional.

In those cases where an increase of fairway width, aimed at avoiding bank effects, cannot be performed it is required to assess manoeuvre simulations considering bank forces in order to check the behaviour of the vessel and the vessel manoeuvring means required to counteract bank effects, as this will have a direct impact on the reserve of manoeuvre to achieve certain operational limits.

Several locations around the world (dredged navigation channels as in river deltas or estuaries like cases in Colombia, Argentina, Pakistan, artificial canals as Panama or Suez, and several Ports around the world …) suffer these effects and Local Pilots learned to deal with

them. Moreover, in some cases they learned how to manage in order to use the bank forces and moments on their benefit in order to sail towards vessels' calling ports.

An example of the usage of bank effects on benefit of the vessel to keep her within the fairway with reduced usage of vessel rudder, as performed by Pilots in real manoeuvres, will be explained. Nevertheless, using bank effects on favour should only be performed by trained and very experienced Pilots or Masters, as suction/repulsion forces can reach values higher than those the vessel rudder is able to compensate.

2 CASE ASSESSED

2.1 VESSEL

The vessel considered in the case described within this paper is a typical LNG carrier with prismatic tanks and single propeller and rudder. This is the "Spirit of Hellas", shown in Figure 1, whose main particulars are: 285 m length and 50.0 m beam.

Figure 1. LNG carrier "Spirit of Hellas"

2.2 FAIRWAY

The fairway considered in the example that is described within this paper is a 10.5 m deep channel with banks on both sides of the channel with slopes close to 1:4. Due to the restricted depth of the fairway, the vessel navigates in the area in partially loaded condition in order to cope with the minimum UKC required. In this case, normal navigation draught of LNG carriers is 9.3 m.

The general layout of the fairway considered has one main straight section which is diverted into a second section, dividing the traffic in two ways, as shown in Figure 2. The first one keeps the straight line heading towards a main port in the area, meanwhile the second one heads towards the mouth of an affluent river. In order to navigate towards the mouth of the river a bend has to be taken in order to change the course of the vessel some 40º.

The following image shows the configuration of the fairway selected for this example.

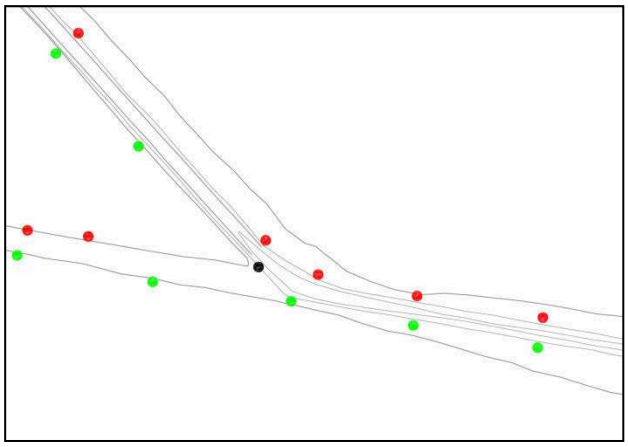

Figure 2. General layout of the fairway considered

This fairway is artificially dredged and it is continuously maintained upon a certain width. Further from this maintained area the surroundings correspond to the natural depth of the river, which is a flatland of some 3 to 5 m depth. As it can be understood this narrow fairway surrounded by shallow flatland waters results in bank forces over the sailing vessels, moreover when the usual navigation speed is approximately 10 to 12 knots.

The bank forces produced by the particular bathymetry over each of the vessels sailing through the fairway has to be considered when manoeuvring in the area, therefore deriving the bank forces is crucial for a proper manoeuvring assessment.

The following section describes the computation of the bank forces by means of specific numerical models and how bank coefficients are derived from those forces.

3 BANK FORCES COEFFICIENTS

3.1 DERIVING BANK FORCES BY NUMERICAL MODELS

Specific numerical models allow us to evaluate the hydrodynamic interaction (forces and moments in six degrees of freedom) that one or more passing vessels generate on one or more moored vessels on the specified area, as well as over the mooring structures, when sailing at navigation fairways (access channels, inner channels, rivers ...), specially in narrow and constrained depth areas.

Therefore the forces and moments produced over the navigating vessel due to the constrains caused by the bathymetry restrictions and the banks can be obtained.

In order to assess the bank forces and moments produced over a vessel under different speeds, at different passing distances and at different drift angles, the numerical model ROPES, developed by PMH BV (Pinkster Marine Hydrodynamics BV, The Netherlands), has been used. An example screenshot of ROPES is shown in Figure 3.

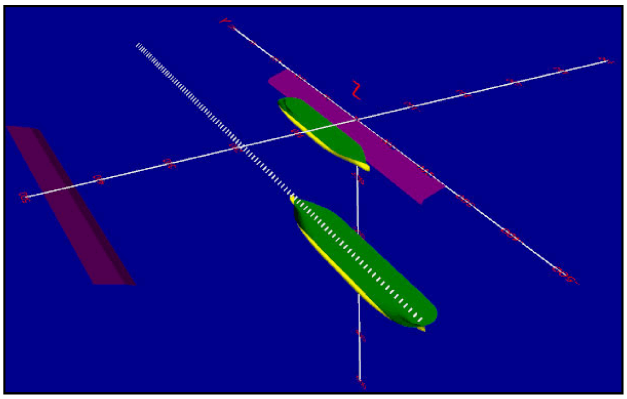

Figure 3. Image of ROPES software of a sailing vessel

The model takes into account the specific hull forms of each vessel, on a established load condition, considering the effects of bathymetry changes and lateral restrictions (navigation channels, vertical structures, slopes,...), and allows the calculations of bank forces and moments for a wide range of passing-distances, even when this passing distances is small (i.e. less than one beam).

The system calculates the forces on the vessels in all 6 degrees of freedom (surge, sway, heave, roll, pitch and yaw) in the time domain, as for example shown in Figure 4. The computations are based on 3-dimensional flow calculations for real hull forms. These flow calculations are based on the double-body flow method.

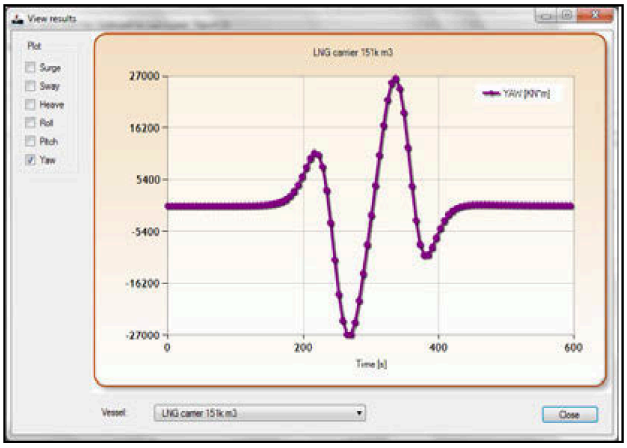

Figure 4. Example of yaw moment time series output of the numerical model ROPES

Once all bank forces and moments are obtained from the numerical model ROPES, the bank coefficients for surge, sway and yaw can be estimated in order to introduce them into the Real-Time Manoeuvring Simulator.

The time series of forces obtained from ROPES have to be transformed into a global singular value; as the geometry is the same, the forces and bank coefficients should also be the same. This singular value is therefore the average force produced over the vessel due to the presence of the bathymetry configuration, including banks.

In order to get the average singular force from the time series it has to be filtered in advance, in order to remove the undesired peaks of the time series produced at the beginning and the end of the banks.

3.2 EXTRACTING BANK COEFFICIENTS FOR REAL-TIME MANOEUVRING SIMULATORS. BANK COEFFICIENTS ESTIMATION

The knowledge of equations governing the computation of bank forces in the Real-Time Manoeuvring Simulator allows us to get the required bank coefficients in order to introduce the bank forces, derived from the numerical model, into the Real-Time Manoeuvring Simulator.

Different Real-Time simulators use different expressions for the bank forces. The governing equations of the bank forces in the case assessed within this paper (Real Time Manoeuvring Simulator MERMAID 500 developed by MARIN, The Netherlands) are the following:

$$X_b = X_{uvB/w} uv\, B/w + X_{uuu/hw}\, u^3/hw \quad (1)$$

$$Y_b = Y_{uv\beta} uv\beta + Y_{\alpha uu} u^2\alpha + Y_{\alpha\alpha\alpha uu} u^2\alpha^3 + Y_{\alpha\alpha uv} uv\alpha^2 \quad (2)$$

$$N_b = N_{uv\beta} uv\beta + N_{\alpha uu} u^2\alpha + N_{\alpha\alpha\alpha uu} u^2\alpha^3 + N_{\alpha\alpha uv} uv\alpha^2 \quad (3)$$

All the parameters of these governing equations, except the bank coefficients, are known for every one of the simulations of the ROPES numerical model. Therefore these bank coefficients, related to the longitudinal and transversal forces, as well as the yaw moment, can be estimated.

Bank coefficients are dependent on:

- Vessel hull forms
- Vessel load condition (draught)
- Banks configuration (fairway slopes)
- Blockage parameter
- Mean depth

Vessel's bank coefficients are independent of:

- Vessel speed
- Vessel drift angle (small angles)
- Asymmetry parameter

Performing a series of different runs for the same bank coefficients dependant factors (vessel, banks, depth, ...) and different independent factors (vessel speed, vessel drift angle and asymmetry parameter) allows us to both, assess the effect of asymmetry parameter, speed and drift angle in the bank forces and estimate the bank coefficients by minimizing the averaged mean quadratic error of the series of forces derived in ROPES and the estimated forces obtained trough successive estimations of the bank coefficients.
Figures 5 and 6 show the variation of the bank force as function of different parameters.

The bank coefficients derived based on a series of different runs with different distances to the banks, drift

angles and vessel speeds are assessed at the same time, therefore the forces derived from the estimated coefficients will have a certain error versus the actual results obtained from the numerical models.

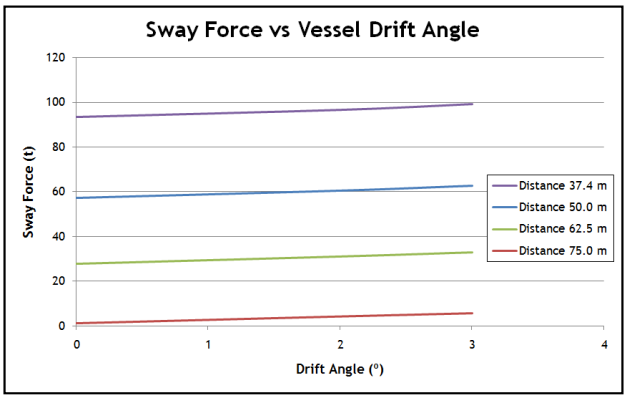

Figure 5. Bank sway forces as a function of vessel drift angle for different distances to the banks

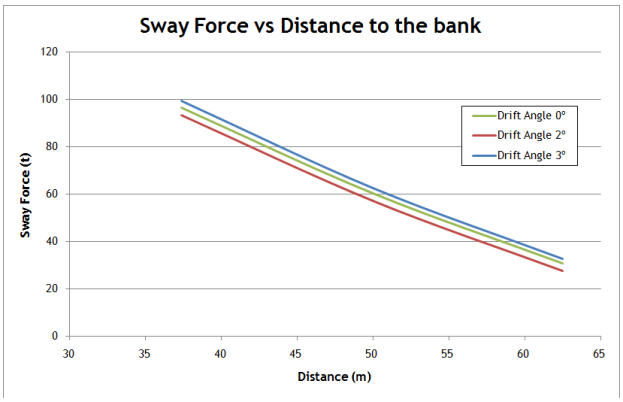

Figure 6. Bank sway forces as a function of distance to the banks for different vessel drift angles

As a reference the errors between the forces obtained in the numerical model ROPES and the forces derived trough the estimated bank coefficients in the assessed case are shown in Table 1.

Table 1. Errors between ROPES forces and forces derived trough bank coefficients estimation

Distance (m)	Speed (kt)	Drift (°)	ROPES Output		Estimated Forces		Differences	
			Y (t)	N (t m)	Y (t)	N (t m)	Y	N
12.5	10	0	27.7	-1550	28.0	-1235	-1%	25.6%
12.5	10	2	31.0	38502	30.4	38626	2%	-0.3%
12.5	10	3	32.8	58536	31.6	58497	4%	0.1%
25.1	10	0	57.2	-2634	58.6	-2569	-2%	2.5%
25.1	10	2	60.5	37879	60.8	37834	0%	0.1%
25.1	10	3	62.7	58134	61.8	57976	1%	0.3%
37.6	10	0	93.5	-3927	95.1	-4119	-2%	-4.6%
37.6	10	2	96.7	37412	96.8	37459	0%	-0.1%
37.6	10	3	99.3	58075	97.5	58188	2%	-0.2%

As can be seen in Table 1, these errors are small for the transverse force (less than 5%). For the yaw moment the errors are very limited in terms of percentage in those cases where the force and moment values are quite high in absolute terms (green dotted square), meanwhile the relative errors are higher in some cases when the forces and moment values are small in absolute terms (red dotted square).

This difference over 25% in yaw moment does not have a major impact on the results as the absolute value of the moment is very small, comparing it with the rest of the yaw moments.

Once the bank coefficients have been derived, and the differences in forces and moments have been checked to be limited to a certain percentage, or to a small absolute value, results can be considered to be accurate enough.

The coefficients derived are therefore introduced in the text data files of the Real-Time Manoeuvre Simulator in order to include the bank effects in the manoeuvres performed in the Real-Time Manoeuvre Simulation of the vessel. In this way, the bank forces that would be obtained when manoeuvring in the Real Time Manoeuvring Simulator will be quite close to those obtained in the numerical model, thus increasing the complexity and the accuracy of the simulated scenario.

4 REAL-TIME MANOEUVRE SIMULATIONS WITH BANK EFFECTS

Once the bank coefficients have been estimated for a certain vessel and bottom configuration, and it has been checked that the results are consistent with the forces and moments obtained in the numerical model, they can be introduced in the Real-Time Manoeuvre Simulation. This will allow checking the differences in manoeuvring when bank effects are present or not.

In order to check that the values introduced as input to the Real Time Manoeuvre Simulator derived from ROPES are accurate enough for manoeuvring some Pilots tested the ship behaviour.

A Local Pilot, used to sail considering bank effects and using them in benefit, performed some manoeuvres to verify that the effects produced by the banks and the forces and moments agree with his expertise and knowledge, and calibrate the derived bank coefficients of the vessel's numerical model if necessary, which was not, in this case.

The consequence of bank effect over the vessel is a more or less continuous use of the rudder and engine, required to counteract those external forces. The usage of a certain percentage of the vessel own manoeuvrability to overcome bank forces is directly translated in a reduced reserve of manoeuvrability to overcome the different met-ocean conditions and therefore an eventual reduction in the operational limits of a vessel calling at a certain port.

Figure 7 shows the track of two different manoeuvres in the same area. The first one (blue vessel contour) corresponds to the manoeuvre without considering the bank effects, the second one (red vessel contour) corresponds to the manoeuvre including bank effects.

As can be seen in Figure 7, in both cases the vessel navigates within the limits of the defined fairway, nevertheless the tracks are different as the manoeuvre is also different due to the external force added in the case of the red vessels. In order to properly assess bank effects these manoeuvres have been performed in calm conditions, thus no wind, waves or current were present.

Assessing the results over the mere track plots of the manoeuvres does not give much indication on its own, and results should be accompanied by the time series of the rudder and engine rpm in order to check how different the manoeuvre is.

Nevertheless by means of the track plot the different strategies used by the Pilot at the bend can be easily identified. In the case where bank effects are present the Pilot moves towards the southern bank, thus reducing the "Passing-distance" and therefore increasing the bank yaw moment towards the starboard side. This allows taking the bend without requiring more rudder than in the condition where no bank is present.

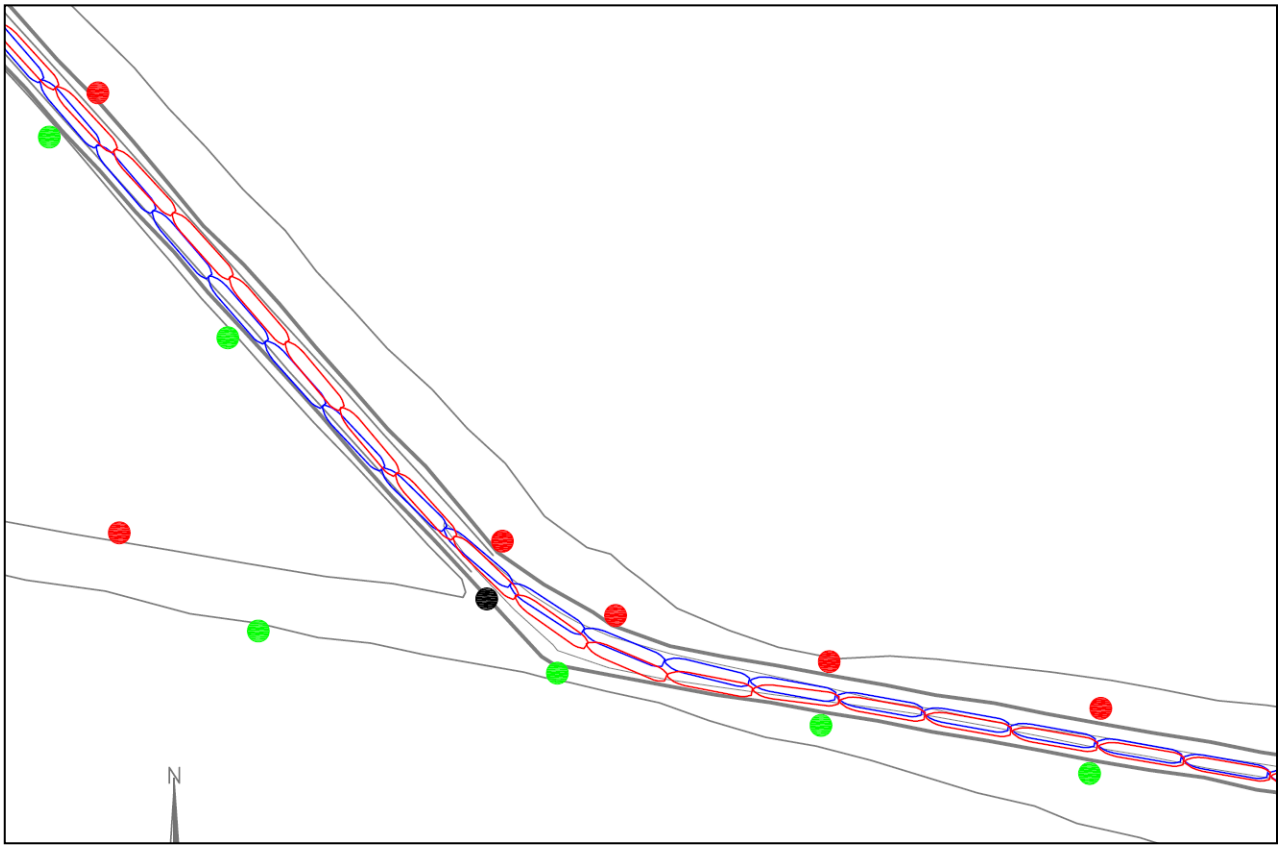

Figure 7. Manoeuvres track plots. Blue vessels = no bank effects. Red vessels = bank effects included

In order to counteract bank forces different rudder angles were required to be set in order to compensate the forces and moments created by the presence of the banks.

Figure 8 shows the rudder angle time series applied during both manoeuvres to safely navigate through the fairway (with and without banks) as a function of the position of the vessel.

The blue line corresponds to the manoeuvre where no banks were present and the red line corresponds to the manoeuvre were banks were present.

The graph clearly shows that in the first part of the track plot (straight line) no rudder was required in the case where no external forces were present (blue line). Once the external bank forces are present a sort of "static" rudder angle close to some 4º was required to safely navigate through that straight section. This rudder angle was required in order to compensate the forces and moments produced by bank effects. And the same occurs in the second straight section.

Nevertheless in the bend a different behaviour is shown. In both cases the maximum rudder angle required is the same (a bit less when banks are present). No extra rudder was required as a certain bank yaw moment force was beneficial in order to initiate the turning towards the starboard side.

Both results, that are visible in the time series plot of the rudder angle, are consistent with the two main points that are the key of the paper.

First of all, the presence of the banks forces the vessel to use certain rudder angle to counteract bank effects, thus the manoeuvrability reserve of the vessel to navigate under different conditions (winds, waves, currents...) is reduced (undesired effects). As a consequence of the reduction of the reserve of manoeuvrability, a reduction in the operational limits for the vessels navigating through areas with presence of banks could be expected.

The second point is the possible use of those external forces in the benefit of the vessels at the bends, using part of the yaw moment created by the presence of the banks in order to limit or reduce the rudder angle initially required to take the bends, even forcing the yaw moment to increase prior to the bends by getting closer to the bank.

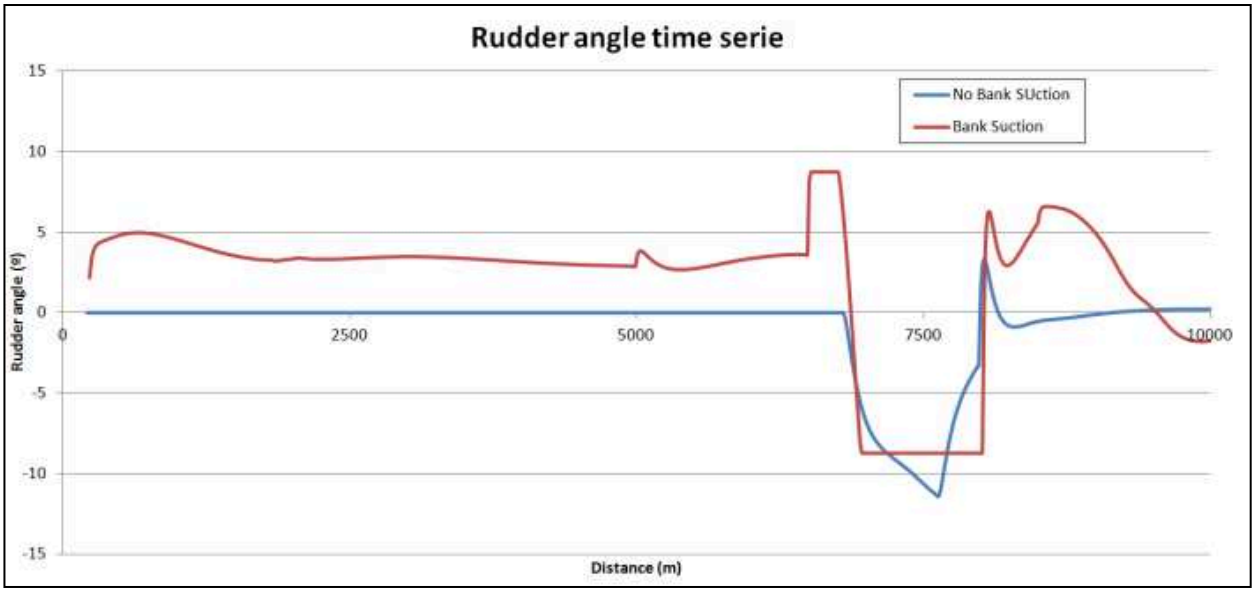

Figure 8. Time series of rudder angle during manoeuvres

Nevertheless, even if there is a part of the bank effect that could be used in the benefit of the vessel it has to be taken into account that bank forces and moments increase exponentially with vessel speed and the reduction of the distance to the banks. Those forces can reach extremely high values, even above those that vessel's manoeuvring means would be able to compensate. Therefore its usage is limited to very experienced Pilots or Masters with a very deep knowledge of the area, the vessel and the channel configuration.

A deep knowledge of the bank effects together with the geometry and the bathymetry of the area allows Local Pilots of certain ports around the world to navigate through narrow fairways using the yaw moment created by bank effects to take bends by reducing the rudder angle that would normally be required, even, in some cases, with the rudder at midships.

5 CONCLUSIONS

Navigation in restricted waters or within a fairway with asymmetrical banks might be exposed to additional “undesirable” external forces due to an asymmetry on the flow surrounding the vessel on her movement. The forces produced by bank effects over the vessels can reach considerably high values and therefore bank effects should be included in manoeuvring models both for port design and training and education of Pilots and Masters.

Sometimes, in port design processes these effects are not taken into account and afterwards a safety margin is included in the fairway width in order to avoid its

occurrence. At least some estimation on bank effects should always be done to be sure if it is really relevant. Nevertheless the bottom configuration of some areas does not allow the designer to avoid bank effects, therefore it should be properly modelled so that minimizing the effects or using them in favour of the vessels can be considered.

As any external force, bank effects usually force the vessel to use her manoeuvring means (rudders and propellers) to compensate the deviation from the desired track produced by the force.

One of the effects of navigating on the presence of banks, is a more or less continuous use of the manoeuvrability means of the own vessel, requiring a "static" rudder angle to compensate the forces produced by the presence of the banks. This reduces the "reserve" of manoeuvrability required to cope with the different met-ocean conditions (winds, waves and current) and therefore a reduction in the operational limits of the vessel at a fairway might be expected.

In such a way, introducing bank effects in Real Time Manoeuvre Simulators allows to asses this aspect, giving a more complete and accurate result, nevertheless a more complex one.

Modelling of bank effects can be performed by using specific numerical models which can be used to obtain the hydrodynamic forces over the vessel hull. Those forces are then used to estimate the bank forces coefficients of the vessel for a specific fairway-vessel configuration which can be used as input parameters in the Real-Time Manoeuvring Simulators. It is highlighted that during the development of ROPES several model tests and real measurements were carried out in order to validate the passing ship effect but validation against bank effects was not analyzed. Therefore, Siport21 validated ROPES based on Pilots' experience as mentioned above. From this point of view, it would be interesting to develop model tests and real measurements to increase the accuracy of the method proposed in this paper.

Nevertheless experienced Pilots with high knowledge of the vessels, the area and the bank effects can use part of the bank forces on their own benefit. In order to obtain this benefit Pilots might force the yaw moment created by the presence of the bank to increase prior to the bends by getting closer to the bank. In this way part of the yaw moment required to take the bend is produced by the banks therefore the rudder angle initially required to take the bends is limited or reduced.

An example of the usage of bank effects on benefit of the vessel to keep her within the fairway with reduced usage of vessel rudders, as performed by Pilots in real manoeuvres, has been described and assessed in this paper. Nevertheless, using bank effects on favour should only be performed by trained and very experienced Pilots or Masters, as bank forces can reach values higher than those the vessel rudder is able to compensate.

6 REFERENCES

1. MARIN (2012). *System User Manual for the Siport XXI simulator*.

2. Pinkster Marine Hydrodynamics (2013). *User Manual for Ropes 1.1*.

3. Verdugo, I.; Iribarren, J.R.; Atienza, R.; Pecharroman, L.; Cal, C.B.; Trejo, I. (2013). Passing Ship Interaction study in Altamira Port (Mexico), *Third International Conference on Ship Manoeuvring in Shallow and Confined Water*, Ghent, Belgium.

4. Pinkster, J.A.; Bhawsinka, K. (2013). A real-time simulation technique for a ship-ship and ship-port interaction, *28th International Workshop on Water Waves and Floating Bodies (IWWWFB 2013)*, L'Isle sur la Sorgue, France

7 AUTHORS' BIOGRAPHIES

Raul Redondo holds the current position of Project Engineer at Siport21. He performs the technical projects. He specializes on moored ship dynamics and ship manoeuvrability in port areas, both using numerical models and real-time simulation.

Raul Atienza holds the current position of Project Manager at Siport21. He coordinates and checks the technical projects. He specializes on moored ship dynamics and ship manoeuvrability in port areas, both using numerical models and real-time simulation. Development of numerical models for the resolution of hydrodynamics problems and ship dynamics. He has previously worked as a teacher in the Technical University of Madrid.

Ignacio Trejo holds the current position of Project Manager at Siport21. He coordinates and checks technical projects. He is a specialist in moored ship dynamics and ship manoeuvrability in port areas, both using numerical models and real-time simulations. He has developed several numerical models for the resolution of hydrodynamics and ship dynamics problems. Specialist in CFD Numerical Models, instrumentation and software developer.

Ismael Verdugo holds the current position of Technical Manager at Siport21. He is responsible for the technical office. He manages, plans and overviews technical projects. He is a specialist in moored ship dynamics and ship manoeuvrability in port areas, both using "Fast-time" and real time simulation of ship manoeuvres.

Jose R. Iribarren holds the current position of General Manager at Siport21 and founded Siport21. He manages, plans and implements corporate policies and strategies. Before, he worked as a project engineer in the head of Port Research Program and Head of Technical and Scientific Program at the Maritime Research Laboratory (Port and Coastal Research Centre, CEDEX, Ministry of Public Works, Spain).

He is specialized in studies on moored ship dynamics and ship manoeuvrability in port areas, both using numerical models and scale models, wave penetration in port areas using scale model tests and "Fast-time" and real time simulation of ship manoeuvres.

In 1998 he was awarded the "Gustave Willems Prize" of PIANC for the paper "Determining the horizontal dimensions of ship manoeuvring areas. General recommendations and simulator studies".

Experimental Measurements

4th MASHCON, Hamburg - Uliczka et al. (eds) - © 2016 Bundesanstalt für Wasserbau ISBN 978-3-939230-38-0 (Online)
DOI: 10.18451/978-3-939230-38-0_27

THE TOWING TANK FOR MANOEUVRES IN SHALLOW WATER

G Delefortrie and **S Geerts,** Flanders Hydraulics Research, Belgium
M Vantorre, Ghent University, Belgium

SUMMARY

The Towing Tank for Manoeuvres in Shallow Water at Flanders Hydraulics Research (FHR) is operated together with the Maritime Technology Division of Ghent University. The possibilities of the tank are continuously updated. This article therefore provides an overview of the capabilities for future reference among the scientific community. The paper also discusses a number of specific challenges characterizing experimental ship model research in shallow and confined water. Although the project of the second towing tank is still under approval, a sneak preview of its characteristics is given as well.

NOMENCLATURE

Fr_h	Froude number (-)
g	acceleration due to gravity (m/s²)
h	water depth (m)
m	blockage factor (-)
T	ship's draft (m)
V	ship's speed (m/s)

1 INTRODUCTION

Most ships are designed and optimised for operation at full ocean, to navigate from port to port at an economic speed and to transport as much cargo as possible. However, almost every ship has to enter a harbour from time to time for loading and unloading her cargo. This harbour can in general only be reached by channels with restrictions in both depth and width, so speed has to be slowed down, bends have to be taken, and external effects, such as wind and current, will become increasingly important. The ship's controllability will be disturbed during transit of these access channels because of hydrodynamic interaction forces caused by the reduction of the distance between the vessel on one hand, and the bottom, the banks of the waterway, and other shipping traffic on the other hand.

The Mobility and Public Works Department of the Flemish Government (Belgium) is responsible for the access channels to the ports of Antwerp, Ghent, Ostend, and Zeebrugge (see Figure 1). With a total maritime cargo traffic of 274 million tons (2015) [1], a considerable part of the European import and export is handled by these ports. Ensuring the accessibility of these ports, as well as the optimal use of the dense inland waterways network, is of crucial importance for maintaining the economic prosperity. Flanders Hydraulics Research in Antwerp is a laboratory of the Mobility department, which investigates the impact of human activity and nature on water systems and the consequences for navigation. The latter focusses on the investigation of the behaviour of ships in shallow and confined water.

Especially in confined waters model testing is still considered to be the most reliable method to acquire knowledge on ship hydrodynamics. The Towing Tank for Manoeuvres in Shallow Water (co-operation Flanders Hydraulics Research - Ghent University) was built in 1992 - 1993. The towing tank is equipped with a planar motion carriage, a wave generator, and auxiliary devices for ship - ship interaction. Most experimental results are used to develop mathematical models for manoeuvring simulations, so that the equipment was designed for captive model testing. Since 2009 free running manoeuvring tests can be carried out as well.

A short overview of the infrastructure will be given, followed by a more detailed description of specific features that have been introduced to improve the quality and the efficiency of the testing facility and an overview of some challenges when dealing with tests in shallow water.

Figure 1. The four seaports of Flanders (Belgium): Antwerp, Ghent, Ostend, and Zeebrugge.

2 MAIN INFRASTRUCTURE

2.1 TOWING TANK

The Towing Tank for Manoeuvres in Shallow Water (co-operation Flanders Hydraulics Research - Ghent University) has a total length of 87.5 m, of which 68.0 m

is useful for experiments, and a width of 7.0 m. These dimensions are rather modest, but sufficient for the execution of manoeuvring and seakeeping tests with ship models with a length over all between 3.5 m and 4.5 m at low or moderate speed (typically < 1.2 m/s on model scale) (see Figure 2 and Table 1). This length range is valid for sea-going vessels and self-propelled inland barges, but can be exceeded considerably for push convoys.

Table 1. Main dimensions of the towing tank

Total length	[m]	87.5
Useful length	[m]	68.0
Width	[m]	7.0
Maximum water depth	[m]	0.50
Length of the ship models	[m]	3.5 – 4.5

Figure 2. General view of the towing tank.

The draft of the ship models used at the towing tank typically varies between 0.10 m and 0.20 m. In practice, the range of under keel clearances may vary between (less than) 10% to 150% of draft in harbours and their access channels, so a variation of the water depth between 0.10 and 0.50 m is required in the towing tank. For that reason the water depth of the towing tank is limited to 0.50 m. While such a range allows to determine experimentally ship behaviour in water depths that are usually considered as very deep for waterways authorities, the vicinity of the bottom may still have an important effect on the ship's hydrodynamics.

2.2 MOTION MECHANISM & INSTRUMENTATION

2.2 (a) Towing carriage

The main carriage is a rectangular frame, composed of two wheel girders, connected by two box girders (see Figure 3). A lateral carriage is guided between the transversal girders and carries a slide in which a yawing table is incorporated (see Figure 4 and Figure 5).

This servo motor driven slide can be positioned manually in vertical direction over 0.4 m to take account of water level variations. Two of the four wheels are driven by brushless AC-servo-motors which are connected to the shaft by means of a gearing. The longitudinal position is determined independently using a measuring wheel. The lateral carriage is driven by means of a pinion - rack combination. The pinion of this combination is driven by a servo motor and a second pinion carries a brake. The rotation angle is measured at the tube, to which a beam is connected by means of a flange.

Figure 3. General layout.

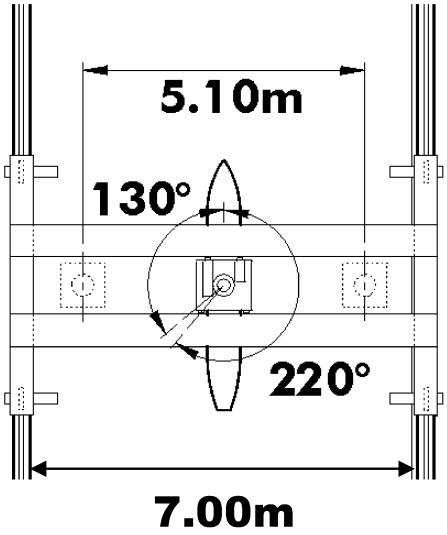

Figure 4. Top view of the towing carriage.

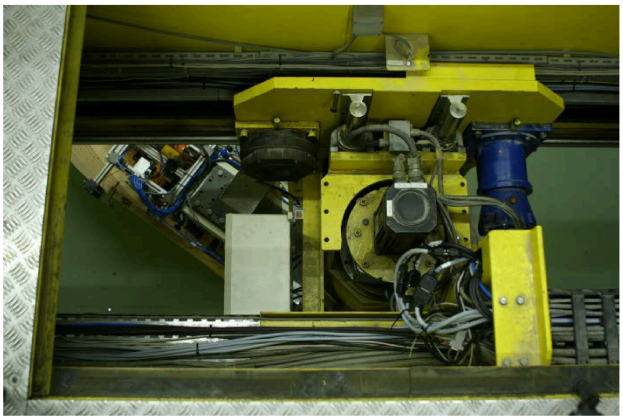

Figure 5. Top view of towing mechanism.

The main kinematic characteristics of the three horizontal motion modes are summarised in Table 2.

Table 2. Range of positions, velocities, and accelerations

	Main carriage	Lateral carriage	Yawing table
Minimal position	0.000 m	-2.550 m	-130.0°
Maximal position	68.000 m	+2.550 m	+220.0°
Maximal velocity	2.01 m/s	1.30 m/s	16.0°/s
Maximal acceleration	0.40 m/s²	0.70 m/s²	8.0 °/s²
Power Output	2 x 7.2 kW	4.3 kW	1.0 kW

2.2 (b) Captive mode

The ship model is attached to this beam by means of a mechanism which provides a rigid connection in the horizontal plane, but allows free heave and pitch; roll can be restrained or free, but will be controllable from 2016 (6.1). See Figure 6 for a typical setup.

2.2 (c) Free running mode

During free running tests there is no rigid connection between the ship model and the towing carriage. The steering forces, the propulsion forces, the steering angle(s), propeller rate(s), and the relative position between the carriage and the model, measured by lasers in six degrees of freedom, are sampled, see Figure 7. An autopilot controls the ship model and the towing carriage follows the free running model as close as possible. As the acceleration and deceleration of the ship model by own propulsion would occupy a significant fraction of the towing tank, the ship model is launched to the desired initial speed by the towing carriage in a captive way. Once this speed is reached, the ship model is released. At the end of the free running test, when the towing carriage can safely stop, the ship model will be clamped "on the fly".

2.2 (d) Instrumentation

The towing tank is equipped with:

- 4 x 2 dynamometers for longitudinal and lateral forces (20, 50, 100, 200 N) (only captive);
- dynamometers for roll moment (only captive);
- measurement of propeller rpm;
- 3 propeller thrust and torque dynamometers (30 N, 0.5 Nm);
- measurement of vertical motion (due to squat or wave action) at different positions;
- measurement of rudder angle;
- 5 rudder force and moment dynamometers (50 N, 2 Nm);
- custom instrumentation such as Z-drives, lateral thrusters, etc. with steering capabilities and force measurements;
- wave height measurement devices;
- visuals system to assess water and wave actions.

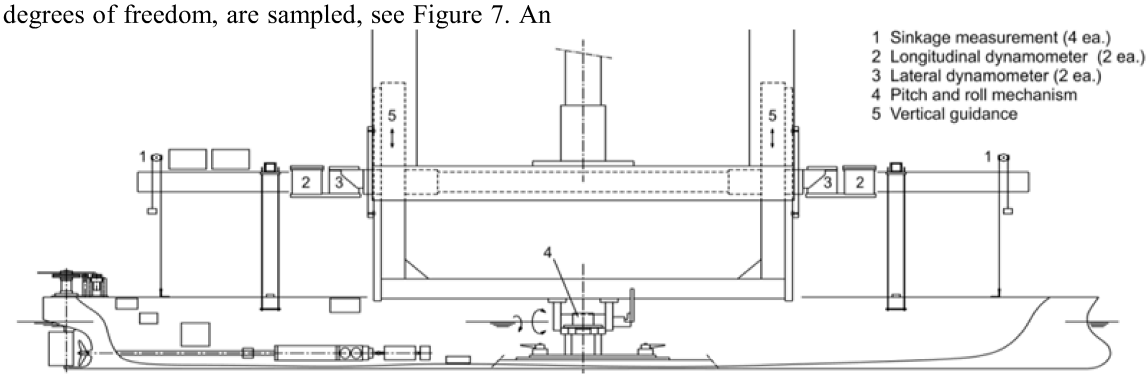

Figure 6. Ship model installation used during captive model tests

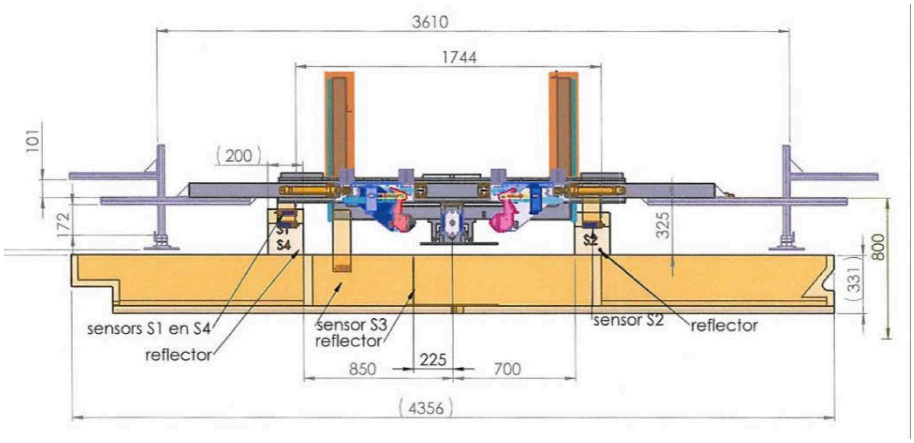

Figure 7. Ship model installation used during free running model tests

2.3 WAVE GENERATOR

The towing tank is equipped with a wave generator to study the vertical vessel motions and horizontal forces and moments induced by waves (see Figure 7). Both regular and irregular long-crested waves can be generated. The piston of this wave generator is driven by an electro-hydraulic unit with kinematical characteristics given in Table 3.

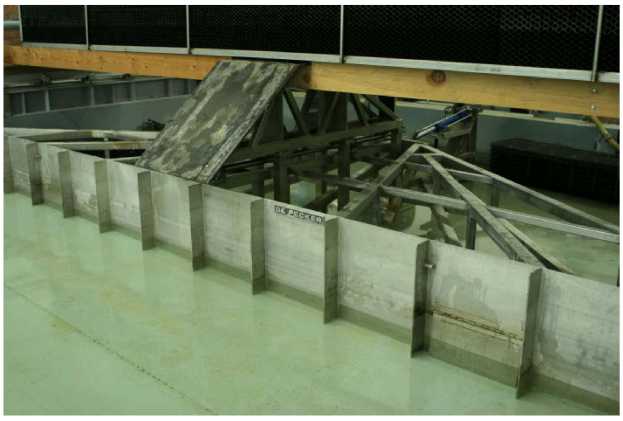

Figure 7. Wave maker.

Table 3. Kinematical characteristics of the wave generator (maximal values)

Stroke	Velocity	Acceleration
0.3 m	0.6 m/s	4.4 m/s

2.4 TEST PREPARATION

2.4 (a) Ship loading

An instrumented ship model has a certain loading distribution (position of centre of gravity, moments of inertia), which can be determined with a physical pendulum, see Figure 8. In order to meet the desired loading condition during tests, an optimization algorithm computes the distribution of ballast weights (0.25 to 10 kg) to be put in the ship model.

Figure 8. Determination of the moments of inertia (principle of the physical pendulum).

2.4 (b) Ship calibration

Ballasting and calibration of the ship model is performed in a smaller section at the end of the tank, which is referred to as the harbour, and offers an easy and dry access for the staff to work on the ship model. Figure 9 shows an example of the calibration of the lateral force. Calibrated weights are used to derive the relationship between the physical units and the voltages measured in the strain gauges.

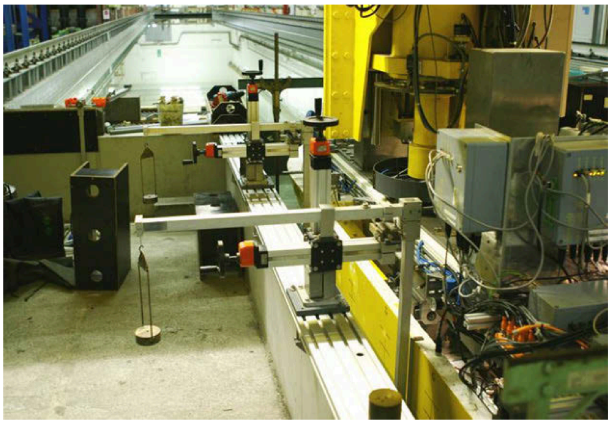

Figure 9. Ship calibration in the harbour of the tank.

3 SPECIFIC TEST SETUP

3.1 SHIP-SHIP INTERACTION TESTS

The tank is equipped with an auxiliary carriage allowing a second ("target") ship model to perform a straight trajectory parallel to the tank walls, according to a prescribed speed history, with a stationary speed between 0.1 and 1.2 m/s (see Figure 10). In this way, ship - ship interaction tests can be carried out with two meeting or overtaking ship models. The auxiliary carriage is connected to a belt driven by an electric motor which is speed controlled. The passing time of both ship models is detected by a proximity sensor. No measurements are performed on the target ship model.

In addition to that forces and moments can be measured on ship models moored alongside a quay or the tank wall [2].

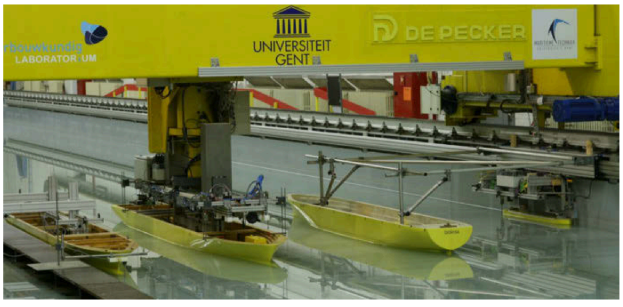

Figure 10. Auxiliary carriage for ship interaction tests.

Figure 11. Second beam for the execution of ship - ship interaction (top: lightering operation between VLCC and Aframax tankers [3]; bottom: ship - tug interaction)

A third type of ship - ship interaction tests can be carried out by attaching an auxiliary beam to the towing carriage (see Figure 11) [3]. With this construction both ship models have the same speed during the test. The second ship can be positioned manually or automatically in the longitudinal direction. The lateral position is set manually and is fixed during a batch of manoeuvring tests.

3.2 BANK EFFECTS

The effect of eccentric navigation of a ship with respect to the centreline of the waterway can be examined by applying an eccentric trajectory in the towing tank. However, the execution of ship – bank interaction tests requires the construction of banks in the towing tank (see Figure 12). The banks have to be built with a high accuracy, which can be controlled making use of the towing carriage for reference. The banks also need to be watertight, particularly at the joints between two bank elements.

Several techniques can be used to build banks into the towing tank. An easy way is to use prefabricated quay elements, made of water-resistant plywood board, constructed with a fixed slope. Alternatively, heavier elements in concrete can be constructed, for instance to counteract the buoyancy. The elements can either be used as a vertical element to construct quay wall or locks, or as a sloping bank. A second, more labour intensive way is often used to construct hydraulic scale models, and makes use of gravel and mortar. This technique is most suitable for banks with a nonlinearly varying slope or width, but for programs of long duration the material tends to dissolve in the water.

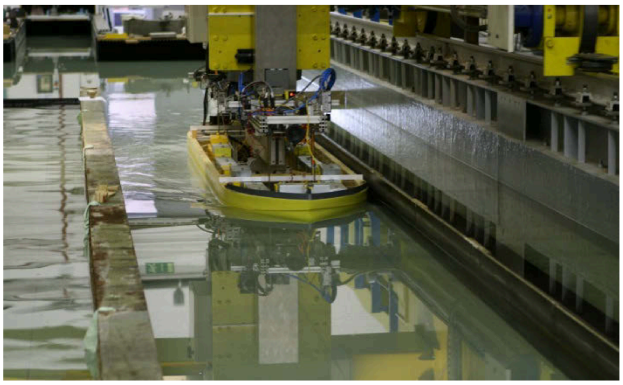

Figure 12. Ship model sailed in an extremely narrow canal

All these techniques have already been applied for the construction of quay walls, surface piercing and submerged sloping banks, sinusoidal banks, variable canal sections, and harbour environments.

3.3 FLOW DETECTION

Registration of the flow occurring around the ship hull, both during calm water and during seakeeping tests, is becoming more important for validation with numerical tools, such as CFD. For common manoeuvring purposes only the undulations of the air water interface are measured with wave gauges (see Figure 3). In more specific research projects the flow can be dyed for visualisation purposes or fluorescent light can be used to track the ship's waterline during seakeeping tests [4]. Some examples are shown in Figure 13.

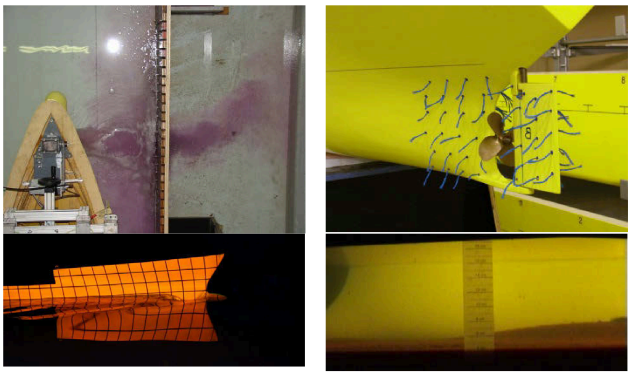

Figure 13. Clockwise from top left: bow thruster jet through semi permeable wall, propeller flow measurement, waterline tracking, rise of water mud interface.

4 AUTOMATIC OPERATION

4.1 TEST CONTROL AND DATA ACQUISITION

The three motion modes, the wave generator, the steering device(s), propeller(s), the auxiliary devices for ship-ship interaction tests, and other external devices are controlled by a PC on the towing carriage and presently up to six PIOCs (Programmable Input Output Control). The PIOCs also assure the sampling and the control of the analogue and digital input signals. The PIOCS can be located on the carriage, in the ship model or ashore. The communication between the PIOCs and the PC occurs over a LAN connection. A directional wireless bridge connects the carriage with the shore. Timing and synchronisation is assured by an implementation of the IEEE 1588 (PTP) timing protocol.

The towing tank application software allows the operator to control the carriage mechanisms and the analogue and digital outputs manually, to manoeuvre into or out of the harbour, to "home" (calibrate the position), to adapt the settings of the software application, and, of course, to execute captive or free running manoeuvring tests. The control system allows unmanned operation, so that experiments can be executed in batch in a fully automatic way during day and night, seven days a week. In spite of the long waiting time between the runs that is required for shallow water tests, see 5.1, an average of 35 tests per 24 hours can be carried out in this way. Safety measures are put in place to safeguard the people around the towing tank from being hit by the carriage.

During captive manoeuvring tests, the ship model follows a predetermined trajectory in the horizontal plane, described in a trajectory file (see 4.3), applied by the towing carriage. During each run, the forces acting on the ship model (hull, propeller(s), and steering device(s)), the propulsion rate(s), the steering angle(s), and the sinkage at four points are measured; depending on the type of test, other signals are sampled as well, e.g. forces on and motions of target vessels, wave gauges mounted at a fixed location in the tank or attached to the towing carriage (see Figure 3 for a typical setup). Each PIOC can sample up to 24 analogue and 20 digital input signals and control up to 4 analogue and 20 digital outputs. The PC controls the positions of the longitudinal, lateral and yawing sub-mechanisms which are stored in a digital way (16 bit). A variable sample frequency up to 200 Hz can be selected.

4.2 PRE-PROCESSING

Software has been developed for the generation of trajectory files in XML format for several types of standard captive and free running manoeuvring tests (see Table 4). The trajectory file contains a sequence of reference values for the sub-mechanism positions and for the analogue and digital outputs as a function of time. In the case of free running tests an additional file is needed which contains the commands for the autopilot. Most captive tests can contain several conditions, e.g. several values for the propeller rate(s) or steering angle(s) during one test run. A graphical user interface allows to input both the common characteristics for all trajectories, e.g. the used ship model and environment, and a number of trajectory rows supplying data typical for each trajectory, e.g. drift angle, propeller rate, rudder angle.

For the specific test type in (ir)regular waves the trajectories are optimized, which means that the optimal start and stop position of the ship model and the optimal starting times for the towing carriage and the wave generator maximise the number of useful encounter periods between the ship model and the wave train. However, it is also possible to use the wave maker to generate regular waves for most test types without this optimization algorithm.

Table 4. Types of standard manoeuvring tests (selection)

Type	Description
	CAPTIVE
bollard pull	propeller and rudder action at zero speed
stationary rectilinear	constant forward or backward speed, propeller and rudder action, drift angle, regular wave climate
oscillation	harmonic variation of longitudinal, lateral or yawing position, at zero speed
PMM sway	constant forward speed, oscillatory sway, propeller action, regular wave climate
PMM yaw	constant forward speed, oscillatory yaw, propeller and rudder action, drift angle, regular wave climate
multimodal	harmonic test to vary at the same time the longitudinal and/or lateral and/or yawing velocity, propeller rate(s) and/or rudder angle(s), regular wave climate
interaction	ship - ship interaction test with two passing or overtaking ship models
(ir)regular waves	model test in regular or irregular (spectrum based) waves with trajectory optimization
	FREE RUNNING
acceleration	determination of the model self-propulsion point
constant	no autopilot control after release
crash stop	perform a stop given a certain propeller reversal law
track keeping	the autopilot tries to keep the ship model on a prescribed track given external disturbances (banks, regular waves,…)
zigzag	the autopilot performs a zigzag test, based on heading or yaw rate

Before the tests can be carried out by the PC of the towing carriage, the trajectory files have to contain a valid signature provided by a validation program. The validation software checks whether the captive trajectory can be executed, taking account of the position, velocity,

and acceleration ranges for each sub-mechanism. It also checks for possible contacts between the ship model and the environment. To validate the model tests the validation program needs additional information such as the carriage parameters, the ship characteristics and the environment geometry. When the tests are validated, the validation software generates a batch file, allowing execution of the test series by automatic operation.

4.3 EXECUTION OF MANOEUVRING TESTS

All information the towing carriage needs to execute a manoeuvring test is stored in the trajectory file. After the trajectory file is read, the ship model is moved to the start position of the trajectory and the waiting time is started. Based on the trajectory file, reference values of the position of the sub-mechanisms at each point of time, the time increment being a multiple of 5 ms, are calculated and stored in the controller memory, with a maximum of 50,000 points. This information is sent to the PIOCs before the test during the waiting time. The waiting in between two tests can be dynamically controlled by monitoring different analogue input signals, such as water levels and forces acting on the waiting ship. The waiting time has a maximum value, after which the test is started disregarding the state of any input signal. A typical waiting time is 2000 s, see also 5.1.

During the test the measurements are only sent to the PC to check the limits of the gauges, an alarm occurs in case a range limit is exceeded. Depending on the settings, alarms can cause either a simple log message or interrupt the test or even the entire batch. The highest alarm level triggers an emergency stop. Alarm warnings can also include an e-mail message or text message which is sent to the operator.

The measurements are saved at the PIOCs during the test and after finishing the test, all measurements are sent to the PC to be stored in a documentation file, an XML text file with all information of the executed manoeuvring test. The documentation file contains the input, output, positioning, ship, and environment files followed by the measurements.

Because of full computer control a series of tests can be carried out consecutively. In a batch file, the trajectory files that have to be executed are listed, separated by the required maximal waiting times. As these batch runs may take several days, the measurement instrumentation is checked by a calibration test which is carried out at the beginning and at the end of the batch file, and after every 60 tests during the batch. The results of these runs are compared and should be equal, otherwise a problem would have occurred with one of the gauges. In this case, corrective actions are required and a calibration check has to be carried out. A full calibration is executed when a new ship is attached to the towing carriage (see also 2.4 (b)). An additional calibration of the hull forces is carried out when the ship's draft is changed. After a calibration the user needs to update the information on analogue and digital in/outputs (conversion of voltage to physical units or vice versa, definitions, acceptable ranges, etc.) in the towing tank program.

4.4 POST-PROCESSING

In order to condense the data in a documentation file, which is in the order of magnitude of 10 MB, post processing software has been developed, which applies corrections of measuring results, e.g. correction of sinkage due to imperfection of the rails according to information based on a rail calibration test (see 5.3 (b)). A running average, based on an interval defined by the user, can be applied to all test results and is stored in a separate XML-file.

Additionally, for captive tests a result file is generated containing a summary of test parameters, and average values (for stationary tests) or amplitudes of 0^{th} to 3^{rd} harmonics (for oscillation tests) for each input channel. Based on this result file or on the running average, a data point file can be generated, containing the results of the tests which can be used for the derivation of mathematical models.

5 SHALLOW WATER CHALLENGES

5.1 EXECUTION TIME

Slow speed, large drift angles and a propeller working in four quadrants are common conditions in harbour manoeuvres. The towing tank was built dedicated for shallow and restricted water tests in harbour conditions. In this way a significant amount of different parameters could be varied. A typical program to derive a mathematical manoeuvring model for one ship at one loading condition and one water depth comprises 300 captive tests with an average execution time of 5 min. The duration of a test program is however heavily affected by the waiting time in between two tests. This waiting time is needed for the water in the towing tank to return to rest. In shallow water this process takes longer, not only due to the decreased wave speed, but also to the natural induction of vortices throughout the tank, especially after a test at large drift angles. At present a standard waiting time is used of 2000 s in between tests. Alternatively the waiting time can be regulated dynamically by continuously monitoring the water motions and forces acting on the ship hull in between two tests. Once an acceptable level is obtained the next test in line can be initiated.

5.2 SPEED AND SINKAGE

The critical speed in shallow water is given by the speed of shallow water waves:

$$V_{crit1} = \sqrt{gh} \rightarrow Fr_{h,crit1} = 1 \qquad (1)$$

h being the water depth. A displacement ship cannot exceed this critical speed which puts an upper limit on the speeds that can be attained in confined water. In a confined environment, such as a towing tank, the critical Froude depth number is given by the more general expression [5]:

$$Fr_{h,crit1} = \left(2sin\left(\frac{arcsin(1-m)}{3}\right)\right)^{3/2} \leq 1 \qquad (2)$$

In this equation m represents the blockage, which is the ratio between the ship's cross section and the cross section of the fairway. The resulting critical speed range is significantly smaller compared to the speed range expressed by equation (1), and will continue decreasing if obstacles, such as banks, are placed in the towing tank, or in case interaction with other ship models takes place. Figure 14 shows for a selection of ship model cross sections in the towing tank the supercritical full scale speed as a function of the water depth and scale factor. This means that the selection of the scale factor also needs to take into account the desired speed range.

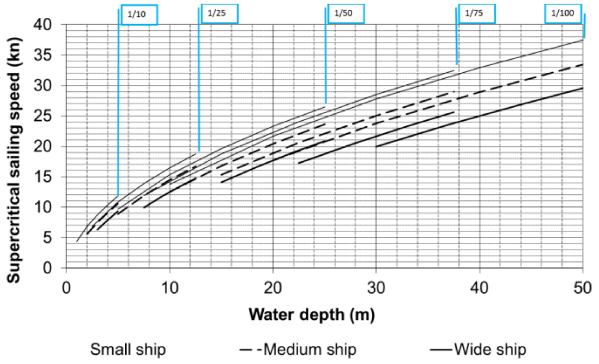

Figure 14. Supercritical sailing speed in function of full scale water depth, without obstacles in the towing tank.

Depending on the speed and the water depth, the ship will squat. To prevent the ship model hitting the bottom, the ship model is equipped with safety contacts (Figure 15). An alarm occurs once a safety contact is touched, which is also registered as the measured forces and motions cannot be considered as reliable in this case.

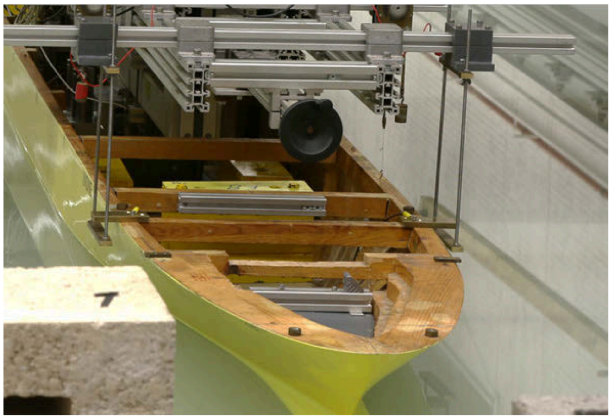

Figure 15. Mechanical safety device to protect the ship model from touching the bottom.

To protect the ship model from touching the bottom of the towing tank or built-in banks, which can cause damage to the hull, rudder, propeller, and/or force gauges, mechanical safety devices were installed fore and aft at both port and starboard sides (see Figure 15).

5.3 ACCURACY

5.3 (a) Requirements

In shallow water the forces acting on a vessel are approximately inversely proportional with the under keel clearance written as $\frac{h}{h-T}$. Moreover, scale models of conventional ships used in the towing tank typically have a draft of 0.2 m, which are tested at under keel clearances up till 10% of the ship's draft. This means that a deviation in either ship's draft or tank bottom of 1 mm causes an uncertainty of 0.5% on the under keel clearance. The position of the rails on which the towing carriage moves is also extremely important, because deviations in both the vertical and the horizontal plane can introduce undesired dynamic effects on the measurements.

5.3 (b) Rails

Train rails of which the upper surface is milled and finished are used to guide the carriage. By means of lateral guiding wheels on one of the rails excessive lateral deviations of the carriage can be avoided. The rails are adjustable in vertical and lateral direction by screw bolts with an in-between distance of approximately 0.5 m, and have to be aligned with high accuracy. The level difference of both rails and the lateral deflection of the guiding rail are less than 0.2 mm; the height difference over the entire length of the rails is less than 1 mm (see Table 5).

Table 5. Rail accuracy

Vertical		Horizontal
Global	Local	
1 mm	0.1 mm/1 m	0.2 mm

Twice a year the position of the rails is checked. This is done at the beginning of the summer and the winter, when the largest temperature deviations occur which lead to extension or shrinkage of the rails. Moreover, during every batch of model tests a rail calibration test is executed, during which the towing carriage moves at 0.03 m/s and the position of the rails is checked indirectly by measuring the sinkage of the ship model. When the results of this test exceed the accuracy limits, a thorough electronic measurement of the rails is executed to re-align the rails between the requested tolerances. The processing of the measurements results into a table presenting rail corrections at each screw bolt, more or less located every m along the towing tank. Several iterations of measurement and adaptation may be needed to obtain the desired accuracy.

5.3 (c) Tank bottom

With respect to the tested under keel clearances, a maximal deviation of the tank bottom level of 1 mm is considered acceptable. After 15 years of operation the bottom was flattened in May 2008 to meet the desired accuracy. The first layers were milled using the towing carriage in manual mode, but when the largest differences had disappeared, the towing carriage was programmed to flatten the bottom automatically. The bottom was flattened in layers of 0.7 mm until the accuracy of ± 1 mm was reached. Stiffness and water tightness of the bottom (and any built in obstacle) is important to correctly measure the ship's responses and manoeuvring forces.

5.4 SHALLOW WATER WAVES

The tests with regular waves in the towing tank are optimized to maximize the useful output. Several criteria have to be met:

- A useful sea state is obtained once the wave train generated by the wave maker has reached the ship model over its full length with an amplitude which is acceptably close to the desired value. The time to reach this point can be computed given the position of the ship, the position of the wave maker, the group and phase velocities of the waves and the start time of the wave generation;
- A wave that reaches the ship model is reflected and sent back to the wave maker where it interferes with the produced wave system. The resulting wave system is different and when it reaches the ship another sea state is obtained. This process is known as diffraction and should be avoided. The time to reach this point is given by the position of the ship, the position of the wave maker, the phase velocity and the start time of the wave generation;
- A wave that has passed the ship model travels further towards the end of the tank where the wave is reflected. If the reflected wave reaches the ship model it interferes with the present wave system. This process is known as reflection and should be avoided as well. The time to reach this point is given by the position of the ship, the position of the wave maker, the wave speed, the position of the tank wall and the start time of the wave generation;
- The ship should be sailing at a stationary speed, thus without acceleration, deceleration or waiting phases.

In addition to the above, interaction between the ship, the wave and the side walls occurs as well. In shallow water this is rather inevitable due to the small ship speeds compared to the wave speed, especially at oblique wave angles and/or drift angles of the ship.

Moreover waves in shallow water are significantly affected by the water depth. Wave braking occurs at smaller wave amplitudes and the wave profile is mostly of higher order with narrow, large crests and wider, shallow troughs which has to be coped with higher order theories.

6 FUTURE DEVELOPMENTS

6.1 ACTUAL TOWING TANK

In 2016 the towing tank will be upgraded by adding forced roll motion as a fourth captive degree of freedom. This will allow to measure forced roll motions, even in combination with yaw and sway motions and to investigate and model the effect of roll on the manoeuvring behaviour of a ship. In 2016-2017, the motor drives of the carriage power will be replaced and the electrical systems refurbished.

Steps are taken towards further automation. In the future the water depth variation should also be included in the batch, which will lead to longer net operational times. Cameras will be added to increase the distant monitoring level, which allows to solve certain alarm issues without necessarily having to be present.

6.2 A SECOND TOWING TANK

The size of the sea-going ships have been increasing since the first towing tank was built in 1992. As a result present scale factors are increasing, which puts a limit on the accuracies that can be achieved. Moreover the mentioned shallow water challenges, such as wave reflection, critical speed,… put a severe limit on the possibilities of the current towing tank.

In 2009 a project was initiated to build a second towing tank. The dimensions of this towing tank are given in Table 6.

Table 6. Main dimensions of the second towing tank

Total length	[m]	174.0
Useful length	[m]	140.0
Width	[m]	20.0
Maximum water depth	[m]	1.0
Length of the ship models	[m]	3.5 – 8.0

FHR has not sufficient space to build a tank of this size at its present location, for this reason a second site has been designed and will be built in Ostend, near the Belgian coast. The tank will also aim at manoeuvring and seakeeping tests in shallow water. It will be equipped with a 4 DOF captive carriage, with possibilities to mount a 6 DOF hexapod and to operate in free running mode.

At present political approval is still needed to release the necessary funds.

7 CONCLUSIONS

Execution of captive manoeuvring and seakeeping tests with ship models in shallow and confined water is time-consuming, not only because of the large number of varying parameters, but also because additional shallow water challenges, such as long waiting times between two test runs have to be taken into account. Experience at Flanders Hydraulics Research in Antwerp has shown that optimisation of a ship model experimental facility can be obtained through intensive automation of the test operations. However, an efficient use of an automatic system also requires the development of reliable pre- and post-processing software to organise the data flow, and the availability of auxiliary infrastructure to investigate interaction effects with the channel environment and other shipping traffic that is integrated into the automated system.

Despite the already high level of automation, further modernization steps are planned, including the construction of a state of the art second, larger towing tank.

8 ACKNOWLEDGEMENTS

The authors wish to expect their gratitude to the operational staff of the towing tank, especially to Luc Van Ostaeyen, who has been an excellent operator since the very beginning, and to Sam Das, who has been able to solve any electronic problem in the complex system.

9 REFERENCES

1. Flemish Port Commision. Quarterly figures total traffic (ton) (Last accessed Feb 25, 2016: http://www.vlaamsehavencommissie.be/en/vhc/page/quarterly-figures-total-traffic-ton)

2. Delefortrie, G.; Vantorre, M.; Cappelle, J.; Ides, S. (2012). The Effect of Shipping Traffic on Moored Ships. *10th International Conference on Hydrodynamics*, St. Petersburg, Russia. 6p.

3. Lataire, E.; Vantorre, M.; Delefortrie, G.; Candries, M. (2012). Mathematical modelling of forces acting on ships during lightering operations. *Ocean Engineering* 55: pp. 101–115. doi:10.1016/ j.oceaneng.2012.07.029

4. Geerts, S.; Van Kerkhove, G.; Vantorre, M.; Delefortrie, G. (2011). Waterline registration using fluorescent lighting. *Advanced Model Measurement Technology for EU Maritime Industry (AMT 2011)*, Newcastle, UK, pp: 61-69.

5. Schijf, J.B. (1949). *XVIIth International Navigation Congress Lisbon Section I Inland Navigation* pp. 61 – 78.

10 AUTHORS' BIOGRAPHIES

Guillaume Delefortrie, naval architect, is expert nautical research at Flanders Hydraulics Research. He is in charge of the research in the Towing Tank for Manoeuvres in Shallow Water and is secretary of the 27th and 28th ITTC Manoeuvring Committee.

Stefan Geerts is naval architect at Flanders Hydraulics Research. He is specialized in the instrumentation and monitoring of physical scale models, among which the Towing Tank for Manoeuvres in Shallow Water.

Marc Vantorre, naval architect, is full senior professor of marine hydrodynamics and head of the Maritime Technology Division at Ghent University, Belgium. His research focuses on ship behaviour in shallow and confined waters, mainly in close co-operation with Flanders Hydraulics Research in Antwerp. He is former member of several PIANC Working Groups and former member and secretary of the ITTC Manoeuvring Committee.

4th MASHCON, Hamburg - Uliczka et al. (eds) - © 2016 Bundesanstalt für Wasserbau ISBN 978-3-939230-38-0 (Online)
DOI: 10.18451/978-3-939230-38-0_28

MEASURED SHIP MOTIONS IN PORT OF GERALDTON APPROACH CHANNEL

J H Ha and **T P Gourlay,** Centre for Marine Science and Technology, Curtin University, Australia
N Nadarajah, Global Navigation Satellite Systems Research Centre, Curtin University, Australia

SUMMARY

This article presents some results from a series of recent full-scale trials on measuring dynamic sinkage, trim and heel of 11 bulk carriers entering and leaving the Port of Geraldton. Measurements were carried out using high-accuracy GNSS receivers and a fixed reference station. Measured dynamic sinkage, trim and heel of three example bulk carriers are discussed in detail. A theoretical method using slender-body shallow-water theory is applied to predict the sinkage and trim of the transits. A comparison between measured and predicted results is made to validate the ship motion software for UKC (under-keel clearance) prediction. It is shown that slender-body theory is able to give good predictions of dynamic sinkage and trim. The measured results will also be in future for validating wave-induced motions software.

NOMENCLATURE

AP	After Perpendicular
AWAC	Acoustic Wave And Current Profiler
AWST	Australian Western Standard Time
B	Ship's beam (m)
C_B	Block coefficient (-)
CD	Chart Datum
C_{s_bow}	Bow sinkage coefficient (-)
C_{s_mid}	Midship sinkage coefficient (-)
C_{s_stern}	Stern sinkage coefficient (-)
C_θ	Trim coefficient (-)
F_h	Depth-based Froude number (-)
FP	Forward Perpendicular
FS	Free Surface
G	GNSS height measurement
g	Acceleration due to gravity (m/s^2)
GM_f	Metacentric height (m), corrected for free surface effect
GNSS	Global Navigation Satellite System
GPS	Global Positioning System
h	Water depth (m)
H_s	Significant wave height (m)
HAT	Highest Astronomical Tide
KG	Height of the ship's centre of gravity above keel (m)
LAT	Lowest Astronomical Tide
LCB	Longitudinal centre of buoyancy (m)
L_{OA}	Ship length overall (m)
L_{PP}	Ship length between perpendiculars (m)
MSL	Mean Sea Level
N	Geoid undulations (m)
S_{bow}	Bow sinkage (m)
S_{mid}	Midship sinkage (m)
S_{stern}	Stern sinkage (m)
T	Instantaneous tide height (m)
Θ	Stern-down change in trim due to squat (radians)
T_m	Mean period of the energy spectrum (s)
T_p	Peak period of the energy spectrum (s)
T_ϕ	Ship's natural roll period (s)
U	Ship speed (m/s)
UKC	Under-Keel Clearance
∇	Ship volume displacement (m^3)

1 INTRODUCTION

Safe under-keel clearance (UKC) management is a critical factor in port marine operations and the shipping industry. Accurate guidelines for the optimized UKC could bring the efficient running of the port as well as safety management. The progressively increasing accuracy of GNSS receivers can provide fundamental information for UKC management by allowing full-scale measurements in actual sea conditions.

In September and October 2015, we carried out full-scale trials on some bulk carriers at the Port of Geraldton, located in the mid-west region of Western Australia, in order to measure vertical ship motions relative to still water level including squat and wave-induced motions in its approach channel. Totally 13 ship transits including 2 trials to measure ship motions at a berth have been measured. Measurements were made using the shore-based receiver method that needs to set up high-accuracy GNSS (or GPS) receivers onboard as well as a fixed base station for an external reference [1], [2].

By comparing the vertical motions of a ship when under way to that at berth, considering the changing tide height and geoid undulations, dynamic sinkage, trim and heel are calculated, as well as wave-induced heave, pitch and roll through the entire transit. The dynamic draught at each point on the ship can then be found using those dynamic results and its static draught. UKC in approach channels is also calculated by comparing elevations of the keel of the vessel relative to the seabed. The largest draught over all of the hull extremities governs the net UKC and hence grounding risk.

With high-quality data for the ship motions and environmental conditions, validation of numerical ship motion modelling may also be achieved at full-scale.

2 DESCRIPTION OF THE TRIALS

At the Port of the Geraldton, full-scale trials were performed on 11 inbound and outbound bulk carriers via its

curved approach channel (see chart AUS81). The procedure for inbound transits is:

- CMST researchers board vessel with pilot and report to Captain on bridge
- Set up GNSS receivers on bow and both port and starboard bridge wings (symmetric positions)
- Data recording throughout pilotage
- Remove equipment and disembark with pilot

The procedure for outbound transits is the reverse of the above. Data recording covers a period of time before departure or after arrival to take a stationary reading at the berth. In our trials, data recording was commenced prior to leaving the berth for the outbound transits and continued until after all mooring work had been completed for the inbound transits. These are then used as a reference value for comparing the vertical height measurements while under way [2].

Three Trimble R10 GNSS receivers were positioned on the bow extremity centreline, and the port and starboard bridge wings for the measurements. A fixed reference station (Trimble R10 GNSS) was located on the pilot wharf to apply differential corrections to the moving receiver results. This shore-based receiver method is described in [1]. The equipment setup yields 10mm horizontal accuracy and 20mm vertical accuracy in the ship motions. All data were recorded at 1.0 Hz. A typical GNSS receivers setup at the Port of Geraldton is shown in Figure 1.

(a)

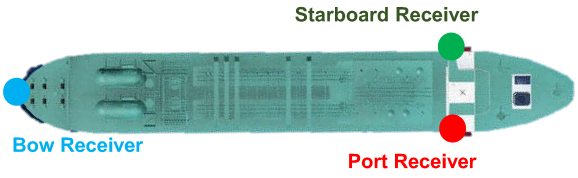

(b) (c) (d)

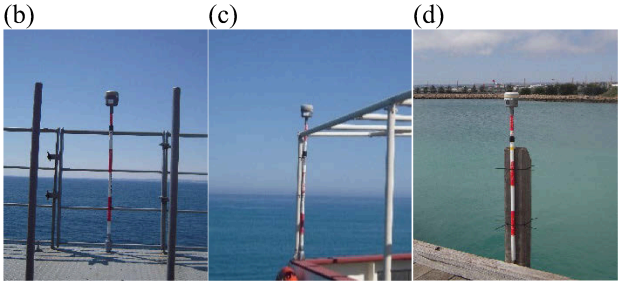

Figure 1. GNSS receivers setup. (a) Plan view of ship receivers. (b) Bow receiver. (c) Port receiver on bridge wing. (d) Base station on pilot wharf.

3 SHIPS AND SHIP TRANSITS ANALYSED IN THIS PAPER

Three transits have been selected for analysis. Table 1 reports pertinent details of these ships that include: *GUO DIAN 17*, built in 2013, a 76,000 DWT Panamax bulk carrier; *FENG HUANG FENG*, built in 2011, a 75,000 DWT Panamax bulk carrier; and *SEA DIAMOND*, built in 2007, a 77,000 DWT Panamax bulk carrier. They each have similar hull dimensions as well as high block coefficient.

Table 1. Details of the ships used for the trials

Particulars	GUO DIAN 17	FENG HUANG FENG	SEA DIAMOND
L_{OA}	225.00 m	225.00 m	224.99 m
L_{PP}	219.00 m	217.00 m	217.00 m
Beam	32.26 m	32.26 m	32.26 m
Summer draught	14.200 m	14.221 m	14.078 m
Displacement	89,800.8 t	88,535.9 t	87,782.0 t
C_B	0.873	0.868	0.869

Displacement and Block coefficient (C_B) are figures at summer draught. C_B is the ratio of displaced volume to (L_{PP}.Beam.Draught).

Since each ship may sail under vastly different conditions, we shall take into account all the available relevant operation conditions. Comparative transit conditions for all the ships are shown in Table 2. Details for GUO DIAN 17 and FENG HUANG FENG are based on the data from "Application for Berth" submitted to the Port of Geraldton no later than 2 hours prior to actual departure. For SEA DIAMOND, a loading condition report was provided by the shipping agent when CMST researchers disembarked after the measurements. Hydrostatic data was obtained from the Trim and Stability Book for FENG HUANG FENG and SEA DIAMOND. From the details, we can see that GUO DIAN 17 and FENG HUANG FENG have nearly fully-loaded draught with almost level static trim while SEA DIAMOND has a comparatively shallower draught and is trimmed by the stern at departure time. Note that all of these transits are outbound cases.

Table 2. Details of the transit conditions

Particulars	GUO DIAN 17	FENG HUANG FENG	SEA DIAMOND
Date and Time	28/09/15 09:18~10:13	29/09/15 21:41~22:53	02/10/15 09:52~10:58
Direction	Outbound	Outbound	Outbound
Draught fwd	12.15 m	12.18 m	8.91 m
Draught aft	12.15 m	12.20 m	10.26 m
Departure displacement	75,571 t	74,788 t	57,427 t
C_B	0.859 @12.15m	0.854 @12.20m	0.835 @9.59m
LCB	-	113.9 m @12.20m	115.05 m @9.59m
KG	5.902 m	6.410 m	8.070 m
GM_f	7.109 m	7.100 m	5.930 m

C_B is calculated based on departure draught. LCB is given as metres forward of Aft Perpendicular (AP). For SEA DIAMOND, average draught of 9.59m is represented for both C_B and LCB.

Figure 2 shows the Port of Geraldton and its approach channel and beacons together with tracks of the three ships. The channel is around 2.8 nautical miles in length and 180m in width (at toe of bottom slope), varying in depth from 12.4m to 14.8m based on the Chart Datum, which is approximately the level of LAT (Lowest Astronomical Tide). An additional depth of up to 1.2 m can be considered by tides, i.e. HAT (Highest Astronomical Tide) and MSL (Mean Sea Level) in the Port of Geraldton are 1.2 and 0.6m respectively (see chart AUS81). For the outbound ships, the measurements were made from the berth until the ships passed the last beacons (Beacon 1 & 2) at the end of the channel.

Since Geraldton is exposed to long-period swells, which cause wave-induced motions of ships in the channel, measured dynamic sinkage includes wave-induced heave, pitch and roll by the swells. During the trials, waves were measured by an AWAC at Beacon 2 (Latitude 28° 45' 28.2" E, Longitude 114° 33' 55.9" S) and by pressure sensors at Beacon 1, Beacon 3, Beacon 5, …, Beacon 19.

Wave data from the AWAC at Beacon 2 is shown in Table 3. The full measured wave data will be used to study wave attenuation along the channel, and wave-induced motions along the channel, in future work.

Table 3. Measured wave data at Beacon 2 during the transits

Transits	AWST	Hs (m)	Tp (sec)	Tm (sec)	Dir (deg)
GUO DIAN 17	28/09/15 09:18	1.49	13.3	8.8	247
	28/09/15 09:38	1.22	12.5	8.2	242
	28/09/15 09:58	1.29	9.2	8.2	244
	28/09/15 10:18	1.12	13.0	7.8	243
FENG HUANG FENG	29/09/15 21:38	0.57	10.8	6.7	240
	29/09/15 21:58	0.55	12.2	6.5	248
	29/09/15 22:18	0.53	12.3	6.4	248
	29/09/15 22:38	0.53	12.5	6.8	251
	29/09/15 22:58	0.52	11.8	6.6	240
SEA DIAMOND	02/10/15 09:58	1.83	13.8	12.1	245
	02/10/15 10:18	1.56	13.8	11.5	246
	02/10/15 10:38	1.51	13.8	11.3	248
	02/10/15 10:58	1.61	15.1	11.5	252

The time of each record is the time at the end of the 20 minutes in which the data was recorded.

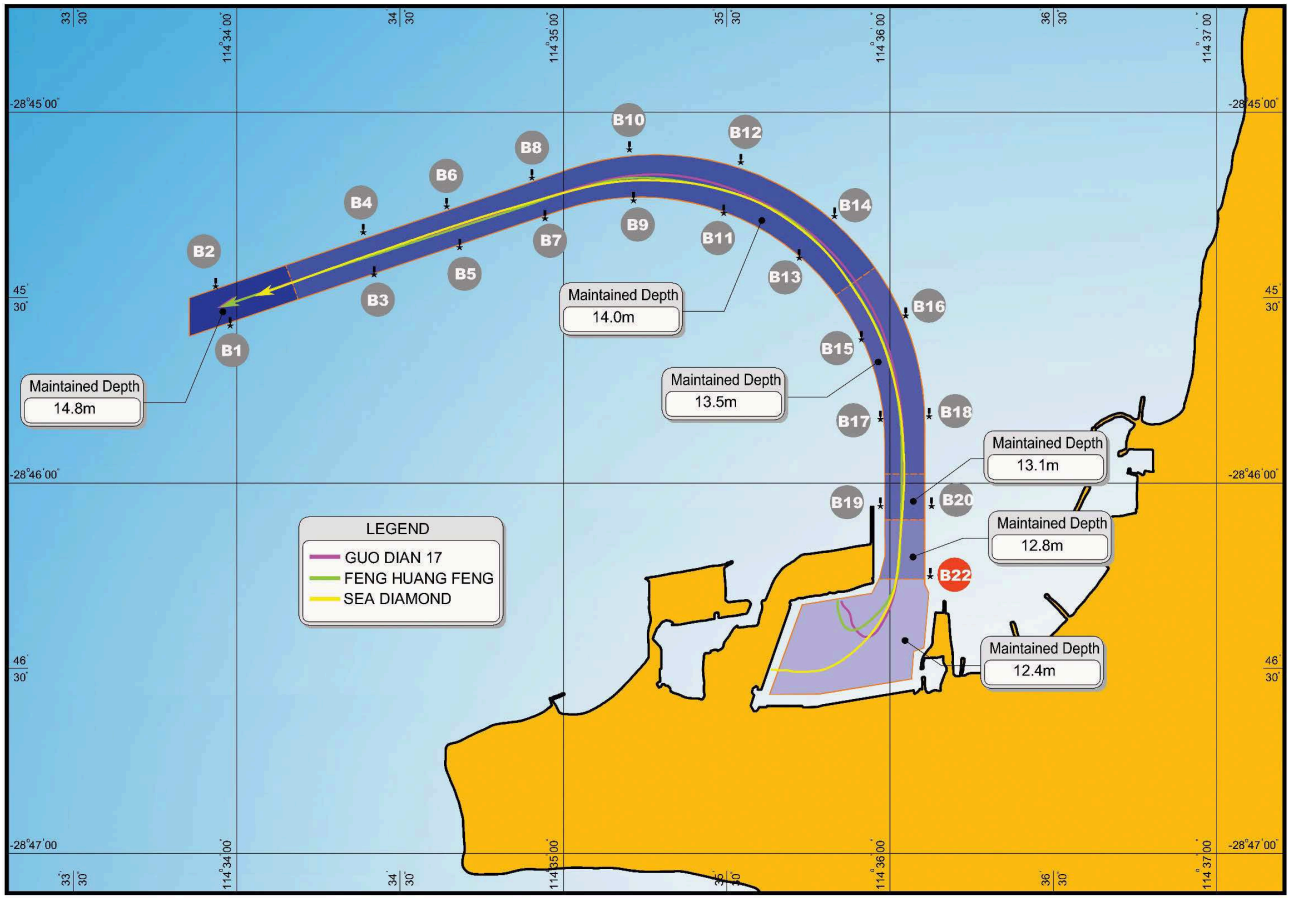

Figure 2. Port of Geraldton approach channel and measured midship tracks.

4 MEASURED DYNAMIC SINKAGE, TRIM AND HEEL

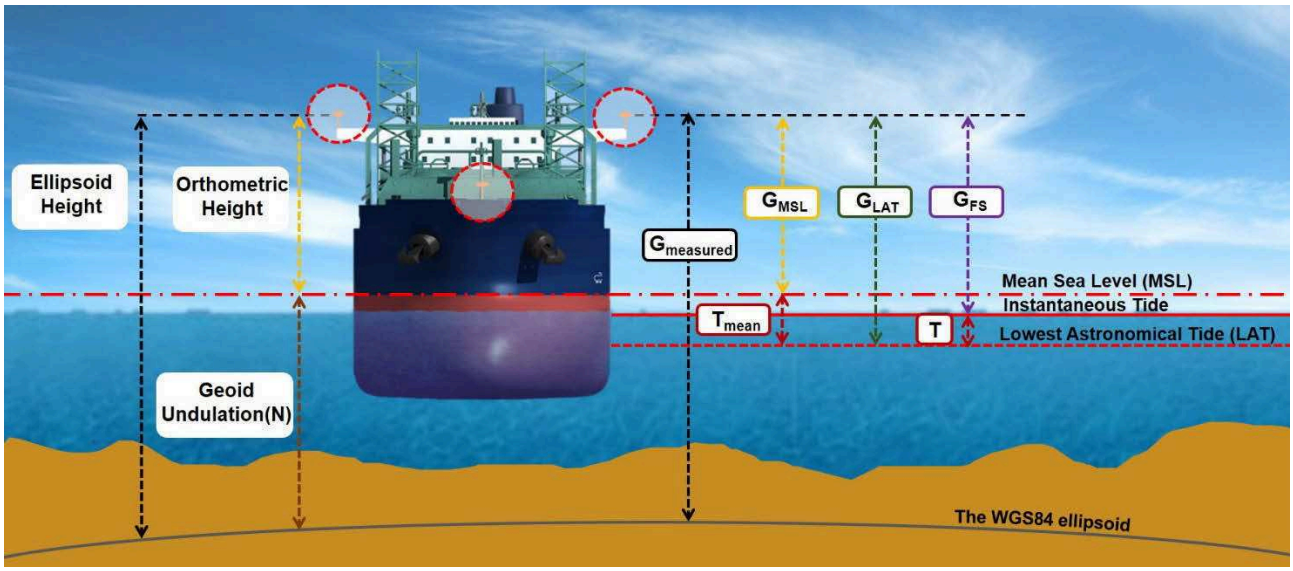

Figure 3. Components for calculating sinkage from GNSS height measurements.

By accurately measuring the vertical elevations of the three GNSS receivers on each ship with respect to the local static waterline, and assuming the ship to be rigid, sinkage at each point of concern of running aground on the ship can be calculated, as well as dynamic trim and dynamic heel. Dynamic heel is here defined as the change in heel angle relative to the static floating position [3], and sinkage is defined as being positive downward.

Figure 3 shows height components for calculating sinkage from GNSS height measurements, and equation (1) is given for their relationship. This method for sinkage calculation is presented in [1], [2].

$$Sinkage = (G_{measured} - N + T_{mean} - T)_{static} - (G_{measured} - N + T_{mean} - T)_{underway} \quad (1)$$

Regarding tidal data, local tide has been extracted from the data that is raw sea surface elevations as measured at Berth 3-4 in the Port of Geraldton, using a low pass filter with a cutoff frequency of 5 minutes.

4.1 DYNAMIC SINKAGE

It would be more effective to see measured vertical motions of the ship against the same horizontal axis that uses cumulative distance from a fixed point for all the ships. The pilots normally state their position in the channel using the beacons, so we use Beacon 22 as the fixed point as marked with a red circle in Figure 2. The horizontal axis is, hence, described as distance out from Beacon 22 in metres and has vertical lines at locations of Beacon 20, Beacon 18, …, Beacon 2 (hereafter referred to as B). Distance within the harbour, therefore, is negative. Note that substantial gaps in the data of GUO DIAN 17 around B16 and B14 are due to GPS fixes being of insufficient quality and being rejected.

Measured sinkage results together with corresponding ship speed profile, as well as the bathymetry along the channel, are shown in Figure 4. With positions of the FP and AP, the forward and aft shoulder of the bilge corners are also plotted as they can be specifically vulnerable to grounding considering the combined effects of dynamic trim and heel and the ships' long parallel midbodies. A parallel body line from the Deck and Profile drawing for SEA DIAMOND is used for the positions of the forward and aft shoulders of the bilge corners, approximately 75.3% and 36.0% of L_{PP} forward of Aft Perpendicular (AP) respectively. These proportions are also applied to those for GUO DIAN 17 and FENG HUANG FENG.

Distance of 89%, 91% and 88% of the half-beam away from the centerline of the ships have been taken for the transversal positions of the bilge corners from the sections of the General Arrangement Plan for GUO DIAN 17, FENG HUANG FENG and SEA DIAMOND respectively. An estimated 90% of that is hence applied to the ships uniformly.

Dynamic sinkage includes a near-steady component due to the Bernoulli Effect at forward speed, which is characterized by a bodily sinkage and a dynamic change in trim. This effect is known as squat, and can be predicted with theoretical or empirical methods. As well as this, the sinkage has oscillations due to wave-induced motions. When swell waves are present, vertical motions of the ship are more intricate with its wave-induced motion that is a combination of heaving, pitching and rolling. For example, the SEA DIAMOND transit was undertaken in large, long period swell conditions (Table 3), and vertical motions are seen to be highly oscillatory (Figure 4) due to wave-induced heave, pitch and roll.

(a)

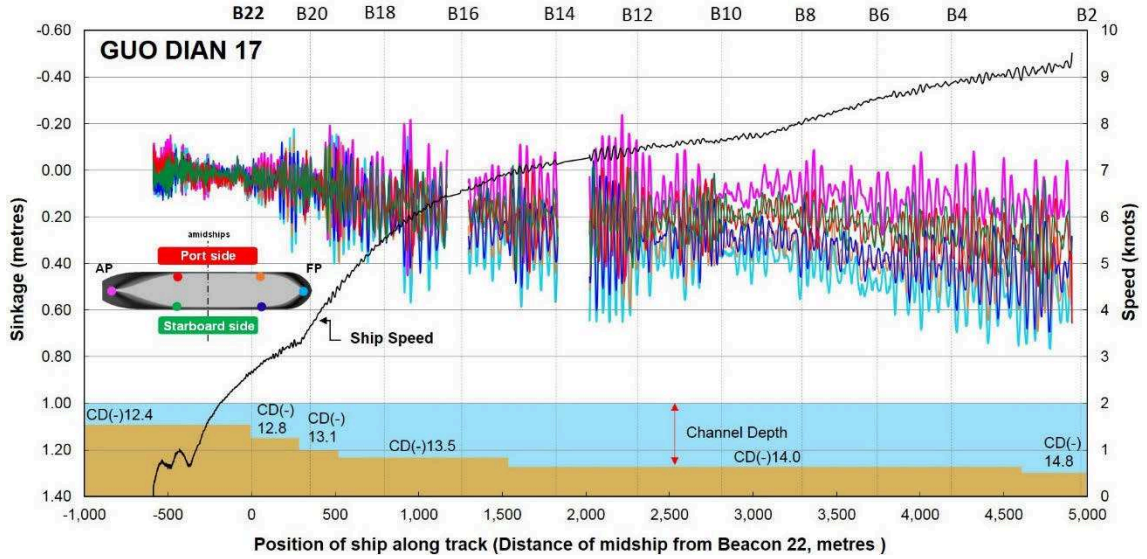

(b)

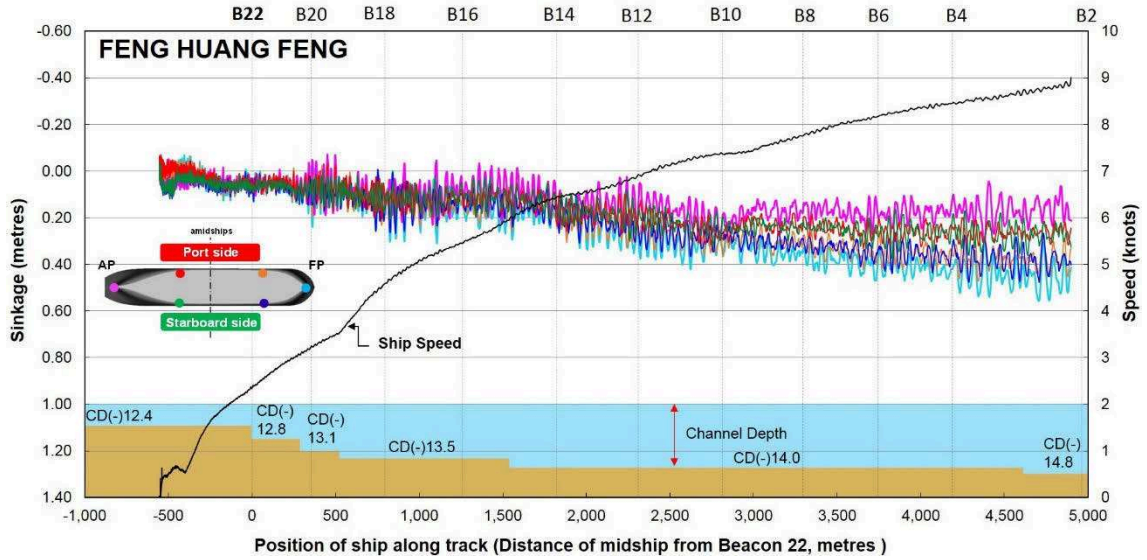

(c)

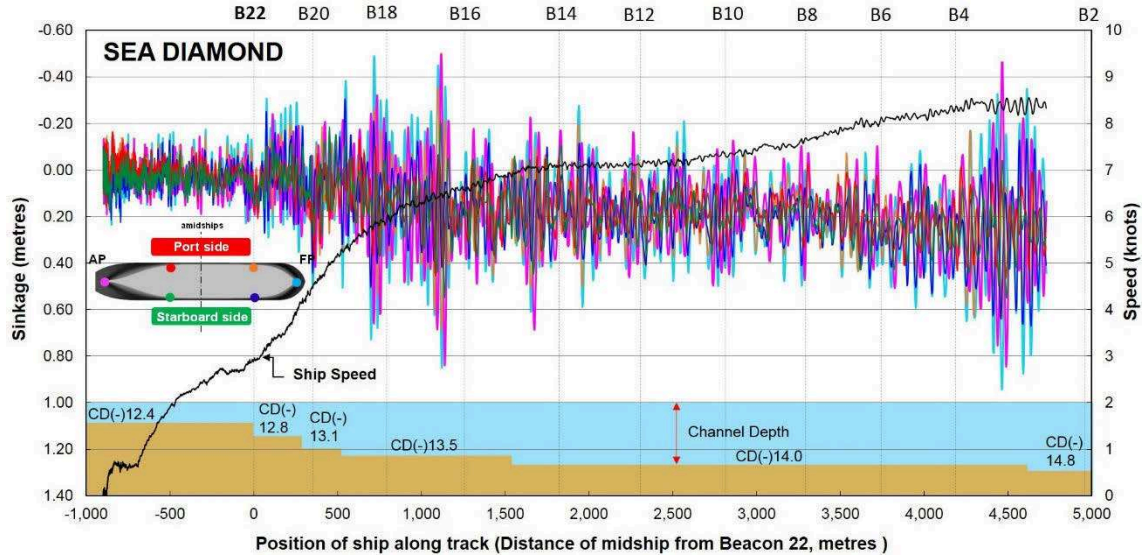

Figure 4. Measured sinkage (positive downward) at six points for (a) GUO DIAN 17, (b) FENG HUANG FENG and (c) SEA DIAMOND. Chart datum depths (not to scale) also shown.

Based on Chart AUS81, outbound transits are on a heading of 0° (North) from B20 to B18, then an approximate 1,200m-radius turn to port, steadying on a heading of 251° from B8 to the end of the channel. By comparing this to directions of the prevailing swells in Table 3, we see that the ships were in port beam seas near B18 and in head seas near B4.

Maximum sinkage is observed at the bow in the vicinity of B2, i.e. near the end of the channel, but significant oscillations also occurred when they are travelling between B20 and B12. This is common to all the ships and might be referable to combined effect of dynamic trim and heel changes due to turning manoeuvres and beam waves in this severely curved section. The maximum sinkage is: 0.77m (0.35% of L_{PP}) for GUO DIAN 17; 0.56m (0.26% of L_{PP}) for FENG HUANG FENG; and 0.94m (0.44% of L_{PP}) for SEA DIAMOND.

With swell present, maximum dynamic draught may occur at the forward shoulders of the bilge corners [4]. This is evidenced by looking at the sinkage at the forward shoulders of the bilge corners that had a greater sinkage than the bow at some instants in the cases of the GUO DIAN 17 and SEA DIAMOND transits. However, with considering the fact that SEA DIAMOND used the static stern-down trim of 1.35m on her departure (see Table 2), the stern still has the maximum dynamic draught (refer to the Appendix). No significant wave-induced heave, pitch and roll in the FENG HUANG FENG transit were seen with calm wind and low swell conditions.

In order to bring further practical support to UKC management in the port, the ship's vertical motions should be addressed with elevations of the ship's keel relative to Chart Datum so that the port may know the actual real-time clearance from the seabed. An Appendix is made to include these vertical elevation changes. The minimum real-time clearance of 0.80, 0.90 and 2.25m is captured for GUO DIAN 17, FENG HUANG FENG and SEA DIAMOND respectively.

The starboard forward shoulder of the bilge corners for GUO DIAN 17 and the starboard aft shoulder of the bilge corners for FENG HUANG FENG are the closest points to the seabed over their entire transits. These closest points are observed in the harbour, and this is primarily due to heel, as tugs pulled the ships to starboard during unberthing. For SEA DIAMOND with having the static stern-down trim, the AP is the point closest to the seabed through the whole transit.

In the appendix, elevations of the FP and AP including changes in tide only, i.e. their static position, not including squat and wave-induced motions, are plotted as broken lines. This shows how much of the sinkage is due to tide changes.

4.2 DYNAMIC TRIM

Bulk carriers with level static trim tend to have dynamic trim by the bow when the ship is under way, see e.g. [5] for model-scale test results, [6] for full-scale test results. This large bow-down trim means that the bow can be the point on the ship most vulnerable to grounding. Figure 5 shows results of dynamic trim for the three transits. Steadily increasing trim by the bow is observed for all the three cases, but is swamped by wave-induced pitching for SEA DIAMOND. Note that dynamic trim is given in metres based on the difference between the FP and AP.

By looking at oscillations of dynamic sinkage (see Figure 4) for each transit, it is identified that dynamic trim is more likely to affect maximum sinkage for bulk carriers rather than dynamic heel which will be discussed subsequently. This situation is different to container ships, where dynamic heel may be the most important factor governing maximum sinkage [2].

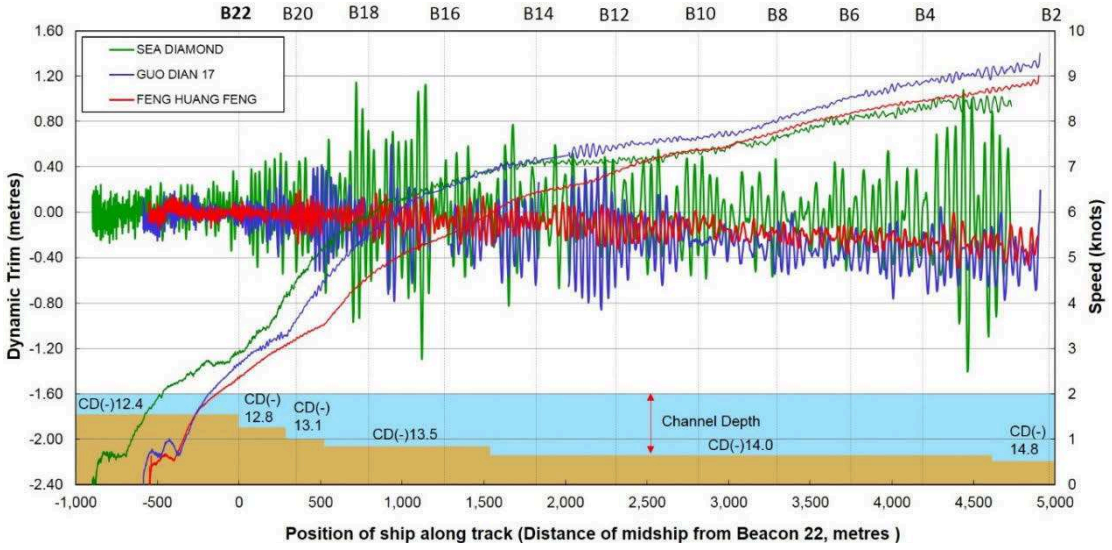

Figure 5. Measured dynamic trim (positive stern-down) for the three transits. Chart datum depths (not to scale) also shown.

According to full-scale tests made by [7] and [8], acceleration and deceleration influence dynamic trim. GUO DIAN 17 and SEA DIAMOND quickly accelerate speed up to 6 knots while they pass between B22 and B18. For the SEA DIAMOND case, some significant oscillations in dynamic trim are seen in the regions of near B18, B16 and the end of the channel. This may be explained considering the operation condition with comparatively larger swell (see Table 3, mostly head sea condition) but lighter displacement.

The maximum dynamic trim by the bow are 0.86m, 0.49m and 1.40m (0.39%, 0.23% and 0.65% of the L_{PP}) for the GUO DIAN 17, FENG HUANG FENG and SEA DIAMOND transit respectively.

4.3 DYNAMIC HEEL

Dynamic heel may cause the bilge corners to be the closest points to the seabed. For ports exposed to long-period swell, large dynamic heel occurs when the wave encounter period is close to a ship's natural roll period [9]. The natural roll period T_ϕ is approximately

$$T_\emptyset = 0.8\frac{B}{\sqrt{GM_f}} \quad (2)$$

More accurate calculations of the natural roll period and wave-induced motions will be done in future publications.
Calculated natural roll periods of the ships measured are shown in Table 4. SEA DIAMOND has smaller GM_f (see Table 2) and hence longer natural roll period.

Table 4. Calculated natural roll period for the trials

Natural roll period	GUO DIAN 17	FENG HUANG FENG	SEA DIAMOND
T_ϕ	9.7 sec	9.7 sec	10.6 sec

By comparing the mean wave period (see Table 3) to the ships' natural roll period, we would expect large roll angles to occur in the GUO DIAN 17 and SEA DIAMOND cases. Measured dynamic heel for the examples are shown in Figure 6. As expected, larger heel oscillations are seen in these cases. Of equal importance is wave height. FENG HUANG FENG travelled in low swell conditions and hence has small roll angles.

An oscillation pattern in dynamic heel between each beacon in the curved section of the channel (between B18 and B10) is equally observed for all the three transits. This repetitive pattern may be partly attributable to rudder-induced heel due to turning manoeuvres. This will be studied further in future work, with reference to the measured rudder changes and calculated wave-induced motions. As mentioned in 4.1, due to tugs for unberthing, considerable heel to starboard is observed in the harbour, i.e. before B22, for all the cases.

Container ships with level static trim generally have significant heel arising from wind and turning in calm water. For example, heel angles in the order 1° to 2° were measured for container ships in Hong Kong [3]. However, bulk carriers have relatively large displacement (for the same ship length), low KG and small above-water profile area, which translated into smaller heel angles due to wind and turning.

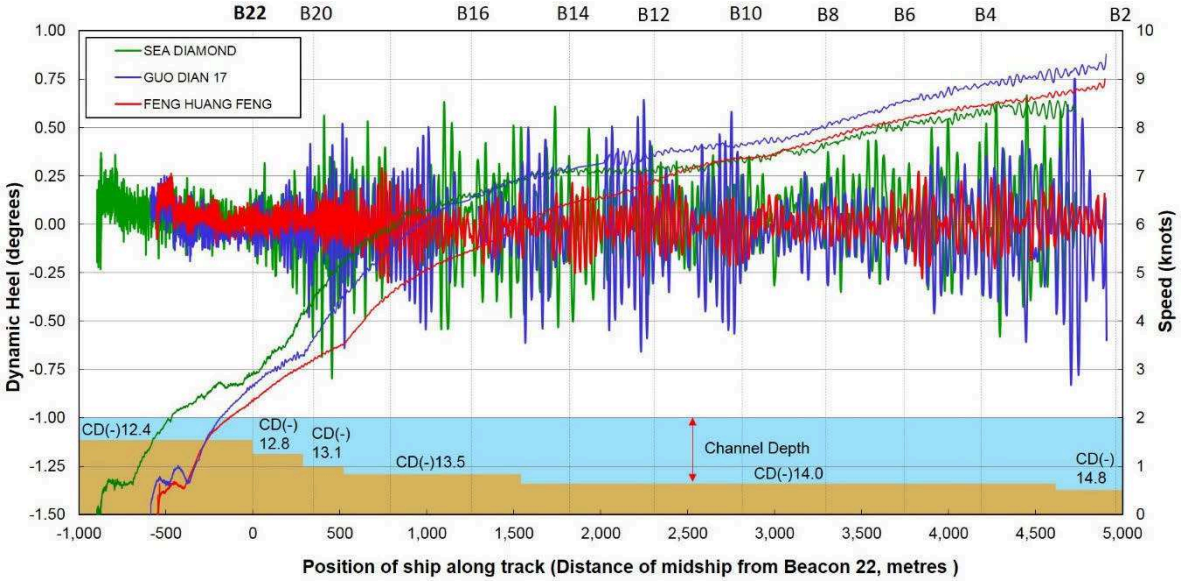

Figure 6. Measured dynamic heel (positive to starboard) for the three ships. Chart datum depths (not to scale) also shown.

5 THEORETICAL SQUAT PREDICTIONS

As Port of Geraldton approach channel is a typically dredged channel in channel dimensions, a differential between channel depth and depths on the side of the channel is observed with bathymetric data on the nautical chart (see chart AUS81), e.g. depths on the side of the channel are around 3m shallower than in the dredged channel in the longest section with a maintained depth of 14.0 m, a conceptual cross section of which is shown in Figure 7.

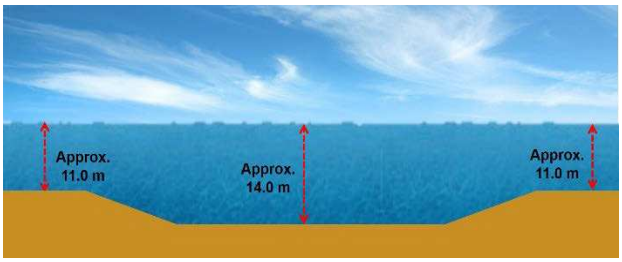

Figure 7. Conceptual cross section of Port of Geraldton approach channel. This view is for illustration only (not to scale).

Some port approach channels in Western Australia including Geraldton have been assessed to see whether a particular ship and channel configuration may be classed as open water, or whether a specific narrow-channel analysis is required. Regarding a Panamax carrier case (L_{PP} 215m), the sinkage coefficient for Geraldton channel has been predicted within 3% of the open-water value using the slender-body theory [10]. For predicting ship sinkage and trim, therefore, the transits can be classed as open water condition since the effect of transverse bathymetries such as channel width and trench depth to the ships having L_{PP} of 217 and 219 m is seen to be minimal.

5.1 TUCK METHOD

A theoretical method used here to compare against the measured ship sinkage and trim is based on slender-body shallow water theory of [11] for open water, modified slightly to make it more applicable to ships with transom sterns, as in [12]. This method uses linearized hull and free-surface boundary conditions. According to that theory, the sinkage at midships (midway of L_{PP}), bow and stern can be written

$$S_{mid} = C_{s\_mid} \frac{\nabla}{{L_{PP}}^2} \frac{F_h^2}{\sqrt{1-F_h^2}} \quad (3)$$

$$S_{bow} = C_{s\_bow} \frac{\nabla}{{L_{PP}}^2} \frac{F_h^2}{\sqrt{1-F_h^2}} \quad (4)$$

$$S_{stern} = C_{s\_stern} \frac{\nabla}{{L_{PP}}^2} \frac{F_h^2}{\sqrt{1-F_h^2}} \quad (5)$$

where F_h is the depth-based Froude number:

$$F_h = \frac{U}{\sqrt{gh}} \quad (6)$$

Similarly, the change in stern-down trim due to squat θ, can be written

$$\theta = C_\theta \frac{\nabla}{{L_{PP}}^3} \frac{F_h^2}{\sqrt{1-F_h^2}} \quad (7)$$

Calculations are done using the slender-body shallow water theory [11], as implemented in the computer programme "ShallowFlow" [13].

5.2 SHIP HULLFORMS MODELLED

Since stability and hydrostatic data were obtained for each ship, but not lines plans or hull offsets, a representative hull that has similar characteristics of the hulls was chosen and modified to match the main hull parameters. For minimum modification, the other dimensionless parameters such as block coefficient (C_B) and longitudinal centre of buoyancy (LCB) should also be reasonably similar.

For the theoretical prediction, FHR ship G, a Panamax bulk carrier hull commissioned by Flanders Hydraulics Research and Ghent University, Belgium [14], [15], has been chosen. Modifications of FHR ship G hull have been made from the supplied IGES file in order to match information on the ships' Trim and Stability Book, as described in [16].

Figure 8 shows an example of the modelled ship G with the bow, stern, profile and bottom views. We see that ship G hull is very block-like with a long parallel midbody and a smaller transom that are considered typical features of bulk carriers in hull shape.

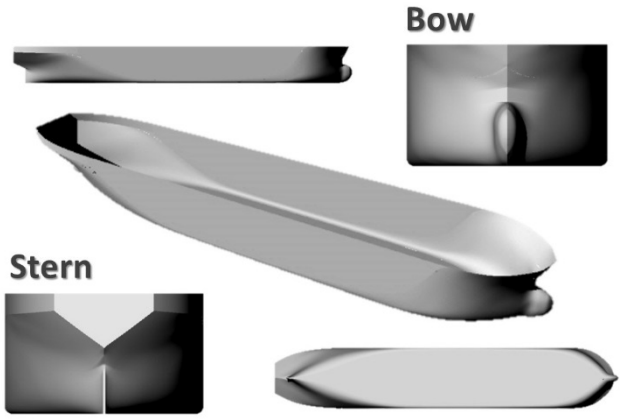

Figure 8. An example of the modelled Ship G.

We have made two kinds of the modified FHR ship G, based on load and ballast conditions for the three ships at the actual departure time. One is applied to SEA DIAMOND, and the other is for both GUO DIAN 17 and FENG HUANG FENG due to the resemblance in transit conditions (see Table 2).

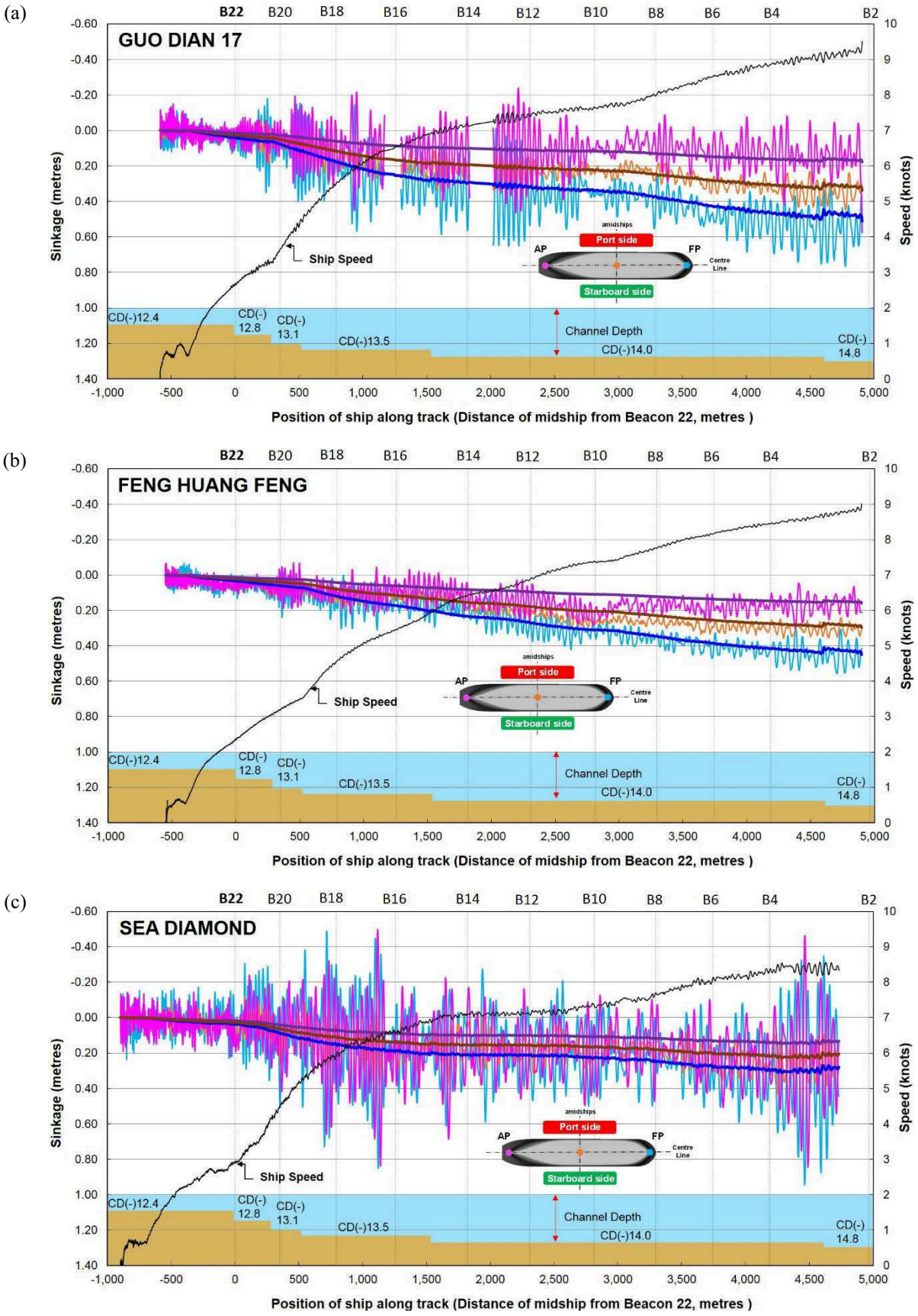

Figure 9. Measured and calculated sinkage (positive downward) at the FP, AP and midship for (a) GUO DIAN 17, (b) FENG HUANG FENG and (c) SEA DIAMOND. Calculations do not include wave-induced motions. Chart datum depths (not to scale) also shown.

5.3 RESULTS

Calculated bow, stern and midship sinkage coefficients for each ship using the slender-body theory of [11] are shown in Table 5. These are then applied to equation (3), (4) and (5) for calculating the theoretical sinkage.

Table 5. Calculated sinkage coefficients for each ship in open water

Sinkage Coefficient (C_s)	GUO DIAN 17	FENG HUANG FENG	SEA DIAMOND
FP (C_{s_bow})	2.00	1.95	1.82
Midship (C_{s_mid})	1.32	1.29	1.33
AP (C_{s_stern})	0.70	0.68	0.87

Comparisons between measured and predicted sinkage for the FP, AP, and midship for the transits, together with measured ship speed and the bathymetry along the channel, are shown in Figure 9.

It is known that Tuck's method [11] tends to under-predict the sinkage of cargo ships in finite-width canal model tests, especially in very narrow canals [17], [18]. No model tests approximating open-water dredged channels are available with which to compare. In the full-scale trials, given that the transits involve significant speed and depth changes along the channel, the overall performance of the theoretical method is quite good, but the theory [11] is still seen to slightly under-predict the sinkage. For FENG HUANG FENG, midship sinkage predictions are on average 13% less than the measurements for speeds above 7 knots. For GUO DIAN 17 and SEA DIAMOND, midship sinkage also appears to be under-predicted, but the measurements are swamped by wave-induced heave.

Reliability of the measurements is made with a vertical accuracy of 20mm of the equipment [19], but there are additional problems in applying Tuck's theory to the transit conditions, such as: the seabed that cannot be perfectly flat in the longitudinal or transverse directions; the seabed condition (e.g. mud, sand, rock, sea grass, and corals); the effect of the approximated hull geometry. These factors all could make application of the theory complicated.

Table 6 lists the theoretical trim coefficients for each ship using equation (7). This is also applied for calculating the theoretical change in stern-down trim due to squat θ. All three transits have negative trim coefficients, indicating negative (bow-down) dynamic trim.

Table 6. Calculated trim coefficients for each ship in open water

Trim Coefficient	GUO DIAN 17	FENG HUANG FENG	SEA DIAMOND
C_θ	- 1.30	- 1.27	- 0.96

The trim coefficient, and hence dynamic trim, is quite sensitive to hull shape, so complete ship offsets are required to accurately calculate dynamic trim using the slender-body theory [11], [20]. Since such offsets are generally confidential for merchant cargo ships, approximations to the hull shape have been made by modifications of FHR ship G hull, as mentioned in 5.2.

Figure 10 shows comparisons between measured and predicted dynamic trim. Dynamic trim is given here in degrees (°).

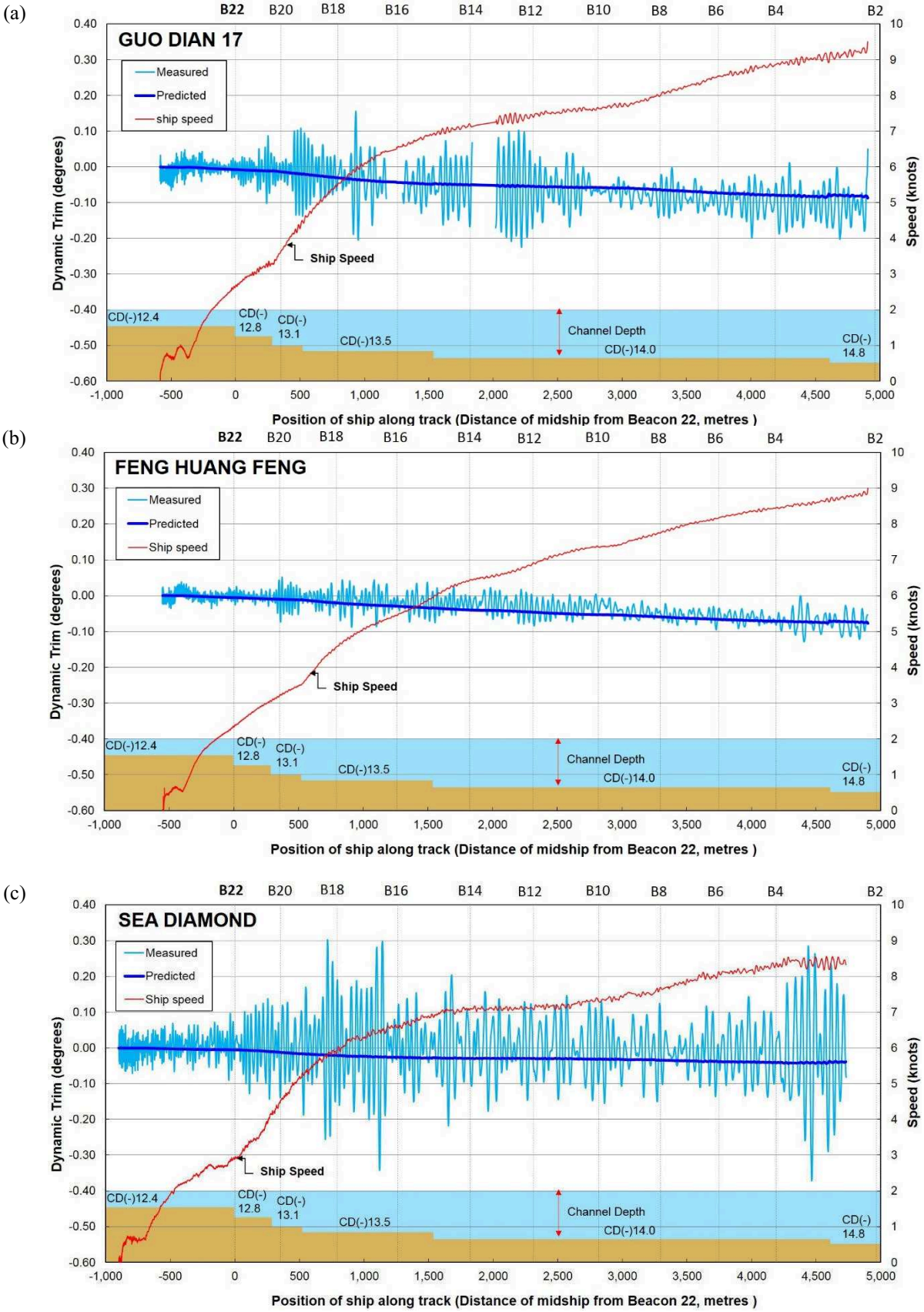

Figure 10. Measured and calculated dynamic trim (positive stern-down) for (a) GUO DIAN 17, (b) FENG HUANG FENG and (c) SEA DIAMOND. Chart datum depths (not to scale) also shown.

Predicted dynamic trim for FENG HUANG FENG and SEA DIAMOND are slightly more bow-down (or less stern-down) than measured whereas GUO DIAN 17 shows a predicted dynamic trim of less bow-down. Considering the above-mentioned approximations, it is found that the theoretical prediction quite closely estimates dynamic trim at full-scale.

6 CONCLUSIONS

For under-keel clearance management, dynamic sinkage, trim and heel of the three outbound bulk carriers have been analysed in detail among a total of 11 measurements in the Port of Geraldton. All measured motion data presented here are from the GNSS receivers with the fixed reference station. The following conclusions are drawn from the study:

- High-quality data have been acquired from the set of full-scale trials
- The trial results will be made publicly-available so that they can be used for validating current UKC practice by ports and as a set of benchmarking data internationally
- Three outbound transits have been chosen for detailed analysis in this paper: a transit in low swell (FENG HUANG FENG); a transit with large swell (SEA DIAMOND) and a transit with medium swell (GUO DIAN 17)
- Maximum sinkage, including the effects of squat and wave-induced motions, occurred at the bow and ranges between 0.26% and 0.44% of L_{PP} for the three ships considered here
- Slender-body theory is able to predict squat (steady sinkage and trim) with reasonable accuracy for bulk carriers at full-scale in open dredged channels. A small empirical correction to the theory is advisable for better UKC prediction

7 ACKNOWLEDGEMENTS

The authors wish to thank all of the marine pilots and staff at Mid West Ports Authority for their assistance, support and enthusiasm in conducting the trials. We would also like to acknowledge the following organizations for their contributions to this research: Tianjin Guodian Shipping, China Shipping Tanker and Hanaro Shipping, who provided access to and hull information for GUO DIAN 17, FENG HUANG FENG and SEA DIAMOND respectively; the GNSS Research Group, Curtin University, who provided the GNSS equipment; Tremarfon Pty Ltd, who provided measured tide and wave data; Flanders Hydraulics Research and Ghent University, who provided hull data for Ship G; and OMC International, who provided surveyed depth data for the channel.

8 REFERENCES

1. Feng, Y.; O'Mahony, S. (1999). Measuring Ship Squat, Trim, and Under-Keel Clearance using On-the-Fly Kinematic GPS Vertical Solutions, *Journal of the Institute of Navigation* 46(2): pp.109-117.

2. Gourlay, T.P.; Klaka, K. (2007). Full-scale measurements of containership sinkage, trim and roll, *Australian Naval Architect* 11(2): pp.30-36.

3. Gourlay, T.P. (2008). Dynamic draught of container ships in shallow water, *International Journal of Maritime Engineering* 150(4): pp.43-56.

4. Gourlay, T.P. (2007). Ship Underkeel Clearance in Waves, *Proceedings of the Coasts & Ports 2007 Conferenc*e, Melbourne, Australia.

5. Dand, I.W.; Ferguson, A.M. (1973). The squat of full form ships in shallow water, *Trans. RINA* 115: pp.237-255.

6. Härting, A.; Laupichler, A.; Reinking, J. (2009). Considerations on the squat of unevenly trimmed ships, *Ocean Engineering* 36(2): pp.193-201.

7. Ferguson, A.M.; McGregor, R.C. (1986). On the Squatting of Ships in Shallow and Restricted Water, *Coastal Engineering Proceedings* 1(20).

8. Hatch, T. (1999). Experience measuring full scale squat of full form vessels at Australian ports, *Proceedings of the Coasts & Ports 1999 Conferenc*e, Perth, Australia.

9. Gourlay, T.P. (2015). Ship under-keel clearance. Navigation Accidents and their Causes, *The Nautical Institute*.

10. Ha, J.H.; Gourlay, T.P. (2015). Bow and Stern Sinkage Coefficients for Cargo Ships in Shallow Open Water, *under review*.

11. Tuck, E.O. (1966). Shallow water flows past slender bodies, *Journal of Fluid Mechanics* 26: pp.81-95.

12. Gourlay, T.P. (2008). Slender-body methods for predicting ship squat, *Ocean Engineering* 35(2): pp.191-200.

13. Gourlay, T.P. (2014). ShallowFlow: A Program to Model Ship Hydrodynamics in Shallow Water, *Proceedings of the ASME 33rd International Conference on Ocean, Offshore and Arctic Engineering, OMAE 2014*, San Francisco, California, USA.

14. Vantorre, M.; Journée, J. M. J. (2003). Validation of the strip theory code SEAWAY by model tests in very shallow water, *Numerical Modelling Colloquium*, Flanders Hydraulics Research, Antwerp, October 2003. DUT-SHL Report Nr. 1373-E.

15. Gourlay, T.P.; von Graefe, A.; Shigunov, V.; Lataire, E. (2015). Comparison of AQWA, GL RANKINE, MOSES, OCTOPUS, PDSTRIP and WAMIT with model test results for cargo ship wave-induced motions in shallow water, *Proceedings of the ASME 34th International Conference on Ocean, Offshore and Arctic Engineering, OMAE 2015*, St. John's, Newfoundland, Canada.

16. Gourlay, T.P. (2011). A brief history of mathematical ship-squat prediction, focussing on the contributions of E.O. Tuck, *Journal of Engineering Mathematics* 70: pp. 5-16. doi 10.1007/s10665-010-9435-3.

17. Gourlay, T.P.; Lataire, E.; Delefortrie, G. (2016). Application of potential flow theory to ship squat in different canal widths. To be submitted to *4th International Conference on Ship Manoeuvring in Shallow and Confined Water, MASHCON 2016*, Hamburg, Germany.

18. Gourlay, T.P. (2013). Duisburg Test Case containership squat prediction using ShallowFlow software, *Proceedings of PreSquat Workshop on Numerical Ship Squat Prediction*, Duisburg, Germany.

19. Trimble. (2012). *Trimble R10 GNSS receiver User Guide: Chapter 5 Specifications* (Revision A). California, USA.

20. Gourlay, T.P.; Ha, J.H.; Mucha, P.; Uliczka, K. (2015). Sinkage and trim of modern container ships in shallow water. *Proceedings of the Coasts & Ports 2015 Conference*, Auckland, New Zealand.

9 AUTHORS' BIOGRAPHIES

Jeong Hun Ha is a Ph.D. candidate at the Centre for Marine Science and Technology (CMST) at Curtin University, Australia. His Ph.D. thesis is about ship under-keel clearance in port approach channels. His background is as a Korean civil engineer in the design of port and coastal structures.

Tim Gourlay is a Senior Research Fellow at CMST and is supervising Jeong Hun Ha's Ph.D. thesis. He undertakes research and consulting work in ship under-keel clearance for ports in Australia and internationally. He is the author of ShallowFlow software, and has conducted full-scale ship motion measurements on 42 cargo ships and numerous smaller vessels.

Nandakumaran Nadarajah is a Research Fellow at the GNSS Research Centre at Curtin University, Australia. His main areas of interest are signal processing, target tracking, and relative navigation and attitude determination.

APPENDIX

(a)

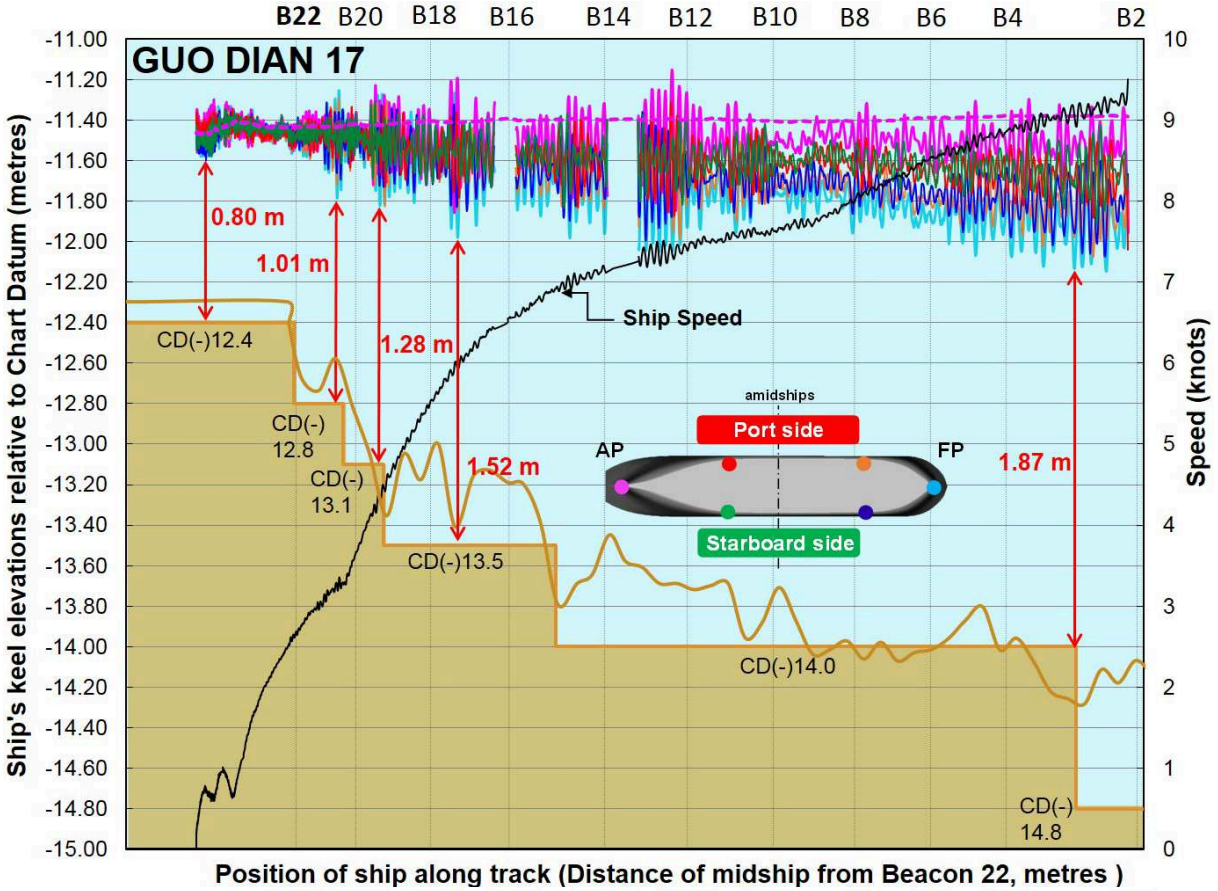
B22 B20 B18 B16 B14 B12 B10 B8 B6 B4 B2
GUO DIAN 17
0.80 m
1.01 m
1.28 m
1.52 m
1.87 m
CD(-)12.4
CD(-)
12.8
CD(-)
13.1
CD(-)13.5
CD(-)14.0
CD(-)
14.8
Ship Speed
amidships
Port side
Starboard side
AP
FP
Ship's keel elevations relative to Chart Datum (metres)
Speed (knots)
Position of ship along track (Distance of midship from Beacon 22, metres)

(b)

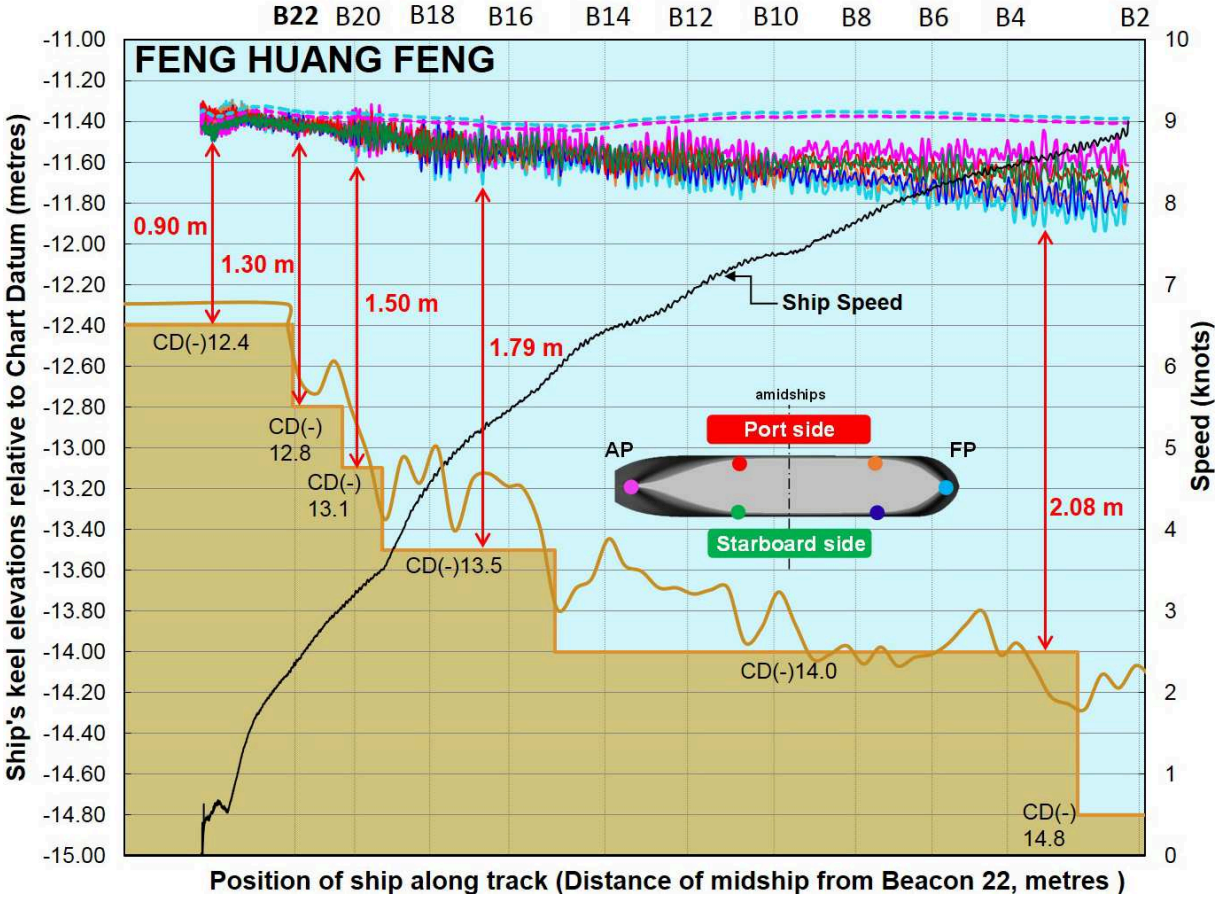
B22 B20 B18 B16 B14 B12 B10 B8 B6 B4 B2
FENG HUANG FENG
0.90 m
1.30 m
1.50 m
1.79 m
2.08 m
CD(-)12.4
CD(-)
12.8
CD(-)
13.1
CD(-)13.5
CD(-)14.0
CD(-)
14.8
Ship Speed
amidships
Port side
Starboard side
AP
FP
Ship's keel elevations relative to Chart Datum (metres)
Speed (knots)
Position of ship along track (Distance of midship from Beacon 22, metres)

(c)

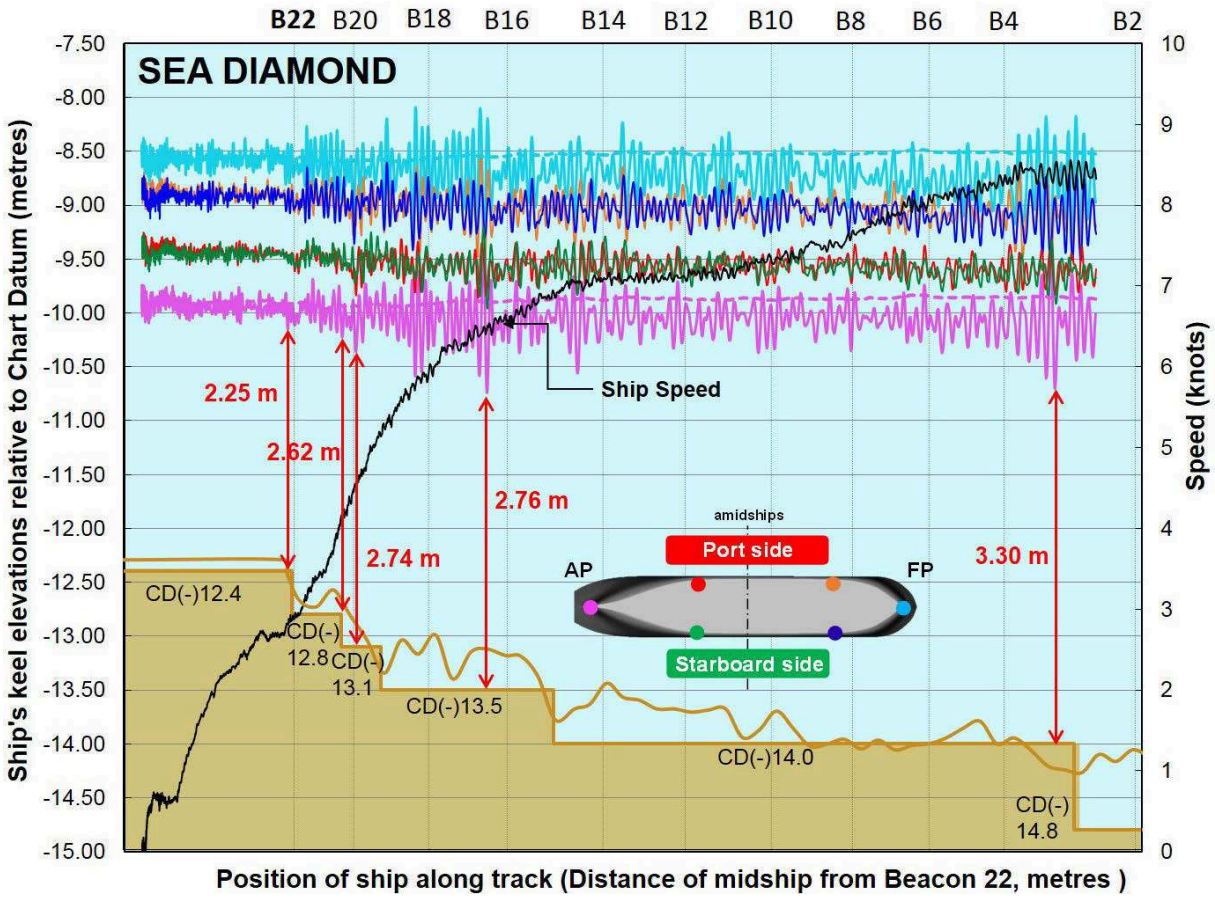

Figure 11. Elevation of the ship's keel relative to chart datum for (a) GUO DIAN 17, (b) FENG HUANG FENG and (c) SEA DIAMOND. Broken lines are elevations of the FP and AP including changes in tide only, i.e. their static position, not including squat and wave-induced motions. A flat seabed line is based on the charted depth on AUS 81, and a fluctuating seabed line is the actual survey line provided by OMC International.

4th MASHCON, Hamburg - Uliczka et al. (eds) - © Bundesanstalt für Wasserbau ISBN 978-3-939230-38-0 (Online)
DOI: 10.18451/978-3-939230-38-0_29

RUNNING SINKAGE AND TRIM OF THE DTC CONTAINER CARRIER IN HARMONIC SWAY AND YAW MOTION: OPEN MODEL TEST DATA FOR VALIDATION PURPOSES

K Eloot, Flanders Hydraulics Research, Ghent University, Belgium
M Vantorre, Ghent University, Belgium
G Delefortrie, Flanders Hydraulics Research, Belgium
E Lataire, Ghent University, Belgium

SUMMARY

After successful conferences on bank effects, ship – ship interaction and ship behaviour in locks, the Fourth International Conference on Ship Manoeuvring in Shallow and Confined Water (MASHCON) has a non-exclusive focus on ship – bottom interaction. With increasing ship sizes in vertical and horizontal dimensions, a clear understanding of the interaction between a ship and the bottom of the waterway will help to improve the operations and increase the safety of manoeuvring ships. To open a joined research effort on the validation and verification of the different research methods, the Knowledge Centre Manoeuvring in Shallow and Confined Water has selected model test data which were obtained while executing tests with the DTC container carrier in the framework of the European SHOPERA project. The benchmark data are harmonic yaw and harmonic sway tests with the bare hull of the DTC at full draft and 20% under keel clearance at rest.

NOMENCLATURE

A_M	Midship section area (m²)
B	Breadth of ship (m)
C_B	Block coefficient (-)
Fr	Froude number based on L_{PP} (-)
Fr_h	Froude number based on water depth h (-)
Fr_{crit}	Critical value of Froude number (based on water depth) accounting for blockage (non-dimensional "Schijf velocity") (-)
GM_T	Transverse metacentric height (m)
h	Water depth (m)
I_{xx}	Mass moment of inertia about Ox-axis (kg m²)
I_{yy}	Mass moment of inertia about Oy-axis (kg m²)
I_{zz}	Mass moment of inertia about Oz-axis (kg m²)
KG	Height of centre of gravity above keel (m)
L_{PP}	Length between perpendiculars (m)
n	Propeller rate (rps)
N	Yaw moment (Nm)
O_0	Origin of the earth-bound axis system
$O_0x_0y_0z_0$	Earth-bound reference system
O	Origin of the ship-bound axis system
Oxyz	Ship-bound reference system
O'	Origin of the horizontal bound towing carriage system
O'x'y'z'	Horizontal bound towing carriage system
p	Roll velocity (rad/s)
q	Pitch velocity (rad/s)
r	Yaw velocity (rad/s)
r_A	Amplitude of yaw velocity (rad/s)
S	Wetted surface (m²)
t	Time (s)
t_{harm}	Start time of harmonic motion (s)
Δt	Time interval (s)
T	Test period (s)
T_{design}	Design draft (m)
u	Longitudinal velocity component (m/s)
v	Lateral velocity component (m/s)
v_A	Amplitude of sway velocity (m/s)
V	Velocity (m/s)
w	Vertical velocity component (m/s)
x_G	Longitudinal coordinate of the centre of gravity (m)
X	Longitudinal force (N)
Y	Lateral force (N)
$y_{0,A}$	Sway amplitude (m)
β	Drift angle (deg)
δ_R	Rudder angle (deg)
φ	Roll angle (deg)
θ	Pitch angle (deg)
ψ	Course angle (deg)
ψ_A	Yaw amplitude (deg)
Ω	Canal cross section area (m²)
AP	Aft Perpendicular
CG	Centre of Gravity
DTC	Duisburg Test Case
FHR	Flanders Hydraulics Research
FP	Fore Perpendicular
LCB	Longitudinal Centre of Buoyancy
UKC	Under Keel Clearance

1 INTRODUCTION

After successful conferences on bank effects [1] (Antwerp, May 2009), ship – ship interaction [2] (Trondheim, May 2011) and ship behaviour in locks [3] (Ghent, May 2013), the Fourth Conference on Manoeuvring in Shallow and Confined Water (MASHCON) has a non-exclusive focus on ship – bottom interaction. This conference is organised in Hamburg, Germany, from 23 to 25 May 2016, by the Federal Waterways Engineering and Research Institute, Flanders Hydraulics Research and Ghent University (Maritime Technology Division). The initiative to organise these conferences is taken in the frame of the activities of the Knowledge Centre Manoeuvring in Shallow and Confined water, which aims to consolidate, extend and disseminate knowledge on the behaviour of ships in navigation areas with major vertical and horizontal restrictions.

With increasing ship sizes in all dimensions and optimisations in the design and maintenance of waterways, a clear understanding of the interaction between a ship and the bottom of the waterway helps to improve the operations and to increase the safety of manoeuvring ships. The extension of knowledge on ship-bottom interaction focusses on:

- Squat
- Shallow water effects on ship behaviour
- Effect of bottom topography on ship behaviour
- Effect of fluid mud layers on ship behaviour
- Probability and hydrodynamic aspects of bottom contact
- Required manoeuvring margin
- Regulations and design guidelines
- Nautical bottom – equivalent bottom: definition and determination

These topics are covered from different points of view:

- Practical aspects
- Simulation models
- Field observations
- Experimental results
- Numerical calculations, including CFD

To open a joined research effort on the validation and verification of the different research methods, the Knowledge Centre has selected model test data which were obtained while executing tests with a container carrier in the framework of the European SHOPERA project (Energy Efficient Safe SHip OPERAtion [4]).

2 MODEL TEST SET-UP

Tests have been executed with a scale model of the Duisburg Test Case (DTC) container ship in the Towing Tank for Manoeuvres in Shallow Water (cooperation Flanders Hydraulics Research – Ghent University, Antwerp Belgium).

The following sections describe the ship model, the towing tank, the chosen reference axis systems and the environmental conditions.

2.1 SHIP MODEL

The Duisburg Test Case (DTC) is a hull design of a typical 14,000 TEU container ship, developed at the Institute of Ship Technology, Ocean Engineering and Transport Systems for benchmarking and validation of numerical methods [5].

The DTC is a single-screw vessel with a bulbous bow, large bow flare, large stern overhang and a transom stern. The ship is tested as bare hull and as appended hull equipped with a fixed-pitch five-bladed propeller with right rotation and a twisted rudder with a Costa bulb.

The ship particulars are presented in
Table 1. The ship model is made at a scale of 1:89.11.

Table 1. Ship particulars

Particulars		Ship	Model
Scale	-	1	1:89.11
L_{PP}	m	355	3.984
B	m	51	0.572
T_{design}	m	14.5	0.163
Displacement	m^3	173,925	0.2458
C_B	-	0.661	0.661
S	m^2	22,051	2.777
LCB from AP	m	174.032	1.953
KG	m	19.78	0.222
GM_T	m	5.17	0.058
I_{xx}	kgm^2	7.6976E+10	13.7
I_{yy}	kgm^2	1.1889E+12	211.6
I_{zz}	kgm^2	1.2316E+12	219.2

2.2 TOWING TANK

The characteristics of the towing tank also determine the model test set-up. The dimensions of the towing tank (Table 2) allow the use of ship models with a length of typically 4 m. The particulars and possibilities of the towing tank have been extensively described in [6]. In captive mode the ship model can be positioned in the three horizontal degrees of freedom (surge, sway and yaw) with roll fixed or free and heave and pitch always free. Roll was fixed during the tests.

Table 2. Main dimensions of the towing tank at FHR

Total length	87.5 m
Effective length	68.0 m
Width	7.0 m
Maximum water depth	0.5 m
Length of ship models	3.5 to 4.5 m

2.3 REFERENCE AXIS SYSTEMS

In Figure 1, Figure 2 and Figure 3 three rectangular and right-handed coordinate systems are presented. $O_0x_0y_0z_0$ is the earth-bound reference system of the towing tank. The vertical O_0z_0-axis points downwards, while the horizontal O_0x_0- and O_0y_0-axes are located at the free water surface at rest. $O_0x_0z_0$ is the longitudinal vertical symmetry plane of the towing tank.

Oxyz is a ship-bound coordinate system: the origin O is located at the intersection of the midship's section (at ½ L_{PP} fore of AP and ½ L_{PP} aft of FP) Oyz, the ship's vertical longitudinal plane of symmetry Oxz and the waterline Oxy at rest. The orientations of the positive coordinate axes are directed from stern to bow for the longitudinal axis Ox, towards starboard for the transversal axis Oy and from the waterline towards the keel for the Oz-axis. For a right-handed axis system looking in the positive direction of each axis, the rotation angles are positive clockwise in common science definition.

O'x'y'z' is a horizontal-bound towing carriage coordinate system with origin O' that does not change with heave, pitch nor roll motions of the ship; as a result, O'x'y' always remains horizontal. At rest, Oxyz and O'x'y'z' coincide. O'x'y'z' is used during testing and thus also during modelling the ship hydrodynamics based upon model tests.

For clarification the body Oz-axis in Figure 2 is rotated with θ (Oxz-plane) and in Figure 3 with φ (Oyz-plane) with respect to the axis O_0z_0 or the towing carriage axis O'z'. As mentioned above, during the benchmark tests the roll angle φ was kept fixed at 0 deg.

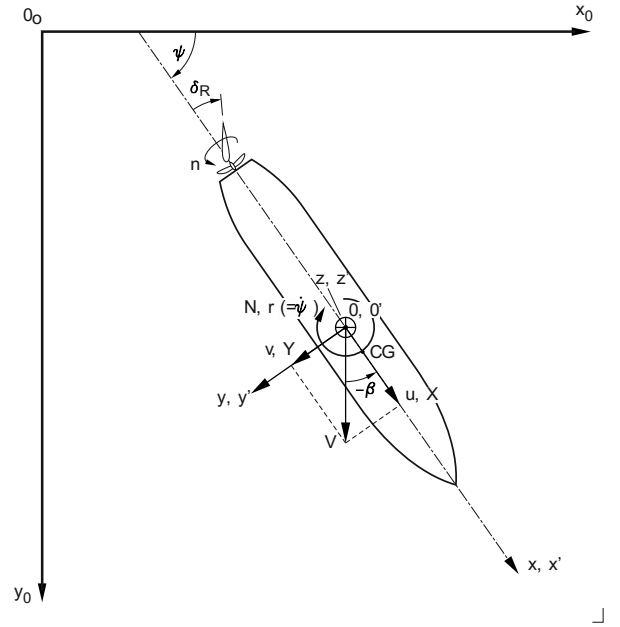

Figure 1. Ship- and earth-bound (towing tank) coordinate system: projection on the $O_0x_0y_0$ plane

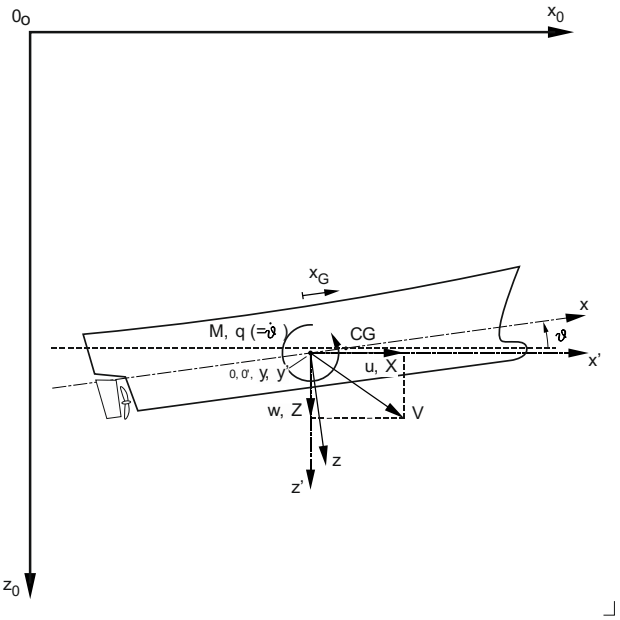

Figure 2. Ship- and earth-bound (towing tank) coordinate system: projection on the $O_0x_0z_0$ plane

2.4 ENVIRONMENTAL CONDITION

Although the DTC has been tested at the maximal possible water depth for free-running tests in the towing tank of FHR (which is 200% of the draft) and in a shallow water depth corresponding to 120% of the draft, only test results with the shallow water condition, 20% UKC, will be reported and used for the benchmark data. At this UKC, the water depth is 17.4 m at full scale and 0.195 m at model scale. The tests were conducted in still water.

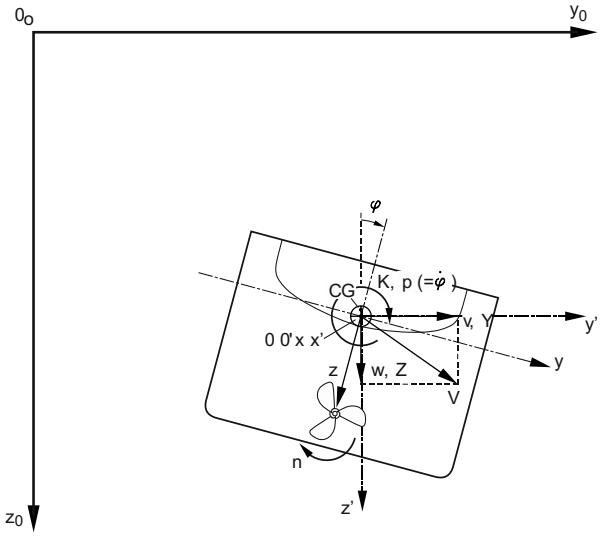

Figure 3. Ship- and earth-bound (towing tank) coordinate system: projection on the $O_0y_0z_0$ plane

2.5 MODEL TEST PROGRAM

The benchmark data are harmonic yaw and harmonic sway tests with the bare hull of the DTC. The ship model executes a pure sway motion with a prescribed sway amplitude and test period during the harmonic sway test. During the harmonic yaw test the ship model executes a pure yaw motion with a chosen yaw amplitude and test period. The ship model has a zero drift angle during the harmonic yaw tests. During both types of tests, the longitudinal component *u* is kept at a constant value.

Tests have also been executed with the appended hull at zero propeller rate and at the model self-propulsion point. Other test types, such as stationary tests at constant speed with or without drift and without yaw, are added as a reference to illustrate the dependence of the test type and kinematical test parameters. These tests are only reported to frame the benchmark data in a broader test matrix.

Table 3. Tested forward speeds

Full scale speed (knots)	Model speed (m/s)	$Fr = \frac{V}{\sqrt{gLpp}}$	$Fr_h = \frac{V}{\sqrt{gh}}$	Fr_h/Fr_{crit}
11	0.599	0.096	0.433	0.63
16	0.872	0.139	0.630	0.91

The selected tests are executed according to full scale ship speeds of 11 and 16 knots which correspond to Froude numbers Fr (based upon the ship length L_{PP}) of 0.096 and 0.139 (Table 3). While these speeds can be considered as moderate for a container carrier at full sea, they are in the higher range for the 20% UKC environmental condition, taking account of the corresponding Froude depth numbers Fr_h of 0.43 and 0.63, as displayed in Table 3. Apparently, the highest test speed comes close to the critical speed ("Schijf speed", see [8]), which takes a value of 0.95 m/s at model scale (17.4 knots at full scale):

$$Fr_{crit} = \left(2\sin\left(\frac{Arcsin\left(1-\frac{A_M}{\Omega}\right)}{3}\right)\right)^{\frac{3}{2}} \quad (1)$$

The ratio of the highest test speed and this critical speed is 91%, which is larger than the 84% cut-off value for subcritical speeds as determined in [9].

2.6 MEASUREMENTS

The results of the sinkages are presented as a mean running sinkage z_{VM} and trim. The trim is positive bow up and the sinkage is positive downwards. Sinkage is presented as the vertical displacement at the midship position. The trim is presented as the difference in vertical position at the fore and aft perpendicular, made non-dimensional with the length between perpendiculars. The sinkages at the fore and aft perpendicular are not shown to reduce the number of derived values in this paper but can nevertheless be calculated from the mean sinkage and trim.

The forces and moments measured in the horizontal-bound towing carriage coordinate system have contributions of the velocity and acceleration dependent parts. The longitudinal force X is pure resistance for the bare hull, and oscillates with the harmonic motion as do the lateral force Y, the yaw moment N and the roll moment K.

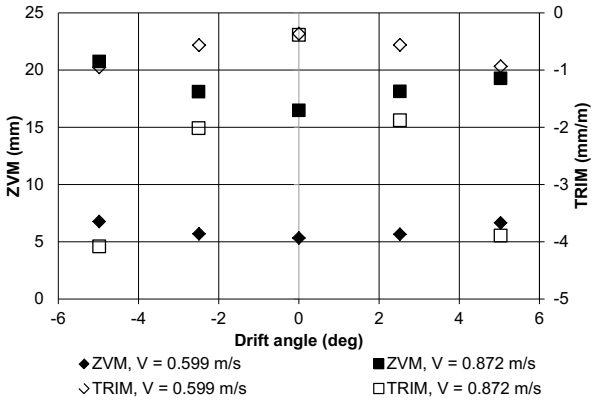

Figure 4. Mean sinkage and trim at stationary tests with the bare hull (V = model speed)

3 STATIONARY TEST DATA

Stationary tests have been executed at the same two Froude numbers as mentioned in section 2.5 with and without drift angle. The results for the mean sinkage and the trim are shown in Figure 4 for the bare hull and in Figure 5 for the appended hull (propeller and rudder attached) with zero propeller rate and according to self-propulsion. The following conclusions can be summarised based on Figure 4:

- The mean sinkage at Fr = 0.096 and zero drift angle is 5 mm.

- The mean sinkage at Fr = 0.139 and zero drift angle is 16.5 mm. The sinkage increases with drift and reaches values of 19.3 mm and 20.7 mm, for positive and negative drift angles, respectively.
- The trim is always negative or thus bow down for both Froude numbers and increases considerably (more negative values) with increasing drift (for example a value of approximately -4 mm/m at +/- 5 degrees drift for the largest Fr).

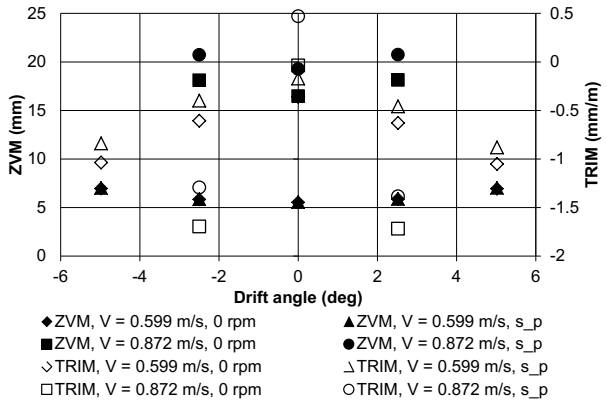

Figure 5. Mean sinkage and trim at stationary tests, appended hull, 0 rpm and model self-propulsion point (s_p)

Some differences between the results for the appended (Figure 5) and the bare hull can be observed:

- The +/- 5 degrees drift for the largest Fr is not carried out with the appended hull.
- Compared to tests at zero propeller rate, tests at the model self-propulsion points, generate higher values for the mean sinkage and more positive values for the trim.

4 BENCHMARK DATA

The harmonic yaw and sway tests with bare hull are referenced with 2016 as prefix (Table 4). The test names differ according to the test conditions:

- harmonic yaw or sway;
- model speed 0.599 m/s or 0.872 m/s;
- test type specific parameters (Table 5 and Table 6).

Table 4. Test names and general parameters of bare hull tests

	Type	u	v_A	r_A
Test name		(m/s)	(m/s)	(deg/s)
2016_A	Yaw	0.599	0	3.8
2016_B	Yaw	0.872	0	3.8
2016_C	Sway	0.599	0.063	0
2016_D	Sway	0.872	0.063	0

4.1 HARMONIC YAW TEST

The harmonic yaw test parameters are summarised in Table 5. During this type of test, the ship's longitudinal speed component u takes a constant value, while the lateral speed component v is equal to zero; therefore, the drift angle is zero. The heading is varying harmonically as a function of time with a large yaw amplitude ψ_A of 15 degrees, equation (2).

$$\Psi(t+\Delta t) = \Psi(t) - \Psi_A \frac{2\pi}{T} \sin\left[\frac{2\pi(t-t_{harm})}{T}\right] \Delta t \qquad (2)$$

The course / yaw angle change during the tests at both ship velocities are presented in Figure 6 as function of the longitudinal position in the towing tank. This position gives a time dependence taking into account the constant longitudinal velocity component u.

Table 5. Test parameters of harmonic yaw tests

	u	v	Ψ_A	T
Test name	(m/s)	(m/s)	(deg)	(s)
2016_A	0.599	0	15	25
2016_B	0.872	0	15	25

The following important conclusions can be made:

- Considering the entire harmonic test run the influence of the harmonic varying course, rate of turn and yaw acceleration on the mean sinkage and trim are minor.
- In the first half period of the harmonic yaw test the mean sinkage increases considerably, especially at the largest Froude number. The trim is small, positive (bow up) at the start of the test (after the acceleration phase) and negative (bow down) while the harmonic yaw test is proceeding.

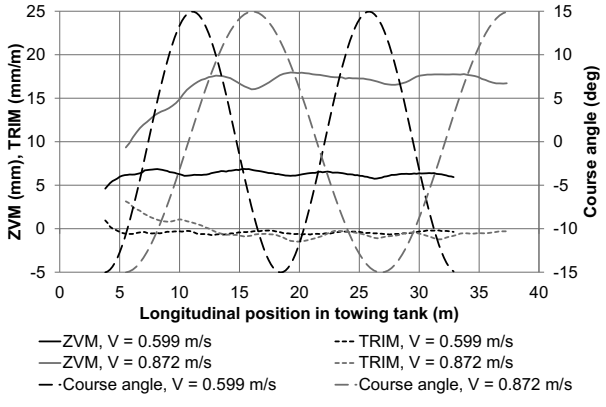

Figure 6. Time series for mean sinkage and trim at harmonic yaw

As the influence of the harmonic yaw motion on the sinkage is small, the values, once a kind of regime in oscillation is obtained after the acceleration phase, could be compared with stationary tests.

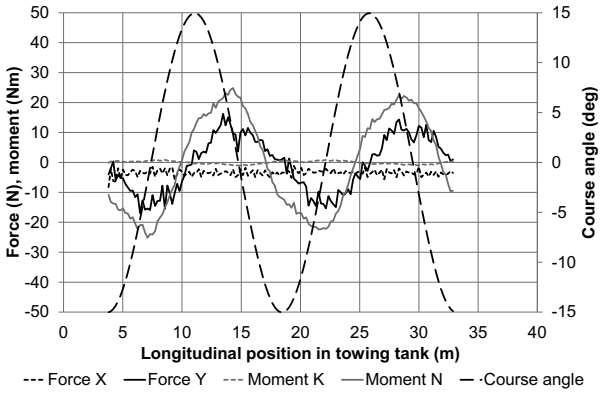

Figure 7. Time series for forces and moments at harmonic yaw and model speed 0.599 m/s

The measured forces and moments are shown in Figure 7 for Fr = 0.096 and in Figure 8 for Fr = 0.139. The longitudinal force X (resistance for bare hull) and the roll moment K have small values, while the lateral force Y and the yaw moment N clearly oscillate with the harmonic motion. Nevertheless, no stable oscillatory force and moment are measured especially for the largest Froude number, so that a Fourier analysis is disregarded. For the lateral force, in particular, the positive peak value, running at the larger velocity, has a significantly larger magnitude compared to the negative peak value. For the yaw moment, on the other hand, the opposite is observed. At maximum yaw angle / yaw acceleration, the lateral force and moment cross the zero ordinate line, so that maximum forces and moments are measured around maximum yaw velocity.

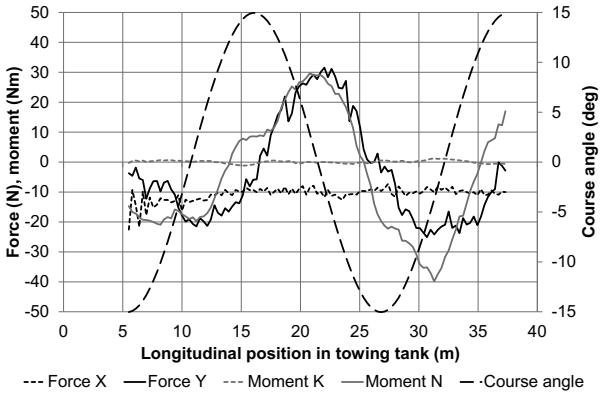

Figure 8. Time series for forces and moments at harmonic yaw and model speed 0.872 m/s

The resulting graphs for sinkages, forces and moment of each benchmark harmonic yaw test are repeated in full form in Appendix 1.

4.2 HARMONIC SWAY TEST

During harmonic sway tests, the ship's longitudinal speed component u takes a constant value, while the lateral speed component v oscillates harmonically as a function of time. The heading is constant and, hence, the rate of turn is zero during the test.

$$y_0(t) = y_{0,A}\cos\frac{2\pi(t-t_{harm})}{T} \quad (2)$$

The harmonic sway tests are summarised in Table 6.

Table 6. Test parameters of harmonic sway tests

Test name	u (m/s)	v_A (m/s)	$y_{0,A}$ (m)	T (s)	β_A (deg)
2016_C	0.599	0.063	0.2	20	6.0
2016_D	0.872	0.063	0.2	20	4.1

Sway tests with small sway amplitudes are chosen as in shallow water this results in values for the acceleration dependent derivatives which are less sensitive to the oscillation frequency [7].

The mean sinkage and trim are presented in Figure 9 for the tests at 11 and 16 knots full scale. Even for the lower velocity a clear oscillation in the time series for sinkage and trim occurs. Nevertheless at the higher Froude number 0.139 the magnitude of the oscillating sinkage and trim gradually increases; no steady oscillation is reached before the end of the test run.

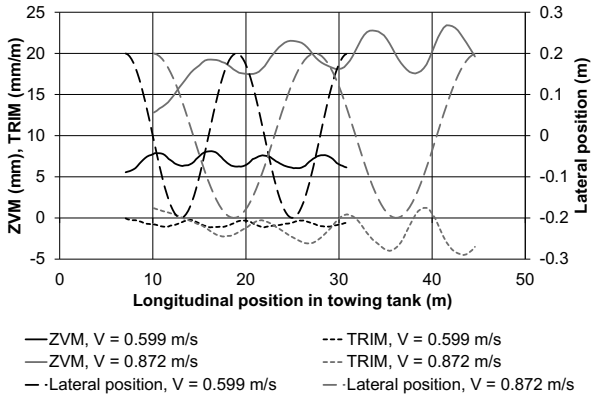

Figure 9. Time series for mean sinkage and trim at harmonic sway

The following important conclusions can be made:

- The peak values of the sinkage and trim occur at non-zero lateral position or thus at a combined non-zero sway velocity and sway acceleration.
- The mean sinkage and trim run in phase so that a maximum sinkage corresponds to a maximum trim magnitude.
- The trim is generally negative and thus bow down.
- For the test run at Fr 0.139 the critical velocity is almost reached which gives an increasing amplitude of the mean sinkage and the trim. Compared to the harmonic yaw test where there is almost no influence of the critical velocity and a mean sinkage of 16 to 17 mm is measured with a trim of -1 to -2 mm/m, for the harmonic sway test the mean sinkage reaches values of 18 to 23 mm (minimum and maximum) at the last

cycle and the trim oscillates between -4.5 and +1.5 mm/m.

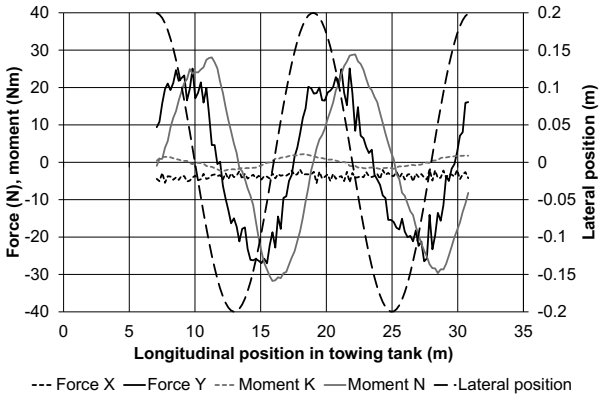

Figure 10. Time series for forces and moments at harmonic sway and model speed 0.599 m/s

The measured forces and moments are shown in Figure 10 for Fr = 0.096 and Figure 11 for Fr = 0.139. The longitudinal force X act similar as the same force during the harmonic yaw tests.
The roll moment K oscillates considerably more than during the harmonic yaw test although the values remain small.
The lateral force Y and the yaw moment N have a stable oscillating pattern at Fr = 0.096 but increase while the test is running with high maximum values at Fr = 0.139 (minimum value lower than -100 Nm). The critical velocity influences the test sequence.

At Fr = 0.096 an peak value for the yaw moment is measured when the ship is at the middle of the tank on the x_0 axis which means that the sway motion and sway acceleration are zero. Zero-crossing of the lateral force occurs at a combined non-zero sway velocity and acceleration.

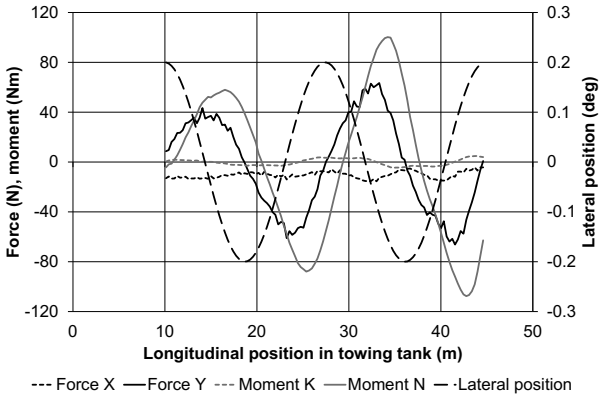

Figure 11. Time series for forces and moments at harmonic sway and model speed 0.872 m/s

The resulting graphs for sinkages, forces and moment of each benchmark harmonic sway test are repeated in full form in Appendix 2.

4.3 COMPARISON WITH STATIONARY TESTS

Comparing the values for sinkage and trim between stationary and harmonic tests, the following conclusions can be made:

- The mean sinkage at Fr = 0.096 and zero drift angle for stationary tests (value of 5 mm) corresponds to the starting value measured at the first period of the harmonic yaw and sway tests. For both yaw and sway tests the mean sinkage then gradually increases to a higher value.
- The mean sinkage at Fr = 0.139 and zero drift angle for stationary tests (value of 16.5 mm) corresponds to the mean value over the complete harmonic yaw test and the minimum value of the harmonic sway test. The sinkage increases with drift and reaches values of 19.3 mm and 20.7 mm. These values are still lower than the values measured during the harmonic sway tests with a maximum drift angle of 4.1 degrees at Fr = 0.139.

5 HARMONIC TEST DATA WITH APPENDED HULL

5.1 HARMONIC YAW TEST

The time series of mean sinkage and trim are shown in Figure 12 for the harmonic yaw tests at both Froude numbers with the fully appended hull and zero propeller rate. The differences with Figure 6 are minor.

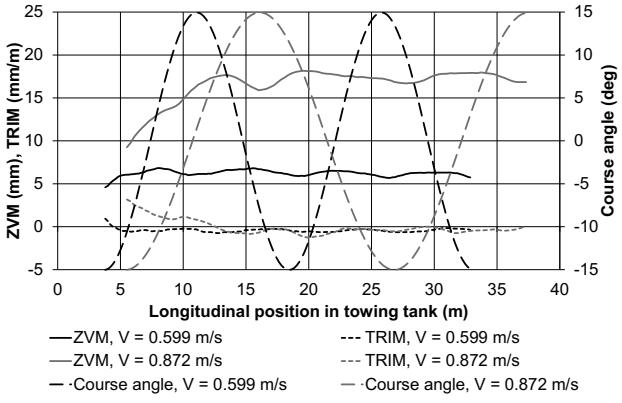

Figure 12. Mean sinkage and trim at harmonic yaw tests, appended hull - 0 rpm

5.2 HARMONIC SWAY TEST

The harmonic sway tests executed with the appended hull are presented in Figure 13. The differences at zero propeller rate are again minor compared to the bare hull results in Figure 9 but the mean sinkage at model speed 0.872 m/s shows more steep variations in the maximum sinkage range. The presence of the propeller and rudder influences the pattern of the time series. If the propeller is running at the model self-propulsion point, slightly

higher sinkages are measured and a more regular oscillation pattern is observed.

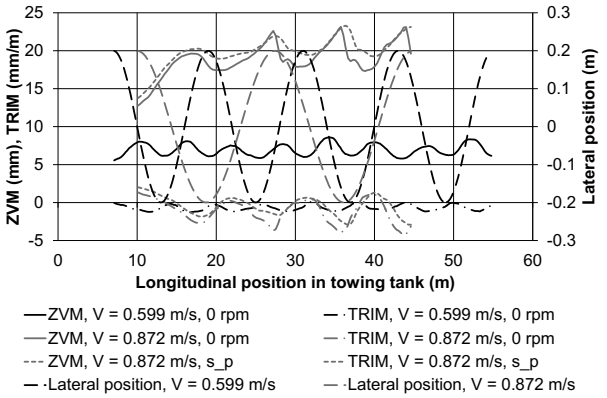

Figure 13. Time series for mean sinkage and trim at harmonic sway, appended hull, 0 rpm and model self-propulsion point

6 CONCLUSIONS

This paper introduces four benchmark tests carried out with the DTC container carrier at 20% under keel clearance. Two speeds were selected, corresponding to 11 and 16 knots full scale, at which both harmonic yaw tests and harmonic sway tests were carried out. The tests at 11 knots show a more consistent behaviour. At 16 knots nearly supercritical effects start to occur in the towing tank.

The data not only present the sinkage and trim during the four benchmark data tests but also the forces and moments. The test results are further considered in a broader test matrix comparing the bare hull benchmark tests with tests executed with the appended hull at zero propeller rate or self-propulsion. Stationary test results additionally show the reference data values for the harmonic test type time series.

The benchmark data are open and digitally available and can be ordered on request at info@shallowwater.be.

7 ACKNOWLEDGEMENTS

The authors would like to thank the SHOPERA consortium for the permission to publish the data and the Flemish Government for the financial support for the maintenance and operation of the Towing Tank for Manoeuvres in Shallow Water (cooperation Flanders Hydraulics Research – Ghent University).

8 REFERENCES

1. Eloot, K.; Vantorre, M. (editors)(2009). *International Conference on Ship Manoeuvring in Shallow and Confined Water: Bank Effects (Antwerp, May 2009)*. The Royal Institution of Naval Architects, London.

2. Pettersen, B.; Berg, T.E.; Eloot, K.; Vantorre, M. (editors)(2011). *2nd International Conference on Ship Manoeuvring in Shallow and Confined Water: Ship to Ship Interaction (May 18-20, 2011, Trondheim, Norway)*. The Royal Institution of Naval Architects, London.

3. Eloot, K.; Vantorre, M.; Delefortrie, G.; Lataire, E.; Candries, M. (editors)(2013). *3rd International Conference on Ship Manoeuvring in Shallow and Confined Water: Ship Behaviour in Locks (June 3-5, 2013, Ghent, Belgium)*. The Royal Institution of Naval Architects, London.

4. SHOPERA "Energy Efficient Safe Ship Operation" www.shopera.org

5. El Moctar, O.; Shigunov, V.; Zorn, T. (2012). Duisburg Test Case: Post-Panamax Container Ship for Benchmarking. *Ship Technology Research*, Schiffstechnik Vol. 59, No. 3.

6. Van Kerkhove, G.; Vantorre, M.; Delefortrie, G. (2009). Advanced Model Testing Techniques for Ship Behaviour in Shallow and Confined Water, *Proceedings of AMT*, Nantes, France.

7. Eloot, K. (2006). Selection, Experimental Determination and Evaluation of a Mathematical Model for Ship Manoeuvring in Shallow Water, *PhD thesis*, Ghent University, Ghent.

8. Briggs, M.; Vantorre, M.; Uliczka, K.; Debaillon, P. (2009). Prediction of Squat for Underkeel Clearance, *Handbook of Coastal and Ocean Engineering*. (Ed.: YOUNG, C.K). World Scientific, pp. 723–774.

9. Lataire, E. (2014). Experiment Based Mathematical Modelling of Ship-Bank Interaction, *PhD thesis*, Ghent University, Ghent.

9 AUTHORS' BIOGRAPHIES

Katrien Eloot holds the current position of senior expert at Flanders Hydraulics Research, Flemish Government and guest professor at Ghent University. She is responsible for simulation studies and fundamental research related to ship hydrodynamics and especially manoeuvring in shallow and confined water. She is member of PIANC InCom Working Group 141 and AVT-183 and AVT-216 of NATO STO.

Marc Vantorre, naval architect, is full senior professor of marine hydrodynamics and head of the Maritime Technology Division at Ghent University, Belgium. His research focuses on ship behaviour in shallow and confined waters, mainly in close co-operation with Flanders Hydraulics Research in Antwerp. He is member of PIANC Working Groups and former member of the ITTC Manoeuvring Committee.

Guillaume Delefortrie is expert nautical research at Flanders Hydraulics Research. He is in charge of the research in the Towing Tank for Manoeuvres in Shallow Water (cooperation Flanders Hydraulics Research – Ghent University) and is secretary of the 27th and 28th ITTC Manoeuvring Committee.

Evert Lataire is currently assistant at the Maritime Technology Division of Ghent University. He has made a PhD on the topic of bank effects mainly based upon model tests carried out in the shallow water towing tank of FHR. His ten year experience includes research on ship manoeuvring in shallow and confined water such as ship-ship interaction, ship-bottom interaction and ship-bank interaction.

Appendix 1 Benchmark harmonic yaw test

2016_A

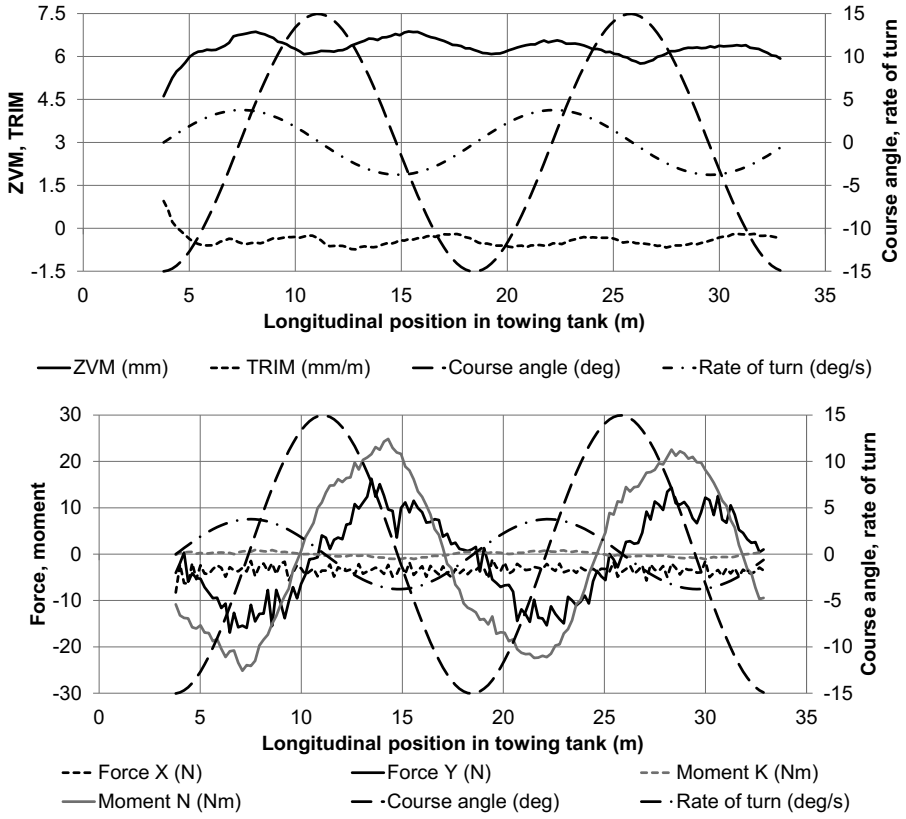

2016_B

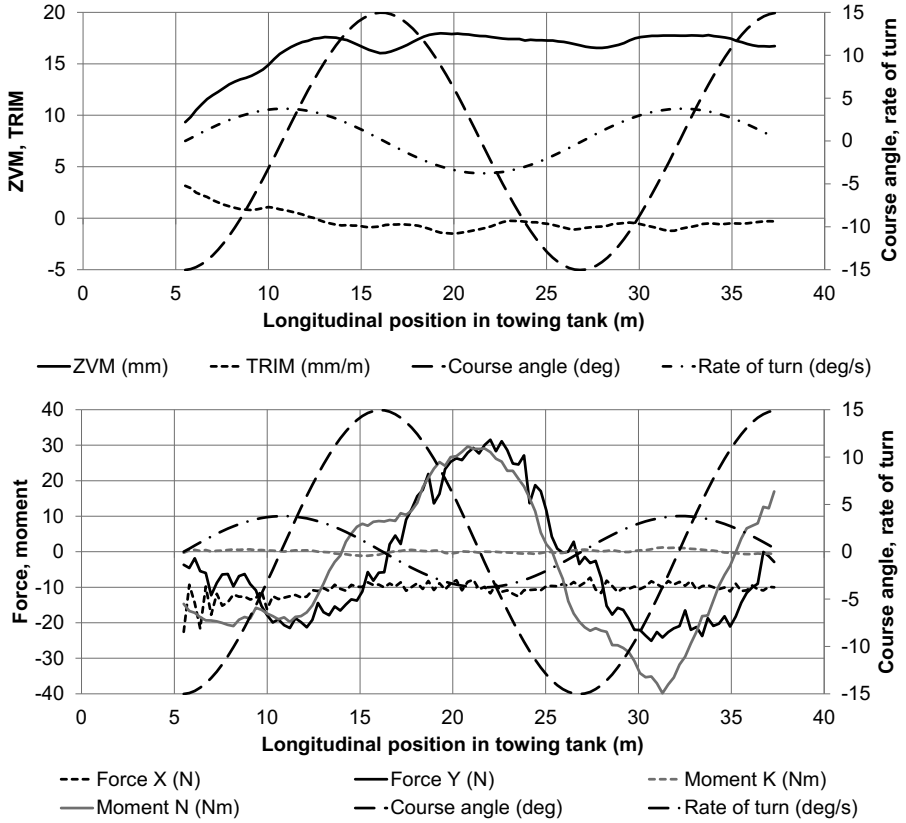

Appendix 2 Benchmark harmonic sway test

2016_C

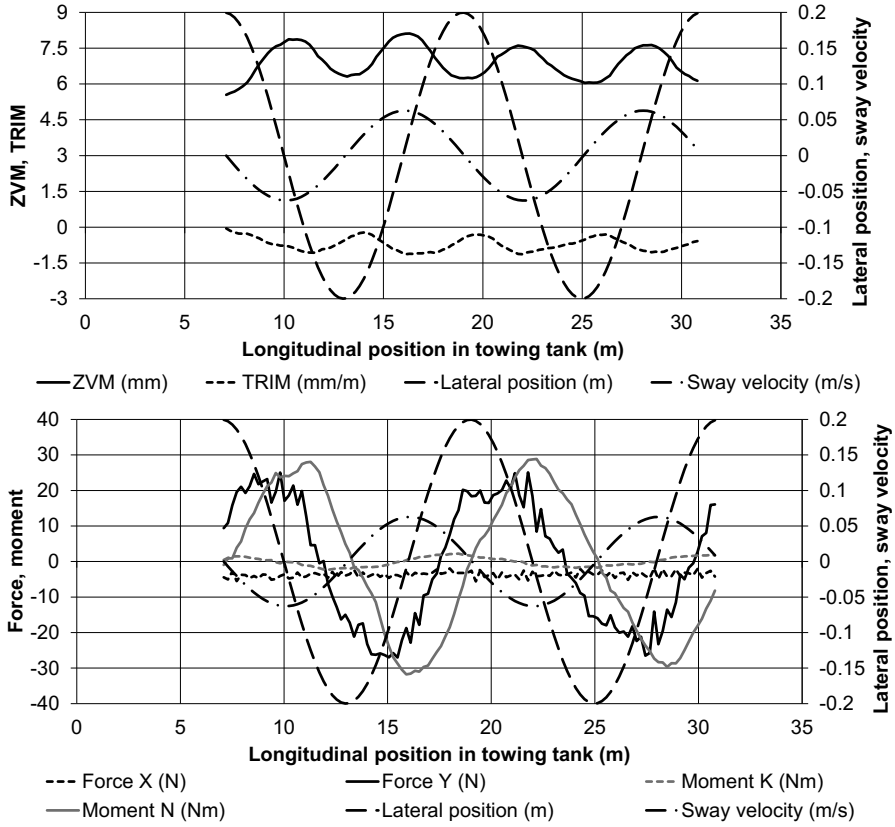

2016_D

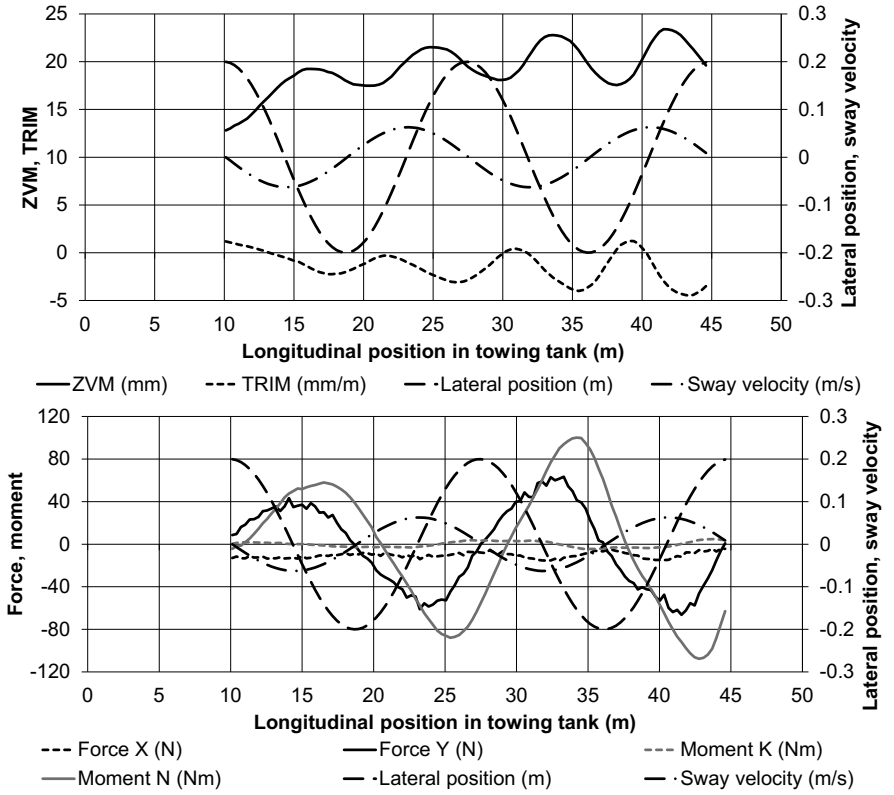

4th MASHCON, Hamburg - Uliczka et al. (eds) - © Bundesanstalt für Wasserbau ISBN 978-3-939230-38-0 (Online)
DOI: 10.18451/978-3-939230-38-0_30

MANOEUVRING WITH NEGATIVE UNDERKEEL CLEARANCE: 2ND FULL SCALE FIELD TEST IN THE PORT OF DELFZIJL

R Barth and **C J A W van der Made,** Wiertsema & Partners, The Netherlands
L Bourgonjen and **J van Dijken,** Groningen Seaports, The Netherlands
M Vantorre, Ghent University, Belgium
J Verwilligen, Flanders Hydraulics Research, Belgium

SUMMARY

Wiertsema & Partners (Short: W&P) together with Flanders Hydraulics Research (short: FHR) investigated on behalf of Groningen Seaports (Short: GSP) the influence on the manoeuvrability of a vessel when sailing with a small and negative under keel clearance in the harbour of Delfzijl by performing a full scale field test. The full scale field test was performed in May 2015 during spring tide corresponding to a negative under keel clearance up to -5% UKC at low tide. Several trials were performed during the full scale field test in the harbour entrance channel with different under keel clearances and changing from going inbound to outbound. The paper gives a summary of the full scale field test, used measuring techniques for qualifying the mud layer, an overview of interactions between involved parties and the results.

NOMENCLATURE

cm	Centimetre
FHR	Flanders Hydraulic Research
GSP	Groningen Seaports
kHz	Kilohertz
kn	Knots (nautical speed)
KSN	Keep Sediments Navigable
N.A.P.	Normaal Amsterdams Peil (reference height)
m	Meter
Pa.s	Pascal second
UKC	Under Keel Clearance
W&P	Wiertsema & Partners
UKC210kHz	UKC with respect to 210kHz based on survey of 2nd of May 2015
UKC33kHz	UKC with respect to 33kHz based on survey of 2nd of May 2015

1 INTRODUCTION

The field test is part of the overall project 'Sustainable Port Management' for the port of Delfzijl.

One of the primary goals of the project Sustainable Port Management is to investigate whether it is possible to optimize the tidal window of the port without a significant increase of the maintenance dredging volumes. One of the realistic approaches to increase the tidal window of the port is to implement the Keep Sediments Navigable (short: KSN) method. This method has already been successfully applied in the port of Emden.

According to PIANC [1] the nautical depth can be defined as 'the level where physical characteristics of the bottom reach a critical limit beyond which contact with a vessel's keel causes either damage or unacceptable effects on controllability and manoeuvrability'. Accordingly, nautical depth can be defined as: the instantaneous and local vertical distance between the nautical bottom and the undisturbed free water surface.

The project 'Sustainable Port Management' for the ports of Delfzijl and Harlingen is conducted in four separate phases. The first three phases were executed from 2010 until 2013. In 2013 a full scale field test was executed consisting of a sailing trial with the vessel 'CSL Rhine' and dredging trials using the dredgers 'Meerval' and 'Airset'. The dredger "Meerval" is also used in the port of Emden to implement the KSN method [2].

Based on the feasibility study in the first phase of the project it was concluded that, based on the mud conditions at that time, it was realistic to implement the KSN-methodology for both ports. To further test the feasibility of the KSN-methodology computer simulations were carried out during the second phase of the project. For these simulations, the lay-out of the port of Delfzijl including the mud and current conditions were implemented into a ship manoeuvring simulator using the expertise and facilities of FHR in Antwerp and Ghent University (Maritime Technology Division).

The influence of sailing at very low and even negative Under Keel Clearance (short: UKC) with respect to the mud layer on the inbound and outbound sailing to/from the port of Delfzijl were investigated in a full mission bridge simulator. During these tests the thickness of the mud layer and the mud density were varied systematically. In order to perform simulations as realistic as possible local pilots, experienced with the port of Delfzijl, did participate in the study. The investigations carried out during the second phase of the project confirmed that it was realistic to implement the KSN-methodology for the port of Delfzijl.

The third phase of the project was a full scale field test. The test was executed in the port of Delfzijl. The first full scale field trial with the CSL Rhine was carried out successfully and provided sufficient reference data for further field trials. The data gathered was sufficient to

make recommendations for the next field trial to determine the nautical depth under present dredging practices.

The results of the simulation studies and the field trial were presented to an international audience on the occasion of the 33th PIANC Congress in San Francisco (USA) [3]. Referring to comprehensive model test studies performed at FHR [5], the major impact of the presence of fluid mud in situations with a relatively high UKC (10% - 20%) with respect to the mud-water interface on the manoeuvrability and propulsion of the vessel is due to the hindered flow towards the propeller and rudder. An important phenomenon in this respect is the internal wave which is generated by a sailing vessel in the mud-water interface in case of sediments with weak rheology , which appears to affect the ship's behaviour particularly in a speed range which corresponds to the speed applied in the entrance channel. Especially in case of rather thick mud layers, these phenomena appear to smoothen if the mud layer is penetrated by the ship's keel, which gives reason to a significant potential reduction of the UKC with respect to the mud-water interface.

Based on the results of the earlier simulation study and the field trial with the CSL Rhine it was thought acceptable to start with the second full scale field test.

The main aim of the field trials was verification of the simulator results by full scale field tests with an instrumented representative vessel with adjusted UKC conditions in agreement with the captain and the pilot. The tests were performed in the port of Delfzijl.

2 SECOND FULL SCALE FIELD TEST

2.1 FIELD TEST DESCRIPTION

The full scale field test was executed in the port of Delfzijl in the early morning from 05:38AM until 09:19AM on the 20th of May 2015. The dredger 'Geopotes 15' from Van Oord Nederland b.v. was used for the trial runs.

The second full scale field test consisted of four trial runs with the selected vessel. Each trial run was started at predefined tide levels in order to experience a wide range of UKC. These different departures are numbered, subsequently T0, T1, T3 and T4. Departure T0 is the reference measurement with an UKC_{Gross} >10% with respect to top fluid mud (210kHz). This condition corresponds to the actual accessibility regulation of the port. Departure T1 was executed before the low tide, T3 was executed at low tide and T4 after low tide.

During the departures, the vessel's behaviour (use of propeller, rudder, thruster and tugs including corresponding speeds and yaw velocities) was monitored and analysed in a similar manner as during the computer simulation runs (FHR) from the second phase of the project and the first full scale field test.

During the field trial an assisting tug from Wagenborg Shipping named the 'Waterstroom' was assisting the trials. The 'Waterstroom' has a maximum bollard pull of 60 ton. If necessary the tug would be attached to the aft of the vessel to mitigate any risk of an uncontrollable vessel.

Before the trials and after each run the in-situ density profiles of the fluid mud were measured at pre-defined locations with the support vessel 'Havenschap 1'. Multi beam surveys were performed from this before and after the field trial as well.

The planning for the field trial was based on the predicted astronomical tides supplied by the Dutch governmental organization Rijkswaterstaat.

2.2 TIME SCHEDULE

The different timings for the trial runs of the second full scale field test are presented in Table 1. Run T2 was scheduled in the first planning but during the kick-off meeting on 2015-05-19 this run was cancelled due to expected lack of time after run T1. Run T3 was scheduled at low tide and could therefore not be shifted.

Table 1. Time schedule trial runs

Run	Time	Trial run locations
T0	05:30AM – 06:15AM	B05 → B17
T1	06:15AM – 07:00AM	B08 ← B17
T3	08:05AM – 08:30AM	B08 → B17
T4	08:45AM – 09:25AM	B05 ← B17

2.3 LOCATION

The trial runs were executed in the area with a known amount of sediment (fluid and consolidated mud) which was from reference point B05 until B17 (Figure 2). This is a total length of approximately 3400 meters as can be seen in Figure 1.

Due to the low tide it was not possible to execute the trial runs over the total length of the entrance channel during all runs, as the normal applicable safety precaution in the port of Delfzijl of 10% UKC_{Gross} was maintained towards the hard soil (33kHz survey). This led to a shorter run for trial run T1 and T3 of around 2200 meters. In Figure 1 the track covered during the four trial runs is presented.

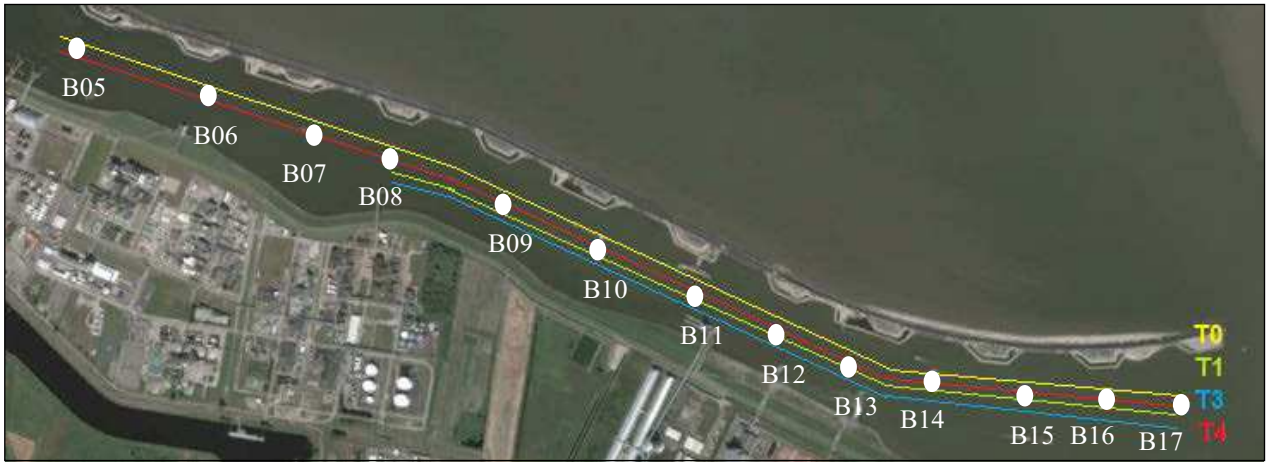

Figure 1. Location of the different trial runs (Source: Google Earth and W&P)

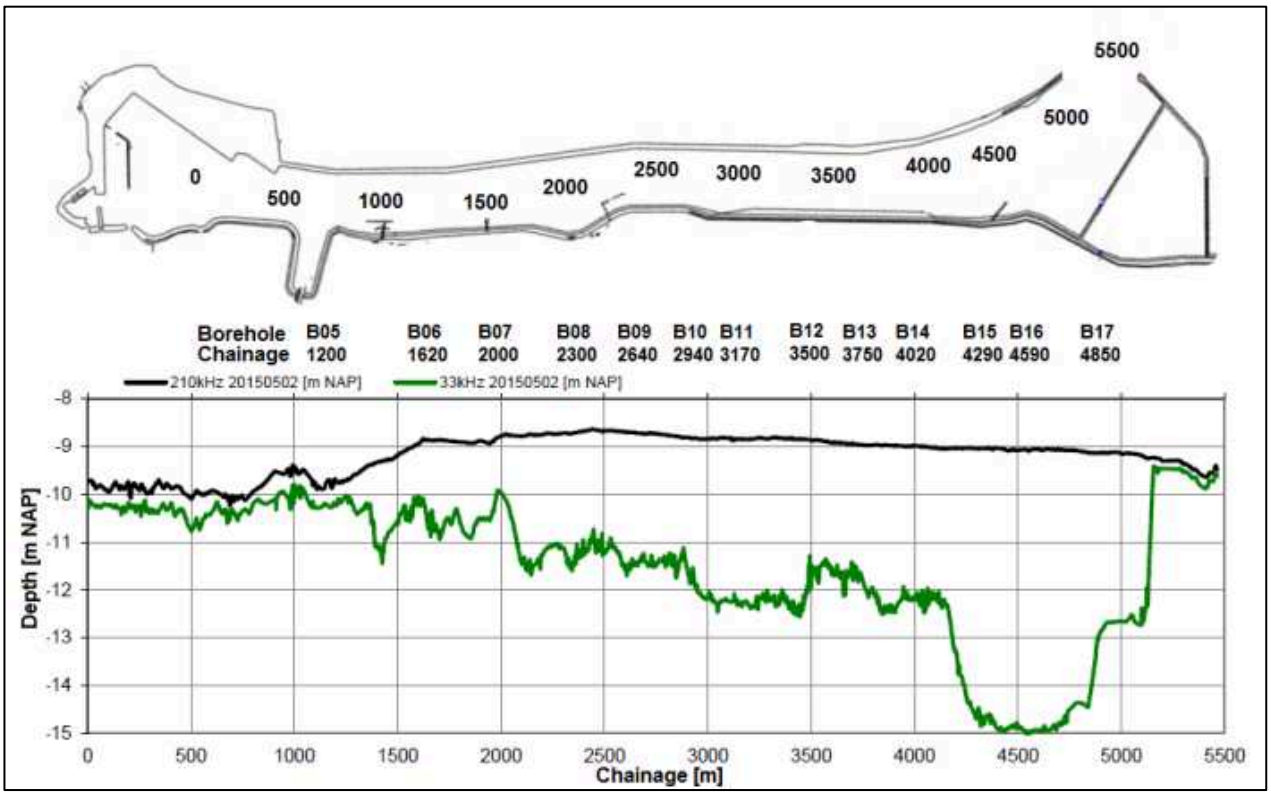

Figure 2. Location of the reference points on a longitudinal scale (source: FHR and W&P). The black line represents the 210 kHz reflection (top fluid mud), the green line in the bottom window represents the 33 kHz reflection (hard bottom).

2.4 VESSEL

During the simulation study a container carrying vessel was used.

For the second full scale field test it was preferred to monitor a vessel which has more or less equal dimensions as the vessel used for the simulation study. Although there is a difference between the vessels used in the simulation study and field test, the vessel used for the field test is representative for the port of Delfzijl. This is also confirmed by the pilot. All expected effects based on the simulation study were experienced during the field trial.

The second full scale field trial was executed with the 'Geopotes 15' from Van Oord Nederland. This vessel is a trailing suction hopper dredger and has the following main characteristics:

- Length 132 meter
- Width 23.6 meter
- Draft 7.4 meter (filled with water)
  9.40 meter (dredging mark)
- Propellers 2

During the trials the vessel was partially loaded with sand in the hopper, to ensure no water would flow out of the hopper and consequently changing the draft of the vessel.

3 RESULTS MEASUREMENTS

3.1 IN-SITU MEASUREMENTS

3.1 (a) Survey

Bathymetric survey was performed by GSP with the support vessel 'Havenschap 1'. The 'hard' soil can be surveyed with a 33kHz survey and the top of the fluid mud with a 210kHz survey. Several surveys were executed and presented in Table 2 and Figure 3.

Table 2. Bathymetric surveys

Date in May 2015	Survey
2nd	Multibeam 33kHz and 210kHz
20th (1 hr. before T0)	Multibeam 210kHz
20th (2 hrs. after T4)	Multibeam 210kHz
22nd	Multibeam 210kHz

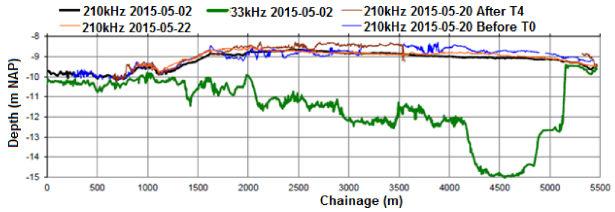

Figure 3. Longitudinal section and surveys executed in May 2015 (Source: FHR)

Figure 3 shows that the 210 kHz reflections on the day of the trials are at a higher position than the reflections measured on the 2nd and 22nd of May 2015. One possible explanation for the difference of the sediment thickness is the earlier passages of Geopotes 15. Since the differences in altitude can reach up to 0.7 m they have a significant impact on the UKC towards top sediment for a vessel with draft 7.4 m (see figure 4 for visualization). To illustrate the differences in UKC during the field test, the values of UKC_{Net} to the top of the sediment, were compared for a position halfway trial run T3, corresponding to different surveys carried out in May 2015:

- -4.6% based on survey 2nd of May 2015;
- -9.2% based on survey 20th of May 2015, prior to the test runs;
- -11.7% based on survey 20th of May 2015, after the test runs;
- -4.1% based on survey 22nd of May 2015.

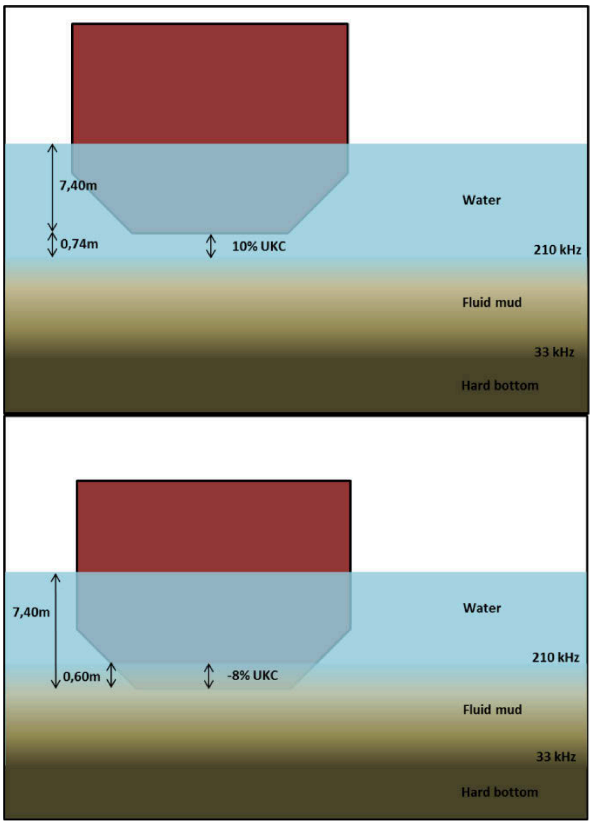

Figure 4. Schematic presentation of +10% UKC_{Gross} and -8% UKC_{Gross} conditions in respect to the 210 kHz reflection of the single beam measurements.

3.1 (b) Density profiles

The in-situ density profiles were measured on the 18th and 20th of May with the SoniDens. The SoniDens is an accurate piece of equipment for the measurement of the in-situ density of fluid mud (unconsolidated sediment).

3.1 (c) Sampling

On the 18th of May 2015 fluid mud samples were taken at 4 different locations with a Sludge Sampler (see figure 5).

The Sludge Sampler is a sampling tool for taking samples of the fluid mud layer which is present in the entrance channel of the Port of Delfzijl. The Sludge Sampler takes 11 samples over a height of 211cm. The samples were collected in jars with a volume of 720ml.

Figure 5. Taking fluid mud samples using the Sludge Sampler

3.1 (d) Water level

The water level during the trial runs at three different locations was measured with a Diver datalogger. The Diver datalogger measures the water pressure and temperature in time.

The Diver data loggers were situated along the entrance channel of the port of Delfzijl. During the tide the port is filled with seawater, which runs in and out via the entrance channel. Differences in water level height will occur due to the inflow and outflow of water in the entrance channel. Therefore three pressure sensors were installed along the route of the trial run to measure the exact water level.

Based on the measurements the uncertainty of the water level measurement was estimated at 8cm. This is an additional uncertainty of 1.1% in the determination of the UKC during the field runs.

3.1 (e) Wind

The average wind speed and direction was measured by Groningen Seaports with equipment installed permanently at the Diver 1 location in the entrance channel.

3.1 (f) Temperature air and water

The average air temperature was measured with a Baro Diver at diver 1 location in the entrance channel.

The water temperature was measured during the in-situ density profiles. The values are different per location and over depth. The average temperature for the brackish water in the port was between 8° and 12° Celsius.

3.1 (g) Maintenance dredging

The sediment in the entrance channel is conditioned by an air injection dredger called the 'Airset'. The Airset technique is presently used in Delfzijl for maintenance dredging. The conditioning of the mud is done during the outgoing tide from chainage 4500m towards 5500m.

3.2 LABORATORY MEASUREMENTS

3.2 (a) Samples

The samples were tested for physical and rheological properties in the laboratory of W&P in Tolbert (NL). The laboratory results were checked by the sediment laboratory of FHR. Below paragraphs describe the different tests and results.

Important for navigability at minimal or negative UKC is the resistance of the 'muddy sediment' against the vessel's movement. The resistance of 'muddy' sediment is generally shear stress dependent. Rheological properties to be tested regarding this resistance are the yield point and dynamic viscosity. The rheological properties differ over time and therefore tests were performed on samples after stirring and 2 days after stirring.

The rheological properties were determined with the Brookfield DV3T. The ratio of shear stress and shear rate of the dynamic viscosity and the yield stress is determined by applying the Bingham method [4] on the flow curve (shear rate against shear stress).

The wet and dry densities were determined for all fluid mud samples for which rheological tests were executed. The wet density was acquired by filling a ring with known volume (approximately 17 cm^3) with the fluid mud. The ring is weighted and the wet density is calculated. The dry density is acquired by drying this sample and weighing this again.

Average organic content of the fluid mud was 17.4% and average carbonate content was 9.15%.

4 RESULTS MONITORING VESSEL POSITIONS AND ORIENTATIONS

The vessel's positions and orientations during the field test were measured and processed in time series for each trial run. The evolution of the manoeuvrability of the vessel is described with the interaction between the fluid mud layer and the propeller.

The following items were monitored during the field test:

- The position of the vessel in six degrees of freedom,
- Rudder angles,
- Propeller pitch,
- Draft,
- Vertical position.

4.2 MONITORING EQUIPMENT

4.2 (a) Vessel positions in 6 degrees of freedom

The measuring equipment consists of a F185 positioning system from Coda Octopus (developed on behalf of FHR) which is placed inside a rigid housing with a span width of 2 meter. The raw data as well as the processed position, speed, and acceleration data is transmitted via Wi-Fi to a laptop situated on the bridge.

4.2 (b) Rudder angles

The evolution of the rudder angles during the field test is monitored by means of photo-cameras (1Hz) which capture the rudder angle indicator on the bridge of the vessel.

4.2 (c) Propeller pitch

The Geopotes 15 is equipped with two CPP (controllable pitch propeller) propellers. With CPP propellers the propulsion is realized and controlled by a variance in pitch of the propeller blades. The evolution of the propeller pitch is acquired via the datalogger of the vessel.

4.2 (d) Draft

In the datalogger the draft of the vessel, hopper volume and vessel speed was logged.

This draft measurement is based on pressure measurements in the hull. In the event that the vessel achieves an important speed through the water, the pressure around the body is influenced by the flow along the hull, and the depth measurement is therefore unreliable. The depth measurement therefore only delivers reliable values with negligible speed of the vessel. The static draft (draft at cruising speed equal to zero) varied during the trial run. The reason for this is that the water volume in the hopper tanks leaked and was replenished in order to compensate so that the mass of the vessel (and hence the static draft) remained almost constant.

The periods during which trial runs were conducted (5h30 to 7h00 and 8h05 to 9h25) the drafts fore and aft deviate relatively little from 7.4 m (at around 10 centimetre). A deviation of 10 cm in static draft gives rise to a deviation in the UKC equal to 1.4%.

4.2 (e) Vertical position

The vertical position of the vessel is influenced by the vertical position of the reference point, the roll angle and trim angle. The static values of the roll angle (list) and trim angle were calculated as the average during the first part of the measurement when the vessel was not moving and did not use the propellers. The trim and roll angles varied little in this period.

Due to the variable static draft during the measurement campaign (due to a variable content of the hopper tanks) the squat of the vessel could not be accurately estimated.

Due to the uncertainty about the static drafts and water level measurements on one hand, and by the accurate determination of the vertical distance between the measuring point and vessel's keel on the other hand, the UKC is defined as the vertical distance between keel and bottom. This UKC corresponds to the so-called UKC_{Net}, while the UKC_{Gross} is reduced with the squat of the vessel. UKC_{Net} will have a lower value than UKC_{Gross} (defined based on static draft), see figure 6.

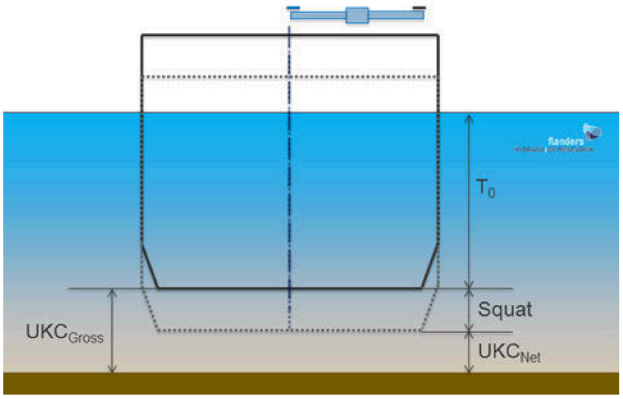

Figure 6. Definition of the UKC (Source: FHR).

5 ANALYSIS

5.1 MUD CHARACTERISTICS

5.1 (a) Physical properties

The average organic content of the fluid mud is 17.4%.

The average carbonate content is 9.1%.

The particle size distribution shows an average silt content of 34.7%.

5.1 (b) Rheological properties

The rheological properties of the fluid mud samples taken before the field test are compared to the previous investigations for this project and the ports of Emden, Rotterdam and Antwerp (Deurganck Dock).

The results of the rheological tests show the difference in characteristics directly after stirring and 2 days after stirring, see figure 7. As expected and found in previous investigations in Delfzijl the yield point was higher for the same density after 2 days. This is due to the thixotropic behaviour of the mud and its ability to regain strength after conditioning.

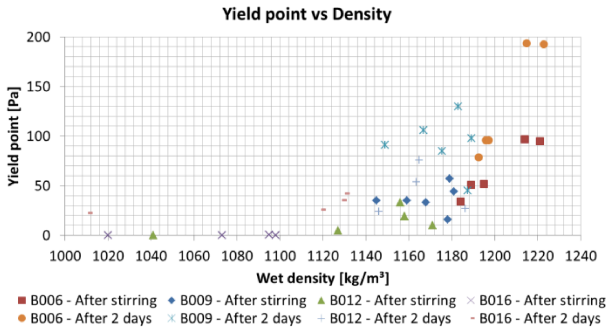

Figure 7. Yield point vs Density (Source: W&P).

Figure 7 shows a figure in which the yield point is presented against the measured density. The yield point increases with density for all samples taken over the length of the entrance channel.

The rheological properties can be positioned in between Rotterdam/Emden and Antwerp (Deurganck Dock). When the mud is conditioned (after stirring) it shows to be more fluid and tends towards behaviour similar to Emden port.

The wet density at the yield point threshold (defined in previous feasibility study at 100 Pa) is for the stirred mud around 1210 kg/m³ and for the unstirred mud after 2 days around 1150 kg/m³ based on the rheological tests performed over the length of the entrance channel.

The mud conditions used for the model tests (performed by FHR) during an earlier phase of the project are different from the conditions presented in this paper. The dynamic viscosity density combinations used during the model tests in Antwerp were as follows:

- Mud D, 1108 kg/m³, viscosity 0.03 Pa.s.
- Mud C, 1149 kg/m³, viscosity 0.06 Pa.s.
- Mud B, 1179 kg/m³, viscosity 0.10 Pa.s.
- Mud H, 1207 kg/m³, viscosity 0.19 Pa.s.

The dynamic viscosity of the samples taken during the field test are compared with the dynamic viscosities used with the model tests.

The dynamic viscosity results after stirring (conditioning) are closest to the model tests mud characteristics. The tests after 2 days give a higher result than after stirring for the same density.

During an earlier phase of the project the effect of temperature on the dynamic viscosity of the samples was investigated. Comparing these results with the current results, for the tests after stirring, it was concluded that the differences at the lower densities could not be explained by differences in temperature.

The dynamic viscosities at certain densities used for the model tests are lower than during the field tests. The effect on the ship's behaviour, however, is negligible because the viscosities are within the same range [6].

5.2 DENSITY PROFILES

The mud density profiles taken on the 18th of May before the trial runs were compared to the results of the samples taken with the Sludge Sampler. The densities determined in the laboratory are corresponding with the densities of the in-situ density profiles. No discrepancies were observed.

Based on the density profiles and 210kHz -33kHz survey data the test area is subdivided in three sections based on:

- Thickness of the mud layer;
- Intensity of maintenance dredging by the 'Airset'.

In all three sections (B05 until B07 and B08 until B14 and B15 until B17) of analysed density profiles a decrease in in-situ densities is observed below the top of the fluid mud layer (210 kHz) after trial runs T3 and T4, which could be explained due to the turbulence of the propeller which is in contact with the fluid mud layer. The influence by the propeller could reach several meters below the initial top of the fluid mud layer (210 kHz). The clear distinction of the top of the fluid mud layer is changed in an unclear density profile where the density gradually increases over depth.

In section 3 (B15 until B17) the fluid mud is conditioned by the 'Airset'. Lower initial densities were present, before trial runs took place, compared to the initial densities of section 1 (B05 until B07).

Section 2 has a clear difference between the initial densities and the densities after the trial runs. The dense fluid mud layer was clearly diluted and distributed over the depth.

The mud in section 1 was less than 1.8 meter thick and situated furthest away from the entrance of the channel. The initial profile shows a density which is clearly higher than the initial densities in section 2 and 3. The diluted fluid mud is seen at the same density as the other sections after trial runs T3 and T4.

The average density profiles between different measurements of section 2 are very clear (figure 8). The fluid mud is diluted roughly 3 times until around 2.5 meter below the 210kHz line. The arrows show the decrease in density below the 210kHz line and the increase in density above the 210kHz line.

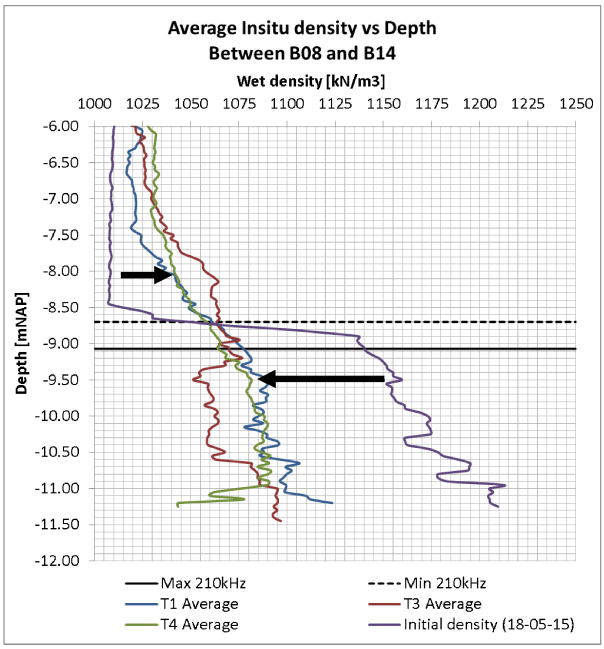

Figure 8. Average Insitu Density versus Depth for the area between B08 and B14.

5.3 MONITORING

The different runs during the field trial are analysed based on the vessel's manoeuvrability and presented in the following paragraphs. In this analysis the mud-water interface was assumed to correspond to the 210kHz survey performed on May 2nd. However, analysis of the density profiles (figure 8) revealed that as a result of consecutive distortions of the mud, the water-mud layer was not well defined during the full scale tests.

5.3 (a) Trial run T0

The results of the T0 run performed with the 'Geopotes 15' appear to be similar to those observed for the 'CSL Rhine' with respect to the evolution of the speed of the vessel. Regarding the manoeuvring behaviour it shows that the disturbance, caused by the sediment-run at $UKC210kHz_{Net}$ equal to approximately 14%, is less than it was on the 'CSL Rhine'. It can be stated that the 'Geopotes 15' is a suitable vessel to assess the impact of different soil conditions and under keel clearances on the vessel's behaviour.

The vessel's speed at a propeller pitch ratio equal to 41% was found to decrease from initial 5.5 kn (CPP at 40%) when the 'Geopotes 15' reached the sediment layer to 2.83 kn at the location of the sediment trap. The rudder angle required appeared to be limited to the execution of the manoeuvres above sediment. The largest rudder angles that had to be handled during the T0-run, can be ascribed to bank effects.

At the height of borehole location B10 a relatively large speed reduction occurred. The master and pilot also noticed vibrations in the vessel, although the strength of the vibrations was definitely not assessed as exceptional or alarming.

5.3 (b) Trial run T1

During sailing into the entrance channel a major rudder change and associated yaw movement must be realized when the vessel reaches the port mouth at relatively high speed. Trial run T1 shows that for UKC_{Gross} in accordance with the current accessibility criteria ($UKC210kHz_{Gross}$ > 10%) there is a significant influence of the sediment on the vessel's behaviour. For example, when the vessel was located above the sediment layer, despite the combination of propeller pitch ratios 41% with maximum rudder angles, the initial yaw speed dropped completely resulted in. Also the vessel's speed showed a significant drop over a relative short distance from 5kn to 2.14kn. Limited temporary increases in propeller pitch (up to a maximum of 78%) was found necessary in order to go through a favourable route.

After the required course change was realized in the port mouth, T1 showed a straight trajectory accompanied by small rudder angles and low yaw velocities. During this process the vessel's speed showed a minimum at the same location as was the case in the trial T0 (at borehole location B15).

The reduction of the sediment layer thickness and the reduction of UKC33kHz when sailing out from the sediment trap gave reason to a limited speed reduction. After this the ship speed stayed constant throughout seven minutes at approximately 2.3kn, although the $UKC210kHz_{Net}$ decreased from 11.3% to 7.2%. It was further noted that during the T0-trial run at the same straight trajectory the speed stagnated at 3.65kn and a $UKC210kHz_{Net}$ equal to 15%.
A further reduction of the $UKC210kHz_{Net}$ (from 7.2% to 5%) gave rise to an increase in vessel speed towards 2.87kn at the end of the trial run.

5.3 (c) Trial run T3

The trial run T3 performed with $UKC210kHz_{Net}$ ranging between -5% and +1% had a very good result. With the same propeller settings higher speeds could be achieved than in T0 and T1. This indicates an improved propeller efficiency with keel penetration compared to the case of UKC_{Net} towards top sediment of more than +7%. The manoeuvrability of the vessel was found similar to the manoeuvrability during the T0 trial run.

Remarkable during trial run T3 was that the ship speed seemed to be mainly influenced by the thickness of the sediment layer where thicker mud layers, despite the higher UKC to solid soil that accompanied it, gave reason for lower ship speeds.

Both captain and pilot were positively surprised by the vessel's behaviour during the trial conducted at T3 with

negative UKC_{Net}. Despite the realistic ship speed with moderate propeller use, the vessel showed good manoeuvrability and vessel's vibrations were limited.

5.3 (d) Trial run T4

Trial run T4 was accompanied by UKC_{Net} towards top sediment which reached small and alternating positive and negative values. At the start of the trial run an unfavourable manoeuvring behaviour seemed to occur above the sediment trap with $UKC210kHz_{Net}$ up to +3%. In the same area also the minimum ship speed in this field run occurred. During the further course of the trial run T4 the ship speed still showed different extremes which could always be related to bottom conditions.

Summarizing it could be stated that small negative $UKC210Khz_{Net}$ (in this trial to -2%) result in higher ship speeds and better manoeuvrability than small positive UKC_{Net} (in this trial run around +3%). Moreover the T4 trial run shows that with small positive UKC_{Net} with respect to the mud-water interface a larger thickness (in spite of the larger UKC with respect to the solid soil) corresponded to a less favourable manoeuvring behaviour.

6 CONCLUSIONS

Summarizing it can be stated that based on the trial runs an UKC_{Net} between 0% and roughly +14% (up to 20%) has a significant influence on the vessel's behaviour, see figure 9. It should be noted that the current minimum operational UKC_{Gross} of +10% is already in the unfavourable range. Based on the trial runs, no reduced manoeuvrability is expected for an UKC less than +10% to penetration in to the sediment up to an UKC of -5%.

From reference [6] it is known that the major impact of relatively high UKC (10% - 20%) on the manoeuvrability and propulsion of the vessel is due to the hindered flow to the propeller and rudder. Especially in cases where sediment layers are present with a weak rheology, a sailing vessel generates an internal wave at the interface of sediment and water. In a speed range of a vessel, corresponding to typical speeds in the entrance channel, a significant reduction of the clearance between the keel and the sediment water interface (see Figure 1) can be allowed without jeopardizing safe shipping. The field trials with the 'CSL Rhine' and the 'Geopotes 15' confirm these findings.

Although the full scale field tests reveal an important relation between the UKC with respect to the mud-water interface, the mud layer thickness and the ship behaviour on both manoeuvrability and ship speed (figure 9), it should be noticed that, as a result of consecutive disturbance of the mud layer, the mud-water interface was not clearly defined during the tests (figure 8). In order to validate the conclusions of the full scale field tests in case of an undisturbed mud layer, recommendation is made for a supplementary full scale test in this condition.

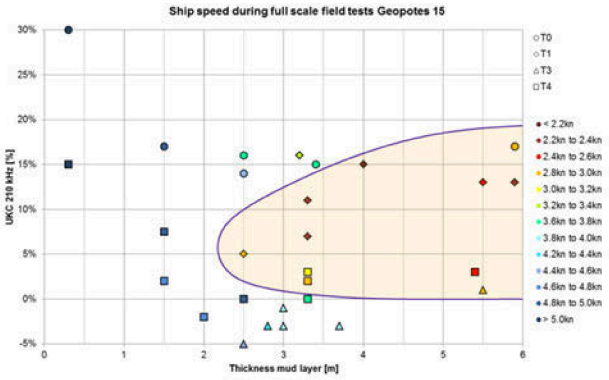

Figure 9. Summarizing graph of the evolution of the speed of the 'Geopotes 15' in function of the sediment layer thickness and the under keel clearance to the top of the fluid mud layer (source FHR).

7 REFERENCES

1. PIANC (2008), Minimising Harbour Siltation. *PIANC REPORT N° 102*, PIANC Secrétariat Général: Bruxelles, Belgium. ISBN 2-87223-169-2

2. Wurpts, R.; Torn, P. (2005), 15 Years Experience with Fluid Mud: Definition of the Nautical Bottom with Rheological Parameters. *Terra et Aqua number* 99: pp. 22-32.

3. Verwilligen, J.; Vantorre M.; Delefortrie, G.; Kamphuis, J.; Meinsma, R.; Van der Made, C.; (2014). Manoeuvrability in proximity of nautical bottom in the harbour of Delfzijl, *33rd PIANC World congress*, San Francisco, USA 2014.

4. Bingham, E.C (1916), An Investigation of the Laws of Plastic Flow, *U.S. Bureau of Standards Bulletin*, 13, 309-353

5. Delefortrie, G.; Vantorre, M.; Eloot, K. (2005). Modelling navigation in muddy areas through captive model tests. *Journal of Marine Science and Technology*, 10, 188-202.

6. Delefortrie, G.; Vantorre, M. (2009). Prediction of the forces acting on container carriers in muddy navigation areas using a fluidization parameter. *Journal of Marine Science and Technology*, 14, 51-68

8 AUTHORS' BIOGRAPHIES

René Barth holds the current position of Engineer at Wiertsema & Partners. He is responsible for geotechnical consults and field investigations relating to sediments. His previous experience includes managing dredging activities in UAE, consulting on fluid mud slopes in England and he was involved in the previous phases of this project.

Kees-Jan van der Made holds the current position of Engineer at Wiertsema & Partners. He is responsible for geotechnical consults and field investigations relating to sediments. His previous experience includes dredging consults for the expansion of Eemshaven and new industrial areas in this harbour, consults regarding maintenance dredging and the reuse of dredged material e.g. for the construction of nature reserve island

Leendert Bourgonjen holds the current position of unit manager Dredging & Surveying and project manager at Groningen Seaports. The unit Dredging & Surveying is responsible for maintenance dredging works in the 4 harbours of GSP in Delfzijl and Eemshaven. His previous experience includes deepening and widening the harbour of Eemshaven.

Joop van Dijken holds the current position of project engineer Dredging & Surveying at Groningen Seaports. He is responsible for contracting and coordinating the dredging works and getting those works more sustainable. His previous experience includes the previous phases of this project.

Jeroen Verwilligen holds the current position of senior expert in nautical research at Flanders Hydraulics Research. He is experienced with simulation studies, nautical accessibility studies and full scale measurements. He is member of the PIANC MarCom WG 171 on Ship Handling Simulation Dedicated to Channel and Harbour Design.

Marc Vantorre, naval architect, is full senior professor of marine hydrodynamics and head of the Maritime Technology Division at Ghent University, Belgium. His research focuses on ship behaviour in shallow and confined waters, mainly in close co-operation with Flanders Hydraulics Research in Antwerp. He is member of PIANC Working Groups and former member of the ITTC Manoeuvring Committee. The investigation of manoeuvring behaviour in muddy areas has been a topic throughout his career.

Manoeuvring in Shallow Water

4th MASHCON, Hamburg - Uliczka et al. (eds) - © 2016 Bundesanstalt für Wasserbau ISBN 978-3-939230-38-0 (Online)
DOI: 10.18451/978-3-939230-38-0_31

CAPTIVE MODEL TESTS BASED 6 DOF SHALLOW WATER MANOEUVRING MODEL

G Delefortrie, Flanders Hydraulics Research, Belgium
K Eloot, Flanders Hydraulics Research, Belgium and Ghent University, Belgium
E Lataire, Ghent University, Belgium
W Van Hoydonck, Flanders Hydraulics Research, Belgium
M Vantorre, Ghent University, Belgium

SUMMARY

This article presents the formulation of the 6 DOF manoeuvring model in calm water for ships with conventional propulsion and steering (1 fixed propeller, 1 stock rudder) as it is used on the ship manoeuvring simulators at Flanders Hydraulics Research (FHR). The coefficients are determined based on the results of captive model tests carried out in the Towing Tank for Manoeuvres in Shallow Water at FHR (co-operation with Ghent University). In this article the benchmark ship KVLCC2 is used as an example for discussion, based on the tests that were carried out at full draft and water depths of 180%, 130% and 120% of the draft. Fast time simulations have been carried out based on the developed manoeuvring model and the trajectories in 6 DOF are compared with the SIMMAN 2014 benchmark manoeuvres.

NOMENCLATURE

a_H	parameter (-)
A_R	rudder area (m²)
A_W	waterline area (m²)
B	breadth (m)
C_B	block coefficient (-)
C_D	drag coefficient (-)
C_L	lift coefficient (-)
C_Q	torque coefficient (-)
C_T	thrust coefficient (-)
D_P	propeller diameter (m)
F_N	force, perpendicular on the rudder (N)
Fr_h	water depth based Froude number (-)
F_X	longitudinal rudder force (N)
F_Y	lateral rudder force (N)
g	gravity acceleration (m/s²)
$\overline{GM}_T$	initial transverse stability lever (m)
$\overline{GM}_L$	initial longitudinal stability lever (m)
h	water depth (m)
$\bar{I}$	inertia tensor (kgm²)
I_{**}	moment or product of inertia (kgm²)
K	roll moment (Nm)
$\overline{KM}_T$	transverse metacentric height (m)
$\overline{KM}_L$	longitudinal metacentric height (m)
k	~ distance propeller – rudder (-)
L	length (m)
M	pitch moment (Nm)
m	ship's mass (kg)
N	yaw moment (Nm)
n	propeller rate (1/s)
p	roll velocity (rad/s)
q	pitch velocity (rad/s)
Q_P	propeller shaft torque (Nm)
r	yaw velocity (rad/s)
T	draft (m)
t	time (s); thrust deduction factor (-)
T_P	propeller thrust (N)
Tu_h	Tuck parameter, eq. 27 (-)
u	longitudinal ship velocity (m/s)
u_R	longitudinal velocity near rudder (m/s)
ukc	under keel clearance
V	total ship velocity (m/s)
v	lateral ship velocity (m/s)
v_R	lateral velocity near rudder (m/s)
w	vertical ship velocity (m/s)
w_R	wake factor for the rudder (-)
w_T	wake factor for the thrust (-)
X	longitudinal force (N)
x	longitudinal coordinate (m)
$\overline{\boldsymbol{x}}_{\boldsymbol{G}}$	position of centre of gravity (m)
x_G	longitudinal centre of gravity (m)
x_H	parameter (-)
x_R	longitudinal position of rudder (m)
Y	sway force (N)
y	lateral coordinate (m)
y_G	lateral centre of gravity (m)
Z	heave force (N)
z_G	vertical centre of gravity (m)
z_H	parameter (-)
z_{HX}	parameter (-)
z_R	vertical position rudder centreline (m)
α	inflow angle (deg)
β	drift angle (deg)
β_R	drift angle near rudder (deg)
γ	yaw angle (deg)
γ^*	propeller loading angle for yaw (deg)
Δ	displacement (N)
δ	rudder angle (deg)
δ_0	rudder asymmetry correction (deg)
$\varepsilon^{(*)}$	(apparent) propeller loading angle (deg)
η	propeller diameter ÷ rudder height (-)
θ	pitch angle (deg)
ξ	parameter (-)
ρ	water density (kg/m³)
φ	heel angle (deg)
φ^*	propeller loading angle for sway (deg)
φ_*	phase angle (deg)
χ	yaw-drift correlation angle (deg)

Subscripts

0	tank fixed
IC	inertial and centrifugal
H	hull
hyd	hydrostatic
OA	over all
P	propeller
PP	between perpendiculars
R	rudder
ret	retardation

Superscripts

.	time derivative
n	propeller dependent

1 INTRODUCTION

Mathematical manoeuvring models commonly focus on the prediction of the longitudinal force, sway force and yawing moment acting on the ship to predict her path in the horizontal plane. At Flanders Hydraulics Research (FHR), manoeuvring models with three degrees of freedom (3 DOF) have been applied successfully to study the ship's manoeuvring behaviour in different shallow water areas. This manoeuvring model was presented in [1].

In 2009 the roll motion was added as a fourth degree of freedom, specifically to include the roll motion for inland ships in the, at that time, newly built inland navigation simulator Lara. Since then the roll motion has been studied for seagoing vessels as well due to the interaction of the roll motion with the other degrees of freedom.

The sinkage and trim of the vessel were mostly treated separately from the measured forces. This is mainly due to the setup of the tests in the Towing Tank for Manoeuvres in Shallow Water at FHR [2] (co-operation with Ghent University) where the ship models are always free to heave and pitch. As such the sinkage and trim were only occasionally added to the simulation models through kinematic squat mathematical models. However, since the IMO issued the Energy Efficiency Design Index with specific regulations considering the manoeuvring behaviour in wind and waves, the research in this topic has received a growing interest.

To cope with the manoeuvring behaviour in waves and give attention to all degrees of freedom, a 6 DOF manoeuvring model is compulsory. Even in calm shallow water conditions a 6 DOF manoeuvring model offers advantages, such as the inclusion of squat and assessment of the dynamic under keel clearance. As a stepping stone towards a full 6 DOF model to cope with manoeuvring in waves, a 6 DOF manoeuvring model in calm water has been under development since 2012.

In this article this mathematical model will be presented, applied to the benchmark ship KVLCC2 [6]. The mathematical model is based mainly on the outcome of captive manoeuvring tests carried out in the towing tank of FHR. Some simulations are presented as well, which compare the free running model tests carried out with the KVLCC2 in the frame of SIMMAN2014, as such this research is a follow up of [3,4].

2 EXPERIMENTAL PROGRAM

2.1 KVLCC2

The KVLCC2 is a benchmark ship developed at KRISO in Korea. FHR possesses a 1/75 scale model of this ship, called T0Z. The full scale particulars are presented in Table 1. The mass distributions of the ship model during captive and free running tests can be found in Tables 2 and 3.

Table 1. Ship data of T0Z at tested draft (even keel)

KVLCC2 (T0Z) – single propeller – single rudder			
L_{OA} (m)	325.0	#propeller blades	4
L_{PP} (m)	320.0	D_P (m)	9.86
B (m)	58.0	$P/_D$ (-)	0.721
T (m)	20.8	AEP (-)	0.431
C_B (-)	0.810	A_R (m²)	111.7
m (kg)	3.130 10^8	Model scale	1:75
$\overline{KM}_T$ (m)	24.29	$\overline{KM}_L$ (m)	398.5

Table 2. Loading condition during captive model tests (model scale)

$$\bar{x}_G = \begin{bmatrix} 0.151 \pm 0.002 \\ 0 \\ 0.0 \pm 0.003 \end{bmatrix} m;$$

$$\bar{I} = \begin{bmatrix} 42.9 \pm 2 & 0 & NA \\ 0 & 837.2 \pm 2 & 0 \\ NA & 0 & 867.2 \pm 2 \end{bmatrix} kgm^2$$

Table 3. Loading condition during free running model tests (model scale)

$$\bar{x}_G = \begin{bmatrix} 0.149 \pm 0.002 \\ 0 \\ 0.012 \pm 0.003 \end{bmatrix} m;$$

$$\bar{I} = \begin{bmatrix} 49.4 \pm 2 & 0 & NA \\ 0 & 839.6 \pm 2 & 0 \\ NA & 0 & 877.5 \pm 2 \end{bmatrix} kgm^2$$

2.2 CAPTIVE MODEL TESTS

The captive model tests were carried out in 2012 and 2015 in the towing tank at FHR at three different under keel clearances, see Table 4.

Table 4. Tested under keel clearances (captive mode)

Environment	ukc	Execution date
T0Z06A01	80%	August 2012
T0Z09A01	30%	March 2015
T0Z06A03	20%	September 2012

For each under keel clearance about 300 tests have been carried out. The speeds were varied between -3.5 knots and 15.5 knots. A large range of kinematic and control parameters was covered to be able to simulate four quadrant harbour manoeuvres. Both drift and yaw angle were varied over 360 deg. Rudder angles between hard port and hard starboard (±35 deflection angles) were combined with propeller rates between harbour full ahead and astern.

The experimental programme consisted of:

- bollard pull tests;
- stationary tests;
- harmonic sway tests;
- harmonic yaw tests;
- multimodal tests with variable speed, rudder angle and/or propeller rate.

The following data were measured:

- longitudinal force;
- lateral force components fore and aft;
- roll moment;
- vertical motion (4 measuring posts: fore/aft, port/starboard);
- rudder parameters (normal and tangential forces, torque, angle);
- propeller parameters (torque, thrust, rpm).

The coefficients of the mathematical model have been determined for each ukc. For an arbitrary ukc the hydrodynamic forces are linearly interpolated between the calculated forces from the available mathematical models.

2.3 FREE RUNNING MODEL TESTS

In 2010 free running model tests were carried out for SIMMAN2014. In this article all the repetitions of the free running model tests carried out at an ukc of 20% will be used as a basis for comparison. The approach speed was always according to 7 knots full scale. The following tests have been carried out:

- 10/2.5 zigzag test, both starting to port and to starboard;
- 20/5 zigzag test, both starting to port and to starboard;
- Partial turning circle at 35 deg rudder deflection, both starting to port and to starboard.

The following data were measured:

- ship position in the horizontal plane;
- vertical motion (3 measuring posts to cover heave, roll and pitch);
- rudder parameters (normal and tangential forces, torque, angle);
- propeller parameters (torque, thrust, rpm).

3 DYNAMICS IN 6 DOF

3.1 COORDINATE SYSTEM

Figure 1 shows the used horizontal bound right handed coordinate system for a regular ship in 6 degrees of freedom. The shown coordinate systems are the tank-fixed ($O_0x_0y_0z_0$), the ship-fixed ($Oxyz$) and the ship-fixed horizontal bound ($Ox'y'z'$) coordinate systems. The expected vertical motions during calm water manoeuvring are small, so that the ship fixed system can be considered equal to the horizontal bound.

The origin O of the ship fixed system is determined as follows:

- located amidships;
- on the static waterline corresponding to the static loading condition;
- in the longitudinal plane of symmetry of the ship.

As a consequence the moments of centrifugal terms and other inertia forces must be taken into account.

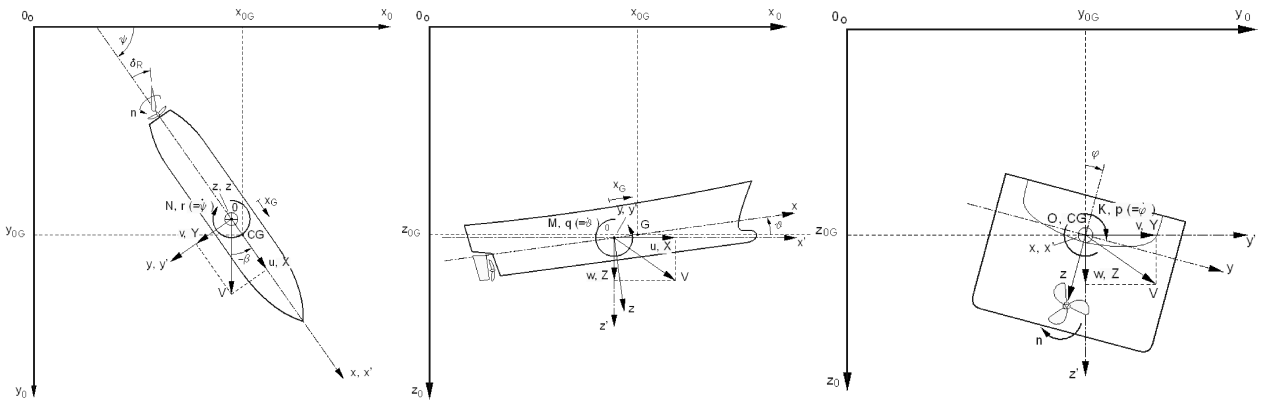

Figure 1. Ship and earth fixed coordinate systems in 6 degrees of freedom: projections on the x_0y_0-plane, y_0z_0-plane and z_0x_0-plane.

3.2 ASSUMPTIONS

Apart from the assumption that the ship fixed coordinate system is horizontal bound, additional assumptions are needed.

The vessel is always free to heave and pitch, but for simulation purposes, the pitch moment and the heave force are needed for formulating the corresponding equations of motion. It is assumed that the mean sinkage and the trim can be considered solely the result of the counteracting hydrostatic heave force Z and the counteracting pitch moment M. The displacement of the ship and the counteracting buoyancy force are left out of the equations (the heave force is the disturbance force). In reality the squat of the vessel is caused by the hydrodynamic equilibrium with the free surface deformation around the ship and not by an external heave or pitch moment.

Due to the limitations of the towing tank carriage, which only enables steering in the horizontal plane, the presented 6 DOF manoeuvring model is to be considered a 3+3 DOF model where only the horizontal motions are fully coupled with the forces and moments in 6 degrees. The effect of vertical motions are either implicitly covered, found by other means or simply neglected.

3.3 FORMULATION

3.3 (a) Inertia and centrifugal terms

Because the KVLCC2 possesses a longitudinal plane of symmetry ($y_G = 0$) the following set of equations, expressed in the ship bound axis system, may be used:

$$X = m[\dot{u} - vr + wq - x_G(q^2 + r^2) + z_G(\dot{q} + pr)] \quad (1)$$

$$Y = m[\dot{v} + ur - wp + x_G(\dot{r} + pq) + z_G(-\dot{p} + qr)] \quad (2)$$

$$Z = m[\dot{w} + uq - vp + x_G(-\dot{q} + pr) - z_G(p^2 + q^2)] \quad (3)$$

$$K = (I_{xx}\dot{p} - I_{xz}\dot{r}) - I_{xz}pq + \left(I_{zz} - I_{yy}\right)qr - m(\dot{v} + ur - wp)z_G \quad (4)$$

$$M = I_{yy}\dot{q} + (I_{xx} - I_{zz})pr + I_{xz}(p^2 - r^2) + m[-(\dot{w} + vp - uq)x_G + (\dot{u} - vr + wq)z_G] \quad (5)$$

$$N = (-I_{xz}\dot{p} + I_{zz}\dot{r}) + I_{xz}qr + \left(I_{yy} - I_{xx}\right)pq + m(\dot{v} + ur - wp)x_G \quad (6)$$

The inertia (acceleration dependent) and centrifugal (speed dependent) terms are supposedly included with the hull forces. Adding the effect of the hydrodynamic inertia terms to be modelled, leads to the reordered equations (7) – (12).

$$X_{IC} = (X_{\dot{u}} - m)\dot{u} + \left(X_{\dot{q}} - mz_G\right)\dot{q} + m(vr - wq) + mx_G(r^2 + q^2) - mz_G pr \quad (7)$$

$$Y_{IC} = (Y_{\dot{v}} - m)\dot{v} + \left(Y_{\dot{p}} + mz_G\right)\dot{p} + (Y_{\dot{r}} - mx_G)\dot{r} + m(wp - ur) - mx_G pq - mz_G qr \quad (8)$$

$$Z_{IC} = (Z_{\dot{w}} - m)\dot{w} + \left(Z_{\dot{q}} + mx_G\right)\dot{q} + m(vp - uq) - mx_G pr + mz_G(p^2 + q^2) \quad (9)$$

$$K_{IC} = (K_{\dot{v}} + mz_G)\dot{v} + \left(K_{\dot{p}} - I_{xx}\right)\dot{p} + (K_{\dot{r}} + I_{xz})\dot{r} + I_{xz}pq - \left(I_{zz} - I_{yy}\right)qr + mz_G(ur - wp) \quad (10)$$

$$M_{IC} = (M_{\dot{u}} - mz_G)\dot{u} + (M_{\dot{w}} + mx_G)\dot{w} + \left(M_{\dot{q}} - I_{yy}\right)\dot{q} - (I_{xx} - I_{zz})pr - I_{xz}(p^2 - r^2) + mx_G(vp - uq) - mz_G(wq - vr) \quad (11)$$

$$N_{IC} = (N_{\dot{v}} - mx_G)\dot{v} + \left(N_{\dot{p}} + I_{xz}\right)\dot{p} + (N_{\dot{r}} - I_{zz})\dot{r} - I_{xz}qr - \left(I_{yy} - I_{xx}\right)pq - mx_G(ur - wp) \quad (12)$$

The blue parameters are mostly found with a regression analysis based on the captive towing tank measurements. Due to the horizontal 3 DOF nature of the carriage, these parameters have to be found by other means:

- $Z_{\dot{w}}, Z_{\dot{q}}, M_{\dot{w}}, M_{\dot{q}}$ have to be computed numerically, although the available software is mostly not accurate enough in shallow water. Alternatively they can be determined based on labour intensive pitch and heave decay tests. They are only determined for the natural frequency.
- $K_{\dot{p}}$ is found after execution of roll decay tests.
- The grey values are unknown, but are supposed to be rather small and therefore neglected. For instance I_{xz} has a magnitude of 1 kgm² on model scale (but was not determined for the KVLCC2, *NA* in Table 2 and 3). At present they are simply neglected in the simulator.

The left hand side of equations (1) – (6) are the sum of external forces (e.g. wind, tugs,…, not considered in this article), the speed-dependent hydrodynamic forces, the control forces and the hydrostatic terms. The speed-dependent behaviour (hydrodynamic damping) is considered together with some retardation terms, hydrostatic terms, inertia and centrifugal terms as hull forces. The modelling of these will be tackled in section 4. The modelling of the control forces is dealt with in sections 5 and 6.

3.3 (b) Retardation terms

The ship's squat shows retardation during acceleration of the ship model. Until now this retardation is modelled using equations (13) – (14).

$$Z_{ret} = Z_{\dot{u}}\dot{u} + Z_{\dot{v}}|\dot{v}| + Z_{\dot{r}}|\dot{r}| \quad (13)$$

$$M_{ret} = M_{\dot{v}}|\dot{v}| + M_{\dot{r}}|\dot{r}| \quad (14)$$

It should be emphasized that the present formulation is a pragmatic one, but leaves room for improvement, as it could have undesirable results during the simulation process. The other degrees of freedom do not include retardation. $M_{\dot{u}}$ is already included in equation (11) but is expected to have implicit retardation.

3.3 (c) Hydrostatic terms

In the vertical degrees of freedom hydrostatic equilibrium is achieved with the following equations:

$$Z_{hyd} = -\frac{\partial \Delta}{\partial T} dT \approx -\rho g A_W z \quad (15)$$

$$K_{hyd} = -\Delta \overline{GM}_T \varphi \quad (16)$$

$$M_{hyd} = -\Delta \overline{GM}_L \theta \quad (17)$$

The use of (constant) $\overline{GM}_T$ and $\overline{GM}_L$ is acceptable due to the assumption of small vertical movement in calm water.

4 MATHEMATICAL MODEL: HULL FORCES

4.1 OVERVIEW

The hull forces are expressed according to equations (18) – (23).

$$X_H = X_{IC} + \frac{1}{2}\rho LT(u^2+v^2)X'^{(\beta)} + \frac{1}{2}\rho LT\left(u^2+\left(\frac{1}{2}rL\right)^2\right)X'^{(\gamma)} + \frac{1}{2}\rho LT\left(v^2+\left(\frac{1}{2}rL\right)^2\right)X'^{(\chi)} \quad (18)$$

$$Y_H = Y_{IC} + \frac{1}{2}\rho LT(u^2+v^2)Y'^{(\beta)} + \frac{1}{2}\rho LT\left(u^2+\left(\frac{1}{2}rL\right)^2\right)Y'^{(\gamma)} + \frac{1}{2}\rho LT\left(v^2+\left(\frac{1}{2}rL\right)^2\right)Y'^{(\chi)} \quad (19)$$

$$Z_H = Z_{IC} + Z_{ret} + Z_{hyd} + \Delta T u_h Z'^{(\beta)} + \frac{1}{2}\rho LT\left(u^2+\left(\frac{1}{2}rL\right)^2\right)Z'^{(\gamma)} + \frac{1}{2}\rho LT\left(v^2+\left(\frac{1}{2}rL\right)^2\right)Z'^{(\chi)} + Z_w w + Z_q q \quad (20)$$

$$K_H = K_{IC} + K_{hyd} + \frac{1}{2}\rho LT^2(u^2+v^2)K'^{(\beta)} + \frac{1}{2}\rho LT^2\left(u^2+\left(\frac{1}{2}rL\right)^2\right)K'^{(\gamma)} + \frac{1}{2}\rho LT^2\left(v^2+\left(\frac{1}{2}rL\right)^2\right)K'^{(\chi)} + \left[K_p - |\varphi|\sqrt{\Delta \overline{GM}_T\left((-K_{\dot{p}} + I_{xx})\right)}\right]p + K_{up}up \quad (21)$$

$$M_H = M_{IC} + M_{ret} + M_{hyd} + \Delta LT u_h M'^{(\beta)} + \frac{1}{2}\rho L^2 T\left(u^2+\left(\frac{1}{2}rL\right)^2\right)M'^{(\gamma)} + \frac{1}{2}\rho L^2 T\left(v^2+\left(\frac{1}{2}rL\right)^2\right)M'^{(\chi)} + M_w w + M_q q \quad (22)$$

$$N_H = N_{IC} + \frac{1}{2}\rho L^2 T(u^2+v^2)N'^{(\beta)} + \frac{1}{2}\rho L^2 T\left(u^2+\left(\frac{1}{2}rL\right)^2\right)N'^{(\gamma)} + \frac{1}{2}\rho L^2 T\left(v^2+\left(\frac{1}{2}rL\right)^2\right)N'^{(\chi)} \quad (23)$$

In the above equations the following parameters have been introduced:

- The hydrodynamic angles (horizontal speed combinations):

  $$\beta = \arctan\left(\frac{-v}{u}\right) \quad (24)$$

  $$\gamma = \arctan\left(\frac{0.5rL}{u}\right) \quad (25)$$

  $$\chi = \arctan\left(\frac{0.5rL}{v}\right) \quad (26)$$

  respectively referred to as drift, yaw and drift-yaw correlation angle. The range of the arctan function is extended to [-π,π] for four quadrants.
- The Tuck parameter [5]:

  $$Tu_h = \frac{Fr_h}{\sqrt{1-Fr_h^2}} \quad (27)$$

  expressed as a function of the depth-related Froude number:

  $$Fr_h = \frac{V}{\sqrt{gh}} \quad (28)$$

The blue terms in equations (18) – (23) need to be modelled. The way this is performed depends on the term:

- The effect of the hydrodynamic angles is based on the results of the captive manoeuvring tests. The influence is modelled in a tabular way, meaning that a function is built with discrete values for a selection of angles β, γ and χ. In between two values a linear interpolation is applied. The results of the regression are highly dependent on a good selection of the discrete values. They should correspond with values obtained during the captive model tests.
- The vertical speed dependencies can be obtained as follows:
  - K_p, K_{up} are determined based on roll decay tests, performed at different forward speeds.
  - Z_w, Z_q, M_w, M_q have to be computed using a similar method as for the corresponding acceleration dependent derivatives.

Within this article it is impossible to discuss every expression in detail. In the following paragraphs some examples of drift and yaw functions will be given.

4.2 DRIFT FORCES

Figure 2 shows the influence of the ship's drift angle on the force components in 6 DOF. The drift force is to be considered as the main force component, i.e. at zero drift, yaw and yaw-drift correlation angle, the entire force component is considered as a drift force.

For all DOFs, except roll, an increasing trend is observed for decreasing under keel clearance. Pure sway motion mainly affects the sway and heave forces and the roll moment. The other degrees of freedom are affected when surge and sway velocity are of the same magnitude.
Clear symmetry patterns can be observed in the different functions, however perfect symmetry is not achieved due to imperfections of the hull, carriage, modelling… Prior to simulations the functions are made (anti-)symmetric.

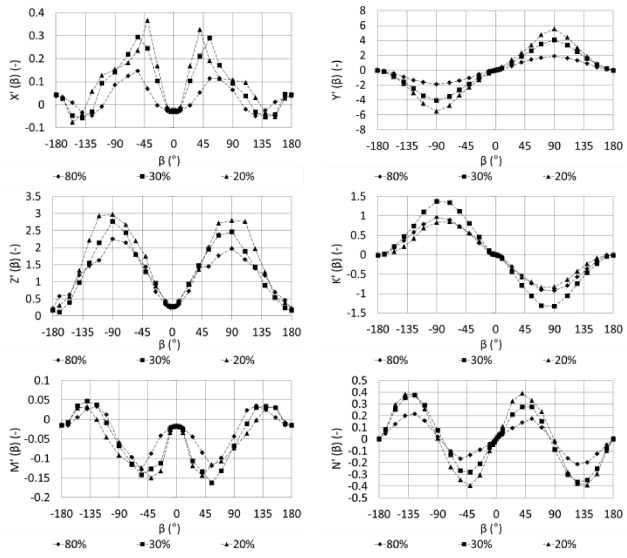

Figure 2. Drift functions in 6 DOF for the tested under keel clearances.

4.3 YAW FORCES

The influence of the yaw angle on the 6 DOF force components is shown in Figure 3. Increasing the yaw rate and decreasing the under keel clearance will increase the magnitude of the force or moment. As for the drift force, symmetry patterns are clearly visible.

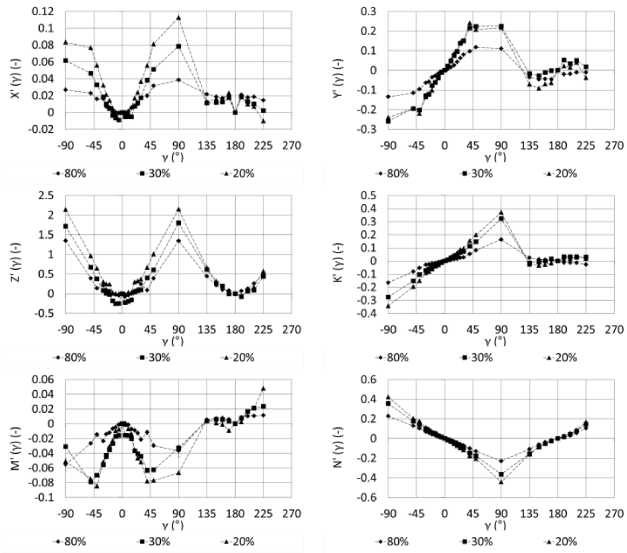

Figure 3. Yaw functions in 6 DOF for the tested under keel clearances.

5 MATHEMATICAL MODEL: PROPULSION FORCES

5.1 PROPELLER THRUST AND TORQUE

The propeller thrust is modelled by determining the wake factor in:

$$\varepsilon = \arctan\left(\frac{(1-w_T)u}{0.7\pi n D_P}\right) \tag{29}$$

So that the thrust can be predicted as follows:

$$T_P = \frac{0.7^2}{8}\pi^3 \rho n^2 D_P^4 C_T(\varepsilon)(1+\tan^2\varepsilon) \tag{30}$$

in which C_T is an alternative formulation of K_T to allow for four quadrant operations:

- Quadrant 1: $u \geq 0; n \geq 0$
- Quadrant 2: $u \geq 0; n < 0$
- Quadrant 3: $u < 0; n \leq 0$
- Quadrant 4: $u < 0; n > 0$

The propeller thrust in open water was determined and it is found to be comparable to the open water characteristic of the HMRI model available on the SIMMAN2014 website [6]. Analogously, the propeller shaft torque is modelled using the expression:

$$Q_P = \frac{0.7^2}{8}\pi^3 \rho n^2 D_P^5 C_Q(\varepsilon)(1+\tan^2\varepsilon) \tag{31}$$

In most cases a slightly different wake factor is needed for the propeller shaft torque. Both wake factors are expressed as a function of the apparent propeller loading,

$$\varepsilon^* = \arctan\left(\frac{u}{0.7\pi n D_P}\right) \tag{32}$$

see Figure 4, for the first quadrant. The model self-propulsion point during simulations is $\varepsilon^* \approx 12°$. In the other quadrants the wake factor equals zero, however, between the first and the fourth quadrant a smooth transition is needed.

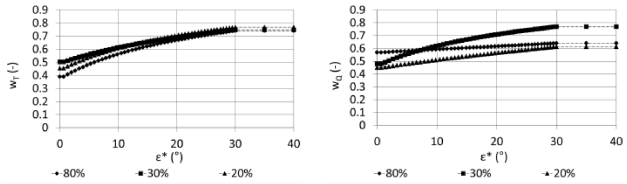

Figure 4. Wake factors for the propeller thrust (T) and shaft torque (Q).

5.2 PROPELLER INDUCED FORCES

5.2 (a) Longitudinal force

The propulsion induced longitudinal force is modelled with a thrust deduction factor:

$$X_P = \big(1 - t(\varepsilon^*, \varphi^*, \gamma^*)\big)T_P \tag{33}$$

which depends on different propeller loading angles:

$$\varphi^* = \arctan\left(\frac{|v|}{0.7\pi n D_P}\right) \tag{34}$$

$$\gamma^* = \arctan\left(\frac{|0.5rL|}{0.7\pi n D_P}\right) \tag{35}$$

as follows:

$$t = f(\varepsilon^*) + q_1(\varepsilon^*)\varphi^*\xi_1 + q_3(\varepsilon^*)\varphi^*\xi_3 + q_4(\varepsilon^*)\gamma^*\xi_4 \tag{36}$$

$q_j(\varepsilon^*)$ is equal to 1 in quadrant j and equal to zero in the other quadrants.

Figure 5 shows the thrust deduction in the first quadrant near the model self-propulsion point. Thrust deduction increases with decreasing propeller loading and with decreasing water depth (80% versus 20-30 % ukc), but for bollard pull the opposite seems true.

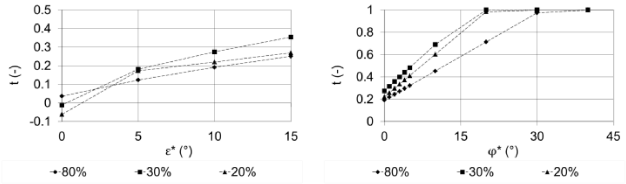

Figure 5. Thrust deduction factors close to the model self propulsion point.

5.2 (b) Forces in other DOF

The propeller induced forces in the other degrees of freedom are expressed using equations (37) – (41). The effect can be split in three parts:

- the propeller action affects the hydrodynamic inertia derivatives;
- a constant force or moment is observed, which depends on the thrust, yaw and drift angle;
- in the even quadrants, oscillations occur. The characteristics of these oscillations depend on the propeller loading.

In equations (37) – (41) the following parameters appear:

- K_1 equals the ship length based Froude number in the first quadrant and is 1 in the other quadrants;
- K_2 depends on the degree of oscillation, based on the yaw rate [1];
- K_3 equals the Tuck parameter (27) in the first quadrant and is 1 in the other quadrants.

In [7] the propulsion effect on squat has been modelled using an additional speed V_T which is a function of the propeller thrust T_P. To be more compliant with the mathematical models for the other degrees of freedom new equations are proposed. In contrast with the current work, the squat model in [7] accounted for the confinement of the waterway, but did not consider other quadrants than the first one.

As an example, Figure 6 shows the mean propeller induced forces and moments, while the amplitude of the oscillations are shown in Figure 7 for the second quadrant.

The propeller action mostly increases with decreasing under keel clearance and increasing yaw or drift angle. The oscillations are more pronounced in shallow water conditions.

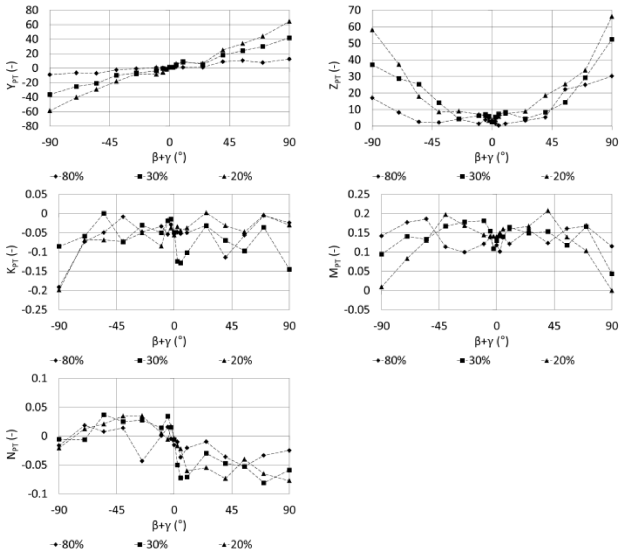

Figure 6. Mean propeller induced forces and moments in the first quadrant

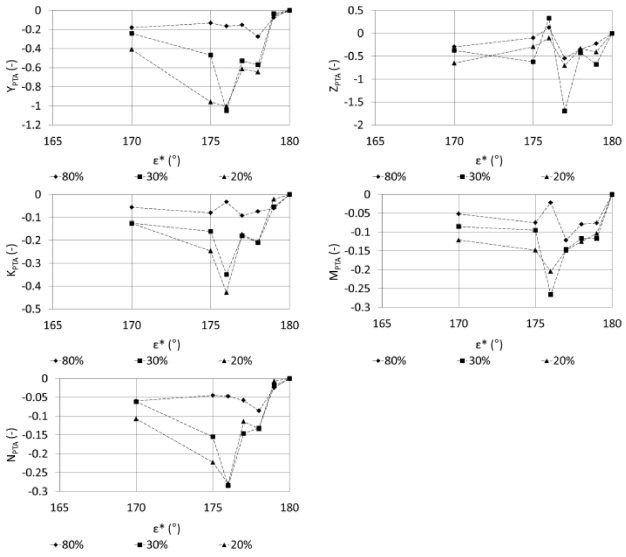

Figure 7. Amplitude of the propeller induced forces and moments in the second quadrant

$$Y_P = \left|\frac{n}{n_{MAX}}\right| [Y_{\dot{v}}^n \dot{v} + Y_{\dot{r}}^n \dot{r}] + \left[K_1[Y_{PT}(\beta, \varepsilon^*) + Y_{PT}(\gamma, \varepsilon^*)] + K_2 Y_{PTA}(\varepsilon^*) \cos\left(\omega(\varepsilon^*)t + \varphi_Y(\varepsilon^*)\right)\right] T_P(\varepsilon^*) \quad (37)$$

$$Z_P = \left[K_3[Z_{PT}(\beta, \varepsilon^*) + Z_{PT}(\gamma, \varepsilon^*)] + K_2 Z_{PTA}(\varepsilon^*) \cos\left(\omega(\varepsilon^*)t + \varphi_z(\varepsilon^*)\right)\right] T_P(\varepsilon^*) \quad (38)$$

$$K_P = \left|\frac{n}{n_{MAX}}\right| [K_{\dot{v}}^n \dot{v} + K_{\dot{r}}^n \dot{r}] + \left[[K_{PT}(\beta, \varepsilon^*) + K_{PT}(\gamma, \varepsilon^*)] + K_2 K_{PTA}(\varepsilon^*) \cos\left(\omega(\varepsilon^*)t + \varphi_K(\varepsilon^*)\right)\right] TT_P(\varepsilon^*) \quad (39)$$

$$M_P = \left[M_{PT}(\beta, \varepsilon^*) + M_{PT}(\gamma, \varepsilon^*) + K_2 M_{PTA}(\varepsilon^*) \cos\left(\omega(\varepsilon^*)t + \varphi_M(\varepsilon^*)\right)\right] LT_P(\varepsilon^*) \quad (40)$$

$$N_P = \left|\frac{n}{n_{MAX}}\right| [N_{\dot{v}}^n \dot{v} + N_{\dot{r}}^n \dot{r}] + \left[[N_{PT}(\beta, \varepsilon^*) + N_{PT}(\gamma, \varepsilon^*)] + K_2 N_{PTA}(\varepsilon^*) \cos\left(\omega(\varepsilon^*)t + \varphi_N(\varepsilon^*)\right)\right] LT_P(\varepsilon^*) \quad (41)$$

6 MATHEMATICAL MODEL: STEERING FORCES

6.1 FORCES ACTING ON THE RUDDER

6.1 (a) Formulation

Similar to the propeller thrust, the forces acting on the rudder are based on a model of the wake factor. To determine the open water lift and drag coefficients of the rudder, tests have been carried out with solely the rudder for a variety of inflow angles α (Fig.8).

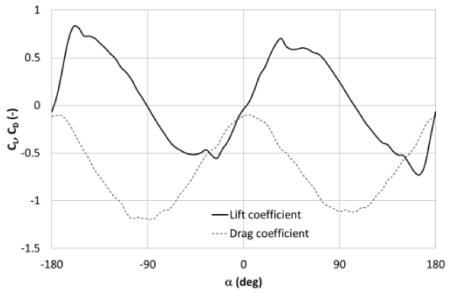

Figure 8. Measured lift and drag on the rudder of the KVLCC2 in open water.

When the rudder is behind the ship the inflow is affected, which is modelled with the effective rudder angle and drift near the rudder:

$$\alpha = \delta + \delta_0 + \beta_R \quad (42)$$

δ_0 (the rudder angle where the normal force F_N acting on the rudder becomes zero) is an offset for flow asymmetry:

$$\delta_0 = -\delta(F_N = 0) \quad (43)$$

β_R is the local drift angle at the rudder:

$$\beta_R = \arctan\left(\frac{-v_R}{u_R}\right) \quad (44)$$

u_R, v_R being the longitudinal and transverse component of the flow velocity near the rudder:

$$V_R = \sqrt{u_R^2 + v_R^2} \quad (45)$$

This way the forces on the rudder can be expressed as:

$$F_X = \frac{1}{2}\rho A_R V_R^2 [C_L \sin\beta_R + C_D \cos\beta_R] \quad (46)$$

$$F_Y = \frac{1}{2}\rho A_R V_R^2 [C_L \cos\beta_R - C_D \sin\beta_R] \quad (47)$$

6.1 (b) Modelling the inflow speed to the rudder

The problem is then to predict the velocity components near the rudder. The lateral component is assumed to be:

$$v_R = v + r x_R \quad (48)$$

The longitudinal component of the inflow speed is affected by both the propeller action and the hull. The formulation is based on impulse theory, which results in expression (52) for the first quadrant.

For the fourth quadrant the inflow is more complex due to the opposite flow generated by ship and propeller. The following methodology is used:

- Step 1: resolve the following implicit equations to determine the dominant flow component:

$$A = 0 \Leftrightarrow \sin\varepsilon = -k\sqrt{\frac{|C_T|}{\left(1+2k+\sqrt{\frac{1-\eta}{\eta}}\right)\left(1+\sqrt{\frac{1-\eta}{\eta}}\right)}} \quad (49)$$

$$B = 0 \Leftrightarrow \sin\varepsilon = -k\sqrt{\frac{|C_T|}{\left(1+2k-\sqrt{\frac{1-\eta}{\eta}}\right)\left(1-\sqrt{\frac{1-\eta}{\eta}}\right)}} \quad (50)$$

- Step 2:
  - if the propeller loading ε is smaller than B then the inflow velocity is determined by equation (53) and $\mathrm{sgn}(u_{RP})$ is negative;
  - if the propeller loading ε is larger than A then the inflow velocity is determined by the average of equations (53) and (54) with $\mathrm{sgn}(u_{RP})$ positive;
  - for intermediate points a linear interpolation, based on the propeller rate, is applied between the inflow velocity at point A and the inflow velocity at point B.

In the second and the third quadrant the forces acting on the rudder are rather small and the following simple expression for the inflow velocity is used:

$$u_R = \xi n + (1 - w_R)u \quad (51)$$

$$u_R = \frac{1-w_R}{1-w_T}\sqrt{\left\{\eta\left[(1-k)\sin\varepsilon + k\sqrt{C_T + \sin^2\varepsilon}\right]^2 + (1-\eta)\sin^2\varepsilon\right\}\{[(1-w_T)u]^2 + [0.7\pi n D_P]^2\}} \quad (52)$$

$$u_R = \frac{1-w_R}{1-w_T}sgn(u_{RP})\sqrt{\left\{\eta\left[(1+k)\sin\varepsilon + k\sqrt{|C_T| + \sin^2\varepsilon}\right]^2 - sgn(u_{RP})(1-\eta)\sin^2\varepsilon\right\}\{[(1-w_T)u]^2 + [0.7\pi n D_P]^2\}} \quad (53)$$

$$u_R = \frac{1-w_R}{1-w_T}sgn(u_{RP})\sqrt{\left\{\eta\left[(1+k)\sin\varepsilon + k\sqrt{|C_T| + \sin^2\varepsilon}\right]^2 - sgn(u_{RP})(1-\eta)\sin^2\varepsilon\right\}\{[(1-w_T)u]^2 + [0.7\pi n D_P]^2\}} \quad (54)$$

The wake factor w_R in the above equations can be expressed as a tabular function of the rudder angle. A different function is necessary for the longitudinal and the lateral rudder force. As can be seen on Figure 9 the wake factor is also affected by the under keel clearance.

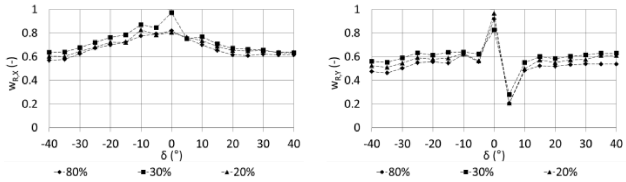

Figure 9. Wake factors for longitudinal (X) and lateral (Y) rudder force.

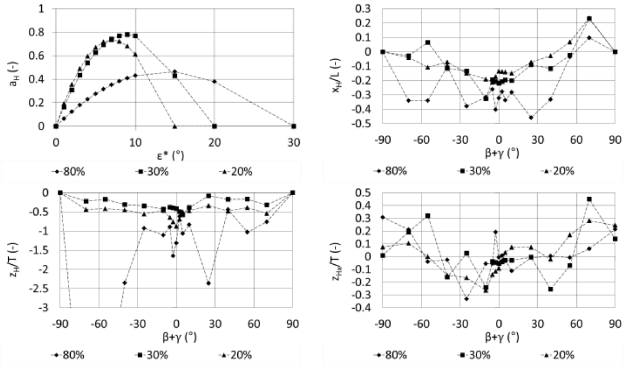

Figure 10. Rudder induced correlation coefficients for the first quadrant.

6.2 STEERING INDUCED FORCES

Once the hull and propeller induced forces are computed the remainder of the measured forces is used to compute the rudder induced part with the following equations:

$$X_R = F_X \quad (55)$$

$$Y_R = \big(1 + a_H(\varepsilon^*, \beta)\big)F_Y \quad (56)$$

$$Z_R = 0 \quad (57)$$

$$K_R = -\big(z_R + a_H(\varepsilon^*, \beta)z_H(\beta)\big)F_Y \quad (58)$$

$$M_R = z_{HX}(\beta)F_X \quad (59)$$

$$N_R = \big(x_R + a_H(\varepsilon^*, \beta)x_H(\beta)\big)F_Y \quad (60)$$

The longitudinal rudder force can be directly transferred to the ship's longitudinal force. The heave does not seem to be affected by the rudder, but the sway force and the moments depend on the rudder forces and the extra asymmetries induced by the hull. Figure 10 shows values of the different correlation coefficients in the first quadrant. The a_H parameter increases with decreasing under keel clearance, but at the same time the application points x_H and z_H move towards zero.

7 VALIDATION

7.1 CAPTIVE

Figure 11a, presented in Appendix 1, shows the correlation between the measured and modelled forces, moments or positions in every degree of freedom for 20% ukc. The correlation coefficient is always more than 90%, the trim being the most difficult degree of freedom to model.

Some captive runs were not used to determine the model coefficients, but to check the prediction capabilities of the simulation model in a rather complex trajectory. Two examples are shown in Figures 11b and 11c. In validation test 1 the longitudinal ship speed was constant and equal to 0.125 m/s (2.1 knots at full scale), while the rudder was harmonically varied between ± 35 deg. In validation test 2 the rudder was also varied harmonically between ± 35 deg and the longitudinal speed between 0 and 0.25 m/s (4.2 knots at full scale). The other kinematic and control parameters were varied according to the bottom graphs of Figure 11b and 11c.

Overall, the longitudinal force, sway force and yawing moment are accurately predicted. In the other degrees of freedom the predictions are fair enough for their intended purpose. The mean sinkage for instance has some underestimation, but was very small during the validation tests.

7.2 FREE RUNNING

In Figure 12 (see Appendix 2) all SIMMAN 2014 free running manoeuvres at 20% ukc are compared with the simulation prediction. In every graph the SIMMAN results are presented with grey curves. A black line is the prediction of the 6 DOF model presented in this article. In some graphs a dashed line is present, which is the prediction of the model presented in [3,4]. A coloured line is a prediction with modifications to the 6 DOF model, see section 8. Both the simulations and the free running results were scaled to full scale by means of Froude scaling only.

The 6 DOF manoeuvring model is better at predicting the trajectories than the model based on a limited number of tests. This was already suggested in [3] and illustrated in [4] based on the shortcomings of a 4 DOF model derived from only 97 captive model tests. Nevertheless, the 6 DOF manoeuvring model seems to underestimate the overshoot angles during the zigzag tests with larger discrepancies for the 10/2.5 zigzag tests. This underestimation was not only the case for the previous mathematical model described in [3] but is also observed for other ship models in very shallow water. As was concluded in [4] both empirical and PMM based mathematical models predict a more course stable KVLCC2 in 20% UKC. The global speed evolution during the manoeuvres seems well predicted, but both the drift angle and the yaw rate should be larger.

The largest deviations are seen for the roll angle (only shown for the partial turns). However, the roll angle during the free running tests is always towards starboard side, which suggests that the measurement in the free running tests is probably biased. In general the sinkage and trim of the vessel are reasonably well predicted, with a small underestimation for the sinkage.

8 SENSITIVITY ANALYSIS

In order to predict the SIMMAN 2014 free running manoeuvres in an accurate way, some coefficients of the mathematical model can be tuned. In theory any coefficient could be tuned and many possibilities exist to reach the same trajectory. In this case the period of the zigzag manoeuvres and the turning circle radius seems correctly predicted, which means that rudder forces and the yawing moment are adequately predicted.

The lower overshoots and corresponding low rate of turn and drift angle mean an unbalance, which can also be observed in the so-called pivot point (defined by $-v/r$, shown in Figure 13) which is the longitudinal position on the ship that is not subjected to lateral movement referred to the ship's trajectory. In a zigzag manoeuvre this pivot point shifts with every rudder reversal, but in the simulations the shift occurs too fast (low overshoot). In addition, the average position seems to be closer to midships compared to the free running trials. The shift towards midships is a typical phenomenon in shallow water, which was already observed for captive model tests in [8], but perhaps this does not happen during free running trials in very shallow water which are more scarcely available.

The position of the pivot point can be influenced by decreasing $Y'^{(\beta)}$, $Y'^{(\gamma)}$ or $Y'^{(\chi)}$ rather significantly, which was performed here for the 20/5 zigzag tests. The results are represented by the coloured curves in Figures 12 and 13. This way the simulations and the free running results are in agreement for the 20/5 zigzag tests. Further tuning would be needed for the 10/2.5 zigzag tests. Yet, it does not explain why in the captive tests a larger sway force in drift and/or yaw is measured than what can be expected during free running tests. More research is needed, for instance on the influence of the turning point during captive harmonic yaw tests. As already mentioned in [4] flow measurements in captive and free-running tests could help in understanding the steady or transient behaviour of the water flow in the tank. These flows could further be compared with flow predictions from RANS calculations using CFD techniques so that the specific hydrodynamics in shallow water are better understood.

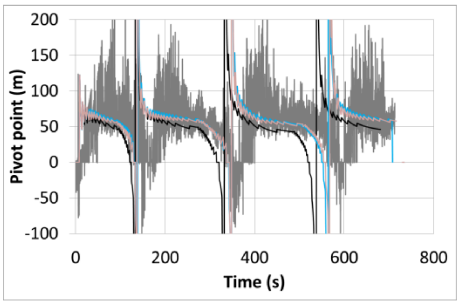

Figure 13. Evolution of pivot point during 20/5 zigzag test, starting to portside.

9 CONCLUSIONS

In this article the 6 DOF mathematical manoeuvring model is introduced, presently in use at FHR. The main input for this mathematical model is based on captive model tests, where the ship's motion is forced in the 3 horizontal degrees of freedom, while the ship's roll angle is fixed (and kept at 0 deg) and the heave and pitch motions are free. To use such test results, some assumptions are needed and sometimes numerical input is needed to assess the ship's response in the vertical degrees of freedom.

The predictions of the mathematical model for the KVLCC2 have been compared with the outcome of the SIMMAN 2014 free running tests at 20% ukc. The agreement is acceptable, except for the underprediction of the drift and yaw rate. This phenomenon has been observed for other ship models at very low under keel clearance and will receive more attention in future research.

10 REFERENCES

1. Delefortrie, G.; Vantorre, M.; Eloot, K. (2005). Modelling navigation in muddy areas through captive model tests. *J. Mar. Sci. Technol.* 10(4): pp. 188-202. dx.doi.org/10.1007/s00773-005-0210-5.

2. Delefortrie, G.; Geerts, S.; Vantorre, M. (2016). The Towing Tank for Manoeuvres in Shallow Water. *MASHCON 2016*, Hamburg, Germany.

3. Delefortrie, G.; Eloot, K. (2014). Mathematical Model for Shallow Water Manoeuvres with the KVLCC2 as used in SIMMAN 2014. *Preprints of SIMMAN 2014*, Lyngby, Denmark.

4. Eloot, K.; Delefortrie, G.; Vantorre, M.; Quadvlieg, F. (2015). Validation of Ship Manoeuvring in Shallow Water through Free Running Tests. *OMAE 2015-41912*, St. John's, Canada.

5. Tuck, E.O. (1966). Shallow-water flows past slender bodies. *J. Fluid Mech.* 26: pp. 81–95

6. www.SIMMAN2014.dk

7. Lataire, E.; Vantorre, M.; Delefortrie, G. (2012). A prediction method for squat in restricted and unrestricted rectangular fairways. *Ocean Engineering* 55: pp. 71-80. dx.doi.org/10.1016/j.oceaneng.2012.07.009

8. Vantorre, M.; Delefortrie, G.; Laforce, E.; De Vlieger, H.; Claeys, S. (2003) Ship manoeuvring at very small and negative under keel clearance, *MCMC 2003*, pp. 55-60.

11 AUTHORS' BIOGRAPHIES

Guillaume Delefortrie, naval architect, is expert nautical research at Flanders Hydraulics Research. He is in charge of the research in the Towing Tank for Manoeuvres in Shallow Water, development of mathematical models based on model tests and is secretary of the 27th and 28th ITTC Manoeuvring Committee.

Katrien Eloot, naval architect, is senior expert nautical research at Flanders Hydraulics Research and guest professor at Ghent University. She is involved in research concerning ship hydrodynamics in shallow and confined water through experimental fluid dynamics and ship manoeuvring simulation. She is member of the PIANC Working Group 141 for Design Guidelines for Inland Waterways and working groups of the NATO Science and Technology Organisation.

Evert Lataire, naval architect, is currently assistant at the division of Maritime Technology at Ghent University. He has written a PhD on the topic of bank effects mainly based upon model tests carried out in the shallow water towing tank of FHR. His ten year experience includes research on ship manoeuvring in shallow and confined water such as ship-ship interaction, ship-bottom interaction and ship-bank interaction.

Wim Van Hoydonck, aerospace engineer, is nautical researcher at Flanders Hydraulics Research. He is involved in research concerning ship hydrodynamics and hydraulic constructions using Computational Fluid Dynamics (CFD). He is a member of working groups of the NATO Science and Technology Organisation.

Marc Vantorre, naval architect, is full senior professor of marine hydrodynamics and head of the Maritime Technology Division at Ghent University, Belgium. His research focuses on ship behaviour in shallow and confined waters, mainly in close co-operation with Flanders Hydraulics Research in Antwerp. He is former member of several PIANC Working Groups and former member and secretary of the ITTC Manoeuvring Committee.

Appendix 1. Comparison between measured and modelled forces at 20% ukc. Captive validation tests.

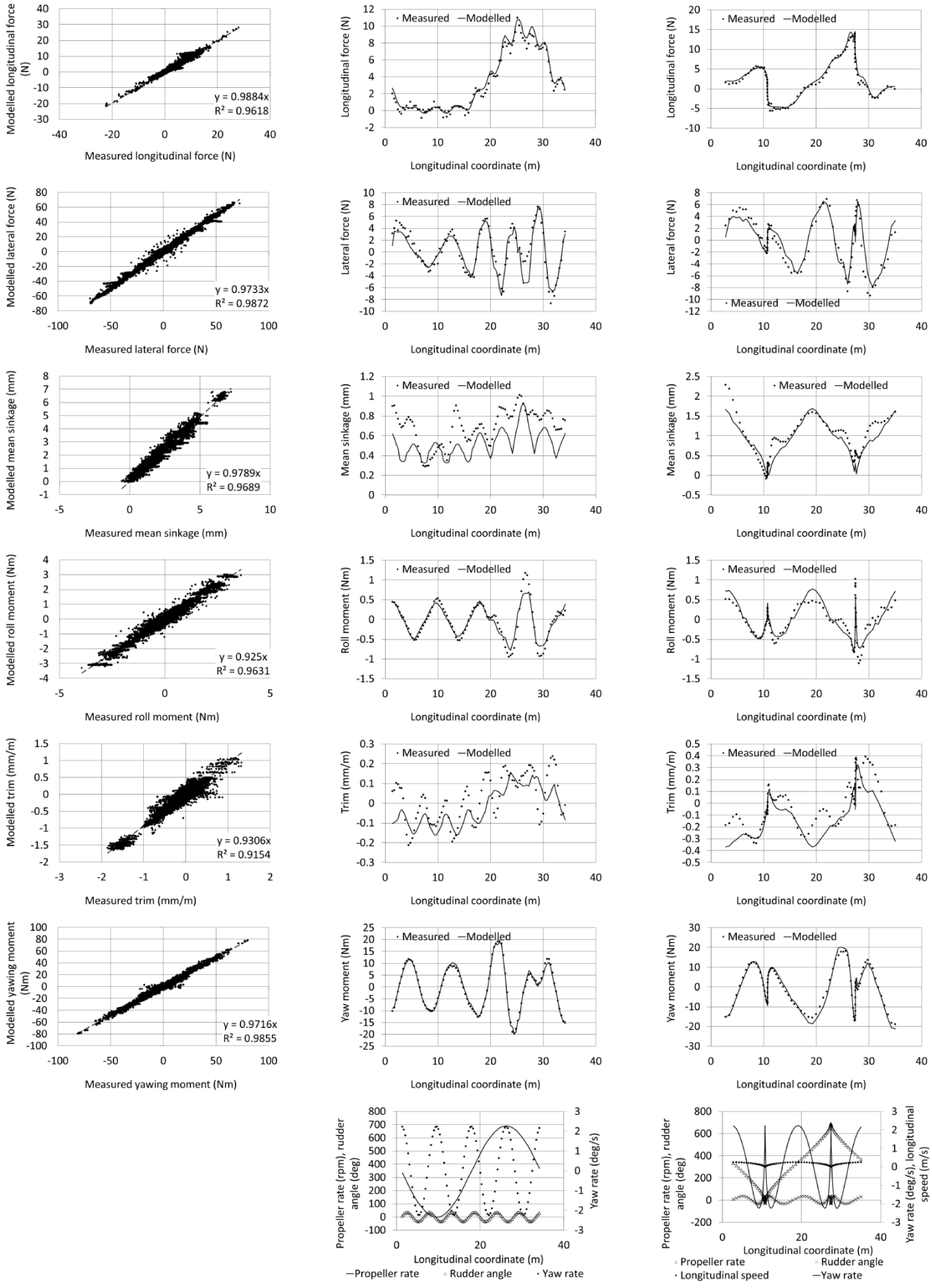

a) All tests b) Validation test 1 c) Validation test 2

Figure 11. Comparison between the measured and modelled forces and moments in captive model tests at 20% ukc.

Appendix 2. Comparison manoeuvring model with SIMMAN 2014 free running model tests

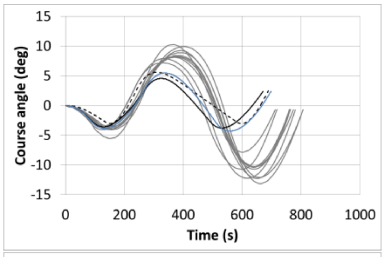

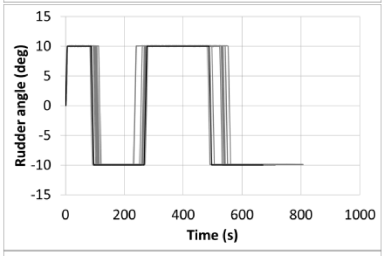

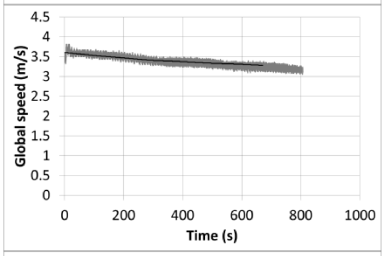

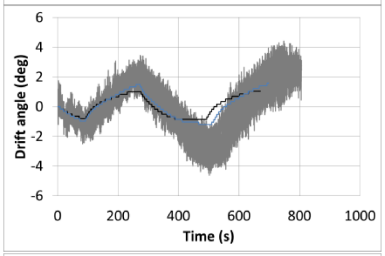

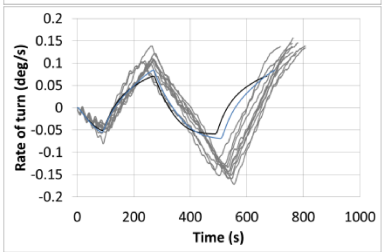

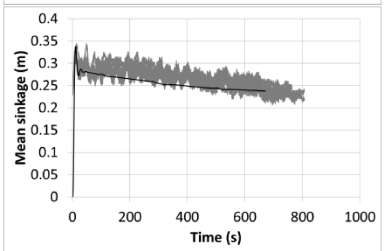

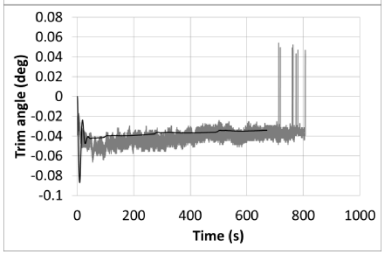

a) 10/2.5 zigzag test, starting to portside

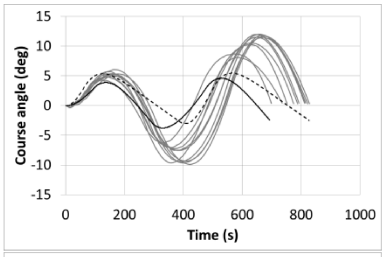

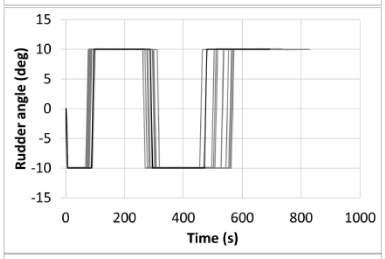

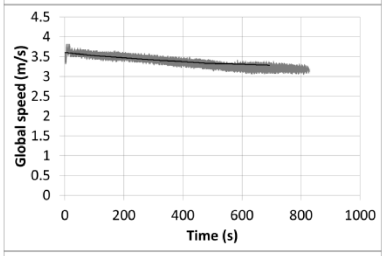

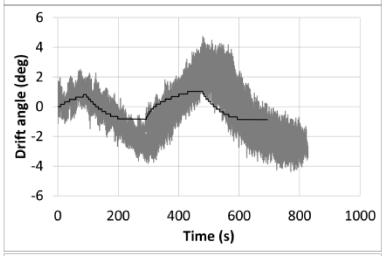

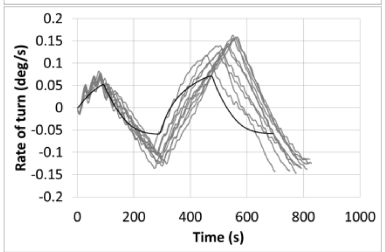

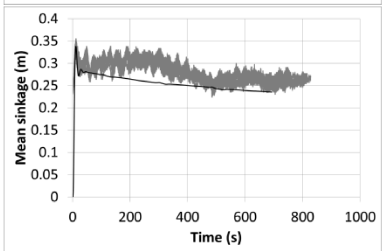

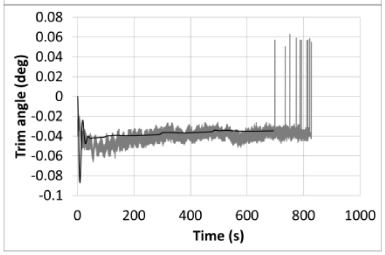

b) 10/2.5 zigzag test, starting to starboard side

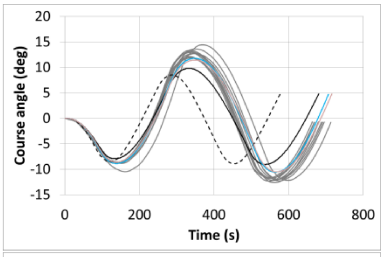

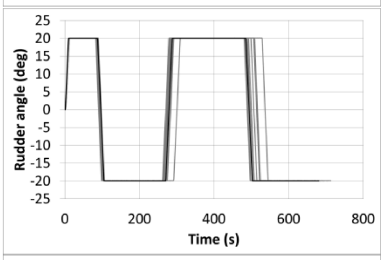

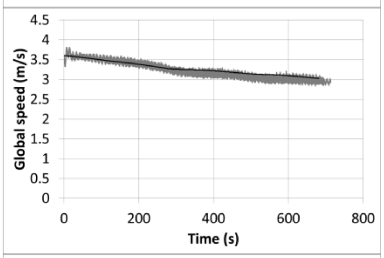

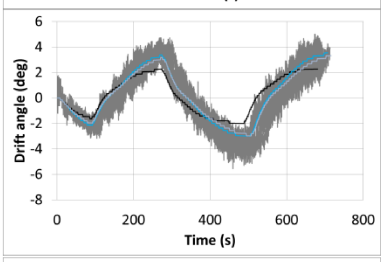

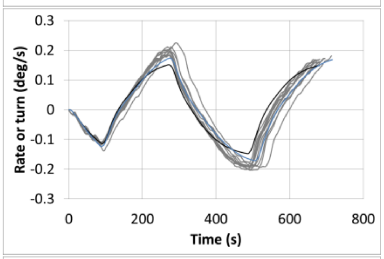

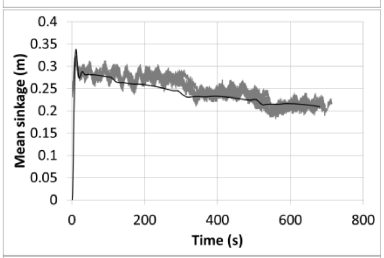

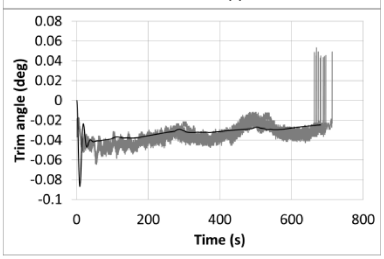

c) 20/5 zigzag test, starting to portside

{continues on next page}

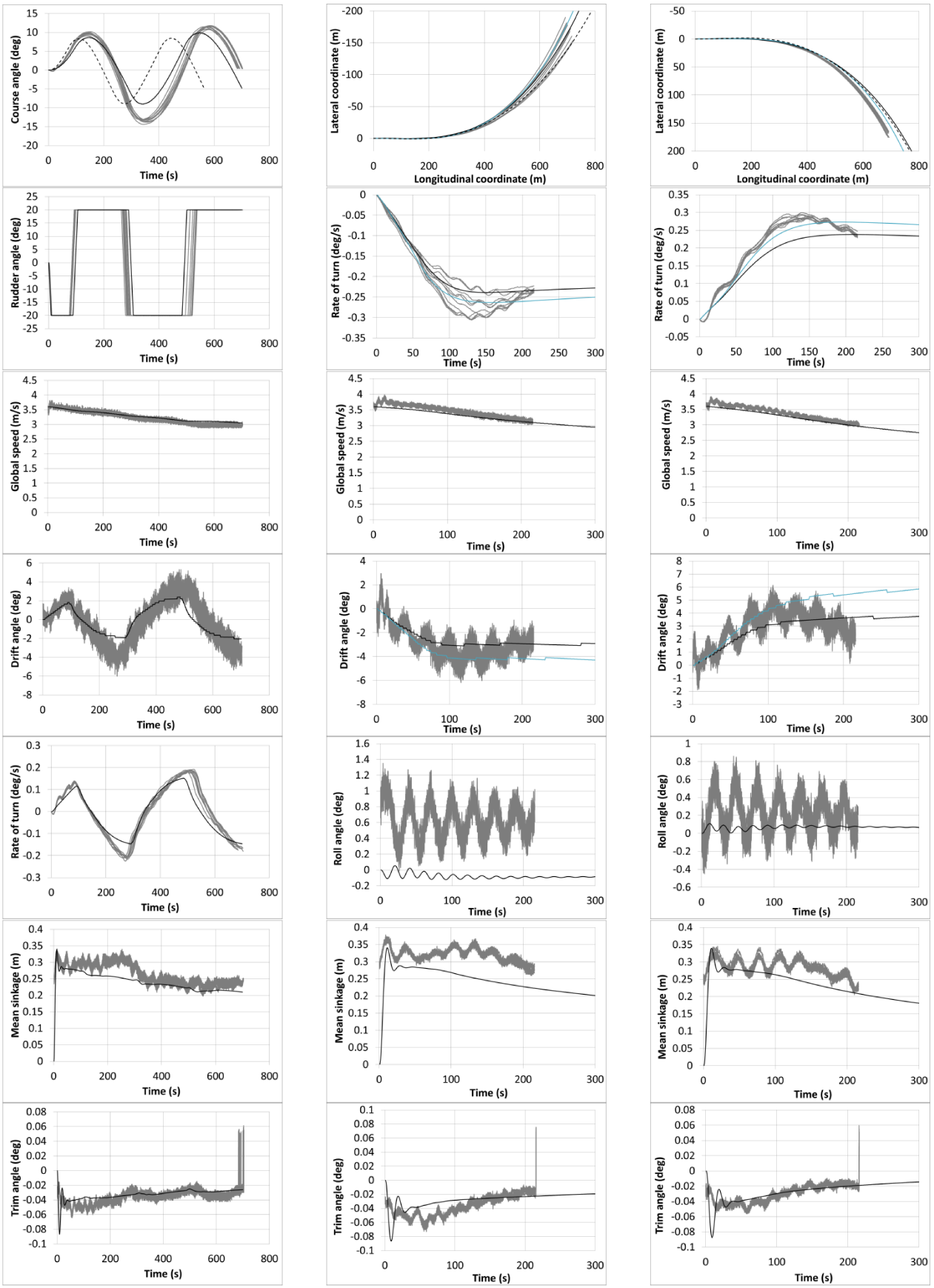

d) 20/5 zigzag test, starting to starboardside

e) 35 deg turn to portside

f) 35 deg turn to starboardside

Figure 12. Comparison between the SIMMAN 2014 model tests and the simulated manoeuvres (in prototype).

4th MASHCON, Hamburg - Uliczka et al. (eds) - © 2016 Bundesanstalt für Wasserbau ISBN 978-3-939230-38-0 (Online)
DOI: 10.18451/978-3-939230-38-0_32

EXPERIMENTAL STUDY ON THE MANOEUVRABILITY OF KVLCC 2 IN SHALLOW WATER

D J Yeo, K Yun and **Y Kim,** Korea Research Institute of Ships and Ocean engineering, Rep. of Korea

SUMMARY

Manoeuvring of ships in shallow water region is known as hard and risky, so phenomena in the shallow water region should be carefully studied for the safe voyages of ships. Ship manoeuvring in shallow and confined waters has become an issue again to people those have been interested in safe manoeuvring. Reflecting this interest, KRISO (Korea Research Institute of Ships and Ocean Engineering) had conducted a project entitled "Enhancement of simulation technique for navigation of a ship in confined waterway [PES171E]". As a part of the project, experimental studies on the manoeuvring characteristics of KVLCC 2 were conducted. Both Free Running Model Tests (FRMTs) and Horizontal Planar Motion Mechanism (HPMM) tests were conducted on false bottom of KRISO's towing tank. Based on the hydrodynamic coefficients estimated from HPMM test results, numerical simulations of turning and zigzag manoeuvres were conducted. The simulation results were compared with the results of FRMTs, especially focusing on the change in manoeuvrability due to change of water depth.

1 INTRODUCTION

Recently, several studies on a ship's manoeuvrability in shallow water were conducted. This movement is meaningful not only because manoeuvring of ships in shallow water region is known as hard and risky, but also is inevitable for most ships. Furthermore, in shallow water region, there happens many interesting hydrodynamic phenomena of a ship such as squat. Therefore, phenomena happened in the shallow water region should be carefully studied for the safe navigation of ships. SIMMAN 2014 of which purpose was to benchmark the capabilities of different ship manoeuvring simulation methods including systems based and CFD based methods, set manoeuvring in shallow water as one of its' theme.

To match the purpose of SIMMAN 2014, KRISO (Korea Research Institute of Ships and Ocean Engineering) conducted a project entitled "Enhancement of simulation technique for navigation of a ship in confined waterway [PES171E]". As a part of this project, captive manoeuvring model tests for three different ships (KCS, KVLCC 2, KLNG) were conducted to estimate manoeuvring characteristics of ships in shallow waters [4] [5] [6] [7]. Some manoeuvring trials were simulated based on hydrodynamic coefficients estimated through the captive model tests of KVLCC 2 [6]. Simulated results were compared with free running model tests conducted in the KRISO's towing tank, using false bottom facility [8].

2 HPMM MODEL TEST

2.1 SETUP & DEVICES

2.1 (a) Towing Tank

All the tests were conducted in the KRISO's towing tank. Since 1978, towing tank of the KRISO has made all the efforts to provide accurate and reliable experimental results and numerical simulations for almost 1,600 model ships over 38 years with the most sophisticated facilities and highly experienced staffs. The dimensions & characteristics of the KRISO towing tank & carriage are shown in Table 1. In Figures 1 and 2, the top view and photograph of towing tank are displayed.

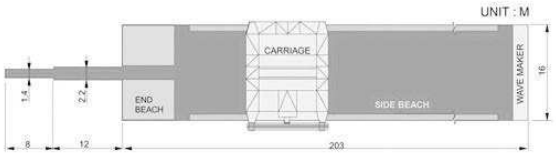

Figure 1. Top view of towing tank.

Figure 2. Photograph of KRISO towing tank.

Table 1. Dimensions & characteristics of KRISO towing tank.

	Items	Value	Remark
Towing Tank	Length	200 m	
	Breadth	16 m	
	Depth	7 m	
Carriage system	Low speed	0.04 ~ 1 m/s	2 small motors
	General speed	0.04 ~ 6 m/s	8 large motors
	Max. acceleration	1 m/s^2	

Figure 3. Picture of KRISO's false bottom facility.

2.1 (b) False-bottom

To mimic the shallow water condition, a false-bottom facility was used. The false-bottom facility was built in the KRISO's towing tank in 2011, and had been used for several purposes including these captive manoeuvring model tests. The vertical position of false-bottom facility is adjustable to make 0~7m water depth. In Fig 3, a picture of false bottom facility (L x B: 54m x 10m) is displayed [3].

2.1 (c) HPMM Device

A Horizontal Planar Motion Mechanism (HPMM) device was used for the captive manoeuvring model tests. KRISO's HPMM device has been used for estimating a ship's manoeuvrability over 30 years. The specification of KRISO's HPMM device is summarized in Table 2.

Table 2. Specification of KRISO's HPMM device.

Specifications		**Value**
Item	***unit***	
Max. Sway amplitude	*m*	1.5
Max. Yaw amplitude	*deg*	40.0
Drift available	*deg*	±360

Figure 4. HPMM device and model ship on the false-bottom.

Table 3. Principal dimensions of KVLCC 2 (model).

Dimensions		**Value**
Item	*unit*	
Scale ratio	-	39.44
Lpp	*m*	8.1136
Breadth	*m*	1.4706
Depth	*m*	0.7606
Draft	*m*	0.5273
Displacement	m^3	5.0958
Rudder area	m^2	0.1757
DP	*m*	0.25
U	*m/s*	0.5734

2.2 MODEL SHIP

A 1:39.44 scale model ship was used for the shallow water captive manoeuvring model test. Principal dimensions of the model are shown in Table 3. In figure 4, KVLCC 2 model mounted to HPMM device is displayed.

2.3 TEST MATRIX

2.3 (a) Depth over Draft (H/T) Cases and Self-Propulsion Point

Depths to draft conditions were set to be H/T = 1.2, H/T = 1.5, and H/T = 2.0. Tests were conducted with model's self-propulsion condition. To find propeller revolution at self-propulsive condition, simple self-propulsion tests were conducted. Propeller RPS at self-propulsion condition were found to be 4.28, 4.31 and 4.47 at H/T = 2.0, H/T = 1.5, and H/T=1.2 respectively.

2.3 (b) Test Matrix

Test matrices were set as Table 4 and 5 considering conventional HPMM test matrix in deep water condition and the specification of HPMM device.

Table 4. Static test matrix.

Type of Test	**Drift Angle (°)**	**Rudder Angle (°)**	**rps (1/sec)**
Static Rudder	0°	0°, ±5°, ±10°, ±15°, ±25°, ±35°	4.47 (H/T=1.2)
Drift & Rudder	0°, ±4°, ±8°, ±12°	3 Rudder Angles	4.31 (H/T=1.5)
Static Drift	0°, ±2°, ±4°, ±6°, ±10°, ±15°, ±20°	0°	4.28 (H/T=2.0)

Table 5. Dynamic test matrix.

Type of Test	Drift Angle	Independent Variable (nondimensionalized)	rps (1/sec)
Pure Sway	0°	$\dot{v}'$ =-0.24, -0.28, -0.32, -0.36 (- sign means the start direction of motion)	4.47 (H/T=1.2)
Pure Yaw	0°	r' =0.45, 0.48, 0.51, 0.54, 0.57	4.31 (H/T=1.5)
Yaw with Drift	4° 8° 12°	r' =0.45, 0.48, 0.51, 0.54, 0.57	4.28 (H/T=2.0)

3 ANALYSIS & SIMULATION

3.1 COORDINATES SYSTEM

The following right handed orthogonal coordinates system are used for the modeling of a ship's manoeuvring motion. The coordinate is moving with a body, with the origin fixed at the midship of the body [1]. The sign conventions are shown in figure 5.

3.2 MATHEMATICAL MODEL

To describe a ship's manoeuvring motion, a modular type manoeuvring equations of motion was used, based on the prescribed coordinates system.

$$\mathrm{m}(\dot{u} - vr - x_G r^2) = X_H + X_P + X_R$$
$$\mathrm{m}(\dot{v} - ur + x_G \dot{r}) = Y_H + Y_R$$
$$I_Z \dot{r} + m x_G (\dot{v} + ur) = N_H + N_R$$

where the terms with subscripts H, P and R represent the hull forces, the propeller forces and the rudder forces, respectively.

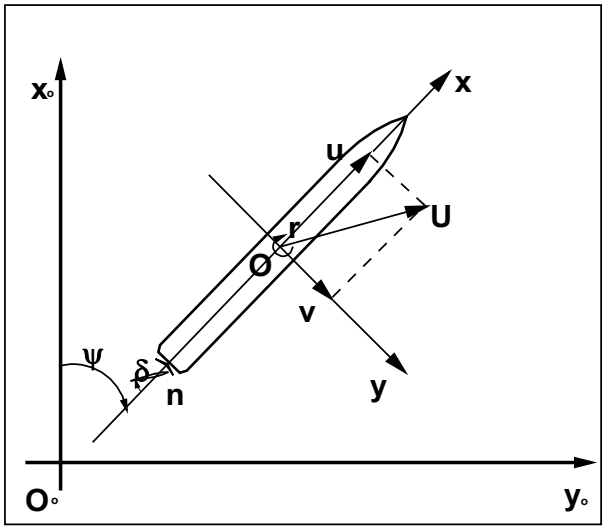

Figure 5. Coordinates system.

3.2 (a) Hull Forces

Hull forces are described as follows.

$$X_H = X_{\dot{u}}\dot{u} + \mathrm{X}_{vv}v^2 + \mathrm{X}_{vr}vr + \mathrm{X}_{rr}r^2 + X(u)$$
$$Y_H = Y_{\dot{v}}\dot{v} + Y_{\dot{r}}\dot{r} + \mathrm{Y}_v v + \mathrm{Y}_r r + \mathrm{Y}_{v|v|}v|v| + \mathrm{Y}_{r|r|}r|r| + \mathrm{Y}_{vvr}v^2 r + \mathrm{Y}_{vrr}vr^2$$
$$N_H = N_{\dot{v}}\dot{v} + N_{\dot{r}}\dot{r} + \mathrm{N}_v v + \mathrm{N}_r r + \mathrm{N}_{v|v|}v|v| + \mathrm{N}_{r|r|}r|r| + \mathrm{N}_{vvr}v^2 r + \mathrm{N}_{vrr}vr^2$$

where resistance force $X(u)$ is obtained from the resistance test.

3.2 (b) Propeller Force

Propeller force was considered as follows.

$$X_P = (1 - \mathrm{t})\rho n^2 D^4 K_T(J_P)$$

where
$J_P = u(1 - w_P)/(nD)$, n: rps, D: diameter

where
t: thrust deduction factor and w_P: the effective propeller wake fraction.

3.2 (c) Rudder Forces

Rudder forces model are described as follows.

$$X_R = -(1 - \mathrm{t}_R)F_N sin\delta$$
$$Y_R = (1 - \mathrm{a}_H)F_N cos\delta$$
$$N_R = (\mathrm{x}_R + \mathrm{a}_H \mathrm{x}_H)F_N cos\delta$$

$$F_N = \frac{1}{2}\rho \mathrm{A}_R \mathrm{U}_R{}^2 f_\alpha sin\alpha_R$$

where
A_R: rudder area, U_R: effective inflow velocity, f_α: rudder normal force coefficient, α_R: effective inflow angle, F_N: rudder normal force, t_R: rudder force deduction factor, a_H: hull force factor, x_H: hull moment factor, x_R: rudder position in x-axis, and δ: rudder angle.

3.3 SIMULATION CASES

Based on the mathematical model described in the previous section and the manoeuvring coefficients estimated from the captive manoeuvring model tests, numerical simulations for 1:39.44 scale model KVLCC 2 were conducted. Numerical turning and zigzag simulations were conducted, and results of those simulations were compared with free running model tests results those were conducted also on the false-bottom in KRISO's towing tank.

In table 6, cases for numerical simulations are summarized.

Table 6. Cases for numerical simulations & FRMTs.

Type	Rudder	Direction	H/T
Turning Circle	35°	STBD, PORT	1.2, 1.5 and 2.0
Zigzag	20°/10°	STBD, PORT	1.2 and 1.5
	20°/5°	STBD, PORT	1.2 and 1.5

4 COMPARISON OF TEST RESULTS

4.1 FREE RUNNING MODEL TEST

FRMTs in shallow water condition were carried out to obtain data to be compared with simulation results from HPMM tests. All of the data were converted into 1:39.44 scale to be drawn with the simulation results from the scale of HPMM tests model.

4.1 (a) Model Ship

1:83.74 scale model ship was selected for FRMTs when the size of the false-bottom and the speed of KVLCC2 were taken into consideration. Principal dimensions of selected model are shown in table 7. Figure 6 shows the figure of KVLCC 2 model with FRMTs devices on the false-bottom.

4.1 (b) Devices & Setup

FRMTs in shallow water depth were conducted indoor with navigational devices. To obtain position data and other navigation data, the devices in table 8 were installed in the model ship and the facility.

Table 7. Principal dimensions of KVLCC 2 (model for FRMTs).

Item	*Unit*	Value
Scale ratio	-	83.7403
Lpp	*m*	3.8213
Breadth	*m*	0.6926
Depth	*m*	0.3583
Draft	*m*	0.2484
U	*m/s*	0.3935

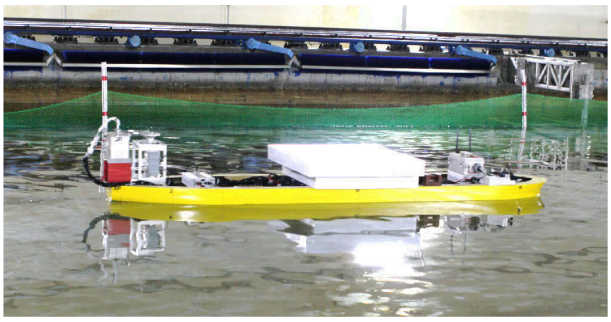

Figure 6. KVLCC2 model ship on the false-bottom.

Table 8. Devices in model ship and facility [8].

Item	Name	Specification
Camera	Sony, XCG-5005E	2448/2048 pixels, 15FPS
Lens	-	56.3° HFOV, 43.7° VFOV
Gyro	Hitachi, HOFG-1(A)	-180 to 180°, -60 to 60°/s
Inclinometer	Tamagawa, TA4270	-45 to 45°
DAQ	NI 9239	4CH, 24bit
Modem	Acksys, WLg-Link	802.11 a/b/g/h

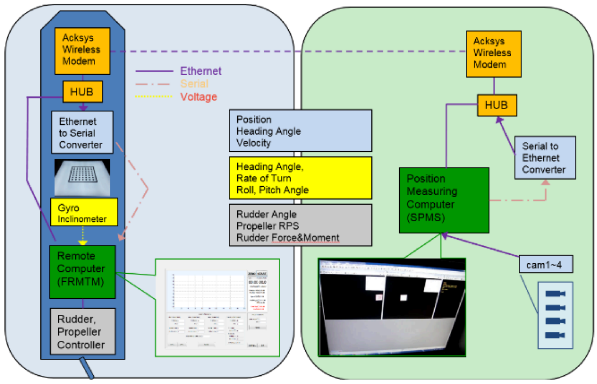

Figure 7. Diagram of data exchange [8].

Figure 7 shows the flow of navigation data and control data between the model ship and the control devices.
The model ship was loaded with devices and weights to meet test conditions such as GM, Izz, and Ixx. Final GM value was within 96.5% of designed value. Final moment of inertia for z and x axis were within 106.5% and 93.5% of designed values respectively.

4.1 (c) Test Matrix

Turning circle tests (±35°) and zigzag tests (±20 ° /5 °, ±20 ° /10 °) were carried out in three water depth conditions: 1.2, 1.5, and 2.0. Test matrix for FRMTs is shown in table 6. This test matrix was selected considering the model test specification by SIMMAN 2014 [2].
Before the model ship enters the test scenario, it has to go straightly along the false-bottom while the speed of the model ship reaches the design speed of 0.3935m/s. PD controller was adapted with neutral rudder angle in this stage. After turning circle and zigzag tests, all of the result values from FRMTs were averaged with STBD and PORT tests due to asymmetry of the model ship which has a propeller and a rudder. Figure 8 shows the process of turning circle test to STBD in H/T condition of 1.5.

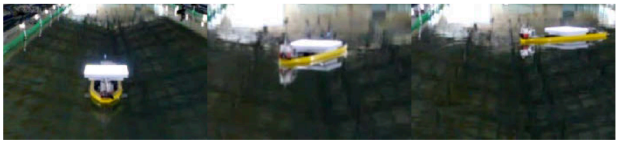

Figure 8. Turning circle test

Because of the limit of the false-bottom size, the graphs only show initial stages of turning tests and the 1st overshoots of zigzag tests.

4.2 COMPARISONS

4.2 (a) Turning

Figures 9-11 show comparisons of numerical simulations and FRMT results of 35° turning. Both numerical simulations and FRMT results show the tendency that heading angle changes slower in relatively shallower water cases. By comparisons of results of different water depth, the tendency is more clearly shown when the results of H/T conditions between 1.2 and 1.5 are compared. With this results, and considering hydrodynamic forces grows exponentially with decrease of water depth, it can be suspected that the shallow water effect on manoeuvrability also grows exponentially according to water depth.

4.2 (b) Zigzag

Figures 12~15 show comparisons of numerical simulations and FRMT results of 20°/5° and 20°/10° zigzag. Both numerical simulations and FRMT show the tendency that 1st overshoot of heading angle becomes slightly larger in H/T=1.5 condition. It can also be seen that the time to reach 1st overshoot is faster in H/T=1.2 condition. With these results, it can be deduced that a ship becomes more stable as H/T becomes small.

4.3 OVERALL COMPARISON

Both FRMT results and numerical simulation results show asymmetry between port and starboard, but asymmetric tendencies are relatively small at numerical simulation results.

Even though FRMT results seem to have slight initial turning rate to starboard side in all cases, the results of FRMT are somewhat different from those of numerical simulation.

In all cases, it can be found that the heading changes of FRMTs are faster than simulated results. Times to reach 1st overshoot are smaller at FRMT cases. The tendency to have more turning rate to port-side is more clearly seen in FRMT cases.

These differences are suspected to have relation with the difference of model scale and test condition of self-propulsion. As are mentioned in the previous sections, 1:83.74 and 1:39.44 models were used for FRMTs and captive manoeuvring model tests, respectively. Both tests were conducted at self-propulsion condition of each model scale, so it can be suspected that the rudder effectiveness at FRMT condition is larger than that at captive manoeuvring model test condition. Therefore, it can be expected that a FRMT model has better response to rudder movement, due to better rudder effectiveness condition.

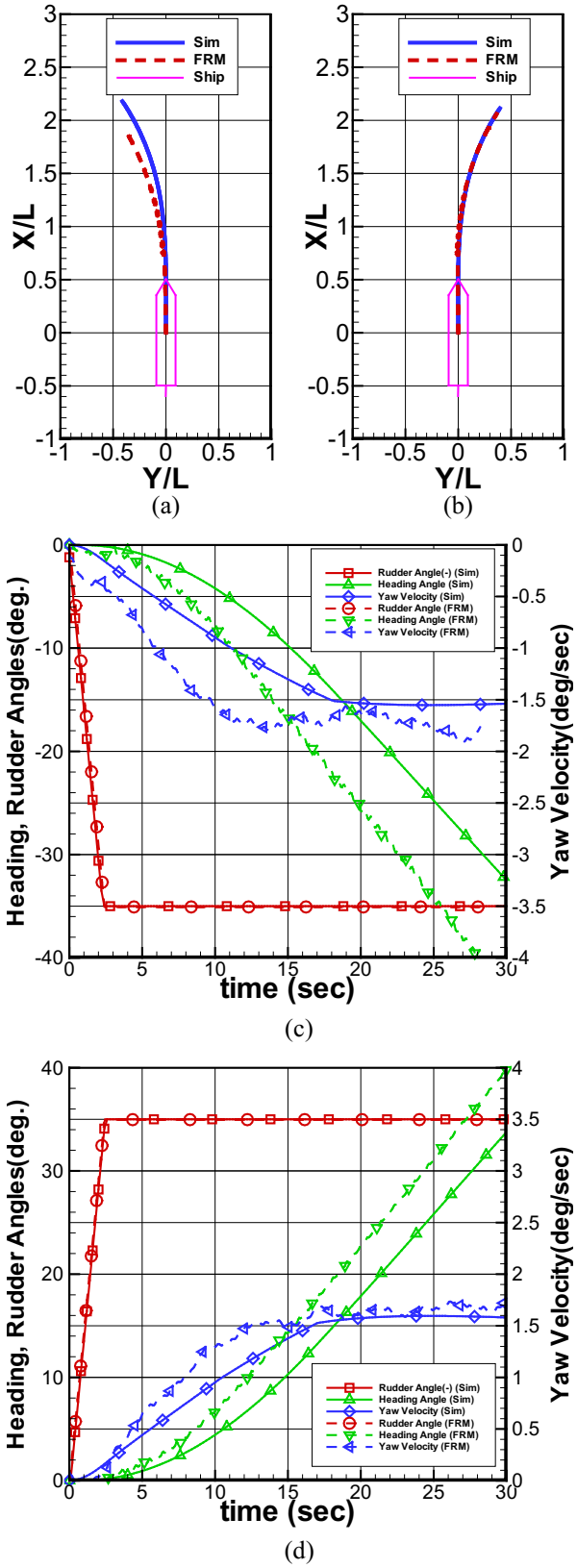

Figure 9. Comparison of 35° turning, H/T=1.2 ((a): PORT-trajectory, (b): STBD-trajectory, (c) PORT-Angles (d): STBD-Angles).

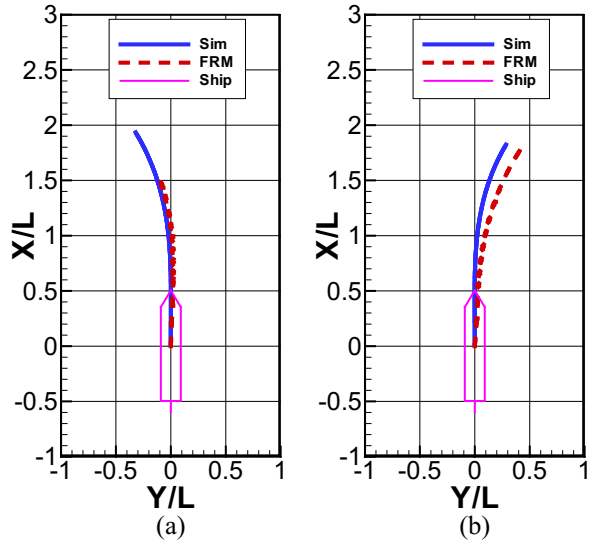

(a) (b)

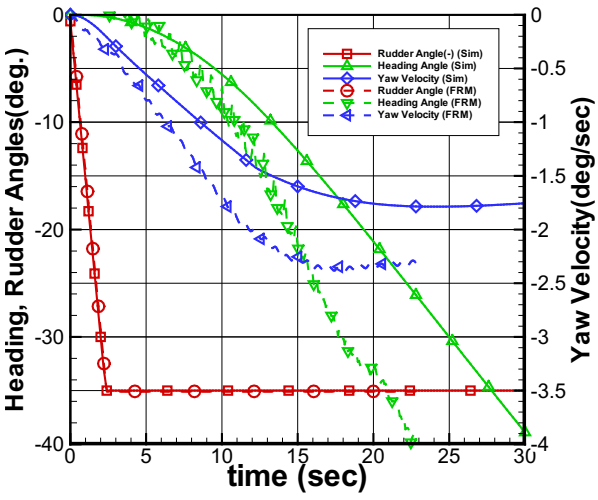

(c)

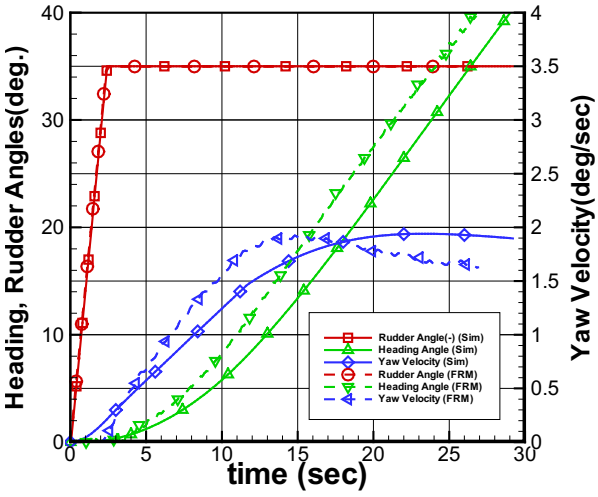

(d)

Figure 10. Comparison of 35° turning, H/T=1.2 ((a): PORT-trajectory, (b): STBD-trajectory, (c) PORT-Angles (d): STBD-Angles).

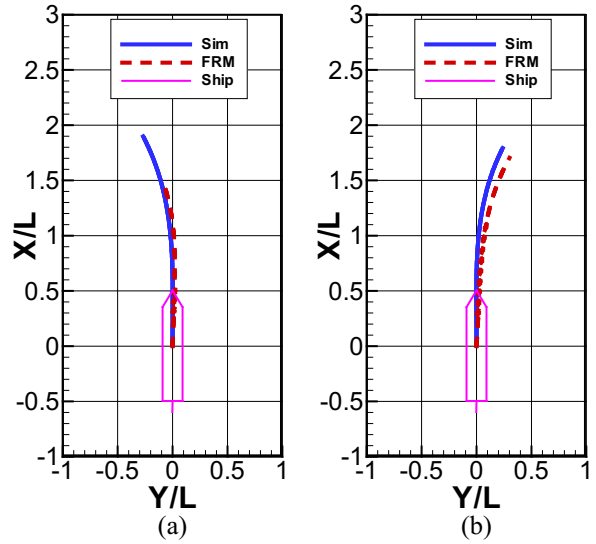

(a) (b)

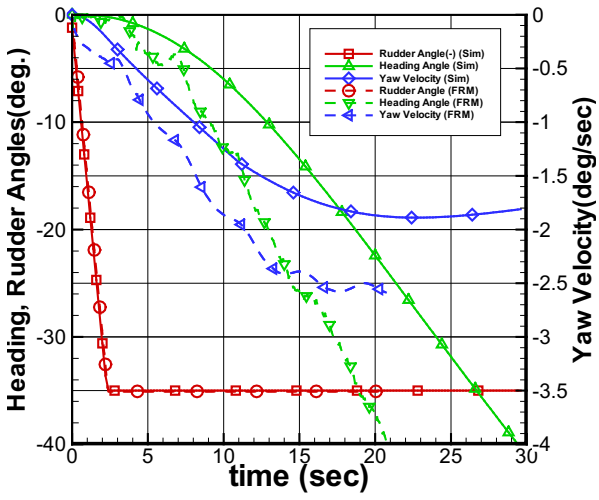

(c)

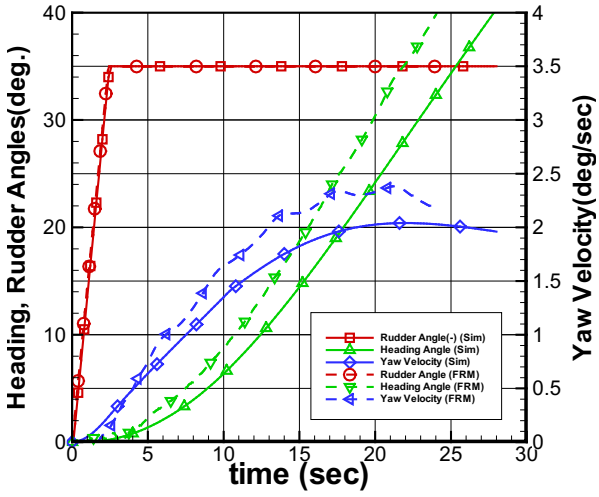

(d)

Figure 11. Comparison of 35° turning, H/T=1.2 ((a): PORT-trajectory, (b): STBD-trajectory, (c) PORT-Angles (d): STBD-Angles).

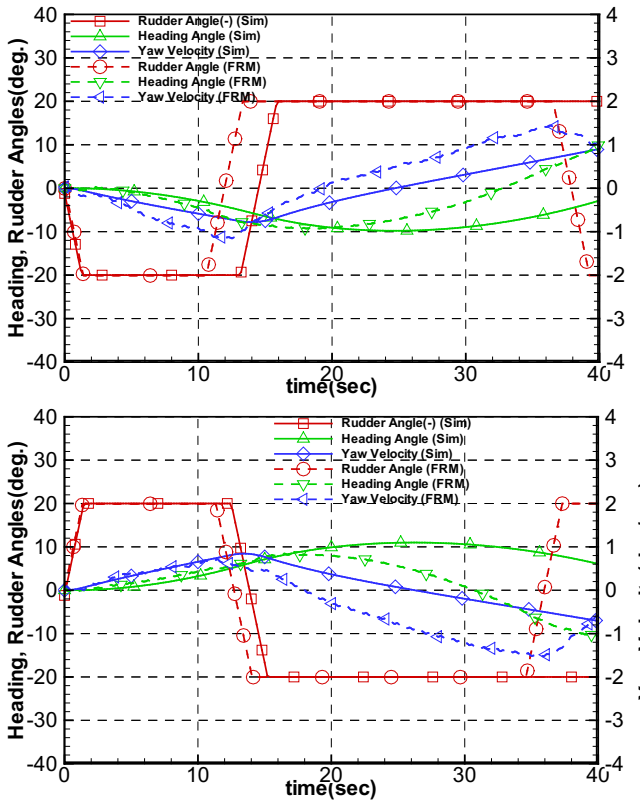

Figure 12. Comparison of 20°/5° zigzag, H/T=1.2 (upper: PORT, lower: STBD).

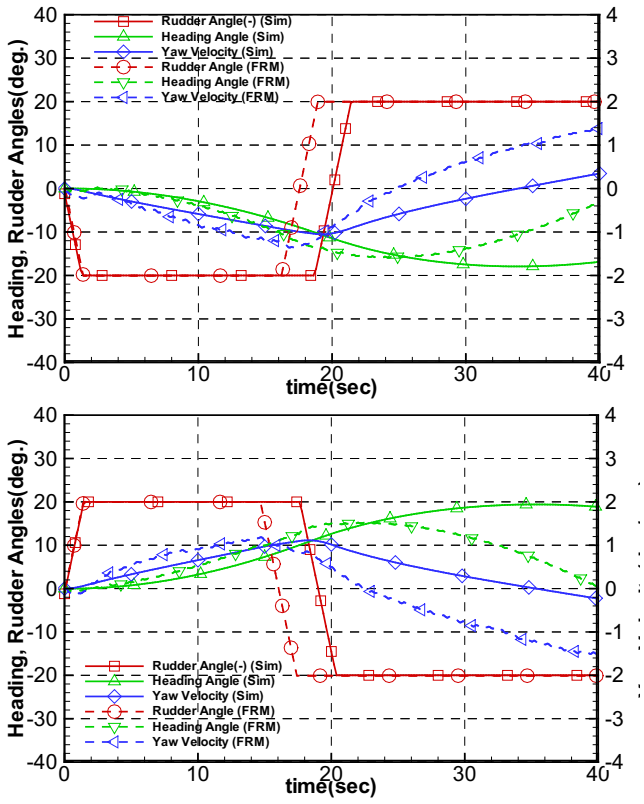

Figure 13. Comparison of 20°/10° zigzag, H/T=1.2 (upper: PORT, lower: STBD).

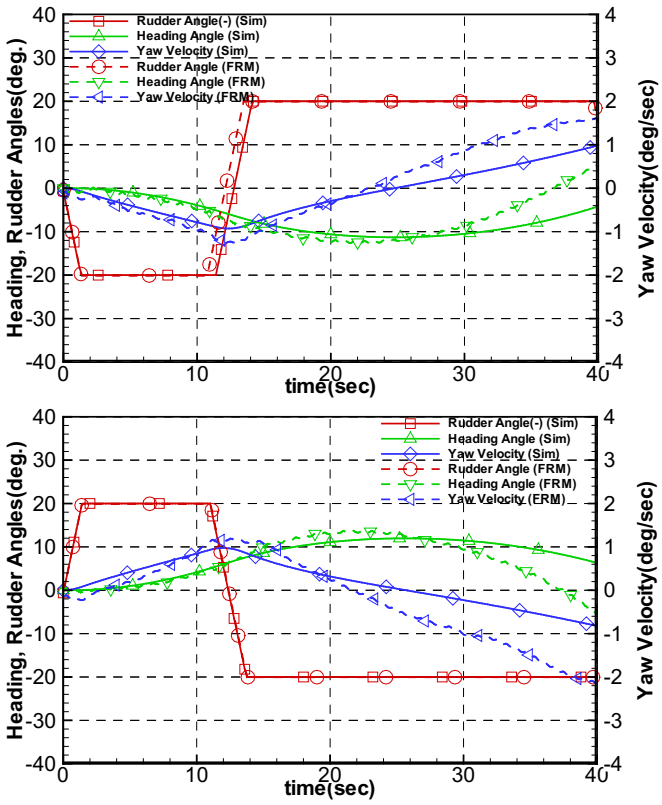

Figure 14. Comparison of 20°/5° zigzag, H/T=1.5 (upper: PORT, lower: STBD).

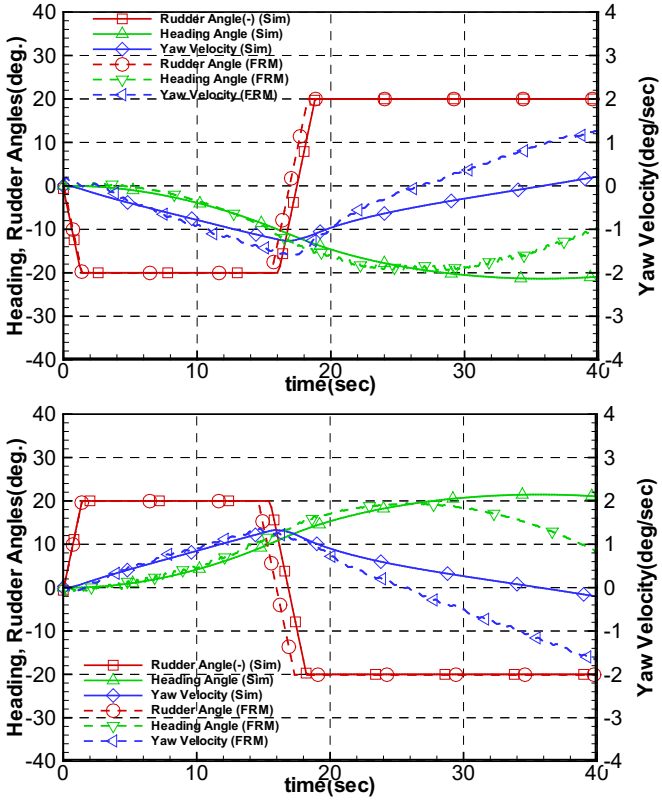

Figure 15. Comparison of 20°/10° zigzag, H/T=1.5 (upper: PORT, lower: STBD).

5 CONCLUSIONS

In this paper, the manoeuvrability of KVLCC 2 in shallow water region was investigated through experimental studies. FRMTs and captive manoeuvring model tests were conducted in KRISO's towing tank with false-bottom facility. The results of captive manoeuvring model tests were used to estimate the manoeuvring coefficients of KVLCC 2, and then numerical simulations of turning and zigzag manoeuvres were conducted based on the estimated coefficients. By comparisons between the simulation results and the results of FRMTs, these conclusions can be deduced:

- Both numerical simulations and FRMTs show the tendency that heading angle changes slower in relatively shallower water cases.
- Both numerical simulations and FRMTs show the well-known tendency that a ship becomes more stable as H/T becomes small.
- It can be suspected that the shallow water effect on manoeuvrability also grows exponentially according to water depth.

The heading changes of FRMTs were faster than simulated results, and tendencies to have more turning rate to port-side were more clearly seen in FRMT cases. These differences are suspected to have relation with the difference of model scale and propulsion conditions for each model.

6 ACKNOWLEDGEMENTS

This study was supported by the projects: "Enhancement of simulation technique for navigation of a ship in confined waterway [PES171E]" and "Development of core technology for the analysis & reproduction of maritime accidents through simulations [PES2200]".

7 REFERENCES

1. Kim, S. Y.; Yang, S.I.; Gong, I.Y.; Kim, B.Y. (1988). Development of manoeuvring evaluation procedure. *KIMM report, UCE4061328.D.*

2. Tonelli, R. (2014). Experimental fluid dynamics - free running model tests. *Workshop on Verification and Validation of Ship Manoeuvring Simulation Methods (SIMMAN)* 2014, Copenhagen, Denmark.

3. Van, S. H.; Ahn H.; Lee, Y.Y.; Kim, C.M.; Hwang, S.; Park, Y., Moon, I.S.; Park, C.S.; Seol, H.; Kim, G.D.; Lee, C.J.; Cho, S.R.; Jeong, S.Y.; Rim, D.W.; Lee, J.; Ha, I.; Bae, S.G.; Hwang, I.S.; Kwon, K.J.; Lee, C.Y.; Gong, I.Y.; Kim, Y.G.; Son, N.S.; Kim, S.Y.; Yun, K.H. (2012). Development of New Experiment Technique for Towing Tank and Large Tunnel Facility. *KORDI report.*

4. Yeo, D. J.; Yun, K.; Kim, Y.G.; Ryu, K.H. (2012). Manoeuvring captive model tests of KCS container ship in shallow water. *Proceedings of the 12th Asian Conference on Maritime System and Safety Research (ACMSSR),* Philippines.

5. Yeo, D. J.; Yun, K.; Kim, Y.G.; Kim, S.Y. (2013). Benchmark HPMM test of KCS container ship in shallow water. *Proceedings of the 3rd International Conference on Ship Manoeuvring in Shallow and Confined Water,* Ghent, Belgium.

6. Yeo, D. J.; Yun, K.; Kim, Y.G. (2014). Manoeuvring Captive Model Tests of KVLCC 2 in Shallow Waters. *Proceedings of the 14th Asian Conference on Maritime System and Safety Research (ACMSSR),* Tainan, Taiwan.

7. Yeo, D. J.; Yun, K.; Kim, Y.G.; Park, B. (2015). Manoeuvring Captive Model Tests of KLNG in Shallow Waters. *Proceedings of the 15th Asian Conference on Maritime System and Safety Research (ACMSSR),* Tokyo, Japan.

8. Yun, K.; Yeo D.J.; Ryu, G.; Lee, Y.J. (2015). Experimental study on manoeuvrability of KVLCC2 in shallow water by free running model test. *Proceedings of the International Conference on Ship Manoeuvrability and Maritime Simulation (MARSIM)*, Newcastle, UK.

8 AUTHORS' BIOGRAPHIES

Dong Jin Yeo holds the current position of principal researcher at Korea Research Institute of Ships and Ocean Engineering. He is responsible for identification, performance prediction, and control of ocean vehicles' dynamics. His previous experience includes design of optimal inputs for the identification of ocean vehicles' dynamics, modeling of ocean vehicles' dynamics, etc.

Kunhang Yun holds the current position of senior researcher at Korea Research Institute of Ships and Ocean Engineering. He is responsible for manoeuvring simulation of maritime vehicles and maritime simulator.

Yeon-gyu Kim holds the current position of principal researcher at Korea Research Institute of Ships and Ocean Engineering. He is responsible for prediction of manoeuvrability of ships and submersible bodies.

4th MASHCON, Hamburg - Uliczka et al. (eds) - © 2016 Bundesanstalt für Wasserbau ISBN 978-3-939230-38-0 (Online)
DOI: 10.18451/978-3-939230-38-0_33

SHALLOW WATER EFFECTS ON LONGITUDINAL COMPONENTS OF HYDRODYNAMIC DERIVATIVES

Y Furukawa, H Ibaragi, Y Nakiri and **K Kijima,** Kyushu University, Fukuoka, Japan

SUMMARY

In order to evaluate ship manoeuvrability in shallow water condition by numerical simulation based on MMG mathematical model, it is important to use hydrodynamic coefficients on which shallow water effects are considered properly. The authors have carried out captive model tests to measure hydrodynamic forces acting on the bare hulls of eighteen model ships of tankers, bulk carriers and so on both in deep and shallow water conditions and accumulated the measured forces as a database. In this paper, the authors present shallow water effects on the longitudinal components of hydrodynamic derivatives based on the analysis of the measured forces in the database. The variation of the longitudinal components of hydrodynamic derivatives by principal particulars of ships or water depth is investigated.

NOMENCLATURE

B	Breadth of ship (m)
C_b	Block coefficient of ship (-)
H	Depth of water (m)
L	Length of ship (m)
m	Mass of ship (kg)
m_y	Lateral component of added mass of ship (kg)
R_0	Resistance of ship in forward straight motion measured at midship (N)
r	Yaw rate (rad/s)
T	Draught of ship (m)
U	Ship speed at midship (m/s)
v	Lateral component of ship speed at midship (m/s)
X_H	Longitudinal component of hydrodynamic force acting on ship hull measured at midship (N)
$X'_{\beta r}$, X'_{uu}, X'_{vv}, X'_{vvvv}, X'_{vr}, X'_{rr}, X'_{vvr}	Hydrodynamic derivatives (-)
x_G	Longitudinal coordinate of centre of gravity of ship (m)
β	Drift angle (rad)
ρ	Density of water (kg/m^3)
$'$	Non-dimensional quantity (-)

1 INTRODUCTION

In order to evaluate ship manoeuvrability in shallow water condition by numerical simulation based on MMG (Manoeuvring Mathematical Modelling Group in Japan Towing Tank Committee) mathematical model, it is important to use hydrodynamic coefficients on which shallow water effects are considered properly. Performing captive model tests is a steady way to get the hydrodynamic coefficients but the number of facilities which have capability to conduct captive model tests in shallow water condition is few. There are several published papers [1-6] reporting the results of captive model tests both in deep and shallow water conditions. In these papers, the influence of water depth on lateral force and yawing moment is mainly paid attention and the discussion of water depth effect on longitudinal force is often omitted.

CFD calculations [7-10] are promising methods to evaluate the shallow water effect on hydrodynamic forces, but it will still take a while before captive model tests are replaced with CFD and it is also a time consuming method. Therefore an empirical prediction method based on the database of measured hydrodynamic forces by captive model tests would be still useful at a design stage.

The authors have carried out captive model tests to measure longitudinal and lateral forces and yawing moment acting on the bare hulls of ten model ships both in deep and shallow water conditions and accumulated the measured forces as a database. The basic settings of the ratio of water depth (H) for draught (T) in the shallow water conditions are $H/T = 2.0$, 1.5 and 1.3 or 1.2. Based on the database, some empirical formulae for estimating linear hydrodynamic derivatives for lateral force and yawing moment in deep and shallow water conditions had been proposed by the authors [11].

As for the longitudinal components of hydrodynamic derivatives, there are few empirical methods to estimate them even in deep water condition. An estimation chart for X'_{vr} was presented by Hasegawa [12] and Yoshimura et al. [13] proposed regression formulae for the hydrodynamic derivatives of longitudinal force based on their hydrodynamic force database.

In this paper, the authors present shallow water effects on the longitudinal components of hydrodynamic derivatives based on the analysis of the measured forces in the database. The variation of the longitudinal components of hydrodynamic derivatives by principal particulars of ships or water depth is investigated.

Table 1. Principal dimensions of model ships and conditions of water depth / draught ratio.

Ship	Ship type	L (m)	L/B	B/T	C_b	H/T 6.0	2.0	1.5	1.3	1.2
Ship A	Tanker	2.5	5.5175	2.7885	0.8099	✓	✓	✓		✓
Ship B	Tanker	2.5	5.5175	2.7885	0.8101	✓				
Ship C	Tanker	2.5	6.1320	2.4039	0.8310	✓		✓		✓
Ship D	Tanker	2.5	5.7405	2.7686	0.8023	✓	✓	✓	✓	
Ship E	Bulk carrier	2.5	5.0000	4.7619	0.8232	✓	✓	✓		✓
Ship F	Bulk carrier	2.5	5.5556	2.6627	over 0.8	✓		✓		✓
Ship G	Bulk carrier	2.5	5.3487	3.3079	over 0.8	✓	✓	✓		✓
Ship H	Bulk carrier	2.5	5.2521	3.9016	over 0.8	✓	✓			
Ship I	Bulk carrier	2.5	5.6433	2.8397	over 0.8	✓				
Ship J	Bulk carrier	2.5	5.3763	3.3696	over 0.8	✓				
Ship K	Bulk carrier	2.5	6.7150	3.3723	over 0.8	✓				
Ship L	Bulk carrier	2.5	5.3717	3.3725	over 0.8	✓				
Ship M	Coal carrier	2.5	5.5816	3.9463	0.8123	✓		✓		✓
Ship N	Cargo carrier	2.5	5.8221	2.6905	0.8271	✓				
Ship O	Cargo carrier	2.5	6.1244	2.3816	0.7727	✓	✓	✓	✓	
Ship P	Chemical tanker	2.5	5.9552	2.7384	0.7513	✓	✓	✓		
Ship Q	Cable layer	2.5	6.4817	2.8935	0.6326	✓				
Ship R	Container carrier	3.0	6.8966	2.6703	0.5717	✓				

2 MEASURED HYDRODYNAMIC FORCES ACCUMULATED IN A DATABASE

2.1 MODEL SHIPS AND TEST CONDITIONS

The authors have carried out captive model tests to measure longitudinal and lateral forces and yawing moment acting on the bare hulls of ten model ships shown in Table 1 both in deep and shallow water conditions. Most of them are full ships of which C_b is over 0.8. Captive model tests in deep water condition have been also conducted for eight model ships in Table 1. These tests were performed at either old or new Seakeeping and Manoeuvring Basin of Kyushu University. A rotating arm and a towing carriage were used at the old basin (1959-2007) and a CPMC (computerized planar mechanism carriage) was used at the new basin (2008-) to execute oblique towing test and circular motion test. Measured longitudinal forces were nondimensionalized by using the following equation and accumulated in a database.

$$X'_H = \frac{X_H}{(1/2)\rho LTU^2} \tag{1}$$

The basic settings of the conditions of drift angle β, non-dimensional yaw rate r' and water depth / draught ratio H/T are as the following. The range of drift angle is $-10^\circ \le \beta \le 20^\circ$ and non-dimensional yaw rate are varied from 0.0 to 1.0. The step sizes of β and r' are various for each model ship. The value of H/T for deep water condition is normally set greater than 6.0 and those in shallow water conditions are 2.0, 1.5 and 1.3 or 1.2.

2.2 EXAMPLES OF MEASURED FORCES

Symbols in Figure 1 show non-dimensional longitudinal forces $X'_H(\beta, r')$ of the ships A, C and M in deep water condition. The measured forces include inertia force components. It is observed that non-dimensional longitudinal force $X'_H(\beta, 0.0)$ in pure drift motion with small drift angle is almost constant for all ships. As the value of drift angle becomes larger than 10º, the absolute value of X'_H becomes slightly smaller. By paying attention to the value of $X'_H(0^\circ, r')$ on a vertical axis, it is found that its variation for non-dimensional yaw rate is quite different among the ships A, C and M. The value of $X'_H(0^\circ, r')$ for the ship C is almost constant regardless of the value of non-dimensional yaw rate. The absolute value of $X'_H(0^\circ, r')$ for the ship A decreases as non-dimensional yaw rate becomes large. In contrast, that of the ship M increases for the growth of non-dimensional yaw rate.

Longitudinal forces of the ship A in shallow water conditions are shown by symbols in Figure 2. As the depth of water becomes shallow, the nonlinearity of X'_H for drift angle appears remarkably. The value of $X'_H(\beta, 0.0)$ tends to change into the positive direction with the increase of drift angle. This phenomenon was also presented in the references [14-16]. In the condition of $H/T = 1.2$, $X'_H(\beta, 0.0)$ with large drift angle takes a positive value. It means the direction of longitudinal force turns in thrust direction. Although there is the difference in degree, the nonlinearity of X'_H for drift angle is observed for all model ships in shallow water condition.

3 MATHEMATICAL MODELS AND HYDRODYNAMIC DERIVATIVES

3.1 MATHEMATICAL MODELS FOR LONGITUDINAL FORCE ACTING ON SHIP HULL

There are several kinds of mathematical model used for the analysis of longitudinal force acting on a ship hull.

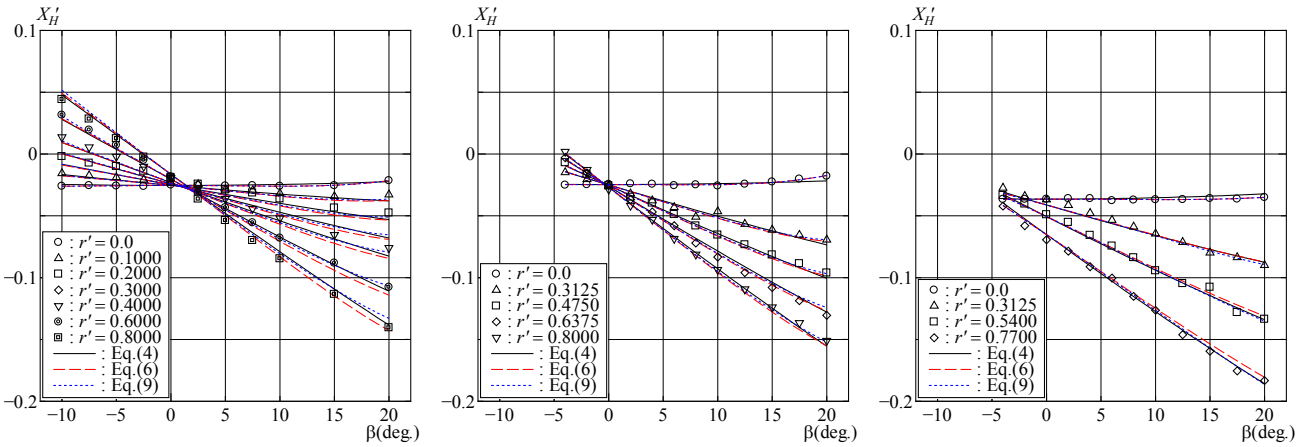

(a) Ship A (b) Ship C (c) Ship M

Figure 1. Measured hydrodynamic forces and fitting curves with mathematical models shown by Eqs. (4), (6) and (9) in deep water condition (Ships A, C and M).

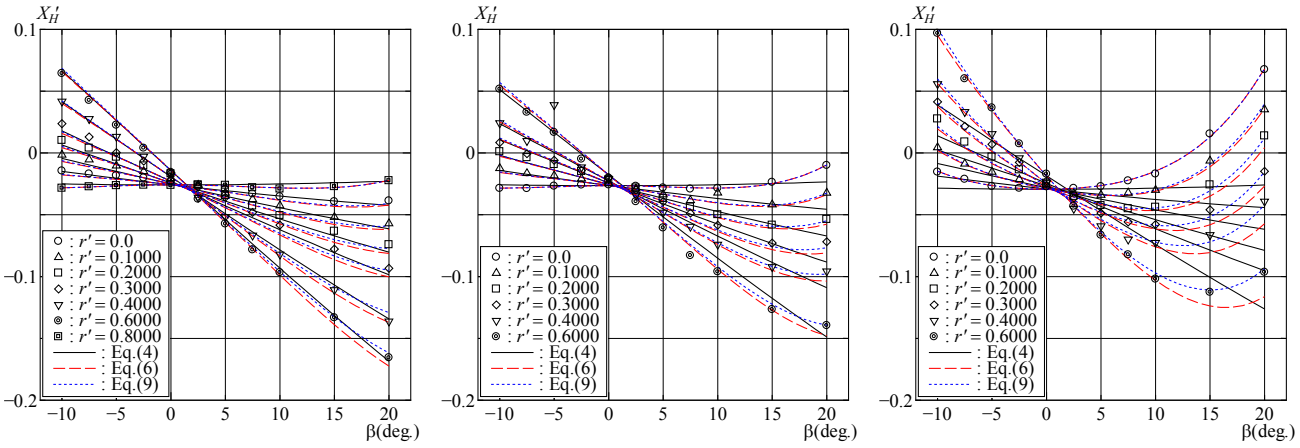

(a) $H/T = 2.0$ (b) $H/T = 1.5$ (c) $H/T = 1.2$

Figure 2. Measured hydrodynamic forces and fitting curves with mathematical models shown by Eqs. (4), (6) and (9) in shallow water conditions (Ship A).

The authors have been using the following expression [17],

$$X'_H = X'_{uu}\cos^2\beta + \{X'_{\beta r} - (m' + m'_y)\}r'\sin\beta + (X'_{rr} + x'_G m')r'^2, \tag{2}$$

where,

$$m', m'_y = \frac{m, m_y}{(1/2)\rho L^2 T}, \quad r' = \frac{rL}{U}, \quad x'_G = \frac{x_G}{L}. \tag{3}$$

The mathematical model shown by Eq.(2) is formulated using drift angle β and non-dimensional yaw rate r'. Ship mass and added mass components are included in the second term of the right side. X'_{uu} is a hydrodynamic derivative which indicates non-dimensional resistance of ship in forward straight motion. A hydrodynamic derivative $X'_{\beta r}$ is a coupling term of β and r' which represents the variation of the slope of longitudinal force for drift angle β due to yaw motion. X'_{rr} is a derivative which shows the change of resistance due to yaw motion. Eq.(2) can be transformed to the following form.

$$\begin{aligned} X'_H &= X'_{uu} - X'_{uu}\sin^2\beta + \{X'_{\beta r} - (m' + m'_y)\}r'\sin\beta \\ &\quad + (X'_{rr} + x'_G m')r'^2 \\ &= X'_{uu} - X'_{uu}v'^2 - \{X'_{\beta r} - (m' + m'_y)\}v'r' \\ &\quad + (X'_{rr} + x'_G m')r'^2, \end{aligned} \tag{4}$$

where,

$$v' = \frac{v}{U} = \frac{-U\sin\beta}{U} = -\sin\beta. \tag{5}$$

It is understood from Eq.(4) that the mathematical model contains the term of v'^2 which is the quadratic component of drift motion and non-dimensional hull resistance X'_{uu} is used in substitution for a derivative for the term. X'_{uu} is often measured in resistance test, then the estimates of the value of $X'_{\beta r}$ and X'_{rr} are required to simulate ship's manoeuvring motion using the mathematical model shown by Eq.(4).

On the other hand, the following expression is proposed in the reference [18] as the standard of mathematical

model for longitudinal force acting on a ship hull in manoeuvring motion,

$$X'_H = -R'_0 + X'_{vv}v'^2 + (X'_{vr} + m' + m'_y)v'r' + (X'_{rr} + x'_G m')r'^2 + X'_{vvvv}v'^4, \quad (6)$$

where,

$$R'_0 = \frac{R_0}{(1/2)\rho LTU^2}. \quad (7)$$

Drift motion is represented by non-dimensional sway velocity v' instead of drift angle β in Eq.(6). Comparing the mathematical models shown by Eq.(6) with the first model shown by Eq.(4), it is understood that an independent derivative X'_{vv} has been adopted for v'^2 and an additional derivative X'_{vvvv} for v'^4 has been introduced. Thus, the estimates of the value of four derivatives X'_{vv}, X'_{vr}, X'_{rr} and X'_{vvvv} are necessary to carry out numerical simulation.

Furthermore the following relations exist between the hydrodynamic derivatives used in the first model shown by Eq.(4) and the second model shown by Eq.(6),

$$X'_{uu} = -R'_0, \quad X'_{\beta r} = -X'_{vr}. \quad (8)$$

In this paper, the measured forces are analyzed by using both mathematical models shown by Eqs.(4) and (6).

3.2 FITTED RESULTS BY THE MATHEMATICAL MODELS

Fitting curves with hydrodynamic derivatives obtained by analyses using the mathematical models shown by Eqs.(4) and (6) for deep water condition are shown by black solid lines and red broken lines respectively in Figure 1 for the ships A, C and M. Both mathematical models can reproduce the measured force well for the three ships in deep water condition.

Fitting curves for the ship A in shallow water conditions are also shown in Figure 2. There exists clear difference between black solid lines and red broken lines representing the two mathematical models. Agreement of measured forces and the fitted results of the first model is not good especially for the conditions of $H/T = 1.5$ and 1.2. As stated in the previous section, the nonlinearity of X'_H for drift angle appears remarkably in shallow water conditions. On the other hand, a derivative for v'^2 in the first model shown by Eq.(4) is substituted by X'_{uu}. For this reason, the nonlinearity of X'_H for drift angle could not be expressed well in shallow water conditions by the first model.

In contrast, the second model shown by Eq.(6) having terms of v'^2 and v'^4 can reproduce the measured forces in shallow water conditions better than the first model. However, it is observed that agreement between measured and fitted results become worse as the value of non-dimensional yaw rate increase. This arises from strengthened nonlinearity for drift angle at large yaw motion, thus the discrepancy can be made small by adding a term of X'_{vvr} which represents the variation of X'_{vv} for r' as the following,

$$X'_H = -R'_0 + X'_{vv}v'^2 + (X'_{vr} + m' + m'_y)v'r' + (X'_{rr} + x'_G m')r'^2 + X'_{vvvv}v'^4 + X'_{vvr}v'^2 r'. \quad (9)$$

Fitting curves with a mathematical model shown by Eq.(9) are shown in blue dotted lines in Figures 1 and 2. Obviously difference between measured and fitted results becomes smaller in shallow water conditions, though extra effort to define the value of X'_{vvr} is required. It is up to required precision of X'_H whether X'_{vvr} is adopted.

In order to get better agreement between measured forces and fitted results by the first mathematical model, the terms of X'_{vv}, X'_{vvvv} and X'_{vvr} should be introduced in Eq.(4). It means that the first mathematical model will have the same form of the third model shown by Eq.(9). Consequently, hydrodynamic derivatives for the third mathematical model shown by Eq.(9) will be presented hereafter.

4 HYDORDYNAMIC DERIVATIVES IN DEEP AND SHALLOW WATER CONDITIONS

4.1 DERIVED HYDRODYNAMIC DERIVATIVES

The hydrodynamic derivatives were derived based on the mathematical model shown by Eq.(9) for the model ships presented in Table 1 using the database of hydrodynamic forces. After having derived the term of $X'_{vr} + m' + m'_y$, non-dimensional mass m' ($= 2C_bB/L$) was excluded from the value of the term. The values of the hydrodynamic derivatives are listed in Table 2 for deep and shallow water conditions.

4.2 HYDRODYNAMIC DERIVATIVES IN DEEP WATER CONDITION

It is ideal to evaluate the relation between the hydrodynamic derivatives and ship type while focusing on a physical phenomenon such as the change of flow field around hull. However, available information from the database is only measured forces and the principal particulars of model ships. Hence correlation coefficients between the hydrodynamic derivatives and non-dimensional parameters comprised of principal particulars were investigated. The non-dimensional parameters used in the calculation of correlation coefficients are C_b, T/L, T/B, B/L and their combinations.

Figure 3 shows each derivative as the function of a parameter indicating the highest correlation and the values of correlation coefficients are shown in Table 3. The ships are classified in two groups of $C_b \geq 0.8$ and $C_b < 0.8$ in Figure 3. It is understood that there is low correlation between each derivative and corresponding non-dimensional parameter. Even $X'_{vr} + m'_y$ which

Table 2. Hydrodynamic derivatives in deep and shallow water conditions.

Ship	H/T	R'_0	$X'_{rr}+x'_G m'$	X'_{vv}	$X'_{vr}+m'_y$	X'_{vvvv}	X'_{vvr}
Ship A	6.0	0.0253	0.0140	-0.0397	0.1827	0.6223	0.1051
	2.0	0.0258	0.0183	-0.1179	0.2986	1.2758	0.1135
	1.5	0.0265	0.0242	-0.1349	0.4215	2.3799	0.1191
	1.2	0.0293	0.0300	0.3651	0.6572	3.9971	0.3213
Ship B	6.0	0.0265	0.0253	-0.0502	0.1727	0.6027	0.1270
Ship C	6.0	0.0246	-0.0035	-0.0265	0.2243	0.7598	0.0323
	1.5	0.0280	-0.0187	0.0674	0.5071	1.9752	0.0154
	1.2	0.0336	-0.0105	0.8000	0.7266	1.9941	0.4875
Ship D	6.0	0.0271	0.0009	-0.0937	0.1738	1.0924	-0.0376
	2.0	0.0307	-0.0216	0.1171	0.0830	-0.2930	-0.2408
	1.5	0.0309	-0.0177	0.1056	0.1817	1.2542	-0.3752
	1.3	0.0355	-0.0534	0.9500	0.4976	-0.2871	0.6037
Ship E	6.0	0.0350	-0.0150	-0.0725	0.1888	0.4541	0.1775
	2.0	0.0386	-0.0198	-0.1393	0.3277	1.1213	0.0765
	1.5	0.0436	-0.0173	-0.0772	0.4997	2.0665	0.3226
	1.2	0.0508	-0.0017	0.7917	0.7184	-0.3953	0.6163
Ship F	6.0	0.0246	0.0016	-0.0658	0.1862	0.9222	0.0795
	1.5	0.0306	-0.0019	-0.0107	0.4908	1.8417	0.3815
	1.2	0.0329	0.0075	0.4986	0.5862	3.4906	0.4833
Ship G	6.0	0.0279	0.0098	-0.0638	0.1475	0.5618	0.0559
	2.0	0.0285	-0.0154	-0.1149	0.2889	1.0689	0.1698
	1.5	0.0318	0.0012	-0.1323	0.4233	2.4418	0.3373
	1.2	0.0366	0.0283	0.6966	0.4962	1.5294	0.3436
Ship H	6.0	0.0327	-0.0045	-0.0149	0.1748	0.1539	0.1107
	2.0	0.0366	-0.0187	-0.1109	0.2923	0.6408	0.1691
Ship I	6.0	0.0253	-0.0206	-0.0680	0.1374	0.5743	0.1256
Ship J	6.0	0.0284	0.0211	-0.0567	0.1732	0.2650	0.0763
Ship K	6.0	0.0384	0.0017	-0.0941	0.2329	0.6866	0.3158
Ship L	6.0	0.0288	0.0044	-0.0008	0.2243	0.1031	0.1057
Ship M	6.0	0.0364	-0.0484	-0.0191	0.1524	0.2667	-0.0644
	1.5	0.0411	-0.0360	-0.0643	0.4000	1.6335	0.2078
	1.2	0.0510	0.0134	0.4233	0.6734	3.2333	-0.0570
Ship N	6.0	0.0255	-0.0034	-0.0909	0.2209	0.8040	-0.0117
Ship O	6.0	0.0202	-0.0377	0.0659	0.1085	-0.4098	0.0134
	2.0	0.0184	-0.0479	-0.1607	0.1771	0.9899	0.0763
	1.5	0.0172	-0.0453	-0.4233	0.3521	3.6515	0.3592
	1.3	0.0218	-0.0457	0.1134	0.4541	3.2435	0.6028
Ship P	6.0	0.0247	-0.0304	-0.0514	0.1724	0.4199	0.1472
	1.5	0.0288	-0.0233	-0.1280	0.4662	2.1014	0.4523
	1.2	0.0327	-0.0055	0.6756	0.5405	0.6160	0.4897
Ship Q	6.0	0.0201	-0.0272	-0.0500	0.0841	0.5013	-0.0041
Ship R	6.0	0.0161	-0.0379	-0.1590	0.1422	1.1370	0.1961

indicates the highest correlation among the derivatives, the value of its correlation coefficient is less than 0.7. However, it can be said that ships of which C_b is less than 0.8 might have negative $X'_{rr}+x'_G m'$.

Yoshimura et al. [13] proposed approximate formulae for the hydrodynamic derivatives of longitudinal force as function of C_bB/L based on their hydrodynamic force database which contains the measured data of medium high speed merchant ships and fishing vessels. The authors also calculated correlation coefficients of the derivatives and C_bB/L and they are presented in Table 4. The values of the correlation coefficients are less than the values shown in Table 3.

According to the results presented in Tables 3 and 4, it seems to be difficult to evaluate each hydrodynamic derivative based on an explanatory variable, therefore multiple regression analysis [19] were carried out using the non-dimensional parameters such as C_b, T/L, T/B, B/L and their combinations. For the purpose of practical use, the number of explanatory variables is limited in 3 or less

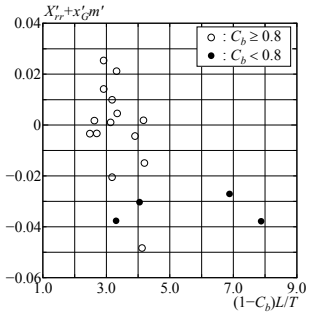

(a) $X'_{rr} + x'_G m'$

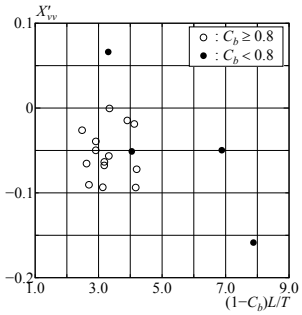

(b) X'_{vv}

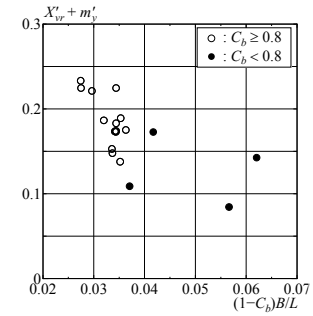

(c) $X'_{vr} + m'_y$

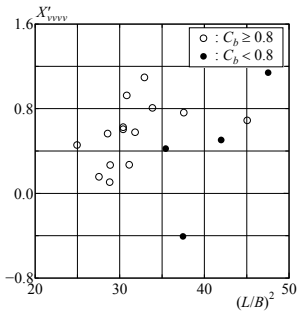

(d) X'_{vvvv}

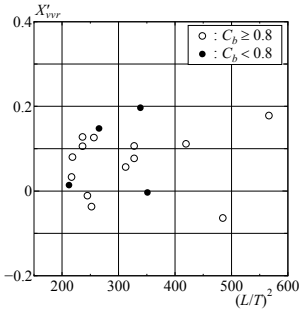

(e) X'_{vvr}

Figure 3. Scattering diagrams of each hydrodynamic derivative for corresponding non-dimensional parameter.

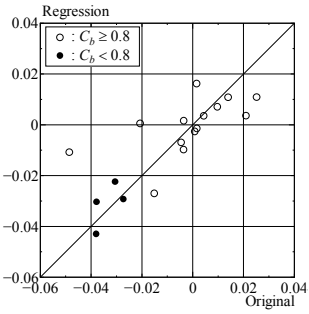

(a) $X'_{rr} + x'_G m'$

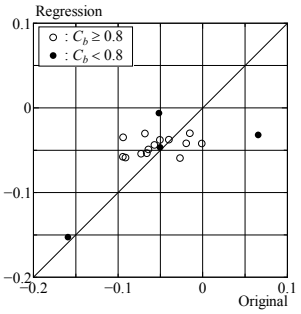

(b) X'_{vv}

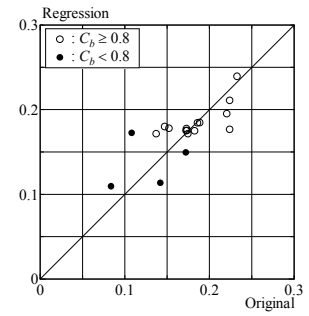

(c) $X'_{vr} + m'_y$

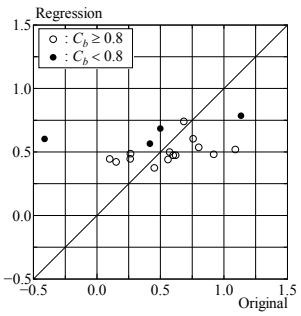

(d) X'_{vvvv}

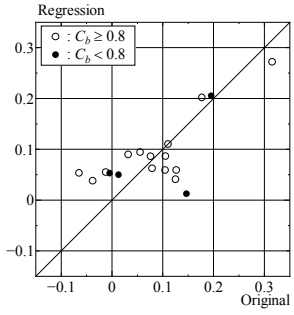

(e) X'_{vvr}

Figure 4. Scattering diagrams of measured and regression values of hydrodynamic derivatives.

Table 3. Correlation coefficients of each hydrodynamic derivative and corresponding non-dimensional parameter.

Derivatives	Parameters	Correlation coefficients
$X'_{rr} + x'_G m'$	$(1-C_b)L/T$	0.55097
X'_{vv}	$(1-C_b)L/T$	0.40707
$X'_{vr} + m'_y$	$(1-C_b)B/L$	0.65634
X'_{vvvv}	$(L/B)^2$	0.30044
X'_{vvr}	$(L/T)^2$	0.36709

Table 4. Correlation coefficients of each hydrodynamic derivative and C_bB/L.

Derivatives	Parameters	Correlation coefficients
$X'_{rr} + x'_G m'$	C_bB/L	0.51695
X'_{vv}	C_bB/L	0.33612
$X'_{vr} + m'_y$	C_bB/L	0.41833
X'_{vvvv}	C_bB/L	0.26454
X'_{vvr}	C_bB/L	0.14153

and a regression formula which has minimum AIC (Akaike Information Criterion) for each derivative was selected as the following,

$$X'_{rr} + x'_G m' = -14.7T/L - 5.20C_bB/L + 107.8BTC_b/L^2 + 0.701 \quad (10)$$

$$X'_{vv} = 7.14C_b + 38.4B/L - 46.6C_bB/L - 5.94 \quad (11)$$

$$X'_{vr} + m'_y = 3.99C_bB/L + 0.0113(L/B)^2 - 0.755 \quad (12)$$

$$X'_{vvvv} = 0.0182(L/B)^2 - 0.0826 \quad (13)$$

$$X'_{vvr} = 0.664C_b - 2.92L/B + 0.253(L/B)^2 + 7.93 \quad (14)$$

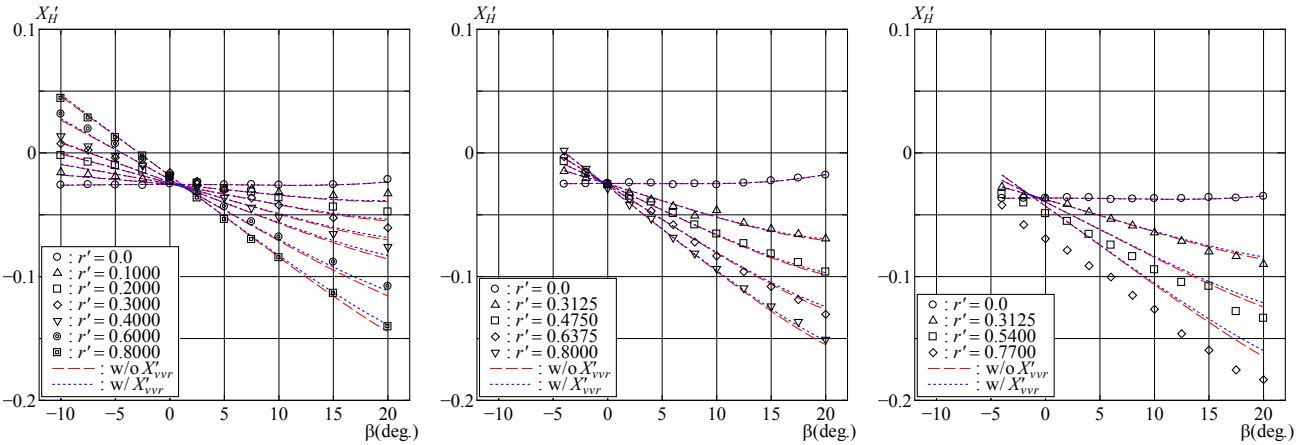

(a) Ship A (b) Ship C (c) Ship M

Figure 5. Regression curves calculated by using hydrodynamic derivatives estimated by Eqs.(10)-(14) in deep water condition (Ships A, C and M).

Figure 4 shows the scatter diagram of the measured and regression values of hydrodynamic derivatives. Although there are a few points which have low correlation between measured and regression values, most of regression values have good correlation with measured values. Fitting curves with the hydrodynamic derivatives for the ships A, C and M calculated by using Eqs.(10)-(14) are shown in Figure 5. Red broken lines and blue dotted lines represent estimated forces either without or with X'_{vvr} term respectively. Good agreement can be observed for the ships A and C, but large discrepancy exists at $\beta = 0°$ for the ship M. This arises from difference between measured and regression values of $X'_{rr} + x'_G m'$. The ship M has the largest value of $|X'_{rr} + x'_G m'|$, but Eq.(10) could not reproduce it.

4.3 HYDRODYNAMIC DERIVATIVES IN SHALLOW WATER CONDITIONS

The variation of hydrodynamic derivatives for the ratio of draught for water depth T/H is shown in Figure 6. The ratio of hydrodynamic derivatives in shallow water conditions for those in deep water condition is chosen as the vertical axis. Rough tendencies are observed in the variation of X'_{vv} and $X'_{vr} + m'_y$ for most of ships. They can be approximately formulated as the following,

$$\frac{[X'_{vv}]_{\text{shallow}}}{[X'_{vv}]_{\text{deep}}} = -70.8(T/H)^4 + 27.7(T/H)^2 + 1, \qquad (15)$$

$$\frac{[X'_{vr} + m'_y]_{\text{shallow}}}{[X'_{vr} + m'_y]_{\text{deep}}} = 1.30(T/H)^2 + 1. \qquad (16)$$

Fitting curves calculated by Eqs.(15) and (16) are shown in Figure 6 by black solid line.

On the other hand, it is difficult to find out the rough trends either in the variation of $X'_{rr} + x'_G m'$, X'_{vvvv} or X'_{vvr}. Although the ratio of $X'_{rr} + x'_G m'$ in shallow and deep water conditions takes a large value, the order of the derivative is relatively small comparing with other derivatives and the variation of the value in itself is not so

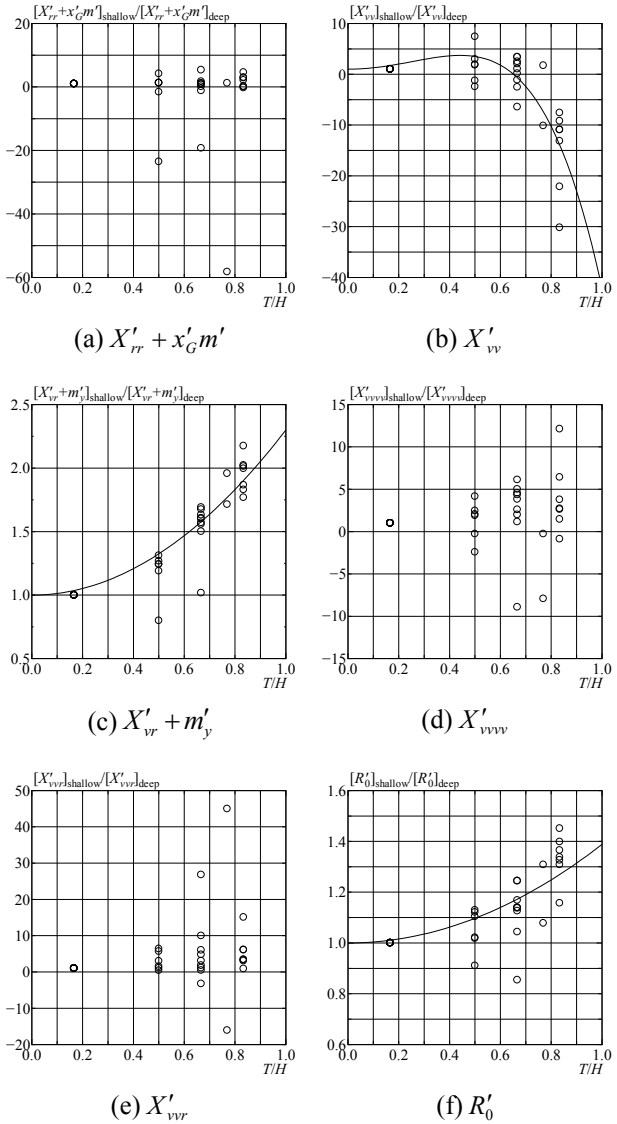

(a) $X'_{rr} + x'_G m'$ (b) X'_{vv}

(c) $X'_{vr} + m'_y$ (d) X'_{vvvv}

(e) X'_{vvr} (f) R'_0

Figure 6. Variation of hydrodynamic derivatives as function of *T*/*H*.

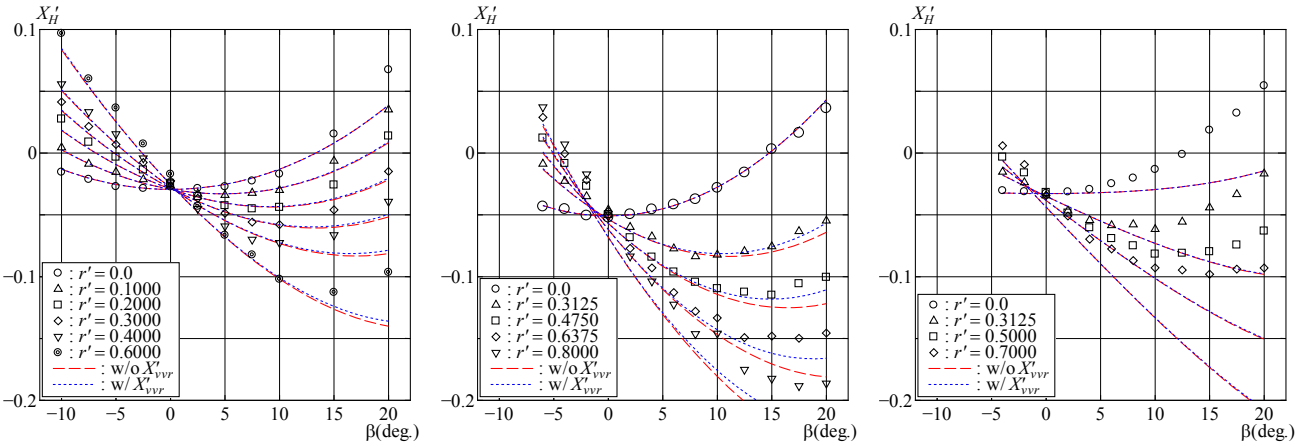

(a) Ship A (b) Ship E (c) Ship P

Figure 7. Regression curves calculated by using hydrodynamic derivatives estimated by Eqs.(10)-(16) in shallow water condition (Ships A, E and P, H/T = 1.2).

significant. Furthermore the contribution of X'_{vvvv} or X'_{vvr} to the total force is smaller than those of X'_{vv} and $X'_{vr} + m'_y$. So it may be possible to use the values of $X'_{rr} + x'_G m'$, X'_{vvvv} and X'_{vvr} in deep water condition instead of those in shallow water conditions.

Resistance coefficient R'_0 is also shown in Figure 6. It seems that the variation of R'_0 for T/H can be formulated roughly as the following,

$$\frac{[R'_0]_{\text{shallow}}}{[R'_0]_{\text{deep}}} = 0.388(T/H)^2 + 1. \qquad (17)$$

However, it would be desirable to use measured value of R'_0 in numerical simulation because R'_0 is the main component of longitudinal force and has much influence on simulation results.

Figure 7 shows fitting curves in shallow water condition (H/T = 1.2) with the hydrodynamic derivatives for the ships A, E and P calculated by using regression formulae shown by Eqs.(10)-(16). As stated above, shallow water effect on $X'_{rr} + x'_G m'$, X'_{vvvv} and X'_{vvr} are not considered in this figure and the measured value of R'_0 is used instead of using Eq.(17). Within the range where the values of drift angle and non-dimensional yaw rate are small, agreement between measured and estimated results is not so bad, but a difference gradually grows with the increase of drift angle and non-dimensional yaw rate and the degree of discrepancy varies according to ships. Significant discrepancy is observed for the ship P of which C_b is 0.7513.

5 CONCLUSIONS

Shallow water effects on the longitudinal components of hydrodynamic derivatives were investigated based on the analyses of hydrodynamic forces measured both in deep and shallow water conditions and regression formulae for the hydrodynamic derivatives as function of non-dimensional explanatory variables were presented. The regression formulae would be applicable for ships of which C_b is about 0.8 or more, because most of ships included in the database used for the analysis are bulk carriers and tankers having large C_b.

Furthermore, the variation of the longitudinal components of hydrodynamic derivatives for the water depth to draught ratio was shown. It was observed that the values of nonlinear derivatives change significantly depending on ships, hence further investigation on the influence of shallow water on the derivatives is necessary.

6 REFERENCES

1. Maimun, A.; Priyanto, A.; Rahimuddin; Baidowi, A.; Nurcholis (2009). Ship Manoeuvring in Shallow Water with Ship-bank Interaction Effects. *Proceedings of International Conference on Ship Manoeuvring in Shallow and Confined Water: Bank Effects*: pp.101–106.

2. Kim, S.W.; Kim, D.J.; Yeo D.J. (2009). Prediction of Manoeuvrability of a Ship at Low Forward Speed in Shallow Water. *Proceedings of International Conference on Ship Manoeuvring in Shallow and Confined Water: Bank Effects*: pp.147–152.

3. Yeo, D.J.; Yun, K.H.; Kim, Y.G.; Ryu, G.H. (2012). Manoeuvring Captive Model Tests of KCS Container Ship in Shallow Water. *Proceedings of 12th Asian Conference on Marine Simulator and Simulation Research (ACMSSR)*: 7pp.

4. Yoon, H.K.; Kang, S. (2013). Experimental Investigation on the Depth Effect of Hydrodynamic Coefficients Obtained by PMM Test in Square Tank. *Proceedings of 3rd International Conference on Ship Manoeuvring in Shallow and Confined Water: Ship Behaviour in Locks*: pp.209–214.

5. Yeo, D.J.; Yun, K.; Kim, Y.G.; Kim, S.Y. (2013). Benchmark HPMM Tests for KCS in Shallow Water. *Proceedings of 3rd International Conference on Ship*

Manoeuvring in Shallow and Confined Water: Ship Behaviour in Locks: pp.249–255.

6. Yeo, D.J. (2013). Investigation of the Depth Dependency of Manoeuvring Coefficients of KCS based on Captive Model Test Results. *Proceedings of 13th Asian Conference on Maritime System and Safety Research (ACMSSR)*: 6pp.

7. Simonsen, C.D.; Stern, F.; Agdrup, K. (2006). CFD with PMM Test Validation for Manoeuvring VLCC2 Tanker in Deep and Shallow Water. *Proceedings of International Conference on Marine Simulation and Ship Manoeuvrability (MARSIM) 2006*: 11pp.

8. Wang, H.M.; Zou, Z.J.; Yao, J.X. (2009). RANS Simulation of the Viscous Flow around a Turning Ship in Shallow Water. *Proceedings of International Conference on Marine Simulation and Ship Manoeuvrability (MARSIM) 2009*: 6pp.

9. Wang, H.M.; Zou, Z.J.; Tian, X.M. (2009). Numerical Simulation of the Viscous Flow around a Ship Undergoing Unsteady Berthing in Shallow Water, *Proceedings of International Conference on Ship Manoeuvring in Shallow and Confined Water: Bank Effects*: pp.121–126.

10. Kimura, Y.; Kobayashi, E.; Tahara, Y.; Koshimura, S. (2011). A Study on Estimation of Hydrodynamic Forces Acting on a Ship Hull in Shallow Water by CFD. *Proceedings of 2nd International Conference on Ship Manoeuvring in Shallow and Confined Water: Ship to Ship Interaction*: pp.193–201.

11. Furukawa, Y.; Nakiri, Y.; Kijima, K. (2011). *Proceedings of 2nd International Conference on Ship Manoeuvring in Shallow and Confined Water: Ship to Ship Interaction*: pp.147–152.

12. Hasegawa, K. (1980). On a Performance Criterion of Autopilot Navigation. *Journal of the Kansai Society of Naval Architects, Japan* No. 178: pp.93–103.

13. Yoshimura, Y.; Masumoto, Y. (2011). Hydrodynamic Force Database with Medium High Speed Merchant Ships Including Fishing Vessels and Investigation into a Manoeuvring Prediction Method (written in Japanese). *Journal of the Japan Society of Naval Architects and Ocean Engineers* Vol. 14: pp.63–73.

14. Yoshimura, Y. (1988). Mathematical Model for the Manoeuvring Ship Motion in Shallow Water (2nd Report) –Mathematical Model at Slow Forward Speed– (written in Japanese). *Journal of the Kansai Society of Naval Architects, Japan* No. 210: pp.77–84.

15. Eloot, K. (2006). Selection, Experimental Determination and Evaluation of a Mathematical Model for Ship Manoeuvring in Shallow Water. *PhD thesis, Ghent University*

16. Delefortrie, G. (2007). Manoeuvring Behaviour of Container Vessels in Muddy Navigation Areas. *PhD thesis, Ghent University*

17. Kijima, K.; Katsuno, T.; Nakiri, Y.; Furukawa, Y. (1990). On the Manoeuvring Performance of a Ship with the Parameter of Loading Condition. *Journal of the Society of Naval Architects of Japan* Vol. 168: pp.141–148.

18. Yasukawa, H.; Yoshimura, Y. (2015). Introduction of MMG Standard Method for Ship Maneuvering. *Journal of Marine Science and Technology* Vol. 20: pp.37–52.

19. Terada, D.; Yasukawa, H.; Furukawa, Y. (2013). A Regressive Model of Maneuvering Hydrodynamic Derivatives Using Hull Principal Particulars (written in Japanese). *Conference Proceedings of the Japan Society of Naval Architects and Ocean Engineers* Vol. 16: pp.13–15.

7 AUTHORS' BIOGRAPHIES

Yoshitaka Furukawa holds the current position of professor at Department of Marine Systems Engineering, Faculty of Engineering, Kyushu University. He is responsible for the research and education of ship dynamics.

Hiroshi Ibaragi holds the current position of assistant professor at Department of Marine Systems Engineering, Faculty of Engineering, Kyushu University. He is responsible for the research and education of ship dynamics.

Yasuaki Nakiri holds the current position of technical staff at Department of Marine Systems Engineering, Faculty of Engineering, Kyushu University. He is responsible for the execution of model experiment and data analysis at the Seakeeping and Manoeuvring Basin.

Katsuro Kijima is emeritus professor of Kyushu University. His previous experience includes the member of 19th and 20th ITTC Manoeuvring Committee and the chairman of 21st ITTC Manoeuvring Committee.

Ship Behaviour in Locks

4th MASHCON, Hamburg - Uliczka et al. (eds) - © 2016 Bundesanstalt für Wasserbau ISBN 978-3-939230-38-0 (Online)
DOI: 10.18451/978-3-939230-38-0_34

CALCULATION OF HYDRODYNAMIC INTERACTION FORCES ON A SHIP ENTERING A LOCK USING CFD

S L Toxopeus and **K Bhawsinka,** Maritime Research Institute Netherlands (MARIN), The Netherlands

SUMMARY

Estimation of hydrodynamic interaction forces experienced by a ship entering a lock plays an important role in the initial design phase of the lock. These forces govern the speed at which a ship can enter the lock and also the tug requirement for facilitating such manoeuvres. Hence hydrodynamic interaction forces can influence the turnaround time and the operational cost of the locks. Traditionally these forces have been calculated using model tests or by potential flow solvers. In this paper, a study is presented on predicting ship-lock interaction effects with the viscous-flow solver ReFRESCO. The scenario consists of a large-beam bulk carrier entering the Pierre Vandamme Lock in Zeebrugge, Belgium. To validate the predictions, existing model tests are used. Furthermore, the results are compared to potential flow computations and CFD results from literature to highlight the benefits of each approach. The paper will show that with careful setup of the computations, reliable predictions of the ship-lock interaction effects can be obtained. In order to capture all physics of the interaction, viscous-flow computations are preferred above potential-flow predictions.

NOMENCLATURE

B	Ship beam (m)
C_B	Block coefficient (-)
Fn	Froude number based on length (-)
Fn_h	Froude number based on water depth (-)
h	Water depth (m)
L_{oa}	Length overall (m)
L_{pp}	Length between perpendiculars (m)
T	Ship draught (m)
V	Ship velocity (m/s)
V_t'	Total flow velocity $\sqrt{V_x^2 + V_y^2 + V_z^2}/V$ (-)
$V_{x,y,z}$	Flow velocity in x, y, z direction (m/s)
x_0	x-position of midship in lock geometry (m)
X	Longitudinal force (N)
y_0	y-position of midship in lock geometry (m)
y_{0CL}	y-position of centre line of lock geometry (m)
Y	Transverse force (N)
N	Yawing moment around midship (Nm)
β	Drift angle (deg)
Δt	Computational time step size (s)

1 INTRODUCTION

Estimation of hydrodynamic interaction forces experienced by a ship entering a lock plays an important role in the initial design phase of the lock. These forces govern the speed at which a ship can enter the lock and also the tug requirement for facilitating such manoeuvres. Hence hydrodynamic interaction forces can influence the turnaround time and the operational cost of the locks. Traditionally these forces have been calculated using model tests 12 or by potential flow solvers 3. However, with the development of computational tools, CFD is increasingly applied to predict the flow around ships during lock entry, see e.g. Wang and Zou 45, using deforming grids, or Meng and Wan 6, using overset grids.

In this paper, a study is presented on ship-lock interaction effects in which the viscous-flow solver ReFRESCO is used to predict the forces and moments on a ship while entering a lock. To model the motion of the ship entering the lock, a combined sliding and deforming grid approach is adopted. The scenario consists of a large-beam bulk carrier entering the Pierre Vandamme Lock in Zeebrugge, Belgium. To validate the predictions, model tests in a 1/75 scale lock configuration conducted by Flanders Hydraulics Research (FHR) are used 12. Furthermore, the results are compared to potential flow computations to highlight the benefits of each approach.
The paper will show that with careful setup of the computations, reliable predictions of the ship-lock interaction effects can be obtained. In order to capture all physics of the interaction, viscous-flow computations are preferred above potential-flow predictions.

2 EXPERIMENTAL DATA

A feasibility study for receiving a large beam bulk carrier in the Pierre Vandamme Lock (lock dimensions are 500m×57m×18.5m) in Zeebrugge was carried out in 1990s by Flanders Hydraulics Research (FHR) and Ghent University in Antwerp. During this study, systematic captive model tests were carried out in FHR's shallow water towing tank.

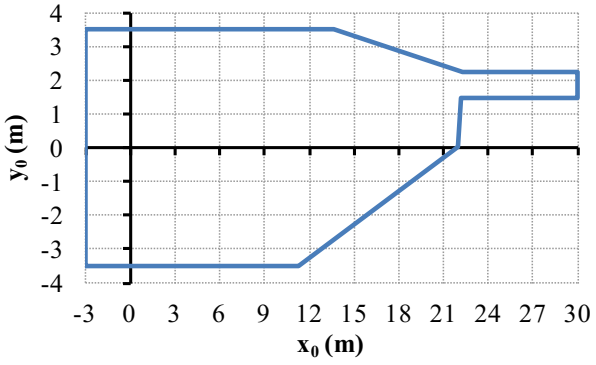

Figure 1. Overview of model lock geometry

Table 1. Main particulars of bulk carrier

Designation	Symbol	Prototype	Model
Length overall	L_{oa} (m)	265.0	3.533
Length between perpendiculars	L_{pp} (m)	259.2	3.456
Beam	B (m)	43.0	0.573
Draught	T (m)	17.342	0.231
Block coefficient	C_B (-)	0.854	0.854

Table 2. Overview of test cases

Case	Water depth to draught ratio h/T (-)	Model speed V (m/s)	Drift angle β (deg)	Eccentricity y_0-y_{0CL} (m)
G	1.2	0.15	0	0.00
H	1.2	0.10	-2	0.00

A 1/75 scale model of the lock configuration was constructed in the towing tank, with special attention to the asymmetric layout of the approach channel. FHR published a limited set of measurements as benchmark data, and more details of the measurements are given in Vantorre et al. 1.

For reference, a short description of the experimental data is repeated in this paper. An overview of the lock configuration as used in the towing tank for the captive model tests is given in Figure 1. The ship model was a 1/75 scale model of the bulk carrier *Mineral Antwerpen* with main dimensions listed in Table 1.

Results of three model tests were made available as benchmark data. During the tests, the model was equipped with a propeller and rudder, but the propeller was turned off. The variation of other parameters is shown in Table 2.

All tests started with the model's midship section at zero x_0 position. After an acceleration phase, the model was towed with constant velocity from a midship position of x_0=2m until x_0=27.5m and was then decelerated over a distance of 0.5m. For each test, the forces and moments measured on the ship model and the vertical displacements of the fore and the aft perpendiculars were obtained 1. All results were provided in model scale dimensions and plotted as a function of the longitudinal position x_0 of the model's midship section.

A ship-fixed coordinate system is used for determining ship kinematics and dynamics. The origin is located on the waterline, at half distance between the fore and the aft perpendiculars. The longitudinal x-axis is pointing ahead, the lateral y-axis is directed towards starboard, and the vertical z-axis is positive in downward direction. As a result, longitudinal forces are positive if directed ahead, lateral forces to starboard are positive, as are moments with the bow to starboard. Eccentricity with respect to the lock centreline is positive if the ship is positioned to the starboard side of the centreline. Concerning vertical motions, a sinkage of the ship is considered to be positive. The drift angle is positive when the bow is turned to starboard.

3 COMPUTATIONAL TOOLS AND SETTINGS

3.1 VISCOUS-FLOW SOLVER REFRESCO

3.1 (a) Description

ReFRESCO is a viscous-flow CFD code that solves multiphase (unsteady) incompressible flows with the RANS equations, complemented with turbulence closure models, cavitation models and volume-fraction transport equations for different phases, see 7. The equations are discretised using a finite-volume approach with cell-centred collocated variables and in strong-conservation form. A pressure-correction equation based on the SIMPLE algorithm is used to ensure mass conservation as discussed by 8. Time integration is performed implicitly with first or second-order backward schemes. At each implicit time step, the non-linear system of velocity and pressure is linearised with Picard's method and either a segregated or coupled approach is used. In the latter, the coupled linear system is solved with a matrix-free Krylov subspace method using a SIMPLE-type preconditioner 8. A segregated approach is always adopted for the solution of all other transport equations. The implementation is face-based, permitting grids with elements consisting of an arbitrary number of faces (hexahedra, tetrahedra, prisms, pyramids, etc.), and, if needed, h-refinement i.e. hanging nodes. State-of-the-art CFD features such as moving, sliding and deforming grids, as well automatic grid refinement 9 are also available in the code.

For turbulence modelling, RANS/URANS, Scale Adaptive Simulation (SAS) 10, ((I)D)DES, Partially Averaged Navier Stokes (PANS) and LES approaches are available, see Pereira et al.11 12 13. The Spalart correction (proposed by Dacles-Mariani 14) to limit the production of turbulence kinetic energy based on the stream-wise vorticity can be activated. Automatic wall functions are available.

The code is parallelised using MPI and sub-domain decomposition, and runs on Linux workstations and HPC clusters. ReFRESCO is currently being developed, verified and validated at MARIN in the Netherlands in collaboration with IST (Lisbon, Portugal), USP-TPN (University of São Paulo, Brazil), Delft University of Technology, the University of Groningen, the University of Southampton, the University of Twente and Chalmers University of Technology.

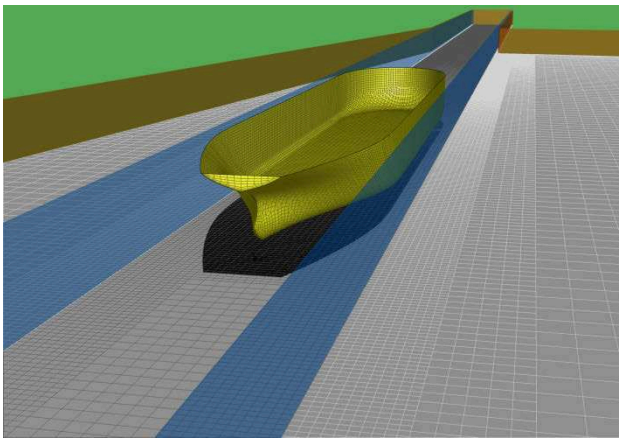

Figure 2. Port side, ship and starboard domains. The interfaces between the domains are indicated in blue.

3.1 (b) Computational domain and setup

To simplify the computations, free surface deformation, dynamic trim and sinkage, and the existence of the rudder and the propeller were neglected. Because of the very low speed during the experiments, i.e. the maximum Froude number was Fn=0.026 and the maximum depth Froude number Fn_h=0.091, it can be expected that the influence of the free surface on the results is small. Furthermore, the non-rotating propeller is expected to mainly produce additional drag. The neglect of the rudder may cause some deviation between the computations and the measurements.

Unstructured grids with hexahedral cells were generated with HEXPRESS. Three domains were made: a domain on port side of the ship, a domain containing the ship and a domain on starboard side of the ship, see Figure 2. To facilitate the motion of the ship while entering the lock, the domain with the ship was deforming, with sliding interfaces between the deforming block and the (non-deforming) port and starboard domains. The deformation of the ship domain was realised using Radial Basis Functions 15.

The port and starboard domains were generated with more-or-less regular grids, but with additional refinement towards the interface in order to improve the transfer of information across the interface. The ship domain was generated with refinements towards the interfaces and towards the ship hull. The average y^+ value was around 40 to 60, so wall functions were used to model the flow close to the hull surface. To maintain the grid quality during the full deformation of the grid for $0 < x_0 < 27$m, the grid was made with the ship at x_0=15.47m and subsequently the grid was deformed such that the computations could start with the ship at x_0=0m.

The size of the computational domain was the same as the lock geometry used during the experiments.
On the hull surface, all external boundaries and the bottoms of the domains, no-slip boundaries were adopted. At the undisturbed water surface, a symmetry boundary condition was applied.

Table 3. Overview of grid densities

	Initial	Fine
Total cells	1645552	4646782
Cells port domain	381114	1490780
Cells ship domain	796368	1541248
Cells starboard domain	468070	1614754
Faces on hull	12412	46590

Two grids were made: an initial grid with about 1.6 million cells, and a finer grid of about 4.6 million cells. Table 3 presents the number of cells in the grids and each domain and the number of faces used to represent the hull. The grid for case H was obtained using the grid of case G and rotating the ship by -2° around the vertical axis through the midship, using mesh deformation.
For the present computations, use was made of the k-ω SST turbulence model 16 and a second order accurate time discretisation.

3.2 POTENTIAL-FLOW SOLVER ROPES

3.2 (a) Description

ROPES has been developed for the prediction of ship-ship interaction forces in shallow water of arbitrary depth. The computational method used in ROPES is based on three-dimensional potential flow and the double-body assumption. This means that free-surface effects of vessels are not accounted for. Furthermore, trailing wakes are not used in ROPES, so the potential flow model does not include lift effects. The flow equations are solved using standard zero-order panels and Rankine sources with or without the effect of restricted water depth and channel walls (see Pinkster 17 and Korsmeyer et al. 18). Based on the solution of the source strengths on the panels describing the various bodies, the hydrodynamic forces on the ships are computed with equations developed by Xiang and Faltinsen 19. These equations are used to compute the complete set of hydrodynamic forces on all bodies. ROPES is applicable to multi-body simulation scenarios involving various ships and port structures.

3.2 (b) Computational domain and setup

A close up view of the panel distribution on the hull and on the lock surface is given in Figure 3. The hull is represented using 1650 panels, while 2091 panels are used to describe the lock surface. For simplicity, the rudder and propeller have not been considered in the ROPES computations. The computations were made for full scale conditions and the interaction force and moment results were obtained. These results were then scaled to obtain model scale results.

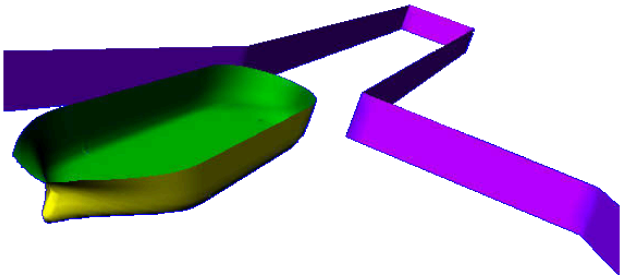

Figure 3. Panelling for ROPES potential flow computation, case G

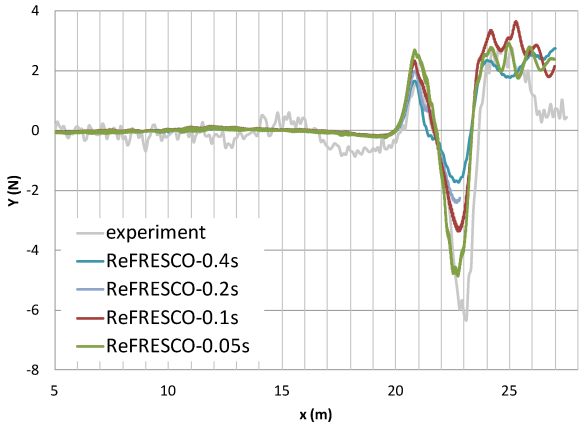

Figure 4. Influence of time step on transverse force, case G, initial grid

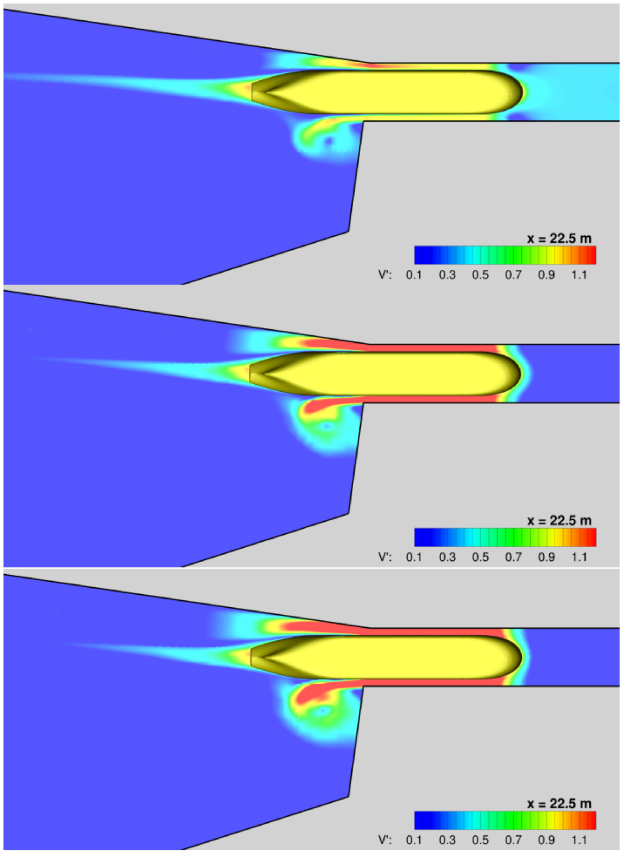

Figure 5. Visualisation of the total velocity field V_t' at the water surface for Δt=0.4s (top), Δt=0.1s (middle) and Δt=0.05s (bottom), case G, initial grid, x_0=22.5m

4 RESULTS

4.1 REFRESCO SOLUTION VERIFICATION

4.1 (a) Iterative convergence

During each time step, the RMS of the residuals were reduced about 4 orders of magnitude. It was found that during the approach phase, lower residuals could be obtained than with the ship near or in the lock entry. This is caused by the increased complexity of the flow when entering the lock.

4.1 (b) Discretisation in time

It was found that the ReFRESCO results were very dependent on the chosen computational time step Δt during the stage of entering the lock entrance, see Figure 4 for the case G results. Therefore ReFRESCO runs were made for various time steps (ranging from 0.4s to 0.025s) to check the influence of the discretization in time. Satisfactory results were obtained for 0.05s time steps. Calculations with an even smaller time step of 0.025s did not improve the results. Figure 5 shows the V_t' velocity field around the ship at a specific position during the case G computation. It is seen that by reducing the time step, significantly different and more complex physics are captured.

Also for case H, the time step size was varied for the computations with the initial grid. The influence of the time step size on the transverse force can be seen in Figure 6. For the flow field, the results are shown for two different time steps in Figure 7. Again, satisfactory results were obtained for Δt=0.05s.

For the lock approach (up to around x_0=17m), a time step size of 0.2s appeared to be sufficient. Therefore, all subsequent simulations were done with a time step Δt of 0.2s ($\approx$1/115 L_{pp}/V) for $0 < x_0 < 17$m and 0.05s ($\approx$1/460 L_{pp}/V) for $x_0 > 17$m.

4.1 (c) Discretisation in space

For case G and H, two different grid sets were used. Some influence of the grid density was seen in the longitudinal force X and marginally in the transverse force and yawing moment for case G, see Figure 8. For these grid densities, the discretisation error due to space was found to be smaller than the error due to discretisation in time.
Also for case H, the influence of the grid was studied, see Figure 9 and a similar grid dependency was observed.

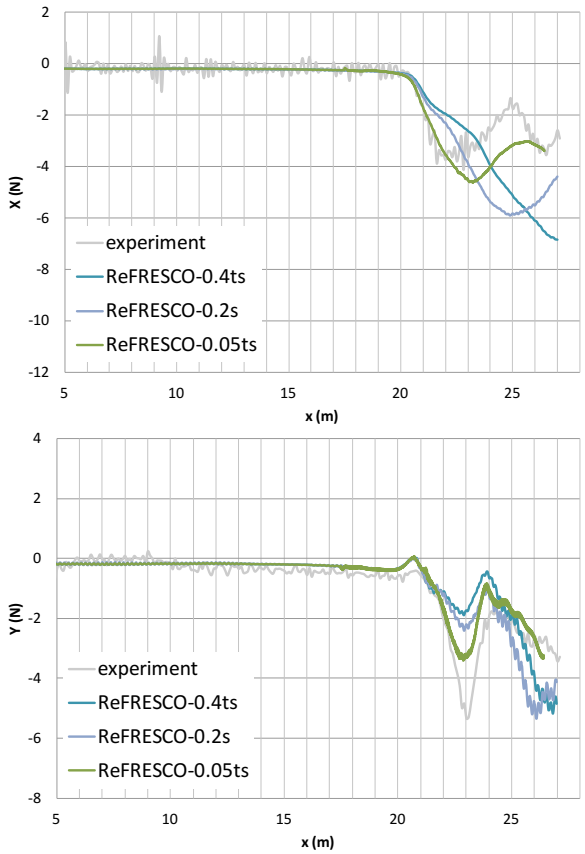

Figure 6. Influence of time step on transverse force, case H, initial grid

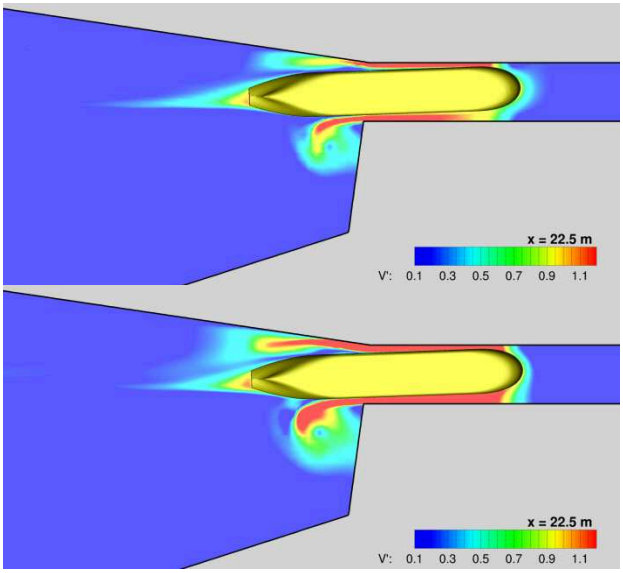

Figure 7. Visualisation of the total velocity field V_t' at the water surface for Δt=0.2s (top) and Δt=0.05s (bottom), case H, initial grid, x_0=22.5m

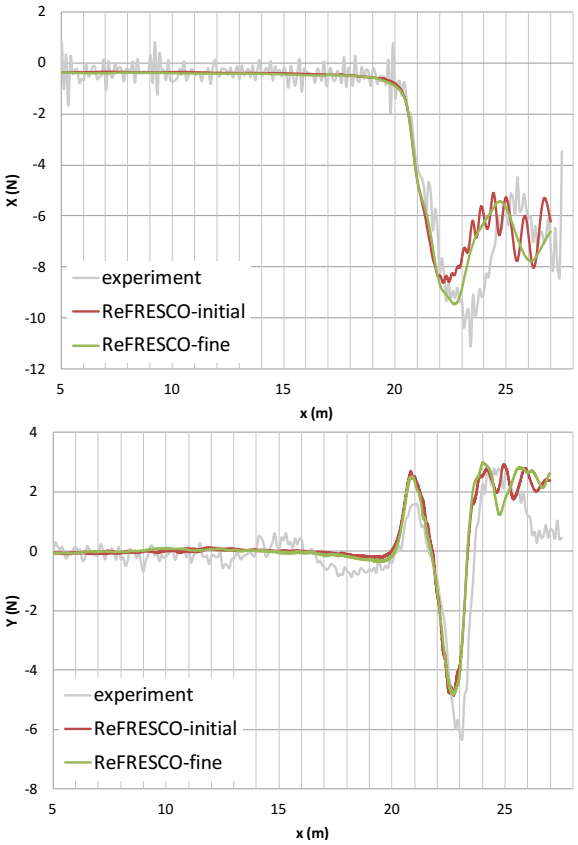

Figure 8. Influence of grid density on longitudinal (top) and transverse force (bottom), case G, Δt=0.05s

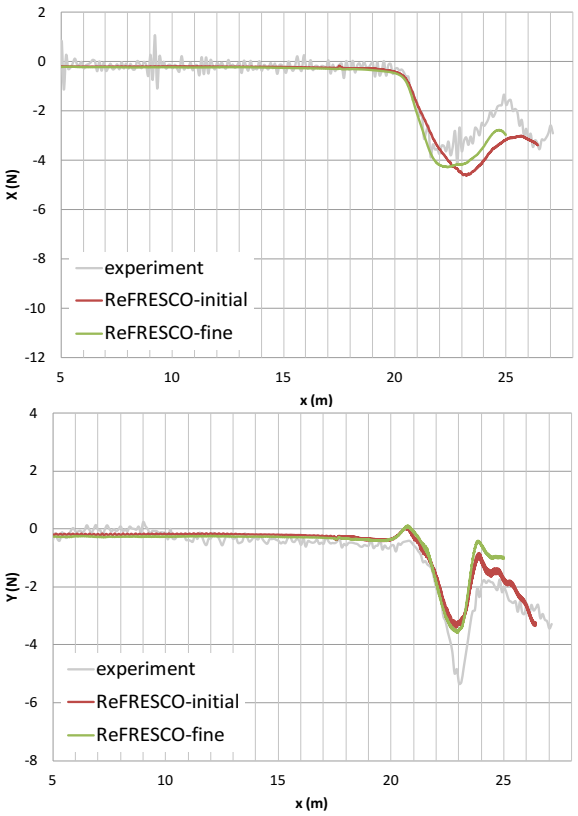

Figure 9. Influence of grid density on longitudinal (top) and transverse force (bottom), case H, Δt=0.05s

4.2 DISCUSSION OF THE FLOW

To better understand the flow during the lock entry, the absolute flow velocity V_t' around the ship calculated by ReFRESCO with a calculation time step of Δt=0.05s is plotted in Figure 10 and Figure 12 for case G and in Figure 11 and Figure 13 for case H, for positions of the midship of x_0=19.5, 20.5, 21.5, 22.5 and 23.5m. These plots give an indication of the development of the flow as the ship enters the lock.

First looking at case G, the asymmetry in the flow due to the asymmetric approach channel design can be seen: at port side, higher velocities can be observed than at starboard. Initially, this results in a slight suction force towards port side (see the evolution of the forces in Figure 14). At x_0=20.5m, the bow reaches the lock gate and a large flow velocity develops between the bow and the starboard side of the lock entrance. A strong side force is generated, combined with a positive yawing moment, both pulling the bow to starboard.

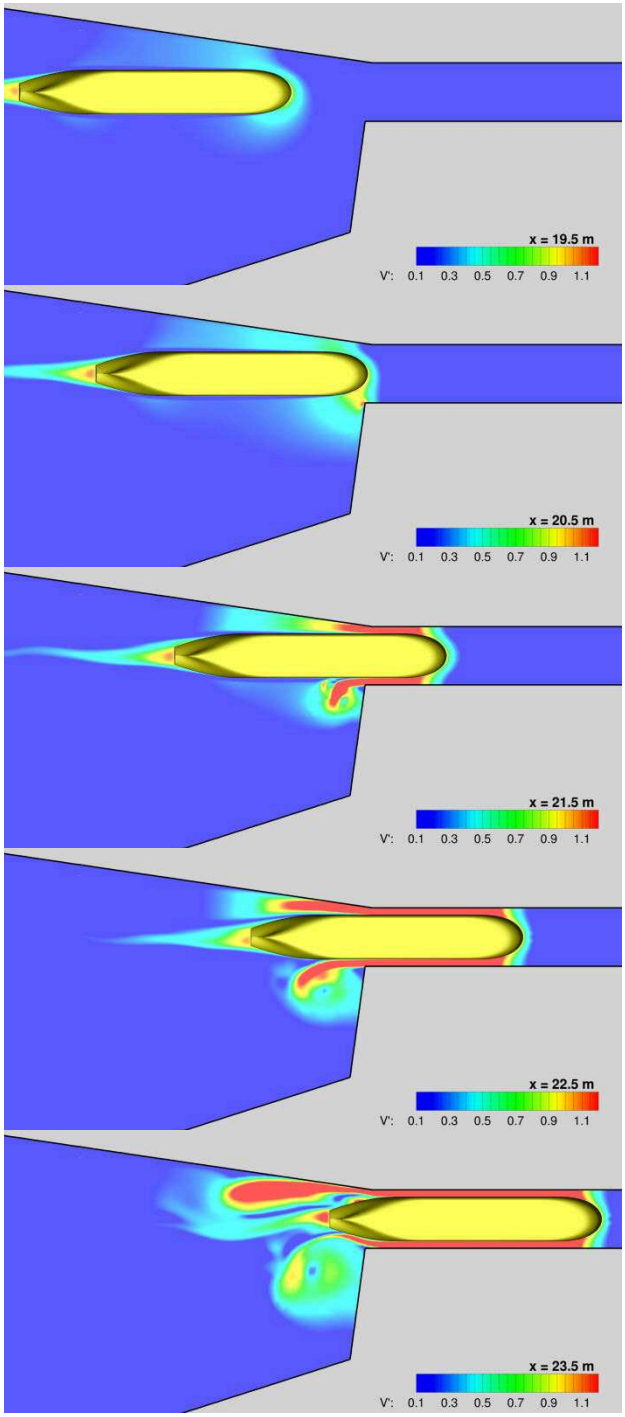

Figure 10. Visualisation of the total velocity field at the water surface, case G, fine grid, Δt=0.05s

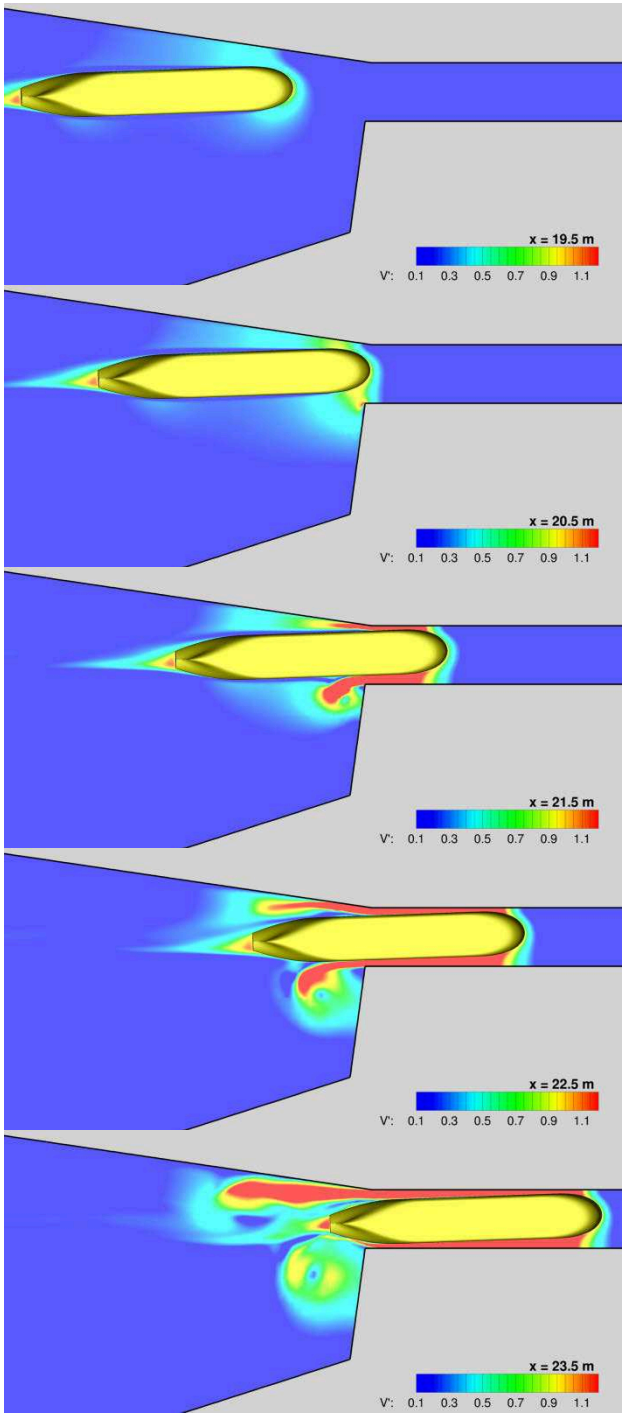

Figure 11. Visualisation of the total velocity field at the water surface, case H, fine grid, Δt=0.05s

When the ship moves further, the water in the lock is pushed outward due to the displacement of the ship and it accelerates around the hull. At port side, the flow along the harbour walls follows the wall without separating, but at starboard, the sharp edge between the lock wall and harbour wall induces a separation of the out flow of the lock and subsequently a large eddy is generated.

These eddies have more space to mix and dissipate with the surrounding flow than the accelerated flow on port side. A large region of return flow develops on port side and with the ship at x_0=22.5m, the accelerated flow extends along the complete length of the ship. Therefore a suction force towards port side is acting on the hull, in combination with a yawing moment pulling the stern to port side.

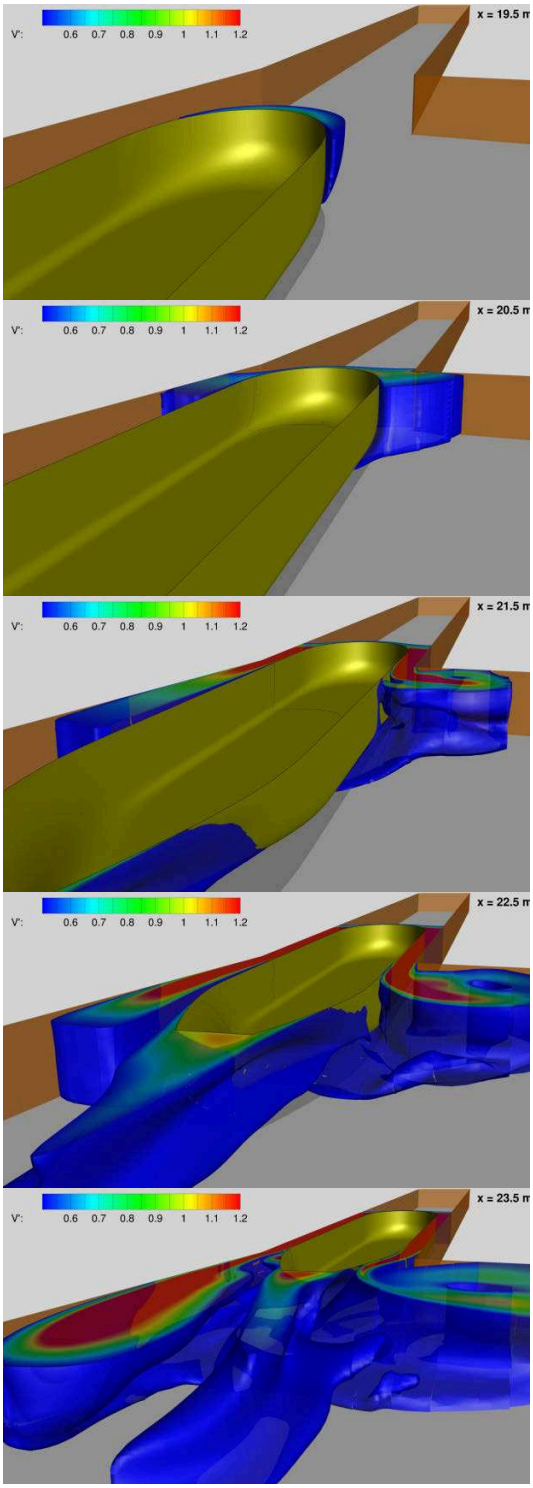

Figure 12. Isosurface of V_t'≥0.5, coloured by V_t', for several longitudinal positions of the model, case G, fine grid, Δt=0.05s

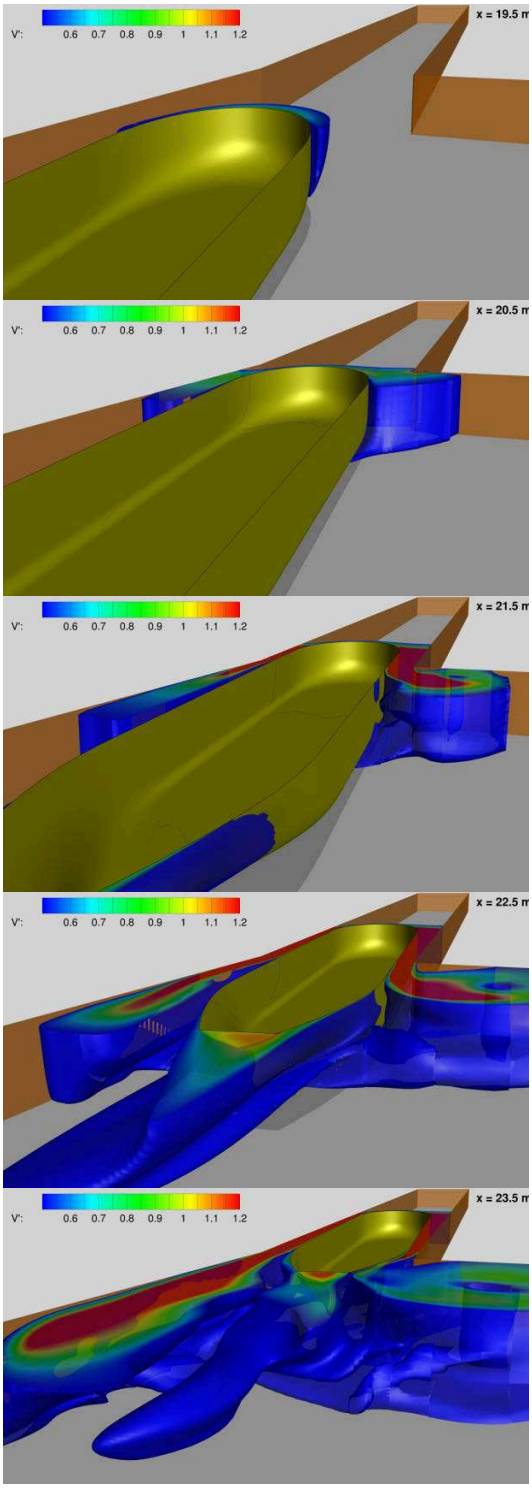

Figure 13. Isosurface of V_t'≥0.5, coloured by V_t', for several longitudinal positions of the model, case H, fine grid, Δt=0.05s

When the stern enters the lock, around x_0=23.5m, the accelerated flow on starboard side follows the shape of the stern without separation, while the flow on port side, with a slightly higher velocity, cannot remain attached and separates from the stern. This generates a low pressure region at the starboard side of the stern and a higher pressure on port side, pushing the stern towards starboard.

For case H, in which the ship sails with a drift angle β of -2 deg, similar flow physics are observed. However, due to the drift angle, the distance between the hull and the lock walls becomes smaller and larger flow gradients occur.

4.3 COMPARISON WITH THE EXPERIMENTS

A comparison of the forces and moment computed by ReFRESCO (fine grid, Δt=0.05s) and ROPES with the experiments for case G is given in Figure 14. It is seen that the ReFRESCO results match very well with the model test results both in terms of trends. The agreement in terms of absolute values is reasonable, although the peak values are not exactly captured. The observed differences can probably be attributed partly to numerical or experimental errors, but also to the neglect of the dynamic trim and sinkage, the free surface deformation, and the propeller and rudder not being incorporated in the CFD results.

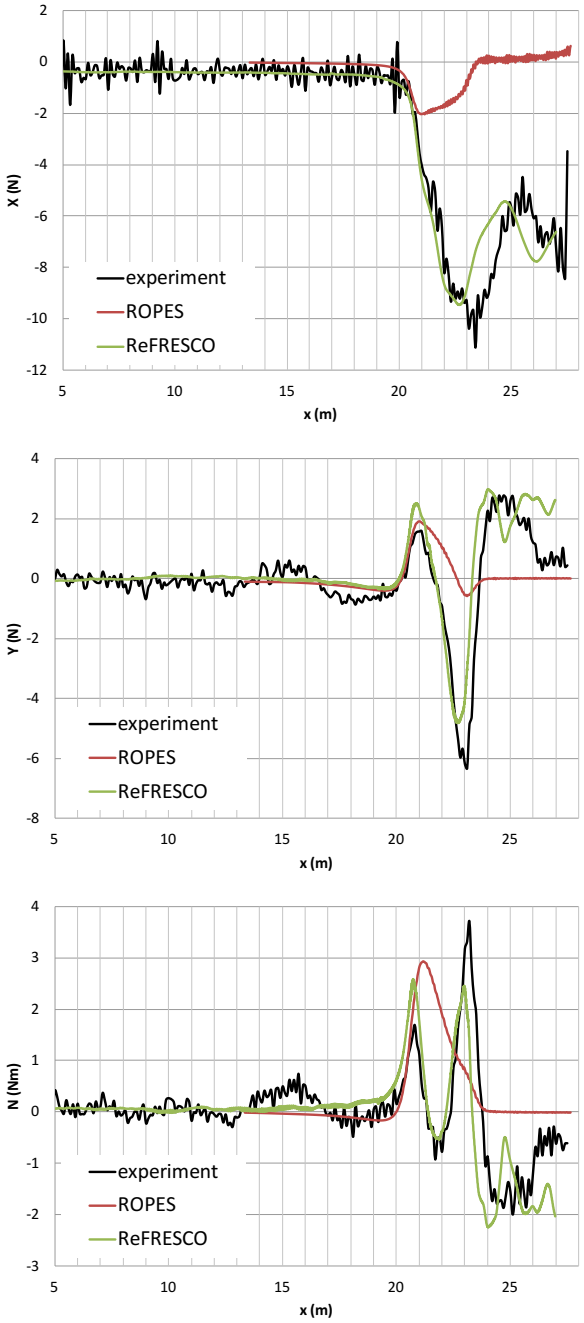

Figure 14. Forces and moment, case G

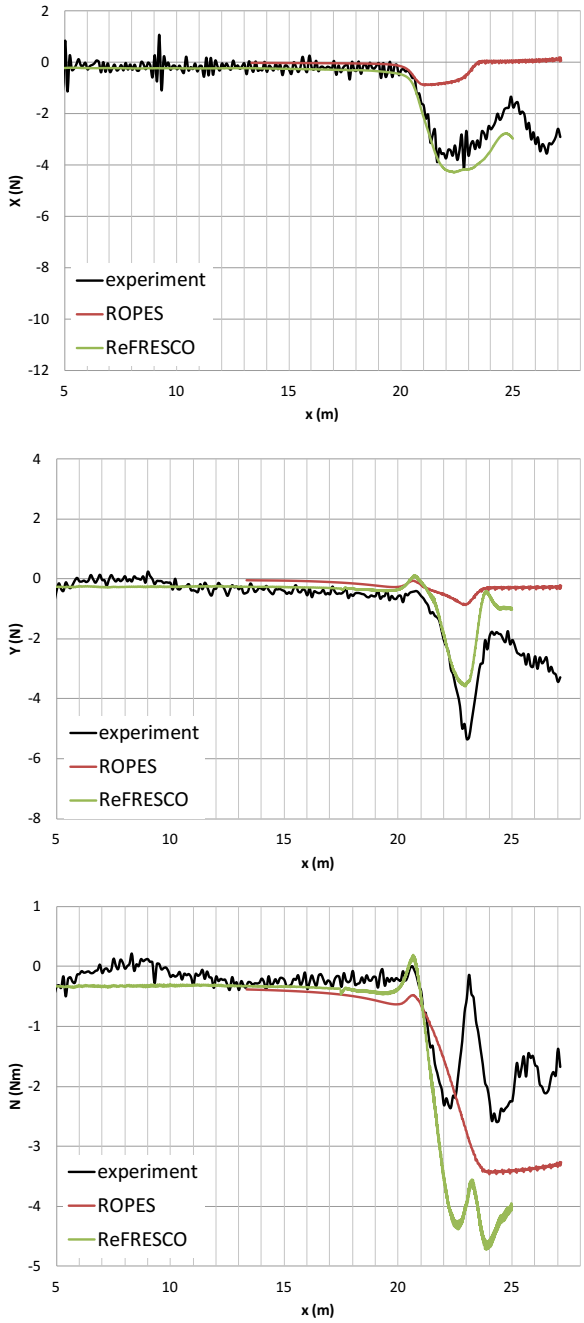

Figure 15. Forces and moment, case H

This demonstrates that even when neglecting the free surface deformation reasonable predictions of the physics of the lock entry can be obtained. The common explanation of a travelling free surface wave in the lock being the primary reason for the large interaction effects can apparently not be applied to the present case.

The comparison for case H is shown in Figure 15. The agreement between the ReFRESCO predictions (fine grid, Δt=0.05s) and the experiments is reasonable for the longitudinal and transverse forces, although also in this case the peak values are not fully captured. However, the agreement of the yaw moment from CFD with the experiments is rather poor, especially when a large portion of the ship is located inside of the lock. This may be caused by the use of a grid that is still coarse near the interface. In particular near the port side of the bow, the grid on both sides of the interface between the port side domain and the ship domain is insufficiently fine to allow accurate interpolation of the flow information across the interface between the two domains. Further computations with a more refined grid, with Δt=0.05s, are recommended.

From these plots, it is found that ROPES highly under predicts the X force. For the hydrodynamic sway force and yaw moment, ROPES only captures the initial interaction effects when the bow reaches the lock entrance, but completely fails to predict the full physics of the flow when the ship is partly or fully into the lock. This demonstrates that viscosity dominates the interaction effects inside the lock, which cannot be captured with a purely potential flow computation.

5 CONCLUSIONS

In the present paper, unsteady CFD computations for a ship entering a lock are presented. Use is made of sliding and deforming grids to model the motion of the ship in the lock geometry. Two cases were considered: one case with the ship entering the lock without drift angle, and a case in which the ship moved at a drift angle of -2 deg.
It is found that the results strongly depend on the time step. For the case with drift angle, the results showed also a grid dependency and further studies are required to see whether a finer grid, in combination with the appropriate time step will results in better agreement between the predictions and the experiments.

It was found that the CFD computations are able to capture the physics of the flow during the lock entry manoeuvre. Even without modelling the free surface, the predicted forces and moments acting on the ship entering the lock without drift angle were close to the experimental data. This shows that the common explanation of a travelling free surface wave in the lock being the primary reason for the large interaction effects can apparently not be applied to the present case.
Computations with a potential flow code demonstrated that the interaction effects inside the lock are of a very viscous nature, which cannot be captured with a purely potential flow computation.

From the outcome of the study, it can be concluded that with unsteady viscous-flow computations, the trends in the hydrodynamic interactions experienced by a ship entering a lock can be predicted well. To be able to quantitatively predict the peak loads during lock entries, further studies are required.

6 ACKNOWLEDGEMENTS

This work has been performed in the context of the *TO2 (Toegepast Onderzoek Organisaties) Natte Kunstwerken van de Toekomst* project.

7 REFERENCES

1. Vantorre, M.; Delefortrie, G.; Mostaert, F. (2012). Behaviour of ships approaching and leaving locks: Open model test data for validation purposes. *Version 2_1, WL Rapporten, WL2012R815_08e*, Flanders Hydraulics Research and Ghent University - Division of Maritime Technology, Antwerp, Belgium.
2. Vantorre, M.; Delefortrie, G. (2013). Behaviour Of Ships Approaching And Leaving Locks: Open Model Test Data For Validation Purposes, *3rd International Conference on Ship Manoeuvring in Shallow and Confined Water: with non-exclusive focus on Ship Behaviour in Locks*, Ghent, Belgium, pp. 337-352.
3. Pinkster, J.A.; Bhawsinka, K. (2013). A real-time simulation technique for ship-ship and ship-port interactions, *28th International Workshop on Water Waves and Floating Bodies*, L'Isle sur la Sorgue, France.
4. Wang, H.-Z.; Zou, Z.-J. (2013) Numerical study on hydrodynamic behaviour of ships sailing in locks, *3rd International Conference on Ship Manoeuvring in Shallow and Confined Water: with non-exclusive focus on Ship Behaviour in Locks*, Ghent, Belgium, pp. 129-134.
5. Wang, H. Z.; Zou, Z. J. (2014). Numerical study on hydrodynamic interaction between a berthed ship and a ship passing through a lock, *Ocean Engineering*, 88: pp. 409-425. doi:10.1016/j.oceaneng.2014.07.001.
6. Meng, Q.; Wan, D. (2015). Numerical Simulations of Viscous Flows around a Ship While Entering a Lock With Overset Grid Technique, *Twenty-fifth International Ocean and Polar Engineering Conference (ISOPE)*. Kona, Big Island, Hawaii.
7. Vaz, G.; Jaouen, F. A. P.; Hoekstra, M. (2009). Free-Surface Viscous Flow Computations. Validation of URANS Code FreSCo, *28th International Conference on Ocean, Offshore and Arctic Engineering*

(OMAE), Honolulu, Hawaii, doi:10.1115/OMAE2009-79398.

8. Klaij, C. M.; Vuik, C. (2013). SIMPLE-type preconditioners for cell-centered, colocated finite volume discretization of incompressible Reynolds-averaged Navier-Stokes equations, *International Journal for Numerical Methods in Fluids*, 71(7): pp. 830-849, doi:10.1002/fld.3686.
9. Windt, J.; Bosschers, J. (2015). Influence Of Local And Adaptive Mesh Refinement On The Tip Vortex Characteristics Of A Wing And Propeller, *VI International Conference on Computational Methods in Marine Engineering (MARINE 2015)*, Rome, Italy.
10. Menter, F. R.; Egorov, Y. (2005). A Scale-Adaptive Simulation Model using Two-Equation Models, *43rd AIAA Aerospace Sciences Meeting and Exhibit*, Reno, Nevada.
11. Pereira, F. S.; Vaz, G.; Eça, L. (2014). On the use of Hybrid Turbulence Models, *17th Numerical Towing Tank Symposium (NuTTS)*, Marstrand, Sweden, pp. 135-140.
12. Pereira, F. S.; Vaz, G.; Eça, L. (2015). On The Numerical Requirements Of RANS And Hybrid Turbulence Models, *VI International Conference on Computational Methods in Marine Engineering (MARINE 2015)*, Rome, Italy.
13. Pereira, F. S.; Vaz, G.; Eça, L. (2015). An assessment of Scale-Resolving Simulation models for the flow around a circular cylinder, *8th International Symposium on Turbulence, Heat and Mass Transfer (THMT'15)*, Sarajevo, Bosnia and Herzegovina.
14. Dacles-Mariani, J.; Zilliac, G. G.; Chow, J. S.; Bradshaw, P. (1995). Numerical/experimental study of a wingtip vortex in the near field, *AIAA Journal*, 33(9): pp. 1561-1568, doi:10.2514/3.12826.
15. Rendall, T.; Allen, C. (2009). Efficient mesh motion using radial basis functions with data reduction algorithms, *Journal of Computational Physics*, 228(17): pp. 6231-6249, doi:10.1016/j.jcp.2009.05.013.
16. Menter, F. R.; Kuntz, M.; Langtry, R. (2003). Ten Years of Industrial Experience with the SST Turbulence Model, *Fourth International Symposium on Turbulence, Heat and Mass Transfer*, Antalya, Turkey.
17. Pinkster, J.A. (2004). The Influence of a Free Surface on Passing Ship Effects, *International Ship Building Progress*, 51(4): pp. 313-338.
18. Korsmeyer, F.T., Lee, C.-H.; Newman, J.N. (1993). Computation of Ship Interaction Forces in Restricted Waters, *Journal of Ship Research*, 37(4): pp 298-306.
19. Xiang, X.; Faltinsen, O.M. (2010). Maneuvering of Two Interacting Ships in Calm Water, *11th International Symposium on Practical Design of Ships and Other Floating Structures (PRADS)*, Rio de Janeiro, Brazil.

8 AUTHORS' BIOGRAPHIES

Serge Toxopeus is a Senior Researcher, Research Coordinator of the Manoeuvring and Nautical studies and Team leader of the R&D CFD Development team at MARIN. He is mainly involved in the development of CFD for manoeuvring applications, including the influence of confined water due to banks or shallow water.

Karan Bhawsinka is a Project Manager at MARIN's nautical centre MSCN. He is mainly involved in research and consultancy projects which use MARIN's full mission bridge and desktop simulators. He specialises in manoeuvring simulations with special focus on shallow and confined water manoeuvres.

Author Index